Galactic Wolf-Rayet stars with Gaia: Origins, Properties and Extragalactic Applications.

Gemma Ann Rate

Department of Physics & Astronomy
The University of Sheffield

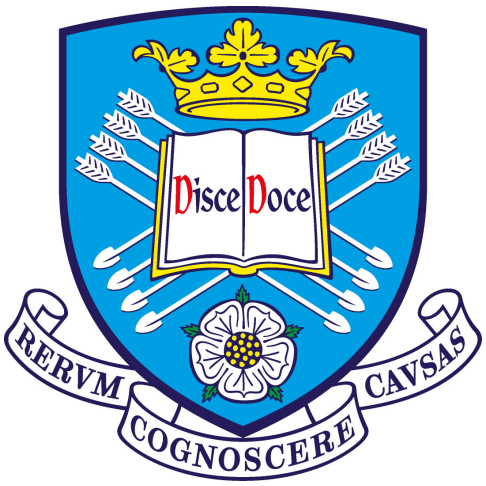

A dissertation submitted in candidature for the degree of Doctor of Philosophy at the University of Sheffield

July 2020

Contents

List of Figures

List of Tables

Declaration

I declare that, unless otherwise stated, the work presented in this thesis is my own. No part of this thesis has been accepted or is currently being submitted for any other qualification at the University of Sheffield or elsewhere.

The work presented in Chapters 2, 3 and 4 has already been published and can be found in Rate & Crowther (2020) (MNRAS volume 493, pg. 1512-1529) and Rate et al. (2020) (MNRAS volume 495, pg. 1209-1226).

Acknowledgments

I am firstly extremely grateful to my supervisor, Paul, for all his academic and pastoral guidance and support throughout the ups and downs of my PhD. Without his patience (especially for my many paper drafts) and immense knowledge, I would never have been able to grow as a researcher and complete even a fraction of the work within this thesis. It has been a pleasure working with him and I hope my contribution to astronomy will help him unlock many more massive star mysteries in the future!

I would also like thank all my collaborators, in particular Richard for his valuable contributions to my second paper. I'm also grateful to Joachim, Andy, Ning-Chen and Justyn of the massive stars and supernovae group, for their insightful discussions and questions during our group meetings in Krebs café. You have all helped me to learn so much more about astronomy and consider my own work from different angles.

Special thanks to the other astro PhD students; my fellow F floor office residents Liam, Johnny and Lydia; past students Martin, Katie, Heloise and Becky; and Emma, Christina, James B, Umar, James W, Rebecca and Alex on E floor. I will never forget all the fun times we had; the hackathons, roleplaying games, conferences and of course CRACK, CREATE and RECAP. I wish you all the best for the future and good luck to those still working on their PhDs, though I'm sure I'll see you around in Sheffield!

Many thanks also go to everyone from the wider astrogroup (both past and present), especially for the seminars, Caper cakes and pub trips over the years. I look forward to hopefully baking for you again in the future!

This thesis would not be complete without mentioning my family, and friends outside academia. I very much appreciate all the encouragement and support from my parents, my brother Matthew and good friend Nel over the last few months. I could not have finished what is nearly eight years of higher education without you!

Final thanks go to the Science and Technology Facilities Council (STFC), for their financial support of this PhD through the Doctoral Training Partnership.

Summary

Wolf-Rayet (WR) stars are the helium core burning descendants of massive O stars. Their strong and dense stellar winds remove outer hydrogen layers from the atmosphere, revealing core burning products, which appear as broad emission lines. As the final evolutionary phase of high mass stars, they can reveal much about massive star origins, evolution and fates. In this thesis, we study Galactic and extragalactic WR stars using results from *Gaia* Data Release 2, which contains parallaxes and proper motions for >1 billion Galactic stars.

We find distances for 383 Galactic WR stars, of which 187 have reliable distances and absolute magnitudes at optical or IR wavelengths. Absolute magnitudes were used to calculate subtype calibrations, which can be applied to estimate distances to other WR stars. Additionally, we find 31 potential runaways by searching for stars far from the Galactic plane.

We also explore WR star origins, using membership of Galactic clusters, associations and star forming regions. At least 59% of WR stars are probably isolated. Simulations suggest they likely result from sparse ($\sim$10 $M_{\odot}\,pc^{-3}$) associations, which dissolve to field densities ($\sim$1–10 $M_{\odot}\,pc^{-3}$) during the WR star lifetime. Many massive stars may therefore form outside cluster environments. We also determine age estimates of clusters containing WR stars. New distances allow us to determine emission line luminosity calibrations at 4600$-$4700Å and 5600$-$5900Å. These can be applied to determine the numbers and subtypes of WR stars within unresolved regions of external galaxies.

Finally, we surveyed the WR population of the spiral galaxy NGC6946 with Gemini GMOS. We find 92 photometric candidates and confirm 61 WC stars spectroscopically using templates. These results are consistent with populations derived from emission line calibrations. We use spectroscopic nebular data to estimate the central metallicity (12+log(O/H)=8.76$\pm$0.2) and extinction, A_V=1.88$\pm$0.09 towards the galaxy, consistent with other studies.

Chapter 1

Introduction

1.1 Massive stars

Usually stars with $>8M_{\odot}$ are massive enough to undergo core collapse at the end of their lives, which is typically associated with a supernova (SN) explosion. $8M_{\odot}$ is therefore usually defined as the minimum mass required for a star to be considered a 'massive star'. During the main sequence, the massive star class consists of early B spectral types and, at $>15M_{\odot}$, O types. These stars have high luminosities ($10^3-10^6L_{\odot}$) and surface temperatures (>20,000K), placing them at the top of the Hertzsprung−Russell (HR) diagram (see Figure 1.1). Due to their high luminosities, they burn through their hydrogen fuel quickly and have short lifetimes. Their lifetimes are <50 Myr for the majority of massive stars and <10 Myr for O stars, with the most massive stars living for just a few million years. This is compared to a ∼10 Gyr lifetime for the Sun and >1000 Gyr for the lowest mass stars.

All forms of the initial mass function (IMF, e.g Salpeter 1955, Kroupa 2001, Chabrier 2003) show massive stars are rare compared to lower mass stars (although 'top heavy' IMFs, with an excess of massive stars relative to the lower mass population, may exist, e.g Schneider et al. 2018). By way of example, Figure 1.2 shows that for a selection of 1000 stars from a Kroupa IMF, only ∼4 stars have $>8M_{\odot}$.

Star formation is thought to occur when turbulence in giant molecular clouds forms dense cores. The cores then collapse under gravity into a protostar and an accretion disk forms around the object. The gravitational potential energy released by the collapse slowly heats up the star and eventually triggers nuclear fusion. This process can be studied much more easily in low mass stars than high mass stars, as the latter are subject to significant extinction and evolve quickly.

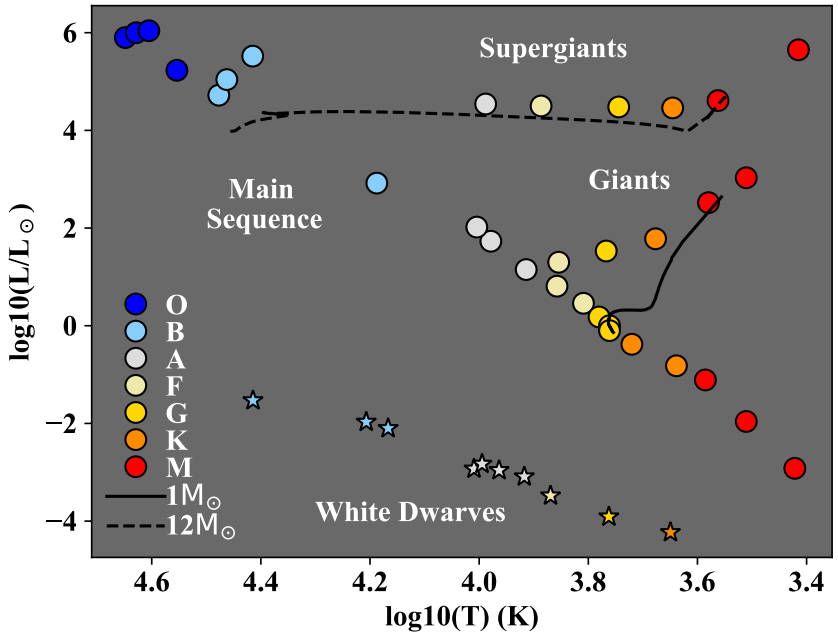

Figure 1.1: Hertzsprung−Russell (HR) diagram showing the main sequence, giants and supergiants for all spectral types, alongside white dwarves. Evolutionary tracks are included for a $1M_{\odot}$ star and a $12M_{\odot}$ massive star (from Ekström et al. 2012). White dwarf data are from Giammichele et al. (2012) and the remaining spectral type data are from Carroll & Ostlie (1996) and Cox (2000), via Lamers & Levesque (2017).

The formation processes of high mass stars are also not simply a scaled up version of low mass star formation. Massive stars produce strong UV radiation, which can evaporate the accretion disk or envelope and affect the environment. Additionally, they spend only around ∼1Myr contracting before reaching the main sequence and destroying their accretion disks, in contrast to ∼30Myr for a solar mass star (Zinnecker & Yorke, 2007). Massive cores may form via monolithic collapse (McKee & Tan, 2003) (where a single gas cloud collapses into a massive star), or through competitive accretion or mergers (Bonnell et al. 1997, Bonnell et al. 2001). The former can happen in dense or sparse environments, whilst the latter is limited to massive stars forming in clusters and other dense regions. Competitive accretion may be important in massive stars (Zinnecker & Yorke, 2007), because large protostellar cores are expected to fragment into smaller cores and would have to accrete gas to become massive.

Alternative formation environments to rich clusters (such as NGC 3603) include sparser regions, such as OB associations (e.g Scorpius OB1, Cygnus OB2) and also small scale groups or clusters of lower mass stars around a single massive star.

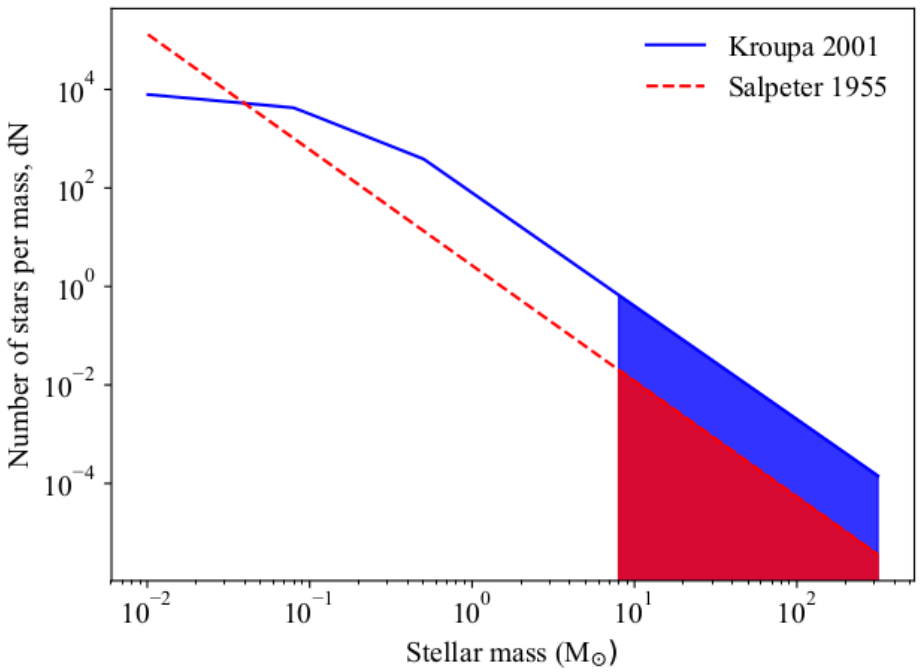

Figure 1.2: IMFs from Salpeter (1955) and Kroupa (2001), normalised for a population of 1000 stars. The shaded region is the integral of the IMF; the number of stars with $>8M_\odot$ (0.12 for Salpeter 1955 and 4.06 for Kroupa 2001).

Most stars were historically thought to form in clusters (Lada & Lada, 2003), which dissolve over time (although this is highly dependent on the definition of a cluster, Bressert et al. 2010). If this is true, then their short lifetimes mean the most massive stars should be still observed within clusters. Any non members could be ejected from the cluster by internal interactions (Poveda et al., 1967), or, if in a binary, by its companion's supernova (Blaauw, 1961). These stars should be travelling quite rapidly and if moving at >30km/s, would qualify as runaways. However, Renzo et al. (2019) uses simulations to suggest that only around 0.5% of stars more massive than $15M_\odot$ are rapid runaways. A further 10% are slower walkaways (>10km/s). Observationally, the fraction of runaways is 10-20% (Gies & Bolton 1986, Tetzlaff et al. 2011, Maíz Apellániz et al. 2018).

Remaining massive stars may therefore appear isolated because their original host clusters have dissolved into associations. This may occur via multiple mechanisms, such as gas expulsion (Tutukov 1978, Lada et al. 1984, Goodwin 1997) or two-body and violent relaxation (where the central region coalesces to a spherical structure to gain virial equilibrium, leaving the outer regions more sparse, Parker et al. 2014b).

However, this process is predicted to take >10Myr, longer than the typical WR

and O star progenitor lifetime (∼5Myr). WR stars should therefore have exploded as supernovae before cluster dissolution is complete. Evidence from *Gaia* DR2 also suggests that associations were not formed by cluster dissolution and instead formed from existing inhomogeneities in the molecular cloud (Ward et al., 2020). A nearby example is Cygnus OB2, which likely did not form via cluster dissolution (Wright et al., 2014). The direct formation of associations is consistent with a hierarchical picture of star formation, in which a variety of environmental densities can coalesce within a single star forming region; ranging from dense clusters to sparse associations.

Existing work on O stars has suggested that massive stars which form outside a cluster are uncommon. de Wit et al. (2005) suggest only a small proportion (4±2%) of O stars formed outside a cluster. Schilbach & Röser (2008) trace 92 field O stars from GOSC (the Galactic O star Catalogue) v2.0 to open clusters and are unable to find an origin for over a third, which may suggest at least some formed in isolation. However, these studies rely mainly on nearby (2−3 kpc in Schilbach & Röser 2008) samples and much larger numbers of O stars will be located further away.

After the main sequence (which, like lower mass stars, lasts ∼80-90% of their lifetime), massive stars will usually evolve into red supergiants, with cooler temperatures (down to ∼3500K) and higher luminosities (up to a factor of 10) than their progenitors, and increased mass loss rates from slow, dust-driven winds. Figure 1.1 illustrates the evolutionary track for a $12M_{\odot}$ massive star, which evolves almost horizontally across the HR diagram after the main sequence.

For solar mass stars, core temperatures are not sufficiently high to allow fusion of elements other than hydrogen and helium, with products of helium, carbon and oxygen respectively. However, in massive stars, core fusion proceeds through carbon, neon, oxygen and silicon burning; ultimately leading to an iron core. At this point, fusion cannot continue to produce energy, because iron is at the peak of the binding energy curve. Therefore, hydrostatic equilibrium cannot be maintained and the star collapses to form a neutron star, usually associated with a supernova. Most massive stars (those below ∼20-30$M_{\odot}$) still maintain their hydrogen envelopes before exploding and their supernova is therefore a type II variety, with hydrogen features. Remnants are usually neutron stars or, if the star is sufficiently massive, a black hole. If the massive star is in a binary system, these remnants may be progenitors of gravitational wave events. Alternatively, very massive stars may create electron positron pairs in their core, causing their collapse as a pair instability supernova (Rakavy & Shaviv 1967, Barkat et al. 1967). This process triggers explosive nuclear burning, which prevents any remnant

from forming.

Though they comprise only a small proportion of the stellar population, massive stars have a significant influence on their surroundings. They provide radiative feedback due to their strong UV emissions and are therefore often embedded in H II regions. Their short lifetimes make these regions markers of recent star formation. Mechanical feedback, mainly from supernovae (but also stellar winds), can create cavities of gas around a massive star. This may trigger star formation where material is compressed at the edge of the cavity, and quench it in the newly cleared region (e.g Baug et al. 2019). At low metallicities, massive stars can help to clear large superbubbles around a cluster (e.g N206 in the LMC Ramachandran et al. 2018, where their mechanical input is comparable to supernovae). Finally, massive stars can disperse metals into the ISM via chemical feedback, either through their stellar winds or explosions as supernovae.

Though most massive stars evolve into red supergiants after the main sequence, the evolutionary process differs for very high mass stars. This is due to the Humphrey Davidson limit, the limiting luminosity at which red supergiants (<15000 K) are observed. This luminosity is $\sim \log L/L_{\odot}=5.8$ (Humphreys & Davidson, 1979) (although this is somewhat controversial, Davies et al. (2018) finds instead that the limit is $\log L/L_{\odot}=5.5$ in most cases). During advanced evolutionary phases, the most massive O stars pass through a blue supergiant or hypergiant phase (which may also exhibit Luminous Blue Variable (LBV) variability, see section 1.3), before progressing through the Wolf-Rayet (WR) phase. Though this evolutionary phase is <10% the length of the O star progenitor's lifetime (Georgy et al., 2012), it has a dramatic impact on the evolution of the star. WR stars have high mass loss rates, which can dramatically affect the evolution of the star and the type of resulting supernova and remnant. Possible outcomes are a stripped envelope supernova and a neutron star or a black hole; or, if significant mass is retained, direct collapse to a black hole with no associated supernova. WR stars are therefore an important evolutionary stage for understanding massive stars in general.

As well as stripped envelope supernovae, WR stars are also the most likely progenitors of long gamma ray bursts (Fruchter et al. 2006, Kelly & Kirshner 2012). They contribute the same chemical enrichment as other massive stars and disperse this material through their strong winds. Their high luminosity means they have extremely short lifetimes and are therefore good markers of recent star formation in distant galaxies.

Studying massive stars and WR stars in particular, is therefore vital for fully understanding stellar environments, transients, compact objects and star formation.

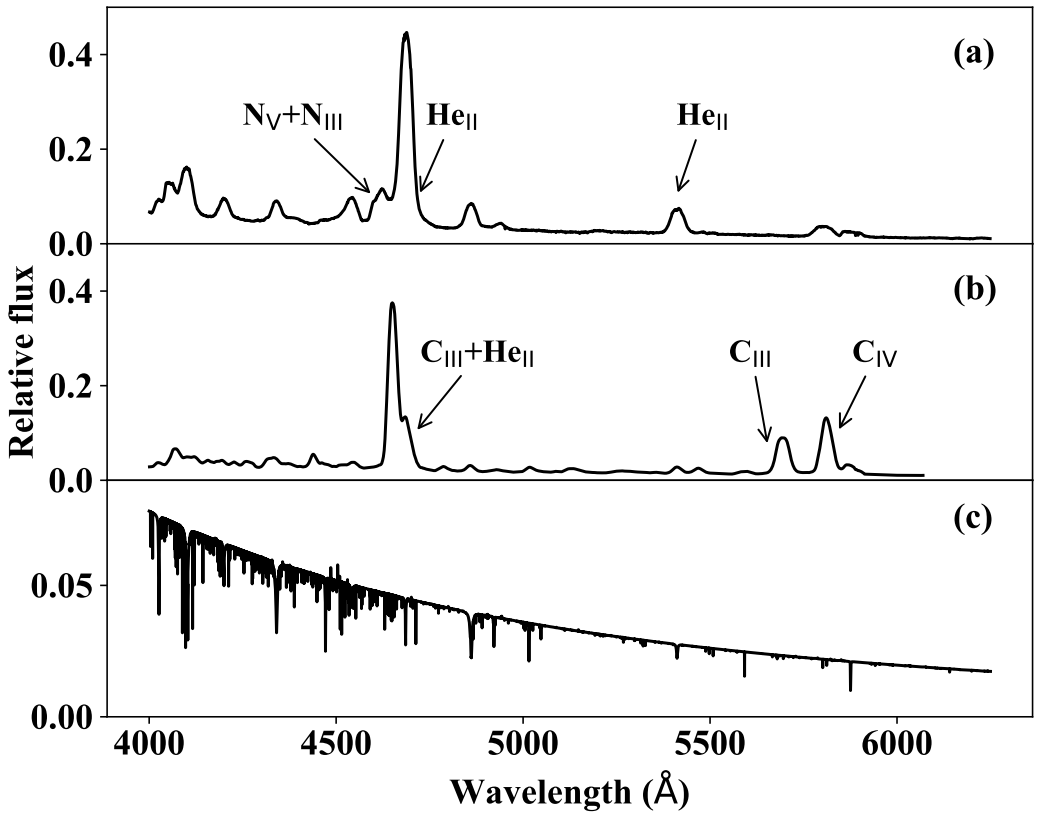

Figure 1.3: Examples of (a) WN4-6, (b) WC7-8 and (c) O7-8V, with the main WN and WC emission lines indicated. The WR stars possess broad emission lines, which are not present in the O star (Hamann & Gräfener 2004 and Todt et al. 2015 for the WN data, Sander et al. 2012 for the WC data and Hainich et al. 2019 for the O star data.)

1.2 Wolf-Rayet stars

WR stars are distinguishable from their O star progenitors by their spectral appearance, Their unusual broad emission line spectra were first identified ∼150 years ago (Wolf & Rayet, 1867). Figure 1.3 shows how the emission lines in WR stars compare to the much more narrow absorption lines of O stars. These emission lines occur due to their strong and dense stellar winds. Mass loss (with high rates of approximately $10^{-4.0}$ to $10^{-5.5}M_{\odot}$/yr, Hamann et al. 2006, Hamann et al. 2019, Sander et al. 2012, Sander et al. 2019) occurs throughout evolution and strips away the outer hydrogen layers. Some are still relatively hydrogen rich, but most exhibit a low fraction ($< 10\%$), or absence of, surface hydrogen.

WR stars also exhibit unusual chemical properties; being helium, nitrogen, carbon

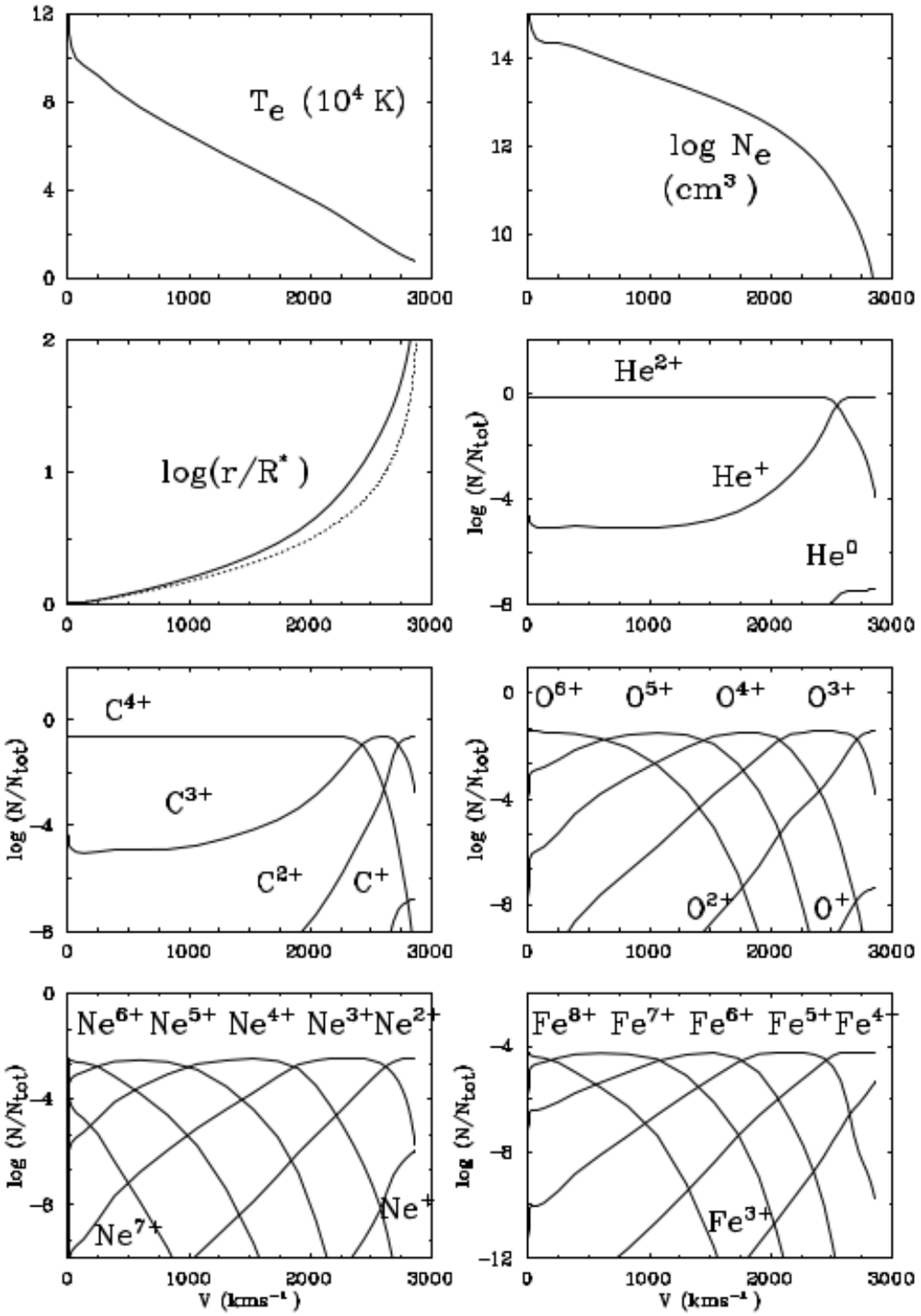

Figure 1.4: Atmosphere structure of an LMC WC4 star. Three panels show the variation in temperature (10^4K), density (cm^3) and radius (R_*), with respect to wind velocity. The other graphs show the ionization balance (N/N_{tot}) for helium, carbon, oxygen, neon and iron (Crowther et al., 2002).

and sometimes oxygen rich. Distinct variations in the spectra mean that WR stars can be sub classified as WN, which show strong helium and nitrogen lines, or WC and WO stars, which have helium, carbon and oxygen emission lines. The differences between WN and WC are shown in the example spectra of Figure 1.3.

In WN stars, the nitrogen and helium are products of core hydrogen burning, which occurred via the CNO cycle. For WC stars, carbon produced by the triple α process during core helium burning and oxygen from α capture are over-abundant compared to nitrogen (Maeder 1983, shown observationally by Lamers et al. 1991 using abundance ratios). This is because the nitrogen is destroyed in a secondary helium fusion process. Atmospheres are highly stratified, with higher ionization levels located closer to the stellar core (see Figure 1.4).

WR stars can be self stripped via strong winds in a single star (Lamers et al., 1991) or, if in a binary, can lose their envelopes via Roche lobe overflow (RLOF) (Paczynski 1973 and references therein) .

WR features are also seen in some central stars of Planetary Nebulae. These are designated [WC] (and occasionally [WN]) and are lower mass stars which have passed through the Asymptotic Giant Branch phase and have shed their outer layers to produce a carbon rich central star of a Planetary Nebula. This thesis will primarily focus on core helium burning, initially high mass 'classic' WR stars. We also include very massive hydrogen 'rich' (with a surface hydrogen fraction of $< 40 - 50\%$) main sequence WNh and WNha stars.

1.3 Single star evolution

After a few million years, massive O stars start to evolve off the main sequence. They first evolve towards the red (during hydrogen shell burning) then move bluewards again as they reach helium core burning. All classical WR stars are located in the blue top left of the HR diagram (see Figure 1.5), which means that they are the likely descendants of O stars (e.g De Loore et al. 1977).

The existence of the Humphrey Davidson limit, suggests that at this evolutionary phase, mass loss occurs in the most luminous stars that prevents further red wards evolution (Humphreys & Davidson, 1979). This mass loss may occur during a Luminous Blue Variable (LBV) phase or, (for objects below the Humphrey Davidson limit), a red supergiant (RSG) phase.

Rotation has a major effect on massive star evolution, leading to mixing and reple-

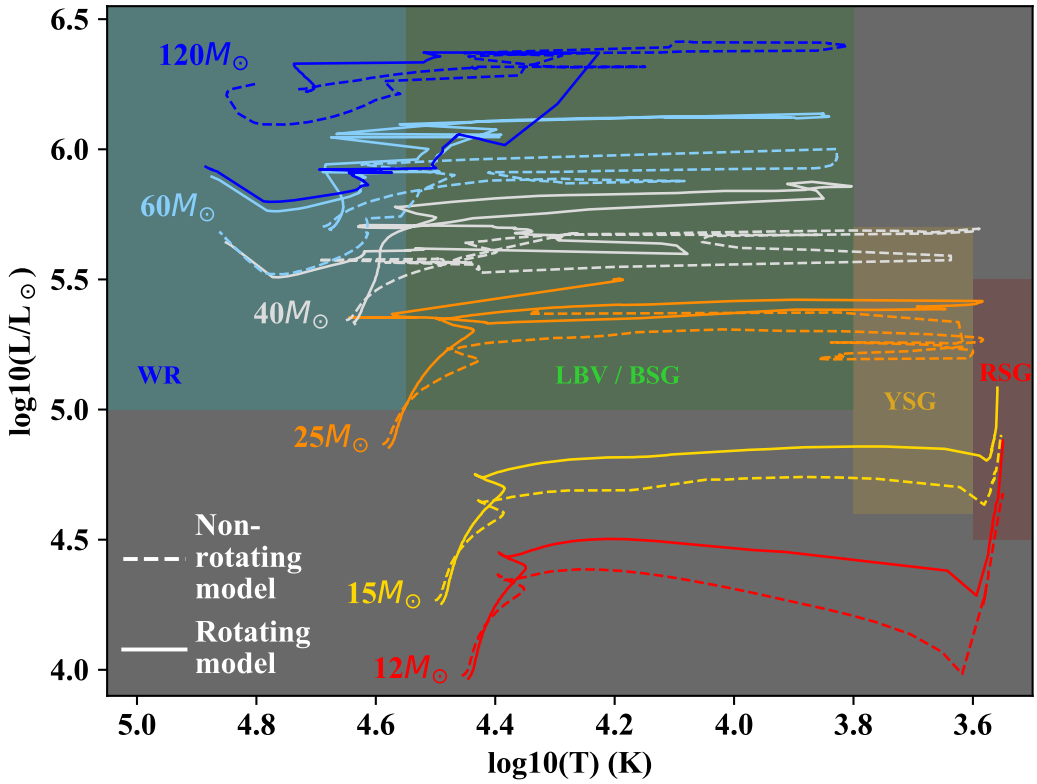

Figure 1.5: Example HR diagram showing stellar tracks from Ekström et al. (2012) and regions where the star appears as a WR, LBV or blue supergiant (BSG), yellow supergiant (YSG) and red supergiant (RSG). The Humphrey Davidson limit for the upper RSG luminosity is taken from the updated result of Davies et al. (2018).

nishing material in and around the core. This prolongs the main sequence phase and ultimately increases the stellar lifetime. Additionally, rotation reduces the minimum mass required to form a WN star. Georgy et al. (2012) find that at solar metallicity and without rotation, only their 120M$_\odot$ model will evolve into a WR star, whilst with rotation, the 60M$_\odot$ model is able to enter the WN phase during the main sequence.

LBVs are a variety of different object types (Conti, 1984) that all share the characteristic of being luminous, hot and variable. One characteristic of some LBVs, such as AG Car, are that they move through the S Dor instability strip; an unstable region of the HR diagram between WR stars and RSGs. They therefore experience S Dor type variability, which causes the peak of their spectral energy distribution to move from the UV at quiescence (with an early B spectral type and bolometric correction BC> -1 to -2) to visible wavelengths at maximum (exhibiting A spectral type, BC=0). Ot-

her LBVs, such at η Car, may experience irregular massive eruptions, which can eject $\sim$10M$_\odot$. Such eruptions could be the mechanism required to remove most of the mass between the O star and WR star phases (Smith & Owocki, 2006). The LBV period usually lasts $10^4 - 10^5$ years (Smith, 2014). Some LBVs, such as AG Car (Smith et al., 1994), exhibit late WN spectral appearance at visual minimum. MCA-1B in M33 was originally classified as a WN9 and was thought to be a dormant LBV (Smith et al., 1995). This was confirmed when it later brightened, indicating an LBV like outburst (Smith et al., 2020). If LBVs do descend from early O star progenitors, they should be located in similar environments (young, massive clusters). However, Smith & Tombleson (2015) claim LBVs are in more isolated environments than WR stars or O stars.

Assuming massive LBVs or RSGs are a progenitor to WR stars, the star will then stabilise and move left across the HR diagram. The outer hydrogen layers will have been removed, leaving a WN star. Depending on the mass, evolution then continues through to WC and WO phases via further mass loss (e.g Tramper et al. 2015). Figure 1.5 shows some model evolutionary tracks, which extend to more evolved objects for higher initial masses.

1.3.1 The Conti Scenario

The complete evolutionary process through the WR phase is known as the Conti scenario' (Conti, 1975). An updated version from Crowther (2007), for stars in the Milky Way with initial masses of $40 - 75$M$_\odot$, is:

O $\rightarrow$ LBV $\rightarrow$ WN(H poor) $\rightarrow$ WC $\rightarrow$ SNIc

A WO phase may occur after the WC phase (Tramper et al., 2015). Lower mass stars between $25 - 40$M$_\odot$ may pass through a red giant phase instead of an LBV period:

O $\rightarrow$ LBV/RSG $\rightarrow$ WN(H poor) $\rightarrow$ SNIb

The evolution process can also be extended to the hydrogen rich, main sequence stars, which are typically above 75M$_\odot$:

O $\rightarrow$ WN(H rich) $\rightarrow$ LBV $\rightarrow$ WN(H poor) $\rightarrow$ WC $\rightarrow$ SNIc

The mass ranges of these evolutionary paths can be shifted upwards at lower metallicity, or downwards at high metallicity.

1.4 Binary evolution

In close binaries, mass can be transferred from one star to the other if the primary overfills its Roche Lobe. This can happen during the main sequence phase for the closest binaries,

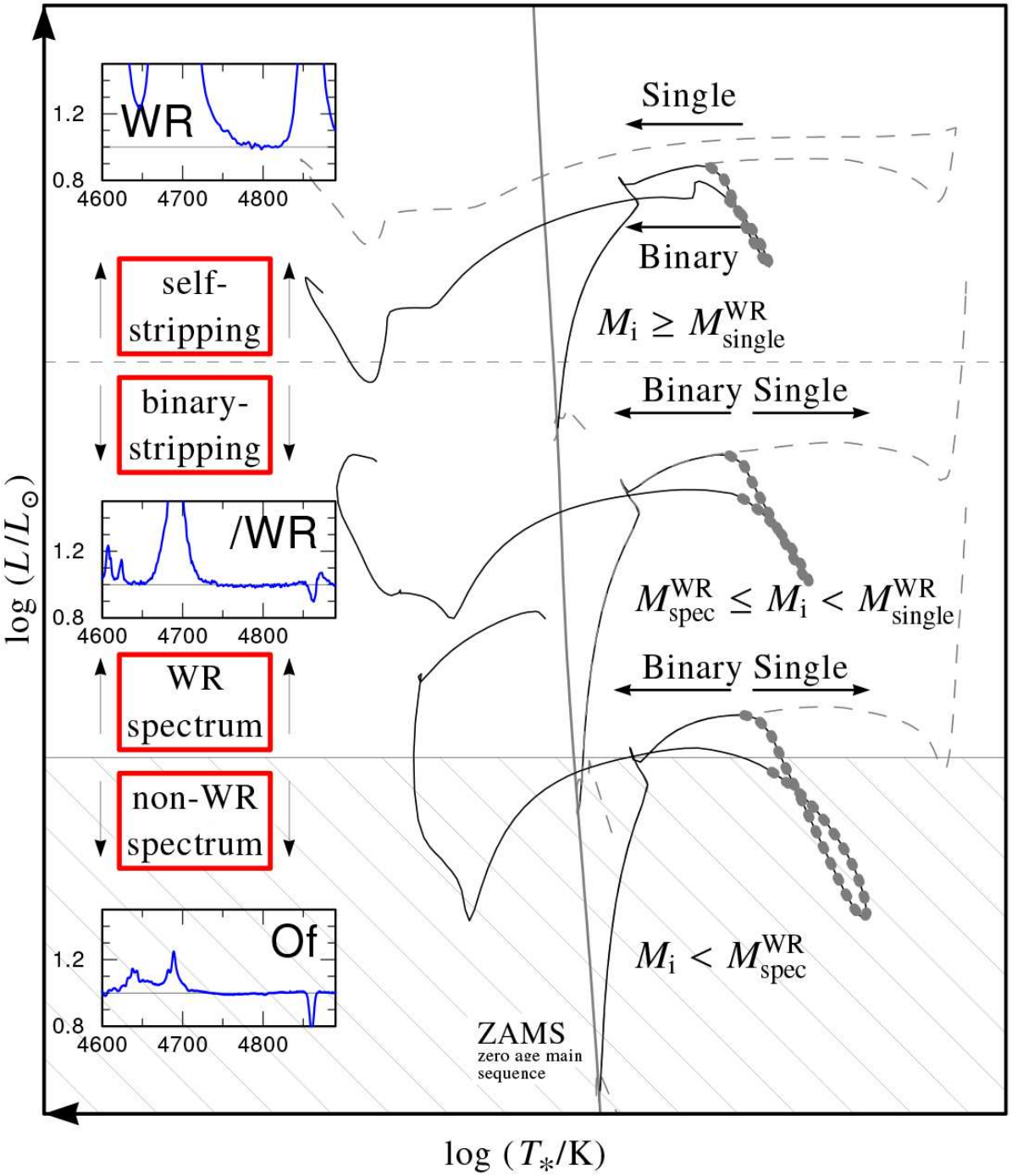

Figure 1.6: Illustrative evolutionary tracks and spectra from Shenar et al. (2020), for WR stars created via self stripping (top) and companion only stripping (middle). The dashed lines correspond to single stars, whilst the solid lines are examples for binary evolution. The top plot shows conventional strong WR emission lines, whilst in the companion stripped middle plot, the emission lines are somewhat weaker. The bottom plot shows a star which is not massive enough to exhibit WR emission lines and instead appears with weaker Of emission features. The differences in evolutionary tracks are also shown, with stars that have undergone binary stripping having lower luminosities than the single models. The grey dotted lines indicate phases of binary mass transfer in the binary models.

or during hydrogen or helium shell burning for wide binaries. The envelope inflation during shell burning allows roche lobe overflow (RLOF) and mass exchange to occur for slightly wider binaries (e.g Kippenhahn & Weigert 1967).

Approximately $\sim>$ 50% of Galactic O stars are in binaries (Mason et al. 2009, Sana et al. 2012), depending on their environment and over 50% of O stars in binary systems are likely to exchange mass (Sana et al., 2013).

To form a WR star, RLOF would strip the outer hydrogen envelope of the primary. This would occur without requiring the strong winds needed to form a single WR star through self stripping. Therefore, RLOF should allow WR stars to form below the single star limit within a given environment (Shenar et al., 2020).

The minimum initial mass required to form a helium star with a WR spectrum via binary stripping, is dependent on the assumed mass loss prescription. Shenar et al. (2020) predict it to be $18M_{\odot}$ at solar metallicity, close to the $14.87M_{\odot}$ from Götberg et al. (2018) and $15M_{\odot}$ from Eldridge et al. (2008). WR stars created via binary stripping would therefore be observed with lower luminosities than their higher mass, self-stripped counterparts. Figure 1.6 shows the differences between evolutionary tracks, with binary stripped WR stars possessing lower final luminosities than their single counterparts.

Georgy et al. (2012) predict that 40% of WR stars at solar metallicity were formed via RLOF. Binary formation channels should therefore dominate lower metallicity environments like the SMC and LMC. However, Foellmi et al. (2003a) find a binary rate of 40% in the SMC and 30% in the LMC (Foellmi et al., 2003b) using the periodic radial velocity variability of 61 WN LMC stars and 11 SMC stars (and statistical discussion to account for any missed variation).. Shenar et al. (2019) do not identify the expected excess of binaries in the LMC, with only $\sim$4% having formed purely via companion mass stripping. Shenar et al. (2016) also finds that binaries do not dominate WR formation at SMC metallicities. Shenar et al. (2020) suggests that low mass ($<18M_{\odot}$) stripped envelope stars will not appear as WR stars and that the minimum mass for a stripped star to have a WR spectrum also increases with decreasing metallicity. The fraction of WR stars produced via the binary channel may therefore not necessarily increase with decreasing metallicity. Figure 1.6 also shows the variation in spectral appearance for self-stripped massive WR stars, companion stripped WR stars and the least massive binary stars with an Of type appearance. Götberg et al. (2018) also shows a similar sequence.

Alternatively, stripped binary WR stars may not be observed directly, due to their faint magnitudes in the visible part of the spectrum with respect to their companions.

Götberg et al. (2017) emphasise that these stars emit most of their light in the extreme UV, which is largely inaccessible to telescopes. However, their strong UV emission may ionize the surrounding ISM (e.g Götberg et al. 2017, Götberg et al. 2019).

1.5 Classification

The earliest WR classification system (Beals & Plaskett, 1936) divided stars into nitrogen and carbon dominated sequences (todays WN and WC respectively). This focussed on ratios of nitrogen, helium, carbon and oxygen lines and included subclasses WN5−WN8 and WC6−WC8. Starting the numbering system with WN5 and WC6, respectively, allowed for extension to lower and higher classes.

The modern classification system builds upon this, extending the numbering of WN stars down to WN2 (high ionization) and up to WN9 or WN11 (at low ionization, also an alternative classification for some stars with Of/WN features). Optical data uses ratios of the peak fluxes of helium and nitrogen lines (Smith 1968a, Smith et al. 1994, Smith et al. 1996). Classes WN2−6/7 are often referred to as 'Early' (WNE) and exhibit higher ionization species than those above WN6/7, which are 'late' (WNL) (nomenclature coined by Vanbeveren & Conti 1980). The WC classes now extend from WC4 to WC11 (Smith 1968a, Crowther et al. 1998). However, the extremes of this classification, WC10−11, only include Planetary Nebulae central stars. Intensities or equivalent widths of carbon and oxygen lines are used for classification (Crowther et al., 1998). The WN/WC classification (Conti & Massey, 1989) with strong C IV lines in WN stars, is a transitional class between WN and WC.

Finally, the classification sequence for rare WO stars extends from WO1−WO4 and typical optical lines used are O IV−O VI and C IV (Barlow & Hummer 1982, Kingsburgh et al. 1995, Crowther et al. 1998). Again, stars in the WO1 class are exclusively Planetary Nebulae central stars (Crowther et al., 1998).

WC stars only have a '1D' classifcation system, with spectral type numbers. However, the WN classification system has been extended to encompass the variation in spectral features. Hiltner & Schild (1966) created a '2D' classification system with WN–A denoting narrow lines and WN–B denoting broad lines, in addition to the usual subtypes.

In the more recent 2D classification scheme, WN stars are divided into broad and narrow lines, using an 's' or 'b' for strong broad lines and 'w' for weak narrow lines. The classification based on their equivalent width of λ5412 Åor FWHM of λ4686 Å(Hamann et al. 1993, Smith et al. 1996). Figure 1.7 shows how these two criteria produce slightly

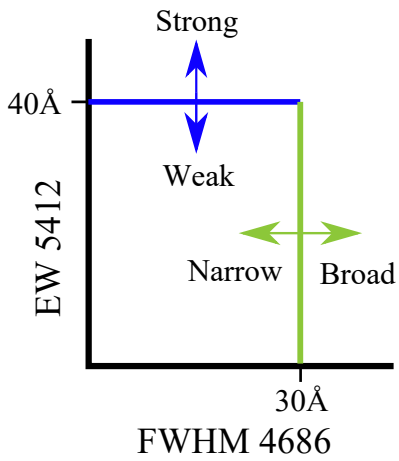

Figure 1.7: Strong line criteria for the 2D classification of WN stars (EW λ5412 > 40Å) from Smith et al. (1996) (secondary diagnostic) and Hamann et al. (1993), compared to broad line criteria (FWHM λ4687 > 30Å) from Smith et al. (1996) (primary diagnostic). A WN star may be classified as broad lined according to one criterion, but not the other.

different cutoffs, such that a star may be considered broad lined under the Smith et al. (1996) scheme, but weak lined according to Hamann et al. (1993). Smith et al. (1996) updated the classification to the 3rd dimension, so that WN stars can also be classified according to the presence of hydrogen in their spectra. This is often indicated by a 'h' after the class name. e.g WN8h. According to the Smith et al. (1996) scheme, stars with no hydrogen are designated with an 'o', e.g WN8o. Finally, the addition of 'a' to the end of the classification can also be used to indicate hydrogen absorption features in the spectra (Smith et al., 1996).

As stated in section, 1.2, these WNha are actually massive main sequence stars (with initial masses above 75$M_{\odot}$, e.g see Langer et al. 1994, Crowther et al. 1995). Of/WN stars are also often grouped with WR stars. These have emission lines in N III and He II, combined with the He I and He II absorption features from typical O stars Conti et al. (2008). Like WNha, many are massive hydrogen core burning objects, but others may be helium core burning and transitioning between the O star and WN phases (Crowther & Walborn, 2011).

Full optical emission line ratios used for the 3D classification scheme and their wavelengths are shown in Table 1.1. The same classification scheme with different emission line criteria is used for IR data (Crowther et al., 2006a), as shown in Table 1.2.

1.6 Physical Properties

Physical properties of early type stars are usually obtained from line blanketed LTE (e.g ATLAS Kurucz 1979) or non-LTE (e.g TLUSTY Hubeny & Lanz 1995) atmospheric code, providing temperature (T) and surface gravity (log g). In contrast to other early type stars, WR winds are dense enough to render the photosphere inaccessible. Therefore, spherically extended non LTE model atmospheres are necessary to determine their physical properties. These were developed in the 1980s by Hillier (CMFGEN, e.g Hillier & Miller 1998, Hillier 2012) or the then Kiel group of Hamann and Schmutz (Hamann & Schmutz, 1987), which is now the Potsdam Wolf-Rayet code PoWR (Hamann & Gräfener 2004, Todt et al. 2015 , Sander et al. 2012) These have been refined to include metal line blanketing by iron peak elements.

Luminosity is obtained using photometry, distances and extinctions (from the absolute magnitude); however other parameters (temperature and wind density) must be found using the transformed radius (Schmutz et al. 1989, Hamann & Koesterke 1998)

$$R_t = R_* \left[\frac{v_\infty}{2500 \mathrm{kms}^{-1}} \Big/ \frac{\sqrt{D}\dot{M}}{10^{(-4)} \mathrm{M}_\odot \mathrm{yr}^{-1}} \right] \tag{1.1}$$

which encompasses the mass loss rate $\dot{M}$, clumping factor D (due to inhomogeneities in the atmosphere), stellar radius R_* and terminal wind velocity v_∞. Individual values of these parameters may vary, but when combined, they may lead to the same value of R_t. We can then produce contour maps, of the emission line equivalent widths at different R_t and T.

A single observed equivalent width (or ratio of equivalent widths), therefore corresponds to a series of models with varying R_t and T. By using the intersection of these contours for models from equivalent widths of two different ionization levels (e.g He I and He II), we can obtain the model with the most appropriate R_t and T (Schmutz et al., 1989). By using the luminosity, we can then scale the model to determine other parameters such as the radius and if the wind velocity is known (measured from emission line profile fits or directly from the width), this allows the calculation of the mass loss rate. Once a model has been chosen, a second way to calculate luminosity may be by using the model SED. This could be used to validate the model choice.

Atmospheric models usually define a lower boundary at a Rosseland optical depth of 20 and define this radius as the stellar radius (Conti et al., 2008). Modelled radii vary widely, from less than one $\mathrm{R}_\odot$ for WO and early WC stars (Sander et al. 2012, Tramper et al. 2015, Sander et al. 2019), up to $2 - 10\mathrm{R}_\odot$ for classical WN stars (Hamann et al.,

Table 1.1: Table showing typical optical classification schemes used for WN, WC and WO stars. The values cited for WN stars are peak ratios of lines, but equivalent widths are also often used. Values for WC and WO stars use equivalent widths (denoted by 'EW' in the table). All wavelength units are in angstroms. (a) Smith et al. (1994), (b) Smith et al. (1996) and (c) Crowther et al. (1998).

Citation	WR type	Primary diagnostic	Secondary diagnostic
(a)	WN11	NIV absent, NIII absent, NII strong	
	WN10	NIV absent, NIII=NII	
(b)		Peak HeIIλ5411/ HeIλ5875	Peak NVλ4603-20/ NIIIλ4634-41
	WN9	< 0.1	0
	WN8	$0.1 - 0.65$	$0.05 - 0.25$
	WN7	$0.65 - 1.25$	$0.1 - 0.25$
	WN6	$1.25 - 4$	$0.2 - 0.5$
	WN5	$1.25 - 8$	$0.25 - 2$
	WN4	$4 - 10$	< 2
	WN3	< 10	No NIII
	WN2	No HeI	No NV
(b)	h	$\lambda4861/\sqrt{\lambda4541 \times \lambda5411} - 1 > 0.5$	$\lambda4340/\sqrt{\lambda4200 \times \lambda4541} - 1 > 0.5$
	b (or s)	FWHM $\lambda4687 > 30$Å	EW $\lambda5412 > 40$Å
(c)		log(EW(CIVλ5808/CIIIλ5696))	log(EW(CIVλ5808/CIIλ4267))
	WC11	$\leq$-1.2	$\leq$-1.5
	WC10	-1.2 to -0.7	-1.5 to -0.2
	WC9	-0.7 to -0.3	-0.2 to 1
	WC8	-0.3 to -0.1	≥ 1
			log(EW(CIIIλ5696/OIII-Vλ5590))
	WC7	$0.1 - 0.6$	≥ 1
	WC6	$0.6 - 1.1$	$0 - 0.7$
	WC5	$1.1 - 1.5$	$-0.4 - 0.5$
	WC4	≥ 1.5	$\leq$-0.4
(c)		log(EW(OIVλ3811, 34)/(OVλ5590))	log(EW(OIVλ3811, 34)/(CIVλ5808))
	WO4	$-0.3 - 0.25$	$-1.5 - 1$
	WO3	$0.25 - 0.6$	$-1 - 0.2$
	WO2	$0.6 - 1.1$	≥ 0.2
	WO1	≥ 1.1	≥ 0.2

Table 1.2: Table showing an IR classification scheme, using flux ratios, for WN and WC stars from Crowther et al. (2006a). WN criteria are given for narrow lines, with broad line criteria in brackets. All wavelength units are in micrometers. An updated, more detailed scheme is given in Rosslowe & Crowther (2018). The full table is too large and detailed to be reproduced here.

WR type	Primary diagnostic	Secondary diagnostic	Tertiary diagnostic
	He IIλ1.012/He Iλ1.083	N Vλ2.100/(He I/NIIIλ2.115)	He IIλ2.189/Br γ
WN9	<0.07		<0.1
WN8	0.07 – 0.02		0.1 – 0.4
WN7	0.2 – 0.6 (>0.5)	(blend)	0.5 – 1.2 (1 – 2)
WN6	0.6 – 1.5 (>0.5)	<0.25 (blend)	0.5 – 2.5 (1 – 2)
WN5	1.5 – 3.0	0.2 – 1	1 – 3
WN4	3.0 – 10.0 (>0.8)	1 – 2 (blend)	1 – 3 (>2)
WN3	>10.00	>2	1 – 3
b (or s)	FWHM He IIλ1.012 $\leq$ 65Å		
	C IIIλ0.971/C IIλ0.990	C IVλ1.191/C IIIλ1.198	C IVλ2.076/C IIIλ2.110
WC9	>15	>4	>5
WC8	>15	2 – 4	>4
WC7	>10	0.8 – 2	1 – 4
WC5 – 6	<10	<0.8	<1

2006) and larger (>20$R_\odot$, Hamann et al. 2019) for main sequence WN stars.

For WN stars in the Milky Way, temperatures range from 40kK−50kK for late subtypes (and hydrogen burning subtypes), to 140kK for the earliest subtypes. WN stars have a typical luminosity between $1 \times 10^5 L_\odot$ to $16 \times 10^5 L_\odot$ and current masses of $10 - 50 M_\odot$(Hamann et al. 2006, Hamann et al. 2019), or higher for main sequence WN stars. WC stars have a temperature range of 120 − 40kK and luminosities between $1 \times 10^5 L_\odot$ and $10 \times 10^5 L_\odot$. Typical current masses for WO and WC stars lie between $10 - 30 M_\odot$(Sander et al. 2012, Sander et al. 2019, Table 1.3).

The luminosities of WO stars are comparable to WC stars, but their temperatures are much higher; up to 150 − 210kK (Tramper et al., 2015). Additionally, their elemental abundances differ, with WO stars having up to 25% of their surface mass fraction as oxygen and up to 60% as carbon (Tramper et al., 2015), compared to WC which only have a small fraction of oxygen (Hamann et al., 2006). WO star helium fractions are consequently lower than WC stars, mainly less than 30% (Tramper et al., 2015), whereas for WC stars it is >30%, with ∼40% as carbon, according to Sander et al. (2012).

Table 1.3: Table showing example parameters for WN, WC and WO stars. WO star mass ranges are for initial-final masses of He star models. Unfortunately the WO models did not provide absolute or apparent magnitudes. Citations used are (a) Hamann et al. (2006), Hamann et al. (2019), (b) Sander et al. (2012), Sander et al. (2019) and references therein, and (c)Tramper et al. (2015)

Citation	WR type/example	M($M_\odot$)	R($R_\odot$)	log(L) ($L_\odot$)	T(kK)	log($\dot{M}$) $M_\odot$/yr	M_v (mag)	v_∞ (km/s)
(a)	WN9h / WN108	23/21	16.07	5.77	39.80	-4.9	-6.26	1170
	WN8(h) / WR66	41	19.90	6.15	44.70	-3.9	-7.22	1500
	WN7(WNE-w) / WR120	7	3.78	4.92	50.10	-4.9	-3.81	1225
	WN6-s / WR134	18	5.25	5.61	63.1	-4.4	-5.09	1700
	WN6-w / WR115	20	8.89	5.65	50.1	-4.5	-5.33	1280
	WN5-s / WR110	14	3.73	5.51	70.80	-4.2	-4.85	2300
	WN5-w / WR54	20	5.65	5.67	63.10	-4.7	-4.63	1500
	WN4-s / WR18	38	2.82	6.11	112.20	-4.1	-5.36	1800
	WN4-w / WR51	16	3.72	5.50	70.80	-5.00	-3.85	1500
	WN3-w / WR3	17/15	2.48	5.56	89.10	-5.4	-3.13	2700
	WN2-w / WR2	16	0.89	5.40	141.30	-5.30	-2.43	1800
(b)	WC9 / WR95	10.70	6.86	5.23	45.00	-4.71	-5.25	1900
	WC8 / WR57	21.20	6.36	5.75	63.00	-4.50	-5.61	1787
	WC7 / WR68	21.00	4.96	5.74	71.00	-4.44	-5.16	2100
	WC6 / WR27	11.30	2.35	5.28	79.00	-4.78	-3.92	2100
	WC5 / WR33	16.30	3.25	5.56	79.00	-4.36	-4.77	3342
	WC4 / WR144	9.90	1.06	5.20	112.00	-4.62	-3.28	3500
(c)	WO4 / LH41-1042	17−8.4	0.62	5.26	150.00	-5.05		3500
	WO3 / WR93b	17−8.8	0.58	5.30	160.00	-5.00		5000
	WO2 / WR102	22−9.8	0.39	5.45	210.00	-4.92		5000

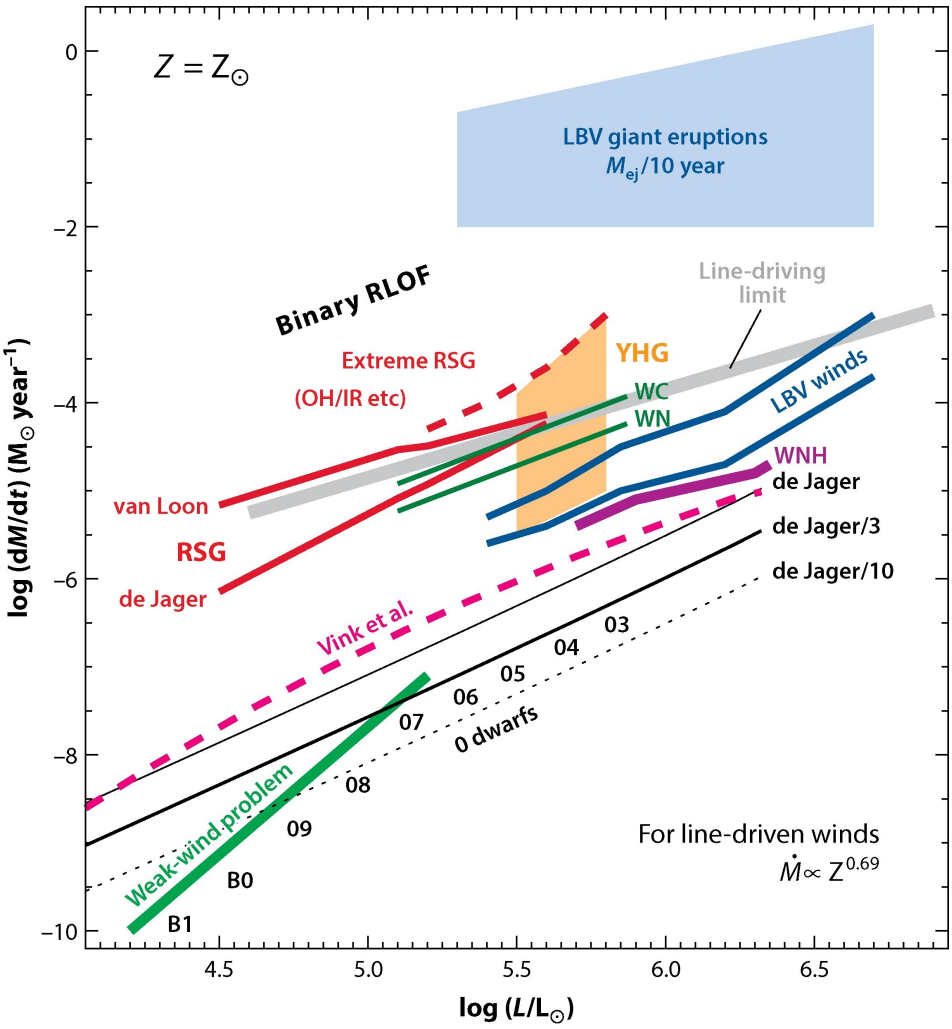

Figure 1.8: Plot from Smith (2014), showing various mass loss prescriptions. Included is the limit of line driven mass loss, which is at least a factor of 10 higher than typical O stars and lower than extreme non line driven mechanisms such as RLOF and LBV eruptions.

1.7 Wind driving mechanism

Hot, luminous stars should have a large classical Eddington parameter, Γ_e, which is the ratio of electron scattering to surface gravity:

$$\Gamma_e = \frac{q\sigma_e}{cm_H G}\frac{L_\odot}{M_\odot} = 10^{-4.5} q \frac{L/L_\odot}{M/M_\odot} \tag{1.2}$$

where σ_e is the Thompson scattering cross section, q is the number of free electrons per atomic mass unit and m_H is the mass of a hydrogen atom. However, the acceleration provided by scattering alone is insufficient to explain mass loss in hot stars; as if $\Gamma_e < 1$,

there would be no wind. An additional mechanism is resonance line absorption (Lucy & Solomon, 1970). This provides extra radiation pressure to accelerate the resonance lines of the wind. Metals make ideal line drivers, as their structure means they are each able to absorb the millions of UV photons required to accelerate the ion to high wind velocities. Therefore, both a high Eddington parameter and line opacity are required for the dense outflows of a WR stellar wind (Castor et al., 1975)

$$v\frac{dv}{dr} = g_{line} - \frac{GM_{\odot}}{r^2}(1-\Gamma_e) \tag{1.3}$$

where v is the wind velocity, r is the stellar radius and g_{line} is the acceleration due to line opacity.

Originally, it was thought that abundant elements such as C and N provided the required acceleration in WR stars (e.g Castor et al. 1975, Lucy & Solomon 1970). However, including iron and line blanketing in models showed iron had a larger influence over the UV (<912 Å) and far-UV (<2000 Å) (Hillier & Miller, 1998). In the inner atmosphere, models have confirmed there is an increase in opacity at a hot iron bump around 160kK, due to the excitation of Fe IX– XVI (Nugis & Lamers 2002, Gräfener & Hamann 2005, Sander et al. 2020). This leads to greater absorption and thus, an increase in the driven efficiency of the wind:

$$\eta = \frac{\dot{M}v_{\infty}}{L/c} \tag{1.4}$$

where $\dot{M}$ is the mass loss rate and v_{∞} is the terminal wind velocity. $\dot{M}v_{\infty}$ is therefore the wind momentum and $\frac{L}{c}$ is the photon scatter momentum. For a typical O star, $\eta < 1$ (where $\eta = 1$ is the 'single scattering limit'), but for a WR star, $\eta > 1$ owing to the extended atmosphere and multiple scattering that can occur. This reliance on iron line driving means that WR stars and their mass loss rates are heavily affected by the metallicity of their environments, with lower metallicity environments causing weaker winds. For instance, Vink & de Koter (2005) find (for $Z/Z_{\odot}$=1−0.01):

$$WN : \dot{M} \propto Z^{0.86} \tag{1.5}$$

$$WC : \dot{M} \propto Z^{0.66} \tag{1.6}$$

Other dependencies have been observed empirically for Galactic, SMC and LMC stars. For example, in Hainich et al. 2015, $\dot{M} \propto Z^{1.2\pm0.1}$, based on the SMC, LMC, Milky Way and M31. In Shenar et al. 2019, based on the LMC WN sample, the dependency

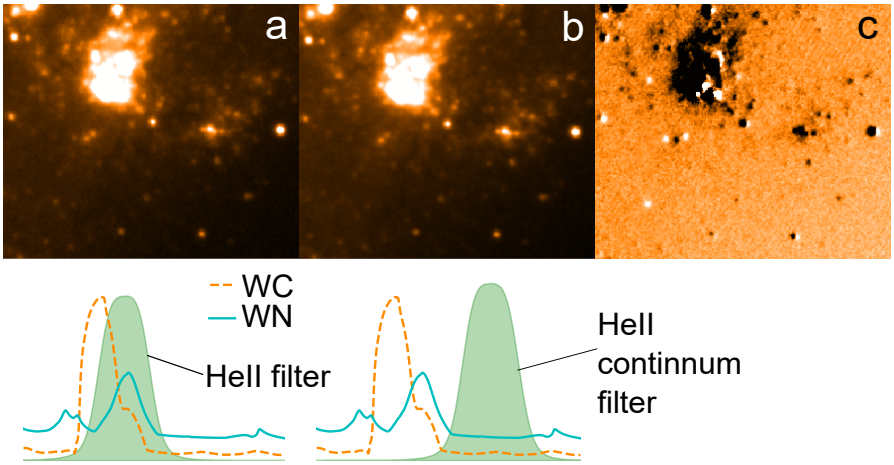

Figure 1.9: Example identification of WR emission line excesses in NGC6946 (using data from Chapter 6) via photometry. The top row shows the images in (a) narrowband (FWHM 80Å) filter centred on the He II 4686 emission line, (b) narrowband filter centred on the continuum near the He II 4686 line and (c) Subtracted image. The WR stars are the bright point sources, which contain excess He II emission. The bottom row shows the corresponding filter position and sample WC and WN spectra.

is more modest, as $\dot{M} \propto Z^{0.81\pm0.09}$. The disagreement in the theoretical and Hainich et al. (2015) empirical results may be because the empirical result strongly depends on assumed galactic metallicities).

1.8 The Milky Way WR population

The Milky Way contains a significant number of WR stars. Rosslowe & Crowther (2015b) estimated the total Galactic WR population as 1200±200, based on a 3D Galactic model of WR subtype and distribution, which was calibrated by comparing the model average absolute magnitudes with observed absolute magnitudes. Therefore, about half may have been detected so far, according to the most recent Galactic Wolf-Rayet catalogue [1]. This nearby sample can be studied at a higher spatial and spectral resolution than more distant WR stars in other galaxies, apart from those that are visually obscured.

1.8.1 Detection methods

The original Galactic catalogues (e.g Campbell 1894,van der Hucht et al. 1981) compiled Galactic WR stars using optical spectra, mainly from objective-prism field surveys (e.g MacConnell & Sanduleak 1970). An alternative detection method is via follow ups to candidate emission line objects identified by (R−I) and (R−Hα) excesses in narrowband Hα surveys (Drew et al. 2004, Hopewell et al. 2005).

Yet another method involves blinking or subtracting continuum from narrow band images to find emission line candidates (e.g Shara et al. 1999). This process uses two narrow band filters. One is centred on a strong emission line and the other on the nearby continuum. By subtracting the continuum image from the line image, regions of excess helium, nitrogen or carbon emission can be located. Alternatively, the two images can be blinked to highlight their differences. (Wray & Corso 1972, Moffat & Shara 1983 and Massey & Conti 1983). Typically the emission line filters are centred on λ4670Å(Moffat & Shara 1983, Massey & Conti 1983) to capture He II and C III lines (Wray & Corso, 1972) or λ4686Å, to capture strong HeII lines. Figure 1.9 shows an example of this process with image subtraction.

However, the high extinction present towards the Galactic centre (A_V >30mag) is a significant barrier to optical identification in that region and within the Galactic disk, as the usual optical features are not visible (see Figure 1.10). More recent work has therefore focused on identifying WR stars using IR data (Hadfield et al. 2007, Mauerhan et al. 2011; Shara et al. 2012; Chené et al. 2013; Kanarek et al. 2015; Rosslowe & Crowther 2018). Approximately half of the known Galactic WR population has been discovered in this way. The WR populations of young, embedded massive clusters, such as Westerlund 1 (e.g Clark & Negueruela 2002; Crowther et al. 2006a) went undetected prior to deep IR searches.

Two different methods can be used for IR detection. The first is the same blink and subtract method as described for optical spectra. Here, emission line filters are centred on He II (here at 2.19μm), He I (2.06 − 2.07μm), C IV (2.08 − 2.09μm) and Br γ (2.165μm) (Crowther et al. 2006a; Shara et al. 2009). Candidates can be selected either from direct excesses above a cutoff (Crowther et al., 2006a), or by calibration with excesses of known WR stars. Using known WR stars for calibration can also enable WN or WC subtype classification (Shara et al., 2009).

The second method uses the IR continuum colour differences between WR stars and the rest of the stellar population. Due to free-free emission in their winds, WR stars have

[1] http://pacrowther.staff.shef.ac.uk/WRcat/index.php, v1.21

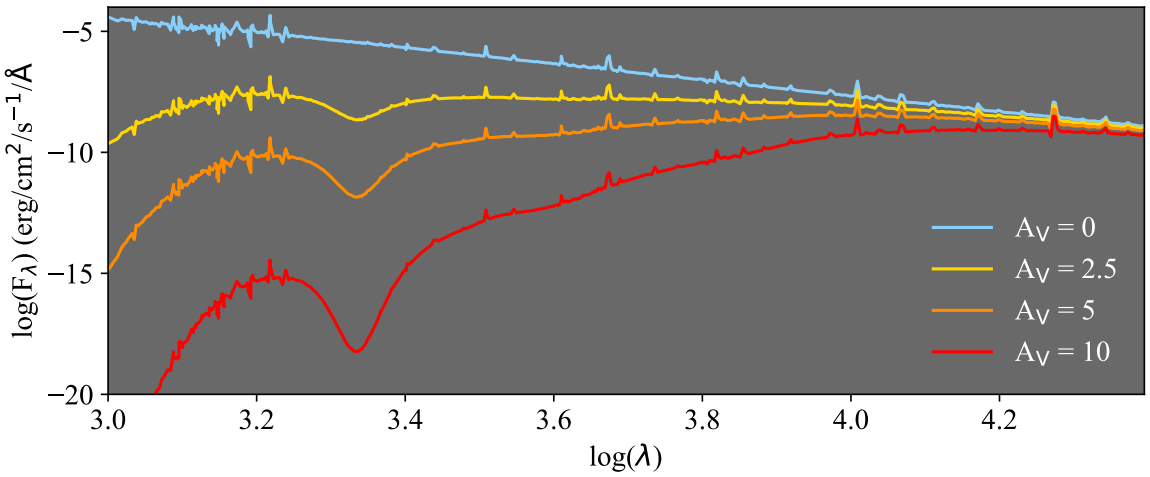

Figure 1.10: WN5−6 SED from PoWR (Hamann & Gräfener 2004 and Todt et al. 2015 for WN, Sander et al. 2012 for WC) model WNE 08–11, reddened using a Cardelli et al. (1989) law with R_V=3.1. This shows how an increasing extinction severely reduces the flux in the optical and UV parts of the spectrum, whilst the IR region is significantly less affected.

a continuum excess in both the near-IR and mid-IR. This allows them to be distinguished from other early type stars using broad band colours. Machine learning can aid in the selection of candidates in colour space (Morello et al., 2018) although there is significant contamination from other stellar populations. Hadfield et al. (2007) found WR star mid-IR excesses of $[3.6\mu\text{m}] - [8.0\mu\text{m}] > 0.5$ and $[3.6\mu\text{m}] - [4.5\mu\text{m}] > 0.1$. For a combination of the mid and near-IR, WR stars had an excess at 8.0μm. Unfortunately, WN and WC stars have similar colours and cannot be distinguished by colour excesses alone. The exceptions are WC stars with dust shells, which have the largest mid IR excesses. The use of such broad band colours allows a greater sensitivity to dusty WC stars than narrow band filter detection (Hadfield et al., 2007). However, this same excess makes determining IR band extinctions towards the stars difficult, as the excess prevents the application of standard extinction laws.

Spectroscopy is required in all cases to confirm and properly classify the detected candidates (see section 1.5).

WR stars can also be detected in the radio part of the spectrum, mainly due to thermal emission in their winds (e.g Andrews et al. 2019). Radio emissions can be used to probe mass loss rates (Wright & Barlow, 1975).

Table 1.4: Overview of identified WR population in the Milky Way, based on v1.24 of the Galactic Wolf-Rayet catalogue.

Region	WN, WN/WC and Of/WN	WC and WO	Total
Optical+IR visible	174	118	292
IR visible only	211	163	374
Total	385	281	666

1.8.2 WR population

Table 1.4 shows the number of currently detected WR stars observable in either both the visible and IR parts of the spectrum, or only at IR wavelengths. Rosslowe & Crowther (2015b) also shows that most of these detections are still within the neighbourhood of the Sun and follow the spiral arms, and that most stars on the other side of the Galactic Centre have not yet been identified.

Distances to these stars are highly uncertain. Estimates of distances could only be obtained for WR stars in clusters and associations, such as by using the distance modulus after accounting for extinction and the absolute magnitudes of non-WR member stars (e.g Vogt & Moffat 1972)., or by using the absolute magnitudes of extragalactic stars. These distances could in turn be used to derive absolute magnitudes of different WR subtypes, which could be applied to estimate distances to field stars.

van der Hucht (2001) suggests only 35% of optically visible Galactic WR stars are in clusters and associations, whilst Lundström & Stenholm (1984) found that only 10–30% lie within clusters. The known Wolf-Rayet population has expanded substantially since these surveys took place, but the trend continues for recent discoveries in the IR (Mauerhan et al. 2011, Shara et al. 2012, Chené et al. 2013, Kanarek et al. 2015, Rosslowe & Crowther 2018). Therefore, absolute magnitude calibrations for WR subtypes could only be obtained for this small number of WR stars in clusters and associations. This left many subtype calibrations with large uncertainties, which correspondingly propagated to large distance uncertainties of ∼50% (van der Hucht, 2001) for field stars.

Some previous work discussed in Section 1.1, indicated that many massive stars, including WR star progenitors, may have formed in less dense environments than clusters. The WR membership fraction of clusters and associations would be an ideal means by which to test this possibility. However, this existing work assigning WR membership has been hampered by a lack of data for many clusters and associations and a reliance on the assumption that stars within a certain radius of the cluster centre were members (Lundström & Stenholm, 1984). To properly assess the formation environments and processes

of WR stars, we therefore require robust proper motions (to find moving groups of stars) and parallaxes (to determine distance along the line of sight and cluster membership in three dimensions) for the distant clusters and associations that potentially host WR stars.

Improved distances to our Galactic WR population would enable us to reduce the uncertainties of our absolute magnitude calibrations, as well as improving our estimates of WR star fundamental parameters.

1.9 Extragalactic surveys

The influences of metallicity and binarity on WR star evolution are still unclear. The observed WN/WC ratio, as well as WR/O and WR/RSG ratios, can probe the accuracy of evolutionary models. In particular, these ratios depend on the metallicity of the environment and mass loss rates. In Section 1.8, we noted that Milky Way likely contains only approximately 1200±200 WR stars (Rosslowe & Crowther 2015a, Rosslowe & Crowther 2015b) and it also has a limited range of metallicities. Therefore, to properly study the metallicity dependence of WR evolution and compile a WR catalogue for future type Ibc supernovae, we must study the WR populations of external galaxies.

1.9.1 Candidate detection

WR star candidates can be found by searching for sources with strong optical emissions over the background continuum. This is done using the same optical narrow band filter blink and subtraction technique as outlined in Section 1.8.1.

Again, photometric candidates require spectra to confirm the presence of nitrogen, carbon or oxygen lines. The extracted spectrum can then be classified according to its line characteristics. However, WC stars possess a median line strength around 4 times higher than WN stars (Massey & Johnson 1998) which means that the emission line excesses of WN stars in external galaxies are weaker and more difficult to detect than those from WC stars. This may lead to biases towards detecting WC stars over WN stars, and skew the WN/WC ratio.

Due to their strong emission line spectra, it is not possible to identify WR stars using UBV photometry or distinguish amongst other early type stars. Additionally, WR emission lines may inflate the values of results of broad band photometry. By contrast Figure 1.11 shows that narrow band filters (Smith 1968b, Massey 1984) can avoid the lines and sample only the continuum. Unfortunately, Figure 1.10 shows that

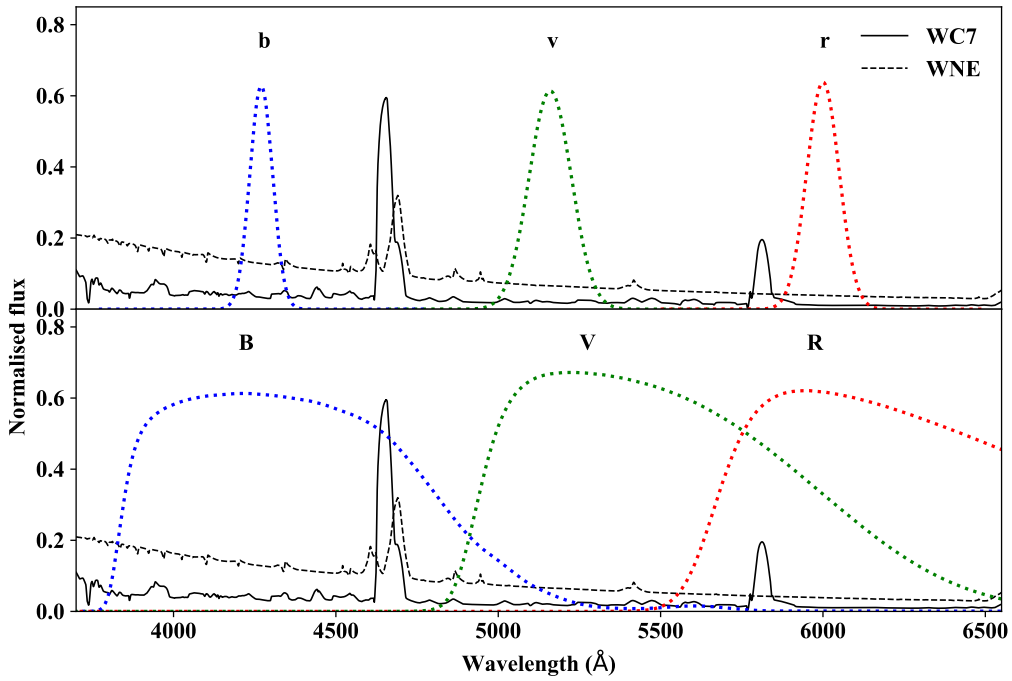

Figure 1.11: Example WN and WC spectra, together with narrowband filters from Smith (1968b) (b and v band) and Massey (1984) (r band) (top) and broadband Johnson filters (bottom). For both classes of WR stars, the wavelength range of the broadband filters encompasses the WR emission lines which are avoided by narrow band filters.

neglecting extinction, WR stars are much fainter at IR wavelengths. The significant distance moduli of external galaxies will therefore render them too faint to be detected at these wavelengths.

The process of identifying WR stars in photometry and then following up with spectroscopy, can be significantly sped up by using integral field units (IFUs). IFUs can be used to obtain simultaneous photometry and spectroscopy, as a full spectrum is obtained for each pixel of the image. The key advantage of this technique is that WR stars can be identified and confirmed without the need for follow up spectroscopy.The small fields of view for IFUs, (e.g 1x1 arcmin^2 for MUSE) mean it is currently impractical to use them for surveying entire galaxies. However, they are ideal for studying individual H II regions and star forming complexes; regions which are the most rich in massive stars. They can be used to simultaneously identify the WR stars and study the properties of their environments (e.g McLeod et al. 2020).

1.10 Metallicity dependence

The metallicity dependence of winds means the WN/WC ratio of WR populations and their total numbers are dependent on their environments. The lack of more luminous RSGs in metal rich environments also suggests that higher luminosity stars there go on to become WR stars instead of RSGs (e.g Shenar et al. 2020, originally studied by Maeder et al. 1980).

The effect is clear when comparing the Milky Way to the Small Magellanic Cloud (SMC), which has a low metallicity of $\sim 0.3 Z_{\odot}$ (log[O/H]+12=8.1). Here, WC stars are absent, although there is one WO star present (Hainich et al., 2015). Table 1.5 shows that the WC/WN ratio is 0.08 (as the WO can be counted as similar to a WC). Stronger winds means WN stars are more likely to evolve into WC due to further mass loss. In the Large Magellanic Cloud (LMC), which has a slightly higher metallicity $\sim 0.5 Z_{\odot}$ (log[O/H]+12=8.4), the ratio of WC/WN is correspondingly higher at 0.21. Table 1.5 suggests that in the Galaxy ($\sim Z_{\odot}$, log[O/H]+12=8.7) the ratio is higher still, at 0.73, although the survey is still highly incomplete.

Low metallicity environments also increase the minimum progenitor mass for WR formation via the single star channel. Such environments reduce wind strengths and thus also mass loss rates. Shenar et al. (2020) uses models calibrated using the lowest luminosity WR stars to find minimum initial masses of self stripped WR stars, obtaining 20−30, 30−60 and >40 $M_{\odot}$ for the Galaxy, LMC and SMC respectively. For very low metallicity models (Z=0.0004, compared to solar Z=0.014), Groh et al. (2019) anticipate no WR stars will form via the single star scenario.

This metallicity dependence extends to WN subtypes (Crowther et al., 2002). Amongst WC stars, early types dominate in metal poor environments, owing to their weaker winds. An example is the outer regions of M33, whilst more metal rich central regions host later types (Neugent & Massey, 2011). Bibby & Crowther 2010 also see a deficit of WC4−6 stars with strong winds in the metal rich inner regions of NGC7793. The LMC ($\sim$ log[O/H]+12=8.4) is also dominated by WN and Of/WN stars (Neugent et al., 2018) and the WC stars that are present are overwhelmingly early subtypes.

Some galaxies have not followed this trend, such as IC10. This galaxy has a similar metallicity to the LMC, but a confirmed WC/WN ratio of 1 (see Figure 1.12). However, including candidates, which are assumed to be WN stars, this fraction falls to 0.7 (Tehrani et al., 2017). Weak WN emission lines may therefore be responsible for such high WC/WN ratios (see Section 1.9.1, on the greater WC median line strengths compared to WN, Massey & Johnson 1998).

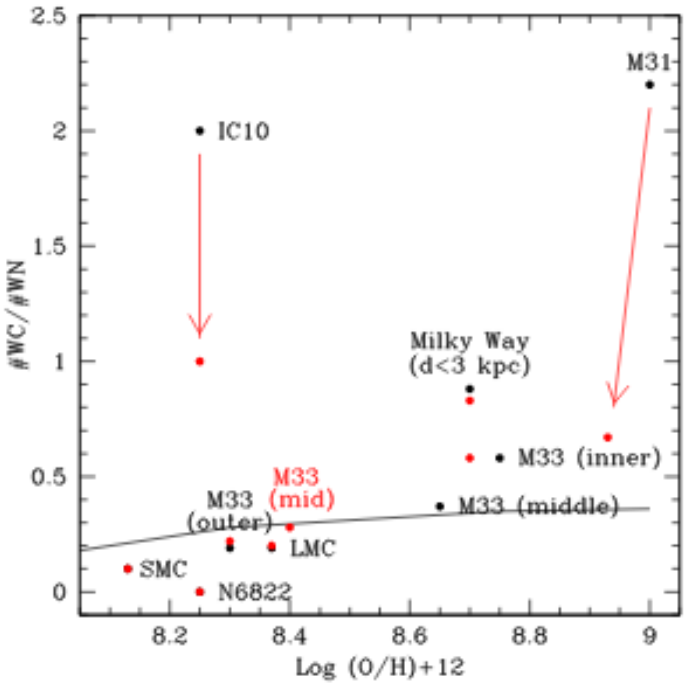

Figure 1.12: Plot from Neugent & Massey (2019) showing the WN/WC ratio of IC10, in relation to other surveys, including M31. The black dot is the WN/WC ratio around the year 2000 and the red dot is the current ratio, after the surveys of Tehrani et al. (2017) for IC10 and Neugent & Massey (2011) for M31 increased the known WN populations in these galaxies. The black line is the prediction of how the WC/WN ratio varies with metallicity, from the 2005 Geneva evolutionary models (which include rotation).'

1.11 Survey overview and completeness

The LMC and SMC have been thoroughly surveyed for WR stars. The LMC hosts a total of 154 WR stars (Neugent et al., 2018) and in particular, the giant H II region of 30 Doradus contains a rich main sequence WR population, including the most massive known WR star (R136a1, whose initial mass is estimated at 320$M_{\odot}$, Crowther et al. 2010) in its central cluster R136. The SMC hosts just 12 WR stars, 11 WN and 1 WO (Neugent & Massey, 2019).

Further afield, the local group galaxies M31 (Neugent et al. 2012; Shara et al. 2016), M33 (Neugent & Massey, 2011), and IC10 (Crowther et al. 2003; Tehrani et al. 2017), have also been surveyed for WR stars. M33 shows a gradient in metallicity; as does M31, with results suggesting most WR stars are located in regions with $>Z_{\odot}$ metallicity.

More distant galaxies, including NGC3125 (Hadfield & Crowther, 2006), IC 4662 (Bibby & Crowther, 2010), NGC 625 (Monreal-Ibero et al., 2017) and M101 (Pledger et al., 2018), all host WR populations. Dwarf galaxies (e.g NGC3125, IC4662) mainly

have a lower metallicity than the Milky Way and some are undergoing starbursts (e.g potentially IC4662).

Finally, more distant regions including spiral galaxies NGC5086 (Bibby & Crowther, 2012) at 5.45Mpc and NGC1313 (Hadfield & Crowther, 2007) at 4.1Mpc, have been surveyed for WR stars as potential type Ibc progenitors. M83 contains an exceptional WR population within ≈200 regions (Hadfield et al., 2005), possibly due to the galaxy's high metallicity. The WC population also mainly consists of late types, although the WN early to late type ratio is more even, though still highly incomplete.

Table 1.5, shows that many catalogues remain incomplete, preventing the determination of accurate WN/WC ratios. Intrinsically weak WR lines from very low metallicity regions or dilution from a binary companion (e.g Pledger et al. 2018) may render some WR stars undetectable, whilst some galaxies like IC10 experiences high reddening due to their location behind the Galactic plane (Tehrani et al., 2017).

Unresolved populations in star forming regions can be studied using their integrated properties. These manifest as a 'blue bump', primarily from WN stars, containing He II 4686Å and N V 4620Å + N III 4640Å blended emission, and a red bump from WC stars due to their C III 5696Å and C IV 5808Å lines. The numbers of WR stars in such regions can be identified in spectra by using templates or average emission line luminosities with the correct metallicity (e.g Hadfield & Crowther 2006; López-Sánchez & Esteban 2010; Miralles-Caballero et al. 2016). The subtypes of photometric candidates can be estimated using average absolute magnitudes for WR subtypes, again, accounting for metallicity.

Table 1.5: Table showing measured and estimated total WR populations for different surveyed galaxies. (1) Rosslowe & Crowther (2015a), (2) Rosslowe & Crowther (2015b), (3) Chomiuk & Povich (2011), (4) Neugent et al. (2012) and references therein, (5) Shara et al. (2016), (6) Hα luminosity from Kennicutt et al. (2008), converted to SFR using Kennicutt (1998b), (7) (Neugent & Massey, 2011) and references therein, (8) Crowther et al. (2007) and references therein, (9) Bibby & Crowther (2010) and references therein, (10) Hadfield & Crowther (2007) and references therein, (11) Hadfield et al. (2005) and references therein, (12) Pledger et al. (2018) and references therein, (13) (Kennicutt et al., 1995), (14) Neugent et al. (2018) and references therein, (no ref. for dist or metallicity) (15) Neugent & Massey (2019) and references therein, (16) Monreal-Ibero et al. (2017) and references therein, (17) Tehrani et al. (2017), (18) Hadfield & Crowther (2006) and references therein, (19) Bibby & Crowther (2012) and references therein. Note: IC4662 was not included in the table, due to the uncertain number of WR stars it hosts and their subtypes.

Galaxy	Confirmed WN, WN/WC and Of/WN	Confirmed WC and WO	Current total	Estimated total	Metallicity (log[O/H]+12)	SFR ($M_\odot yr^{-1}$)	Distance (Mpc)	Reference
—Spiral—								
Milky Way	385	281	665	1200±200	8.85−8.55	≈2	...	1, 2, 3
M31	93	62	155	160-170	≈8.9	0.21	0.76	4, 5, 6
M33	153	53	206	214	8.72−8.29	0.26	0.84	6, 7
NGC300	16	15	31	40	8.6	0.06	1.88	8
NGC7793	27	25	52	105	8.6−8.2	$0.45^{+0.11}_{-0.13}$	3.1	9
NGC1313	51	32	83	115	8.23±0.06	0.6	4.1	10
M83	471±130	564±170	1035±300	3000	9.0−9.2	1.41	4.5±0.3	6, 11
M101	4	11	15	3000	8.23±0.06	1.7−3.3	6.4	12
–Dwarf/Irregular–								
LMC	127	27	154	...	8.37	0.22	0.05	13, 14
SMC	11	1	12	...	8.13	0.04	0.05	13, 15
NGC 625	23	5	28	...	8.14±0.02	≈2	3.9±0.2	16
IC10	15	14	29	...	8.40±0.04	0.045±0.023	0.74±0.02	17
NGC3125	200	40	240	...	≈8.4	0.37	11.5	6, 18
NGC5068	18	24	42	170	8.74−8.23	$0.63^{+0.11}_{-0.13}$	5.45	19

1.12 Fate

At the end of a WR lifetime (duration $\sim 0.1 - 1$Myr for classical helium burning single WR stars, but dependent on mass, rotation and metallicity, Georgy et al. 2012), the star undergoes core collapse and may explode as a stripped envelope supernova (SN). WN stars are expected to be associated with hydrogen deficient type Ib SN, whilst WC stars are expected to explode as hydrogen and helium deficient type Ic SN (Georgy et al., 2009). Other possible SN results are type IIb (hydrogen which disappears as the spectrum evolves) and type Ibn (including narrow lines, indicating an ejecta nebula surrounds the star. Ibn SN are therefore thought to result from LBVs).

The distributions of type Ib and Ic SN correlate well with the distributions of star forming environments. Ic SN are found in brighter environments, close to the galaxy centre, whilst Ib SN follow the galaxy light curve (Kelly et al., 2008). WC and WN stars have the same distribution and so are are potential progenitors of these SN (Leloudas et al. 2010, Leloudas 2012).

Broad line type Ic SN also show an association with long gamma ray bursts (LGRBs), which suggests WC stars in metal poor environments are LGRB progenitors (Modjaz et al. 2008, Leloudas et al. 2010, Leloudas 2012).

By contrast, RSG from somewhat less massive stars retain their hydrogen and thus explode as type II supernovae (e.g Smartt et al. 2009). The supernova progenitors can be identified by comparing pre and post supernova imaging from archives (e.g HST). Before the supernova, the progenitor star should be detected, whereas it will have vanished after the supernova has occurred. The progenitor photometry can be fitted with an SED to determine the stellar subtype, temperature and luminosity and then compared with stellar models on a HR diagram to determine the mass (e.g Mattila et al. 2008).

However, finding WR progenitors in this way is not possible. As stated in Section 1.9, it's not possible to distinguish WR stars from other types of blue massive stars within broad band photometry and most surveys which capture pre supernova explosion images were taken with broad band photometry. Additionally, models of massive stars at the WR stage are still very uncertain.

There has, however, been tentative evidence of massive stars producing type Ibc SN. Spectral model fits to images of the source show SN 2007gr was most likely produced by a massive yellow supergiant, that could potentially have evolved into a WR star (Maund & Ramirez-Ruiz, 2016).

The binary formation channel also impacts the number of observed Ib and Ic SN. Leloudas (2012) found from their studies of WR stars and GRBs, that 20%−30% of

their examined SN should originate from lower mass binaries. Based on analysis of rates for different SN types, a binary population model and limits on type Ibc progenitors, Eldridge et al. (2013) suggest the majority of type Ibc SN arise from lower mass stars in binaries that are stripped by their companion. A similar analysis by Smith et al. (2011) suggests that at least half, if not most, type Ibc SN come from binaries.

An example of a Ib SN which may originate from a binary, is iPTF13bvn. The initial mass of the progenitor was constrained to between $10-12M_{\odot}$, suggesting it was a helium star formed by RLOF with a lower mass companion (Eldridge & Maund, 2016). Maund et al. (2004) also located a binary companion to a type IIb SN progenitor. This progenitor had likely lost its outer hydrogen layers in RLOF. Sun et al. (2020) also finds that the progenitor of Ibn SN 2006jc was likely to be a lower mass star in a binary, which underwent stripping from its companion. The surrounding population of both SN 2006jc and SN 2015G suggests they are unlikely to have originated from high mass single WR stars.

The dominant formation channel for stripped envelope supernovae is therefore unclear. Crowther & Hadfield (2007) sought to link a Ibc SN to a known WR star, by creating a catalogue of ∼10 nearby galaxies containing more than 10^4 WR stars. With such a large sample, a type Ib or Ic SN with definitive connections to a WR progenitor would be expected in the next few decades (although this is challenging since the WN fraction is incomplete at large distances).

The core collapse SN leaves behind either a neutron star or a black hole remnant. The nature of the remnant depends on the metallicity, which affects the mass lost. For example, Georgy et al. (2009) predicted that below Z=0.01 all stars above $30M_{\odot}$ produce black holes, but at high enough metallicities (Z>0.04), no single WR stars produce black holes. Extremely massive stars are also predicted to produce direct collapse black holes, where a supernovae is not observed because the ejected material immediately falls back onto the remnant. Thus far, the only possible candidate for a direct collapse black hole is NGC6946-BH1 (Adams et al., 2017) which may have descended from either a red supergiant or a yellow hypergiant (Humphreys, 2019).

1.13 Overview of this thesis

As outlined in this introduction, the evolutionary stages of massive stars, in particular the WR phase, are still highly uncertain. Key questions relating to WR stars are:

1. What are the most common formation environments of WR star progenitors (the

most massive O stars)? Do they mainly form in rich clusters, as historically anticipated, or in more sparse environments? What does this suggest about their formation mechanisms?

2. What is the evolutionary process of self stripped WR stars? Are LBVs a progenitor phase of WR stars? What is the impact of rotation and mass on how stars progress through the WN, WC and WO phases? What is the lower mass limit required to produce a single WR star?

3. What are the effects of mass loss rates on the later phases of massive star evolution and how does this affect WR star evolution?

4. What is the impact of binary companions on WR star evolution? In particular, what fraction of WR stars form through Roche Lobe overflow, vs single star self stripping? What is the lower mass limit required to produce a WR star through the binary channel?

5. What are the effects of metallicity on WR star evolution? In particular, how does it contribute to the binary formation channel, the WN/WC ratio and the distribution of WN and WC subtypes?

6. What are ultimate fates of WR stars? Are massive WR stars progenitors of stripped envelope supernovae and gamma ray bursts or do many collapse directly to black holes? Additionally, which mass ranges produce neutron stars and black holes and how are these are influenced by mass loss and metallicity?

This thesis aims to produce results that can help to address the problem of WR star origins (question 1), determine their properties and survey extragalactic populations (relating to questions 5 and 6). Data from the ESA *Gaia* mission grants us access to highly precise parallaxes of WR stars. In Chapter 2, we outline our methods for transforming these parallaxes to robust distances of Galactic WR stars. These new distances can be used to help determine key parameters of WR stars, such as luminosities and mass loss rates. Chapter 3 continues our analysis, using these distances to determine absolute magnitudes for WR subtypes and identify possible runaway stars.

The new *Gaia* data is also used to assign cluster and association membership to Galactic WR stars in Chapter 4, and explore their formation environments. In Chapter 5, we use the distances to determine updated emission line luminosities. We apply these emission line templates to a survey of the galaxy NGC6946 in Chapter 6, to determine

the numbers and subtypes of WR stars in unresolved star forming regions. We also use nebular emission lines to calculate the metallicity and extinction of the galaxy.

Finally, we summarise our findings in Chapter 7 and discuss potential future work.

Chapter 2

Gaia DR2 Methods

Content from this chapter is taken from the publication Rate & Crowther (2020) (RC20). Paul Crowther selected the WR star PoWR models in Table 2.1. The artificial Photometry used to produce the conversions in Table 2.3, was produced by Josep Manel Carrasco and Carme Jordi from the University of Barcelona.

2.1 Introduction

Determining fundamental parameters of WR stars, such as their mass loss rates, relies on fitting observations to grids of stellar atmospheres using their emission line equivalent widths and luminosities (Chapter 1). Whilst the equivalent widths can be obtained directly from the spectra, luminosities rely on accurate distances to WR stars. As stated in Section 1.8.2, these distances were previously limited to the small number of WR stars in clusters and associations. These were used to develop absolute magnitude calibrations, which could be applied to determine distances to field stars. However, the resulting distances were highly uncertain, which propagated to uncertainties in the key parameters.

As part of this thesis, we determine the distances to WR stars directly using *Gaia* DR2 parallaxes; removing the previous reliance on calibrations from a small numbers of Galactic WR stars. Using this much larger sample of stars with reliable distances, we can also determine new and more accurate absolute magnitude calibrations.

In this chapter, we present the technical details of the methods used to calculate these distances and absolute magnitudes. In Section 2.2, we discuss the extraction of WR star coordinates from the *Gaia* DR2 catalogue and Section 2.2.1 presents the Bayesian method used to obtain distances from the resulting *Gaia* parallaxes. Finally,

we introduce the methods to obtain absolute magnitudes in Section 2.4.

2.2 *Gaia* DR2 catalogue

The parallax and errors used to calculate distances were taken directly from the *Gaia* DR2 catalogue (Gaia Collaboration et al., 2018a), via the *Gaia* archive. Our distance calculations also made use of G band magnitudes, astrometric excess noise (to identify potentially spurious results) and *Gaia* RA and DEC coordinates.

A python ASTROQUERY (Astropy Collaboration et al. 2013a, Astropy Collaboration et al. 2018) script downloaded data from the *Gaia* archive (Salgado et al., 2017), using the ADQL query

```
SELECT TOP 10 DISTANCE(POINT('ICRS', ra, dec), POINT('ICRS',
WRra, WRdec)) AS dist, *
FROM gaiadr2.gaia_source
WHERE CONTAINS(POINT('ICRS', ra, dec), CIRCLE('ICRS', WRra, WR-
dec, search_radius))=1
ORDER BY dist ASC
```

where WRra and WRdec are the WR RA and DEC search coordinates in decimal format and the `search_radius` is one arcsecond. The query selects the top ten closest points (arranged in distance order) that are within a 1" radius circle of the WR search coordinates.

The majority (370) of 415 successful search coordinates came from the Galactic WR catalogue (van der Hucht 2001 and Kanarek et al. 2015). However, 45 coordinates from the catalogue did not lead to correct *Gaia* detections. In these instances, coordinates from SIMBAD were used instead (Wenger et al. 2000, accessed on 23/05/2018). We checked the coordinates for accuracy, and that the 1" search radius had identified isolated stars, using images from VPHAS+ DR3 (Drew et al., 2014) [1], IPHAS DR2 (Barentsen et al. 2014, Drew et al. 2005) and 2MASS (Skrutskie et al., 2006), to ensure that the detected *Gaia* coordinates overlapped with a bright, isolated point source and were consistent with the Galactic catalogue coordinates.

For stars in IPHAS and VPHAS, 150 stars were included in the Hα filter, whilst an extra 8 stars were present in the r band filter. For WR stars that were not present in the VPHAS or IPHAS catalogue, we used results from 2MASS. In total, we identified

[1] Accessed via the ESO archive.

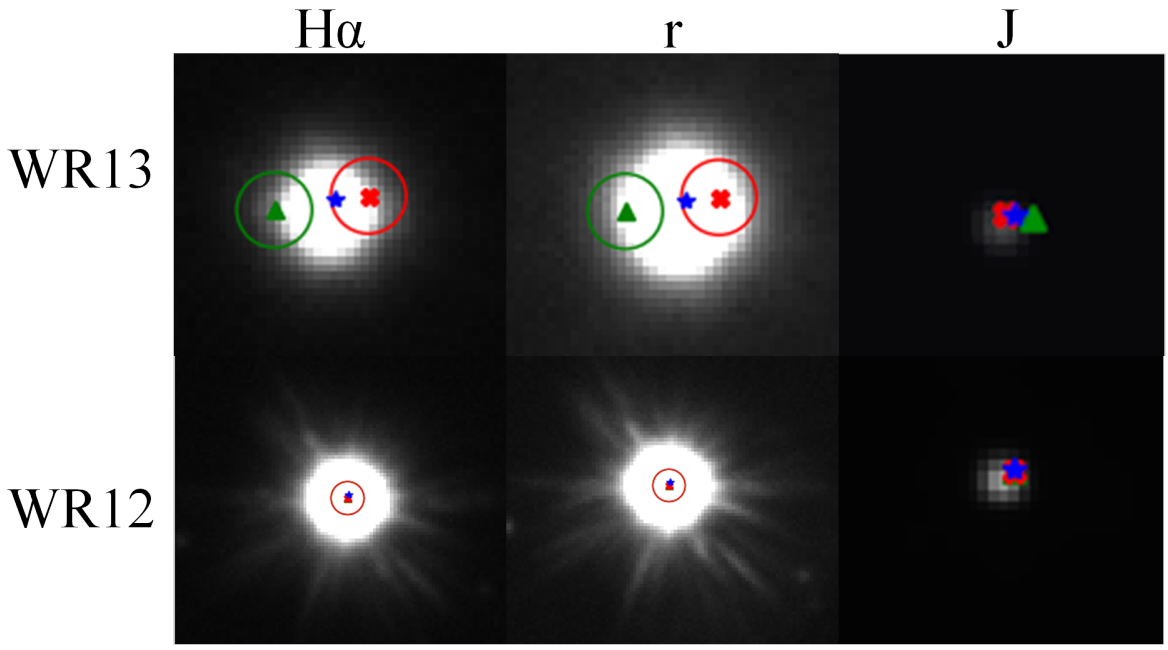

Figure 2.1: WR12 and WR13 identified in VPHAS, IPHAS and 2MASS. The blue star is the detected *Gaia* DR2 coordinates, whilst the green triangles are the Galactic Wolf-Rayet star catalogue coordinates and the red crosses are coordinates from SIMBAD . Also marked around the SIMBAD and Galactic catalogue coordinates (in the Hα and r band images) are the 1" search radius regions. For WR12, all three coordinate systems agree reasonably well. However, WR13 highlights the slight offsets in astrometry between the Galactic catalogue coordinates and SIMBAD, showing that the *Gaia* coordinates are the most accurate. The image size is $\sim$ 9x9 arcsec for WR13 and $\sim$ 18x18 arcsec for WR12 in the Hα and r band images. In the J band, it is $\sim$81x81 arcsec for both stars.

656 sources this latter catalogue, almost every star in the WR catalogue. Figure 2.1 shows the identifications for WR12 and WR13, highlighting their Galactic WR catalogue coordinates, SIMBAD coordinates and the chosen *Gaia* sources.

The 1" search radius detected *Gaia* sources that corresponded well to almost all WR stars. However, WR 43A and 43B are not included in the final distance catalogue as the same *Gaia* source was detected for both stars. The detection for WR43C is also spurious, as the position overlaps with other objects. These stars are located in the compact cluster NGC 3603 (Melena et al. 2008, Crowther & Dessart 1998) and therefore blending is to be expected. Additionally, for a small minority of sources (<10), which were faint in the *Gaia* G band (>13 mag), we found our method had detected very faint background sources, rather than the star itself. The correct coordinates for these stars were obtained by comparing V band magnitudes to G band magnitudes of nearby sources and choosing the source with the most appropriate G band magnitude.

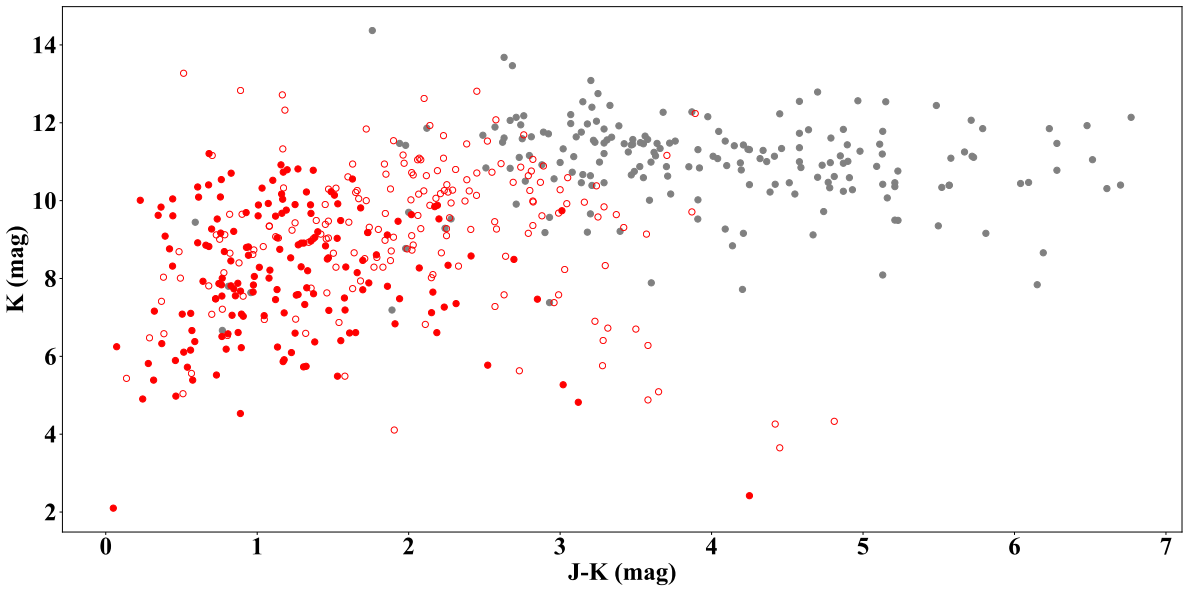

Figure 2.2: The colour magnitude diagram of Galactic WR stars from the catalogue detected by *Gaia* (red) and WR stars only observed at IR wavelengths (grey). Stars not observed by *Gaia* have larger (>3) J−K colours, indicating significant extinction. Filled red circles are stars with the most reliable distances, these are limited to bright sources (K<12) with J−K<3.

The remaining 243 WR stars yielded no successful results with either the SIMBAD or WR Galactic catalogue coordinates. Figure 2.2 shows most of these (>230) have J–K > 3 mag ($\sim A_V > 14$), indicating significant foreground dust extinction and are therefore inaccessible to Gaia.

383 stars (∼58% of the total) from the Galactic WR catalogue [2] have *Gaia* parallaxes. Of those, 305 have positive parallaxes. Figure 2.3 shows that both the total WR population, and the sample containing only the results with reliable distances, appear to be relatively complete up to G ∼13 mag. However, for results with robust absolute magnitudes, the distribution falls off more quickly beyond G ∼13 mag. This is because fainter magnitudes are preferentially removed due to their larger astrometric excess noise and increased incidence of negative parallaxes (which are more likely to produce unacceptable absolute magnitudes).

2.2.1 Bayesian methods

We use Bayesian methods to obtain distances to our WR stars, because the conversion of *Gaia* parallaxes to distances significantly modifies the shape of the original parallax

[2] http://pacrowther.staff.shef.ac.uk/WRcat/index.php

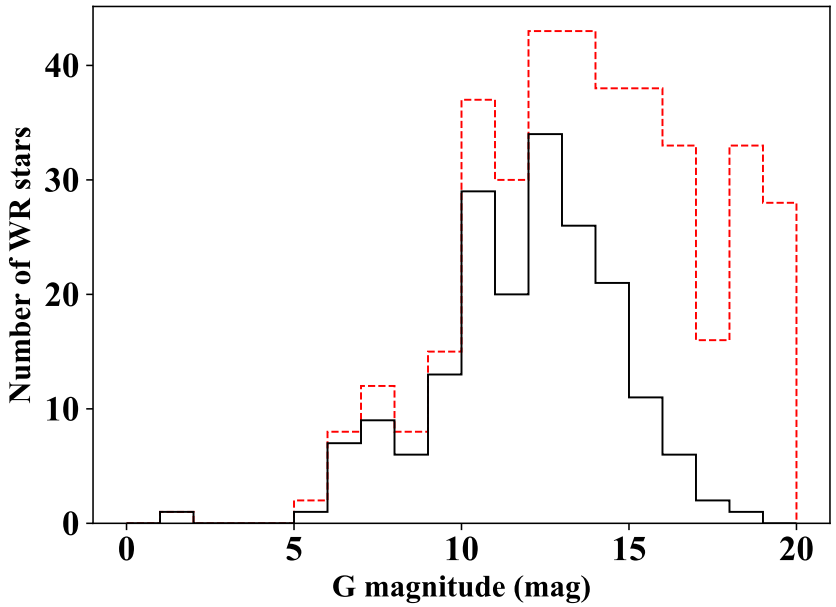

Figure 2.3: Histogram of G band magnitudes for Gaia DR2 detected WR stars. The solid line (black) involves 187 WR stars with reliable absolute magnitudes (Chapter 3) and the dashed line (red) involves the full sample of 383 WR stars.

(ω) probability distribution and uncertainties therefore do not transform symmetrically. This occurs unless the parallax errors (σ_ω) are very small ($\sigma_\omega/\omega < 0.1$, Bailer-Jones 2015), which is not the case for most of our DR2 sources Additionally, many sources have negative parallaxes; a consequence of the data processing algorithm fitting noisy observations (Luri et al., 2018) and of the variation in parallax zero points (see Section 2.2.1).

Bayesian inference is therefore the recommended way to transform parallaxes to distances (Luri et al., 2018). The end result is a probability distribution with correct uncertainties, reflecting the non symmetric transformation of parallax to distance. Bayesian methods are also capable of elegantly accounting for unphysical parallaxes and so there is no need to cut negative data from the sample (Luri et al., 2018).

The inferred distribution of distances (the posterior $P(r|\Psi, \sigma_\Psi)$) is calculated using

$$P(r|\Psi, \sigma_\Psi) = \frac{1}{Z} P(\Psi|r, \sigma_\Psi) P(r) \tag{2.1}$$

(Bailer-Jones, 2015), where $P(\Psi|r, \sigma_\Psi)$ is the likelihood (the probability distribution of measured parallaxes, $P(r)$ is the prior (the expected distribution of the distances) and Z is a normalisation constant.

Likelihoods

The likelihood, $P(\Psi|r, \sigma_\Psi)$, can be constructed by assuming the parallax distribution is Gaussian, with a mean at the parallax measured by *Gaia* and the parallax error as the standard deviation (Hogg 2018, Luri et al. 2018, Bailer-Jones 2015).

The parallaxes quoted by *Gaia* are not corrected for the global zero point. As our sample of WR stars is spread over the sky and the zero point will therefore not be dominated by regional systematics, we choose to apply this global correction to the distance calculation (Arenou et al., 2018). In light of the variation in measured zero points and the fact that Lindegren et al. (2018a) states that the zero point is likely multivariate, with no general process currently available to calculate it, we choose to use the globally measured QSO zero point of −0.029 mas (Lindegren et al. 2018b, Luri et al. 2018). One possible effect of this on the final distances is that if the full multivariate zero point could be used, some small negative parallaxes could be converted to positive values.

Additionally, analysis from Arenou et al. (2018) suggests that, when compared to external data, the errors of DR2 parallaxes in the catalogue are underestimated. This is because they are consistent with the internal uncertainties, and do not account for systematics. The underestimation varies with G band magnitude and is particularly acute for results in the range 12<G<15, which could be underestimated by 30–50% (Gaia Collaboration et al., 2018a).

To account for this, we calibrate the uncertainties of Gaia parallaxes using parallaxes from previous surveys. Arenou et al. (2018) provide in their Table 1 the unit weight error calculated using a variety of comparative surveys and the median G band of these surveys. It is possible to fit a combined Gaussian and straight line to the Arenou et al. (2018) data, which can increase the size of the uncertainties in proportion to the G band magnitude

$$X = -0.01319G + 1.376 + \frac{1.1}{\sqrt{2\pi}1.35} \exp\left[-\frac{1}{2(1.35)^2}\Big(G - 14.59\Big)^2 \right] \tag{2.2}$$

where G is the WR *Gaia* G band magnitude and X is the factor by which the error is estimated to increase. Using this data, we present the conversion curve shown in Figure 2.4. This is similar to the approach of Lindegren et al. (2018a), although our model neglects the HST measurement (1.9 unit weight error at G=8 mag).

The updated parallax (in mas) ω and error σ_ω (also in mas) parallax inputs to the likelihood are therefore given by

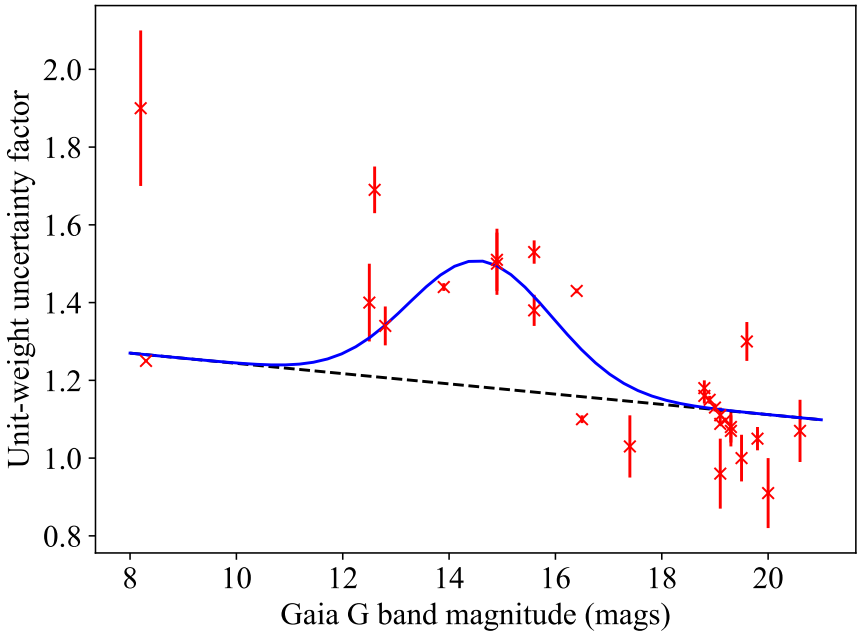

Figure 2.4: Weighted fit to the unit weight uncertainty factors from Arenou et al. (2018), used to increase the uncertainties σ_ω, to account for underestimation in the *Gaia* catalogue. The dotted line is the linear component of the fit, whilst the solid line is the total fit and the red crosses are the unit weight uncertainties of the external data.

$$\omega = \Psi + 0.029 \tag{2.3}$$

$$\sigma_\omega = \sigma_\Psi X \tag{2.4}$$

where Ψ is the original parallax from the *Gaia* catalogue. These increased uncertainties were applied to our WR parallaxes and lead to a likelihood that is appropriate for the WR population

$$P(\omega|r,\sigma_\omega) = \frac{1}{\sqrt{2\pi}\sigma_\omega}\exp\left[-\frac{1}{2\sigma_\omega^2}\left(\omega - \frac{1}{r}\right)^2\right] \tag{2.5}$$

Prior

The prior is a probability distribution of expected distances for a given WR star. Previous work with *Gaia* (Bailer-Jones et al., 2018) has opted for a smooth, exponentially decreasing prior, with a single parameter that can be tuned based on galactic latitude and longitude. This is designed to follow the distribution of all observed stars within

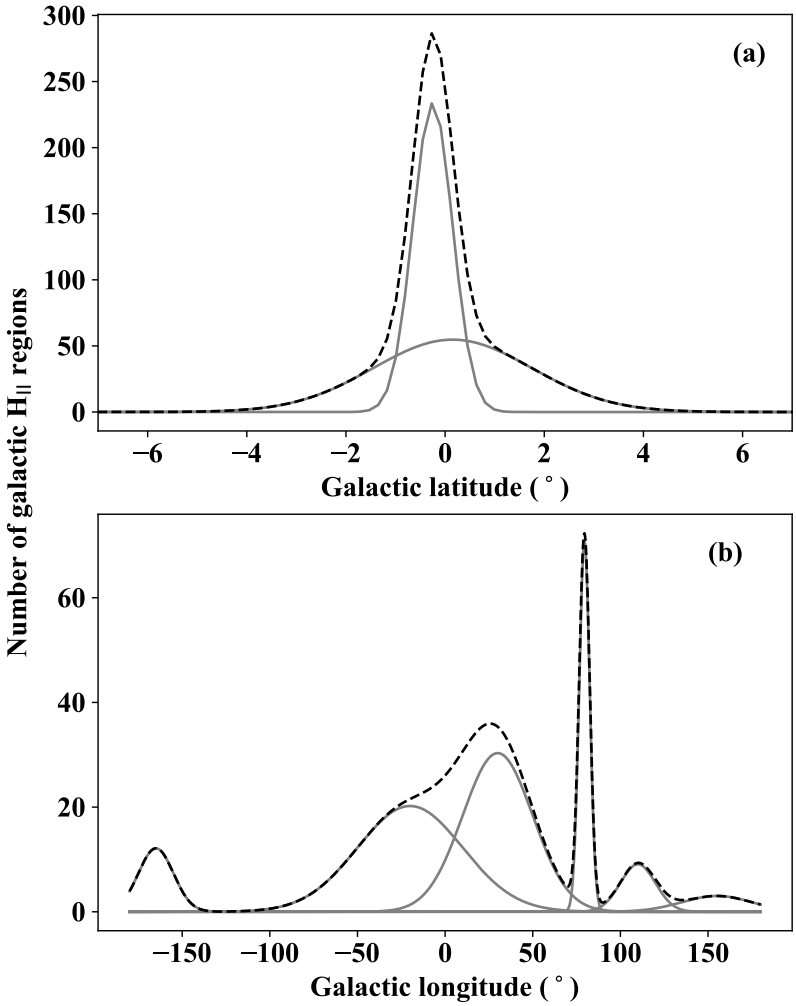

Figure 2.5: A mixture of Gaussians showing the number of H II regions over (a) Galactic latitude and (b) Galactic longitude, based on Figure 6 and data from Paladini et al. (2003). The solid lines are the individual Gaussians and the black dotted line is the overall fit. The parameters for individual gaussians were chosen to match the histograms from Figure 6 of Paladini et al. (2003) as closely as possible. The peak around l=75-90° is the Cygnus X region.

the Milky Way and to provide a distance derived purely from a geometric model.

Almost all WR stars are found at large (kiloparsec) distances and lie preferentially in the Galactic plane, so their observed distribution will be significantly affected by extinction. Previous priors do not properly account for this, which could be problematic

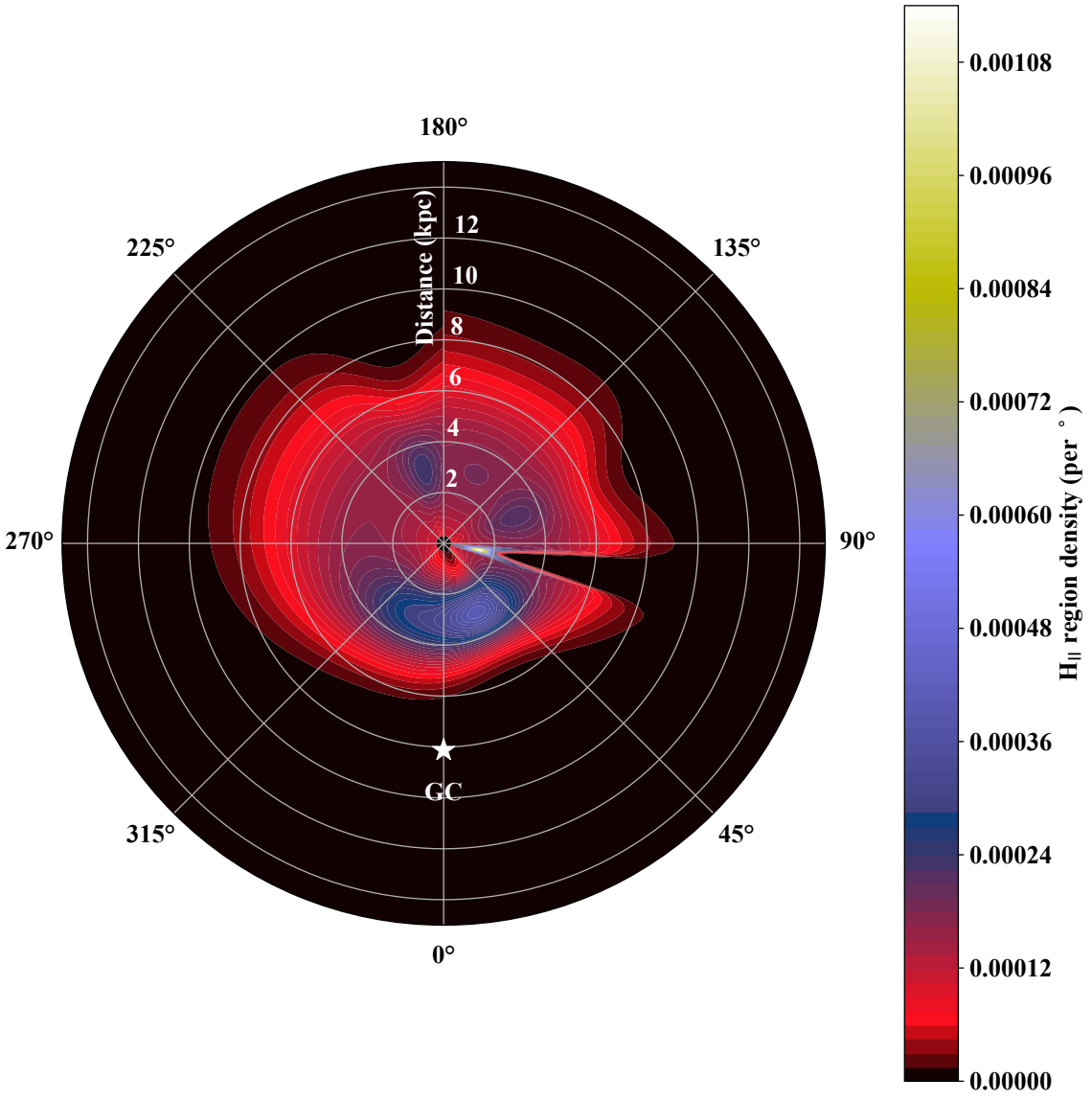

Figure 2.6: Density of Galactic H II regions over distance and longitude, at zero latitude, before extinction is applied (based on Paladini et al. 2004 and Paladini et al. 2003). The coordinate system is centred on the Sun, with the Galactic Centre at 8.122 kpc.

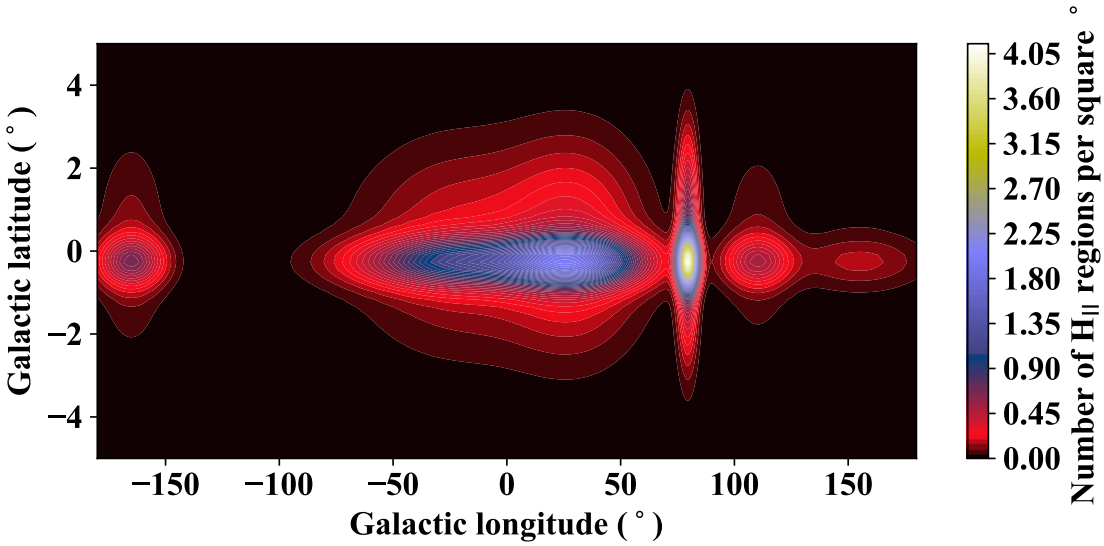

Figure 2.7: Density of Galactic H II regions across different latitudes, viewed from the Sun and based on Paladini et al. (2003).

for our sample.

Instead, we build a prior using H II regions and a dust model for extinction. H II regions approximate the spatial distribution of massive stars. They are independent of previous WR distribution maps, avoiding any bias from previous incorrect results and are well sampled across the galaxy (as they are detectable at a broad range of wavelengths).

To find the overall distribution, we considered H II region density (D) along each line of sight. Figure 2.5 shows a mixture of Gaussians fitted to binned Galactic latitude and longitude distributions, which gave normalised numbers of H II regions at a given latitude or longitude coordinate. These were then multiplied together to get a total number density along the line of sight.

Along the third dimension, distance, the prior covered distances between 0 and 15 kpc at a resolution of 1 pc. The probability is zero below 300 pc, as we do not expect to find any WR stars detected with Gaia closer than this distance. we chose a Gaussian centred on 3000 pc from the sun (based on Figure 12 from Paladini et al. 2004). Over varying Galactic longitudes and latitudes, the number of H II regions and their spread over distance changes. To alter the distribution for different lines of sight, the standard deviation was modified based on the H II region number density D, at a given latitude and longitude. The standard deviations range from 1-3 kpc, depending on the longitude and latitude of the line of sight. Figure 2.6 shows the resulting distribution over different longitudes at different distances and 2.7 shows the distribution over latitudes.

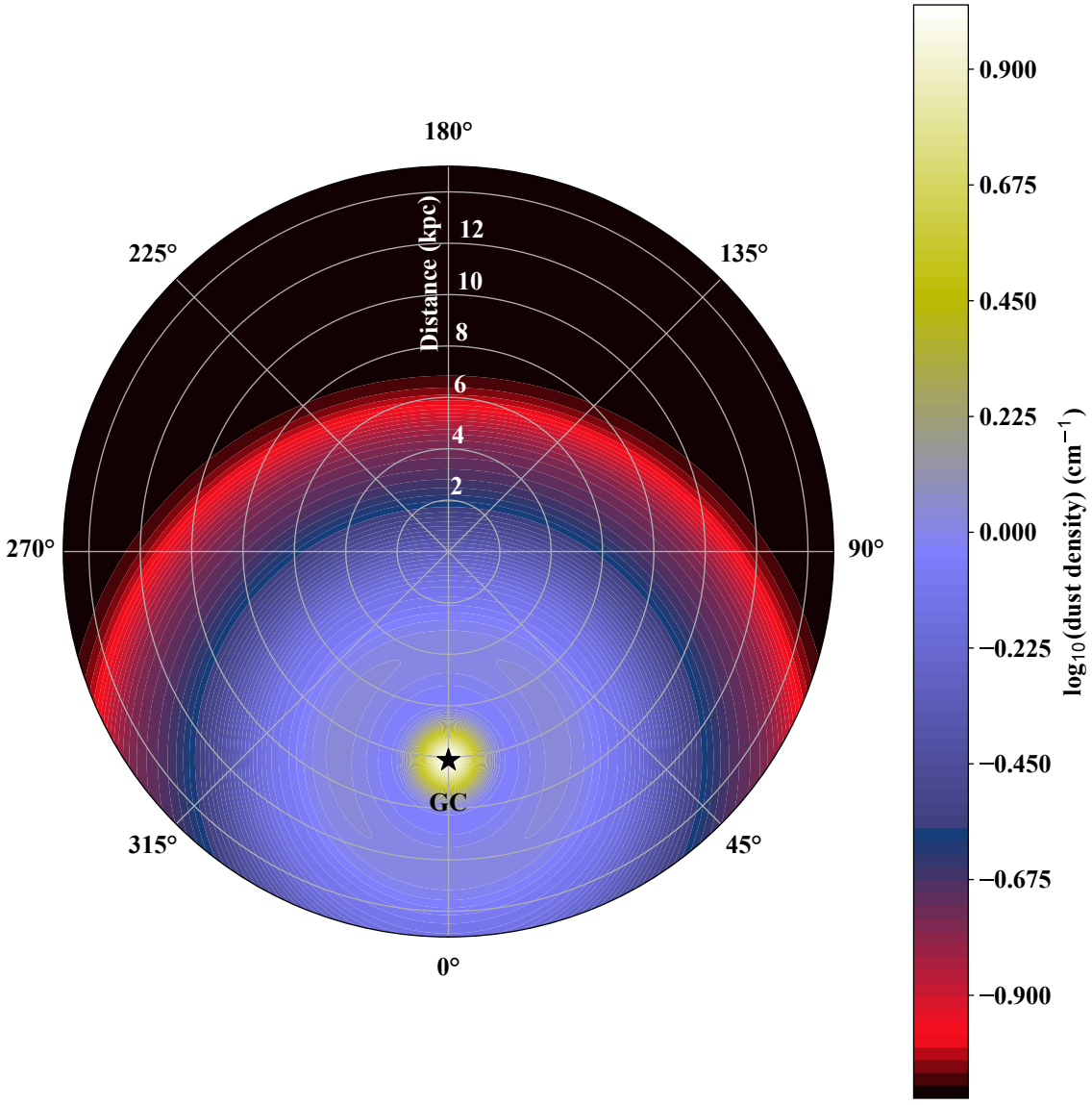

Figure 2.8: Dust distribution over longitude and distance, at zero latitude, in the simple disk model.

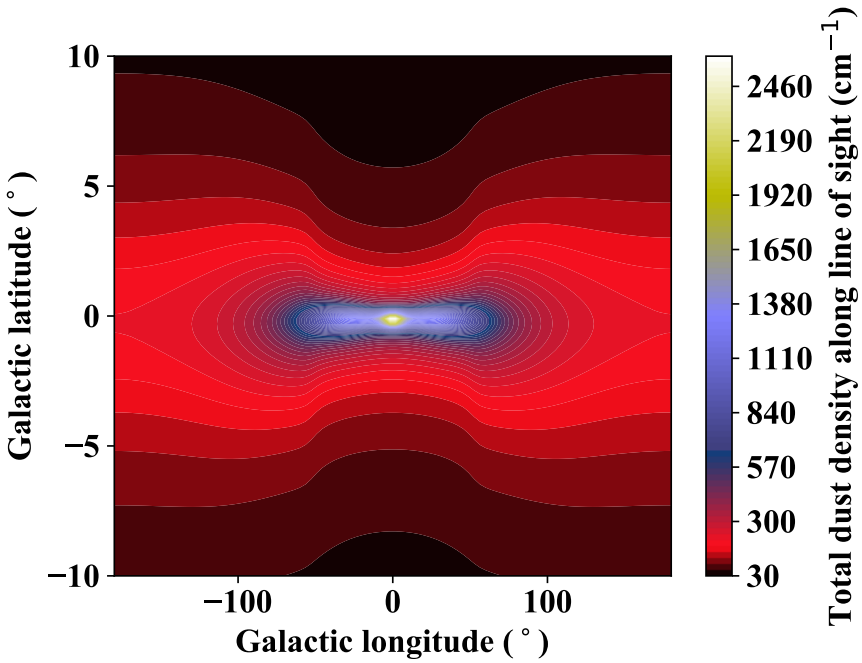

Figure 2.9: The variation of dust integrated along line of sight with latitude, viewed from the Sun. The coordinate system is centred on the Sun, with the Galactic Centre at 8.122 kpc.

There is a particularly large excess probability around l=73-86° and -3≤b≤-4° due to the Cygnus X region (as stated in Paladini et al. 2003). Over these coordinates, the mean of the Gaussian is instead centred on 1400 pc and the standard deviation is correspondingly lower.

We then used a simple dust model from Rosslowe & Crowther (2015a) to account for the effects of extinction. This consists of both molecular and atomic gas, to replicate the thin and thick disks. For the Sun, we chose a distance of 8.122 kpc (Gravity Collaboration et al., 2018) to the Galactic Centre and a height of 20.8 pc (Bennett & Bovy, 2019) above the plane. (see Figure 2.8 for the variation in longitude and 2.9 for the latitude).

Our primary goal was to determine how extinction affected the observable distances along each line of sight. In regions of high extinction, the peak of the prior would be moved towards the Sun, as the probability of detecting a WR star at a greater distance would decrease. The I band (which peaks at ∼8000Å) is best suited for this, as it operates towards the extreme red end of the *Gaia* G band (at 10500Å). Any distance that is too faint to observe in this wavelength range would therefore be very faint in G and only have a small probability of hosting a WR star that is visible to *Gaia*. At each

distance, the dust was integrated along the line of sight and normalised to the extinction at the Galactic centre.

Unfortunately, it was not possible to reliably convert A_I to A_G, as the conversion relationship given in Evans et al. (2018) does not extend to the large values of $V - I_c$ at the Galactic centre.

Galactic centre extinction in the I band was calculated by assuming the V band extinction at the same point is 32 mag (based on averaging optical extinction at 0.55μm from Fritz et al. 2011) and multiplying by A_I/A_V =0.48 Cardelli et al. (1989) (giving 15.36 magnitudes) to account for the difference in reddening. Figure 2.10 shows the resulting extinction variation with Galactic longitude.

We then converted the extinction to a factor which could be applied to the probability at each distance, to simulate the reduction of flux from extinction

$$\delta = 2.512^{(-A_I)} \tag{2.6}$$

where A_I is the I band extinction at that distance, calculated from $A_I = 0.48A_V$ (where A_V is the V band extinction).

This conversion factor was then combined with the H II region distribution, to give the final distribution. This incorporates both the radio H II region observations and dust extinction, and so approximates what might be seen by *Gaia*. This final distribution is shown in Figure 2.11. As compared to Figure 2.6, the peak of the prior has moved significantly closer to the Sun (within 1-3 kpc, depending on longitude).

The final form of the prior therefore varies from Gaussian like in regions with a pronounced H II region peak or low extinction, to exponential like in regions with a less pronounced peak or high extinction.

Posterior

For our likelihood and prior, the resulting posterior distribution is

$$P(\omega|r,\sigma_\omega) = \frac{1}{\sqrt{2\pi}\sigma_\omega\sigma_p}\exp\left[-\frac{1}{2}\left(\frac{\left(\omega-\frac{1}{r}\right)^2}{\sigma_\omega^2}+\frac{(r-\mu_p)^2}{\sigma_p^2}\right)\right]\delta \tag{2.7}$$

where σ_p is the standard deviation of the Gaussian from the H II region prior in the direction of the WR and μ_p is the mean. We do not account for errors in the WR position, as these are insignificant compared to the simplifications in the prior (such as the simplification of the dust distribution).

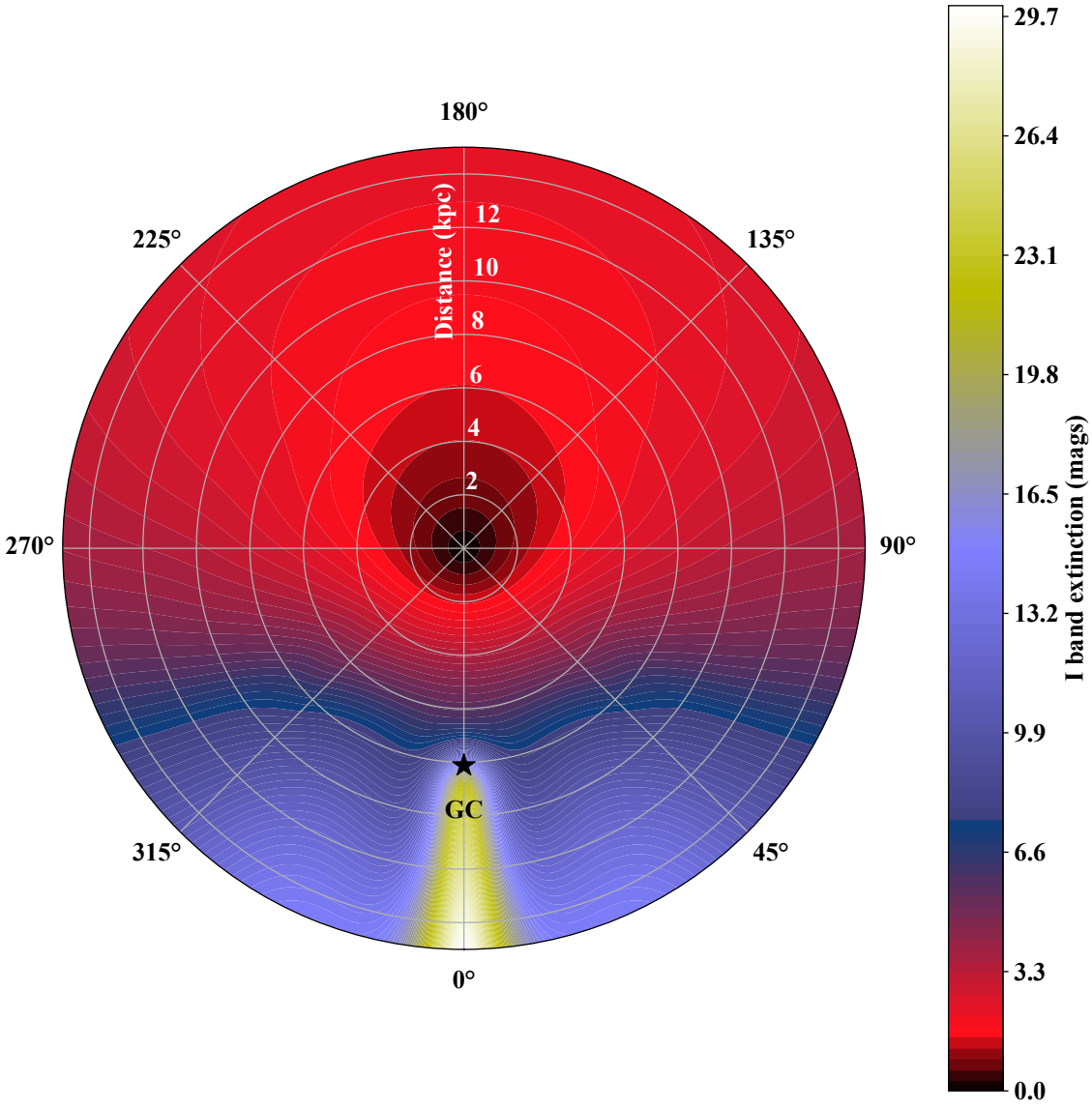

Figure 2.10: Extinction variation with distance and Galactic longitude, at zero latitude, as calculated using the dust model. The plot is centred on the Sun, with the Galactic Centre at 8.122 kpc.

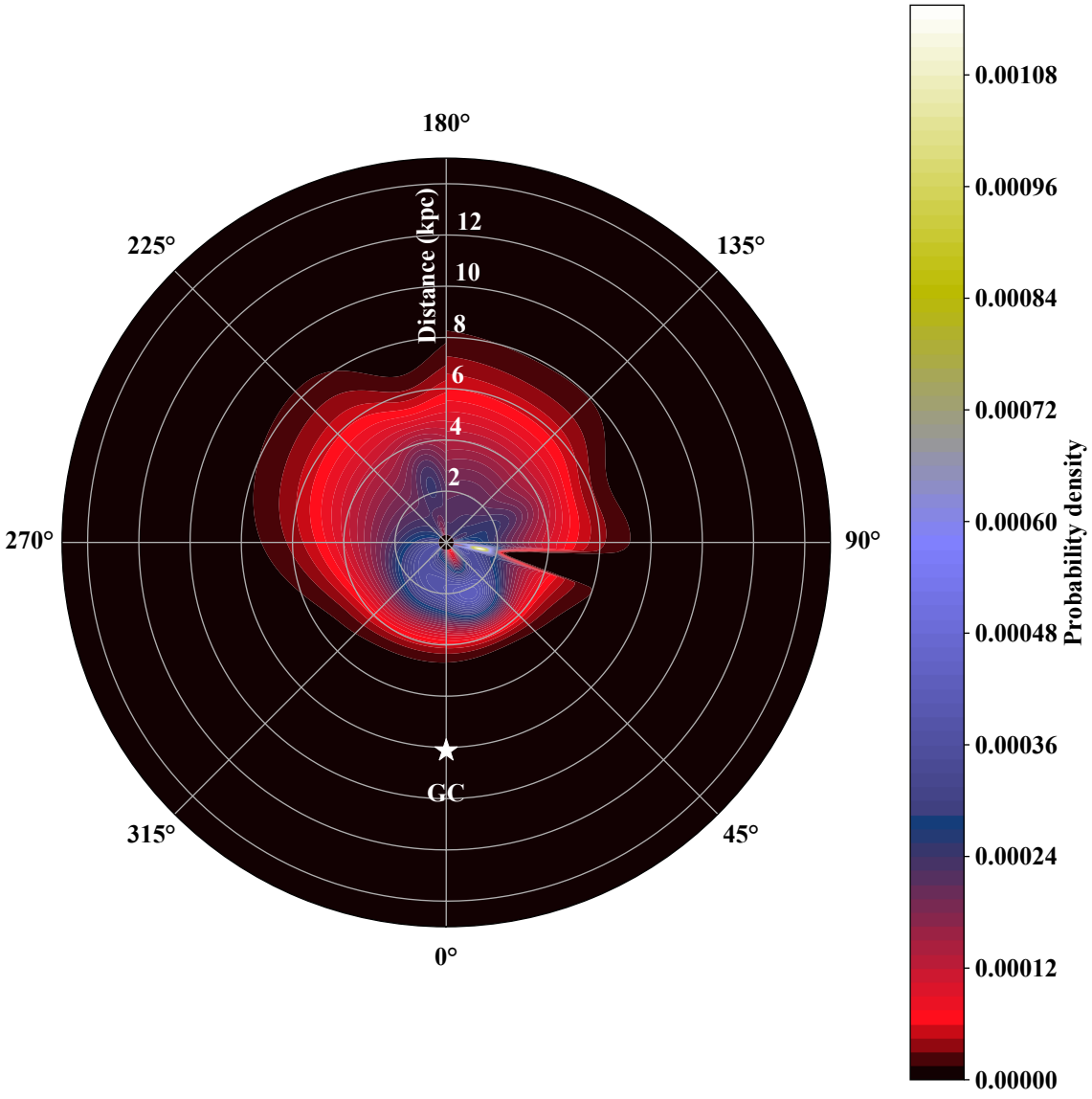

Figure 2.11: Combined prior, consisting of H II region prior and dust extinction.

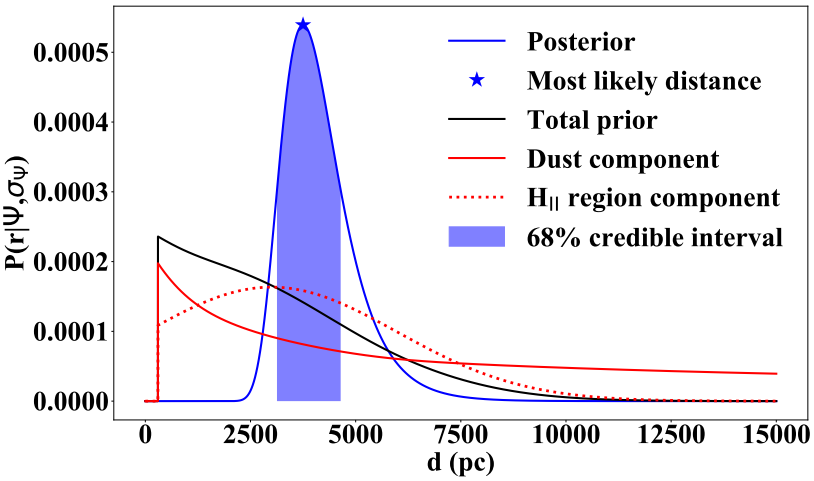

Figure 2.12: Posterior distribution for WR4, shown alongside the prior components and credible interval. The filled star is the most likely distance to WR4 ($3.75^{+0.89}_{-0.62}$ kpc, compared to $3.71^{+0.65}_{-0.49}$ kpc from Bailer-Jones et al. 2018).

Figure 2.12 shows an example of this for WR4, together with the prior and its components. We determine a distance of $3.75^{+0.89}_{-0.62}$ kpc, compared to $3.71^{+0.65}_{-0.49}$ kpc from Bailer-Jones et al. 2018.

Use of the numerical dust model meant we could not differentiate the posterior and produce an analytical solution for the maximum likelihood. Instead the peak of the distribution was taken as the most likely distance. We calculated the credible intervals (uncertainties, similar to those used in Bailer-Jones et al. 2018) , by cycling through each of the calculated probabilities, beginning with the maximum. At each probability, the corresponding distances either side of the distribution peak were selected. The area under the curve for this distance range could then be compared to the target area (e.g 68% for one sigma uncertainties). The process was repeated until the area integrated reached or exceeded the required credible interval.

Due to the use of a discrete grid of values, slight deviations from the specified 68% area occurred, the largest of which was for WR11 (which reached 68.5% of the area). However, these deviations led to typical interval changes of a few pc or less, below the reasonable precision of our distance calculation.

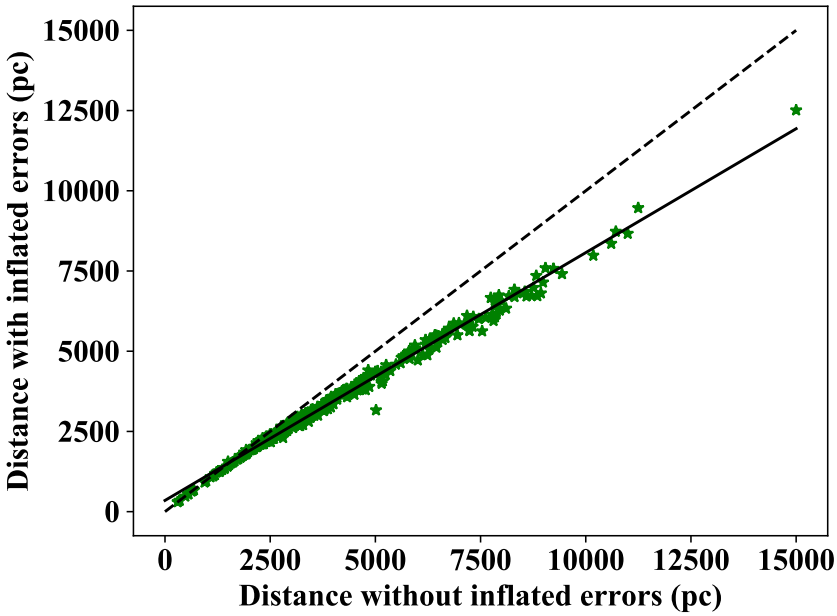

Figure 2.13: A comparison between distances with and without the modelled error increase. The dashed line denotes where the two distance calculations are the same and the solid line is the fit from equation 2.8

2.3 Impact of uncertainties

Figure 2.13 shows that underestimated parallax errors from *Gaia* have a significant effect on the most probable distance. Beyond ∼1.4 kpc, the adjusted errors result in systematically closer distances, compared to data with no uncertainty increases. This occurs because the larger parallax to error ratio means the prior has a greater influence on the resulting distance.

We can compare the distance obtained using the increased uncertainties, with the distance from the original parallax and determine a conversion

$$d_e = 0.7724d + 349.25 \tag{2.8}$$

where d_e is the distance with increased errors and d contains no error modification. The deviations between this fit and a line x=y indicate a typical contribution of 24% at 10 kpc, decreasing towards zero at 1.5 kpc. Below this distance, the difference begins to increase again because the increased errors have little effect and the fit is no longer accurate. For isolated cases, the maximum deviation was higher, up to ∼50%.

In most instances, the differences between the distances from the original *Gaia* ca-

talogue parallax error and the distances from the increased parallax error, fall within uncertainties. A major limitation is that the error rescaling used here, may not account for individual errors which are still underestimated.

Overall, the data show that underestimated parallax errors have a significant effect on many distances and that these underestimates need to be accounted for in distance calculations.

2.3.1 Flags from *Gaia*

The validity of the distances is determined primarily by the quality of the parallax data. A significantly negative parallax (less than the zero point), will result in a smaller likelihood than a positive parallax and will increase the proportional size of the prior. Negative parallaxes can also indicate unreliable *Gaia* data. Similarly, a large error (on the scale of the data itself) will also result in a much smaller likelihood and a greater influence from the prior.

Negative parallaxes and large uncertainties mainly arise from badly fitted parallax solutions, which can be identified using parameters in the *Gaia* catalogue. We chose astrometric excess noise (the observational noise which needs to be added to the data to match the solution residuals) as this identifier. Large values can indicate that a solution does not fit the data well. We chose to use this parameter, as it was the quality indicator with the clearest cut-off and acted as a good benchmark for removing bad values when calculating absolute magnitudes. The excess noise can also account for modelling errors, which are not included in the observational noise. Significant astrometric excess noise is mainly applied to fainter objects, in particular those with brighter neighbours.

The *Gaia* documentation (Hambly et al., 2018) states that high excess noise will be present in early releases and suggests that users apply their own cut-offs to determine erroneous values. The ideal excess for results with distances is zero, which indicates a good fit. However, excluding an outlier with excess noise 18 mas, the average value for our sample is 0.71 mas and the standard deviation is 0.98 mas. Therefore, we flag all results with noise above 1 mas.

Combined, our three criteria for flagging *Gaia* data quality are

`a = astrometric_excess_noise`>1

e = $|\sigma_\omega/\omega| > 1$

n = $\omega < 0$.

Results without any of these issues are given the 'g' flag. These flags are applied to the distances in the next Chapter.

We apply the flags to the zero point corrected parallaxes and the increased errors, as these are the values are used to calculate distance. A star can be flagged if it satisfies one or more of the criteria. If all three are applied, then ∼37% of the WR stars with parallaxes have an a, e or n flag.

59% of the flagged results had more than one negative flag. This reflects the way such errors are intertwined, where a poor solution fit due to noisy observations can lead to a large astrometric excess noise, sizeable errors and negative parallaxes all at once.

The relations between flags are shown in Figure 2.14. In general, WR stars with large astrometric excess noise are supposedly located closer than 4 kpc, and in many cases closer than 2 kpc. This latter group further breaks down into brighter objects at around G=11 mag (WR146 and WR115) and G=15 mag (including WR77p) and fainter objects with G >17 mag. The fainter objects may have high excess noise because of astrometric modelling difficulties, caused by issues like binarity or a badly determined spacecraft attitude during a given time interval (Hambly et al. 2018, Lindegren et al. 2018b). These problems would make it difficult for the *Gaia* AGIS algorithm to reliably extract astrometric parameters. The brighter objects may have high excess noise for a variety of reasons, such as issues with instrument calibration (Lindegren et al., 2018b). High astrometric excess noise can also occur if the stars are in binaries (WR146) or potential binaries (WR115).

The other two flags show a less clear breakdown. Negative parallaxes can occur at all magnitudes and distances, but have non zero excess noise. Only a small fraction of results with large error ratios have zero astrometric excess noise and none at all occur below G=12 mag. Both flags become increasingly common beyond G=15 mag and only a few points beyond G=18 mag are not flagged. This is expected given that highly reddened objects at any distance are more difficult for *Gaia* to observe.

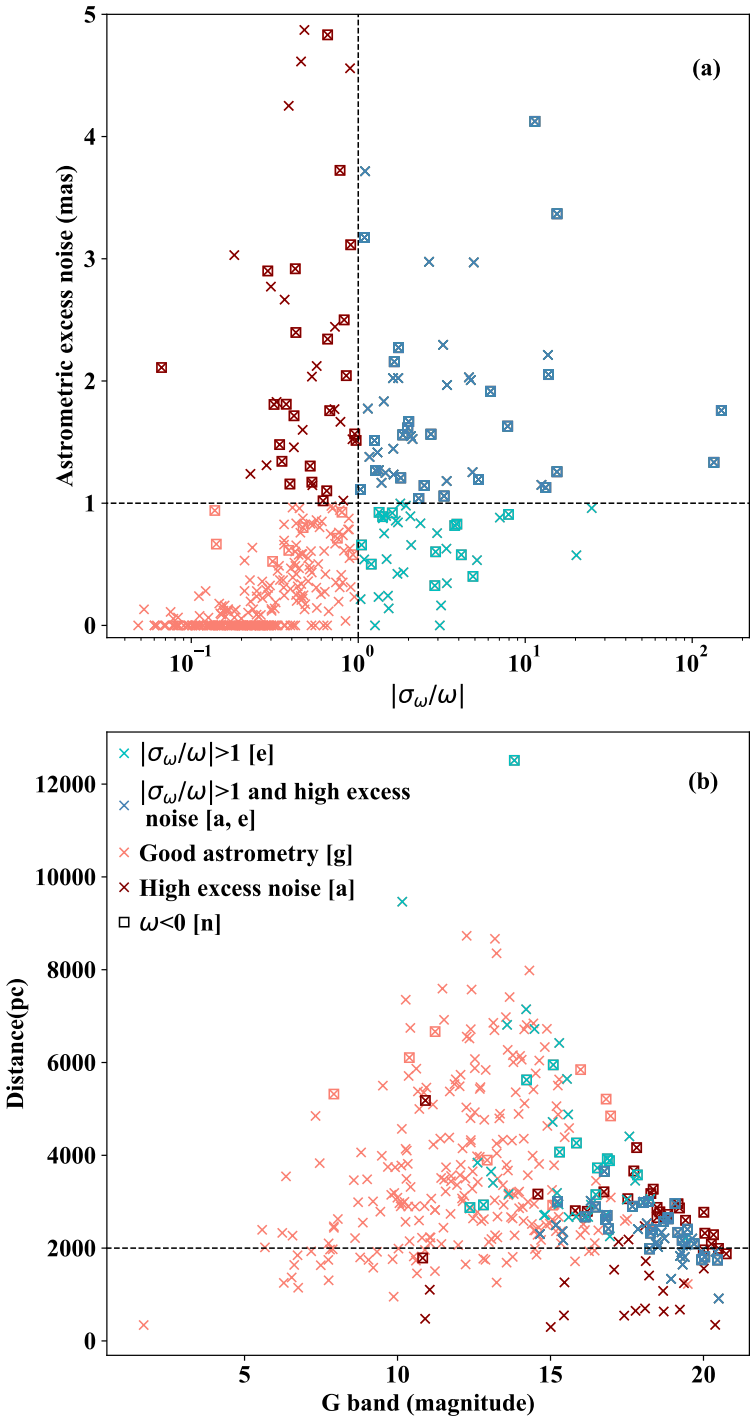

Figure 2.14: (a) Comparison between parallax error $|\sigma_\omega/\omega|$ and astrometric error noise (mas) for Galactic WR stars from *Gaia* DR2, for which dotted lines indicate values of unity for each parameter to highlight data quality flags a, e, g, n; (b) Comparison between G band magnitudes and inferred distances (pc) for Galactic WR stars from *Gaia* DR2, with the dotted line marking a distance of 2 kpc.

Table 2.1: Intrinsic colours of WR stars from PoWR models (Hamann & Gräfener 2004 and Todt et al. 2015 for WN, Sander et al. 2012 for WC) for $(b-v)_0^{WR}$ and monochromatic $(J-K)_0^{mono}$ and $(H-K)_0^{mono}$, and Rosslowe & Crowther (2015a) for $(J-K_s)_0$ and $(H-K_s)_0$.

WR subtype	PoWR model	$\log(T/k)$	$\log(R_t)$	$(b-v)_0^{WR}$	$(J-K_s)_0$	$(H-K_s)_0$	$(J-K)_0^{mono}$	$(H-K)_0^{mono}$
WN3-4	WNE 12-11	4.95	1.0	−0.32±0.1	−0.11±0.1	−0.03±0.1	0.24	0.16
WN4b-7b	WNE 12-18	4.95	0.3	−0.18±0.1	0.37±0.1	0.27±0.1	0.63	0.40
WN5-6	WNE 08-11	4.75	1.0	−0.28±0.1	0.18±0.1	0.16±0.1	0.30	0.20
WN7-9	WNL 06-13	4.65	0.8	−0.15±0.1	0.13±0.1	0.11±0.1	0.30	0.18
WN6ha	WNL 07-07	4.70	1.4	−0.33±0.1	−0.015±0.1	0.03±0.1	0.00	0.00
WN7ha	WNL 07-07	4.70	1.4	−0.33±0.1	−0.04±0.1	0.01±0.1	0.00	0.00
WN8-9ha	WNL 05-07	4.60	1.4	−0.32±0.1	−0.04±0.1	0.01±0.1	0.01	0.00
Of/WN	WNL 07-06	4.65	1.5	−0.34±0.1	−0.11±0.1	−0.07±0.1	−0.04	−0.03
WO2-3	WC 17-12	5.20	0.9	−0.37±0.1	0.11±0.1	0.00±0.1	0.20	0.11
WC4-7	WC 11-16	4.90	0.5	−0.20±0.2	0.62±0.1	0.58±0.2	0.54	0.33
WC8	WC 09-14	4.80	0.7	−0.37±0.1	0.43±0.1	0.38±0.1	0.38	0.21
WC9	WC 06-12	4.65	0.9	−0.32±0.1	0.23±0.1	0.26±0.1	0.12	0.09
WN/WC				−0.23±0.1	0.37±0.1	0.27±0.1		

2.4 Absolute magnitudes

In addition to the *Gaia* data quality flags, we checked the validity of the distance results by calculating absolute magnitudes in the v^{WR}- band (Smith, 1968b)[3] (designed to avoid WR emission lines, as discussed in the introduction), and the K_s band. As part of this, we calculated extinction using intrinsic colours and an adopted extinction law. The result was then combined with distances and apparent magnitudes to obtain absolute magnitudes.

2.4.1 Intrinsic colours for single stars

Intrinsic optical colours were taken from PoWR grids (Hamann & Gräfener 2004 and Todt et al. 2015 for WN, Sander et al. 2012 for WC), for single stars in the v^{WR} band (see Table 2.1). The exception is for WN/WC stars, as the value $(b-v)_0^{WR} = -0.23$ is averaged from the $E(b-v)^{WR}$ values of Sander et al. (2012) and the b^{WR} and v^{WR} apparent magnitudes of each star. Intrinsic colours for the J, H and K_s bands are taken from Rosslowe & Crowther (2015a), with monochromatic near-IR PoWR synthetic colours also included.

2.4.2 Intrinsic colours for binary systems

16% (61 stars) of our WR sample were classified as binaries. For these systems, we calculated absolute magnitudes in the same manner as single stars, but included the companion in the intrinsic colour by measuring the dilution of the strongest optical emission lines. These are HeII 4686Å for WN stars, and CIV 5808Å and CIII 5696Å for WC stars. We fit the relation of the equivalent width to subtype for single stars (see Figs 2.15–2.16), to obtain the equivalent width of a 'typical' single star with a particular subtype.

For WC stars, we used CIV 5808Å to obtain the typical equivalent width of a single WR star with subtype 4, 5 or 6. In subtypes 8 and 9, the dominant line is instead CIII 5696Å . The fractions for WC7, which can contain either line, were the average dilution of the two. The fractional contribution of the WR's visible light ($\frac{F_{WR}}{F_{sys}}$) to the binary was then found using:

$$\frac{F_{WR}}{F_{sys}} = \frac{EW_b}{EW_s} \tag{2.9}$$

[3] A 'WR' superscript is added to distinguish the Smith v filter from the standard Johnson V-band filter

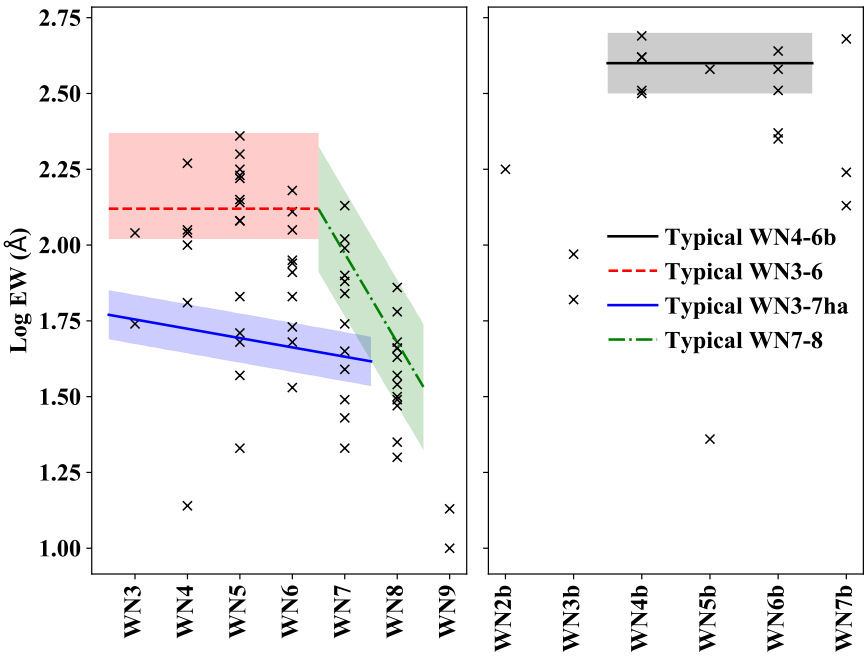

Figure 2.15: WN stars with HeII 4686Å equivalent widths from Conti & Massey (1989) and Smith et al. (1996). The lines show the equivalent width for a typical single WN star at each subtype. The shaded regions should contain only single stars.

where EW_b is the WR equivalent width for the binary and EW_s is the equivalent width for a single star. We summed the intrinsic colour of each component, weighted by contribution fraction, to obtain the colour for the system.

WR stars contribute a higher fraction of the continuum flux to the binary at near-IR wavelengths with respect to the visual (see Table 2.2). To illustrate this, we compare template spectra from WR stars of different subtypes to an O star from a Kurucz ATLAS model ($T_{\rm eff}$ = 37500K and $\log g$ = 5). Each template spectrum is set to the same V-band continuum flux. The fraction of light contributed by the template O star at IR wavelengths can then be calculated. We use this to obtain the intrinsic colours of the binary in the same way as optical wavelength colours.

For WR11, we used the light ratio derived in De Marco et al. (2000) and for WR104, we used the ratio from Williams & van der Hucht (2000). For WR30a, we estimated the fraction of light contributed by the WR was 10%, based on the emission line strength of similar WO4 star BAT99-123 (Br93, Sand 2). For WR64-4, we used the HeII 1.16μm, 1.69μm and 2.19μm IR lines to find contribution ratios, as no optical data were available. For WR35a, a reverse approach was followed based on the absolute magnitude of the system and assuming an absolute V magnitude for the O8.5V companion (from Martins

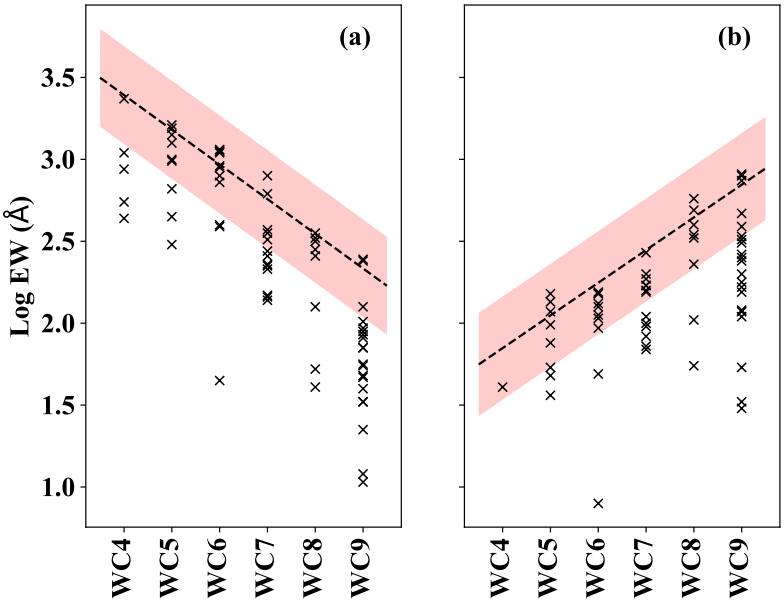

Figure 2.16: Equivalent widths of (a) C IV 5808Å and (b) C III 5696Å from Torres et al. (1986), Conti & Massey (1989), Smith et al. (1990), Cohen et al. (1991), Mauerhan et al. (2009) and Zhekov et al. (2014) showing the relation between line strengths and spectral types for both single and binary stars. The dashed line shows the equivalent width for a typical single WC star at each subtype. The shaded region is the one sigma standard deviation and should contain only single stars.

& Plez 2006b), to calculate the absolute magnitude of the WR component.

2.4.3 Optical and IR extinctions

We calculate dust extinctions using the intrinsic colours (Table 2.1) and apparent magnitudes in the v^{WR} band taken from the Galactic Wolf-Rayet catalogue, which was primarily compiled from van der Hucht (2001) and Torres-Dodgen & Massey (1988). J, H and K_s band magnitudes were primarily sourced from the 2MASS catalogue. The K_s band extinction, A_{Ks}, was calculated using the standard extinction law $A_{Ks} = 0.107A_v^{WR}$ (obtained from $A_{Ks} = 0.118A_V$ from Cardelli et al. 1989 and $A_v^{WR} = 1.1A_V$ from Turner 1982), if values of A_v^{WR} were available.

Though we have used the standard Cardelli et al. 1989 extinction law, we note that a range of possible alternatives are available. For instance, Fitzpatrick & Massa (2009) find a variable law for near IR wavelengths and Maíz Apellániz & Barbá (2018) derive a law based on Galactic O stars. Use of different laws somewhat changes our absolute

Table 2.2: The relative continuum flux contribution of WR stars to O-type companions at near-IR wavelengths for various subtypes, adopting a Kurucz ATLAS O star model with $T_{\rm eff} = 37500$K and $\log g = 5$ for the companion, assuming each contribute 50% of the V-band continuum flux.

WR subtypes	F_{WR}/F_0			
	V	J	H	K
WNE-w	1	1.33	1.56	1.94
WNE-s	1	2.45	3.35	4.56
WN6ha	1	1.22	1.38	1.63
WN8	1	2.03	2.70	3.55
WN9	1	1.33	1.5	1.78
Of/WN	1	1.17	1.22	1.33
WC4-5	1	2.03	2.57	3.55
WC6-7	1	1.94	2.45	3.35
WC8	1	1.86	2.23	3.00
WC9	1	1.70	2.13	2.57

magnitude results. For a WR star with $A_v^{WR} = 10$ (one of the largest extinctions in our WR sample), the extinction law from Cardelli et al. 1989 gives $A_{Ks} = 1.07$, but using the much steeper law from Wang & Chen (2019) leads instead to $A_{Ks} = 0.605$. For most stars, this difference should be within the typical uncertainty $\pm 0.2-0.7$ for an individual absolute magnitude.

If A_v^{WR} was unavailable, A_{Ks} was calculated with the relations of A_H and A_J to A_{Ks} (using parameters from Fritz et al. 2011 towards the Galactic Centre and Stead & Hoare 2009 elsewhere, as in Rosslowe & Crowther 2015a).

For WR25, known to have an anomalous extinction curve, we calculated A_v^{WR} using $R_v^{WR} = 6.2$ from Crowther et al. (1995).

Since dust extinction preferentially attenuates blue wavelengths, the *Gaia* $G_{BP}-G_{RP}$ can be used as a proxy for extinction. Some stars had unusually high K_s band extinctions (possibly due to incorrect photometry), which led to erroneous absolute magnitudes. Figure 2.17(a) shows the relationship between $(G_{BP}-G_{RP})$ and A_{Ks}, while Fig 2.17(b) compares $(G_{BP}-G_{RP})$ and A_v^{WR}. The erroneously high K_s extinctions are not shown on Figure 2.17, but the region of stars with low A_{Ks} corresponds to results where the Cardelli et al. 1989 extinction law was not applied (as A_v^{WR} was unavailable) and the relations of A_H and A_J to A_{Ks} were used instead. A 5σ (grey dashed lines) cut-off from the line of best fit (black solid line) was used to exclude incorrect extinctions. Some values of A_v^{WR} were also excluded for being outliers, indicating an issue either with some

Table 2.3: Conversion equations between narrowband v^{WR} and *Gaia* G band filters for $(G_{BP} - G_{RP})_0$ of different spectral types, using results from Carrasco & Jordi (valid for $A_v < 12$).

WR class	$(G_{BP} - G_{RP})_0$	A_v^{WR} to A_G
WNE-w	−0.421	$-0.0169{A_v}^2+0.894A_v$
WNE-s	−0.136	$-0.0159{A_v}^2+0.871A_v$
WN6ha	−0.406	$-0.0166{A_v}^2+0.891A_v$
WN8	−0.163	$-0.0157{A_v}^2+0.868A_v$
WN9	−0.359	$-0.0163{A_v}^2+0.886A_v$
WC5	−0.619	$-0.0178{A_v}^2+0.933A_v$
WC7	−0.479	$-0.0182{A_v}^2+0.921A_v$
WC8	−0.360	$-0.0178{A_v}^2+0.901A_v$
WC9	−0.159	$-0.0156{A_v}^2+0.870A_v$
B0V SED	−0.430	

photometry or the $G_{BP} - G_{RP}$ magnitudes.

We chose to use the model data as it allowed us to exclude results clearly far outside the typical mean and scatter, whilst not excluding points which may be a product of the A_H and A_J to A_{Ks} conversion. We found that this exclusion method, using the 5σ cutoff was best for excluding values in both the A_{Ks} and A_v^{WR} bands.

To obtain meaningful results at low $G_{BP} - G_{RP}$ (where we have no observations) we ensure that the extinction is zero at the intrinsic colour, $(G_{BP} - G_{RP})_0$. We obtain $(G_{BP} - G_{RP})_0$ for a generic blue energy distribution, namely a B0 V spectral type, with $V - I$=−0.44 in the Johnson filter (Ducati et al., 2001). We transform this relation to the Cousins system (Bessell, 1979) and finally to $(G_{BP} - G_{RP})_0 = -0.43$, using the $V - I$ to $G_{BP} - G_{RP}$ calibration in Evans et al. (2018).

Carrasco & Jordi (priv. comm) (using methodology from Jordi et al. 2010) provide the transformation from A_V to A_G by artificially reddening template PoWR WR spectra with different extinctions (from $A_V \sim 0.5$ to 36 mag). Synthetic photometry for the *Gaia* (Maíz Apellániz & Weiler, 2018) passbands was then obtained at each A_V. This allowed for the calculation of $E(G_{BP} - G_{RP})$ and A_G. The results from Carrasco & Jordi allow us to find the intrinsic colour $(G_{BP} - G_{RP})_0$ for each WR subtype. The generic B0 V model we have used to calculate $(G_{BP} - G_{RP})_0$, is within the uncertainty of the average WR value $(G_{BP} - G_{RP})_0 = -0.35 \pm 0.14$ of the subtypes in Table 2.3.

For the K_s band, we obtain the $G_{BP} - G_{RP}$ to A_{Ks} relationship using data with $G_{BP} - G_{RP} < 3$. This is the regime in which A_{Ks} follows the extinction law, as these stars are also observed in the v^{WR} band. At higher $G_{BP} - G_{RP}$, the calculated extinction

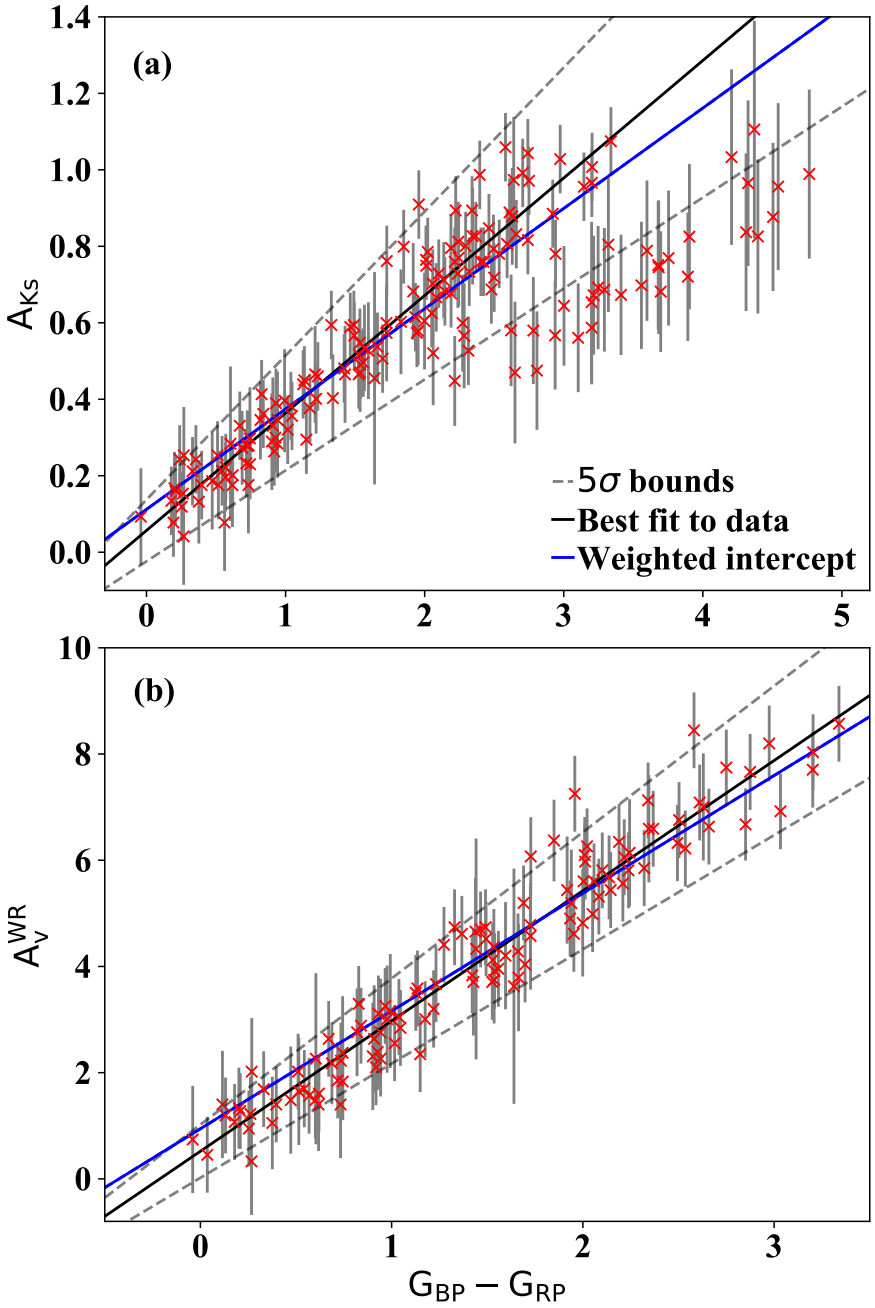

Figure 2.17: *Gaia* $G_{BP} - G_{RP}$ colours for Galactic WR stars compared to (a) K_s-band and (b) v^{WR} band extinctions. In (a), the solid black line presents the best fit to data with $G_{BP} - G_{RP}$ <3 while in (b), the solid line is a best fit to all data. The grey dashed lines are the 5σ bounds, based on the uncertainties of the fit parameters. The solid blue line is also the best fit to the data, but weighted so that it passes through $A_v^{WR} = A_{Ks}$=0 at $(G_{BP} - G_{RP})_0 = -0.43$, as expected for a generic B0 V star.

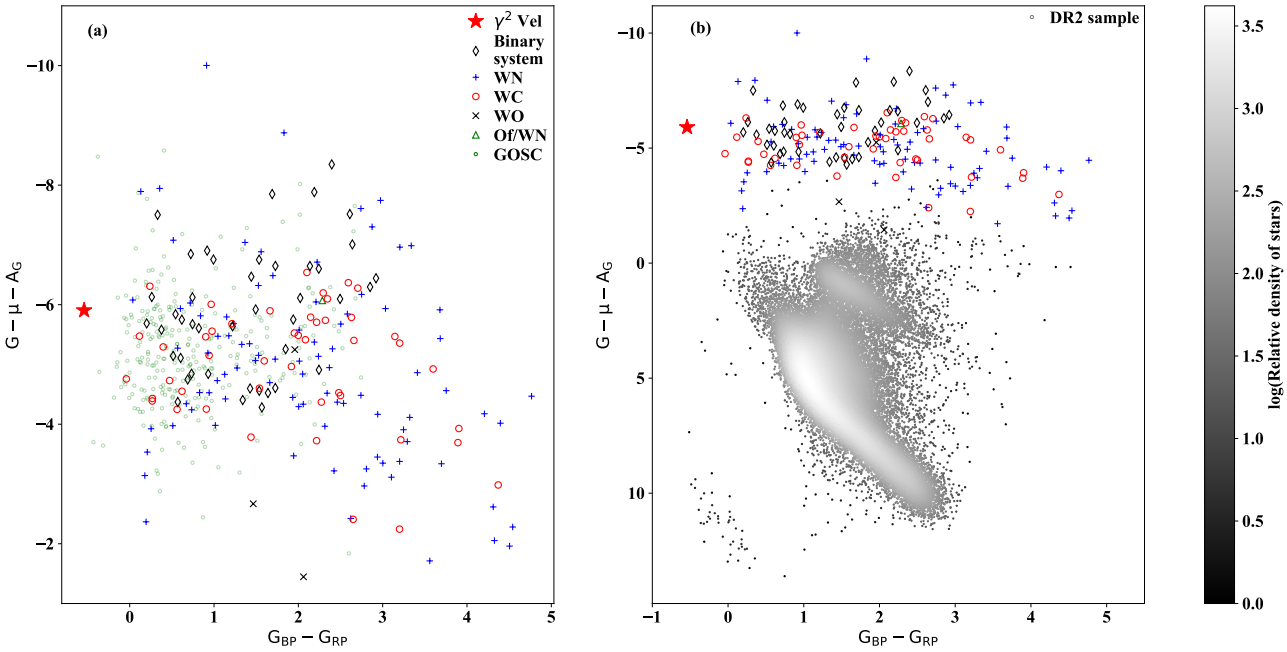

Figure 2.18: (a) *Gaia* DR2 colour magnitude diagram for Galactic WR stars plus O stars from GOSC (v4.1, Maíz Apellániz et al. 2013). Absolute magnitudes are calculated using our inferred distance moduli μ and A_G (converted from $A_v^{\rm WR}$ using the relation from Carrasco & Jordi). The red star is the WR component of γ Velorum, the only WR star with a trigonometric parallax from *Hipparcos*; (b) *Gaia* DR2 colour magnitude diagram for Galactic WR stars plus 70,000 stars from DR2, satisfying the selection criteria from section 2.1 of Gaia Collaboration et al. (2018b).

begins to deviate from this relationship. The empirical fit is shown in blue in Figure 2.17(a) and has the form:

$$A = X(G_{BP} - G_{RP}) + Y \tag{2.10}$$

where $G_{BP} - G_{RP}$ is the value from the *Gaia* catalogue, X=0.2250 and Y=0.0961. The $v^{\rm WR}$ band, shown in Figure 2.17(b), was much more closely grouped around the line of best fit, with X=2.217 and Y=0.9436. The gradient is 9.85 times the gradient for the K_s band. This is slightly larger than the $A_{Ks} = A_v^{WR}/9.35$ extinction law used to calculate values of A_{Ks} with A_v^{WR}. The deviation reflects the fact that some values of A_{Ks} were not calculated using that extinction law.

We can also use the synthetic photometry from Carrasco & Jordi to calculate the conversion relationship from A_v^{WR} to A_G (also shown in Table 2.3), by converting A_V in

their relationship to A_v^{WR}. This enables us to calculate the absolute *Gaia* G magnitude and present the *Gaia* colour magnitude diagram (CMD) in Figure 2.18, for the most reliable WR results. Fig. 2.18(a) presents a CMD for Galactic WR stars plus visually bright O stars from v4.1 of the Galactic O Star Catalogue (GOSC, Maíz Apellániz et al. 2013), while Fig. 2.18(b) compares the CMD of WR stars to 70,000 DR2 stars from Gaia Collaboration et al. (2018b). Two exceptionally bright stars are the extreme hypergiants He 3-519 (WR31a) and AG Car (WR31b), which exhibit very late WN characteristics at extreme visual minima (Smith et al., 1994).

2.4.4 Bootstrapping and fits to absolute magnitudes

We used the extinctions, distances and apparent magnitudes to calculate the absolute magnitudes for stars that have reliable extinctions (within the 5σ bounds of Figure 2.17). Repeating the calculation using a Monte Carlo selection (bootstrapping with replacement) from the distributions of the three parameters, produced a binned histogram of absolute magnitude against frequency. This acted as a proxy for the probability distribution of each absolute magnitude. A Gaussian or Weibull distribution was fit to the binned data, to find the most likely absolute magnitude and uncertainties.

For the bootstrapping procedure, we sample 1000 distributions of 20,000 points each (with replacement) from the true distributions of apparent magnitudes (assumed to be a Gaussian with the peak at the measured value and the standard deviation as the uncertainty), distances and extinction. This generated a distribution of absolute magnitudes which could be fitted with a Gaussian if the χ^2 value was below 0.005 (setting the limit below this value made it difficult to fit stars). Alternatively, if the χ^2 value was above 0.005, a Weibull distribution (non symmetric with left or right skew) was fitted instead

$$y = \frac{\gamma}{\lambda}\left(\frac{M_{range}}{\lambda}\right)^{(\gamma-1)} e^{-(M_{range}/\lambda)^{\gamma}} \tag{2.11}$$

where γ is the shape parameter, λ is the scale parameter and M_{range} is the range of absolute magnitude values over which the fit is made. As the Weibull distribution is only valid over a positive interval, we add a constant to transform the negative absolute magnitudes to positive values

$$M_{mod} = M_{range} + M_{max} + 0.1 \tag{2.12}$$

where M_{mod} is the transformed range and M_{max} is the maximum value in the fit

range.

Both distribution types were fitted using a least squares curve fit in the python SCIPY package. The most likely absolute magnitude was the average of the Gaussian, or the mode M_{mode} of the Weibull distribution, transformed back to negative values

$$M_{mode} = \lambda\left(\frac{\gamma - 1}{\gamma}\right)^{(1/\gamma)} - (M_{max} + 0.1) \tag{2.13}$$

Credible intervals were again used for 68% uncertainties on individual magnitudes. The typical variation between Monte Carlo runs (due to different data selections), was less than +/-0.05. In a small number of cases, the distribution fitting failed. In these instances, we calculated the point value of absolute magnitude, using the peaks of the distance, apparent magnitude and extinction probability curves. We decided not to use the 16th, 50th and 84th percentiles from the samples for a point estimate and uncertainty, due to random anomalies with sampling that appeared in some histograms. In these distributions, certain (random) bins showed significant 'spikes', indicating that a large number of points were placed in the same bin. This could potentially have skewed the percentile distribution and thus the calculated medians and uncertainties. Due to the non Gaussian nature of the distance distributions, however, there was some offset (usually on the scale of 0.1 mag) between the peaks fitted to full distributions and these point values.

An example of a Gaussian and a Weibull fit to WR18 in the v^{WR} and K_s band, is shown in Figure 2.19.

2.4.5 Absolute magnitudes for WR components of binaries

For binaries, the absolute magnitudes obtained using the bootstrapping procedure were the total system magnitudes. The magnitudes of the WR components therefore needed to be separated. To do this, we start with the calculation for the apparent magnitude of the system, m_{sys}

$$m_{sys} = -2.5 log_{10} F_{sys} + c \tag{2.14}$$

where F_{sys} is the total flux from the system and c is a constant. Similarly, the apparent magnitude for the individual WR star, m_{WR}, is

$$m_{WR} = -2.5 log_{10} F_{WR} + c \tag{2.15}$$

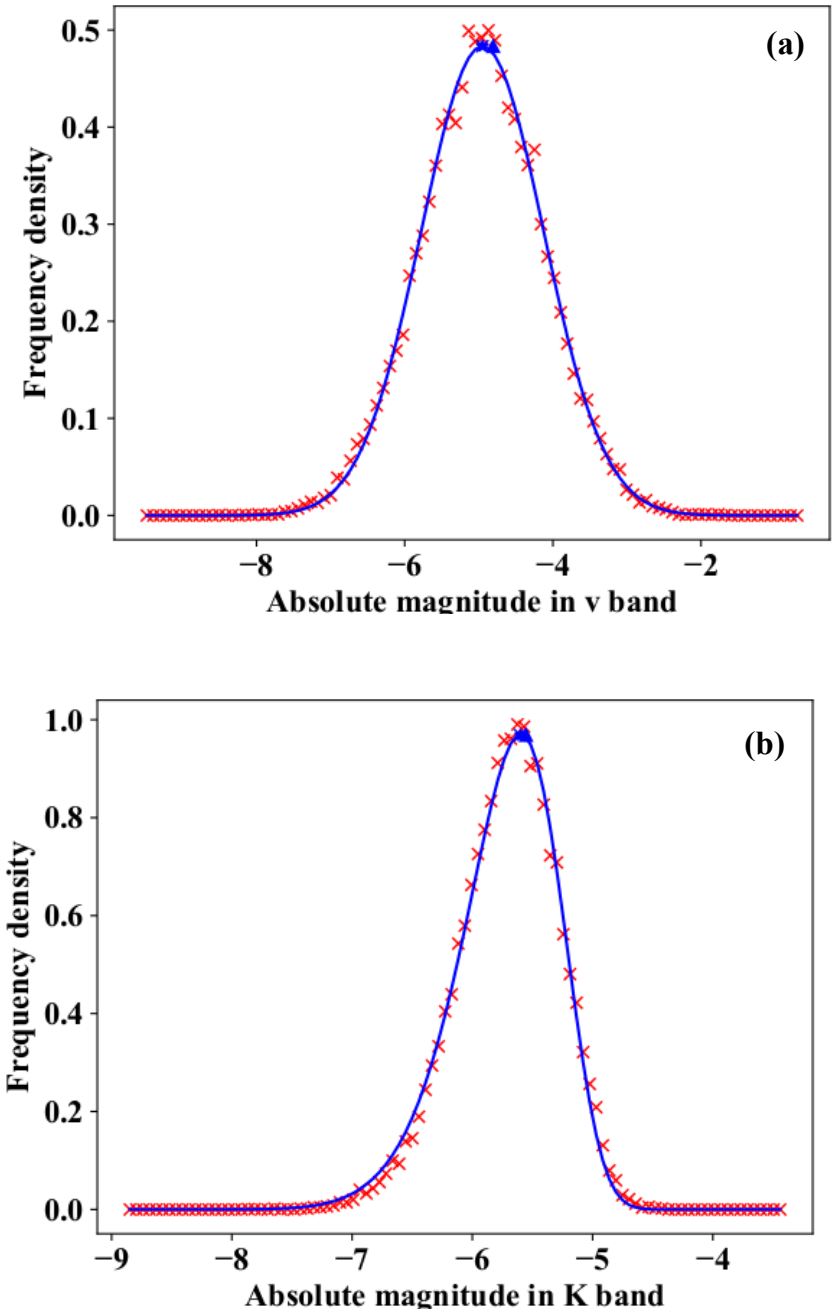

Figure 2.19: Fits to 20,000 binned absolute magnitudes from a Monte Carlo selection of distance, apparent magnitude and extinction distributions for WR18. The red crosses are the centre of each bin. The triangle is the point value calculated by taking the most likely distances, apparent magnitudes and extinctions. (a) is a Gaussian fit to the v^{WR} band distribution and (b) is a Weibull distribution fit to the K_s selected distribution.

where F_{WR} is the WR flux in the binary and again c is a constant. We can eliminate the constant c, using

$$m_{sys} - m_{WR} = -2.5log_{10}F_{sys} + 2.5log_{10}F_{WR} \tag{2.16}$$

which is equal to

$$m_{WR} = m_{sys} - 2.5log_{10}\frac{F_{WR}}{F_{sys}} \tag{2.17}$$

where $\frac{F_{WR}}{F_{sys}}$ is equal to the fractional contribution of the WR's visible light to the binary, as calculated in Equation 2.9 of Section 2.4.2. We can convert the apparent magnitudes to absolute magnitudes, M_{WR} and M_{sys}, using their distances d and extinctions A

$$M_{WR} = m_{WR} - 5(log_{10}(d) - 1) - A \tag{2.18}$$

$$M_{sys} = m_{sys} - 5(log_{10}(d) - 1) - A \tag{2.19}$$

As the system and its WR star component have the same distance and extinction, Equation 2.17 simplifies to

$$M_{WR} = M_{sys} - 2.5log_{10}\frac{F_{WR}}{F_{sys}} \tag{2.20}$$

2.4.6 Average absolute magnitudes for WR subtypes

After obtaining absolute magnitudes for individual WR stars, we calculate updated absolute magnitude calibrations for all subtypes of WR stars, using a multi step process of sigma clipping.

First, stars with high astrometric excess noise, or unrealistically low absolute magnitudes (≥ -1 mag) were removed from the sample. We then calculated the averages of the remaining stars in each subtype class. Stars with unusually high or low absolute magnitudes (defined as were greater than one sample standard deviation, from the mean) were then cut from the sample. This cut-off provided a good balance between excluding clearly incorrect values and including valid ones across all subtypes.

The remaining sample contained only the most reliable absolute magnitude results in each subclass and were used to calculate the averages presented in the results chapter.

2.4.7 Photometric Flags

In addition to the *Gaia* flag, we identify results with potentially spurious absolute magnitudes. As stars with incorrect extinctions were removed, spurious results can indicate either incorrect apparent magnitudes, or an incorrect *Gaia* parallax, whose distance generates the wrong absolute magnitude. We therefore adopt two different flags, one where the absolute magnitude is implausible and another where the absolute magnitude only just falls outside the uncertainty of the subtype average. The latter does not necessarily indicate a bad result, but these data should be treated with caution.

M >upper$_{initial}$ or M <lower$_{initial}$ = b

M >upper$_{final}$ or M < lower$_{final}$ = b:

where upper and lower are the upper and lower magnitude bounds of the absolute magnitude average. $_{initial}$ denotes the averages calculated before sigma clipping (Section 2.4), $_{final}$ are the final absolute magnitude boundaries (as in Table 3.1) and M is the absolute magnitude of individual WR stars. Results with a 'b' flag are highly implausible and lie well outside the range of acceptable absolute magnitudes, whilst those with a 'b:' flag are still acceptable, but fall outside the 1σ uncertainties of the results in Table 3.1. Again, results without any of these issues are given the 'g' flag. Results without any absolute magnitudes are flagged with 'u'. These stars were included to provide the reader with the distance moduli of the stars and any other helpful information (e.g apparent magnitudes), if their absolute magnitudes could not be calculated.

For all subsequent analysis we use only the most photometrically reliable results, which have a 'b:' or 'g' flag in either the v^{WR} band, or the K_s band. These data do not have high astrometric excess noise ('a') Gaia data quality flags. Results with, for example, two 'b' flags were excluded. These flags are applied to the absolute magnitudes in Table A.2 and A.3.

We note that 13 objects retained in this selection process had either negative parallax ('n') or high error to parallax ratio ('e') *Gaia* flags.

2.5 Summary

We have introduced the process used to obtain the parallaxes of Galactic WR stars from the *Gaia* DR2 catalogue, and the Bayesian method used to calculate their distances. We use Bayesian methods to properly transform the parallax uncertainties to distance uncertainties and to obtain distances from negative parallaxes. Our Bayesian prior accounts for extinction using a Galactic dust model and the specific distribution of massive stars

using H II regions. Potential underestimates of parallax uncertainties and the zero point error are accounted for in our calculation. We also show that these distances can be used to determine their absolute magnitudes, via a Monte Carlo bootstrapping procedure.

In the Chapter 3, we present the distances and absolute magnitudes obtained and determine possible runaways using the distances from the Galactic plane.

Chapter 3

Gaia DR2 Results

The content of this chapter is taken from the publication Rate & Crowther (2020). My supervisor Paul Crowther, produced the comparison to Green et al. (2015) and the luminosity rescaling in Table 1.

In Chapter 2, we outlined the Bayesian methods used to transform *Gaia* DR2 parallaxes into distances and the Monte Carlo method used to obtain absolute magnitudes. Here, we present the results and an assessment of the vertical distances of WR stars from the Galactic plane.

In Section 3.1, we discuss the absolute magnitudes in both v^{WR} and K_s bands for individual stars, and averages for subtypes. Then in Section 3.2, we present the new distances and compare these to alternatives (also found using *Gaia*), and previous results.

The new distances are used in Section 3.3 to compile a list of potential WR star runaways, based on their distances from the Galactic plane. We additionally discuss why we did not use our results to calculate WR star parameters like luminosities and masses in Section 3.4. Finally, Section 3.5 presents the conclusions of these chapters on *Gaia* and outlines how the results will be used in future chapters.

3.1 Absolute magnitudes

Absolute K_s band magnitudes and uncertainties for each subtype are shown in Figure 3.1. These are compared with corresponding values from Rosslowe & Crowther (2015a), who also calculated absolute magnitudes for 126 stars using their apparent magnitudes and intrinsic colours from Crowther et al. (2006a) (with unpublished WO models). The distances for most of these stars were obtained from their host cluster or association. A minority were isolated and instead kinematic distances were derived from their associated

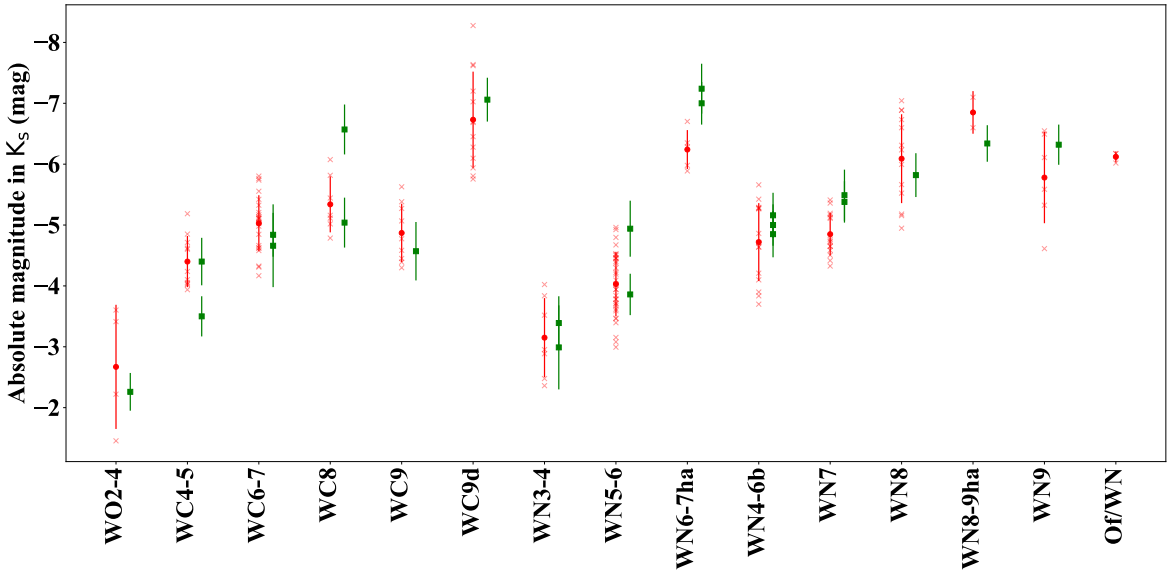

Figure 3.1: Absolute magnitudes in the K_s band. Red crosses are individual WR star results (remaining after sigma clipping) and the red circle is the average for each spectral subtype (with the sample standard deviation of the data as the uncertainties). Green squares are the comparative data from Rosslowe & Crowther (2015a), also with the sample standard deviation of the weighted mean shown.

nebula.

Figure 3.2 shows the same distribution for the v^{WR} band, compared with van der Hucht (2001) and Tables A.2 and A.3 in Appendix A.2 give details on the results for individual stars.

We additionally plot the absolute magnitudes for 116 LMC stars in Figure 3.2, using results from Hainich et al. (2014) for single WN and Of supergiant stars (excluding WN2b), Shenar et al. (2019) for stars in binaries, Crowther et al. (2002) for single WC stars and reddenings from Tramper et al. (2015) and v^{WR} band magnitudes from Torres-Dodgen & Massey (1988) for BAT99-123 (WO4). We adopt spectral types of LMC late WN stars from Crowther & Smith (1997) instead of Schnurr et al. (2008).

From Figure 3.2, absolute v^{WR} magnitudes of LMC stars are often brighter than their Galactic analogues, so it is inappropriate to apply LMC WR absolute magnitudes to Galactic stars. LMC WN5–6 stars are particularly bright, since this sample includes the luminous H-rich main sequence WN5–6h stars whose closest Galactic analogues are WN6–7ha stars, which are amongst the visually brightest WR stars in the Milky Way.

In total, realistic absolute magnitudes, extinctions and no *Gaia* excess noise flags, were obtained in 187 cases. Absolute magnitudes for almost all WR subtypes revealed

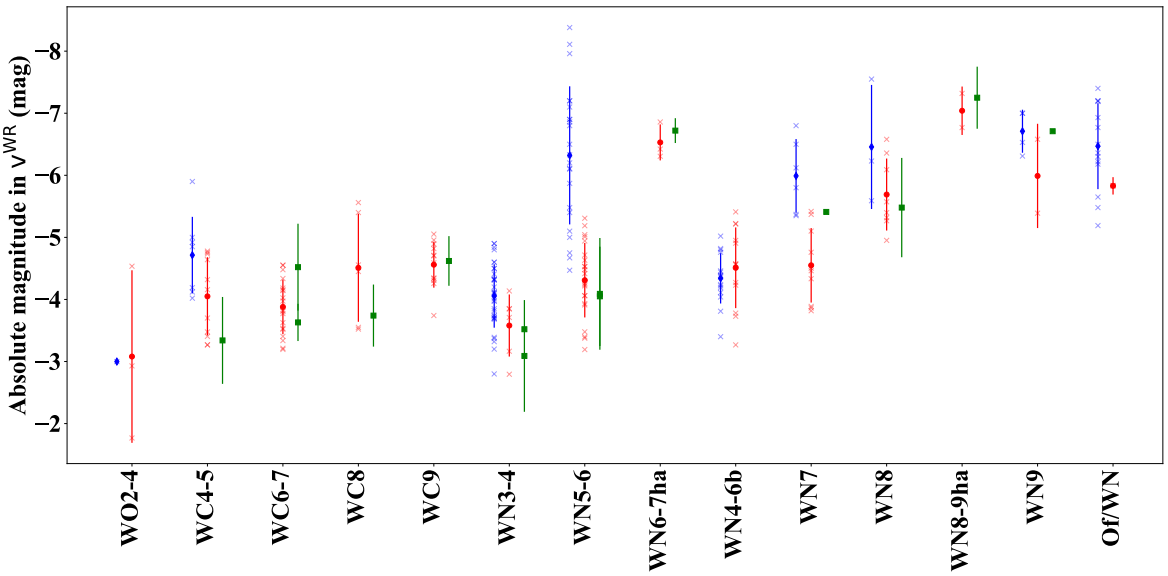

Figure 3.2: Absolute magnitudes in the v^{WR} band. Red crosses are individual WR star results (again, for the stars remaining after sigma clipping) and the red circle is the average for each spectral subtype (with the sample standard deviation of the data as the uncertainties). Green squares are the comparative data from van der Hucht (2001) and sample standard deviation for those results. Results from the LMC (Hainich et al. 2014, Shenar et al. 2019 and Crowther et al. 2002) are shown in blue, with crosses for individual stars and the diamond the average for each subtype. LMC WN5-6 stars include very luminous H-rich main sequence WN5–6h stars. Results for WO were calculated using Tramper et al. (2015) and Torres-Dodgen & Massey (1988)

standard deviations that overlapped with the uncertainty range of the previous results in both the v^{WR} and the K_s bands. The differences between values can be attributed to the improved distance estimates and the increased number of stars with distances. Some stars, such as WR2 (the only WN2 star, Chené et al. 2019), were not present in the *Gaia* catalogue.

There is a clear trend across both filters of increasing absolute magnitudes with increasing subtype. In both filters, WN4-6b are brighter than their weak-lined counterparts (Hamann et al., 2006) and WNLha stars are known to be highly luminous, and conform to this expectation.

The spread in absolute magnitudes is similar to those previously obtained in the near-IR, but slightly larger in the v^{WR} band. Rosslowe & Crowther (2015a) quote a range of 0.3-0.6 mag, whilst the standard deviation in our K_s band results spans 0.1-1.0 mag, but is also more typically 0.3-0.6 mag. For the v^{WR} band, the standard deviations range from 0.3-1.4 mag, though most standard deviations are between 0.4-0.6 mag.

We therefore corroborate the findings of Sander et al. (2019) that WC stars of the same subtype have a broader range of absolute magnitudes than expected. We also posit this is true for WN stars (Hamann et al. 2019 also note the relations between absolute magnitude and subtype are not strict). The uncertainties show no systematic differences between WC and WN classes or regular variation across subtypes. However, particularly in the v^{WR} band, some classes suffered from very small numbers of WR stars (only 2 WN9 stars had v^{WR} band magnitudes, for instance). This increases the size of the uncertainties on the mean result.

Due to this intrinsic variation, we advise caution when using averages as absolute magnitude calibrations and recommend accounting for the large uncertainties by exploring other methods, such as a Bayesian approach with a probability distribution centred on the average magnitude. We also recommend continued use of the intrinsic colours in Table 2.1, rather than calculating new values using our methods and results. The large uncertainties of our absolute magnitudes, mean that propagated uncertainties of any resulting intrinsic colours are correspondingly large. These new uncertainties are far larger than those in the intrinsic colours from Table 2.1.

We also present the average absolute magnitudes in Table 3.1. WR20-2, WR42-1, WR43-2 and WR43-3 were excluded from the averages, owing to uncertain subtypes.

We obtain K_s band results for dusty subtypes (WC8d and WC9d) by converting A_v^{WR} to A_{Ks}, using the standard extinction law (as v^{WR} band data is free of significant dust emission). This method prevents the IR dust emission from contaminating the extinction calculation. The absolute magnitudes could then be calculated for each subtype and in each filter, with the standard deviation providing upper and lower bounds on the typical absolute magnitudes. The WC9d were combined with WC9 in the v^{WR} band, but not in the K_s band, as their IR excess renders them brighter than dust free WR stars. As there were only three WC8d (WR48a, WR53 and WR113) in the final sample, these stars were grouped with the non dusty WC8 stars and only WR113 was used to calculate the final absolute K_s in Table 3.1. Excluding WR113 from the average, we obtain M_{Ks}=–5.3 mag for WC8 stars, the same result as Table 3.1.

3.1.1 Sensitivity of results to adopted intrinsic colours

We test the sensitivity of the results to the intrinsic colours. For the v^{WR} band, this is straightforward in that any difference in $(b-v)_0^{WR}$ is propagated through to the extinction. According to Turner (1982), A_v^{WR}=4.12E$(b-v)^{WR}$. So as $(b-v)^{WR}$ remains the same, the difference in $(b-v)_0^{WR}$ can be multiplied by 4.12, to give the difference

Table 3.1: Mean absolute magnitudes for Galactic Wolf-Rayet subtypes in v^{WR} and K_s band filters. In the v^{WR} band, the WC9d sample has been combined with non dusty WC9 stars.

WR subtypes	$M_{v^{WR}}$ (mag)	N(v^{WR})	M_{Ks} (mag)	N(K_s)
WN3-4	-3.6 ± 0.5	6	-3.1 ± 0.6	7
WN5-6	-4.3 ± 0.6	22	-4.0 ± 0.5	33
WN6-7ha	-6.5 ± 0.3	3	-6.2 ± 0.3	5
WN4-6b	-4.5 ± 0.6	13	-4.6 ± 0.7	15
WN7	-4.6 ± 0.6	10	-4.8 ± 0.3	15
WN8	-5.7 ± 0.6	8	-6.0 ± 0.8	13
WN8-9ha	-7.0 ± 0.4	2	-6.8 ± 0.4	2
WN9	-6.0 ± 0.8	2	-5.7 ± 0.7	6
Of/WN	-5.8 ± 0.1	2	-6.1 ± 0.1	3
WO2-4	-3.1 ± 1.4	3	-2.6 ± 1.0	4
WC4-5	-4.1 ± 0.6	11	-4.3 ± 0.4	11
WC6-7	-3.9 ± 0.4	19	-4.9 ± 0.4	22
WC8	-4.5 ± 0.9	6	-5.3 ± 0.5	7
WC9	-4.6 ± 0.4	12	-4.8 ± 0.5	9
WC9d			-6.6 ± 0.8	13

from the existing A_v^{WR}. However, within the K_s band, the combination of $(J-K_s)_0$ and $(H-K_s)_0$ complicates this somewhat and we test the effects by calculating M_{Ks} with alternative $J-K_s$ and $H-K_s$ synthetic colours. These are taken from the PoWR grids (Hamann & Gräfener 2004 and Todt et al. 2015 for WN, Sander et al. 2012 for WC), using the same models as Table 2.1. Unlike the $(b-v)^{WR}$ colours, these are only valid at the monochromatic wavelengths and not the whole filter bands, which are affected by emission lines, especially for early-type WC stars. The difference in absolute magnitudes are between 0.05 for WN5-6 and 0.2 for WC6-7 and WN2-4 (as emission lines fall within the filter band and are not included in the monochromatic result), with most subtypes falling between 0.1 and 0.2. In all instances, this was well within the uncertainties on individual magnitudes.

3.2 New distances to WR stars and comparison to other *Gaia* derived distances

We can compare the WR star sample from *Gaia* to the total population. There is no substantial difference between the latitude and longitude distribution of WR stars detected in *Gaia* and the total known WR distribution. The exception is for some regions, such as around Westerlund 1 and towards the Galactic Centre, which went undetected by *Gaia* due to their exceptionally high extinctions (with $A_V > 30$ mag in the latter case).

Crowding presented an additional challenge. WR 43A and 43B are not included in the final distance catalogue as the same *Gaia* source was detected for both stars. The detection for WR43C is also spurious, as the position overlaps with other objects. These stars are located in the compact cluster NGC 3603 (Melena et al. 2008, Crowther & Dessart 1998) and therefore blending is to be expected. It is possible that further stars are missing parallaxes due to crowding, as this issue would reduce the quality of the *Gaia* five parameter solution below acceptable limits, and cause it to be excluded from the *Gaia* catalogue.

Finally, some stars may not have been detected due to their close binary companions. Arenou et al. (2018) shows that completeness falls for separations below 2", to a limit at 0.12". This may account for three missing stars with narrowband $v^{WR} < 15$ mag (WR2, WR63 and WR86), two of which (WR63 and WR86) have known companions.

Table A.1 in Appendix A.1 includes distances for each WR star with measured parallaxes. Also included are the 68% credible intervals. Table 3.2 lists, in WR catalogue order, the closest WR stars (with reliable results) within 2 kpc of the Sun. We find 25 WR stars within this distance, similar to the 30 WR stars within 2 kpc from Conti et al. (1983). We also calculate distances to O stars using our Bayesian prior and GOSC v4.1 (Maíz Apellániz et al., 2013). For the O star population within 2 kpc, we obtain a WR/O ratio of 0.09. This ratio is within the 0.07–0.10 range of Conti et al. (1983), found by comparing lifetimes of H and He core burning phases from massive star models, as an analogue to O star and WR star phases. However, our ratio includes all O stars, and not just the most massive population that WR stars are descended from. Conti et al. (1983) also calculate a WR/O ratio with only O stars>40$M_\odot$, and find a much higher ratio of 0.36±0.15.

Table 3.2 also includes K_s-band extinctions, and extinctions per kpc for these nearby WR stars, with average A_{K_s}/kpc $\sim$ 0.26 mag, albeit with significant star-to-star varia-

tion. Dust extinctions of stars in common with the 3D dust map from Pan-STARRS1 and 2MASS Green et al. (2015) show reasonable overall agreement.

3.2.1 Comparison with previous WR distances

Rosslowe & Crowther (2015a) provide distance estimates for 228 Galactic WR stars based on previous absolute magnitude calibrations. Of those, 87 have reliable distances from this work. Fig. 3.3(a) compares distances to Galactic WR stars in common with Rosslowe & Crowther (2015a). Agreement is reasonable up to ∼2 kpc. This is the subset of *Gaia* sources with the lowest uncertainties and extinction, enabling accurate applications of our prior and absolute magnitude calibrations. Beyond 2 kpc, there is significant scatter, with many stars closer than previously thought. These are principally more highly reddened WR stars that have been discovered recently. Conversely many stars that were thought to be nearby based on calibrations, have significantly larger distances (e.g. WR57 is revised from 2.98±0.52 kpc to $5.50^{+1.49}_{-1.06}$ kpc).

All of our 187 stars with reliable absolute magnitudes have distance estimates from Bailer-Jones et al. (2018). Comparisons are presented in Figure 3.3(b). Again, good agreement is obtained up to ∼2 kpc, beyond which the Bailer-Jones et al. (2018) distances are generally larger than our results. The average σ_ω/ω for stars at distances beyond 2.5 kpc is −0.71. The error is therefore a substantial proportion of the total parallax, which suggests disparities stem primarily from limitations in the *Gaia* data and the differences between the two priors. At large distances and so proportionally large parallax errors, the prior dominates the data and the peak of the posterior shifts closer to the peak of the prior.

For this work, the peak of the prior probability defaults to <3 kpc, depending on longitude. If the peak in the Bailer-Jones prior is substantially closer or further, this results in a large divergence between the two measures. Our prior differs significantly from Bailer-Jones et al. (2018) as it more directly accounts for extinction and the specific distribution of massive stars. The red stars/black crosses in Figure 3.3(b) show the contrast between results calculated with/without the dust extinction model. In most instances, the stars had results more in line with Bailer-Jones et al. (2018) when dust was excluded. Therefore, in the vast majority of cases, dust extinction in the prior is the primary factor leading to different results.

Since distances from Bailer-Jones et al. (2018) formed the basis of the recent spectroscopic studies of Galactic WR stars by Sander et al. (2019) and Hamann et al. (2019), use of distances from this study (with no warning flags) would lead to generally modest 0.05

Table 3.2: WR stars within 2 kpc of the Sun, including colour excess, K_s-band extinction and A_{Ks}/kpc, extinction per kpc.

WR Number	Alias	Spectral type	Distance (kpc)	Flags	E(B-V)	A_{Ks}	A_{Ks}/kpc
WR11	γ Vel	WC8+O7.5III-V	$0.34^{+0.04}_{-0.03}$	...	0.00±0.30	0.00±0.11	$0.00^{+0.32}_{-0.32}$
WR25	HD 93162	O2.5If*/WN6+O	$1.97^{+0.18}_{-0.15}$	g	0.93±0.32	0.34±0.11	$0.17^{+0.06}_{-0.06}$
WR52	HD 115473	WC4	$1.75^{+0.16}_{-0.13}$	g	0.59±0.30	0.22±0.11	$0.12^{+0.06}_{-0.06}$
WR70-5	WM10 11b	WC9	$1.95^{+0.75}_{-0.47}$	g		1.26±0.26	$0.65^{+0.28}_{-0.21}$
WR78	HD 151932	WN7h	$1.25^{+0.15}_{-0.12}$	g	0.44±0.21	0.16±0.08	$0.13^{+0.06}_{-0.06}$
WR79	HR 6265	WC7+O5-8	$1.37^{+0.12}_{-0.10}$	g	0.31±0.26	0.11±0.09	$0.08^{+0.07}_{-0.07}$
WR85	HD 155603B	WN6h	$1.99^{+0.30}_{-0.24}$	g	1.03±0.21	0.37±0.08	$0.19^{+0.05}_{-0.04}$
WR90	HD 156385	WC7	$1.15^{+0.11}_{-0.09}$	g	0.10±0.30	0.04±0.11	$0.03^{+0.09}_{-0.03}$
WR93	Th10-19	WC7+O7-9	$1.76^{+0.19}_{-0.15}$	g	1.67±0.23	0.61±0.08	$0.34^{+0.06}_{-0.06}$
WR94	HD 158860	WN5o	$0.95^{+0.06}_{-0.06}$	g	1.24±0.21	0.45±0.08	$0.47^{+0.09}_{-0.08}$
WR98	HDE 318016	WN8o/C7	$1.96^{+0.31}_{-0.24}$	g	1.59±0.21	0.58±0.08	$0.29^{+0.06}_{-0.05}$
WR105	NS 4	WN9h	$1.73^{+0.32}_{-0.23}$	g	2.41±0.21	0.88±0.08	$0.51^{+0.10}_{-0.08}$
WR110	HD 165688	WN5-6b	$1.58^{+0.15}_{-0.12}$	g	1.13±0.21	0.41±0.08	$0.26^{+0.05}_{-0.05}$
WR111	HD 165763	WC5	$1.63^{+0.32}_{-0.23}$	g	0.22±0.30	0.08±0.11	$0.05^{+0.07}_{-0.05}$
WR113	HD 168206	WC8d+O8-9IV	$1.80^{+0.24}_{-0.19}$	g	0.94±0.21	0.34±0.08	$0.19^{+0.05}_{-0.05}$
WR113-2	SMG09 1425_47	WC5-6	$1.86^{+0.90}_{-0.56}$	g		0.65±0.21	$0.35^{+0.21}_{-0.16}$
WR133	HD 190918	WN5o+O9I	$1.85^{+0.16}_{-0.14}$	g	0.36±0.21	0.13±0.07	$0.07^{+0.04}_{-0.04}$
WR134	HD 191765	WN6b	$1.75^{+0.13}_{-0.11}$	g	0.46±0.21	0.17±0.08	$0.10^{+0.04}_{-0.04}$
WR135	HD 192103	WC8	$1.98^{+0.18}_{-0.15}$	g	0.41±0.21	0.15±0.08	$0.08^{+0.04}_{-0.04}$
WR139	HD 193576	WN5o+O6III-V	$1.31^{+0.07}_{-0.06}$	g	0.81±0.24	0.30±0.09	$0.23^{+0.07}_{-0.07}$
WR142	Sand 5	WO2	$1.65^{+0.11}_{-0.09}$	g	2.13±0.21	0.78±0.08	$0.47^{+0.06}_{-0.05}$
WR142a	PCG02 1	WC8	$1.81^{+0.61}_{-0.37}$	g		0.83±0.19	$0.46^{+0.19}_{-0.14}$
WR142-1	HBHalpha 4203-27	WN6o	$1.77^{+0.23}_{-0.18}$	g		0.69±0.16	$0.39^{+0.10}_{-0.10}$
WR144	HM19-1	WC4	$1.75^{+0.24}_{-0.19}$	g		0.47±0.19	$0.27^{+0.11}_{-0.11}$
WR145	AS 422	WN7o/CE+?	$1.46^{+0.12}_{-0.10}$	g	2.28±0.39	0.83±0.14	$0.57^{+0.11}_{-0.10}$

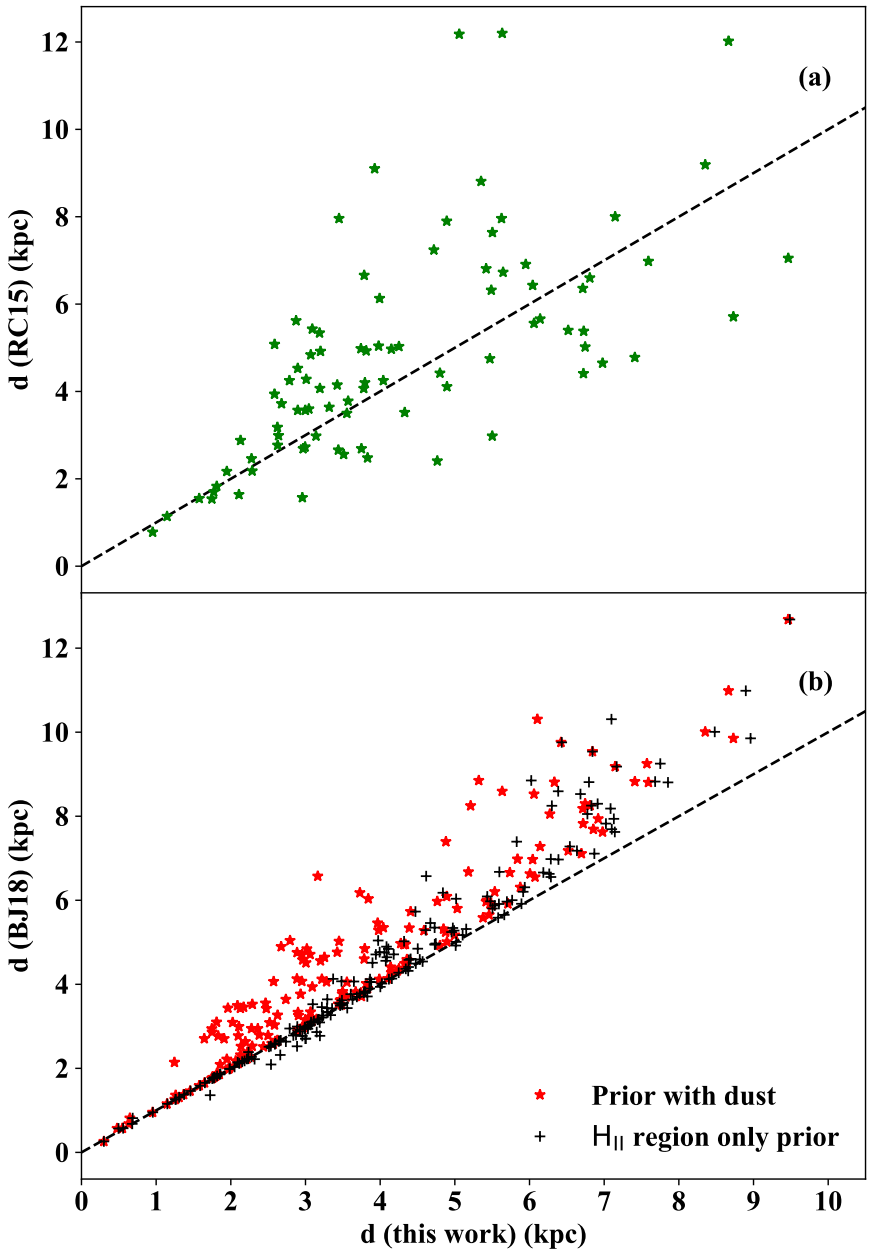

Figure 3.3: (a) A comparison between distances to Galactic WR stars in common between this work and Rosslowe & Crowther (2015a). The black dashed line indicates one-to-one agreement. Error bars from Rosslowe & Crowther (2015a) have been omitted for clarity; (b) A comparison between WR distances obtained in this work and Bailer-Jones et al. (2018). We illustrate the effect of extinction by presenting the full prior including both dust and H II regions (red stars) and a prior with only H II regions (black cross).

dex reductions in stellar luminosity. These are included in Table A.1, with higher reductions for relatively distant stars including WR74 (WN7o, 0.24 dex), WR91 (WN7b, 0.23 dex) ,WR56 (WC7, 0.20 dex) and WR64 (WC7, 0.20 dex).

We also compare the distances to a Galactic LBV (WR31b = AG Car) and LBV candidate (WR31a = He 3-519) which are in common with Smith et al. (2019). They obtain a distance of $7.12^{+2.53}_{-1.67}$ kpc to WR31a, versus $7.35^{+1.45}_{-1.18}$ kpc from this work, and $4.65^{+1.43}_{-0.92}$ kpc to WR31b, versus $4.85^{+0.93}_{-0.70}$ kpc from this work. These are well within the uncertainties of both stars, particularly given WR31a has a high error to parallax ratio of 0.72 (as measured directly from the catalogue values). Smith et al. (2019) adopt a different zero point to our study, namely -0.05 mas as an initial value and model some uncertainty in this as part of their calculation. This decision is based on the variety of different zero points found in the literature (e.g Riess et al. 2018, Zinn et al. 2019, Stassun & Torres 2018 and Graczyk et al. 2019).

Therefore, the Smith et al. (2019) distances are systematically closer than those from Bailer-Jones et al. (2018). This result agrees both with our findings and Schönrich et al. (2019), who also find that Bailer-Jones et al. (2018) appear to systematically overestimate distances. As Smith et al. (2019) adopts a similar prior to that of Bailer-Jones et al. (2018), the overlapping results therefore indicate that the larger zero point is performing much the same function as our dust model, acting to moderate the distances of Bailer-Jones et al. (2018).

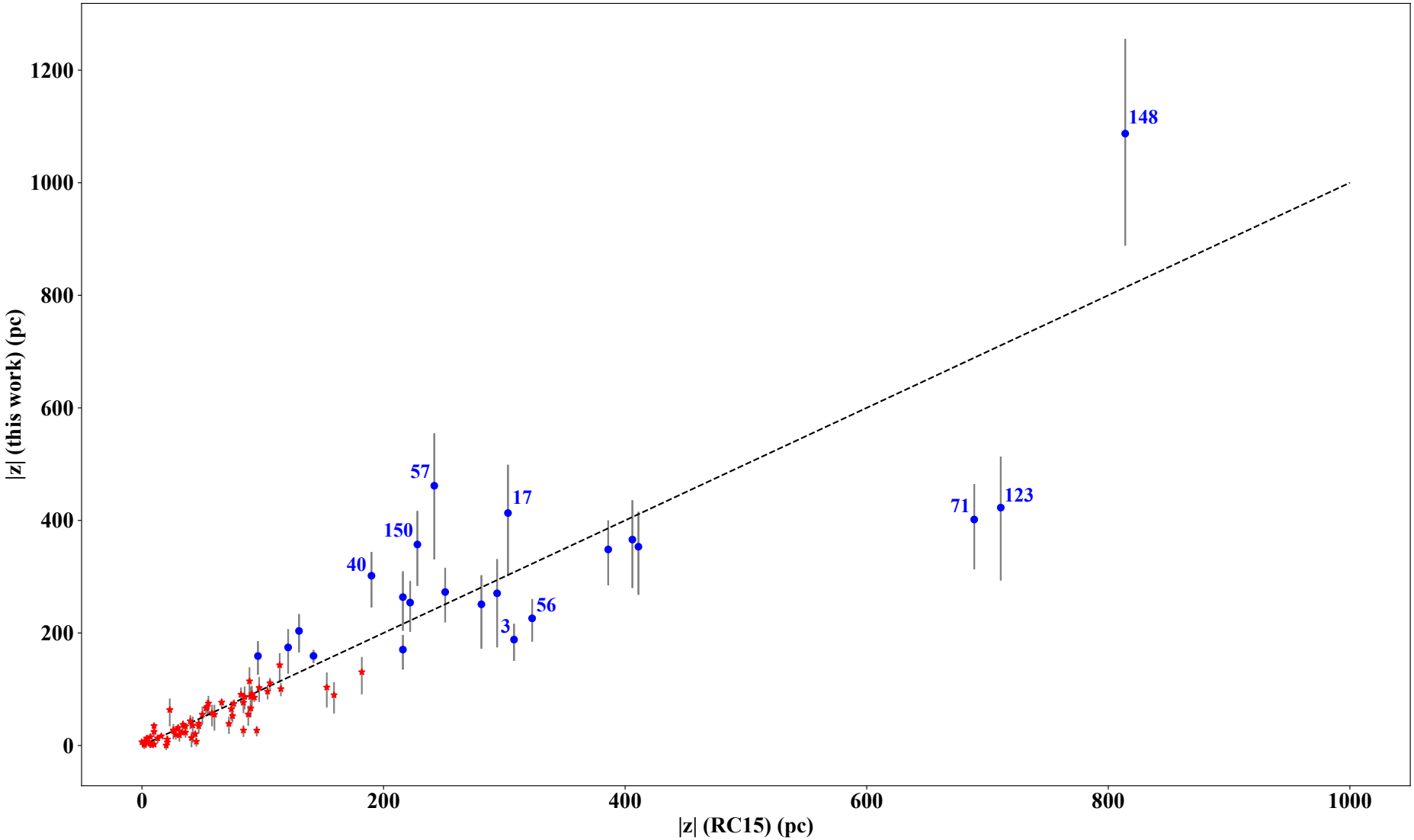

Figure 3.4: A comparison between the WR distances from the midplane from Rosslowe & Crowther (2015a) and this work. Blue circles are the points from this work with distances greater than 3σ, where σ is the H II region scale height. The dotted line indicates parity between the two measures. Stars with the largest differences between our results and those from Rosslowe & Crowther (2015a) are labelled with their WR numbers.

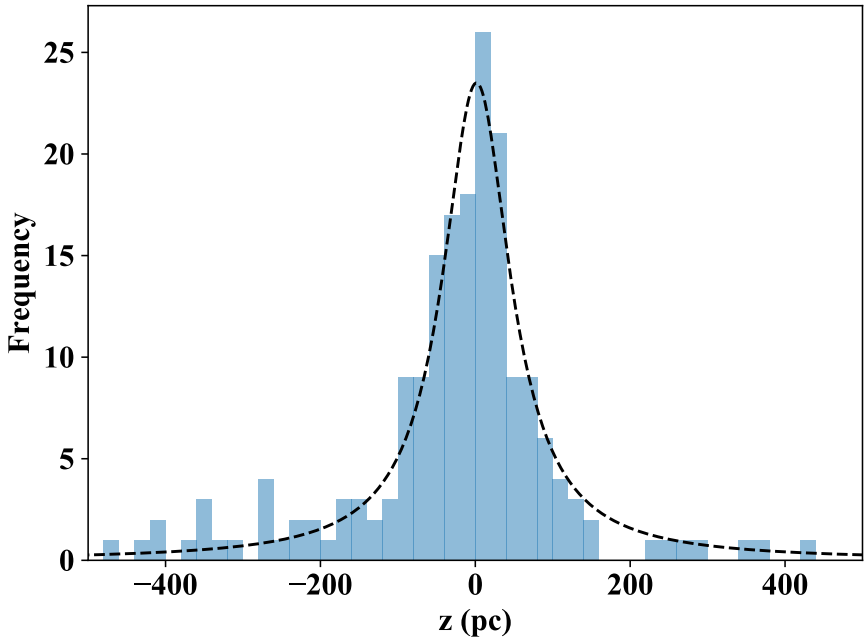

Figure 3.5: A histogram distribution of WR distances from the Galactic disk. The dotted line shows the Cauchy fit from Equation 3.1.

3.3 Distances from the Galactic disk

To identify potential runaway stars, we calculated distances from the Galactic plane using the most likely distance from the Sun and the Galactic latitude of the star, with the addition of the 20.8 pc (Bennett & Bovy, 2019) for the Sun's distance above the midplane. The 68% distance uncertainty intervals were scaled to give height uncertainties.

The new midplane distances in Table A.1 are compared with results from Rosslowe & Crowther (2015a) in Figure 3.4. In general, the deviation from previous results increases with height, reflecting the uncertainty of distances to very remote WR stars. The scale heights, σ, of H II regions loosely trace massive star formation sites and can therefore highlight potential runaways. Based on the median north scale height between 3.9 kpc and 5.6 kpc in Paladini et al. (2004), σ is 52 pc. The south scale heights contained too few points to be reliable.

We additionally calculated the scale height of the WR population. The histogram of WR distances from the midplane is presented in Figure 3.5 and can be fit with a Cauchy distribution

$$g = \frac{A}{\pi\gamma}\frac{\gamma^2}{(z-c)^2+\gamma^2} \tag{3.1}$$

where A is the scale constant, c is the distribution centre and γ is the scale parameter,

specifying the half width half maximum (HWHM). Fitting these parameters gives a centre of 1.5 pc and a HWHM of 53.4 pc. The central value of our distribution is similar to Rosslowe & Crowther (2015a) (1.9 pc), though their HWHM is somewhat smaller, at 39.2 pc. The central value would suggest many WR stars are slightly above the plane, but this may be due to planar dust extinction rendering WR stars which sit below the disk being inaccessible to *Gaia*.

Our results are similar to Conti & Vacca (1990), who find a WR scale height of 45±5 pc using an isothermal disk model and Bobylev & Bajkova (2016), who obtained a height 51.3±3.7 pc using the same method. However, this latter value relies on a sample at <4 kpc (excluding distant stars to avoid the effects of Galactic disk warp) and thus only covers about half the WR stars in our sample.

To identify only the most extreme runaways and ensure they did not form in situ, we apply a 3σ cut-off using the H II region scale height. Since a velocity of 1 $\mathrm{km\,s^{-1}}$ equates to 1 $\mathrm{pc\,Myr^{-1}}$, runaways ($\geq$30 $\mathrm{km\,s^{-1}}$) will travel in excess of 150 pc over a typical WR lifetime of 5 Myr. 91% of 383 WR stars in *Gaia* reside within three scale heights from the Galactic plane, so 9 % of WR stars are located far from the Galactic plane. Table 3.3 presents the $|z|$ distances for each of these stars.

However, the resulting runaway list does not account for the known warp in the Galactic disk. Romero-Gómez et al. (2019) estimate the warp begins at a radius of 12–13 kpc from the Galactic centre for their sample of young, bright stars (which they refer to as the OB sample). All but two of our WR stars are within 12 kpc of the Galactic centre and by this measure, would be unaffected. However, their results show some complex structures that in fact suggest some of our sample may be affected by the warp. An alternative measure from Li et al. (2019), estimates that the Galactic disk instead begins to warp at a radius of 9.2 kpc. 20 stars are further from the centre than this distance, and so their heights would need to account for the warp.

To obtain a robust candidate list of runaways with $\geq$30 $\mathrm{km\,s^{-1}}$, we used the Galactic warp model and onset from Li et al. (2019) to calculate the height of the Galactic plane at the position of each of the 383 WR stars with distances. We subtracted the height of this Galactic warp, which produced a distance from the midplane for each star, which accounted for the warp. These distances were then used to exclude any stars which were not 3σ from the plane, once the warp was accounted for. Using this method, we excluded WR8 and WR12 from our runaway list in Table 3.3. Therefore, 31 stars (8% of WR stars in *Gaia*) are robust runaway candidates.

We do not apply the warp to our full list of distances from the plane in Table A.1,

as the warp onset and model are still uncertain.

The runaways identified in Rosslowe & Crowther (2015a) generally remain far from the plane. However, many of the more extreme distances from the plane are now moderated, due to reduced distances from the Sun. This suggests that extreme runaways are less common than previously thought. WR93a and WR64 are not included, as they were identified as having abnormal v^{WR} band extinction (Section 3.1), which meant it was not possible to calculate their absolute magnitudes, so their distances could not be validated.

Two main evolutionary paths may have created these runaways. The first is the disruption of a binary system when the primary star explodes as a supernova and ejects the remaining companion (Blaauw, 1961). The second scenario is dynamical ejection from a dense cluster, which can eject both binary and single stars (Poveda et al., 1967). The majority of outliers with $>3\sigma$ distances are apparently single stars, as only WR30 and WR69 have confirmed OB companions.

As both single stars and binaries can be ejected from clusters, it is not possible for us to definitively state which mechanism is dominant. We defer a discussion of the origin of runaways to the next chapter, which considers the association of WR stars with star clusters or OB associations. However, we note that recent simulations suggest fast runaways from either mechanism are anticipated to be very rare (Renzo et al., 2019; Oh & Kroupa, 2016), in stark contrast with the high fraction of WR stars at extreme distances from the Galactic plane.

Two stars merit individual consideration. The high velocity runaway WR124 is now located at $|z|$=360 pc, compared to previous estimates of 217 pc (Rosslowe & Crowther, 2015a), 193 pc (Marchenko et al., 2010) and 250 pc (Moffat et al., 1982). This confirms its runaway status, although our work places it significantly further from the Sun (5.9 kpc instead of 3.3 kpc from Marchenko et al. 2010).

WR148 is located furthest from the Galactic plane. Drissen et al. (1986) suggested it as a possible WR+compact object binary disrupted by a SN, however, Munoz et al. (2017) claim it is instead a WN+O binary. If the latter is true, our data suggests that WR148 is a binary system that has been ejected from a cluster, concurring with Munoz et al. (2017). Assuming a lifetime of 5 Myr and a straight vertical trajectory from the Galactic disk, the minimum possible velocity for WR148 is 212 km s^{-1}, making it a very rapid cluster ejection.

Moffat (1989) suggested WN8-9 were over represented amongst runaways, a finding which was corroborated by Rosslowe & Crowther (2015a). However amongst our sample,

Table 3.3: Distance of WR stars from the midplane $|z|$, for which excesses exceed 3σ, where σ=52 pc, the H II region scale height of 52 pc. Previously identified runaways with $|z|$ ≥300 pc according to Rosslowe & Crowther (2015a) are also indicated

WR Number	Spectral type	Dist (kpc)	$\|z\|$ (pc)	H II σ	Known runaway
WR148	WN8h+	$9.47^{+1.77}_{-1.49}$	1087^{+199}_{-168}	$20.9^{+3.8}_{-3.2}$	Yes
WR57	WC8	$5.50^{+1.49}_{-1.06}$	462^{+131}_{-93}	$8.9^{+2.5}_{-1.8}$	No
WR123	WN8o	$5.35^{+1.56}_{-1.09}$	423^{+129}_{-91}	$8.1^{+2.5}_{-1.7}$	Yes
WR73	WC9d	$6.81^{+1.85}_{-1.47}$	423^{+109}_{-87}	$8.1^{+2.1}_{-1.7}$	No
WR17	WC5	$6.75^{+1.74}_{-1.33}$	413^{+112}_{-86}	$7.9^{+2.1}_{-1.6}$	Yes
WR71	WN6o	$3.19^{+0.67}_{-0.48}$	402^{+89}_{-63}	$7.7^{+1.7}_{-1.2}$	Yes
WR6	WN4b	$2.27^{+0.42}_{-0.31}$	376^{+73}_{-54}	$7.2^{+1.4}_{-1.0}$	No
WR75c	WC9	$7.15^{+1.78}_{-1.45}$	366^{+86}_{-70}	$7.0^{+1.7}_{-1.3}$	Yes
WR124	WN8h	$5.87^{+1.48}_{-1.09}$	360^{+85}_{-63}	$6.9^{+1.6}_{-1.2}$	Yes
WR150	WC5	$8.73^{+1.70}_{-1.38}$	357^{+73}_{-60}	$6.9^{+1.4}_{-1.1}$	No
WR61	WN5o	$5.49^{+1.25}_{-0.91}$	353^{+85}_{-62}	$6.8^{+1.6}_{-1.2}$	Yes
WR49	WN5(h)	$8.35^{+1.44}_{-1.17}$	348^{+64}_{-52}	$6.7^{+1.2}_{-1.0}$	Yes
WR58	WN4b/CE	$5.88^{+1.42}_{-1.04}$	337^{+86}_{-63}	$6.5^{+1.7}_{-1.2}$	No
WR40	WN8h	$3.83^{+0.67}_{-0.50}$	302^{+56}_{-42}	$5.8^{+1.1}_{-0.8}$	No
WR126	WC5/WN	$7.57^{+1.49}_{-1.19}$	300^{+55}_{-44}	$5.8^{+1.1}_{-0.8}$	No
WR103	WC9d+?	$3.46^{+1.28}_{-0.77}$	275^{+109}_{-65}	$5.3^{+2.1}_{-1.3}$	No
WR33	WC5; WC6	$7.59^{+1.62}_{-1.30}$	273^{+54}_{-43}	$5.2^{+1.0}_{-0.8}$	No
WR69	WC9d+OB	$3.48^{+0.64}_{-0.47}$	272^{+54}_{-40}	$5.2^{+1.0}_{-0.8}$	No
WR92	WC9	$3.78^{+1.25}_{-0.79}$	271^{+96}_{-61}	$5.2^{+1.8}_{-1.2}$	No
WR54	WN5o	$6.52^{+1.37}_{-1.05}$	264^{+60}_{-46}	$5.1^{+1.1}_{-0.9}$	Yes
WR129	WN4o	$5.47^{+1.22}_{-0.90}$	254^{+52}_{-38}	$4.9^{+1.0}_{-0.7}$	No
WR83	WN5o	$3.80^{+1.10}_{-0.72}$	251^{+79}_{-52}	$4.8^{+1.5}_{-1.0}$	No
WR131	WN7h+abs	$6.92^{+1.40}_{-1.09}$	227^{+42}_{-32}	$4.4^{+0.8}_{-0.6}$	No
WR56	WC7	$8.67^{+1.46}_{-1.20}$	226^{+41}_{-34}	$4.3^{+0.8}_{-0.7}$	Yes
WR30	WC6+O6-8	$5.09^{+0.99}_{-0.74}$	211^{+45}_{-33}	$4.1^{+0.9}_{-0.6}$	No
WR20	WN5o	$6.98^{+1.18}_{-0.93}$	204^{+38}_{-30}	$3.9^{+0.7}_{-0.6}$	No
WR3	WN3ha	$2.90^{+0.52}_{-0.39}$	188^{+38}_{-28}	$3.6^{+0.7}_{-0.5}$	Yes
WR4	WC5+?	$3.75^{+0.89}_{-0.62}$	174^{+47}_{-32}	$3.4^{+0.9}_{-0.6}$	No
WR128	WN4(h)	$2.90^{+0.54}_{-0.39}$	170^{+35}_{-26}	$3.3^{+0.7}_{-0.5}$	No
WR52	WC4	$1.75^{+0.16}_{-0.13}$	159^{+13}_{-11}	$3.1^{+0.2}_{-0.2}$	No
WR34	WN5o	$7.41^{+1.37}_{-1.09}$	159^{+33}_{-26}	$3.1^{+0.6}_{-0.5}$	No

only 4 out of 31 stars are of the WN8-9 subtype. The previous over representation disappears with the drop in extreme runaways. If our sample is representative of the wider WR star population, this suggests that the observed distribution was due to overestimated distance measurements, which would have made the stars appear further from the plane than they truly are.

3.4 WR star parameters

We attempted to calculate WR physical and wind parameters (including luminosities, masses and mass loss rates) using our absolute magnitude results. To do this, we calculated bolometric corrections for individual stars using the absolute magnitudes and luminosities from the model fits of Hamann et al. (2019) and Sander et al. (2019). These could then be averaged to give corrections for each WR subtype.

However, there was a wide variation in the bolometric corrections of individual stars within a subtype class (e.g Figure 3.6 shows the range of corrections as obtained from Hamann et al. (2019) and Sander et al. (2019), compared to average values). This propagates to large inaccuracies in the luminosities and the subsequent masses, mass loss rates and other parameters. For example, for broad lined WN4–6 stars, bolometric corrections for individual stars vary from –4 to –6 mag. Use of the latter correction would lead to a luminosity ∼6.3 times higher (or 0.8 dex larger) than the former.

Instead, we prefer to scale the luminosities of individual stars analysed by Hamann et al. (2006) and Sander et al. (2012) using our distances and include them in Table A.1 in the Appendix.

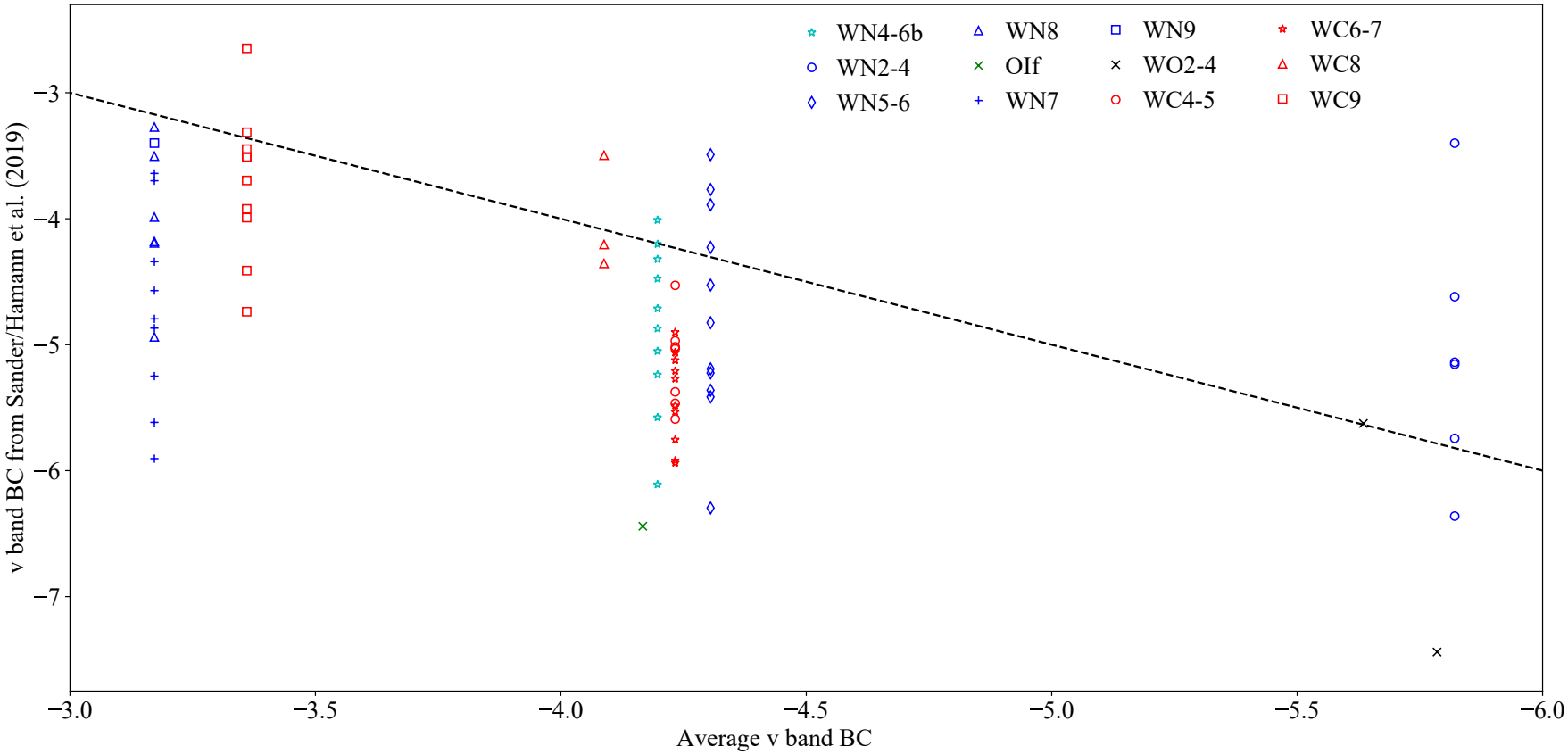

Figure 3.6: Averaged bolometric corrections as calculated using Hamann et al. (2019) and Sander et al. (2019), for different WR subtypes. This shows the large spread in corrections for a given subtype, and why using averages does not produce reliable luminosities for individual stars.

3.5 Conclusions

In this chapter, we have calculated distances and absolute magnitudes of 383 Galactic WR stars with *Gaia* DR2 parallaxes:

- The distances agree well with both the previous calibration (Rosslowe & Crowther, 2015a) and DR2 distances from Bailer-Jones et al. (2018) up to 2 kpc. Deviations above 2 kpc are due primarily to the large uncertainties of the *Gaia* parallaxes. Distances from Bailer-Jones et al. (2018) formed the basis of recent spectroscopic studies of Galactic WR stars by Sander et al. (2019) and Hamann et al. (2019). Use of distances from this study would generally lead to modest 0.05 dex reductions in stellar luminosities, albeit with reductions of up to 0.2 dex for relatively distant stars.

- 25 WR stars are found within 2 kpc, compared to 30 WR stars from Conti et al. (1983). Based on the population in GOSC v4.1 (Maíz Apellániz et al., 2013), the WR/O star ratio in this region is 0.09.

- We calculate absolute magnitudes for WR stars, in both the v^{WR} and K_s bands. Of these, 187 stars have an absolute magnitude in either band and were used to generate subtype averages for calibrations. Both WN and WC stars are found to be more diverse in their absolute magnitude ranges than anticipated and therefore we recommend avoiding use of calibrations without accounting for this large intrinsic spread.

- We have applied our new distances to identify 31 potential runaways from the Galactic disk, accounting for the Galactic warp. H II region scale heights define the cut-offs for runaway status. 20 of these WR stars with $|z|$ >156 pc are new detections. The vast majority of the runaway stars are single. However, as both companion supernovae and dynamical ejection from clusters can produce single star runaways, it was not possible for us to determine the dominant runaway production mechanism.

In the next chapter, we use these distances and the *Gaia* proper motions to analyse cluster and association memberships. We also apply the distances to derive emission line luminosities in Chapter 5. These can be used to determine the WR population of unresolved regions in external galaxies.

Chapter 4

Cluster and Association membership

Content from this chapter is taken from the publication Rate et al. (2020) (RCP20). Paul Crowther compiled the statistics on O star cluster membership, (including Table 4.1), added embedded cluster literature results to Tables 4.3 and 4.6 and star forming region results to Table 4.6, compiled the lists used to determine cluster ages in Section 4.4 and the discussions of proximity of supernovae to star forming regions in Section 4.6. The simulations and explanations in Section 4.5 were created by Richard Parker.

4.1 Introduction

In Section 1.1, we noted the possible formation mechanisms of massive stars in different environments. Competitive accretion or mergers may occur only in dense environments such as clusters, whilst monolithic collapse can take place in dense or isolated environments. The majority of stars are thought to form in clusters (Lada & Lada, 2003) which dissolve into associations; with the cluster dissolution process taking longer than a WR star lifetime (>5Myr). WR stars which formed in star clusters should thus remain there, unless they have been ejected dynamically or by the core collapse supernova of a binary companion. The current environments of WR stars may therefore be used to probe massive star formation processes.

However, Section 1.8.2 notes that at most 35% of optically visible Galactic WR stars are in clusters and associations, whilst many WR stars only detected at IR wavelengths are also found in the field. Additionally, v3 of the Galactic O star Catalogue (Maíz Apellániz et al., 2013) suggests that only 42% of O stars are thought to be members of star clusters, with almost three quarters located in OB associations and/or low density (<100s stars pc^{-3}) star forming regions (Table 4.1). These statistics are likely to be upper

Table 4.1: Summary of membership of clusters, OB associations of radio/infrared-selected star forming regions for stars included in v3 of the Galactic O star Catalogue (Maíz Apellániz et al., 2013).

Sample	Cluster Member	OB Assoc Member	S.F. region Member	Isolated
611	258 (42%)	441 (72%)	445 (73%)	82 (13%)

limits given membership has not been confirmed from *Gaia* proper motions/parallaxes, although some comparisons with earlier distance estimates have been undertaken (Shull & Danforth, 2019). Data from *Gaia* also supports the notion that not all stars are born in clusters (Ward et al., 2020).

Evidence discussed in Section 1.12 also suggests that type Ib and Ic SN (stripped envelope SN) may originate primarily from lower mass binaries, rather than the most massive stars as historically anticipated. However, studies of their environments suggest that stripped envelope SN are most closely associated with star-forming regions (Anderson et al., 2012; Kuncarayakti et al., 2018), which would imply that they have high mass progenitors. Therefore, there is conflicting evidence for and against WR stars as the progenitors of highly stripped SN, some of which directly involves their immediate environments.

In Chapter 2, we used *Gaia* parallaxes to calculate distances for Galactic WR stars. Here we use these new distances, along with *Gaia* proper motions, to analyse WR membership of Galactic clusters and associations, supplemented by IR surveys for sources inaccessible to *Gaia*. We outline the methods in Section 4.2. Cluster/association membership and distances are presented in Section 4.3 and ages are estimated in Section 4.4. Finally, implications for massive star formation and their environments, informed by N-body simulations, are presented in Section 4.5. This is followed with a discussion and brief conclusions in Section 4.6.

4.2 Assessment of cluster/association membership

4.2.1 Cluster/association candidates

The Galactic Wolf-Rayet catalogue [1] includes 663 WR stars (v1.23, July 2019) and lists the supposed members of star clusters and OB associations. To assess which WR stars

[1] http://pacrowther.staff.shef.ac.uk/WRcat/index.php

Table 4.2: Clusters and associations (in parentheses) excluded from *Gaia* DR2 membership analysis. Claimed membership from Lundström & Stenholm (1984), van der Hucht (2001), Borissova et al. (2012), Wallace et al. (2005), Messineo et al. (2009), de la Fuente et al. (2015), Davies et al. (2012b), Bibby et al. (2008), Kurtev et al. (2007) and Chené et al. (2013).

No reliable membership data	No parallaxes or proper motions from *Gaia* (high A_V)	Few objects from membership list detected by *Gaia*
AG Car	Arches	C1104-610 a
(Anon. Cen OB)	[DBS2003] 179	C1104-610 b
(Anon. Pup a)	Galactic Centre	NGC 6871
(Anon. Pup b)	Mercer 20	(Serpens OB1)
(Anon. Sct OB)	Mercer 70	(Serpens OB2)
(Anon. Sco OB)	Mercer 81	VVV CL099
(Anon. Vel a)	SGR 1806-20	
(Anon. Vel b)	Sher 1	
(Crux OB 4)	Quartet	
Dolidze 29	Quintuplet	
Henize 3	VVV CL011	
(Norma OB4)	VVV CL036	
(Vulpecula OB2)	VVV CL073	
	VVV CL074	
	W43	
	(Cas OB1)	

are genuine members of a named cluster or association, we obtain lists of all candidate members from the literature and use these to determine the proper motions and distances of the clusters and OB associations. The results were then compared to the proper motions and distances of the individual WR stars.

Of course, historical definitions of Galactic OB associations (Humphreys, 1978) were undertaken from observations of visually bright O and B-type stars, so are inevitably limited to stars located within a couple of kpc from the Sun. The majority of star clusters and OB associations are also associated with optical nebulosities, drawn from one or more historical catalogues, namely the New General Catalogue (Dreyer, 1888), Index Catalogue (Dreyer, 1910), Sharpless 2 (Sharpless, 1959) or RCW (Rodgers et al., 1960).

Table 4.1, gives the percentages of stars in v3 of the Galactic O star Catalogue (Maíz Apellániz et al., 2013) which, according to literature (included in the catalogue), are members of various regions. Numbers in different columns overlap because the O stars may be identified as members of both clusters and associations (due to hierarchical star formation) and an individual star may also have surrounding nebulosity in addition to cluster or association membership.

In contrast, only ∼7% of the Galactic WR population detected by *Gaia* lies within 2 kpc (Chapter 3), such that only a small fraction may lie within catalogued OB associations. Ideally, membership of star-forming regions identified from radio (Russeil, 2003) or infrared (Conti & Crowther, 2004; Rahman & Murray, 2010; Urquhart et al., 2014) surveys would be more revealing, although this is beyond the capabilities of *Gaia*.

Consequently, here we focus on O and B star members of clusters and/or associations selected, where possible, to ensure a bright sample that could be reliably detected by *Gaia* DR2 and fit the same distribution as our prior for WR stars (Chapter 2), (which results in somewhat lower distances with respect to Bailer-Jones et al. 2018). Our prior consisted of a H II region model, based on radio observations from Paladini et al. 2004 and Paladini et al. 2003. This was combined with a dust disk model from Rosslowe & Crowther (2015a). The dust was converted to an I band extinction map by calibrating the total dust along line of sight, with the maximum extinction at the Galactic centre. This map could be applied to the H II region model, to approximate the H II region distribution as observed by Gaia's white light G band.

Unfortunately, some cluster members lacked spectral type information. In these instances, we used the SIMBAD database to obtain the most recently assigned spectral type. However, many candidates remain unclassified. Additionally, for some larger

candidate catalogues, we used only the 20 brightest stars, as this provided a reasonable number of members for comparison and ensured these objects would be observed by *Gaia*. Overall, we were able to use *Gaia* data to assess the WR star membership in 28 clusters and 15 associations. We will revisit the issue of visually obscured WR stars in Section 4.5.

4.2.2 Excluded clusters and associations

Table 4.2 lists specific clusters and associations excluded from our *Gaia* analysis. There are three main reasons why individual clusters and associations were omitted. No membership lists could be identified for Dolidze 29 or Henize 3. Anonymous associations in Cen, Pup, Sct, Sco and Vel, plus Norma OB4 and Crux OB4 also lacked membership information. Star lists were available for the parent region of Vulpecula OB2, but these did not break down into lists for specific OB associations.

The membership lists of other excluded clusters and associations were too small to test the WR membership, or were not available to *Gaia*. Only 3 members of NGC 6871 were available in the *Gaia* DR2 catalogue, including WR113, and the only stars detected by *Gaia* for Sagittarius OB7, Serpens OB1 and Serpens OB2 were their supposed WR members.

The remaining clusters were not observed by *Gaia*, as they are only accessible to IR observations, owing to high dust extinctions. For completeness, we include WR membership of embedded clusters in the Galactic disk, but only summarise previous results for the 110 WR stars within the Galactic Centre region ($l = 360 \pm 1°$, $b = 0 \pm 1°$), which includes the Galactic Centre, Quintuplet and Arches clusters.

4.2.3 Selection criteria

To assess cluster and association membership, we identified groups of stars by eye in RA and DEC proper motion space. We then compared this to the WR star proper motions, to determine if the latter were part of the groups. The *Gaia* proper motion zero point is far smaller than the proper motion measurements ($\sim$10μas yr^{-1}, compared to mas scale proper motions, Lindegren et al. 2018b) and therefore no corrections needed to be applied. Additionally, the uncertainties tended to be small when compared with parallax and distance uncertainties.

We assign individual WR stars as members of clusters/associations, possible members or non-members, depending on the similarity of proper motions with respect to other

members. This was a 'by eye' judgement and the proximity required for membership depends on the proper motion dispersions of the cluster or association. 4 WR stars in clusters and 4 WR stars in associations showed possible evidence of ejection, in which the star is located near the cluster or association in proper motion space (travelling within one or two mas yr^{-1} in most cases), but is clearly isolated from the main group. It is possible that other clusters and associations could contain ejected stars, but these are masked by the scatter in the proper motion data. By way of example, Drew et al. (2018) support WR20aa and WR20c as potential stellar ejections from Westerlund 2 approximately 0.5 Myr ago.

Distances were used as a secondary check, to remove foreground and background stars. Parallaxes were converted to distances using the same prior and bayesian method as Chapter 2. The prior was based on H II regions and extinction, and so is applicable to other OB cluster members. If WR stars showed strong agreement in proper motion space but disagreed in distance, they were assigned either as members or possible members, depending on how distant they were from the main cluster or association.

We checked our membership assignment was reasonable using the Python scikit-learn (Pedregosa et al., 2011) implementation of DBSCAN. However, compared to the manual classification, the automated method had a number of limitations. When defining clusters in proper motion and parallax space, it struggled with boundary stars and could not account for sparse or scattered data. Additionally, it was difficult for this algorithm to properly weight the more reliable feature (proper motion) and account for quality indicators such as astrometric excess noise. We therefore chose not to use this automated method and used our manual classification to make the final membership decision.

As part of our analysis, we have obtained *Gaia* DR2 distances to the clusters/associations. Although we could not model the shape and distance of each cluster simultaneously, (as recommended by Luri et al. 2018) it was still possible to get an approximation using the distances of individual members. To do this, we averaged positive parallaxes for all supposed members with astrometric excess noise <1. The systematic parallax uncertainty of the cluster or association could then be found by adapting the correlated error calculation outlined in (Lindegren et al. 2018a, 2018b)

$$\sigma_{clust} = \sqrt{\frac{1}{n}\langle\sigma_\omega^2\rangle + \frac{n-1}{n}\langle\langle V_\omega(\theta_{i,j})\rangle\rangle} \tag{4.1}$$

where n is the number of stars used to calculate the uncertainty, σ_ω (described in Chapter 2) is the inflated uncertainty of each star's parallax, averaged for the cluster. The

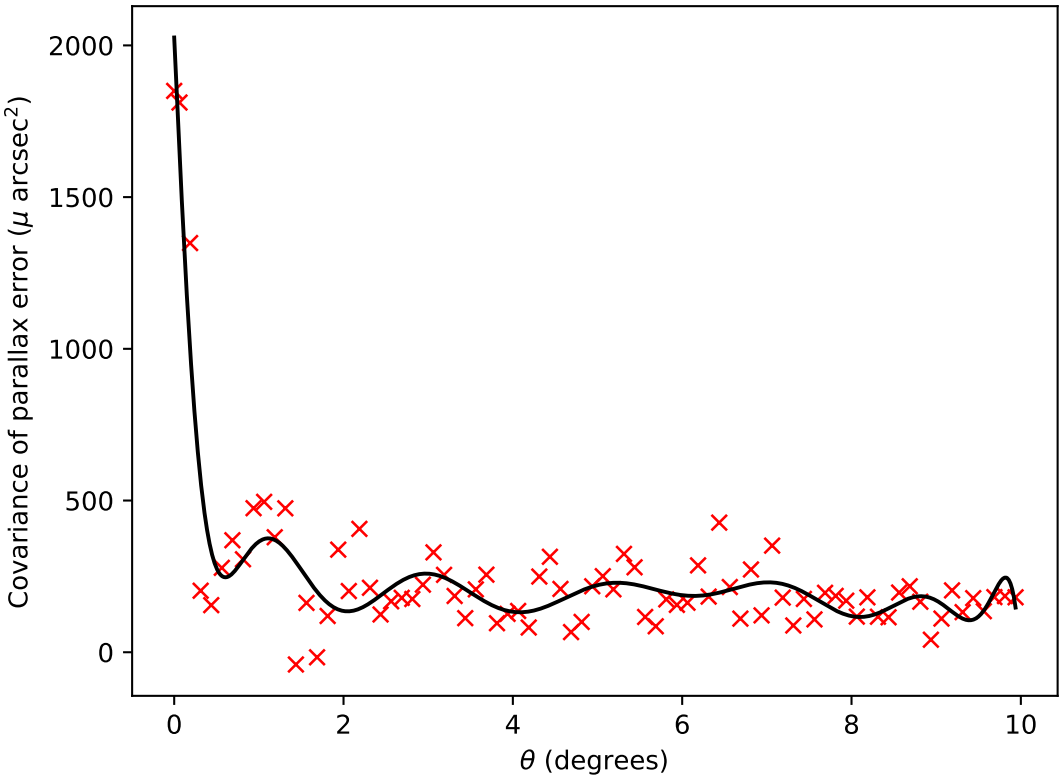

Figure 4.1: Polynomial fit of binned parallax covariance $V_\omega(\theta)$, to angular separation between two stars in the cluster Θ.

$\sqrt{\frac{1}{n}\langle\sigma_\omega^2\rangle}$ term accounts for the random error and variance of the systematic error, using the external calibration with data from Table 1 of Arenou et al. (2018). However, it does not account for the spatial covariance function, $V_\omega(\theta)$, which is required to calculate the systematic errors for the mean parallax of stars in a cluster (Lindegren et al., 2018a). The full systematic term, $\frac{n-1}{n}\langle\langle V_\omega(\theta_{i,j})\rangle\rangle$ (where $\langle\langle V_\omega(\theta_{i,j})\rangle\rangle$ is the average $V_\omega(\theta)$ of n(n-1)/2 non redundant pairs of stars (i and j) in the cluster) is therefore required.

The initial binned $V_\omega(\theta)$ values from Lindegren et al. (2018b) were not sufficiently high enough resolution to account for the small angular separations between the stars in our clusters. We therefore fit a polynomial (with 14 parameters, although the results were not sensitive to changes in the number of these parameters) to the $V_\omega(\theta)$ data, in a similar manner to the bottom panel of figure 14 of Lindegren et al. (2018b). The resulting fit is shown in Figure 4.1.

The polynomial fit was compared with an interpolation between the binned data.

The differences between the resulting distances produced by each method were small (~ 0.07 kpc for NGC3603, the most distant cluster in the sample and more often ~ 0.01 kpc for more nearby clusters). We selected the polynomial fit method, as it would be less strongly affected by any uncertainty in the individual values.

We then apply our prior from Chapter 2 to the average parallax and uncertainty, to obtain the distance and its uncertainty. For some clusters that may be obscured (e.g Danks 2), the distances in Tables 4.7 and 4.8 are located further away than the mean distances for cluster members would indicate. This is because the average uncertainties of the clusters are much smaller than the uncertainties of individual stars. The prior therefore dominates more for individual stars and moves them somewhat closer than the cluster distance. However, the large uncertainties for individual star distances and uncertainties of clusters mean that the cluster distances are still appropriate for the group overall.

In many cases, foreground or background objects had been misidentified as members and were contaminating the mean parallax. We therefore apply parallax cuts to remove these from the averages. These cuts were not performed via sigma clipping, but by manually identifying and removing clear outliers (e.g, if the star or group was ∼kpc in the foreground of a cluster, the parallax required to remove these stars would be identified and used as the cutoff). The uncertainties of the excluded stars had to be clearly separated from the furthest foreground or background star that was connected to the main cluster group. We do not apply any cuts to associations (aside from removing a foreground star from Puppis OB2), as they may comprise multiple subregions, with different distances.

4.3 WR membership

Table 4.3 summarises WR membership of star clusters in the Galactic disk, drawn from *Gaia* DR2 proper motions (bold) or literature results for embedded clusters (non bold). Table 4.4 provides a summary of WR membership of OB associations drawn from *Gaia* DR2, supplemented by results for Chené et al. (2019) for WR2 (Cas OB1).

Table 4.3 reveals that only 43 WR stars from 62 claimed cluster members were confirmed from our analysis. Only 11% of WR stars with *Gaia* DR2 distances are in clusters, rising to 15% if possible members are additionally included (58 stars altogether). For associations, only 23 WR stars from 48 claimed members were confirmed, including WR11 in the γ Vel group (see Table 4.4). However, membership of associations proved

to be more challenging than clusters owing to greater scatter in proper motions and distances.

Combining cluster and association membership (including WR25 and the members of Mercer 30, which are both association and cluster members, and WR24, WR79, WR79a and WR137 which are possible cluster members but confirmed association members), this rises to 17% of the total WR sample with *Gaia* DR2 distances. Additionally, in many cases, only a few cluster/association members were detected by *Gaia* DR2. This leaves the full proper motion and distance range of the cluster or association uncertain, which would potentially exclude WR members.

Several physically small or sparsely populated clusters, like Pismis 24 and Berkeley 86, were thought to host WR stars but do not. In the former's case, this is a cluster with few members and WR93 (WC7+O) has a radically different proper motion. Lundström & Stenholm (1984) only regarded it as a possible member and we can confirm it is not. For Berkeley 86, Lundström & Stenholm (1984) consider WR139 (WN5o+O) as a probable cluster member, but note it sits outside the apparent cluster and has a lower colour excess. We find that WR139 differs from known members in its proper motion and distance. Therefore we do not consider it a member.

A number of other clusters and associations did not have any confirmed members. This is because their proper motions are highly scattered, possibly because they are unbound, or broken down into subgroups along the line of sight. This made it difficult to locate the main proper motion centre of the cluster. For instance, Cassiopeia OB7 included a couple of possible members at a similar distance to WR1 (WN4b), but with no coherent proper motions.

Additionally, the existence of some clusters and associations is questionable. Ara OB1 shows a large scatter in proper motions, which indicates there is no relation between the supposed members. The catalogue for Kharchenko et al. (2013) also suggests it may not be a cluster. Collinder 121 also contains stars with a wide range of proper motions, though they are all at approximately the same distance. Other clusters and associations with no or few members detected by *Gaia*, such Serpens OB1, may also be chance alignments.

The proper motions of proposed WR members of Cir OB1 (WR65, WR67) agreed with other members; although their distances were in tension. In these instances future improvements to distance accuracy from *Gaia*, would help with membership identification.

Table 4.3: WR star membership of clusters for *Gaia* DR2 sources (bold) and non *Gaia* sources (non bold), external to the Galactic Centre region. (a) Decision was made based on proper motion and parallax clustering, not distances. (b) Large scatter in the data points. (c) Decision was made based on very few data points. (d) Possible former member ejected from cluster.

Cluster	WR cat # of member(s)	Possible member	Non member	References	Notes
Berkeley 86			**139**	1	
Berkeley 87	**142**			2	
Bochum 7	**12**			3	
Bochum 10	**23**			4	WEBDA. No spectral types.
Bochum 14	**104**			3	No spectral types.
Cl 1813-178	**111-4**	**111-2**^{d}		5	
Collinder 121		**6**		3	20 brightest objects in the J band. Probability of membership>80%.
Collinder 228		**24**^{b}		6	GOSC.
Danks 1	**48a, 48-7**	**48-8, 48-9**		7	
	48-10	**48-4**			
Danks 2	**48-2**^{cb}			7	
[DBS2003] 179	84-1, 84-6, 84-7			8	
Dolidze 3		**137**^{ab}		3	20 brightest objects in the J band. Probability of membership>80%.
Dolidze 33		**120**^{ab}		3	20 brightest objects in the J band. Probability of membership>80%.
Havlen-Moffat 1		**87**^{d}	**89**	6	GOSC.
Hogg 15		**47**^{c}		4	No spectral type information.
Markarian 50	**157**			2	
Mercer 23	**125-3**^{a}			9	

Cluster	WR cat # of member(s)	Possible member	Non member	References	Notes
Mercer 30	**46-3, 46-4, 46-5, 46-6**			10	
Mercer 70	70-12			11	
Mercer 81	76-2, 76-3, 76-4, 76-5, 76-6, 76-7, 76-8, 76-9			12	
NGC 3603	**43-2, 42-1**[a]			13	
	43A, 43B, 43C				WR43A, WR43B and WR43C unresolved by *Gaia*.
NGC 6231		**79**[b], **79a**[b]	**78**	6	GOSC.
Pismis 20		**67**[c]		2	
Pismis 24			**93**	6	GOSC.
Quartet	118-1, 118-2, 118-3			14	
Ruprecht 44	**10**			2	
SGR 0806–20	111a, 111b, 111c, 111d			15	
Trumpler 16	**25**[a]			6	GOSC.
Trumpler 27	**95, 98**			2	
VVV CL009	**45-5**			16	
VVV CL036	60-6			16	
VVV CL041	**62-2**			17	Selected cluster members, with J<16
VVV CL073	75-25, 75-26			16	
VVV CL074	75-27, 75-28, 75-29, 75-32			16, 18	
VVV CL099	84-8, 84-9, 84-10			16	
W43	121a			19	
Westerlund 1[a]	**77aa, 77a, b**	**77p**[a,d], **77r**[d]		20	
	77c, d, f, h, i, j				

Cluster	WR cat # of member(s)	Possible member	Non member	References	Notes
	77m, n, o, q, s, sa				
	77sb, sc, sd				
	77e, g, k, l				
Westerlund 2	**20a, 20b**[a]			21	Stars with spectra (in table 3).

(1) Massey et al. (1995), (2) Massey et al. (2001) and references therein, (3) Dias et al. (2014c), Dias et al. (2014b) (4) Lasker et al. (1990), (5) Messineo et al. (2011), (6) Maíz Apellániz et al. (2013), (7) Davies et al. (2012a), (8) Borissova et al. (2012), (9) Hanson et al. (2010), (10) de la Fuente et al. (2016), (11) de la Fuente et al. (2015), (12) Davies et al. (2012b), (13) Melena et al. (2008) , (14) Messineo et al. (2009), (15) Bibby et al. (2008), (16) Chené et al. (2013), (17) Chené et al. (2015), (18) Martins et al. (2019), (19) Blum et al. (1999), (20) Clark et al. (2005), (21) Vargas Álvarez et al. (2013)

We can compare our WR membership classifications to those from Cantat-Gaudin et al. (2018), which assigns cluster members based on an unsupervised machine learning algorithm. Table 4.5 shows the probability of membership from Cantat-Gaudin et al. (2018) for 10 clusters in common with our data. Their numerical membership probability (between 0 and 1) is divided into three groups, roughly corresponding to our classification categories. A high (>0.6) membership probability suggests the WR star is a member. An intermediate (0.4−0.6) membership probability suggests a candidate and low (<0.4) membership probability implies the star is a non member. In most cases, our confirmed members from Table 4.3 were assigned membership probabilities >0.7 by Cantat-Gaudin et al. (2018).

Of the stars classified as possible members in Table 4.3, four could be reclassified as confirmed members based on the probabilities from Cantat-Gaudin et al. (2018). However, four of our confirmed members could also be reclassified as possible members (again, based on Cantat-Gaudin et al. (2018) results), resulting in no change to the overall membership fractions. Similarly WR67, which we consider a candidate member of Pismis 20, only has a membership probability of 0.1 in Cantat-Gaudin et al. (2018) and could thus be alternatively classified as a non member. However simultaneously WR89 had a high (0.7) Cantat-Gaudin et al. (2018) membership probability, but was classified by us as a non member. Accounting for the different classifications of these two stars also does not change the percentage of *Gaia* WR stars which are cluster members or candidates.

Table 4.4: Possible WR star membership of OB associations for *Gaia* DR2 sources (bold) and non-*Gaia* sources (non-bold), external to the Galactic Centre. (a) Decision was made based on pmra/pmdec and parallax clustering, not distances. (b) Large scatter in the data points. (c) Decision was made based on very few data points. (d) Possible former member ejected from cluster, (e) Result taken directly from Chené et al. (2019).

Association	WR cat # of member(s)	Possible member	Non-member	References	Notes
Ara OB1			**77**^{b}	1	GOSC.
Carina OB1 (incl Tr 16, Coll 232)	**22, 24, 25**	**18**^{d}, **23**^{d}		1	GOSC.
Cassiopeia OB1		2^{e}		2	No *Gaia* astrometry.
Cassiopeia OB7			**1**^{c}	1	GOSC.
Centaurus OB1	**48**^{b}			1	GOSC.
Cephus OB1		**152**^{abc}, **153**^{abc} **154**^{abc}, **155**^{abc}		1	GOSC.
Circinus OB1		**67**^{ab}	**65, 66, 68**^{ab}	3	20 brightest objects in the J band with membership probability >80%. No spectral types.
Cygnus OB1	**137**^{b}, **138**^{ab} **141**^{b}		**136, 139**	1	GOSC.
Cygnus OB2	**144, 145**	**142a**^{d}		1	GOSC.
Cygnus OB3	**135**^{b}		**134**	1	GOSC.
Cygnus OB9	**142a**^{cb}			1	GOSC.
Dragonfish	**46-2, 46-3, 46-4, 46-5, 46-6, 46-8, 46-9, 46-16, 46-17**		**46-10**	4	
Puppis OB2	**10**			5, 6	
Scorpius OB1	**79, 79a**	**78**^{d}		1	GOSC.
Sagittarius OB1			**108, 104** **105**^{bc}, **110**^{bc}, **111**^{bc}	1	GOSC.
Gamma Velorum	11			7, 8	WR 11 from Hipparcos. No spectral types.

(1) Maíz Apellániz et al. (2013), (2) Chené et al. (2019), (3) Kharchenko et al. (2013), (4) Rahman et al. (2011), (5) Mel'nik & Dambis (2017), (6) Turner (1981), (7) van Leeuwen (2007), (8) Jeffries et al. (2014a)

Table 4.5: Probability of membership from Cantat-Gaudin et al. (2018), for clusters and WR stars in Table 4.3. Stars classed as members in Table 4.3 are shown in bold, those classed as candidates are underlined and stars classed by us as non members do not have any formatting.

Cluster	High (>0.6) membership probability (Members)	Intermediate (0.4−0.6) membership probability (Candidates)	Low (<0.4) membership probability (Non members)
Danks 1	48-8, 48-9	**48a**, **48-10**	
Danks 2	**48-2**		
Havlen-Moffat 1	89		
Hogg 15	47		
Markarian 50	**157**		
NGC 3603	**43-2, 42-1**		
NGC 6231	79		
Pismis 20			67
Westerlund 1	**77aa, 77a**		
	77c, d, f, h, i		
	77m, n, o, q, sa	**77s**	
	77sc	**77sb**	
Westerlund 2	**20a, 20b**		

Therefore, considering the results from Cantat-Gaudin et al. (2018) does not change the fraction of isolated WR stars in *Gaia*.

Tables 4.3–4.4 also include literature results for embedded clusters within the Galactic disk, which are inaccessible to *Gaia*. Results are summarised in Table 4.6, and reveal that only 18% of 553 WR stars in the Galactic disk are confirmed members of clusters or OB associations.

OB associations included in the WR catalogue are nearby and have low associated extinction. However, the majority of WR stars are at $\sim$ kpc distances from the Sun and so beyond the extent of these catalogued associations. Additionally, more distant, moderately obscured star forming regions are historically detected at IR wavelengths but not at optical wavelengths and so these are not included in the OB associations of the WR star catalogue.

To account for this and incorporate these more distant star forming regions we have compared the location of WR stars to radio-selected H II regions from Russeil (2003) and infrared selected star forming regions from Conti & Crowther (2004), Rahman & Murray (2010), and Urquhart et al. (2014). In particular, Urquhart et al. (2014) provide star-forming complexes from the Red MSX Source (RMS) survey of massive star forming regions within the Galactic disk. Accounting for potential membership of obscured star forming regions, the fraction associated with star clusters, OB associations or obscured star formation in the Galactic disk could be as high as $\sim$ 36%.

If we include the 110 WR stars within the Galactic Centre region, of which 13 are members of the Arches cluster (Clark et al., 2018a), 19 are members of the Quintuplet cluster (Clark et al., 2018b) and 36 lie within the Central Cluster (Krabbe et al., 1995; Tanner et al., 2005; Paumard et al., 2006; Fritz et al., 2010), 25% of 663 WR stars are confirmed members of clusters or associations, rising to 41% if potential association with radio/infrared star forming regions are confirmed.

We can check these membership statistics have not been skewed by the lack of OB associations identified beyond $\sim$2kpc, by comparing the results to those for WR stars within 2kpc of the Sun. Extinctions within this region are low (Table 3.2 shows A_{Ks} <1 in most cases), and small parallax uncertainties mean the resulting distances are not substantially affected by our prior. The list of known young associations within this region should therefore be fairly complete and these WR stars should have robust distances.

In Section 3, we found 27 WR stars are located within 2kpc of the Sun (listed in Table 3.2). 18 of these 27 WR stars were identified as potential cluster and association members. Of the possible members, 10 were confirmed, with 6 assigned as non members

Table 4.6: Summary of membership of clusters, OB associations and radio/infrared-selected star-forming regions (including candidates from Tables 4.3 and 4.4) for the known Galactic WR population. Some stars were members of both clusters and associations (where the cluster is a sub-region of the association), but we include these objects in the cluster statistics, as the cluster is their primary formation environment. 'Disk non-*Gaia*' refers to stars which are not in the heavily extinguished Galactic Centre region and which were also not detected by *Gaia*. 'Disk *Gaia*' refers to stars in the same region (outside the Galactic Centre), which were observed by *Gaia*.

Region	Cluster	Association	Candidate	Isolated	Total
Within 2kpc of the Sun	3	7	2	15	27
Disk *Gaia*	43	18	65	253	379
Disk non-*Gaia*	37	1	37	99	174
Galactic Centre	68		2	40	110
Total	148	19	104	392	663

Additionally, some stars included in the original *Gaia* distance total (WR11 and the stars in NGC3603) are here not counted as part of the disk Gaia population.

and 2 as candidates. 15 out of 27 stars are therefore isolated. This nearby population has a confirmed cluster and association membership fraction of 37%, which is far larger than the comparative value of 16% for all WR stars with *Gaia* data. However, this excludes a significant number of candidates from Table 4.3, which may still be members. Additionally, as previously discussed, beyond 2kpc OB associations may not be properly identified. It is therefore more sensible to compare the combined statistics of clusters, associations and candidates (associated with a star forming region). Accounting for these increases the number of WR stars within 2kpc classified as cluster, association or candidate members to 44%, which is still somewhat higher than the 33% for all WR stars in *Gaia*.

The high membership number amongst the sample within 2kpc, could be explained by the fact that a proportionally much larger fraction (two thirds) were assigned as possible members in the literature. For the full sample with *Gaia* data, the fraction of stars tested for membership drops to just one quarter.

The results from within 2kpc are broadly consistent with the full dataset, when embedded and Galactic Centre regions are accounted for. 41% of all WR stars are members of a cluster or association, or associated with a star forming region, compared to

the 44% within 2kpc. The slight disagreement between the percentages can be explained by low number statistics in the <2kpc sample, where a single star accounts for roughly 4% of the total membership fraction. By contrast, a single star contributes only 0.15% in the Galaxy wide sample.

Tables 4.7 and 4.8 compare our cluster and association distances with literature results. Both tables contain several DR2 derived distances from Melnik & Dambis (2020). Much like the results from Shull & Danforth (2019), Melnik & Dambis (2020) do not use a Bayesian approach to calculate the cluster distance, instead simply inverting the median cluster parallax. Additionally, they use a much larger parallax zero point of -0.11mas (as opposed to our -0.029mas). Despite this, our distances to most clusters and associations are similar to both the Melnik & Dambis (2020) results and previous estimates. However, we find that distances to Mercer 23, Mercer 30, Dolidze 3, Dolidze 33 and the Dragonfish association are closer than previous estimates. In particular, the revised distance of 5.2 kpc to the Dragonfish association is significantly closer than previous determinations of 12 kpc (de la Fuente et al., 2016) or 7 kpc (Kurtev et al., 2007). However, the member stars are flagged with high (>0.3) astrometric excess noise and error to parallax ratios. This indicates the distance may dominated by the prior and therefore may be inaccurate. This is also relevant to its host cluster Mercer 30, which has a revised distance of 4.7 kpc, on the basis of just two members with positive parallaxes and astrometric excess noise below 1.

Bochum 14 is found to be significantly more distant than previously thought. This distance is likely to be robust, since only one member has astrometric excess noise >0.3 (a further two members were removed for having astrometric excess noises above 1 mas).

15 of our clusters also have distances in Cantat-Gaudin et al. (2018). Cantat-Gaudin et al. (2018) use a maximum likelihood method; determining the cluster distance without a prior. Their distances can therefore be compared to ours, to determine the impact of our prior. Additionally, their results use much larger numbers of member stars than our distances.

Our distances only deviate substantially (>10%) from the Cantat-Gaudin et al. (2018) results for five clusters. These are principally more distant clusters (e.g NGC 3603), or those that are located in highly reddened regions (Danks 1 and Danks 2) and our results are closer than those from Cantat-Gaudin et al. (2018). This is to be anticipated, given the effects of our prior, the small parallaxes and the proportionally large uncertainties. Therefore, our prior does not significantly impact results for most of our cluster distances.

For Markarian 50 and Havlen-Moffat 1, a much larger number of stars (45 and 33 respectively, compared to 8 and 7 in Table 4.7) were used to produce the Cantat-Gaudin et al. (2018) distances, which may explain the discrepancies (though the Markarian 50 distance is within the uncertainties of our result). For NGC3603, there is a difference of almost 3kpc between our distance and the one from Cantat-Gaudin et al. (2018) . However, the uncertainties on our results are proportionally large (∼1.3kpc) and at the upper limit, give a much better agreement with Cantat-Gaudin et al. (2018).

The most surprising deviations from our results, are the Cantat-Gaudin et al. (2018) distances to Danks 1 and 2. Here again, a much larger selection of stars was used in Cantat-Gaudin et al. (2018) and the parallax uncertainties are proportionally large due to the high foreground extinction. As a result, the Cantat-Gaudin et al. (2018) distance is a lot further than both our value, which is moderated by the prior, and the previous 3.8±0.6 kpc distance obtained by Baume et al. (2004).

We now discuss selected rich clusters/associations hosting multiple WR populations.

Table 4.7: Revised distances to star clusters using OB members obtained from *Gaia* DR2 compared to literature values (indicated with DR2 if also obtained from *Gaia*).

Cluster	Distance (this work) (kpc)	Number of stars	Previous distances (kpc)	References	Parallax cut (mas)
Berkeley 86	$1.76^{+0.09}_{-0.08}$	11	1.91, 1.70 (DR2)	1, 2	
Berkley 87	$1.72^{+0.13}_{-0.11}$	18	1.66 (DR2), 1.58	2, 3	
Bochum 10	$2.58^{+0.24}_{-0.20}$	8	2.7	4	ω<0.5
Bochum 14	$2.88^{+0.36}_{-0.29}$	14	0.57	5	ω<0.5
Bochum 7	$5.55^{+1.02}_{-0.78}$	21	5.6±1.7, 4.2±2.1	6, 7	ω<0.3
Cl 1813-178	$2.05^{+0.19}_{-0.16}$	16	2.9±0.8 - $4.8^{+0.25}_{-0.28}$	8	
Collinder 121	$2.52^{+0.14}_{-0.13}$	9	0.75-1.00, 0.55, 0.65 (DR2)	9, 10, 11	ω<0.5
Collinder 228	$2.54^{+0.23}_{-0.20}$	14	3.16, 2.01, 3.10 (DR2), 2.87 (DR2)	3, 10, 11, 12	
Danks 1	$3.41^{+0.53}_{-0.41}$	12	5.32 (DR2), 3.8±0.6	2, 13	
Danks 2	$4.30^{+0.73}_{-0.57}$	5	6.32 (DR2), 3.8±0.6	2, 13	ω<0.5
Dolidze 3	$2.13^{+0.17}_{-0.15}$	21	1.91 (DR2), 1.03	2, 14	
Dolidze 33	$2.96^{+0.36}_{-0.30}$	12	1.07	15	ω<0.5
Havlen-Moffat 1	$3.13^{+0.53}_{-0.40}$	7	4.16 (DR2), 3.30	2, 14	

Cluster	Distance (this work) (kpc)	Number of stars	Previous distances (kpc)	References	Parallax cut (mas)
Hogg 15	$3.20^{+0.44}_{-0.35}$	3	3.39 (DR2), 3.20	2, 5	ω<0.3
Markarian 50	$2.52^{+0.29}_{-0.24}$	8	2.84 (DR2), 3.63, 3.46±0.35	2, 3, 15	
Mercer 23	$3.36^{+0.50}_{-0.39}$	6	6.5±0.3	16	
Mercer 30	$4.72^{+0.71}_{-0.57}$	2	7.2±0.9, 12.6±1.5	17, 18	
NGC 3603	$6.74^{+1.34}_{-1.07}$	8	9.49 (DR2), 7.2±0.1 (DR2), $8.0^{+2.6}_{-1.7}$(DR2)	2, 19, 20	ω<0.1
NGC 6231	$1.60^{+0.11}_{-0.09}$	12	1.62 (DR2), 1.24	2, 5	
Pismis 20	$3.44^{+0.54}_{-0.42}$	5	3.13 (DR2), 3.47, 3.18, 3.38 (DR2)	2, 3, 10, 11	
Pismis 24	$1.71^{+0.12}_{-0.11}$	6	2.51, $1.69^{+0.13}_{-0.11}$(DR2)	3, 20	
Ruprecht 44	$5.38^{+1.08}_{-0.81}$	16	5.54 (DR2), 4.79	2, 3	
Trumpler 16	$2.31^{+0.22}_{-0.18}$	16	2.40 (DR2), 3.16, 2.10, 2.72 (DR2), 2.87 (DR2), ∼2.41 (DR2),	2, 3, 10, 11, 12, 20	ω>0.3
Trumpler 27	$2.43^{+0.25}_{-0.21}$	33	2.88	3	ω<0.5
VVV CL009	$5.62^{+1.27}_{-0.94}$	6	5±1	21	
VVV CL041	$3.56^{+0.59}_{-0.46}$	18	4.2±0.9	22	
Westerlund 1	$3.78^{+0.56}_{-0.46}$	22	3.56 (DR2), $2.6^{+0.6}_{-0.4}$ (DR2), $3.87^{+0.95}_{-0.64}$ (DR2)	2, 23, 24	ω<0.5
Westerlund 2	$4.11^{+0.80}_{-0.59}$	21	4.21 (DR2), $4.73^{+1.13}_{-0.78}$(DR2), 4.16±0.07±0.26	2, 20, 25	ω<0.5

(1) Massey et al. (1995), (2) Cantat-Gaudin et al. (2018), (3) Massey et al. (2001), (4) Patat & Carraro (2001), (5) Dias et al. (2002), Dias et al. (2014a), (6) Corti et al. (2018b), (7) Corti et al. (2007), (8) Messineo et al. (2011), (9) Kaltcheva & Makarov (2007), (10) Mel'nik & Dambis (2017), (11) Melnik & Dambis (2020), (12) Shull & Danforth (2019), (13) Davies et al. (2012a), (14) Vázquez & Baume (2001), (15) Baume et al. (2004), (16) Hanson et al. (2010), (17) Kurtev et al. (2007), (18) de la Fuente et al. (2016), (19) Drew et al. (2019), (20) Maíz Apellániz et al. (2020) (based on one or two individual member stars. Distances are averaged for multiple stars.), (21) Chené et al. (2013), (22) Chené et al. (2015), (23) Aghakhanloo et al. (2020), (24) Davies & Beasor (2019), (25) Vargas Álvarez et al. (2013).

Table 4.8: Revised distances to OB associations using OB members obtained from *Gaia* DR2, compared to literature values (indicated with DR2 if also obtained from *Gaia*).

Associations	Distance (this work) (kpc)	Number of stars	Previous distances (kpc)	References
Ara OB1a, b	$1.64^{+0.05}_{-0.05}$	9	1.3, 1.1/2.78	1, 2
Carina OB1	$2.68^{+0.18}_{-0.16}$	82	1.8-2.8, 2.01, 2.87±0.73 (DR2), 2.99 (DR2)	2, 3, 4, 5
Cassiopeia OB1	2.4	8	2.31 (DR2)	5, 6
Cassiopeia OB7	$3.61^{+0.17}_{-0.16}$	3	2.01, 3.10 (DR2)	2, 5
Centaurus OB1	$2.48^{+0.10}_{-0.09}$	9	1.92, 2.27 (DR2)	2, 5
Cephus OB1	$3.40^{+0.22}_{-0.20}$	10	2.78, 4.32 (DR2)	2,5
Circinus OB1	$1.13^{+0.03}_{-0.03}$	24	2.01, 1.78	2
Cygnus OB1	$1.97^{+0.06}_{-0.06}$	13	1.46, 1.78 (DR2)	2, 5
Cygnus OB2	$1.57^{+0.08}_{-0.07}$	34	1.46, 1.62 (DR2) 1.68 (DR2)	2, 5, 7
Cygnus OB3	$2.05^{+0.08}_{-0.07}$	8	1.83, 1.96 (DR2)	2, 5
Cygnus OB9	$1.62^{+0.04}_{-0.04}$	9	0.96, 1.68 (DR2)	2, 5
Dragonfish	$5.24^{+0.89}_{-0.69}$	12	12.4±1.7, 7.2±0.9	8, 9
Gamma Vel	$0.379^{+0.004}_{-0.004}$	20	$0.345^{+0.001+0.0124}_{-0.001-0.0115}$- $0.383^{+0.0025+0.0153}_{-0.0025-0.0142}$ (DR2)	10
Puppis OB2	$5.56^{+0.55}_{-0.46}$	8	3.18, 5.74 (DR2)	2, 5
Scorpius OB1	$1.65^{+0.07}_{-0.07}$	26	1.53, 1.67 (DR2)	2, 5
Sagittarius OB1	$1.21^{+0.03}_{-0.03}$	6	1.26, 1.40 (DR2)	2, 5

(1) Baume et al. (2011), (2) Mel'nik & Dambis (2017), (3) Molina-Lera et al. (2016), (4) Shull & Danforth (2019), (5) Melnik & Dambis (2020), (6) Chené et al. (2019), (7) Maíz Apellániz et al. (2020) (distances averaged for multiple stars) (8) de la Fuente et al. (2016), (9) Kurtev et al. (2007), (10) Franciosini et al. (2018)

4.3.1 Carina nebula

The Carina nebula (NGC 3572) is the richest optically bright giant H II region in the Milky Way. *Gaia* DR2 confirms that Car OB1 hosts WR22, WR24 and WR25, with WR18 and WR23 possible members. The substructure of the region is quite complex (Buckner et al. 2019, Reiter & Parker 2019), as it also contains the clusters Trumpler 16 and Trumpler 14 (Molina-Lera et al., 2016). WR25 is a member of Trumpler 16, which has a parallax of 0.430±0.115mas, corresponding to a distance of $2.18^{+0.74}_{-0.46}$ kpc. Davidson et al. (2018) proposes a slightly smaller parallax of 0.383±0.017mas, which falls within our uncertainties and Smith (2006c) gives a distance of 2.35±0.05 kpc to η Carinae/Trumpler 14. WR24 is also a possible member of Collinder 228, although this is difficult to confirm, as the cluster contains stars exhibiting a wide range of proper motions.

Molina-Lera et al. (2016) investigate the complex structure of Carina, identifying a foreground population at 1.4–2.3 kpc (corresponding to Trumpler 18), a second population distributed over 2.0–3.3 kpc, plus a background group. Shull & Danforth (2019) obtain 2.87 ± 0.73 kpc[2] for 29 O star members of Trumpler 14–16 and Collinder 228 based on *Gaia* DR2 parallaxes. We also note the bulk of objects in our sample are between 2 and 4 kpc. Molina-Lera et al. (2016) also quote colour excesses of 0.3-0.6 mag. For our WR star sample, WR22, WR24 have values in this range, with E(B-V)=0.50±0.21 and E(B-V)=0.35±0.21, respectively (Chapter 3). WR25 has a higher E(B-V)=0.93±0.31, using an anomalous reddening law of $R_v^{WR} = 6.2$, from Crowther et al. (1995). WR23 has a comparatively low E(B-V)=0.18±0.29 (Chapter 3) which suggests it could be a foreground object. However, the parallax derived distance is consistent with the Carina region and the reddening measurement has a large uncertainty.

4.3.2 Cygnus OB2

Cygnus OB2 is the nearest OB association rich in massive stars (Massey & Thompson, 1991). We find a distance of $1.57^{+0.08}_{-0.07}$ kpc for Cygnus OB2, albeit with some substructure. Figure 4.2 shows the distribution of distances and proper motions, indicating a spread from 1.4 kpc to 1.8 kpc (if uncertainties are included). WR144 is located towards the rear of the association at ∼1.7 kpc, whilst WR145 is closer to ∼1.4 kpc. Both these distances are in line with pre-*Gaia* DR2 literature distances of 1.45 kpc (Wright et al., 2015) and 1.7 kpc (Massey & Thompson, 1991).

[2]Calculated using inverted parallaxes.

Berlanas et al. (2019) have modelled the substructure of the cluster using DR2 data, and have concluded that there are two main groups. One of these, at around 1.76 kpc, they term the 'main' group, with a 'foreground' group at 1.35 kpc. Our results suggest WR145 is a member of the foreground group and WR144 as a member of the more distant main group.

4.3.3 Danks 1 and 2

Danks 1 and 2 clusters are young massive clusters within the G305 star formation complex (Davies et al., 2012a). In Danks 1, three WR stars that were thought to be members have been confirmed, with three possible (but unconfirmed) members. Our membership list has very few entries for Danks 2, but we confirm WR48-2 is a member. The astrometric excess noise of all Danks 1 and 2 WR stars are greater than 0.3 mas, with WR48-4 exceeding 1 mas, indicating potentially unreliable astrometric results.

We find a distance of $3.41^{+0.53}_{-0.41}$ kpc to Danks 1 and $4.30^{+0.73}_{-0.57}$ kpc to Danks 2, in fair agreement with the 3.8±0.6 kpc average distance of the G305 complex (hosting Danks 1 and 2), from Davies et al. (2012a).

Danks 1 and 2 are in regions of high dust extinction, with A_K=1.1±0.16 for Danks 1 and A_K=0.92±0.29 for Danks 2 (Davies et al., 2012a). This is consistent with A_K=0.99±0.22 for WR48-7 and A_K=0.83±0.20 for WR48-10 in Danks 1. However, WR48-2 in Danks 2 has A_K=0.48±0.20, significantly lower than the range for the cluster found by Davies et al. (2012a). In Chapter 3, we found the absolute magnitude for WR48-2 is anomalously faint for a WC7 or WC8 star, suggesting an underestimate of dust extinction, such that WR48-2 is a member of Danks 2.

4.3.4 γ Velorum

WR11, the WC8 component of γ Velorum, is confirmed as a member of its eponymous association. As WR11 is too bright for *Gaia*, we use proper motion and parallax results from *Hipparcos* (van Leeuwen, 2007) to confirm membership. The list of known members was compiled from the 20 brightest members in the V band (Jeffries et al., 2014a). These are not OB stars, because the γ Velorum system is primarily surrounded by low mass stars (Jeffries et al., 2014b).

The association has a wide range of proper motions, consistent with the suggestion by (Jeffries et al., 2014b) that it is barely bound. We find a distance of $0.379^{+0.004}_{-0.004}$ kpc to the group, consistent with the distance to WR11 ($0.342^{+0.038}_{-0.030}$ kpc). It is also consistent with

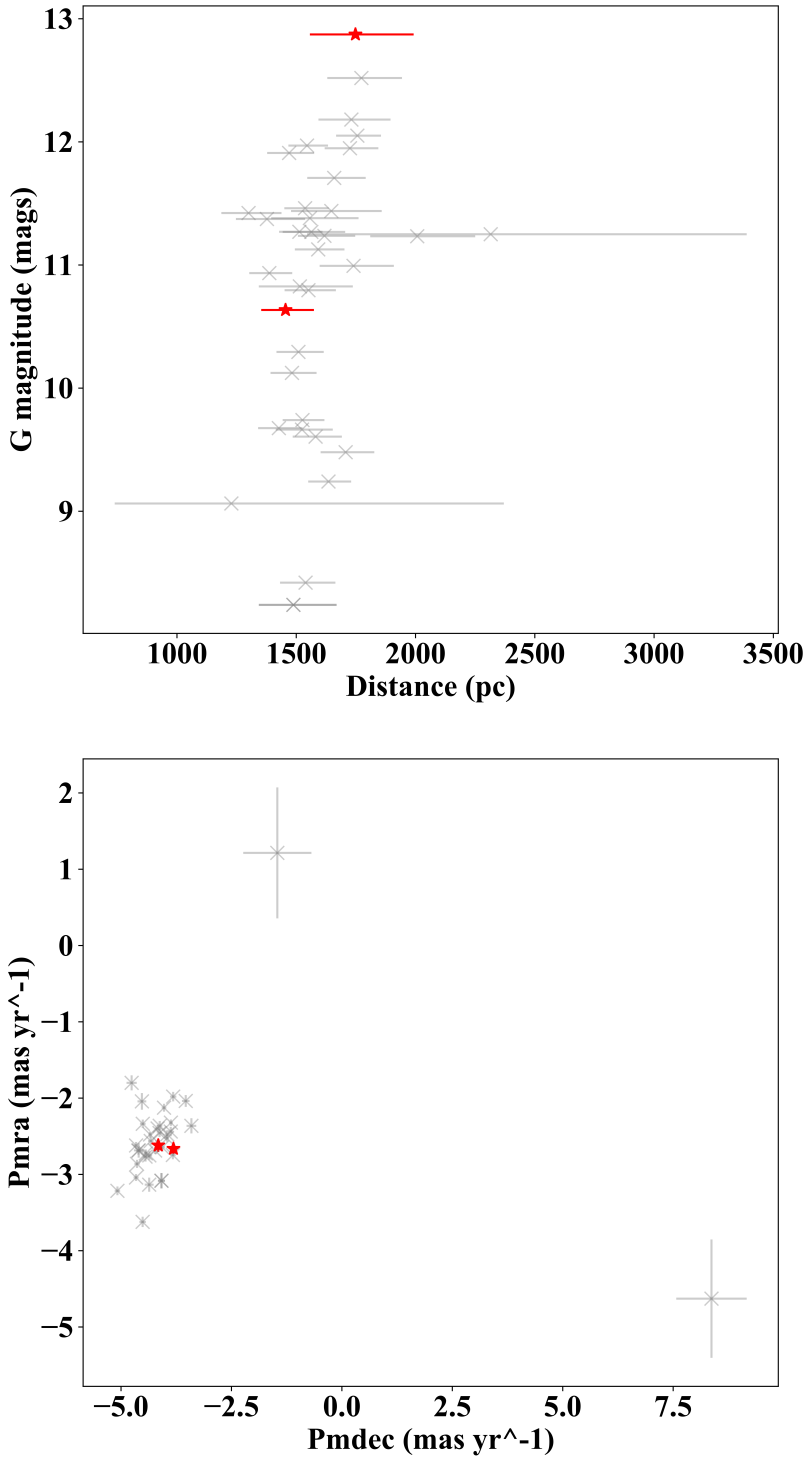

Figure 4.2: Distances vs G magnitudes (upper panel) and proper motions (lower panel) for members of Cyg OB2. Grey crosses are O and B stars from Maíz Apellániz et al. (2013) while red stars are WR stars WR144 and WR145.

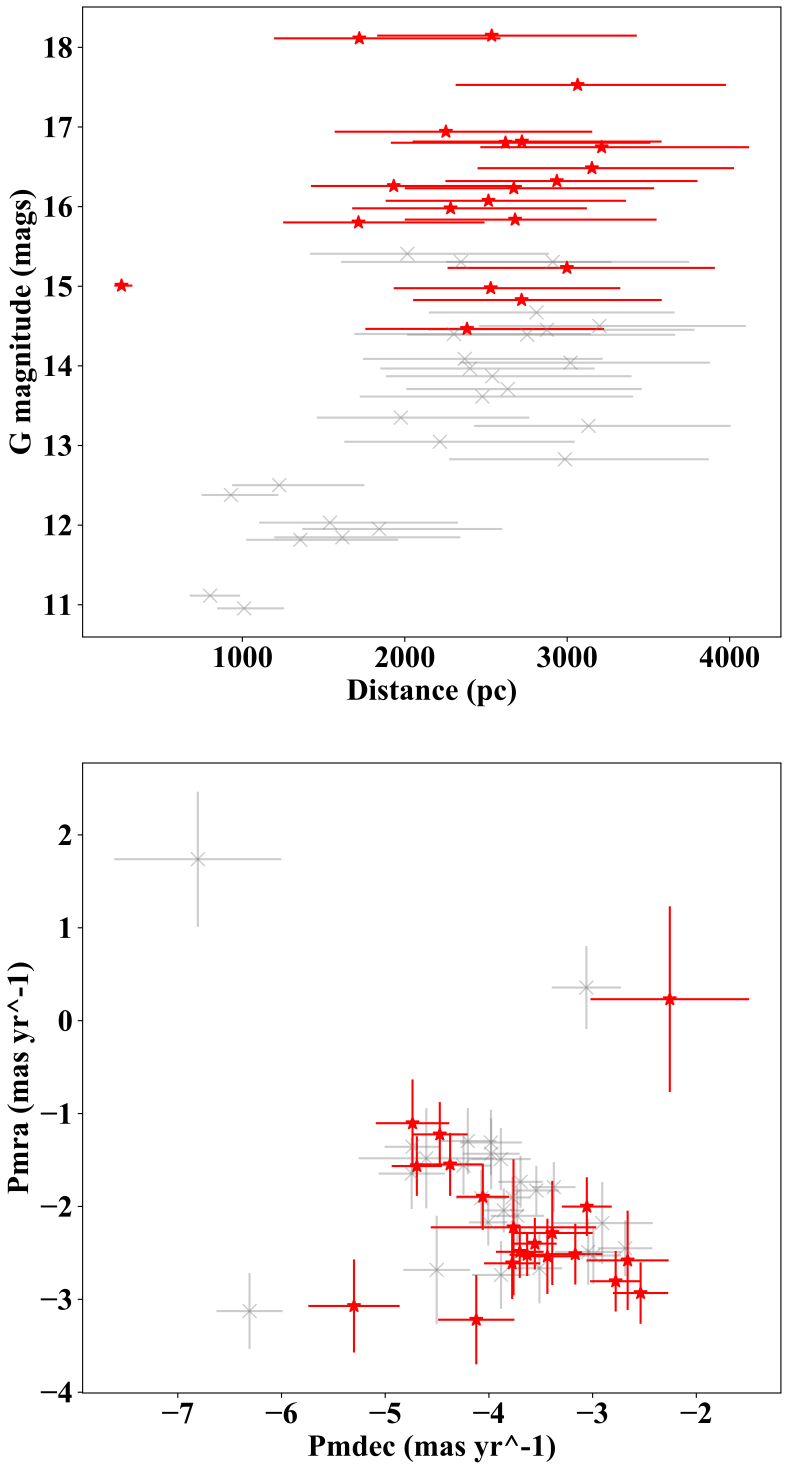

Figure 4.3: Distances vs G magnitudes (upper panel) and proper motions (lower panel) for members of Westerlund 1. Grey crosses are OB stars from Clark et al. (2005) while red stars are WR stars from Crowther et al. (2006a).

results from Franciosini et al. (2018), who obtain two populations at $345.4^{+1.0+12.4}_{-1.0-11.5}$ pc and $383.4^{+2.5+15.3}_{-2.5-14.2}$ pc, respectively (accounting for both systematic and random errors). Two populations were also found by Jeffries et al. (2014b).

However, Cantat-Gaudin et al. (2019) used *Gaia* DR2 to find that the two populations previously identified (e.g Jeffries et al. 2014b, Franciosini et al. 2018) are part of a much larger and more complex region around Vela OB2. These were possibly created by a supernova, which triggered star formation in the surrounding gas cloud.

Unfortunately, the current scope and methods of this work do not allow us to fully disentangle the structure of Vela OB2 and assign membership to a specific subregion. We simply note that it is a member of this region and does therefore not appear to be isolated.

4.3.5 NGC 3603

NGC 3603 is one of the youngest, most compact and high mass star clusters in the Milky Way (Moffat et al., 2002). Unfortunately, young massive WN stars within the cluster core (Crowther & Dessart, 1998) could not be resolved with *Gaia* DR2, but we confirm that WR42-1 and WR43-2 in its periphery are members.

We obtain a distance of $6.74^{+1.34}_{-1.07}$ kpc for NGC 3603, within uncertainty of the literature values of 7.2 kpc (Melnick et al., 1989) and 7.6 kpc (Melena et al., 2008). Recently, Drew et al. (2019) obtained a distance of 7.2±0.1 kpc for a full sample of O star members, increasing to 8.2±0.4 kpc, when restricting the sample to stars within 1 arcmin of the cluster centre.

4.3.6 Westerlund 1

Westerlund 1 is an exceptionally rich star cluster (Clark et al., 2005), thought to host 24 WR stars (Crowther et al., 2006a). *Gaia* DR2 detects 20 of these stars, and we confirm 18 stars as members of Westerlund 1, as shown in Figure 4.3. In two cases membership could not be confirmed, owing to an unphysical distance (WR77p) or discrepant proper motions (WR77r). Unfortunately, many confirmed WR members also have astrometric excess noises above 1 mas, which means their distances are somewhat unreliable. However, our primary membership indicator is proper motion, which is less vulnerable to large fractional uncertainties than parallax. A further 4 stars are not detected by *Gaia*, which we assume to be members.

We estimate a cluster distance of $3.78^{+0.56}_{-0.46}$ kpc (though this excludes many stars

with high excess noise). This is more distant than the $2.6^{+0.6}_{-0.4}$ kpc obtained from the full bayesian combination of cluster member parallaxes from Aghakhanloo et al. (2020). The difference may stem from the fact we excluded some stars, via a parallax cut, as they seemed to be foreground objects. However, our result is consistent with $3.87^{+0.95}_{-0.64}$ kpc from Davies & Beasor (2019). All three results from *Gaia* are closer than the historical distance estimates of around 4–5 kpc (Clark et al., 2005; Crowther et al., 2006a). Davies & Beasor (2019) propose that the zero point is the dominant source of parallax uncertainty, adopting −0.05 mas instead of our −0.03 mas (Chapter 2).

4.3.7 Westerlund 2

Westerlund 2 is another rich, young high mass cluster (Rauw et al., 2007). Proper motions for WR20a and WR20b are comparable to the *Gaia* cluster median of $\mu_\alpha = -5.172$ mas yr^{-1}, $\mu_\delta = 2.990$ mas yr^{-1} (Drew et al., 2018), favouring cluster membership. Drew et al. (2018) infer that WR20c and WR20aa possess proper motions consistent with recent (0.5 Myr) ejection from Westerlund 2. We obtain a distance to the cluster of $4.11^{+0.80}_{-0.59}$ kpc, which is close to the previous estimate of 4.16±0.07 (random) +0.26 (systematic) kpc from Vargas Álvarez et al. (2013). There is some evidence for a background group or association (Drew et al., 2018), to which WR20a is a possible member (a distance of 5 kpc was inferred in Chapter 3). The extinctions of both WR stars are consistent with previous values for the cluster. Vargas Álvarez et al. (2013) lists a range of $5.7 < A_V < 7.5$ mag for OB stars in Westerlund 2, compared with A_V=6.44±0.64 and 7.57±0.64 mag for WR20a and WR20b, respectively, obtained from A_v^{WR} (visual extinction in the Smith narrow band (Smith, 1968b) in Chapter 2, plus A_v^{WR}=1.1A_V from Turner 1982).

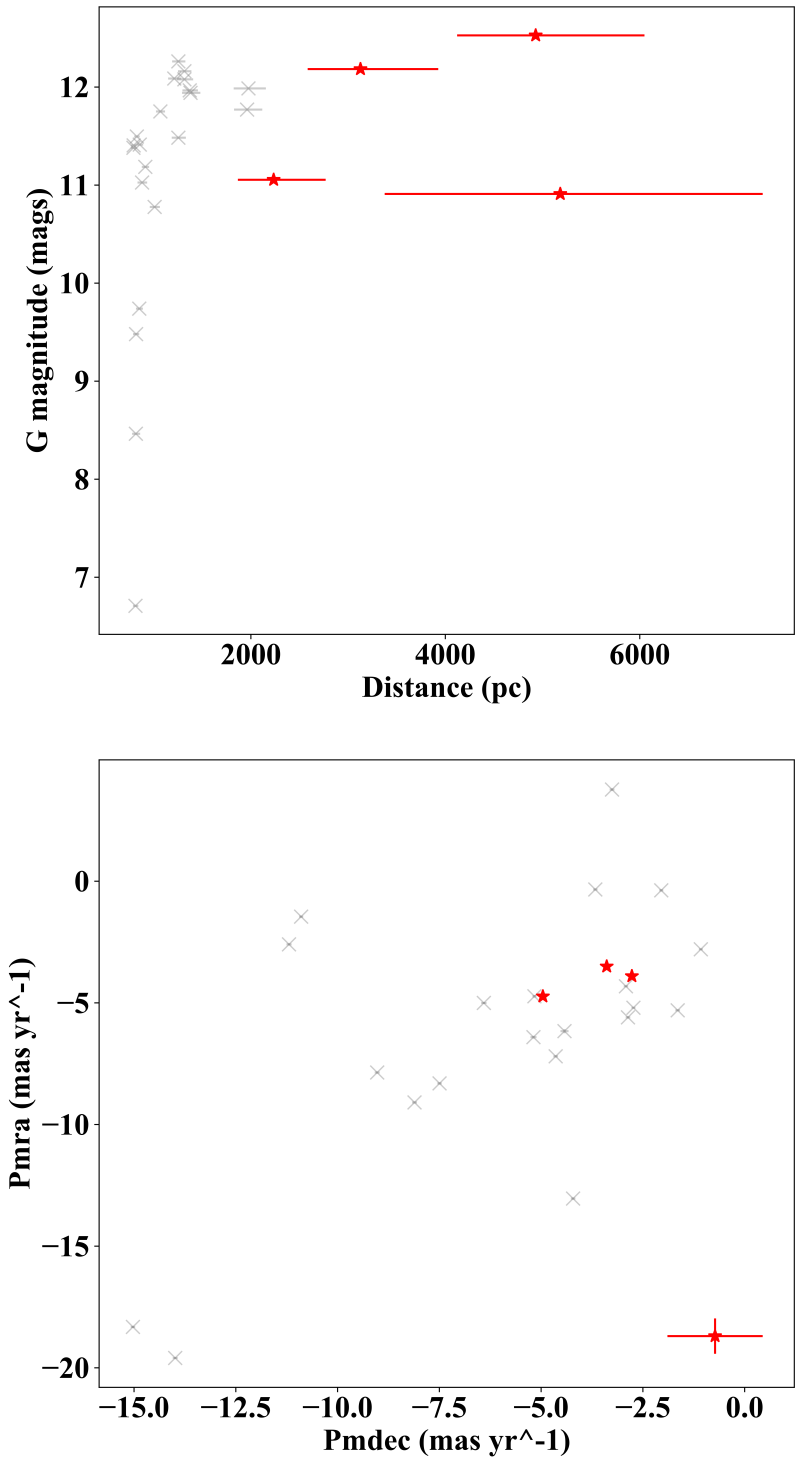

Figure 4.4: Distances vs G magnitudes (upper panel) and proper motions (lower panel) for members of Circinus OB1. Grey crosses are O and B stars from Kharchenko et al. (2013) while red stars are WR65–WR68. This example demonstrates the need for distances in assigning association membership, as proper motions suggest WR65, WR67 and WR68 are members, but distances indicate WR65 and WR68 are behind the association. WR65 may also be a background object, but its distance uncertainty may overlap with the back of the association.

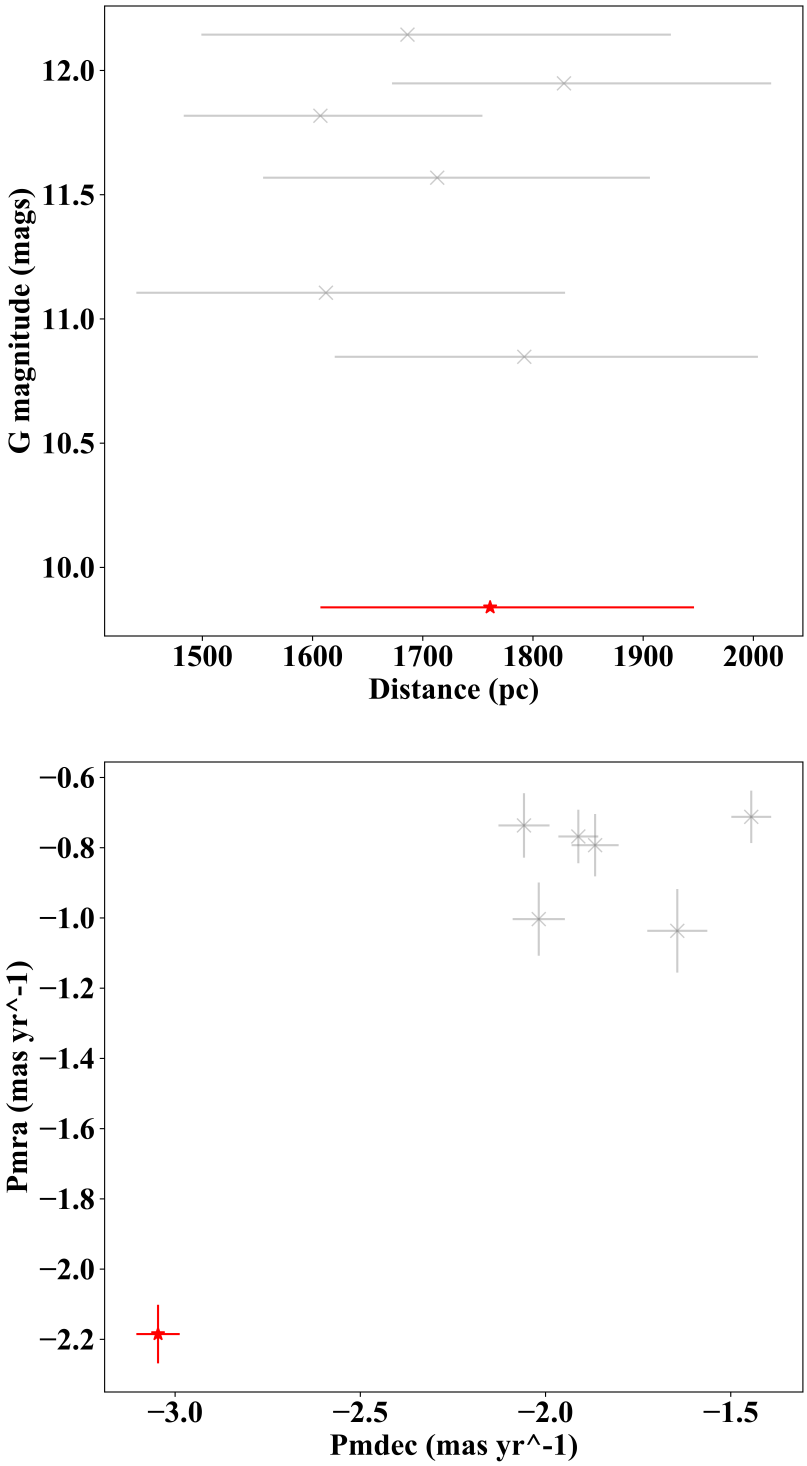

Figure 4.5: Distances vs G magnitudes (upper panel) and proper motions (lower panel) for members of Pismis 20. Grey crosses are OB stars from Maíz Apellániz et al. (2013). The proper motion discrepancy between these data points and the red star, WR93, suggests the latter is not a member of the association.

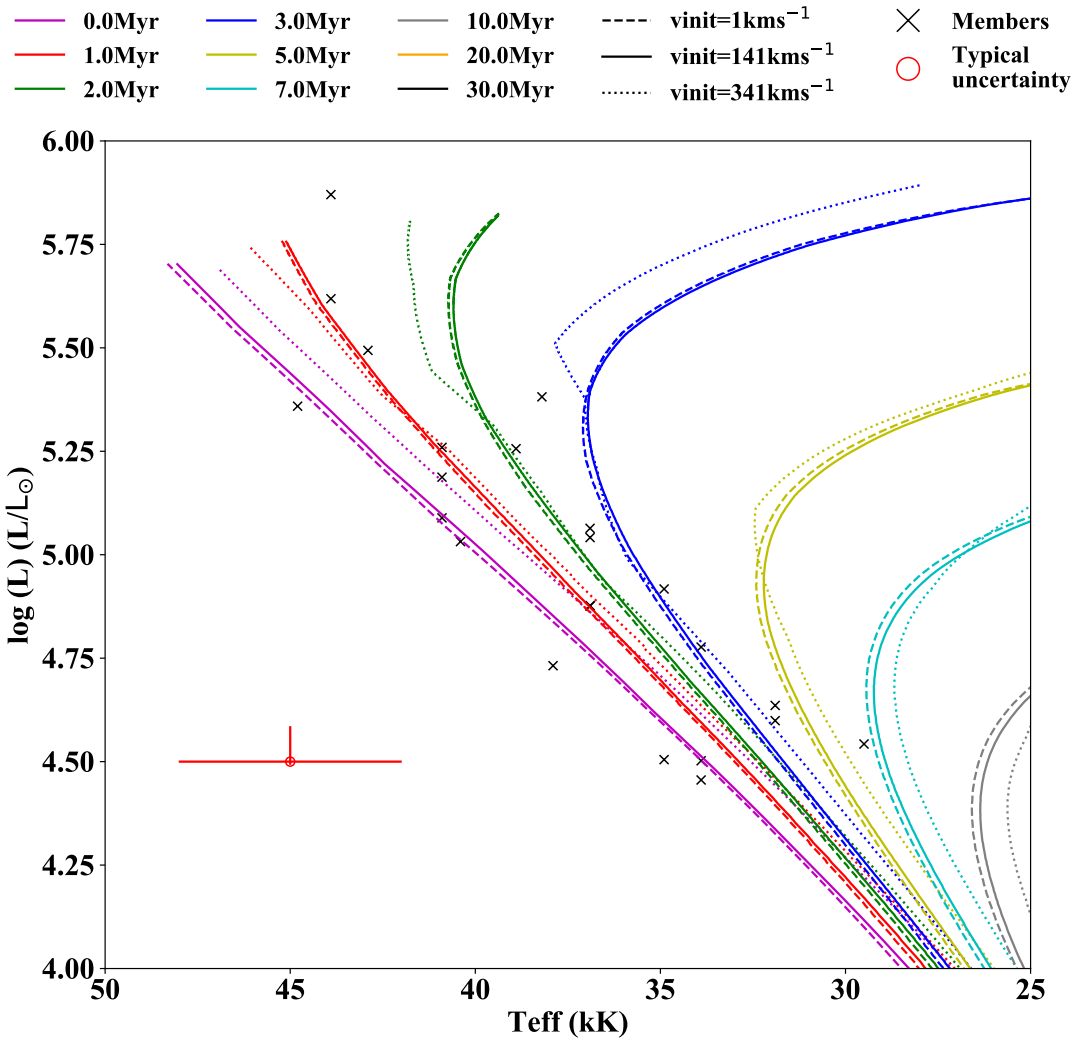

Figure 4.6: Trumpler 16 O and B star cluster members and 0-30 Myr isochrones from Brott et al. (2011). The solid lines denote stars with a 'typical' 141 km s^{-1}(the closest value to the mean from Brott et al. 2011) rotation rate, whilst the dashed line is for a 1 km s^{-1}'non rotating' star and the dotted line is for a 341 km s^{-1}rapid rotator.

4.4 Cluster ages

Armed with our revised distances and confirmed OB, WR members of star clusters, we are able to estimate ages from a comparison between cluster members and solar metallicity isochrones (Brott et al., 2011), following the approach of Massey et al. (2001) and Crowther et al. (2006a). It is important to recognise that these isochrones are based

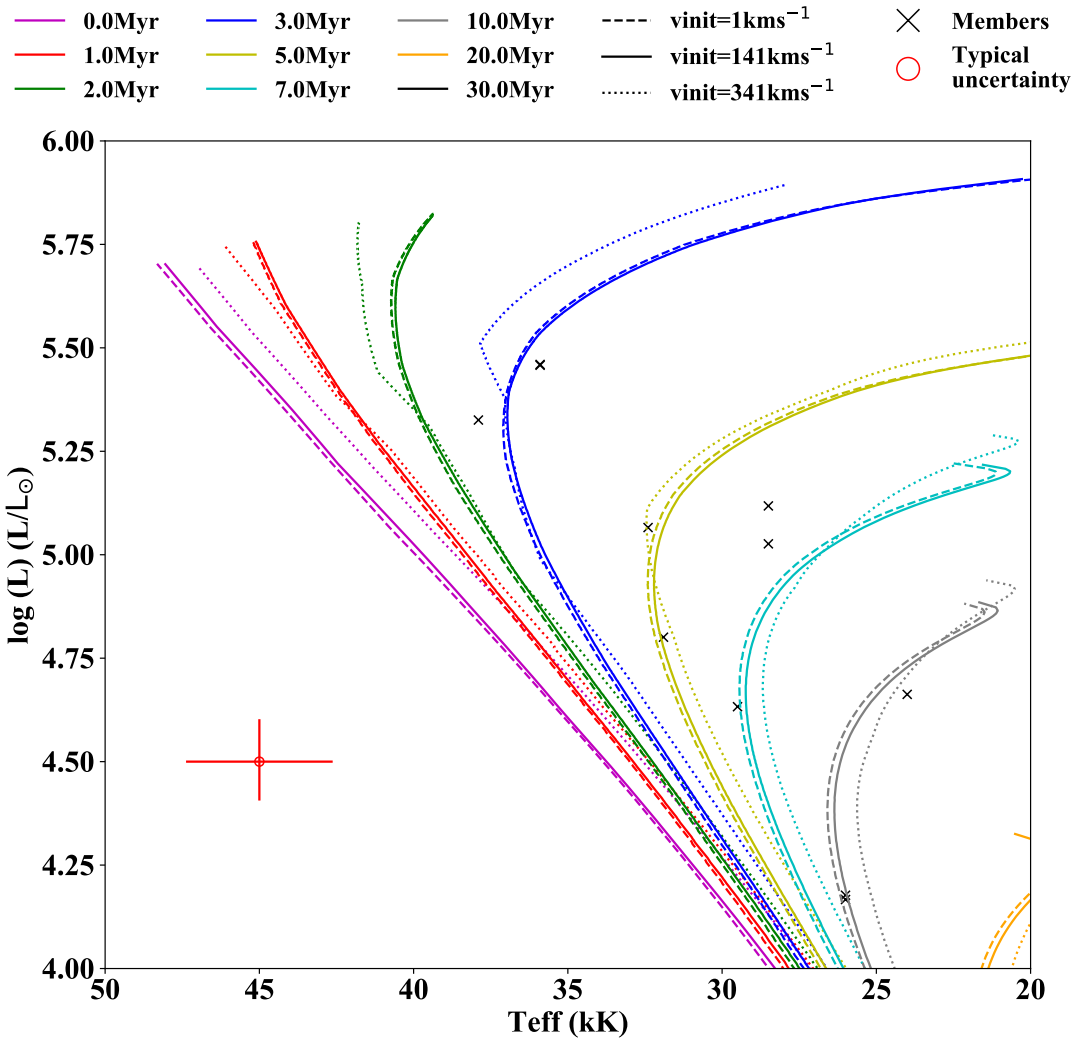

Figure 4.7: Bochum 7 O and B star cluster members and 0-30 Myr isochrones from Brott et al. (2011). The solid lines denote stars with a 'typical' 141 km s^{-1}(the closest value to the mean from Brott et al. 2011) rotation rate, whilst the dashed line is for a 1 km s^{-1}'non rotating' star and the dotted line is for a 341 km s^{-1}rapid rotator.

on single stars and do not account for mass transfer in binaries, which may lead to resulting rejuvenated massive stars. Our results are therefore a lower limit for the true cluster ages (e.g Stevance et al. 2020 find that single star isochrones can underestimate the true ages of H II regions by 0.2 dex, when compared to binary population synthesis models).

Temperature calibrations for O stars are obtained from Martins et al. (2005), whilst

those for B stars are from Conti et al. (2008). O star bolometric corrections and intrinsic colours are from Martins & Plez (2006b) (via Martins & Plez 2006a). Intrinsic colours for B stars are taken from Wegner (1994). Crowther et al. (2006b) provide bolometric corrections for supergiants in the V band, Lanz & Hubeny (2007) provide the bolometric calibration for dwarfs.

Figure 4.6 shows an example for Trumpler 16, where the members are reasonably well gathered around the ∼1 Myr isochrone, with some stars ±1 Myr. However, the results for Bochum 7 (Figure 4.7) are more scattered, with the bulk suggesting an age of ∼5 Myr, but outliers at up to ∼25 Myr. This suggests that multiple populations may have formed within this star forming region.

The clusters Cl 1813-178, Danks 1 and Danks 2, Mercer 23, VVV CL009 and VVV CL041 were excluded from the age analysis, as only IR data was available for these clusters and spectral types for many O and B star cluster members were uncertain.

We categorise clusters with ages of ≤2 Myr as 'young', those with 2–5 Myr ages as intermediate and ≥5 Myr as old. Table 4.9 lists cluster ages, the adopted R_V used to calculate reddening, average extinctions A_V for cluster members, WR members and spectral types of OB stars within the cluster. Unfortunately, no spectral type information was available for the members of Bochum 10 or 14 and so it was not possible to determine their cluster ages.

Table 4.9: Age estimates of star cluster within the Galactic disk host to WR stars, sorted by increasing age. Cluster membership of WR stars from *Gaia* DR2 are indicated in bold. We categorise ages as either young ($\leq$ 2 Myr), intermediate (2–5 Myr) or old ($\geq$ 5 Myr).

Cluster	Age in Myr (V-band)	Photometry Ref	R_V	R_V Ref	Mean A_V (mag)	Age in Myr (literature)	Age Ref	WR members (Sp Type)	OB Sp Type Range	OB Ref
						— Young —				
NGC 3603	1±1	2	3.55	1	4.9	1 ± 1, $1 - 4$	1, 2	**WR43-2** (O2If*/WN5), **WR42-1** (WN4b), WR43A (WN6ha+WN6ha), WR43B (WN6ha), WR43C (O3If*/WN6)	O3V-O8.5V	2
Trumpler 16	1±1	3, 4	3.1		1.7	1.4	5	**WR25** (O2.5If*/WN6+O)	O3.5V-B0V	3, 4
Westerlund 2	2 ± 1	6	4.1	6	7.2	< 1	6	**WR20a** (O3If*/WN6+ O3If*/WN6), **WR20b** (WN6ha)	O3V-O8V	7, 8
Collinder 228	~ 2	5	3.1		1.4			**WR24** (WN6ha)	O5III-9.5V	5
						— Intermediate —				
Westerlund 1	< 5	9	3.1		12.6	4.5-5	10	**WR77aa** (WC9d), **WR77a** (WN6)	O9III-B5Ia	9
Bochum 7	~ 5	11	3.3	12	2.7	< 3	11	**WR12** (WN8h)	O6.5V-B0V	11
						— Old —				
Ruprecht 44	7 ± 3	13, 5	3.1		1.9	3	5	**WR10** (WN5ha)	O8III-B1V	13, 5
Trumpler 27	7^{+3}_{-2}	14, 5	3.1	14	4.7	5	5	**WR95** (WC9d), **WR98** (WN8/C7)	O8III-B8I	15, 5
Berkeley 87	8–9	15, 5	3.1		5.1	3	5	**WR142** (WO2)	O8.5III-B1V	16, 5
Markarian 50	~ 10	5	3.1		2.5	7.4	5	**WR157** (WN5-B1II)	B0III-B1.5V	17, 5

(1) Sung & Bessell (2004), (2) Melena et al. (2008), (3) Massey & Johnson (1993), (4) Smith (2006a), Smith (2006b), (5) Massey et al. (2001), (6) Hur et al. (2015), (7) Rauw et al. (2007), (8) Rauw et al. (2011), (9) Clark et al. (2020), (10) Crowther et al. (2006a), (11) Corti et al. (2018b), Corti et al. (2018a), (12) Sung et al. (1999), (13) Turner (1981), (14) Perren et al. (2012), (15) Moffat et al. (1977), (16) Turner & Forbes (1982), (17) Turner et al. (1983)

All four young clusters host hydrogen-rich main sequence WN stars, Of/WN stars and early O dwarfs. These add to the increasing evidence that main-sequence very massive stars exhibit transition Of/WN or weak-lined WNh spectral morphologies (Crowther et al., 2010). Two clusters have age estimates of ≤5 Myr, so one would expect them to host classical WR stars (hydrogen-deficient WN and WC stars) and mid-type O stars. This is true in both instances and although the age estimate for Westerlund 1 is an upper limit, it is in line with the previous literature value from Crowther et al. (2006a).

Four clusters were assigned ages of >5 Myr, owing to the presence of late O and early B giants. Both Markarian 50 (WR157) and Ruprecht 44 (WR10) also host weak-lined WN5 stars, with previous age estimates for Markarian 50 pointing to ages of 7 Myr or greater (Massey et al., 2001; Crowther et al., 2006a). In contrast, previous estimates of the age of Ruprecht 44 have indicated ∼3 Myr, and the luminosity of WR10 from Hamann et al. (2019) adjusted to the revised distance of Chapter 3 is relatively high ($\log(L/L_\odot)$=5.8) for an age of 7 Myr, suggesting it could be a rejuvenated merger product (Schneider et al., 2014).

Trumpler 27, another old cluster, contains a very late WC and WN/C type; both expected for a younger cluster. However, the uncertainty of the result may mean that the cluster is somewhat younger than 7 Myr, with the younger limit of 5 Myr more in line with previous estimates. The WO star in Berkeley 87 would also appear to be too young for a cluster 8–9 Myr old. However, we note that there is a wide scatter in the possible isochrones that would fit this cluster. The bulk of stars are best fit to the 8–9 Myr isochrone, but there are two outliers at ∼4 Myr (including the only O star in the sample). These younger outliers better match the age result from Massey et al. (2001) and may indicate the presence of multiple populations in Berkeley 87.

For the selected star clusters, there is no evidence of a population of low luminosity WR stars in old clusters, originating from envelope stripping by a close companion. Models from Götberg et al. (2018) indicate that stripped helium stars can exhibit a variety of spectral types depending on their mass. At solar metallicity, progenitors of $\geq 15 M_\odot$ mass donors in close binaries which produce stripped helium stars of $\geq 5 M_\odot$ are anticipated to resemble WN stars. However, due to their low luminosities and/or dilution from an early-type companion (mass gainer), these features may go undetected.

Again, we can compare the cluster ages found using the Cantat-Gaudin et al. (2018) distances to our results. Only the age of NGC3603 differs, increasing to 2^{+2}_{-1}Myr. This is still in the young category, and within the uncertainties of the our age classification from Table 4.9. At the upper limit, it would move into the intermediate age category, but the

stars best fit by this age are later O types and could therefore be part of a slightly older population than the WR star members.

4.5 Implications for massive star formation and environments

We have confirmed literature results of a low cluster membership fraction of 14% for WR stars within the Galactic disk, increasing to 36% after OB association/star-forming region membership is considered (Table 4.6). If the O-type progenitors of WR stars primarily originated in populous, or high mass star clusters, the only way to produce such a low WR cluster membership fraction is if the WR stars are ejected from the cluster, or if the cluster dissolves and is consequently unrecognisable. Only 42% of nearby Galactic O stars currently lie within known star clusters (Table 4.1), so assuming a low ejection fraction or modest ejection velocities, approximately half of WR progenitors formed within clusters have been lost. A relatively high fraction of O stars can be dynamically ejected from dense, relatively massive star clusters over the first few Myr (Poveda et al., 1967), albeit with relatively modest velocities, of order 10 $\mathrm{km\,s^{-1}}$ (Oh & Kroupa, 2016).

Alternatively, the majority of WR progenitors may originate in OB associations, but be ejected following the disruption of their binary systems due to core-collapse supernovae (Blaauw, 1961). Over 70% of Galactic OB stars in the Solar Neighbourhood (few kpc) are found in OB associations/star forming regions, whereas 36% of WR stars external to the Galactic Centre region are associated with a star forming region. Since the majority of massive stars appear to be born in close binary systems (Sana et al., 2012), it is possible that WR stars are ejected through this mechanism. However, simulations suggest only 3% of such binaries lead to runaway WR stars, with $\geq$30 $\mathrm{km\,s^{-1}}$ (Eldridge et al., 2013), with slower moving walkaway stars much more common (Renzo et al., 2019).

It is therefore apparent that WR stars may be ejected either dynamically from dense clusters, or via the disruption of a binary system following a supernova (albeit with relatively modest velocities in most instances). Recalling 1 $\mathrm{km\,s^{-1}}$ equates to 1 pc/Myr, a WR star with an age of 4 Myr moving at 10 $\mathrm{km\,s^{-1}}$ would travel no more than 40 pc from its birth site, usually much less owing to the delayed timescale for dynamical ejection/binary disruption. In contrast, field WR stars dominate the population in the Galactic disk, with runaways relatively common. From Chapter 3, we identified 8% of WR stars from *Gaia* DR2 to lie at least three H II scale heights from the Galactic

midplane, representing a minimum runaway fraction. The true runaway fraction must be higher, since these statistics neglect WR stars ejected within the disk. Indeed, the runaway fraction of O stars is 10–25% (Gies & Bolton, 1986), with a high fraction of runaways amongst the field O star population (de Wit et al., 2005).

The fact that only a minority of O stars are found in open clusters, together with the tension between the scarcity of predicted fast moving WR stars from low-mass clusters/close binaries, and the observed runaway fraction from the field population of WR stars, argues for an alternative to the usual assumption that their progenitors originate in dense clusters. In the following subsections we consider the possibility that WR progenitors originate in low density star-forming regions which are not recognised as clusters/associations, or that their host star cluster has dissolved.

We do not include primordial binaries in these simulations, despite the high incidence of close binaries of massive stars (Sana et al., 2012). If binary systems containing massive stars form via capture, then we implement stellar and binary evolution. However, we do not find any instances of the formation of very close binaries that would subsequently undergo common-envelope evolution in our simulations (and hence lengthen the WR-phase).

The close binary channel may produce main sequence mergers or strip the envelope of the primary through Roche Lobe overflow (de Mink et al., 2014), extending the limit for the formation of WR stars to lower masses. Shenar et al. (2020) suggest a lower initial mass threshold of $18 M_{\odot}$ for solar-metallicity WR stars, while Götberg et al. (2018) suggest 15 $M_{\odot}$, although such helium core masses/luminosities lie below those of WR stars included in our study. Nevertheless, they are considered to dominate the statistics of stripped envelope core-collapse supernovae (Eldridge et al. 2013; Smith et al. 2011).

The simulations presented below thus assume that WR stars originate from (initially) single stars with masses in excess of 25 $M_{\odot}$. According to Meynet & Maeder (2005) the lower mass limit to the formation of single WR stars at solar metallicity is 22 $M_{\odot}$ for rapid rotators, or 37 $M_{\odot}$ for non-rotators, while Shenar et al. (2020) obtain 20–30 $M_{\odot}$.

4.5.1 High mass stars in low-mass clusters and associations

Here we consider the possibility that an apparently isolated WR star is in fact part of a low-mass star-forming region that has formed one massive star, with the remaining stellar content too faint to be observed (Parker & Goodwin, 2007).

One piece of evidence for WR stars in such environments comes from isolated protostellar cores of high mass stars. An example is G328.255–0.532 which may eventually

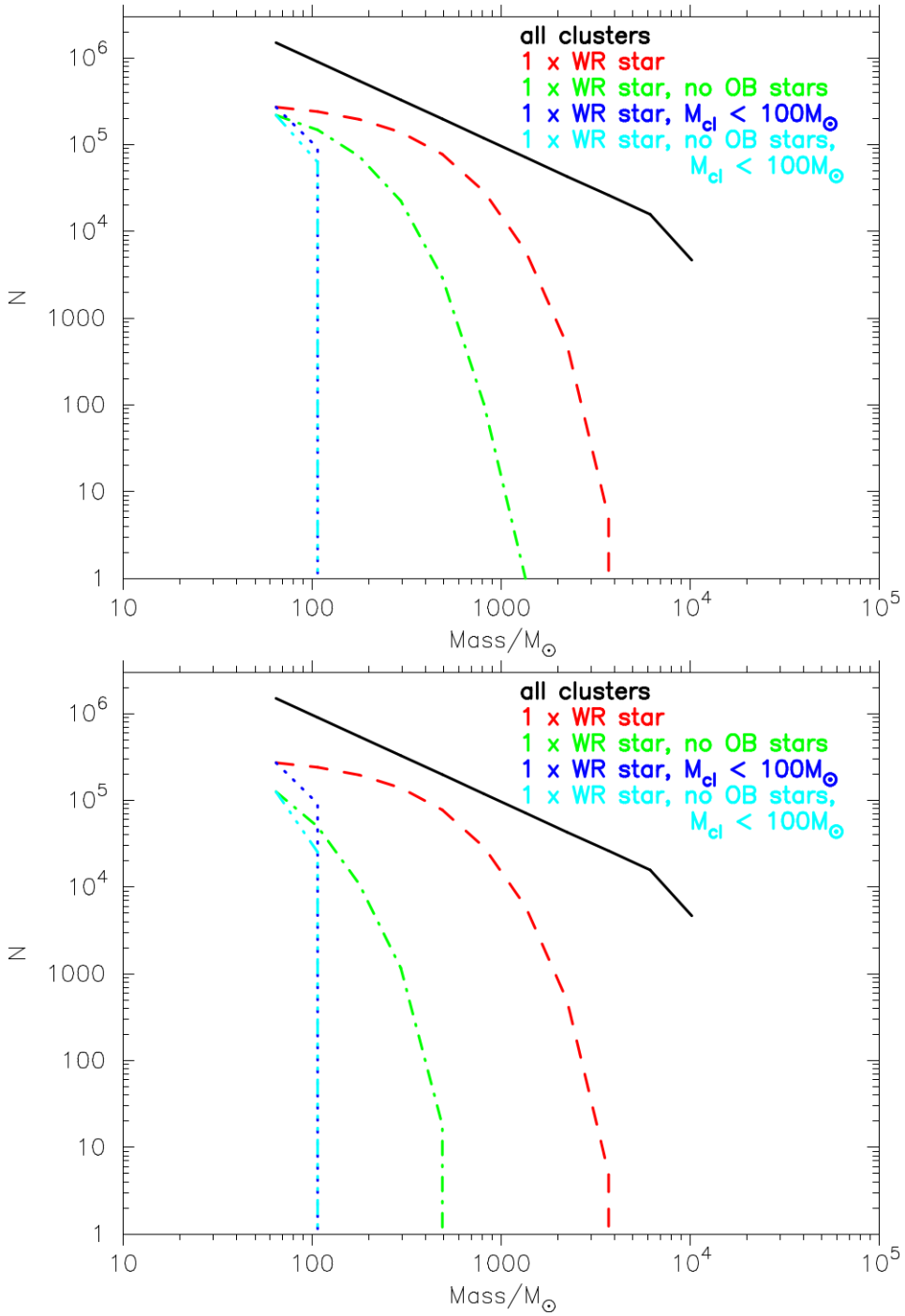

Figure 4.8: Monte Carlo simulations of the number of clusters with different masses, which contain WR stars. Each line shows the relation between cluster mass and number if they contain one WR star. The cutoff applied in the upper panel was >10 $M_\odot$ to OB stars (corresponding to O stars and early B stars, which are the brightest OB subtypes) and >25 $M_\odot$ for WR stars. For the lower panel the cutoff was >5 $M_\odot$ for OB stars (a stricter criterion removing O stars, early B and mid B stars) and >25 $M_\odot$ for WR stars.

form a $\sim$50M$_\odot$ O star (Csengeri et al., 2018).

A notable example of an existing low-mass star forming region host to massive stars is the γ Velorum group (Jeffries et al., 2014b), Additionally, Prisinzano et al. (2016) finds that the total mass of the cluster is only $\sim$100 M$_\odot$. However, accounting for the wider environment, Cantat-Gaudin et al. (2019) find a total mass of $2330 M_\odot$. This potentially indicates that these regions surrounding a single massive star appear low mass, but may be part of much wider, more massive star forming regions.

In order to test the hypothesis that our observed isolated WR stars are the most massive stars within low-mass, faint regions, we perform a Monte Carlo experiment similar to those in Parker & Goodwin (2007) and Tehrani et al. (2019). First, we sample cluster masses, $M_{\rm cl}$ in the range $50 - 10^4$M$_\odot$, from a single power-law of the form

$$N(M_{\rm cl}) \propto M_{\rm cl}^{-\beta}, \tag{4.2}$$

where $\beta = 2$ (Lada & Lada, 2003). Once the cluster mass has been selected, we populate the cluster with stellar masses drawn from a Maschberger (2013) Initial Mass Function, which has a probability density function of the form

$$p(m) \propto \left(\frac{m}{\mu}\right)^{-\alpha} \left(1 + \left(\frac{m}{\mu}\right)^{1-\alpha}\right)^{-\beta}, \tag{4.3}$$

where $\mu = 0.2\,$M$_\odot$ is the average stellar mass, $\alpha = 2.3$ is the Salpeter (1955) power-law exponent for higher mass stars, and $\beta = 1.4$ describes the slope of the IMF for low-mass objects (which also deviates from the log-normal form; Bastian, Covey & Meyer, 2010). We sample this distribution in the mass range 0.1 – 300 M$_\odot$, which allows for the most massive stars known to form (Crowther et al., 2010).

We sample from these distributions until we obtain a total stellar mass of 10^9M$_\odot$. We then determine how many clusters contain one WR star (defined as having an individual mass $>25\,$M$_\odot$, by assuming solar metallicity Crowther 2007) and no other OB stars. These are defined as having individual masses $>5\,$M$_\odot$ (to exclude O stars, early and mid B-type stars, where the latter are the most faint OB spectral types likely to be visible) or $>10\,$M$_\odot$ (to exclude O stars and early B stars, which would be visible in most cases).

Figure 4.8 shows the cluster mass functions for all clusters (solid black line), clusters containing exactly one WR star (red dashed line), clusters containing one WR star and no other OB stars (green dot-dashed line), clusters containing one WR star with the remaining stellar mass $<100\,$M$_\odot$ (the dark blue dotted line) and clusters containing one

Table 4.10: The number and fraction of clusters in each class, as plotted in Figure 4.8. The results are shown for the two lowest mass results bins in the histogram (50-83 $M_\odot$ and 83-138 $M_\odot$) and for both of the OB star cutoff masses (>5 $M_\odot$ and >10 $M_\odot$).

Cutoff mass of OB stars	Total no. of clusters	No. of clusters with exactly 1 WR	No. of clusters with 1 WR and no OB stars	No. of clusters with 1 WR and <100 $M_\odot$	No. of clusters with 1 WR, no OB and <100 $M_\odot$
— Cluster mass bin range 50-83 $M_\odot$ —					
>5 $M_\odot$	1.50x10^6	2.72x10^5 (18.1%)	1.26x10^5 (8.4%)	2.72x10^5 (18.1%)	1.26x10^5 (8.4%)
>10 $M_\odot$	1.50x10^6	2.72x10^5 (18.1%)	2.19x10^5 (14.6%)	2.72x10^5 (18.1%)	2.19x10^5 (14.6%)
— Cluster mass bin range 83-138 $M_\odot$ —					
>5 $M_\odot$	9.00x10^5	2.41x10^5 (26.7%)	4.99x10^4 (5.5%)	9.20x10^4 (10.2%)	2.52x10^4 (2.8%)
>10 $M_\odot$	9.00x10^5	2.42x10^5 (26.8%)	1.49x10^5 (16.5%)	9.22x10^4 (10.2%)	6.32x10^4 (7.0%)

WR star, no OB stars and with the remaining stellar mass <100 $M_\odot$ (the cyan dot-dashed line).

We consider that only WR stars within clusters for which the remaining stellar mass <100 $M_\odot$ could be mis-classified as being isolated. The upper and lower panels of Figure 4.8 show that these low mass (<100 $M_\odot$) clusters containing 1 WR star and no OB stars (defining OB stars as >10 $M_\odot$ and >5 $M_\odot$, respectively), will only form in around 8%–15% of instances (Table 4.10 gives a full breakdown of the number of clusters in each category from Figure 4.8). This is significantly smaller than our observed isolated fraction of 59–75% of WR stars.

4.5.2 Dissolution of star clusters

We now explore the possibility that WR stars appear to be isolated because their birth, or host star clusters have dissolved. Observations indicate that only 10 per cent of star clusters survive beyond an age of 10 Myr (Lada & Lada, 2003). The exact reasons for this rapid destruction of star clusters is still debated. Clusters could be disrupted by the expulsion of gas leftover from the star formation process (Tutukov, 1978; Lada et al., 1984; Goodwin, 1997; Baumgardt & Kroupa, 2007; Shukirgaliyev et al., 2018), although

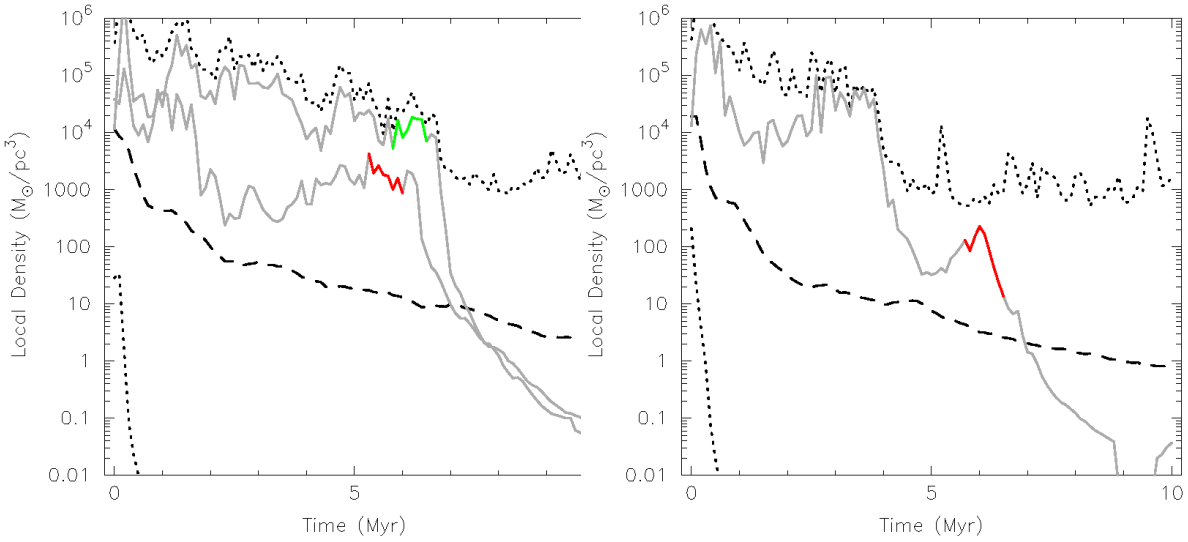

Figure 4.9: Local densities around stars in simulated clusters. The dotted lines are the upper and lower density bounds of the cluster, whilst the dashed line is the median. The solid lines are the stars that will evolve into a WR star, with the coloured segments denoting the WR phase. In the left panel, there are two WR stars in the cluster (red and green), both of which remain in dense regions during their lifetimes. However, in the right panel, the WR star has moved into a reduced densityenvironment during its evolution (though the surroundings are still denser than the median of the cluster).

the effectiveness of this mechanism has been questioned (Kruijssen et al., 2012).

An alternative to gas expulsion is the rapid expansion of a star cluster through two-body and violent relaxation (Parker et al., 2014b), which has been shown to cause clusters to expand significantly, thereby also significantly reducing the stellar density (Moeckel et al., 2012; Gieles et al., 2012; Parker & Meyer, 2012). In this scenario, the rapid (<10 Myr) dynamical expansion of clusters could result in stellar densities similar to the Galactic field ($\sim$0.1 $M_\odot$ pc^{-3}, Korchagin et al., 2003), causing the WR star(s) to appear isolated.

To test this hypothesis, we perform N-body simulations of the evolution of star-forming regions with a range of initial conditions. We use the results to determine the median stellar density during the WR phase of the massive stars, and compare this to the local stellar density surrounding the WR stars. The simulations are modified versions of those presented in Parker et al. (2014a) and Parker et al. (2014b) and we refer the interested reader to those papers for a full description. However, we summarise the initial conditions here.

We draw 1500 stars randomly from the stellar IMF described in Eqn. 4.3. Occasi-

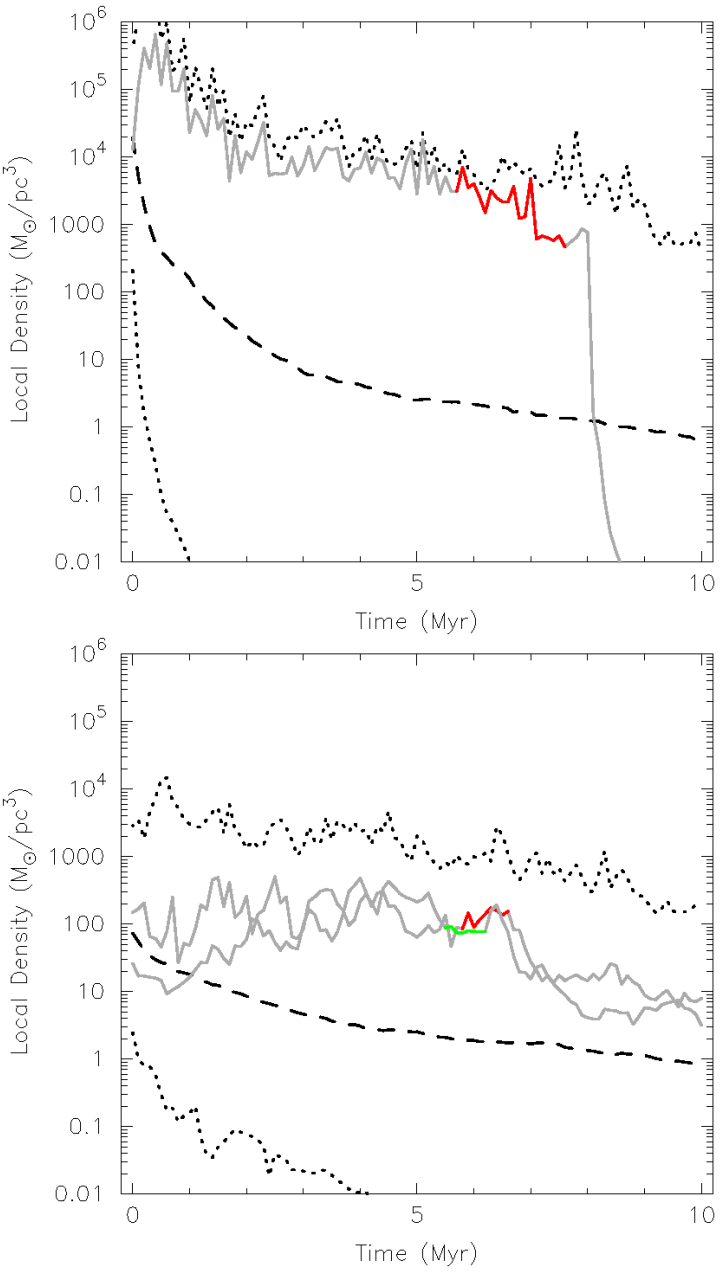

Figure 4.10: Local densities around stars in expanding environments. The upper panel shows an initially dense, highly substructured simulation. The WR star remains in regions of high density due to mass segregation, before being ejected from the cluster. In the lower panel, a moderate density, but highly substructured simulation, the WR stars also remain in moderate or dense surroundings. These regions are still dense enough to be distinguished from the field.

Table 4.11: The variation in initial conditions of our N-body simulations. We show the initial radius, fractal dimension, the resultant initial stellar density, the initial virial state and the figures showing the particular simulation.

Radius	Fractal dimension D	Initial density ($M_\odot\,pc^{-3}$)	Virial state	Figure(s)
1 pc	1.6	10^4	Sub	Fig. 4.9
1 pc	1.6	10^4	Super	Fig. 4.10 (upper panel)
5 pc	1.6	10^2	Super	Fig. 4.10 (lower panel)
5 pc	2.0	10	Super	Fig. 4.11

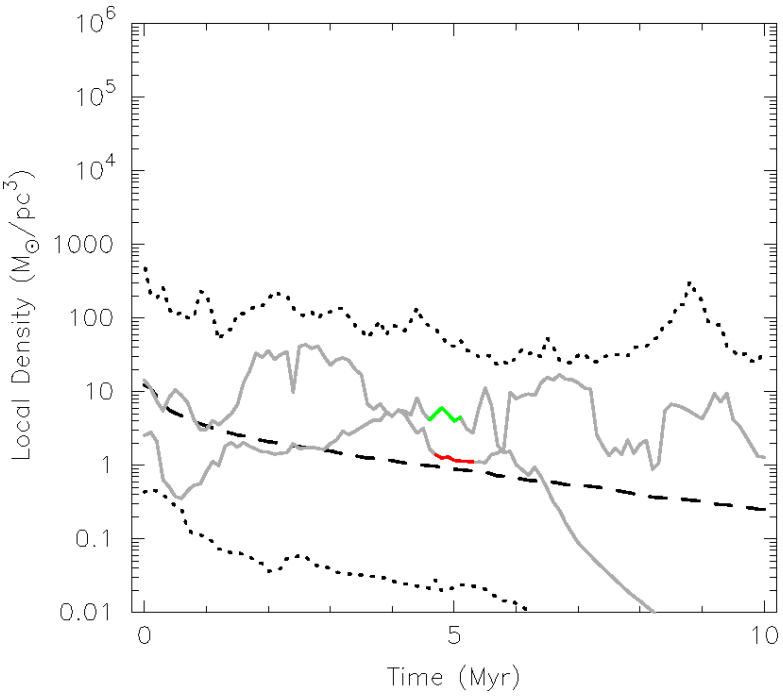

Figure 4.11: An expanding, low density, moderate substructure simulation. Here, the WR stars are in sparse environments and so appear to be isolated.

onally, this results in clusters with no sufficiently massive stars (>25 $M_\odot$), but usually between one and five stars are massive enough to undergo a WR phase. We distribute these stars randomly in space and velocity within a fractal distribution (Goodwin & Whitworth, 2004), which is the most straightforward way of creating the spatially and kinematically sub-structured initial conditions observed in young star-forming regions.

The amount of sub-structure in these fractals is set by the fractal dimension D; a star-forming region with high initial spatial and kinematic substructure has a low fractal dimension ($D = 1.6$), whereas a star-forming region with moderate amounts of substructure has a higher fractal dimension ($D = 2.0$). We run simulations with both degrees of substructure (as observations also indicate a wide range of initial substructure in a star-forming region, Cartwright & Whitworth, 2004). Simulations with a high amount of initial sub-structure have higher local stellar densities relative to those with less substructure. We also vary the *global* density of the simulations by varying the initial radius of the region, which is either 1 or 5 pc.

Finally, we vary the initial virial ratio. Our star-forming regions can be subvirial, which means they collapse into the potential well of the region and form a smooth, spherically symmetric star cluster. Following the formation of the star cluster, two-body relaxation dominates and the cluster expands. In other simulations, the star-forming regions are initially supervirial, which means they expand immediately.

A summary of the initial conditions of our N-body simulations, and the corresponding figure references, are given in Table 4.11. In all simulations, we evolve the star-forming regions for 10 Myr (i.e. long enough for the massive stars to undergo the WR phase before evolving into a stellar remnant). We include stellar evolution using the `SeBa` package (Portegies Zwart & Verbunt, 1996) and the star-forming regions are evolved dynamically using `kira` (Portegies Zwart et al., 1999).

20 simulations were run for each combination of substructure, global density and initial virial ratio parameters. As we used the same 1500 stars for each set of initial conditions, 13 out of 20 simulations contained WR stars regardless of the other initial parameters.

Figure 4.9 shows two of the initially subvirial simulations (i.e. they collapse to form a cluster). The cluster then expands via two-body relaxation. The median, upper and lower bounds of local density variation are plotted over time, alongside the density for stars with initial mass >25 $M_\odot$. The median local density falls during cluster dissolution, as expected. However, due to mass segregation (Allison et al., 2010; Parker et al., 2014b), 90% of WR stars remain preferentially located in regions of high (>1000 $M_\odot pc^{-3}$) density. These regions are still recognizable as clusters, whilst the outer regions have dissolved. This suggests that WR stars in isolated environments are unlikely to originate from dissolved clusters.

We can repeat this analysis for unbound and lower density star-forming regions, which form stellar associations. For initially expanding simulations, with high density

and substructure, the WR stars tend to form in moderate (∼100 $M_{\odot}pc^{-3}$ 45% of WR stars) or high (∼1000 $M_{\odot}pc^{-3}$, 36% of WR stars) density regions and remain in these density enhancements (e.g. upper panel of Figure 4.10).

Moderately dense but highly sub-structured simulations produced a similar result, with 77% of WR stars remaining in moderately or highly dense environments (e.g. lower panel of Figure 4.10). The remaining WR stars were located in low density environments (∼10 $M_{\odot}pc^{-3}$), which are comparable to the field. This implies that such regions can produce WR stars that appear to be isolated, but that they are not the most common formation environment.

However, the expanding simulations with moderate substructure and initially low density in Figure 4.11, led to typical WR densities of around 1-10 $M_{\odot}pc^{-3}$. To an observer, this is comparable to the field density and occurred because the moderate substructure and low-density prevented WR stars from becoming mass segregated. A corresponding collapsing version of this simulation produced WR stars in much more dense environments of 10-1000 $M_{\odot}pc^{-3}$.

The final set of simulations suggest that WR stars primarily form in low density and sub-structured environments within associations. These regions would dissolve to field densities, via very gentle expansion, over the WR progenitor lifetime, which would make the WR star appear isolated.

Cygnus OB2 is an example of one such region. Based on the Wright et al. (2014) surface density of 13.3 stars pc^{-2}, the typical volume density of Cygnus OB2 (which is somewhat lower than the surface density) is ∼5 stars pc^{-3}. With a typical IMF, this results in an average mass density which is similar to the field, at ∼1-10 $M_{\odot}pc^{-3}$.

4.6 Discussion and conclusions

We have exploited *Gaia* DR2 proper motions and parallaxes to reassess the membership fraction of WR stars in clusters and OB associations within the Galactic disk. Only 16% (61 of the 379) of WR stars identified in *Gaia* DR2 are confirmed members of clusters or OB associations, with a further 23 stars possible cluster/association members, plus 42 potential members of visibly obscured star-forming regions. The large distances and high visual extinctions of most WR stars precludes membership of known OB associations. Consequently, 67–84% of the WR stars accessible to *Gaia* DR2 are apparently isolated, in contrast to only 13% of the Galactic O star population within a few kpc of the Sun. The fraction of isolated WR stars within the Galactic disk is largely unchanged if WR stars

inaccessible to *Gaia* are considered (64–82% of 553 WR stars). Once literature results for the WR populations within the Galactic Centre region are included too, 59–75% of 663 Galactic WR stars are isolated. This is illustrated in Figure 4.12.

Our results are broadly consistent with literature results for the membership of Galactic WR stars in clusters or associations (Lundström & Stenholm, 1984) but are much lower than their progenitor O stars, for which over 70% of the 611 O stars in v3 of the Galactic O star Catalogue (Maíz Apellániz et al., 2013) are members of OB associations or star-forming regions. We explore the origin of the high field WR population by undertaking simulations of star forming regions in which WR stars result from progenitors with $\geq$25 $M_{\odot}$.

We find that WR stars in low mass star forming regions lacking other massive stars contribute 8–15% of isolated cases, of which WR11 (WC8+O) in the γ Velorum group may be an example. Additionally, N-body simulations of clusters containing WR stars, reveal that as the median density falls, the outer regions of the cluster dissolve into the field. However, due to mass segregation, WR members remain in high density regions, which would appear as clusters. Only simulations of expanding, moderately sub-structured environments which are already low density, reproduced WR stars that appeared to be isolated. This suggests that most WR form in less dense associations, which are expanding from birth and dissolve to make the WR star appear isolated during its lifetime.

We conclude that only a subset of WR progenitors originate from dense, massive star clusters, such as NGC 3603 or Westerlund 1, with a significant fraction from more modest open clusters, such as Collinder 232, NGC 6231 and Trumpler 16. Considering the global WR population of the Milky Way, 22% are members of clusters, versus 40% of Galactic O stars, indicating that up to half of massive stars are dynamically ejected from such clusters (Oh & Kroupa, 2016; Drew et al., 2018).

From Chapter 3, we identify a minimum of 8% for the runaway fraction of *Gaia* DR2 WR stars owing to being located more than 156 pc (three H II region scale heights) from the Galactic mid-plane. This is in accord with a runaway fraction of 10–25% for O stars according to Gies & Bolton (1986). Although a significant fraction of massive stars are believed to be dynamically ejected from star forming regions (Oh & Kroupa, 2016) or disruption of binaries following a core-collapse supernova (Renzo et al., 2019), runaways are predicted to be extremely rare, in tension with the observed runaway rate.

Overall, based on the observed cluster and association membership fractions, and the simulations conducted, we propose that the isolation of WR stars can be explained by

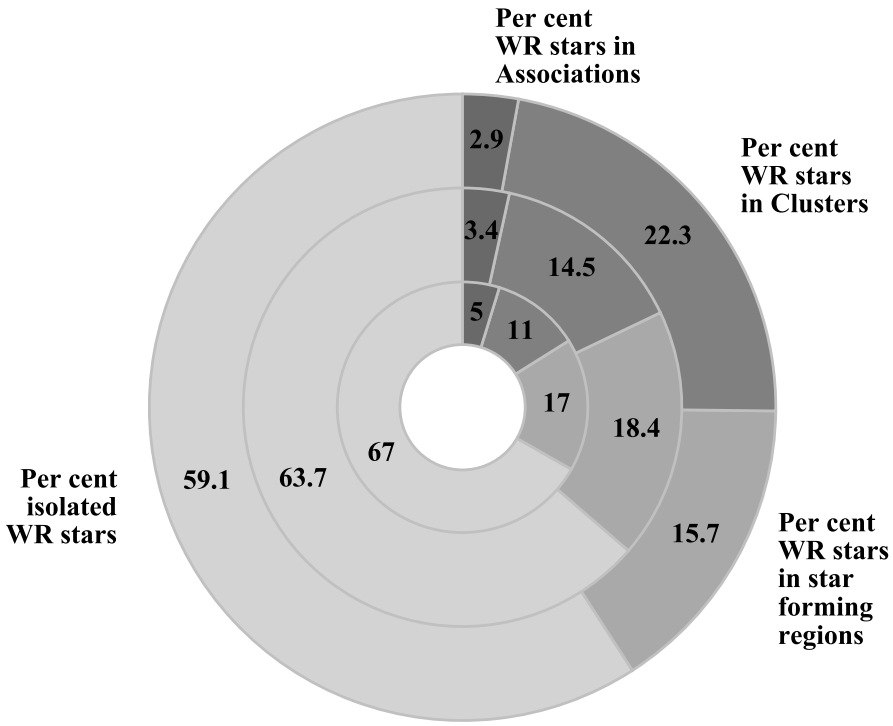

Figure 4.12: Doughnut chart showing the percentages of the WR stars in clusters, associations and star forming regions and isolated environments. The inner ring (379 stars) consists of results for stars with *Gaia* DR2 distances, whilst the middle ring shows both *Gaia* results from the inner ring and embedded Galactic disk membership assignments from the literature (553 stars). The final outer ring shows the *Gaia* assignments, plus all memberships from literature for embedded WR stars both inside and outside the Galactic Centre (663 stars).

the following scenario:

- ∼20% of WR stars form in rich open clusters, such as NGC 3603 (or other clusters in Carina), and remain in situ throughout their lives.
- ∼20% of WR stars appear isolated because they have been ejected from their birth star-forming region, either through dynamical ejection or binary disruption.
- ∼10% are isolated because they have formed in a low mass (∼100 $M_{\odot}$) region, containing only a single WR star and no OB stars. The remainder of the stellar population, aside from the WR star, is therefore too faint to be observed, which makes the WR star appear to be isolated (e.g. WR11 within the γ Velorum group)

- ∼5% of the WR population still reside in non-clustered OB associations/star-forming regions. These regions may be dissolving and have therefore not yet reached field densities, or they may have started out slightly more dense than the typical WR star environment and are therefore taking longer to fully expand.

- The remaining 45% of WR stars originate in low density, moderately sub-structured associations, which expand during the WR star lifetime to ∼1-10$M_{\odot}$ pc^{-3} densities and again make the WR star appear isolated. An observational example of this environment is Cygnus OB2.

To verify this scenario and better constrain the fraction of WR stars in each environment, future work should consider re-assessing the regions around known WR stars (in particular the stars we were not able to firmly classify in this study). This could be done using *Gaia* astrometric data and clustering algorithms, to identify all possible members of the surrounding stellar population; therefore ensuring completeness that may not be present in literature membership lists (e.g Cantat-Gaudin et al. 2019, see Section 4.3.4). The region could then be characterised to determine if it expanded from the moderately dense and sub-structured environments, that may comprise the majority of WR star formation sites.

In addition to establishing the environment of WR stars in the Galactic disk, we have also reassessed the distance to clusters/associations from *Gaia* DR2, considering systematics (Lindegren et al. 2018a, 2018b) and random uncertainties. For those clusters host to WR stars, we used cluster distances, literature photometry and spectral types, to calculate the extinctions and then the luminosities of OB members, from which cluster ages were estimated using isochrones from Brott et al. (2011). Previous results are largely supported, in which young clusters ($\leq$ 2 Myr) host H-rich WN or Of/WN stars, intermediate age clusters (2–5 Myr) host classical WR stars, with older ($\geq$5 Myr) clusters, host to stars which could have been affected by binary evolution (e.g. rejuvenation following a stellar merger), but we do not see a large population of stars which may have evolved via the WR binary formation channel.

Finally, let us return to a topic mentioned in Section 4.1, namely whether core collapse SN environments support WR stars as the primary progenitors of stripped envelope SN. Since the incidence of star-formation increases from the least stripped (II-P, II-L) to the most stripped (IIb, Ib, Ic) SN (Kelly & Kirshner, 2012; Anderson et al., 2012; Kuncarayakti et al., 2018), more massive progenitors are inferred for stripped envelope SN, especially for broad lined Ic SN. By way of example, Crowther (2013) found 70±26%

of nearby type Ib/c SN to be associated with a H II region, versus only 38±11% for type II SN at similar distances.

If WR stars are responsible for (some) stripped envelope SN, how can one reconcile the fact that ≥60% of Galactic WR stars are not associated with star formation (Fig 4.12), yet the overwhelming majority of stripped envelope SN are associated with star forming regions? Recall that the typical distance to a Galactic WR star is 5 kpc (Chapter 3), versus a mean distance of 20 Mpc for stripped envelope SN within large samples (Anderson et al., 2012). 100 parsecs subtends over a degree at the distance of a typical Galactic WR star, versus 1 arcsec for stripped envelope supernovae. Consequently, for a Galactic WR star to be associated with a star-forming region, it needs to lie in the H II region, or in its close proximity (1–5 pc). In contrast, stripped envelope SN are flagged as being associated with a star-forming regions if they lie within 50–100 pc of the H II region.

The size of H II regions spans a wide range (Kennicutt, 1984; Crowther, 2013), from ∼1 pc for compact H II regions (e.g. M42/Orion Nebula Cluster) to ∼1 kpc for super-giant H II regions (e.g. NGC 5461 in M101). According to fig. 8 of Kuncarayakti et al. (2018), 60% of SE-SNe are associated with star forming regions whose Hα luminosities are inferior to that of the Rosette Nebula (NGC 2264), with 30% below M42. Physical dimensions of characteristic extragalactic H II regions are thus ∼10 pc, significantly smaller than the resolution of non-Adaptive Optics, ground-based observations.

Therefore, if one was to relax the condition that a Galactic WR star is associated with a star-forming region by an order of magnitude, from ∼5 parsec to ∼50 parsec, the statistics would of course be far greater than ≤40%. However, such an exercise awaits the combination of more robust *Gaia* parallaxes in future data releases and reliable distances to Galactic star-forming regions (Reid et al., 2019).

Chapter 5

Emission Line Luminosities

Line luminosities of LMC WR stars were provided by my supervisor Paul Crowther.

5.1 Introduction

To study the influence of varying metallicity on massive stars and to catalogue type Ibc supernovae progenitors, we must look beyond the Milky Way. In distant galaxies, individual WR stars will not be resolved, instead residing within larger star forming regions. These may contain many WR stars and their collective emission lines will therefore appear blended into a 'red bump' at around 5600−5900Å and a blue bump at around 4600−4700Å . Galaxies with such features in their spectra were denoted as WR galaxies by Conti & Vacca (1994). Figure 5.1 shows an example of such a region in NGC5398 from figure 7 of Sidoli et al. (2006), with the red (marked as yellow in the figure) and blue bump regions clearly marked.

Previous work has used average WR luminosities to ascertain the numbers of WR stars in these unresolved regions (e.g Bibby & Crowther 2012). For lower metallicity environments, luminosities from LMC stars have been sufficient. The lack of significant extinction towards the LMC and its well determined distance means that the average numbers of stars inferred from these luminosities have relatively small uncertainties, albeit with significant variation within subtypes (Crowther & Hadfield, 2006).

However, results relying on Galactic WR luminosities have a much larger associated uncertainty, which primarily stems from the uncertainties of distances used to calculate them. With our updated distances to WR stars (Chapter 3), we can produce much more robust line luminosities and more accurately determine the populations of extragalactic WR stars in unresolved regions at high metallicity.

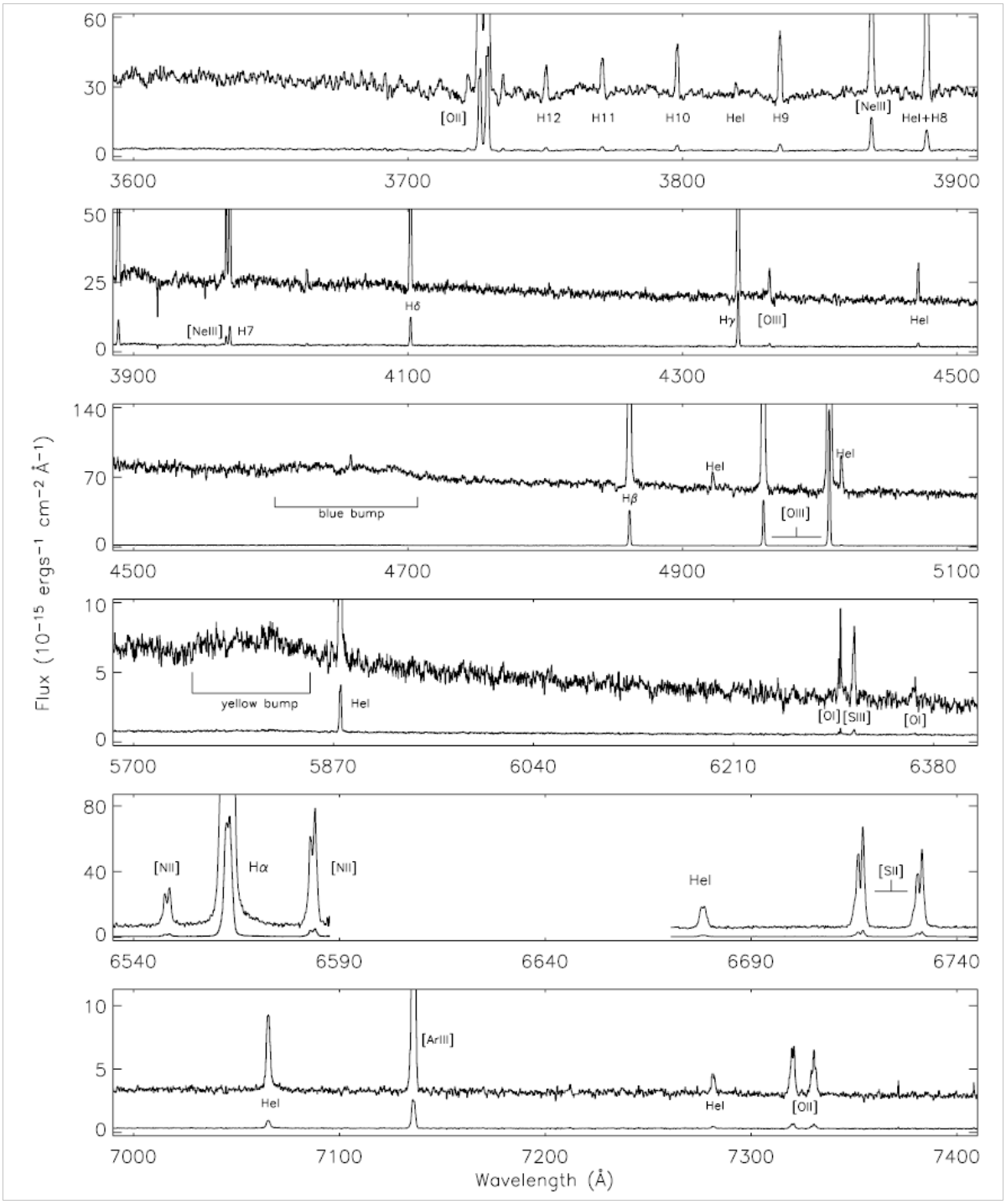

Figure 5.1: Spectrum of WR bumps in Tol89 within NGC5398 around 4600−4700Å and 5600−5900Å from figure 7 of Sidoli et al. (2006).

We therefore obtain the blue and red bump luminosities for different WR subtypes and compare the results to stars from the lower metallicity LMC.

Table 5.1: Sources of WR spectrophotometry used to calculate emission line luminosities. References are from Torres-Dodgen & Massey (1988) (TDM88), Crowther et al. (1995) (C95), Crowther (1997) (C97), Crowther et al. (1998) (C98), Crowther & Smith (1999) (C99), Morris et al. (2000) (M00) and Crowther et al. (2002) (C02).

Telescope	Instrument	Observation date	Wavelength range	Spectral resolution (Å)	Reference	Label
AAT	RGO	Nov 92	3700−4400Å	1.7	C95	AAT92
ANU 2.3m	DBS	Dec 97	3620−6085Å 6410−8770Å 3240−4480Å 8640−11010Å	5-12	C02	ANU97
CTIO	SIT	Nov 1981−Feb 1985	3400−7300Å	10-15	TDM88	CTIO
INT	IDS	Sep 1991	4400−7300Å	2-3	C95	INT91
INT	IDS	Jul 1996	3700−6800Å	1.5-3	C97, C98, M00	INT96
INT	IDS	Sep 2013	3800−10000Å		Priv. comm.	INT13
WHT	ISIS	Jun 1994	3820−7030Å	1.6-1.7	C99	WHT94
WHT	ISIS	Aug 2002	3800−10000Å		Priv. comm.	WHT02

5.2 Fitting methods

We primarily use flux calibrated spectra from Torres-Dodgen & Massey (1988) (TDM88) for the stars present in that catalogue, with additional fluxed spectra from Crowther et al. (1995) (C95) and Crowther et al. (2002) (C02). The sources of the data and observational details are shown in Table 5.1.

For datasets from the Issaac Newton Telescope (INT) and William Herschel Telescope (WHT), several observations were often available. These were taken because the detector did not cover the entire wavelength range required and the two halves of the spectrum had to be combined during data processing. Variable atmospheric conditions meant that these sets of observations differed from each other. To choose the most appropriate observations, we converted v and b narrow band photometry from Torres-Dodgen & Massey (1988) to fluxes and compared these to the fluxes at these wavelengths. We chose the spectrum with the flux closest to the both bands (e.g the flux with an average between them if it was greater than the v band, but lower than the b band).

Regions around the blue (4400Å − 4850Å for WN and WC) and red (5500Å − 6050Å for WN and WC) features were then trimmed from the full spectra to facilitate fitting. Table 5.2 lists the emission lines within each region. Included in the sample

Table 5.2: WR emission lines contained within the red and blue features for different subtypes.

WR Subtype	Blue feature	Red feature
WN	He II 4686Å , N V 4620Å + N III 4640Å blend	C IV 5808Å , He I 5876
WC	He II 4686Å , C III 4650Å	C III 5696Å , C IV 5808Å , He I 5876
WN/WC	He II 4686Å , N V 4620Å + N III 4640Å blend	C III 5696Å , C IV 5808Å , He I 5876
WO	He II 4686Å , C IIV 4860Å	O V 5590Å + O III 5592Å + O VII 5670Å blend (centre at 5600Å , 40 Å standard deviation), C IV 5808Å

are two WO stars, WR30a and WR142, which are fit with the same emission lines as WC stars in the blue region and the oxygen blend and C IV 5808Å in the red. All red and blue regions were first continuum subtracted, using a straight line fit to a series of continuum 'windows' either side of the emission line.

We then fitted emission lines with gaussians, using an automated fitting routine, with the ASTROPY (Astropy Collaboration et al. 2013b, Price-Whelan et al. 2018) modelling module. Where lines were blended, multiple gaussians were fit simultaneously to decompose the blended line. The gaussian fits were constrained to be within 10 Å (for narrow lines in the blue) or 20-30 Å (for the broader lines in the red region) of the emission line centre. Initial 'guesses' were provided for amplitudes and standard deviations, particularly for blended lines. The area below the gaussian could then be integrated to obtain the emission line fluxes.

Figure 5.2 shows the fluxes from our fits, compared to previous results from Smith et al. (1996) (WN) and Smith et al. (1990) (WC). There is generally good agreement, albeit with some variation, particularly for the He I 5876Å and C IV 5808Å lines. This may stem from the difference in decomposing the two blended lines into gaussians. There are also lower flux measurements for the He II 4686Å line, particularly compared to the WN results from Smith et al. (1996). The differences may be due to observational scatter.

The fluxes were dereddened using the extinctions from Chapter 3 to determine the intensity and then adjusted for distances (again from Chapter 3) to calculate the luminosity. The total luminosity for the blue and red features were the sums of the individual emission lines fitted in these regions.

Example fits are shown for WR61 (in Figure 5.3) and WR56 (in Figure 5.4). Unfor-

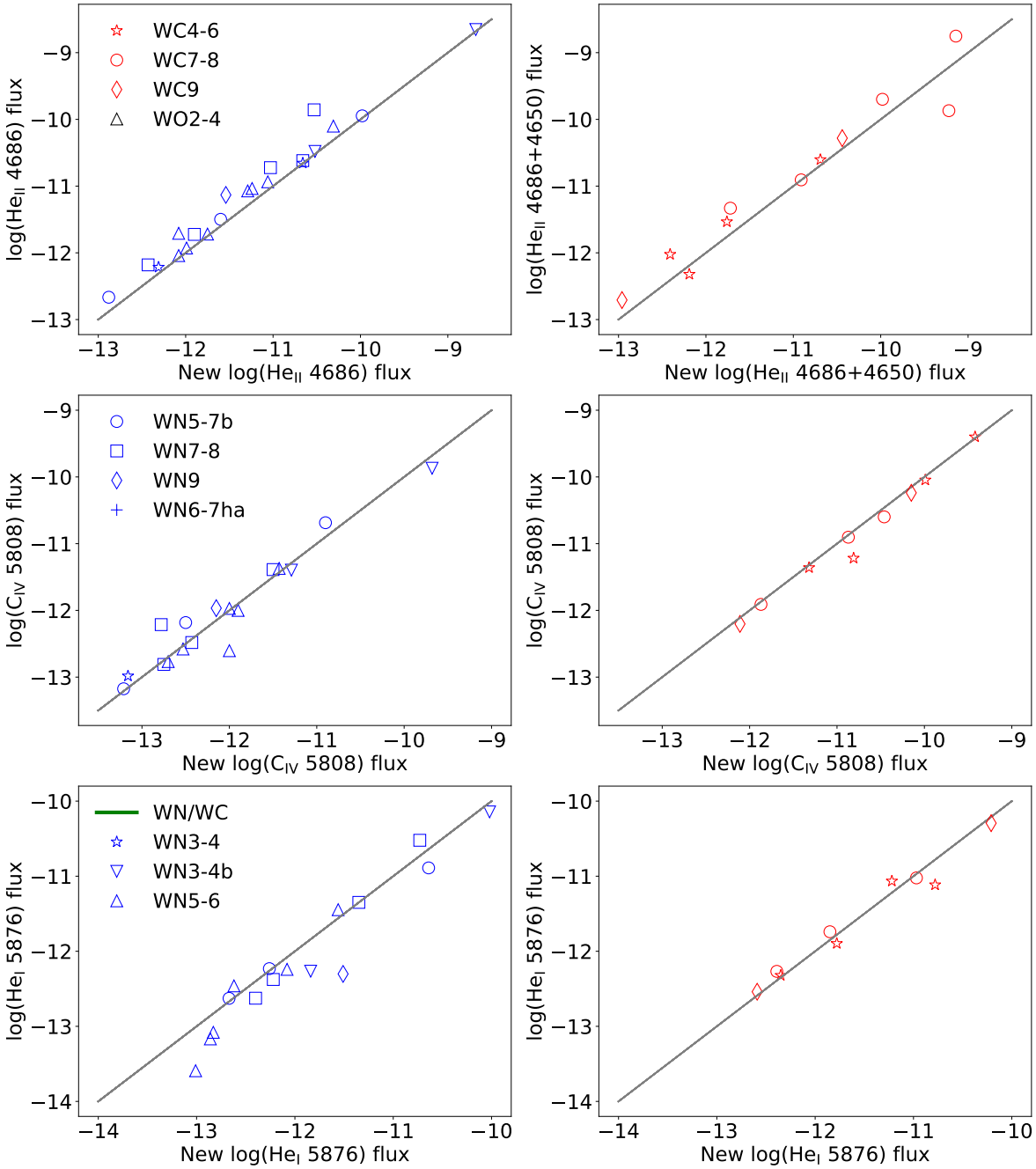

Figure 5.2: Comparison between fluxes for three different emission lines, fitted both in WC and WN stars. Comparison WN flux data (y-axis) was taken from Smith et al. (1996) and WC fluxes from Smith et al. (1990). The grey line denotes the fluxes where the results from this work are equal to the results from Smith et al. (1996) and Smith et al. (1990).

tunately in some instances (particularly the C III 5696Å line in early WC stars) emission lines exhibited a flat topped profile, which was less suitable for a gaussian fit (though

these stars were still included in the averages, as their C IV 5808Å line dominated the red bump luminosity and was well fitted by a gaussian). For WR157 and WR30, the spectra were incomplete, such that parts of emission lines were missing. Owing to these missing data, WR30 and WR157 were not included in the final averages.

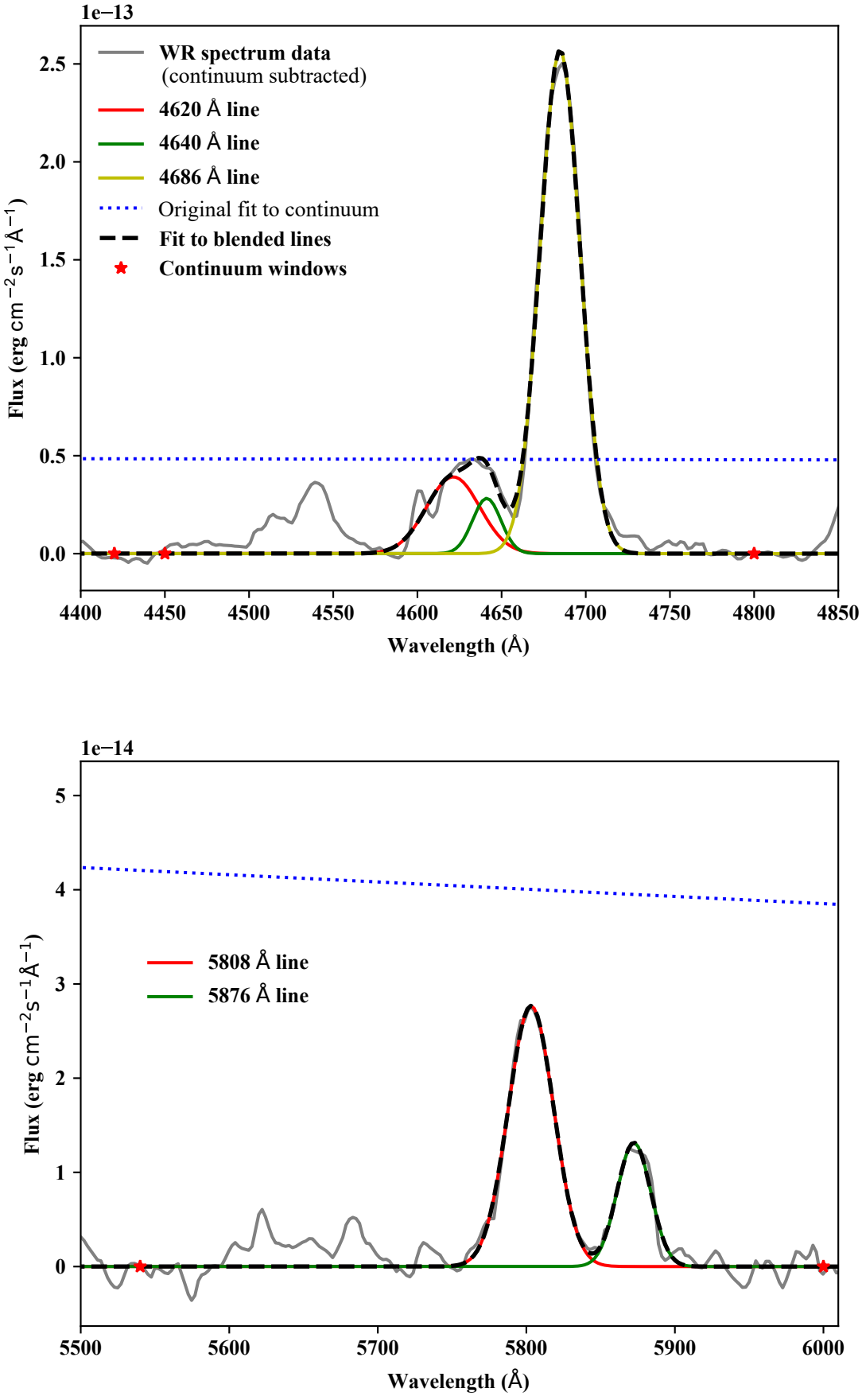

Figure 5.3: Fits to WR61 (WN5) in the blue region (top) and red region (bottom). The best fit is obtained if the centres of the gaussian fits are shifted slightly compared to the emission line centres. For instance, the gaussian mean for the 5808Å line is at 5803Å .

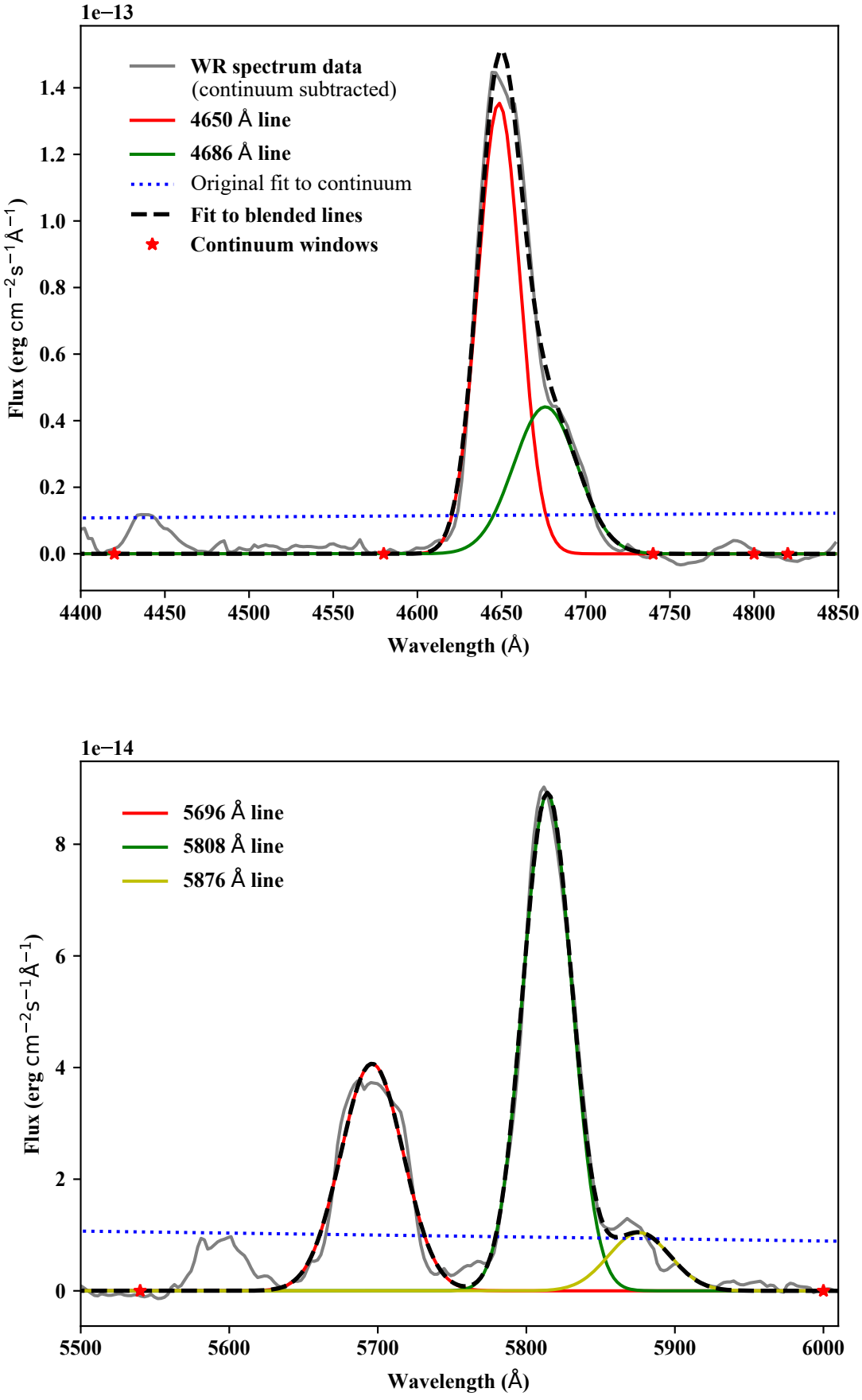

Figure 5.4: Fits to WR56 (WC7) in the blue region (top) and the red region (bottom). The C III 5696Å line appears to have a non gaussian profile, but the C IV 5808Å is still well fitted.

5.3 Results

We can compare the luminosities obtained for individual emission lines, to those from tables 1 and 2 of Schaerer & Vacca (1998) for Galactic and LMC WN and WC stars (Figure 5.5). We find generally good agreement for most WR subtypes and emission lines. However, our results in each subtype category tend to fall on the lower end of the ranges from Schaerer & Vacca (1998). These lower luminosities may be due to the new distances.

The 4650Å emission line for WC4−6 and the WC9 5696Å line appear to be much lower than those from Schaerer & Vacca (1998). However, for their 4650Å emission results, Schaerer & Vacca (1998) do not separate the 4686Å lines, whereas our results remove 4686Å from the 4650Å luminosity. This could have led to an excess of the Schaerer & Vacca (1998) values, as compared to our results. However, the difference for the 5696Å line is likely to be due to the highly uncertain distances to WC9, that existed prior to *Gaia* DR2. Our new distances have therefore resulted in very different emission line luminosities.

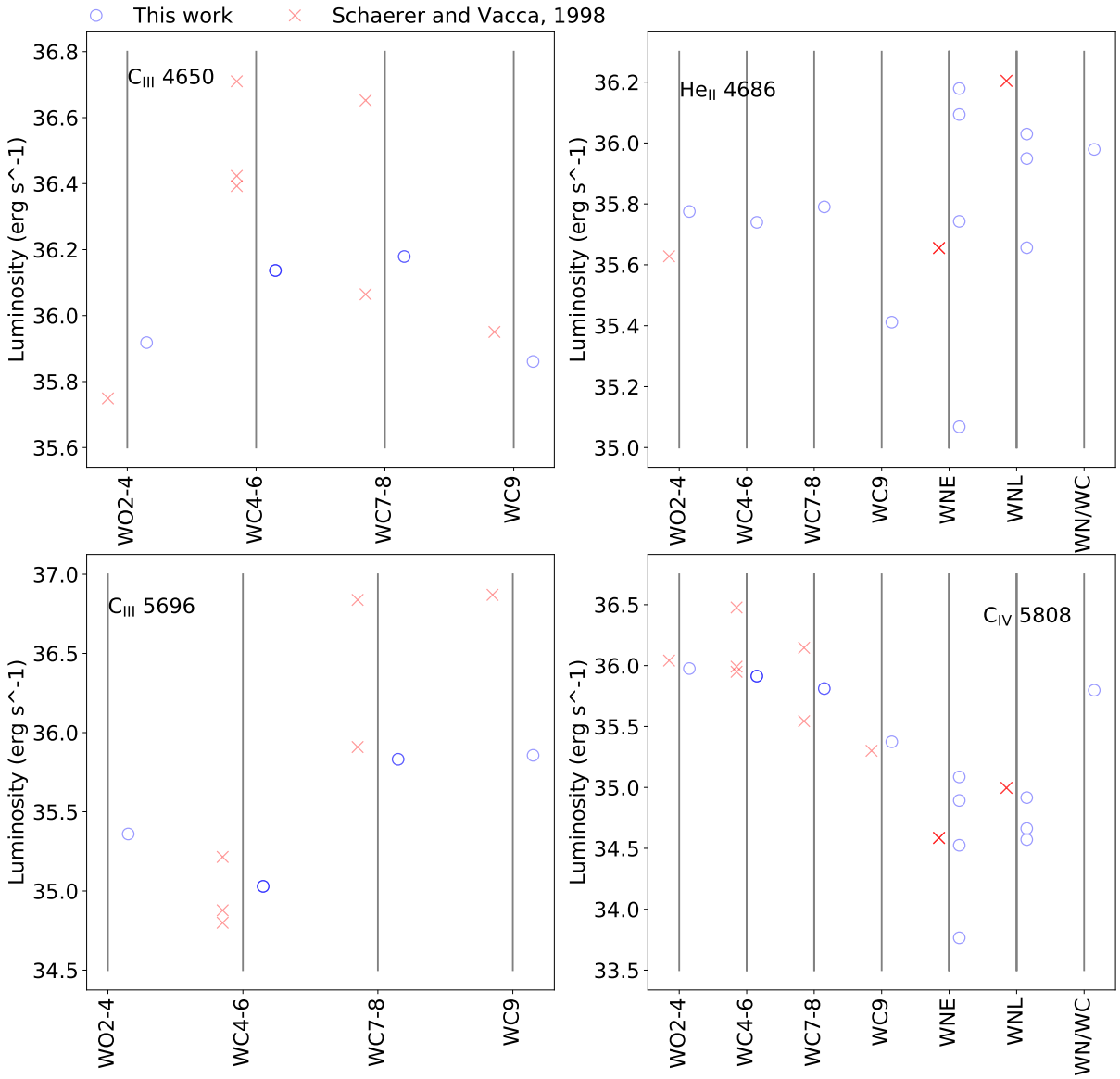

Figure 5.5: Individual emission line luminosities from this work, compared to average line luminosities from Schaerer & Vacca (1998). The data from Schaerer & Vacca (1998) includes both Galactic and LMC stars, for WN and early type WC (WC4). For the LMC WN stars, 4 are WN6h, with one WN4 and one WN8h. The averages of later WC types only contain Galactic stars, as there are no late type WC in the LMC. Individual subtypes from Schaerer & Vacca (1998) have been plotted beside our grouped averages (e.g WC7 was included in the WC7-8 category). Uncertainties are not included due to their large sizes.

Table 5.3: Average luminosities for red and blue bumps in WR stars of different subtypes, within the Galaxy (this work) and LMC (luminosities from Crowther & Hadfield 2006 and WR subtypes from Neugent et al. 2018). The uncertainties are the sample standard deviations.

Subtype	Galactic blue bump (10^{35} ergs s^{-1})	Number of stars	LMC blue bump (10^{35} ergs s^{-1})	Number of stars	Galactic red bump (10^{35} ergs s^{-1})	Number of stars	LMC red bump (10^{35} ergs s^{-1})	Number of stars
WC4−6	19±9.3	16	52±30	19	10±5.4	15	35±21	19
WC7−8	21±17	15			15±12	12		
WC9	9.8±5.5	14			11±5.9	12		
WN/WC	20±12	4			7.2±6.5	4		
WN3−4	1.6±1.3	4	11±9.2	37	0.069±0.068	3	0.8±1.4	37
WN3−4b	18±6.5	5			1.6±0.6	5		
WN5−6	7.3±5.4	17	27±20	18	0.48±0.43	14	1.3±1.3	18
WN5−7b	17±7.8	6			1.7±0.82	5		
WN6−7ha	16±12	5			0.61±0.38	5		
WN7−8	14±9.9	14	13±8.1	5	1.9±2.0	11	1.9±1.2	5
WN9	9.1±4.8	2	3.9±1.2	4	1.1±0.56	2	1.4±0.64	4
WO2−4	14±2.5	2			12±4.5	2		

Table 5.3 shows the average blue and red bump luminosities grouped by WR subtype. WR25, which was the sole Of/WN star in the Galactic sample, was grouped with the WN6−7ha stars, as it is at a similar evolutionary stage.

There is a wide spread of luminosities within subtypes, in many instances, classes had standard deviations on the same order of magnitude as the measurement itself. As anticipated, WC stars have higher red bump luminosities than WN stars. Figure 5.6 shows the results for individual stars. WC7−8 stars have a larger spread of luminosities, with some outliers contributing to the higher average. All of these are WC8 stars, except for WR93, which is in a binary.

WN/WC were plotted with their dominant WN subtypes (though they were separated during averaging). Due to their C IV 5808Å emission line, they are amongst the most luminous subtypes in the red bump. For blue bump luminosities, they have typical emission lines for their WN subtypes. Both WO stars have similar red and blue bump luminosities to early type WC stars.

The full lists of Galactic WR emission line fluxes, intensities and luminosities are in Tables A.4 and A.5 for WN and Tables A.6 and A.7 for WC.

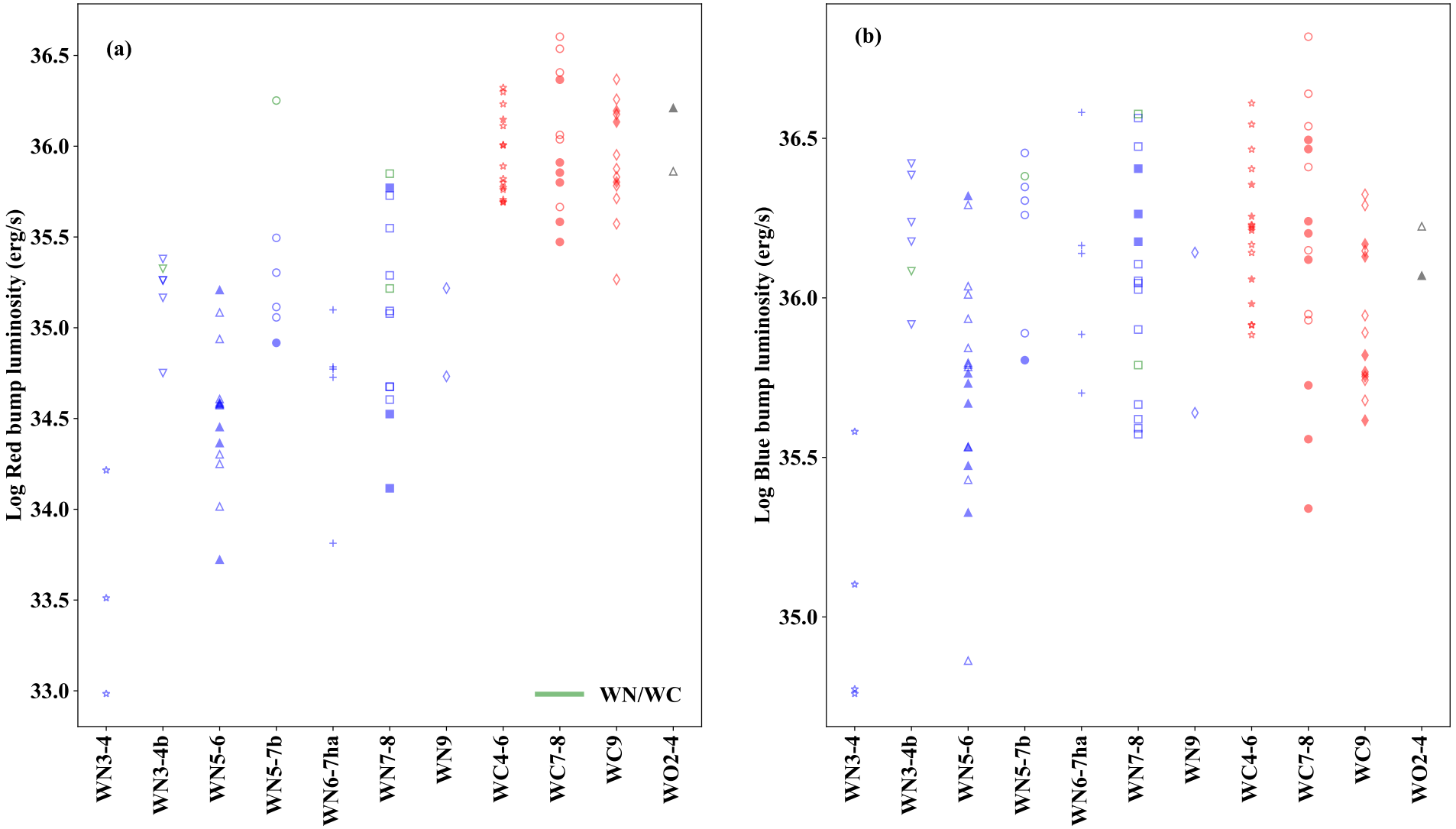

Figure 5.6: (a) Galactic WR star red feature luminosities (b) Galactic WR star blue feature luminosities. Blue points are WN, red are WC and green are WN/WC.

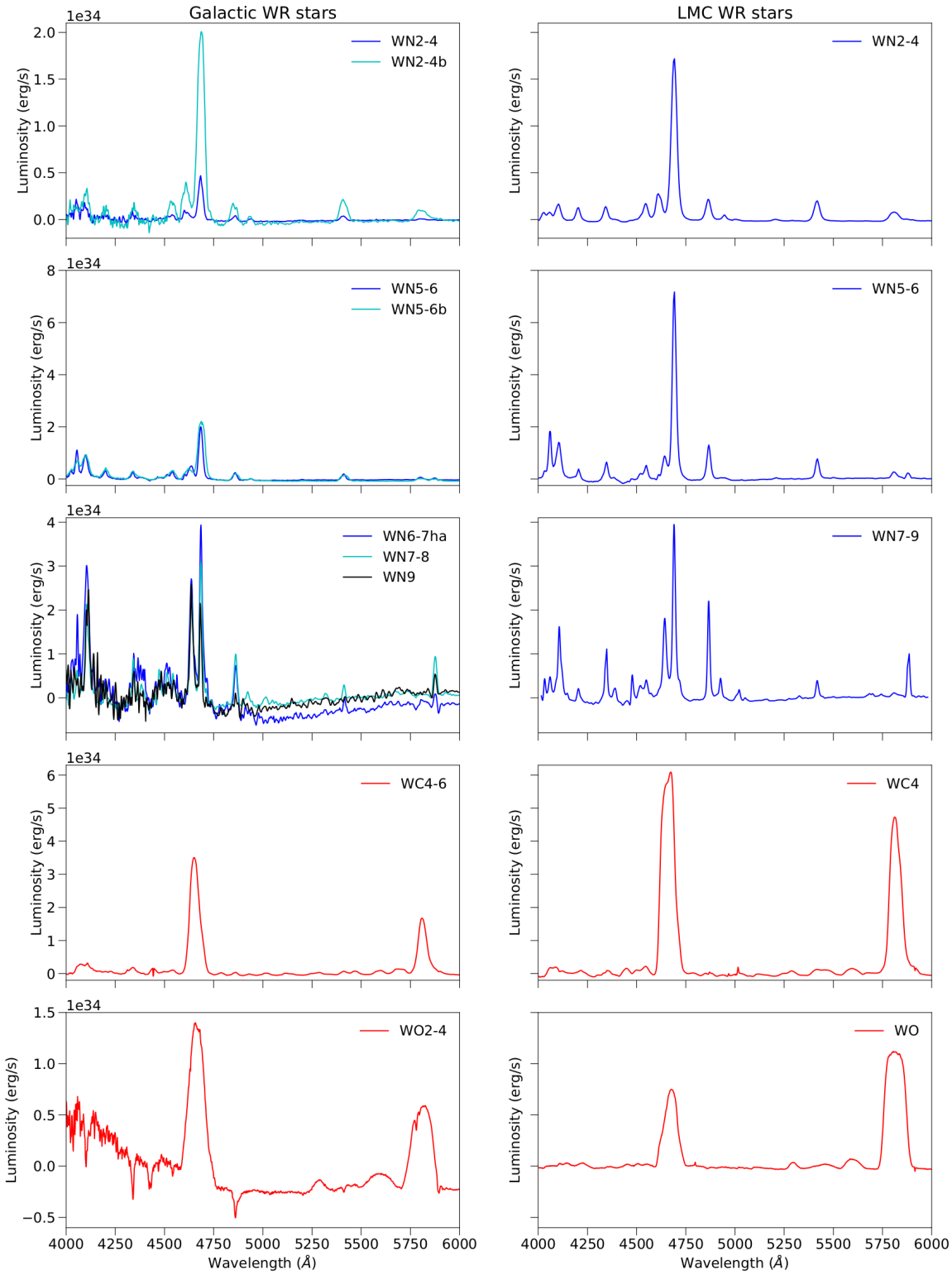

Figure 5.7: Average spectra of the WR categories from Table 5.3 for Galactic WR stars, compared to the same groups in the LMC (showing that the lines are stronger in the LMC stars, the vertical axes scales are the same for all subplots). The seemingly negative luminosities of the late WN and WO Galactic examples are due to difficulty of fitting the shape of the continuum and over subtraction of the continuum models. The shapes and luminosities of the emission lines are not affected.

5.4 Comparison with the LMC

Figure 5.7 shows that the main difference between the Galactic and LMC results are the strengths of the emission lines, with the LMC WR stars possessing much larger peaks and therefore line luminosities, than those in the Galaxy.

Figure (a) from 5.8 shows the red vs blue bump luminosities for Galactic stars. These can be compared with the same diagram for a sample of 89 stars in the LMC in Figure (b), with subtype classifications from the Neugent et al. (2018) LMC WR catalogue and luminosities from Crowther & Hadfield 2006.

Below log(L)=33.8 erg s^{-1}, we could only place lower limits on the red bump luminosities. These were Galactic WR stars with no observed emission lines in the red feature and we therefore took any measured red bump luminosities for these stars as an upper limit. For the LMC, the maximum red bump measurement obtained for a Galactic WR star, without a clear emission line in the feature, was taken as the cutoff for stars with only upper limits.

In both galaxies, the WC stars have significantly higher red bump luminosities than the WN stars. WC4−6 stars in the LMC have a somewhat higher luminosity than their Galactic counterparts in both the red and blue regions. The WN3−4 stars in the LMC break down into two groups. One with luminosities similar to Galactic WN3−4 stars and another with higher luminosities (strong lined stars). Many weak lined LMC WN stars have somewhat broader emission lines than their Galactic counterparts and may therefore have similar luminosities to broad lined Galactic WN, without themselves being classified as broad lined.

In the LMC, WN9 stars have a similar red bump luminosity to Galactic WN9 stars, but appear to cover a much wider range of blue bump luminosities, extending below log(L)=35 erg s^{-1}, whilst the Galactic stars have log(L) >35.5 erg s^{-1}. However, as there are only two WN9 in the Galactic sample, they may simply not be representative of the full range of WN9 luminosities. The small numbers of Galactic WN9 mean the uncertainties on the mean luminosities are much larger than LMC WN9.

The same trend of large variations within blue bump luminosity is observed for low luminosity WN3−4 and WN5−6 stars in the LMC. However, again there are few Galactic WN with these low luminosities in the sample and the larger number of LMC WN may be more representative of the full luminosity range for these stars.

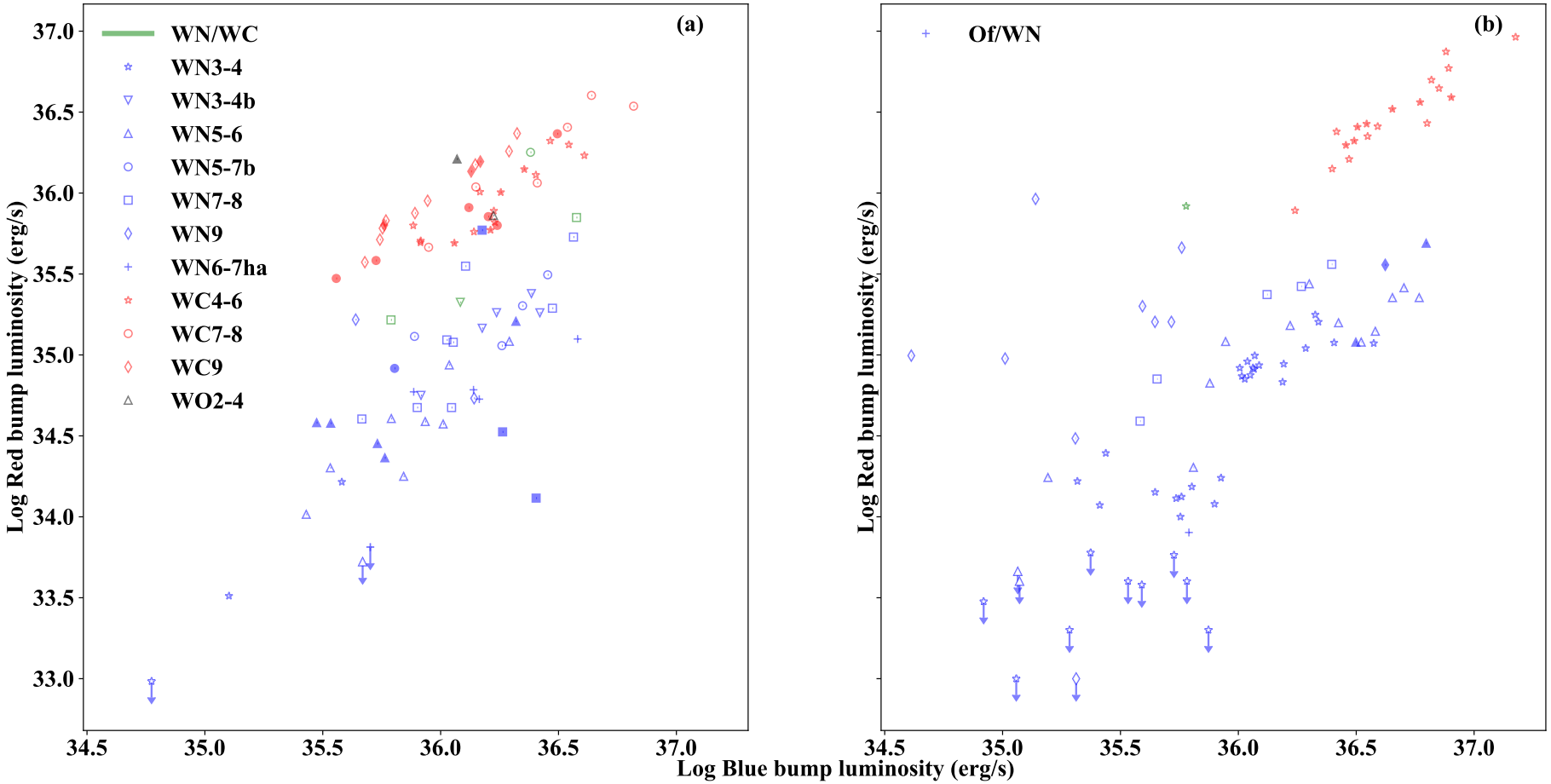

Figure 5.8: (a) Galactic WR star red and blue feature luminosities (b) LMC WR star red and blue feature luminosities. Blue points are WN, red are WC and green are WN/WC.

In general, WN stars in the LMC seem to cover a similar range of red and blue bump luminosities to Galactic stars, but it appears to be more common to find LMC stars on the extreme upper or lower end of this luminosity range. This may be due to the counteracting effects of luminosity, L and mass loss rate $\dot{M}$, which both depend on metallicity Z. Nugis & Lamers (2000) find a mass-loss dependent on luminosity and metallicity as follows for Galactic WR stars

$$\dot{M} \propto Y^{1.7} L^{1.29} Z^{0.5} \tag{5.1}$$

where Y is the mass fraction of helium. As the minimum mass for a WR star to form in the LMC is higher than in the Galaxy (Shenar et al., 2020), this leads to higher LMC WR star luminosities and higher emission line luminosities (if the wind densities are not dependent on metallicity). However, the mass loss rates are reduced at low metallicities, leading to weaker winds and reduced emission line luminosities (e.g Crowther & Hadfield 2006).

Assuming that two stars, one in the Galaxy and the other in the LMC, have the same luminosity and helium mass fractions and that the LMC metallicity is approximately half $Z_{\odot}$,

$$\dot{M_{LMC}} \propto 0.7 \dot{M_G} \tag{5.2}$$

Though the LMC luminosity is equal to the Galactic luminosity, the wind strength is only a factor of $\sim$0.7 times the Galactic wind strength. This explains why, for equal luminosity Galactic and LMC stars, LMC line luminosities may be lower than their Galactic counterparts.

For high luminosity LMC stars, the red and blue line luminosities are greater than in Galactic WR stars of the same luminosity. A possible reason for this is that the most massive stars in the LMC (e.g R136a1 Crowther et al. 2010) experience comparatively minor extinction and are therefore included in the our LMC sample, whereas some of the most massive Galactic WR stars (e.g those in the Arches cluster) are embedded and only visible at IR wavelengths. They are therefore not included in our sample. The most luminous LMC stars may therefore have slightly stronger emission lines than the Galactic stars in our sample, because the most luminous Galactic stars are excluded (although there are fewer extreme luminosity and mass stars than the LMC).

Additionally, the relationship in equation 5.1 may not hold for higher mass, classical WR stars (Vink, 2017) and the relationship of mass loss to luminosity may therefore be more similar the Galactic result.

5.5 Conclusion

In this chapter, we have calculated mean emission line luminosities for Galactic WR stars, based on our updated distances. These luminosities can be applied to other star forming galaxies to determine the number of WR stars with different subtypes within unresolved regions, such as clusters. The spectra can also be used to produce mean solar metallicity templates that can also be applied to extragalactic regions (e.g Figure 5.7).

In the next chapter, we will apply these new Galactic metallicity line luminosities, to an external galaxy (NCG6946) with a similar metallicity to the Milky-Way.

Chapter 6

A survey for WR stars in NGC6946

The data analysed in this Chapter was obtained through proposals GN-2009B-Q-4 and GN2010A-Q-29 at the Gemini North telescope, P.I JL. Bibby.

6.1 Introduction

In Chapter 1, we discussed the WR formation channel, its dependence on metallicity, and whether stripped envelope supernovae arise from massive, self-stripped WR stars, or lower mass companion stripped stars. Answering these questions requires surveys consisting of large numbers of WR stars; observing WR stars in different environments and observing transients in star forming galaxies.

Here, we present the results of a survey for WR stars and their environments in NGC 6946, one of the galaxies selected for observation by Crowther & Hadfield (2007) . NGC 6946 is a grand design spiral galaxy (with an angle of inclination approximately 30°, Sofue et al. 1999) located 6.1±0.6Mpc from the Milky Way (Herrmann et al., 2008). At ∼15kpc in diameter, it is approximately half the size of the Milky Way. It has hosted 10 supernovae in the last century, the most of any individual galaxy, and has a measured star formation rate (SFR) of $2.28 M_{\odot} yr^{-1}$(Kennicutt 1998a; Kennicutt et al. 2008) which is comparable to ∼2 $M_{\odot} yr^{-1}$ for the Milky Way (Chomiuk & Povich, 2011). The Milky Way is estimated to contain 1200±200 WR stars (Rosslowe & Crowther 2015a; Rosslowe & Crowther 2015b) and so if its metallicity is the same as the Milky Way, NGC 6946 likely contains ∼1400 WR (assuming the same IMF). This makes it a good candidate galaxy to search for WR stars, although it is located beyond the Galactic plane (l=95.72°, b=11.67°, according to the NASA Extragalactic Database) and therefore suffers from significant Galactic foreground extinction. Along with the significant distance modulus

of 28.9mag, assuming a total extinction of A_V ∼1.8 from Kessler et al. (2020) means that observing NGC6946 is equivalent to observing a galaxy at 13.8 Mpc. This is a very significant distance at which to be observing WR stars and means that detecting the emission line excesses will be extremely challenging.

The primary goal of our study is to survey WR stars within NGC6946, by finding candidate regions and confirming the presence of WR stars within them. Candidates are identified via photometry, by blinking emission line and continuum images or using continuum subtraction techniques (Section 1.8.1) to highlight WR emission line excesses. Confirmation of these candidates requires spectroscopy, to check for the presence of emission lines in the blue (4600−4700Å) or red (5600−5900Å) bump regions. The main dataset therefore consists of photometry and spectroscopy. Images are taken in six different filter bands; r and g SDSS filters and four narrow emission line (He II and Hα) and continuum bands that can be used to find WR He II emission lines and regions with Hα emission. The images are analysed using PSF subtraction, to obtain reliable photometry in crowded regions such as within the spiral arms. The spectroscopic slits are positioned on WR photometric candidates and regions with Hα nebular emission. The spectroscopy is reduced using the standard Gemini GMOS pipeline. Section 6.2 discusses the photometric and spectroscopic observations in greater detail.

We also use strong nebular lines in our spectra to calculate the galactic metallicity gradient and galactic extinction. The former allows us to study the distribution of WR subtypes, and therefore the effect of metallicity on WR star evolution, whilst the latter is important for calculating luminosity. Section 6.3 discusses the galaxy's metallicity gradient and extinction. Additionally, we use aperture photometry to obtain Hα luminosities for major star forming regions and we determine O star population numbers and the star formation rates within giant H II regions. WR star candidates are then obtained either manually or by calculating magnitude excesses, using blinked and subtracted narrow band filters. Our measurement of extinction allows us to dredden the WR spectra and determine the luminosities of the red and blue bump regions. We finally use the emission line calibrations from Chapter 5 to determine the number of WR stars in these regions. Confirmed and candidate WR population results are presented in Section 6.4 and the overall conclusions of our study and a summary are presented in Section 6.5.

6.2 Observations

Table 6.1: Imaging from Gemini GMOS. N is the number of stacked images and T_{exp} is the exposure time.

Date	Filter (λ_c, FWHM (nm))	Image	T_{exp} (s)	N	sec($\overline{z}$)	Typical FWHM (arcsec)
16/08/2009	Heii_G0320	NGC6946 East	1100	6	1.4	0.75
16/08/2009	(468, 8)	NGC6946 West			1.4	0.65
15/08/2009	Heiic_G0321	NGC6946 East	1100	6	1.4	0.75
17/08/2009	(478, 8)	NGC6946 West			1.3	0.65
16/08/2009	Ha_G0310	NGC6946 East	150	3	1.3	0.75
16/08/2009	(657.7, 6.9)	NGC6946 West			1.3	0.65
16/08/2009	Hac_G0311	NGC6946 East	150	3	1.6	0.75
16/08/2009	(663.2, 6.8)	NGC6946 West			1.3	0.65
15/08/2009	g_G0301	NGC6946 East	75	3	1.5	0.85
17/08/2009	(475, 154)	NGC6946 West		3	1.4	0.65
15/08/2009	r_G0303	NGC6946 East	150	3	1.5	0.65
17/08/2009	(630, 136)	NGC6946 West			1.4	0.65

6.2.1 Imaging

Imaging of NGC6946 was obtained during August 2009 using the GMOS instrument at the Gemini North telescope in Hawaii, with the EEV detectors (consisting of three 2048×4608 detector chips and ∼0.5mm detector gaps). The angular size of the galaxy (9.8×11.5 arcmin) is much larger than the instrumental field of view (5.5×5.5 arcmin)

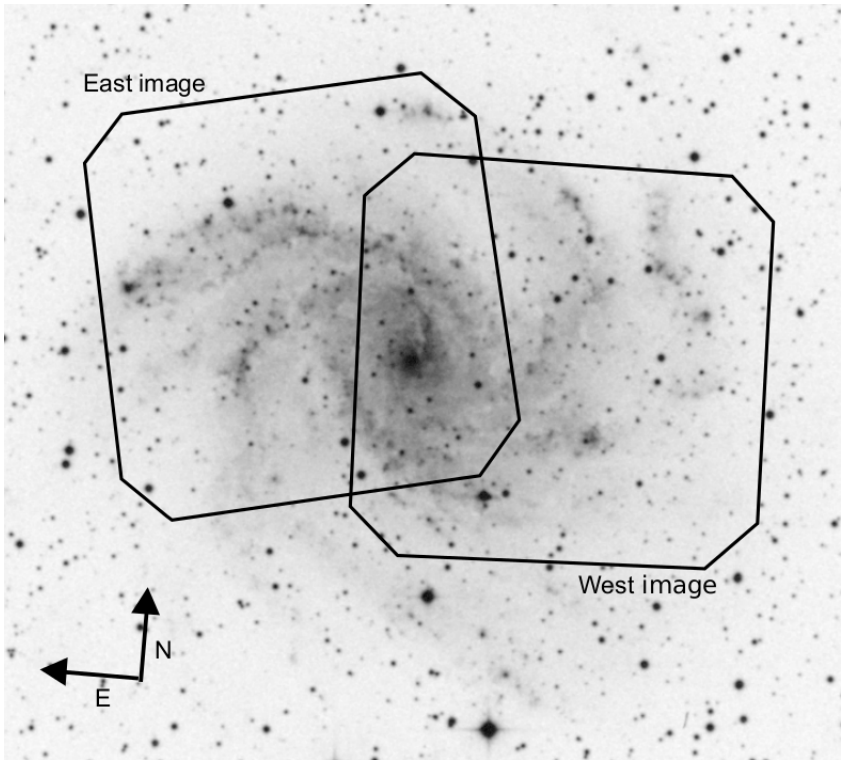

Figure 6.1: R−band Digitized Sky Survey (DSS2) 13×13 arcmin archive image (centre RA=20:34:52.3, DEC=+60:09:13.2) showing NGC 6946 and approximate locations of east and west regions imaged with the Gemini GMOS 5.5×5.5 arcmin field of view.

and so the east and west regions of the galaxy were imaged separately. Figure 6.1 shows the regions observed in each field. These two images were treated separately throughout photometric processing and analysis, allowing us to check the consistency using the overlapping region.

Images were taken in six filters. Narrowband He II (λ_c=468nm, FWHM=8nm) and He II continuum (λ_c=478nm) images were taken to search for characteristic WR emission at HeII 4686 or CIII 4650, using image blinking and subtraction. Hα (λ_c=658nm) and Hα continuum (λ_c=663nm) images were taken to search for ionized H II regions. Broad band r and g images in Sloan filters provided further photometric information. Three exposures with 2x2 binning were taken for the broad band filters and narrowband Hα and HαC filters. Six exposures (again with 2x2 binning) were taken for the narrowband He II and He IIC filters. This allowed for dithering to cover the detector gaps (Figure 6.2).

Calibration images of the spectrophotometric standard star BD+284211, were also taken in the narrowband filters.

All data were reduced using the IRAF Gemini GMOS reduction pipeline, applying bias subtraction but no flat fielding, as none were available. However, the images had

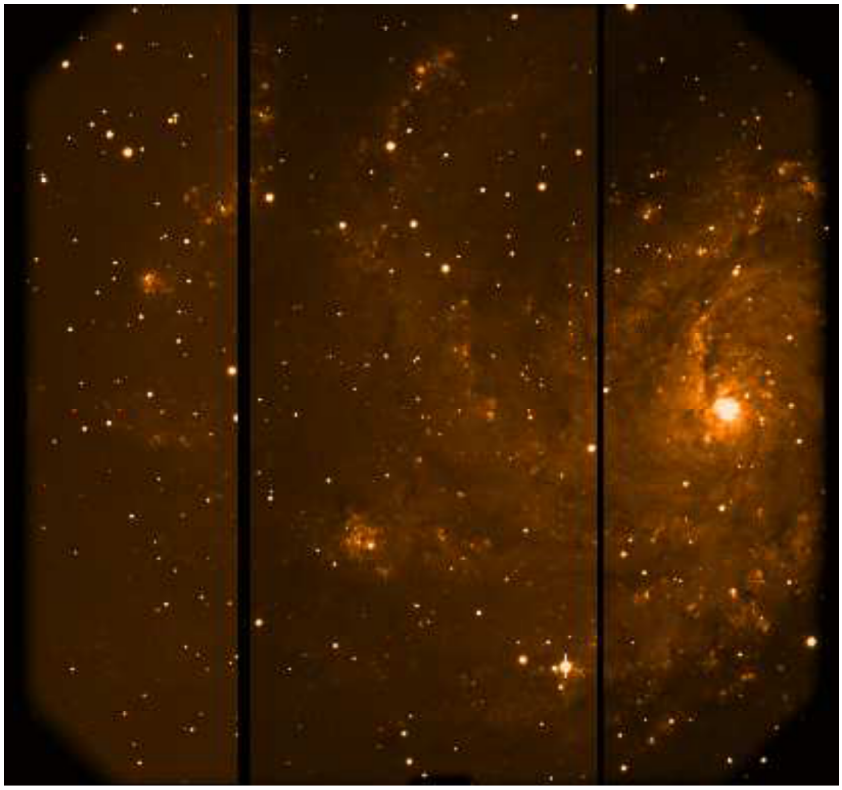

Figure 6.2: One exposure of the r band image, illustrating the gaps between the detectors

no noticeable artefacts or inhomogeneities in illumination over most of the field of view, and so it is unlikely the lack of flat fields has impacted the result. We used the DAOPHOT routine (Stetson, 1987) to fit point spread functions (PSFs) to point sources and obtain magnitudes in all filters.

The process detected point sources in the image, created a PSF and then used subtraction to check it had been properly fitted. However, due to significant variations in the background brightness, we had difficulty fitting PSFs across the full image and some regions showed subtraction residuals. We therefore used an iterative process to find optimal PSF and background settings; balancing the cleanness of subtractions in both faint and bright regions, the quality of the PSF and the consistency in the objects detected between east and west images within the overlapping region. Figure 6.3 shows an example of this process, with (a) being the first attempt and (d) being the result we ultimately decided to use. In image (a), the subtraction and PSF could both be improved. Image (b) shows an example with a somewhat better PSF (as the 'ring' around the central peak was less bright), but poor source subtraction. Though the PSFs for images (c) and (d) look extremely similar, the subtraction image quality differs due to different input

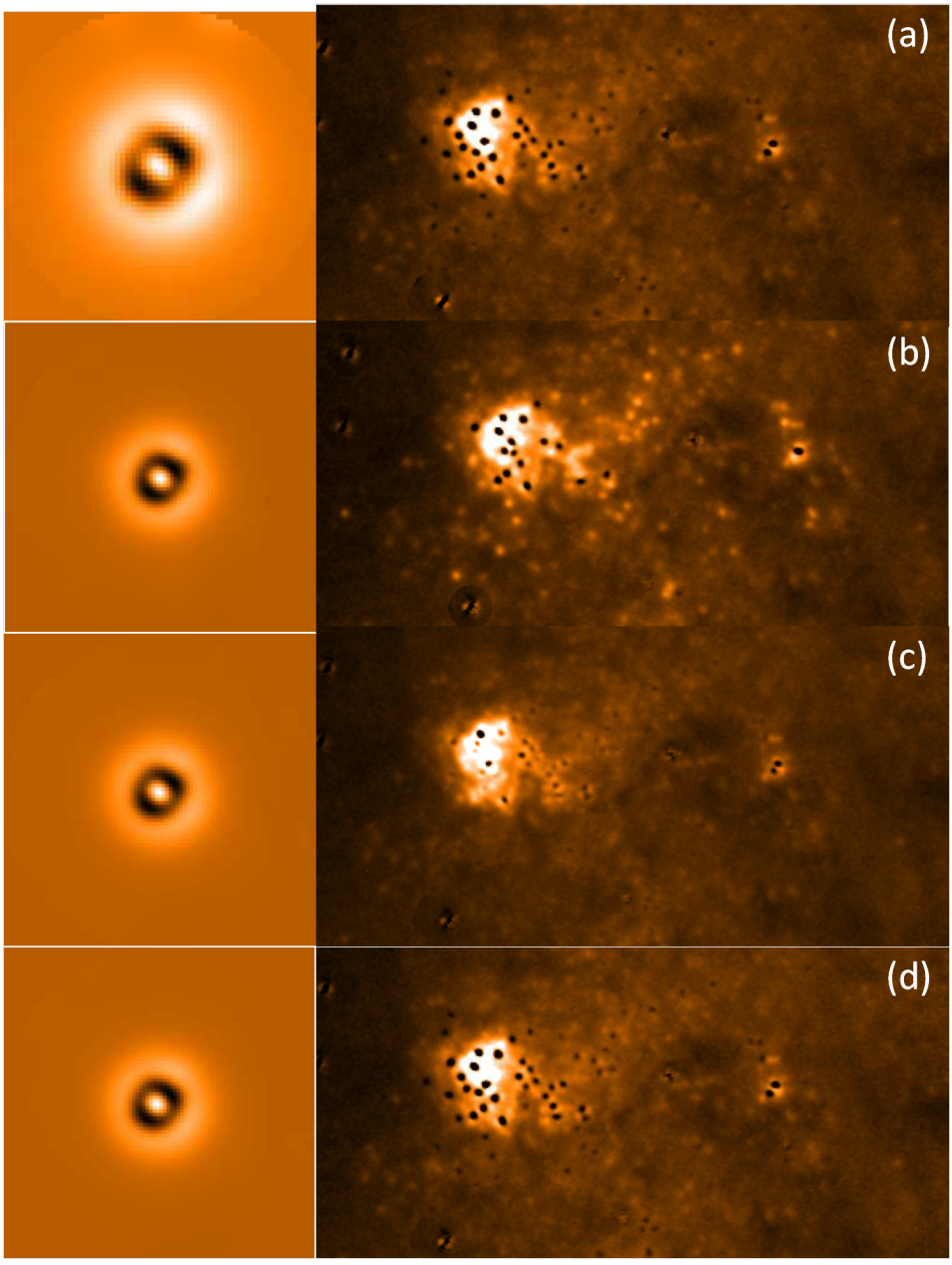

Figure 6.3: The PSF subtraction process for a section of the He II band west image. (a) shows the first attempt, where the PSF has a very bright ring around the central peak and some over subtraction towards the centre. In (b), the PSF was somewhat better, with a less bright ring, but many objects were not subtracted. For (c), the PSF and subtraction balance is much better, but some faint objects that may be spurious were also included in the results. Finally, (d) exhibited the improved PSF and reasonable subtraction without the faint, potentially spurious detections.

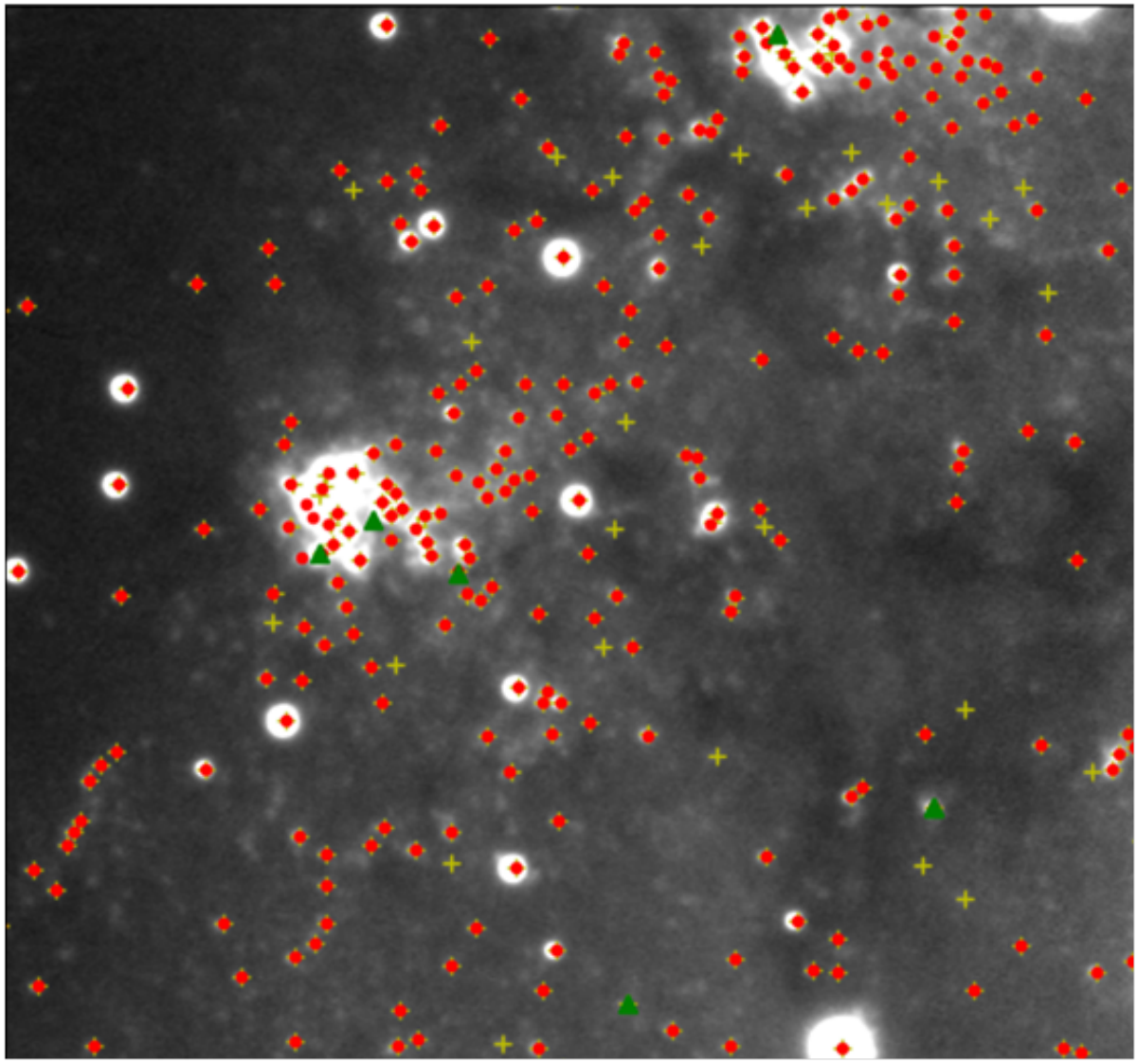

Figure 6.4: Detections from images (d) and (c) within Figure 6.3. The yellow crosses are detections from item (c) whilst the red dots are detections from image (d). Isolated yellow crosses may be potentially spurious detections, confusing nebulosity for stellar objects. The green triangles are sources where a spectrum was taken.

background levels. Image (c) shows better source subtraction overall, though objects in crowded, bright regions were not properly detected. This led to more detections of very faint objects and a different source list to image (d). As shown in Figure 6.4, many of these faint objects appeared to be spurious detections, centred on regions of nebulosity rather than clear point sources. Additionally, analysis of the overlapping region between the east and west images showed inconsistencies in the sources detected when PSF (c) was used. The results from (d), give a good compromise between a reasonable PSF, reasonable subtraction and consistency between the east and west images, whilst avoiding spurious detections.

The resulting fits produced magnitudes for 12723 objects (removing repeated objects, which appear in the overlapping region) in He II , 13083 in Hα , 16502 in g and 19460 in r. BD+284211 and bright stars in the image were then used to obtain a zero point correction for the narrow band filters.

The correction was calculated using equation 5 from Jrgensen (2009), which gives the calibrated values of BD+284211 in all filters m_{calib}, using the zero point correction magnitude m_{zero} and the instrumental magnitude ($m_{inst} = -2.5\log_{10}(N/t) - (a-1)kmk$)

$$m_{calib} = m_{zero} - 2.5\log_{10}(N/t) - (a-1)kmk \tag{6.1}$$

where N is the number of counts, t is the exposure time, a is the airmass and kmk is the median atmosphere extinction at Mauna Kea (and so the final term is the atmospheric extinction correction). The values for kmk were listed in t for the broadband filters, so these were interpolated to produce the values at the wavelengths of narrowband filters. The zero point can therefore be calculated using

$$m_{zero} = m_{calib} - m_{inst} \tag{6.2}$$

As these results are valid for aperture counts and not daophot output values, a conversion between these zero point corrected aperture count magnitudes and the daophot outputs is required. To obtain this, aperture photometry counts were repeated for ten 'standard' stars in each east and west region (the same stars used for alignment) and for each filter. The offsets from the standard star were then added to give the 'real' apparent magnitudes of the stars. The instrumental magnitudes provided by daophot were subtracted from these apparent magnitudes, giving a difference between the instrumental magnitudes for the stars.

As these differed somewhat for each of the stars measured, the overall results were averaged to give a difference that could be added (m_{add}) to convert the instrumental

magnitudes to apparent magnitudes.

$$m_{add} = \frac{(\Sigma(m_{dao} - m_{zcor}))}{10} \tag{6.3}$$

This was applied to the rest of the measurements found by daophot. The error of m_{add} was found by using the standard error on the mean of $m_{dao} - m_{zcor}$ for each of the ten stars.

The average difference between the bright stars and the Pan-STARRS DR1 catalogue data was used for Sloan r and g m_{add} corrections (Chambers et al. 2016; Magnier et al. 2016 and Flewelling et al. 2016). The typical FWHM for the images varied between 0.6 and 0.9 arcseconds, which corresponds to ∼20pc at the 6.1Mpc distance of NGC6946. The raw spatial scale was 0.075 arcseconds pixel^{-1} and 0.15 arcseconds per 2×2 binned pixel in the image.

As the shape and size of the stellar PSFs differed slightly between images, DAOPHOT obtained different centroids for the same point source across different filters. Photometry was matched to objects imaged in different bands by searching a 0.45 arcsec box (3 binned pixels) centred on the object. For He II and He IIC , objects detected in one band, but not the other, were assumed to be beyond the completeness limit in the undetected band. This limit is 22.7 mags in the He II and He IIC bands, based on the turnoff point between the fitted straight line, which tracks how the number of sources N would be expected to increase, and the binned data in Figure 6.5. The slopes of each of the fitted lines are log N = 0.5115m−8.557 for the He II east data, (where m is the magnitude) and log N = 0.5084m−8.471 for He IIC . For the west data, log N = 0.4893m−8.141 for He II and log N = 0.5224m−8.815 for He IIC . Additionally, the fainter objects near the limit have much larger associated errors, >0.1mag (Figure 6.6).

Finally, to obtain good quality positions for individual objects, the astrometry was aligned with the 4th US Naval Observatory (USNO) B1.0 standard catalogue, using the positions for 10 bright, reasonably isolated stars in each of the east and west images. The coordinates for these selected stars were aligned with those from the USNO database with the Starlink Gaia package (Draper et al., 2014). The alignment was accurate to ∼0.1 arcsecond.

Full details on these observations are shown in Table 6.1.

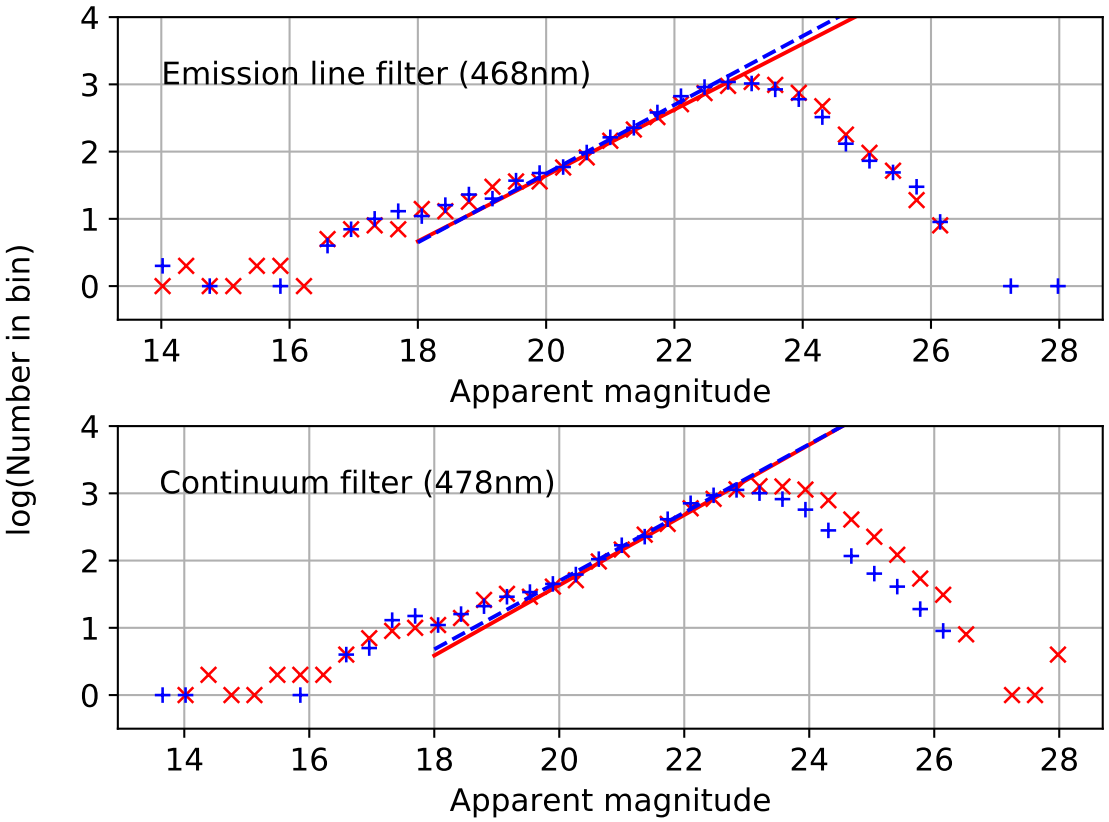

Figure 6.5: The number of sources detected by DAOPHOT at each magnitude in the He II 468nm and He IIC 478nm bands. The blue crosses are the east data and the blue dashed line is the fit to the linear region between 20 and 23mags and the red crosses are the west data, with the red line the fit to the same linear region. The average slope is log N = 0.51m−8.50 for He II and He IIC , where m is the magnitude. There are an increased number of sources at faint magnitudes for the west He IIC data, because a file containing a much larger number of total sources was used. This was to ensure that sources with He II measurements would have a detected He IIC counterpart.

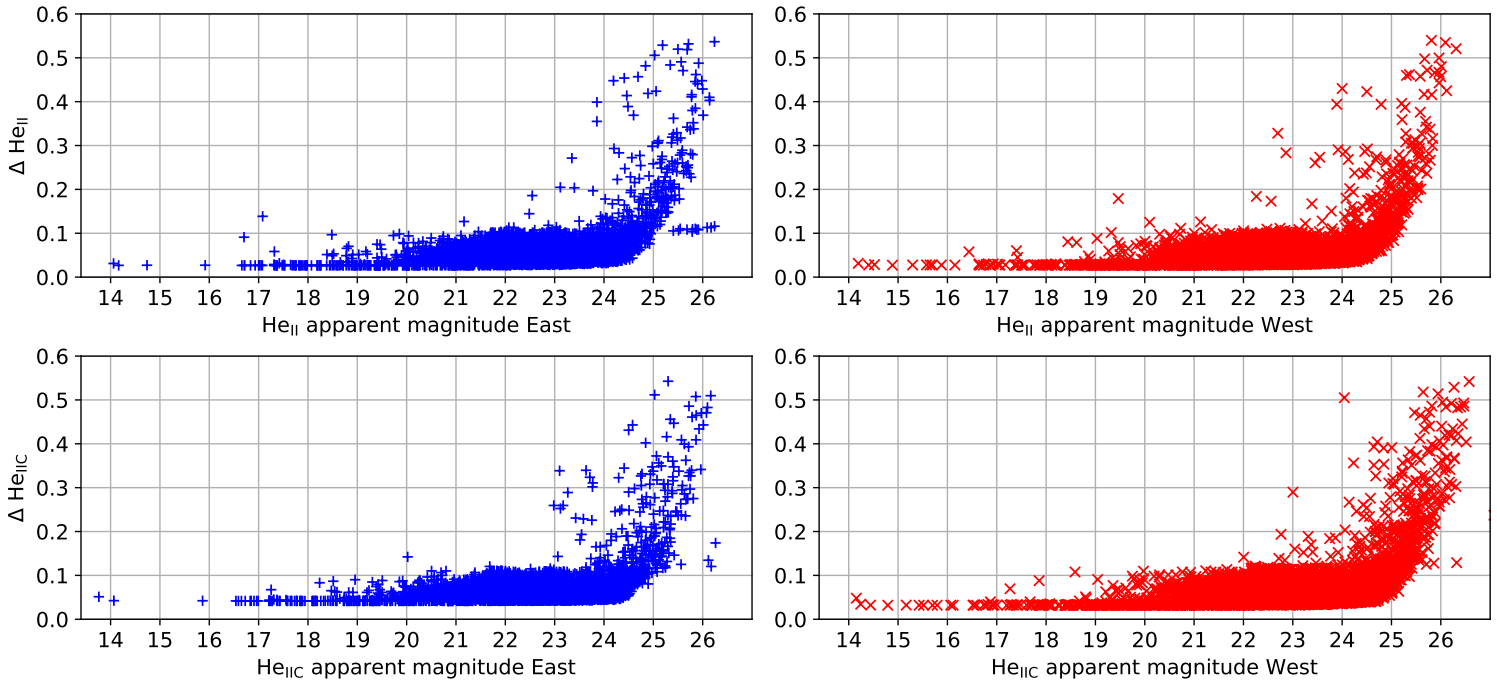

Figure 6.6: Sources detected by DAOPHOT in the He II band and the corresponding errors ΔHe II . These are the internal photometric uncertainties from the PSF fitting in DAOPHOT. They are computed per pixel, based on the CCD count uncertainties and the PSF model intensity. Blue crosses are the east data and red crosses are the west data. There is an approximately exponential relationship between the errors and the apparent magnitudes. There is also an increase in ΔHe II beyond 20mags, likely because of the increased number of sources which only appear at faint magnitudes.

Table 6.2: Spectroscopy from Gemini GMOS. N is the number of stacked images.

Date	Mask	Image	T_{exp} (s)	N	sec(z)
05/06/2010	1	West	1000	2	1.34
18/06/2010	2	West	1900	2	1.35
20/06/2010	3	West	2800	2	1.34
02/07/2010	4	East	1000	2	1.33
02-03/07/2010	5	East	1900	2	1.38
21/06/2010	6	East	2800	2	1.36

6.2.2 Spectroscopy

Spectra were obtained using multi object spectroscopy (MOS), again with Gemini north GMOS (Table 6.2). Six masks were created, to obtain spectra of 166 regions; these were a combination of WR candidates identified from narrowband imaging, and nebulae showing Hα emission. Figure 6.7 shows the positions of the slits within mask 5. We use an R150 grating, with spectra taken for two central wavelengths (5100 and 5300Å). This shifts the positions of the spectral features by 200Å and ensures no data was lost in each of the ∼38 pixel (129Å) wide detector gaps (e.g Figure 6.8). We additionally obtain two exposures for each central wavelength and flat fields for each mask. Slit sizes were 1×5 arcsec, corresponding to 30×150pc at the adopted distance of NGC6946.

The spectral range extended from approximately 4070-9200Å. 2x2 binning was used, to obtain spectral pixel dispersion of ∼3.5 Åpixel^{-1} and a vertical spatial scale of 0.16 arcseconds pixel^{-1}. The data also included arc spectra for the wavelength calibration, from the copper argon (CuAr) lamp at Gemini North.

The IRAF GMOS reduction pipeline applied flat fielding and bias subtraction to the raw images. It then cut the full image into individual spectra, using the multi object spectroscopy header. The two exposures from each central grating were merged, giving 2D spectra (as shown in Figure 6.9) and the IRAF APALL routine was then used to extract the 1D spectra from these chopped images. Figure 6.9 shows two representative examples of this process. For object 26, which has a clearly visible continuum, this process was fairly straightforward. Looking in the spatial direction, the centre of the extraction aperture was placed in the centre of the continuum, at 13.19 pixels. Figure 6.9 shows that the IRAF algorithm then extracts 5.7 pixels either side of the defined centre. An

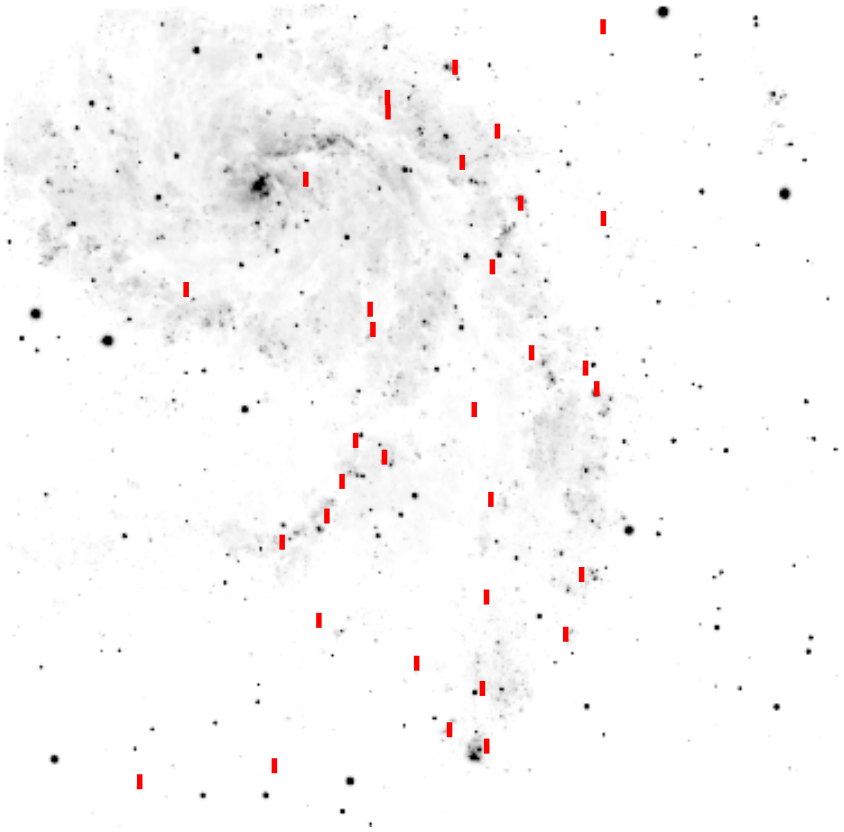

Figure 6.7: East He II image, with 1x5 arcsec slits (red rectangles) from mask 5.

additional four pixels are extracted for the background and are shown as dashed lines on Figure 6.9.

However, for object 10, which does not have a visible continuum, the red bump WR emission lines at 5696Å(if present) and 5808Åare instead used to position the centre of the extraction aperture in the spatial direction. Instead, the high and low extraction regions are 5 pixels either side respectively. Again, four pixels were used to determine the background.

Further IRAF routines applied the wavelength calibration.

Finally, the data was flux calibrated in DIPSO using the spectrophotometric standard star BD+284211. Figure 6.10 illustrates a spectrum before and after flux calibration.

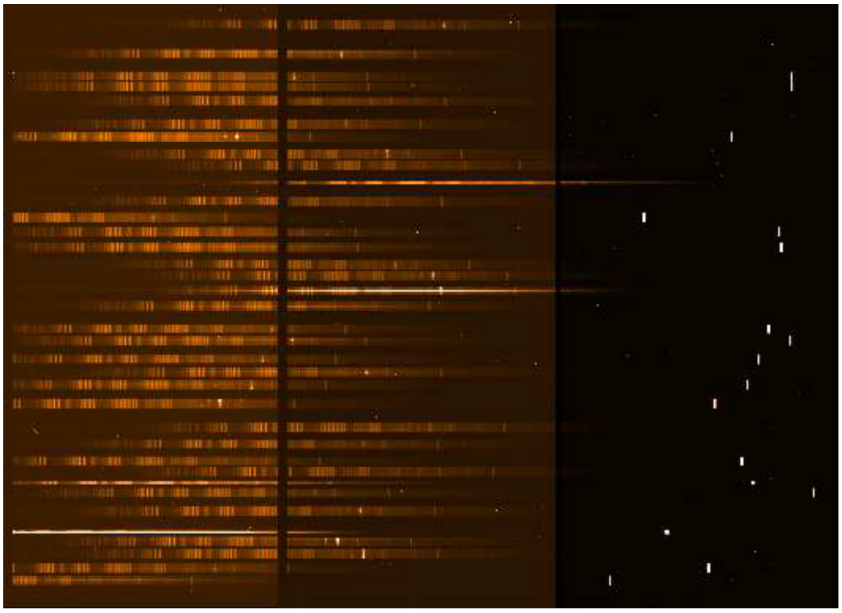

Figure 6.8: Raw multi object spectroscopy image from mask 5.

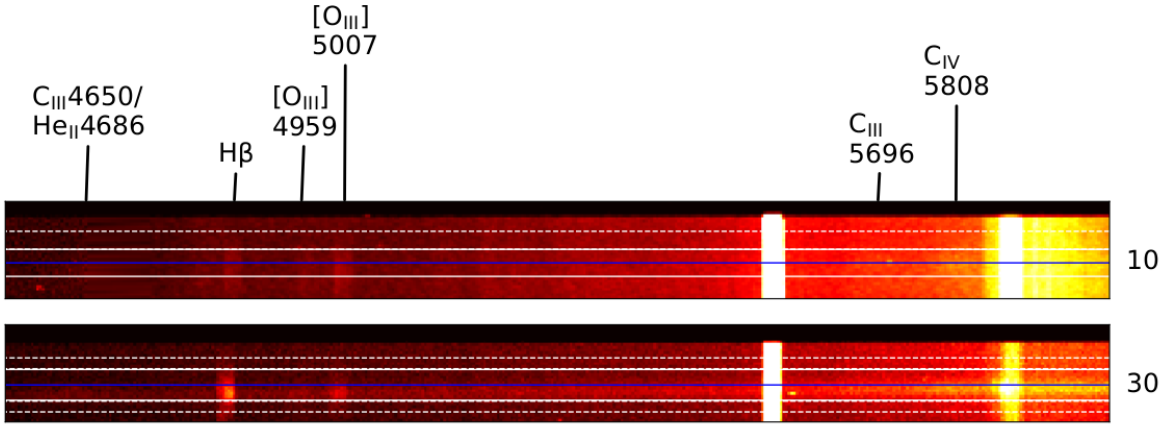

Figure 6.9: Section of 2D spectra, extracted from the MOS image. The upper image is the 5100Å grating image of candidate 10 (from mask 3) and the lower spectrum is the 5300Å grating image of candidate 26 (mask 1). Also marked are the positions of nebular (Hβ and [O III]) and WR emission lines (C III and C IV). Solid white lines denote the spectrum extraction aperture and centre, whilst the dotted white lines are the background regions. Candidate 10 is an example without a visible continuum; where the 1D spectrum was extracted based on the emission lines. Candidate 26 has a clear continuum, which was far easier to extract.

The majority of spectra with data from both 5100 and 5300Å centred gratings were merged to eliminate detector gaps. However, the variation in background levels between images, as well as noise, caused difficulties with background subtraction, which may have

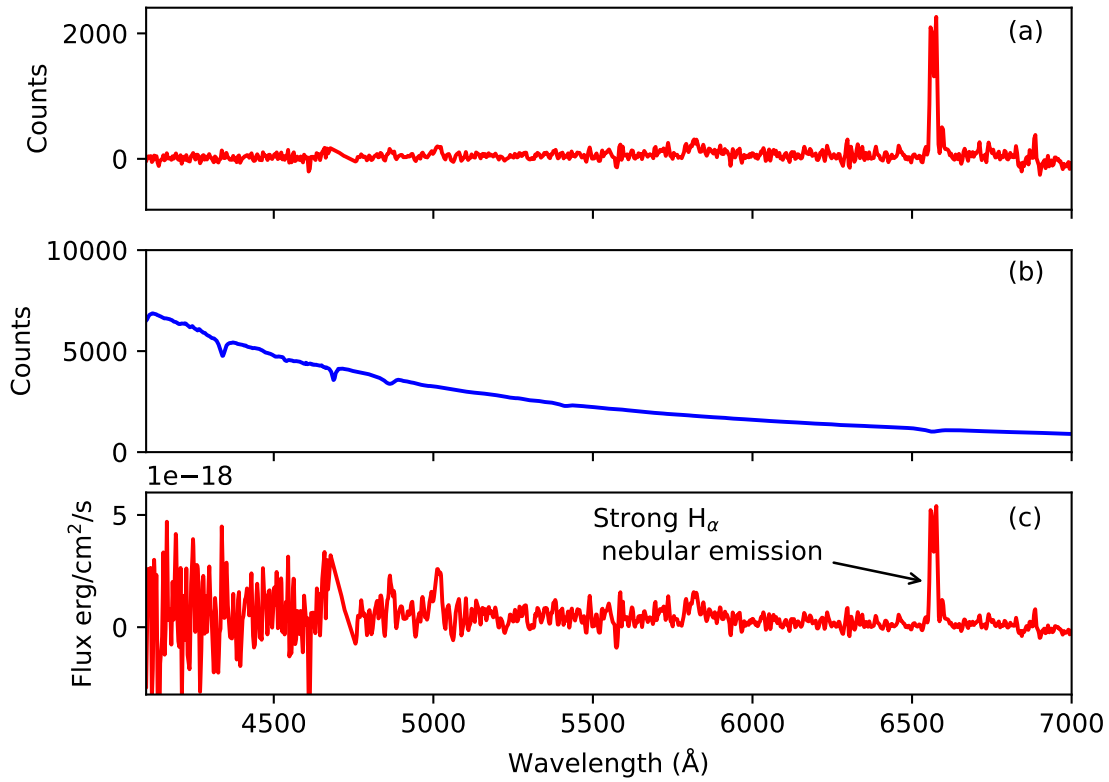

Figure 6.10: Calibration of Candidate 10 (2D spectrum shown in Figure 6.9), from the original 1D extraction in (a) and using the spectrum from standard star BD+284211 (b). The final spectrum (not yet dereddened) is in (c).

led to higher continuum fluxes in one grating compared to the other. Unfortunately, these spectra could not be merged and the detector gaps remained in the data. Non merged spectra were not problematic where the detector gaps occurred outside the region containing most emission lines (4070−7000Å).

Ordinarily, slit loss corrections would be applied using the photometry of the source that the spectrum is centred on. However, contamination from non WR stellar populations led to significant differences between the magnitudes from the photometry and the spectroscopy. Therefore a slit loss correction could not be applied.

6.3 Nebular Analysis

6.3.1 Metallicity

We estimate the metallicity gradient of NGC 6946 using strong nebular emission lines Hα , [N II]6583, Hβ and [O III]5007, to obtain 12+log(O/H) from calibrations at different galactic radii (an example of a spectrum used is in Figure 6.11).

DIPSO was used to fit gaussians to each of the emission lines (using the emission line fitting, ELF, procedure) , which yields line fluxes and allows de-blending of the Hα and [N II]6583 lines.

Unfortunately, in some cases the emission lines often did not conform to gaussian profiles and instead resembled truncated gaussians. Any gaussian fits applied well to the bottom of the curve, but overestimated the height at the peak. In the case of such non-gaussian emission lines, we use the gaussian fits, but obtain an additional measure of flux to determine the degree of overestimation. This additional measure was found using the DIPSO 'flux' command, which integrated the flux below the emission line, by assuming a linear continuum defined between user cursor hits. The method therefore accurately obtained the non-gaussian flux, without relying on gaussian fitting. Conversely it did not give an estimate of individual line errors, as the fluxes for the blended Hα region could not be decomposed into Hα and [N II]6583. However, the differences between fluxes from the gaussian fits and the additional fits were used as a rough guide for uncertainties generated by fitting gaussian emission lines to the non gaussian line profiles.

Typically, formal errors were less than 5 percent for the Hα and N II blended region, whilst results for the Hβ region also have a typical variation of 5 percent (although the maximum was 40 percent). The empirical strong line relations of O3N2 ([O III]5007/Hβ)/([N II]6583/Hα) or N2 ([N II]6583/Hα), to 12+log(O/H) from Pettini & Pagel (2004), were then used to estimate the metallicity (as auroral lines for direct temperature measurements were unavailable).

A total of 28 spectra showed Hα and [N II]6583 emission lines, and so the N2 index was used to calculate the metallicity. A further 47 showed both Hα and [N II]6583 and Hβ and [O III]5007 lines, which meant that the O3N2 index could be used.

The upper and lower bounds of the metallicities were calculated by combining the bounds of emission line fluxes with the systematic errors from Pettini & Pagel (2004). The likely flux uncertainty from the non gaussian emission lines was within the range of these systematic errors. Only results with at least a 3σ detection line width above the error were used.

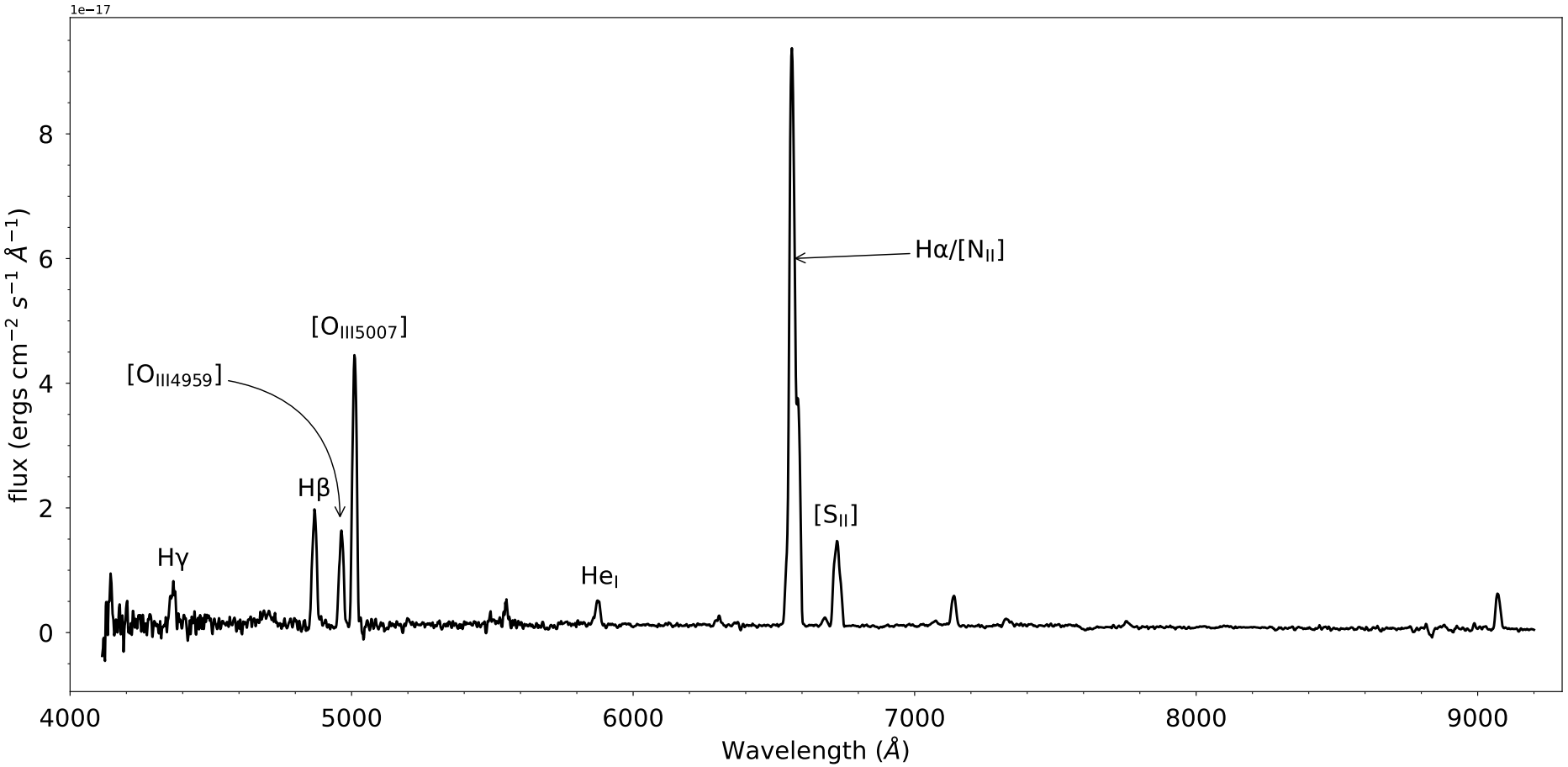

Figure 6.11: Example nebular spectrum used for calculating reddening and metallicities.

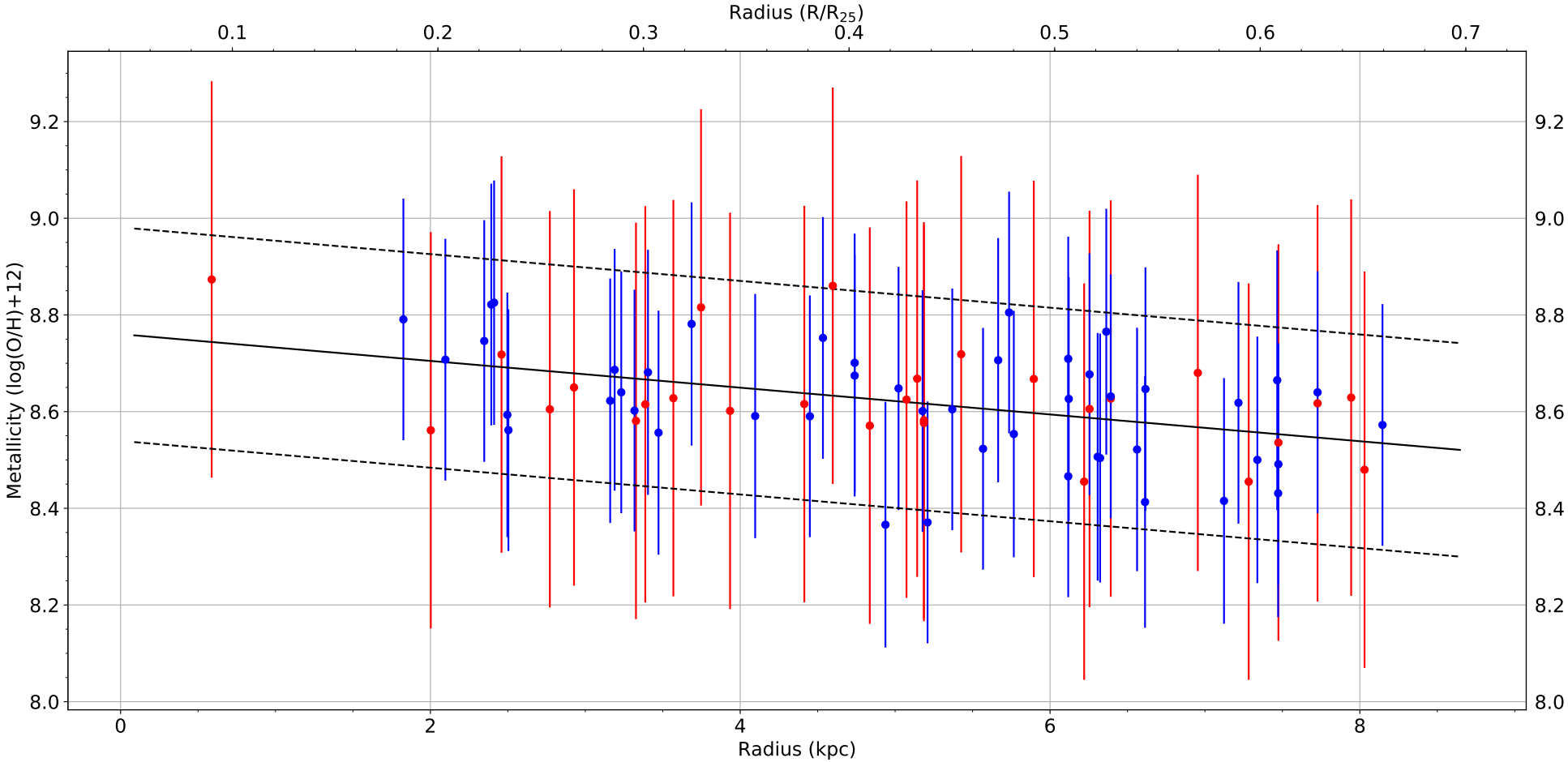

Figure 6.12: Metallicity measurements from nebular emission lines for NGC 6946. Red points are results found using only the N2 index, blue points use the O3N2 index, the solid black line is the best fit gradient (-0.028 ± 0.006 dex/kpc and -0.33 ± 0.07 dex/R_{25}). The dotted lines above and below the best fit line show the 2σ confidence intervals of the gradient (±0.2).

We obtained distances from the galactic centre to the spectroscopic regions, by assuming a projection angle of 30° (Rogstad et al., 1973), a nucleus position at 20 34 52.59 +60 09 12.9 (J2000 epoch, Makarov et al. 2014 from HyperLEDA [1]) and a distance of 6.1±0.6Mpc (Herrmann et al., 2008). The graph in Figure 6.12 shows the resulting metallicity gradient −0.028±0.006 dex/kpc (−0.33±0.07 dex/R_{25}, where R_{25}= 11.48 kpc de Vaucouleurs et al. 1995 and R_{25} is the deprojected isophotal radius of the galaxy, at the point where it reaches a surface brightness of 25mag/arcsec^2 in the B band), with a central metallicity of 12+log(O/H)=8.76±0.2. This gives a result that is closer to Solar metallicity (12+log(O/H)=8.7) than LMC metallicity (12+log(O/H)=8.4), except for the outermost regions beyond approximately 8kpc (albeit with large uncertainties).

6.3.2 Comparison with literature

The metallicity of NGC 6946 has been previously studied by Cedrés et al. (2012) and Moustakas et al. (2010). Both papers calculated metallicity using the R_{23} parameter (where R_{23}=log(([O II]$_{3727,\ 37279}$ + [O III]$_{4959,5007}$)/Hβ)) and calibrations from Pilyugin & Thuan (2005) (which also used an excitation parameter) and Kobulnicky & Kewley (2004), whereas our results used strong nebular line calibrations. Their Kobulnicky & Kewley (2004) calibrated results fall within the uncertainty of this work; Cedrés et al. (2012) find a gradient of −0.29±0.1 dex/R_{25} and Moustakas et al. (2010) find −0.28±0.1 dex/R_{25}. However, our inferred central metallicity is much lower than the Kobulnicky & Kewley (2004) calibrated results of 9.19±0.04 and 9.13±0.04 respectively.

Using the Pilyugin & Thuan (2005) calibration instead gives a central metallicity 8.57±0.04 using Cedrés et al. (2012) and 8.45±0.06 with Moustakas et al. (2010). The gradient from Cedrés et al. (2012) using this calibration is −0.40±0.1 dex/R_{25}, which is again with the uncertainty of our results. However, our value disagrees with the Moustakas et al. (2010) Pilyugin & Thuan (2005) calibrated result of −0.17±0.15 dex/R_{25}.

This shows the strong influence of the calibration of R_{23} to log(O/H), on the resulting metallicity gradient. Unfortunately, calibrations using R_{23} also produce both an upper and a lower value for the same observation, due to the effect of different metallicities on the oxygen emission lines (McGaugh, 1991).

At low metallicities (<0.15$Z_\odot$) hydrogen is the main form of cooling and the oxygen content is low, so the H II regions are on the lower branch. At increased metallicity, (∼0.3$Z_\odot$), with the increasing oxygen content, [O III]$_{4959,5007}$ emission dominates. At high metallicities (>0.5$Z_\odot$), more oxygen content is available for cooling. The temperature of

[1] http://leda.univ-lyon1.fr/

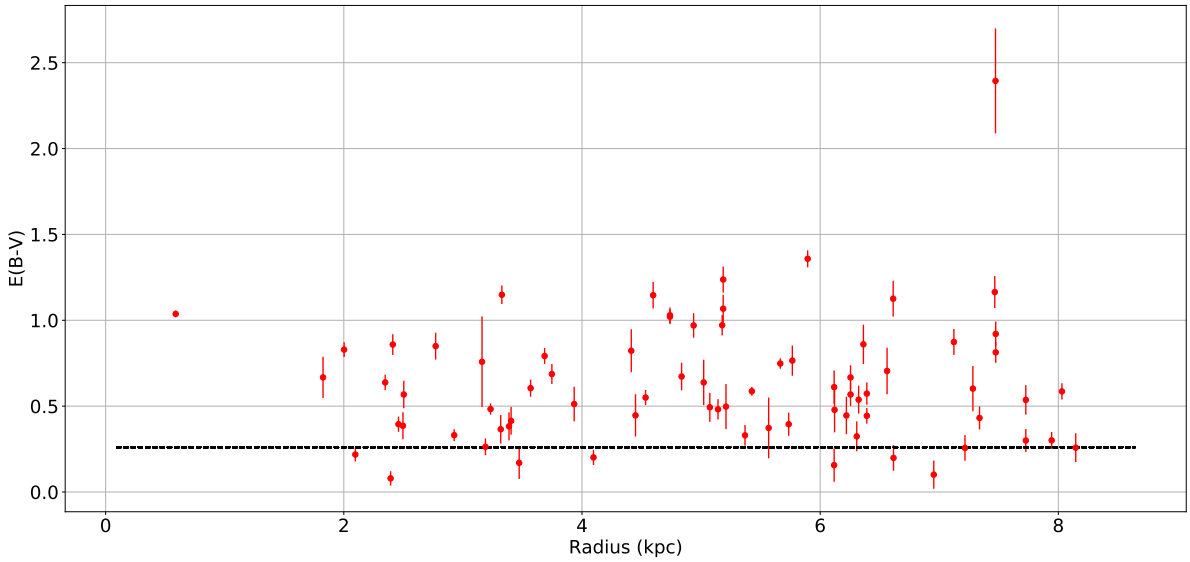

Figure 6.13: Nebular derived reddening for 75 regions showing both Hα and Hβ emission in NGC 6946. The black dotted line denotes the foreground reddening due to the Milky Way (E(B−V)≈0.3 Schlafly & Finkbeiner 2011).

individual oxygen atoms falls and cooling moves to other lines excited at IR wavelengths. The H II regions are therefore on the upper branch (as the number of oxygen atoms is high), whilst the production of the oxygen R_{23} emission lines is reduced (McGaugh, 1991). Therefore, for a single R_{23} measurement at a given galactic radius, two alternative log(O/H) values are possible.

The upper and lower branches are problematic, as an alternative estimation of whether the object is metal rich (and thus lies on the upper branch), or metal poor (and therefore lies on the lower branch), is required. AGN regions and reddening can also introduce errors into the R_{23} parameter and associated calibrations which rely on it. This may particularly apply to metallicities near the galactic centre.

6.3.3 Extinction

The reddening was calculated using the ratios of nebular Hα to Hβ emission lines. The intrinsic intensity ratio is known from Case B recombination theory (Hummer & Storey, 1987) and is $I_{H\alpha}/I_{H\beta}$=2.86 for T=10,000K and N_e=100-1000 cm^{-3}. Using a much higher electron density, N_e=10,000 cm^{-3} makes little difference, as the ratio only decreases slightly to 2.85. Additionally, varying the temperature with N_e=1000 also causes little difference in the intrinsic ratio, which is 2.92 for T=7500K and 2.81 for T=12,500K.

Deviations from $I_{H\alpha}/I_{H\beta}$=2.86 must be caused by interstellar reddening and can be

used to find E(B−V) with the extinction coefficient c(Hβ) (where E(B−V)∼0.7c(Hβ), calculated using Cardelli et al. 1989). We used this method to find the extinction of 75 regions showing nebular emission lines. Uncertainties were again derived using the maximum and minimum possible values of reddening from the emission line fitting errors.

The reddening results are presented in Figure 6.13. Using the galactic dust extinction calibrations from (Schlafly & Finkbeiner, 2011) (queried via IRAS), the mean Milky Way foreground E(B−V)≈0.3 and A_V≈0.9. This foreground reddening is marked on the diagram with a black dotted line and results that fall below it are spurious (as the total extinction is below the Milky Way foreground). 9 results have averages which fall below this line and of those, 5 do not have upper error bars with E(B−V)>0.3 .

The average E(B−V)=0.61±0.03 (weighted average 0.64±0.03), where the uncertainty is the standard error on the mean, and the average A_V=3.1E(B−V) is 1.88±0.09. This result is in good agreement with A_V ∼1.83 from Kessler et al. (2020) (who use Hα and Paβ images, and by converting their median $A_{H\alpha}$ to A_V), but is much higher than the average A_V=0.9 found in Cedrés et al. (2012) (which uses the same ratios of Hα /Hβ and Case B recombination theory as this work).

A much larger number of H II regions were used to calculate the Cedrés et al. (2012) result, which may have included a significant number with low measured reddening (indeed, many of their H II regions are recorded as having no extinction at all). Finally, the non gaussian shapes of some lines in our work may have caused the emission line fits to be over estimated. This would have led to larger Hα fluxes and thus larger measured E(B−V) values, relative to Hβ lines. Unfortunately, this problem is difficult to remove or quantify, as the emission lines cannot easily be decomposed into their individual components without assuming a gaussian shape.

6.3.4 Integrated star formation rate, H II regions and O star population

We investigated both the integrated Hα emission from the whole galaxy and emissions from individual (candidate) giant H II regions. The former was used to calculate the star formation rate of the galaxy and the latter to determine the O star populations of giant H II regions.

The integrated emission was found for both Hα and HαC filters, using the number of counts inside multiple large apertures. Apertures were centred on individual H II regions and sized to encompass emissions above the level of the background (or the surrounding diffuse gas). In both cases, an average background count for each filter was

Table 6.3: Table comparing results with Kennicutt et al. (2008). $F_{H\alpha}$ is the Hα flux, $I_{H\alpha}$ is the dereddened Hα flux and $L_{H\alpha}$ is the Hα luminosity.

	Kennicutt et al. (2008)	This work
Field of view	10.4'x10.4'	6.5'x9.7'
$A_{H\alpha}$ (mags)	0.924	1.549 ± 0.19
Calibration	$A_{H\alpha}$=0.6A_B	(Cardelli et al., 1989)
Distance (Mpc)	5.9	6.1
F(NII6548+6583)/F(Hα)	0.54	0.36 ± 0.03
log(F[NII]6548+6583+Hα) (ergs/s/cm^2)	−10.34 ± 0.03	$-10.79^{+0.13}_{-0.19}$
log($F_{H\alpha}$) (ergs/s/cm^2)	−10.53	$-10.92^{+0.14}_{-0.21}$
log($I_{H\alpha}$) (ergs/s/cm^2)	−10.16	$-10.17^{+0.14}_{-0.21}$
log($L_{H\alpha}$) (ergs/s)	41.46	$41.48^{+0.17}_{-0.28}$
SFR ($M_\odot yr^{-1}$)	2.28	$2.39^{+1.14}_{-1.14}$

found using an aperture centred on a region with no emission. These background values were subtracted from the counts in the emission regions, leaving counts only from Hα and HαC . The count per second to flux conversion was found using spectrophotometric standard star BD+284211 and the fluxes for the combined N II and Hα emissions were then calculated. Finally, the N II and Hα excess was found by subtracting the HαC flux.

The Hα flux (after subtracting N II) and the intensity were then calculated. For the integrated Hα flux, the average [N II6548+6583]/Hα = 0.36 (averaged from the spectral results across all masks) and E(B−V) = 0.61 was used to calculate the contribution of N II and the intensity respectively. For individual H II regions, the N II/Hα ratio and E(B−V) from the spectrum was used, if available. Otherwise, we used the average values for the galaxy. Cardelli et al. (1989) calibrations were used to obtain the extinction in the Hα band ($A_{H\alpha}$ = 2.54E(B−V), with R_V=3.1). Finally, the intensity was converted to the Hα luminosity using the distance to the galaxy.

The integrated star formation rate was then found using the conversion

$$SFR(M_\odot yr^-1) = 7.9 \times 10^{-42} L(H_\alpha) \tag{6.4}$$

from Kennicutt (1998b), where L(Hα) is the total galactic Hα luminosity. This gives

SFR=2.39$M_{\odot}yr^{-1}$, which is similar to the result from Kennicutt et al. (2008). However, this similarity stems from the much lower log($F_{H\alpha}$) flux measured in this work (0.35 times the Kennicutt et al. 2008 data) and the higher extinction correction used (see Table 6.3).

For each individual H II region, the O star content was found by converting the luminosities to the number of ionizing photons using

$$N(Lyc) = 1.36 \times 10^{12} L(H_{\alpha}) \tag{6.5}$$

from Conti et al. (2008). Table 6.4 shows properties of the H II regions studied. All of the brightest regions emit $>10^{50}$ ionizing photons s^{-1} and have diameters on the scale of ∼100pc, so qualify as giant H II regions. O star populations were then calculated by assuming a flux of 10^{49} ionizing photons s^{-1} from a typical O7V star. Catalogue numbers from Hodge & Kennicutt (1983) (identified using HK-0, for example) were used to label individual regions that had already been identified. Exceptions were two regions in the galactic centre (noted with GC in the table), which were unresolved in the original photographic plates, and a region to the north of the galactic centre (noted with N in the table). Unfortunately, the limited (1 arcsec) accuracy of the coordinates and difficulty in reading some of the coordinates from the original paper, made matching HK numbers to their assigned H II regions challenging, and so no label appeared to match these locations. Kessler et al. (2020) also suggest these galactic centre regions have much higher extinction than the rest of the galaxy. The O star populations in these regions may therefore be underestimated.

Results from individual H II regions HK-3 and HK-4 can be compared with those from the integral field spectroscopy in García-Benito et al. (2010). Again, we use the narrowband photometry (Hα and HαC filters) to find the Hα flux from these regions. When using circular apertures the same size as the fibre region diameters given in Table 7 of García-Benito et al. (2010), the F([NII]+Hα) for HK-3 (knot A in García-Benito et al. 2010) measured in this work is approximately 0.68 times that from (García-Benito et al., 2010). For HK-4 (knot C in García-Benito et al. 2010), the fraction is only 0.57. However, García-Benito et al. (2010) notes that these aperture radii are not intended to be accurate, instead giving an order of magnitude estimate of the size. This could mean that García-Benito et al. (2010) used somewhat larger apertures than stated, resulting in the lower flux from this work.

The uncertainties of luminosities and O star populations for individual H II regions were estimated by propagating the uncertainties of counts in the apertures (root N in

each Hα and Hαc filter) and the conversion from the standard star. The uncertainty of Hα extinction was calculated by assuming a conservative uncertainty of 10% for the Hα and Hβ fluxes, with which we obtained an uncertainty of $\sim$17% for c(Hβ) and $\sim$12% for reddening. Additionally, we use the uncertainty of the distance, $\pm$0.6Mpc (Herrmann et al., 2008) and assume a 14% uncertainty of the [NII]/Hα ratio, based on 10% uncertainties for each flux component. For the reddening of the whole galaxy, we instead use the uncertainty of $\pm$0.03 on the reddening average.

Table 6.4: Table showing key information on candidate giant H II regions.

HK-number	RA (aperture centre)	DEC (aperture centre)	E(B−V)	[NII]/Hα	log F([NII]+Hα) (ergs/s/cm^2)	log L(Hα) (ergs/s)	No. of O7V stars	Aperture diameter (arcsec)	Candidates in/near region
473	$20^h34^m34.92^s$	$60°11'38.7''$	0.610±0.073	0.360±0.050	$-12.81^{+0.05}_{-0.05}$	$39.46^{+0.10}_{-0.13}$	212±57	3.38	None
None(N)	$20^h34^m50.93^s$	$60°10'20.9''$	0.638±0.077	0.465±0.065	$-13.01^{+0.05}_{-0.06}$	$39.29^{+0.11}_{-0.14}$	144±40	2.91	None
None(GC)	$20^h34^m52.36^s$	$60°09'14.1''$	0.610±0.073	0.360±0.050	$-12.45^{+0.10}_{-0.13}$	$39.82^{+0.14}_{-0.22}$	487±192	4.97	None
None(GC)	$20^h34^m52.99^s$	$60°09'14.6''$	0.610±0.073	0.360±0.050	$-12.96^{+0.08}_{-0.09}$	$39.31^{+0.12}_{-0.17}$	152±50	3.21	None
95	$20^h35^m08.95^s$	$60°09'31.6''$	0.687±0.082	0.328±0.046	$-13.03^{+0.06}_{-0.07}$	$39.31^{+0.11}_{-0.15}$	152±44	3.11	None
76	$20^h35^m10.99^s$	$60°08'58.6''$	0.610±0.073	0.360±0.050	$-12.72^{+0.05}_{-0.05}$	$39.55^{+0.10}_{-0.14}$	263±70	3.52	None
69	$20^h35^m11.46^s$	$60°09'12.7''$	0.610±0.073	0.360±0.050	$-12.90^{+0.05}_{-0.06}$	$39.37^{+0.10}_{-0.14}$	170±46	3.14	None
29	$20^h35^m16.80^s$	$60°11'00.4''$	0.446±0.054	0.168±0.024	$-12.71^{+0.05}_{-0.05}$	$39.39^{+0.10}_{-0.14}$	180±49	3.75	None
4	$20^h35^m23.60^s$	$60°09'49.8''$	0.874±0.105	0.111±0.016	$-12.89^{+0.05}_{-0.05}$	$39.65^{+0.10}_{-0.14}$	327±88	3.78	None
3	$20^h35^m25.25^s$	$60°09'58.0''$	0.431±0.052	0.192±0.027	$-12.07^{+0.05}_{-0.05}$	$40.01^{+0.10}_{-0.14}$	761±204	6.63	87, 89, 86

6.4 WR Results

6.4.1 Candidate Wolf-Rayet Stars

Photometric candidates were identified using two methods. The first was by blinking or subtracting the He II and He IIC images to show the excess emissions, as described in Section 1.8.1 of Chapter 1. Overall, 49 candidate regions across both images were identified using this method.

The second selection method used the apparent magnitude excesses of the emission line He II band, compared to continuum He IIC (ΔHe IIC $-$He II). To determine if this excess was large enough to be caused by emission lines, the significance of the excess,σ, was calculated by dividing the candidate ΔHe IIC $-$He II by the ΔHe IIC $-$He II from a series of WC+O star binary models (Equations A.1 to A.5 in Section A.6) from combined WC and O star absolute magnitudes. WC star magnitudes were chosen, because these were the only stars detected during our spectroscopic search (Section 6.4.2), and so the only stars that could be used to choose the most appropriate WR absolute magnitude for the model. Additionally, WN emission lines were not visible in the spectra due to noise and extinction, and may therefore not create a clear He II excess in the photometry.

These models could be used to generate anticipated He II excesses, based on the relative magnitudes of the components. The use of a binary model allows us to replicate the He II line dilution that would be expected for WC stars with a companion or in a cluster, whilst much stronger lines would be anticipated for a single WC star. As it is unlikely that all candidates are single WC stars, using a binary model captures many more potential candidates.

We generated models for a range of WC He II and He IIC absolute magnitudes at 0.5mag intervals between -3.5 and -5 (Chapter 3). Absolute magnitudes in the range -2 to -8 were used for the OB star companion. The total absolute magnitudes of the binary (based on a single WC magnitude and the range of O star magnitudes, to simulate different levels of line dilution) were then converted to apparent magnitudes and ΔHe IIC $-$He II excesses (Appendix A.6). The most appropriate absolute magnitude model for the WC star was found to be -4.5, as all spectroscopically confirmed WC stars fell above the curve for this model (the solid black line in Figure 6.14). Photometric results with He II excesses above the model were then selected as possible candidates. Additional values for LMC binaries were also converted to apparent magnitudes at the distance and extinction of NGC6946 and plotted to check the model validity. The final model (with both the selected and the full range of WC magnitudes, to illustrate uncertainty), manually and

model excess selected WR candidates and all other objects with photometry are shown in Figure 6.15.

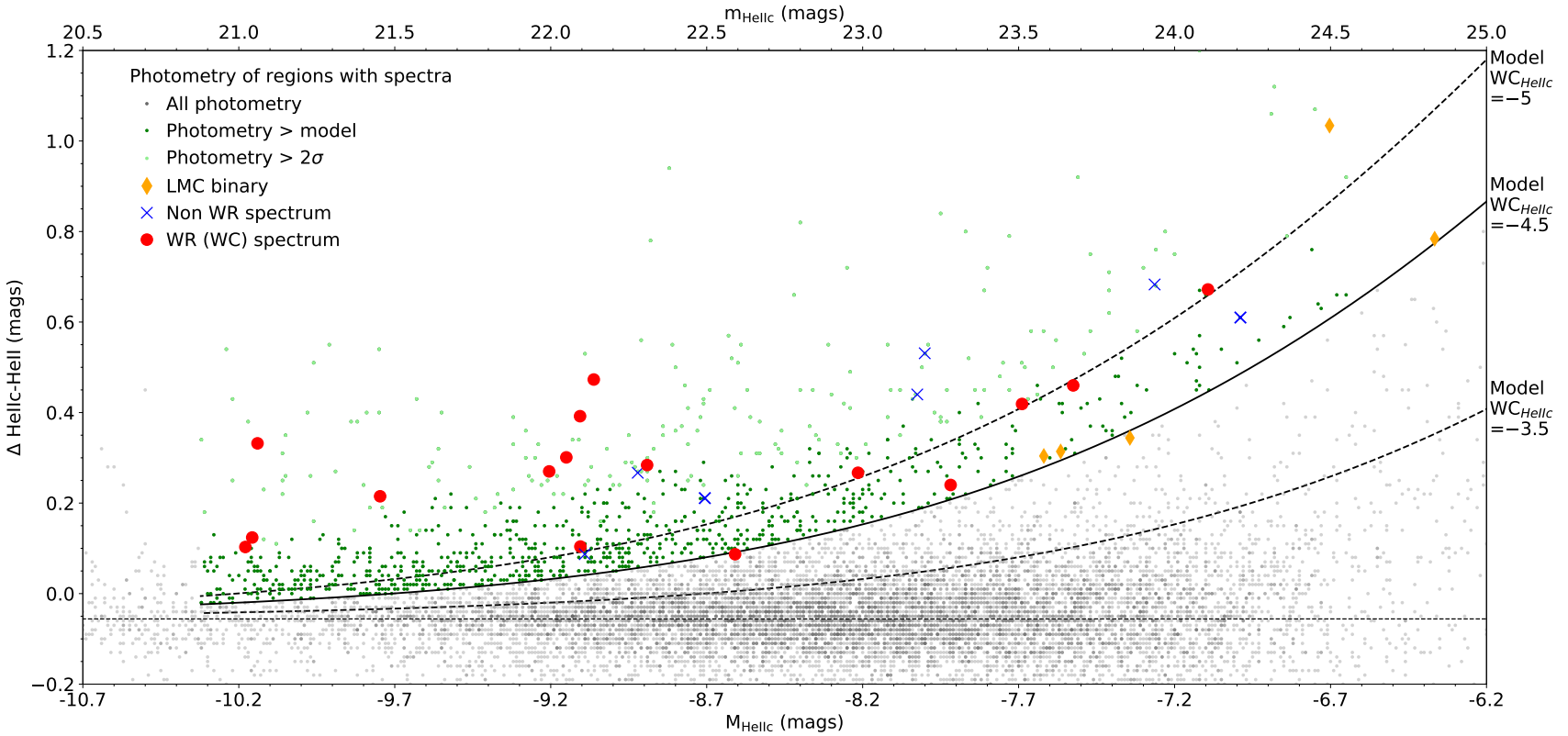

Figure 6.14: Model binary and photometric data for both the east and west images, compared to photometry of regions with associated spectroscopy. The solid black line is the model and the dotted black line is the zero point of the He II -He IIC (−0.056 mags, calculated using the average of all data) used to adjust the model zero point. The dashed lines represent the upper and lower limits of the WC model, based on absolute magnitudes of −3.5 mag and −5 mag. Grey dots are detected photometry from both images (including overlapping regions). Green dots are detected photometry above the model. Orange stars are LMC binaries, plotted to show a comparison to the model. Photometry for spectra with confirmed WC features are labelled as 'WR (WC) Spectrum', whilst 'Non WR spectrum' refers to photometry for spectra without WR features. We selected the model WC magnitude based on the minimum He II excess of spectroscopically confirmed WC regions. He IIC absolute magnitudes were calculated assuming a distance modulus of 28.92 (6.1 Mpc) and extinction in the He IIC band was calculated using A_{HeIIC}=3.7E(B−V) from Cardelli et al. (1989), using the average E(B−V)=0.61 for the whole galaxy.

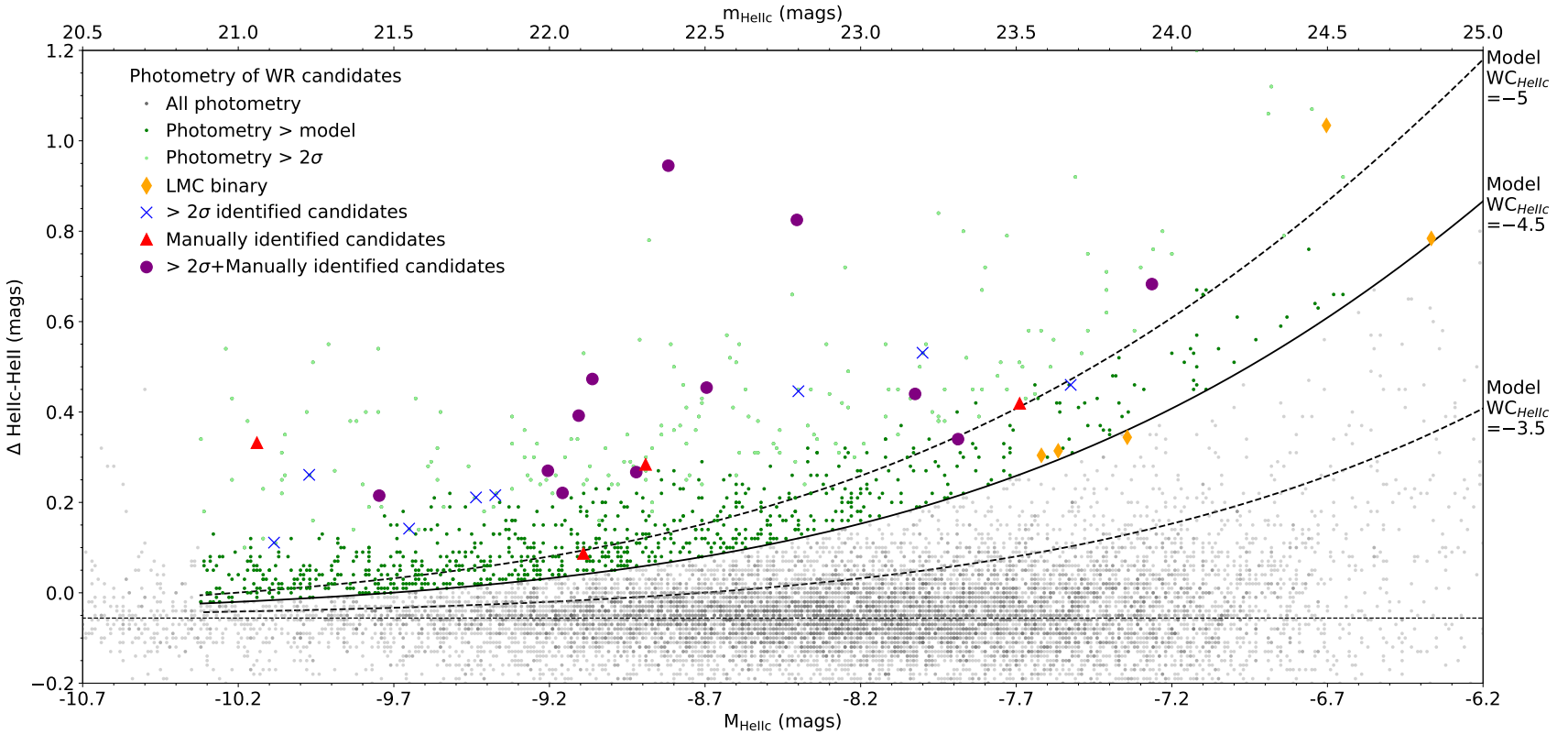

Figure 6.15: Model binary and photometric data for both the east and west images, compared to photometry of WR candidates obtained using various selection methods. The solid black line is the model and the dotted black line is the zero point of the He II -He IIC (−0.056 mags, calculated using the average of all data) used to adjust the model zero point. The dashed lines represent the upper and lower limits of the WC model, based on absolute magnitudes of −3.5 mag and −5 mag. Grey dots are detected photometry from both images (including overlapping regions). Green dots are detected photometry above the model. Orange stars are LMC binaries, plotted to show a comparison to the model. $>2\sigma$ refers to candidates detected with the photometric excess method, whilst Manually identified candidates indicates they were detected via image blink and subtraction. Some candidates were detected with both methods. He IIC absolute magnitudes were calculated assuming a distance modulus of 28.92 (6.1 Mpc) and extinction in the He IIC band was calculated using A_{HeIIC}=3.7E(B−V) from Cardelli et al. (1989), using the average E(B−V)=0.61 for the whole galaxy.

Objects which were at least 2σ detections above the model and flagged as excesses in subtracted and blinked images, were accepted as candidates. Results with measurements in one band but not the other (for example, in He II but not He IIC) were not plotted. This included 8 out of the 22 spectroscopically confirmed candidates and 41 of the 50 candidates selected solely on the basis of excesses in the subtracted image (including all 29 candidates selected from manual excesses only). All photometric candidates have absolute magnitudes greater than the $-3/-4$ mag expected for single WC stars (Chapter 3), which suggests they are in clusters or WC+O star binaries. The full candidate list is provided in Table A.8.

As shown in Figure 6.1, the east and west images overlap. We can compare the photometry in this overlapping region to determine its statistical uncertainty. Figure 6.16 shows the differences between the emission line and continuum photometry (ΔHe IIC $-$He II) for 796 objects in both the east and west images. The median difference between west ΔHe IIC $-$He II and east ΔHe IIC $-$He II is 0.01mag, comparable to the mean, which is 0.014 mag. Most values therefore cluster around zero and the majority of east and west image photometry is consistent. The mean and median are comparable to the uncertainties from DAOPHOT (Figure 6.6), which are on the scale of $\sim$0.05 mag.

The standard deviation of the east and west image differences is much larger, however, at 0.24 mag. The outliers mainly comprise the lines of points stretching in the horizontal and vertical directions. These have marginal excess detections in one image region (either east or west), but strong ($\sim$0.5mag) excesses in the other image. This inconsistency may be caused by a difference in the PSF subtraction within a crowded region (such as where the PSF subtraction in one east or west image filter differs compared to the same filter in the other image) or by image alignment imperfections for a small number of points. In particular, this overlapping region includes much of the galactic centre region, which was very bright and crowded with objects, making it highly susceptible to both of these issues.

We additionally show both candidate and confirmed WR star regions in Figure 6.16. If there was a He II filter excess compared to the He IIC common to the east and west images, the stars would appear in the top right hand quadrant. Figure 6.16 shows this is true for one confirmed WC spectral region (object 43 in Table A.8) and one photometric candidate (object 55). The differences of ΔHe IIC $-$He II between the east and west images are 0.31mag for candidate 55, and 0.23mag for candidate 43. The uncertainty for ΔHe IIC $-$He II in each image is $\sim$0.1. For the candidate 43, this might be enough to explain the discrepancy between the east and west results. However, for object 55,

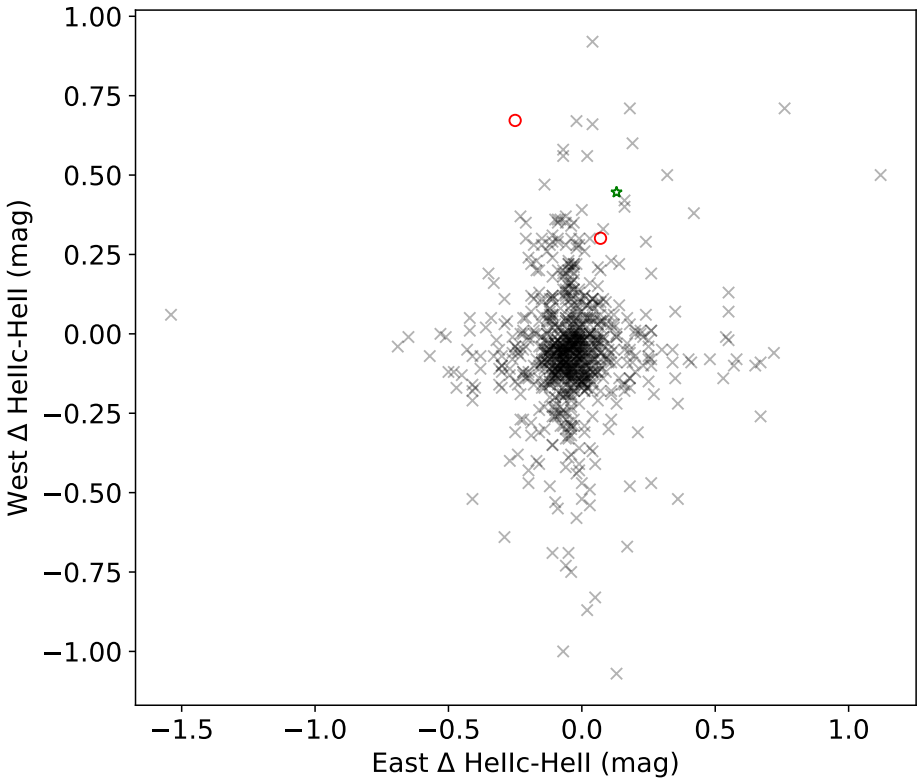

Figure 6.16: A plot showing the differences between the emission line and continuum photometry (ΔHe II$_{\rm C}$ $-$He II) for objects in both the east and west images. The mean and median ΔHe II$_{\rm C}$ $-$He II difference between the east and west images is approximately zero. Three WR stars with photometry in both images and filter bands are shown. Green stars are photometric detections only, red circles are confirmed WC stars and blue triangles are candidate regions with spectra but no confirmed WC stars.

there is still an unaccounted difference of ∼0.1. This shows that some of our candidates may still have statistical uncertainties that are larger than zero.

However, the remaining confirmed WC star (object 53) is an outlier, as it is located in the upper left corner. This indicates there's a clear excess in the west image, but suggests that the continuum is stronger in the east image. Analysis of net (He II −He IIC) images confirms the excess in the west image, but shows no corresponding excess in the east image. The east and west He IIC images were taken on different nights (Table 6.1) and therefore under different conditions (airmasses), which could have masked the excess.

The points from the overlapping region are shown in Figures 6.14 and 6.15 twice.

Figure 6.17 shows the locations of confirmed and candidate WR regions, across the He II , He IIC and net images, whilst Figure 6.18 compares the same data to a net Hα image.

6.4.2 Confirmed Wolf-Rayet Stars

Spectra containing WR emission features were reduced as outlined in Section 6.2.2, with the additional step of dereddening the spectra in DIPSO. To calculate E(B−V) for WR stars without associated nebular emission, we use the difference in He IIC and HαC magnitudes from photometry, and adopted theoretical intrinsic WR colours (He IIC −HαC)$_0$ from Tehrani et al. (2017).

$$\mathrm{E(B-V)}=0.79[(\mathrm{He\ II C}\ \text{-H}\alpha\mathrm{C}\ )\text{-}(\mathrm{He\ II C}\ \text{-H}\alpha\mathrm{C}\ )_0] \tag{6.6}$$

We used the intrinsic colour for a WR+OB binary, (He IIC −HαC)$_0$=−0.21, as the WR stars were most likely to be in binaries or clusters. Nebular reddenings from Section 6.3.3 were also checked using Equation 6.6. Only 13 WR star spectra displayed Hα and Hβ emission lines and of those, only 8 contained photometric detections above the limiting magnitude in both He IIC and HαC filters. Unfortunately, there is a large discrepancy between E(B−V) from Equation 6.6, and E(B−V)=0.7c(Hβ) from nebular emissions. This discrepancy is likely to be because the spectral regions extracted are larger than the FWHM in the photometric psf regions, and so will contain contamination from other stellar populations. This will alter the intrinsic colour, compared to the photometry.

Unfortunately, this inconsistency between the nebular derived reddening and intrinsic WR reddening, made it difficult to apply a correction to the WR stars not showing

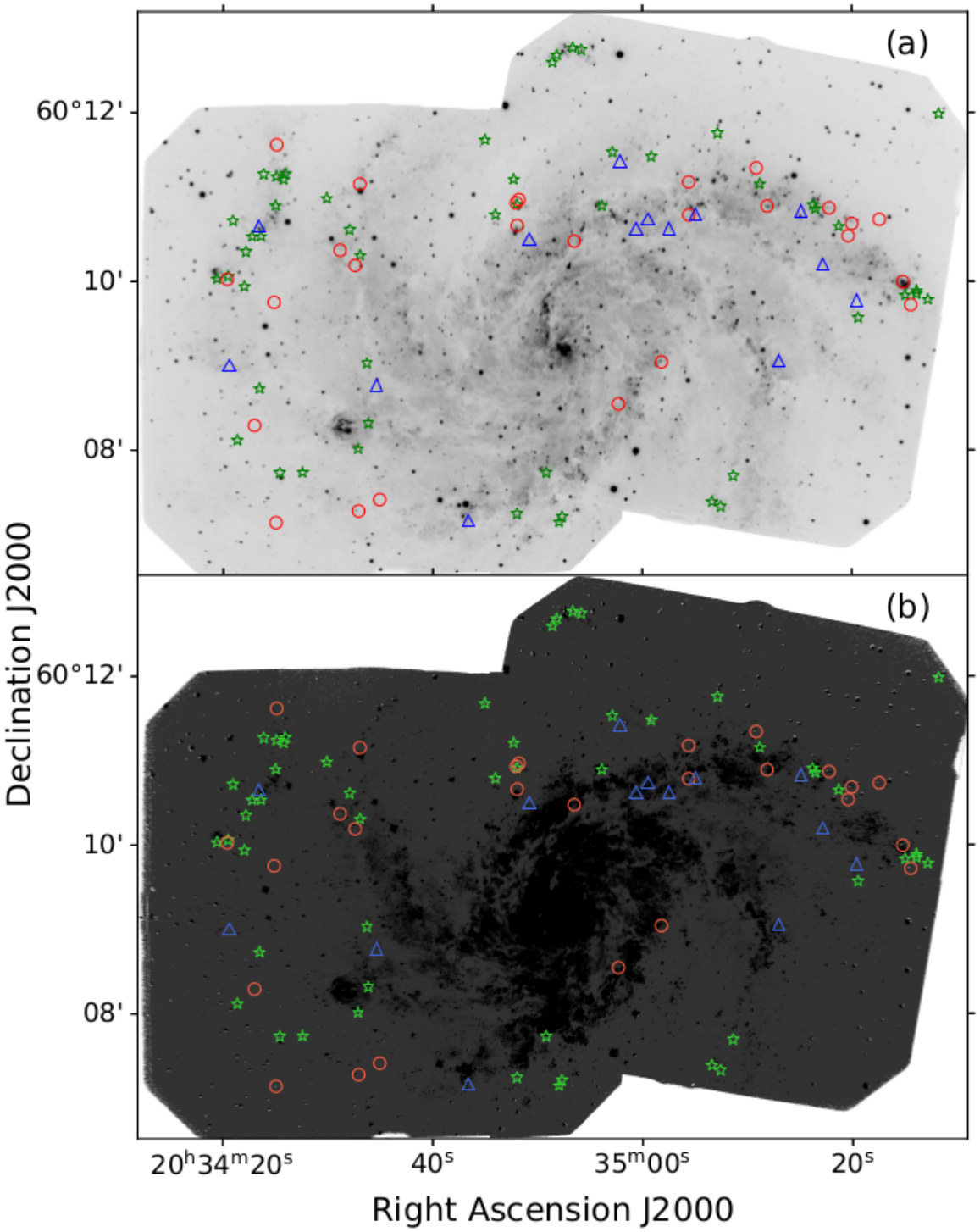

Figure 6.17: Figures showing (a) He II images, (b) He II net image, with confirmed and candidate WR regions. Green stars are photometric detections only, red circles are confirmed WC stars and blue triangles are candidate regions with spectra but no confirmed WC stars. In (b), regions of excess He II emissions show as bright spots.

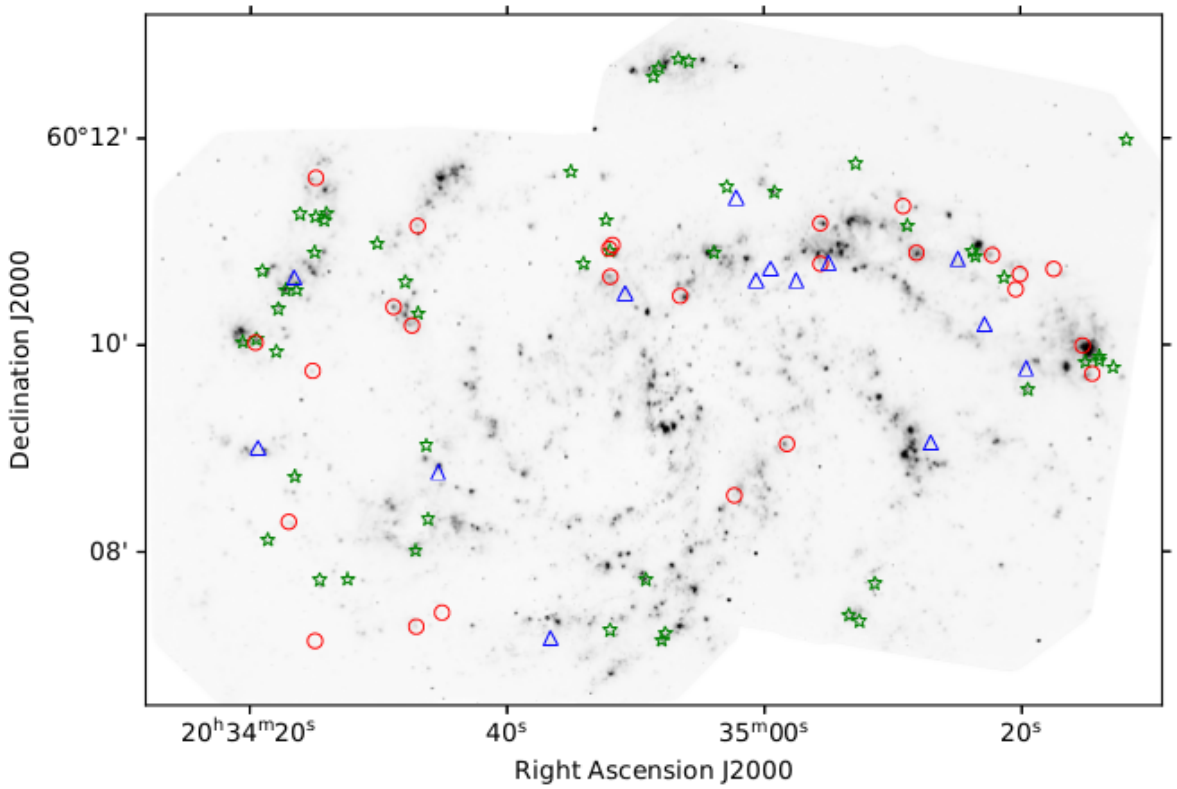

Figure 6.18: Merged Hα net image, with confirmed and candidate WR regions. Green stars are photometric detections only, red circles are confirmed WC stars and blue triangles are candidate regions with spectra but no confirmed WC stars.

nebular emission. Where results from both methods were used, the results were averaged and where no nebular emission was present, E(B−V) values from Equation 6.6 were used alone. If neither value was available, then the E(B−V) that best dereddened the continuum to match other spectra in the mask was used. No reddening correction was therefore applied to some results. The E(B−V) used for each region is shown in Table 6.5.

We can compare our reddening results to those obtained for the same H II regions from Kessler et al. (2020), who use Hα and Paβ photometry to estimate $A_{H\alpha}$. Figure 6.19 shows that, compared to Kessler et al. (2020), our E(B−V) values are somewhat overestimated. In six cases, a pair of H II regions from our work was matched to the same H II region in Kessler et al. (2020). All but two of these results had similar E(B−V values (<0.1 difference) between the two H II reddenings from our data, suggesting that perhaps a region identified as a single object in Kessler et al. (2020), consisted of multiple sources in our work.

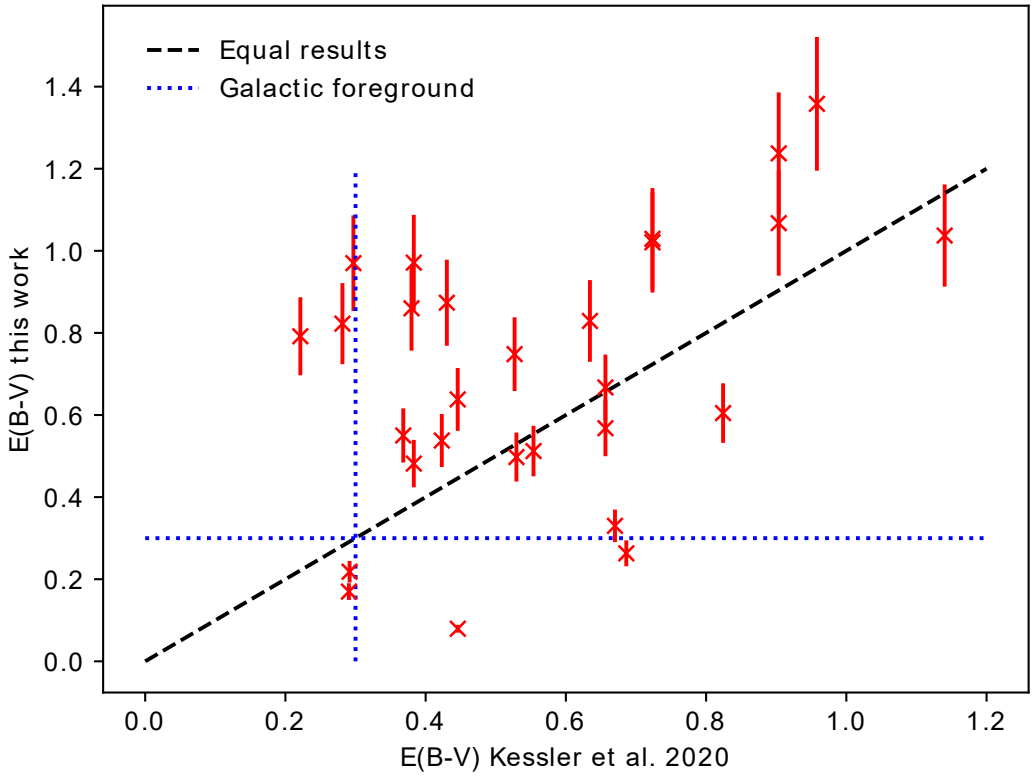

Figure 6.19: Graph comparing reddening obtained for H II regions from Kessler et al. (2020), compared with our values for the same regions from Table 6.5. We match coordinates from Kessler et al. (2020) that are within 1 arcsec of our coordinates, corresponding to $\leq$30 kpc at the 6.1 Mpc distance of NGC6946. Given that most of the H II regions identified likely surround clusters rather than individual stars (and are therefore probably larger than $\sim$30 pc), it's unlikely that the 1 arcsec limit has mismatched unrelated regions. Additionally, decreasing the size of the matching region resulted in very few match regions being identified.

A group of results with E(B$-$V)$>$0.7 in this work, have much lower reddening ($<$0.5) in Kessler et al. (2020). These H II regions seem generally to be located in the far west or north of the galaxy, where inspection of Kessler et al. (2020), suggests that some of the H II regions were not fully within the frames of their images. This would have led to a much lower measured Hα flux than our work. Additionally, several of the Kessler et al. (2020) results and our results have reddenings below the Galactic foreground, which suggests that the results are simply erroneous (in our instance, this may be due to the noisy spectra used to calculate the reddening). Some overestimation, particularly where it seems to increase linearly beyond E(B$-$V)$\sim$0.4, could also be due to our choice of

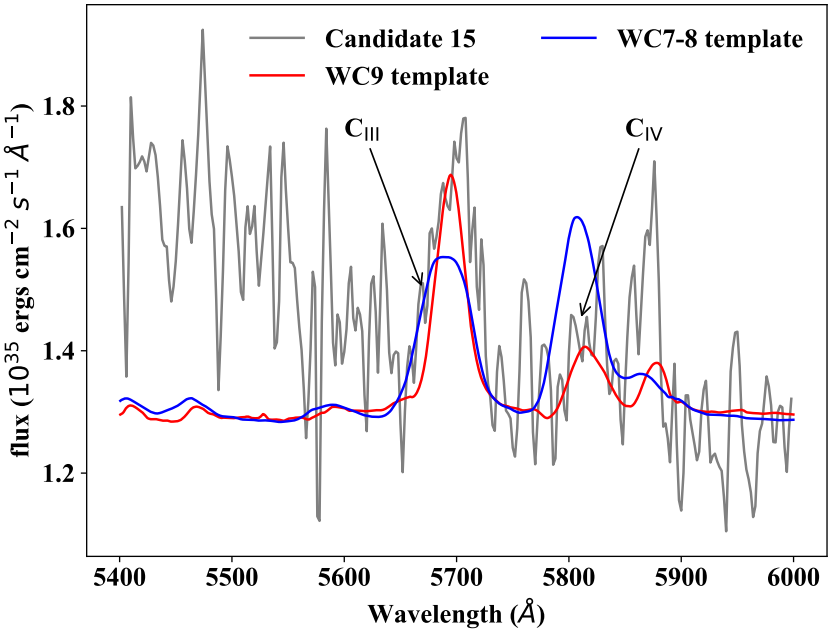

Figure 6.20: The red bump region of Candidate 15, with WC9 and WC7−8 templates (with the continuum adjusted to match the candidate 15 continuum at the wavelengths of the emission lines). The strong C III 5696Å and weak C IV 5808Å is best fit by the WC9 template.

reddening law (used to convert $A_{H\alpha}$ to A_V and then to E(B−V)).

WN stars were then identified by emission in He II 4686Å. WC stars were found from C III 5696Å, the C III 4650Åand He II 4686Åblend and C IV 5800Åemission. A total of 24 regions of 4650+4686Å blend, 5696Å and/or 5800Å emission were identified. Due to the low signal to noise ratio throughout the spectra (particularly towards blue wavelengths) and low fluxes, all identified WR stars were WC stars. This is because they possess an equivalent width 3−4 times as strong as WN stars (Massey & Johnson, 1998), making them easier to observe above a noisy continuum (see Figure 1.3 in Chapter 1).

The 12+log(O/H)=8.76±0.2 metallicity for the central region, is similar to the Galaxy, which means Milky Way WR templates could be applied to these unresolved regions to determine the approximate number of WR stars within them (to within a factor of 2). Figure 6.20 compares two possible WC subtype fits to candidate 15, which was assigned the subtype WC9 based on its strong C III 5696Å line.

These templates are based on the results from Chapter 5 and revealed a total WR population of 61, of which 42 were early type WC. Figure 6.21 shows a comparison between one of these early types and a mid type. Candidate 25 shows significant noise

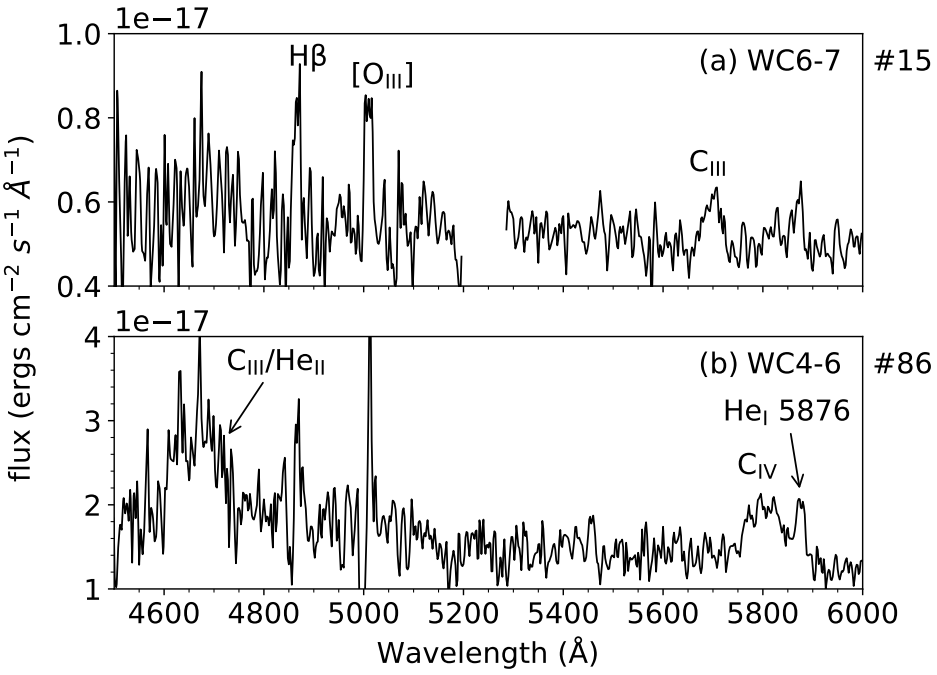

Figure 6.21: (a) Candidate 15 was classified as WC9 on the basis of a strong C III 5696Å line (also with nebular [O III 5007] and Hβ lines). (b) Candidate 86 was classified as WC4−6 on the basis of the C III 4650Å / He II 4686Å blend and C IV 5808Å line (with nebular He I 5876Å).

in its spectrum, meaning it could not definitively be classified as a WR star. It was retained as a candidate as future, less noisy spectra may be able to confirm its status.

All regions with photometry have absolute magnitude ranges comparable to clusters or binaries, as opposed to individual WC stars. Distances from the galactic centre were found using deprojection, assuming a distance of 6.1Mpc and an inclination of 30°. Due to the small number of results, there is no relation between subtype and proximity to the galactic centre. One third of the confirmed WR spectra also showed Hα emission lines, indicating they are in a H II region.

Table 6.5 shows the Hα information on the confirmed WC regions. Only a small number of WR locations were found near Hodge H II regions. This is potentially because the light from the surrounding H II regions diluted the WR emission lines so they were not detected.

We can compare the results obtained with the templates, to those from the Galactic emission line luminosities of Chapter 5. The blue bump was the flux from the C III 4650Å and He II 4686Å lines, whilst the C III5696Å and C IV 5808Å fluxes were combined for the red bump. Table 6.6 shows that in most instances, the uncertainties of the templates

Table 6.5: Key information on confirmed WR regions, including the presence of Hα within the source spectrum and reddening.

Catalogue no.	Hα emission line (indicating H II region)	E(B−V)
2	yes	0.666
10		0.350
15	yes	0.676
18		0.782
19		0.545
26	yes	0.910
30		0.373
41	yes	0.000
43	yes	0.263
45		0.200
53		0.917
57	yes	0.840
62		0.348
64	yes	0.550
65		0.512
71		0.500
73		1.027
79	yes	0.529
81		0.500
82		0.600
85		0.000
86		0.430
88		0.520

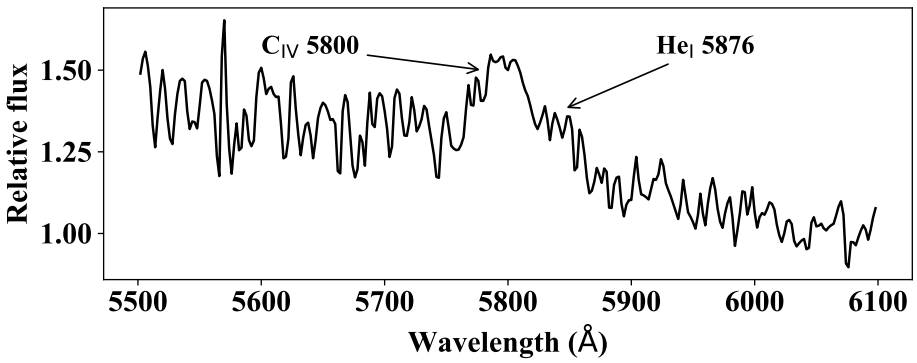

Figure 6.22: The C IV 5800Å line of candidate 73, together with the possible He I 5876Å excess.

and the calibrations mean that there is consistency between the results obtained from each method.

The exceptions to this are sources 86 and 73, which both have much larger WC numbers derived from emission line luminosities. The former is located on the edge of giant H II region HK-3 and both have He IIC apparent magnitudes of ∼21. This corresponds to an absolute magnitude of $M_{HeIIC} \sim -10$ (Figures 6.15 and 6.14), which implies they are both clusters. Additionally, the red bump source from candidate 73 has a broad line excess around 5850Å , which could be from He I 5876Å (Figure 6.22). This excess (unlike the main C IV 5808Å line) is not well fit by the template and suggests that the red bump content is perhaps a mixture of early, mid and late WC subtypes, possibly with some WN. This could have lead to an overestimate in the number of early type WC obtained from the emission line luminosities.

Though Table 6.6 lists the WR numbers derived from both the luminosity calibrations and the template fits, we favour the results from the templates and refer to them in Section 6.5. This is because the template fits can better account for the emission line profiles and the substantial noise in the spectra.

Table 6.6: Emission line fluxes from table 6.5 converted to red and blue bump luminosities and then numbers of WR stars, using the emission line luminosities from Chapter 5.

Cat no.	AV	F(B) (10^{-17}ergs /s/cm^2)	I(B) (10^{-17}ergs /s/cm^2)	L(B) (10^{35} ergs s^{-1})	F(R) (10^{-17}ergs /s/cm^2)	I(R) (10^{-17}ergs /s/cm^2)	L(R) (10^{35} ergs s^{-1})	Template fit	Calibration blue	Calibration red	Subtype
2	2.06±0.25	9.320±1.000	$97.46^{+74.76}_{-48.44}$	$43.51^{+33.65}_{-22.04}$	5.760±1.414	$60.23^{+46.21}_{-29.94}$	$26.89^{+20.80}_{-13.62}$	4±3	2^{+3}_{-2}	2^{+3}_{-2}	WC7-8
10	1.08±0.13				7.530±1.414	$25.85^{+14.12}_{-10.99}$	$11.54^{+6.40}_{-5.04}$	1±1		1^{+1}_{-1}	WC7-8
15	2.10±0.25				4.580±1.414	$49.61^{+38.43}_{-24.76}$	$22.15^{+17.30}_{-11.27}$	1±1		2^{+2}_{-2}	WC9
18	2.42±0.29				3.640±1.414	$57.29^{+49.04}_{-29.85}$	$25.58^{+22.04}_{-13.56}$	1±1		3^{+3}_{-2}	WC4-6
19	1.69±0.20	16.060±1.000	$109.64^{+74.44}_{-51.59}$	$48.95^{+33.58}_{-23.53}$	7.980±1.414	$54.48^{+36.99}_{-25.64}$	$24.32^{+16.69}_{-11.69}$	1±1	3^{+3}_{-2}	2^{+3}_{-2}	WC4-6
26	2.82±0.34	32.700±1.000	$808.05^{+775.11}_{-441.44}$	$360.77^{+347.87}_{-200.26}$	21.250±1.414	$525.11^{+503.70}_{-286.87}$	$234.44^{+226.06}_{-130.14}$	7±4	19^{+21}_{-15}	23^{+26}_{-18}	WC4-6
30	1.16±0.14	6.310±1.000	$23.49^{+13.18}_{-10.12}$	$10.49^{+5.98}_{-4.63}$				1±1	0^{+1}_{0}		WC7-8
41	0.00±0.00	22.850±1.000	$22.85^{+7.62}_{-7.62}$	$10.20^{+3.55}_{-3.55}$	15.510±1.414	$15.51^{+3.72}_{-3.72}$	$6.92^{+1.73}_{-1.73}$	1±1	0^{+1}_{0}	0^{+1}_{-0}	WC7-8
43	0.82±0.10	10.480±1.000	$26.48^{+12.98}_{-10.69}$	$11.82^{+5.91}_{-4.91}$	9.950±1.414	$25.14^{+9.55}_{-7.86}$	$11.22^{+4.35}_{-3.61}$	1±1	1^{+1}_{-1}	1^{+1}_{-1}	WC9
45	0.62±0.07				11.200±1.414	$22.66^{+10.22}_{-8.78}$	$10.12^{+4.67}_{-4.04}$	1±1		1^{+1}_{-1}	WC9
53	2.84±0.34				14.470±1.414	$366.50^{+250.22}_{-141.99}$	$163.63^{+112.29}_{-64.41}$	11±6		11^{+12}_{-10}	WC7-8
57	2.60±0.31				11.560±1.414	$223.20^{+201.35}_{-118.90}$	$99.65^{+90.43}_{-53.98}$	2±1		10^{+11}_{-8}	WC4-6
62	1.08±0.13				23.570±1.414	$80.36^{+43.77}_{-34.12}$	$35.88^{+19.86}_{-15.64}$	1±1		3^{+3}_{-3}	WC9
64	1.71±0.20	25.590±1.000	$177.80^{+121.35}_{-83.87}$	$79.38^{+54.74}_{-38.25}$	11.300±1.414	$78.51^{+53.59}_{-37.03}$	$35.05^{+24.17}_{-16.89}$	1±1	4^{+4}_{-3}	3^{+3}_{-3}	WC4-6
65	1.59±0.19	13.900±1.000	$84.47^{+55.39}_{-39.12}$	$37.71^{+25.01}_{-17.86}$	2.980±1.414	$18.11^{+11.87}_{-8.39}$	$8.09^{+5.36}_{-3.83}$	1±1	2^{+2}_{-2}	1^{+1}_{-1}	WC7-8
71	1.55±0.19	38.170±1.000	$222.36^{+143.93}_{-102.37}$	$99.27^{+65.00}_{-46.74}$	38.120±1.414	$222.06^{+143.75}_{-102.24}$	$99.14^{+64.91}_{-46.68}$	2±1	5^{+5}_{-4}	10^{+9}_{-7}	WC4-6
73	3.18±0.38				29.280±1.414	$1092.82^{+1156.88}_{-620.95}$	$487.90^{+518.73}_{-281.36}$	7±4		48^{+57}_{-38}	WC4-6
79	1.64±0.20	35.440±1.000	$228.67^{+152.67}_{-106.78}$	$102.09^{+68.90}_{-48.72}$	20.180±1.414	$130.21^{+86.93}_{-60.80}$	$58.13^{+39.23}_{-27.74}$	2±1	5^{+5}_{-4}	6^{+5}_{-5}	WC4-6
81	1.55±0.19				15.120±1.414	$88.08^{+57.02}_{-40.55}$	$39.32^{+25.75}_{-18.51}$	1±1		4^{+4}_{-3}	WC4-6
82	1.86±0.22				12.200±1.414	$101.10^{+72.64}_{-48.81}$	$45.14^{+32.73}_{-22.24}$	2±1		4^{+4}_{-4}	WC4-6
85	0.00±0.00				8.980±1.414	$8.98^{+2.99}_{-2.99}$	$4.01^{+1.39}_{-1.39}$	2±1		0^{+1}_{-0}	WC4-6
86	1.33±0.16	128.990±1.000	$587.13^{+351.85}_{-260.80}$	$262.13^{+159.19}_{-119.26}$	54.130±1.414	$246.39^{+147.65}_{-109.44}$	$110.00^{+66.80}_{-50.05}$	3±2	14^{+11}_{-10}	11^{+9}_{-8}	WC4-6
88	1.61±0.19	63.160±1.000	$394.80^{+261.09}_{-183.56}$	$176.27^{+117.85}_{-83.77}$	26.030±1.414	$162.71^{+107.60}_{-75.65}$	$72.64^{+48.57}_{-34.52}$	2±1	9^{+8}_{-7}	7^{+7}_{-6}	WC4-6

6.5 Conclusions and summary

We have surveyed the WR population of NGC 6946 to search for type Ibc supernova or direct collapse black hole progenitors and to investigate the WR population in a different environment (potentially with a different metallicity) to the Milky Way.

We have identified 92 candidates from narrow band He II and He IIC images, using either manual detection (blinking or image subtraction) or a cutoff with 2σ excess of He II − He IIC above a WR+O star binary model, to search for excess He II emission over the continnum. An obstacle to identifying these photometric candidates is the completeness limit of the survey, which is 23 mag across both east and west regions. A comparison with results in Figure 6.15 shows that it's therefore likely that a significant proportion of photometric candidates in regions with absolute magnitudes > -8.2 have not been detected. The absolute magnitudes of individual WR stars are also far fainter than the completeness limit, apart from the brightest WN stars with absolute magnitudes around -6 to -7 mag and large He II excesses.

We also determine the extinction of the galaxy using the ratios of nebular Hα to Hβ, to find the c(Hβ) coefficient. With this we can calculate the average E(B−V), 0.61±0.03, which corresponds to V band extinction 1.88±0.09. Approximately half the extinction is due to foreground reddening within the Milky Way.

The significant distance of the galaxy (6.1 Mpc) also resulted in a large distance modulus (28.92). This significant distance modulus combined with the high extinction, are equivalent to observing an unreddened galaxy at 13.8 Mpc. For a typical WR star with absolute magnitude ~ -4.5, (see Chapter 3) the V band apparent magnitude of an individual WR star is 26.30. Given our completeness limit was 22.7 in the He II and He IIC bands, WR stars were only likely detected as part of clusters, where their emission lines were diluted by the surrounding stellar content. Detecting WR stars was therefore challenging; particularly for WN stars, which have weaker emission lines than WC subtypes.

The high extinction and low sensitivity of the GMOS instrument to the blue part of the spectrum, therefore meant that only WC stars were identified from spectroscopy. Additionally, a visual inspection of H II regions (Figure 6.18) shows that only 3 confirmed WC star populations and 4 photometric candidate regions were identified inside luminous H II regions. A further 5 WC populations and 6 photometric candidate regions were discovered on the edges of major H II regions and 8 WC populations and 21 photometric candidates were found near small H II regions. These results suggest that a further difficulty with WR identification was contamination from cluster continuua,

which diluted WR emission line strengths.

Using the empirical strong line relations from Pettini & Pagel (2004), NGC6946 has a central metallicity comparable to the Galaxy, 12+log(O/H)=8.76±0.2, with very little gradient. We therefore used Galactic templates to identify WR stars in the unresolved regions. We also apply our Galactic red and blue bump emission line calibrations, finding consistency between the results from this method and the templates. However, problems for spectroscopically confirmed WR included finding accurate E(B−V) values in the absence of nebular emissions and large uncertainties of the templates used to fit populations.

We can compare our results to a previous investigation using integral field spectroscopy (IFS) from (García-Benito et al., 2010), which focussed on the ∼2kpc around giant H II region HK-3 and associated smaller H II regions. HK-3 was determined to have a WR population of 125±10 and HK-4 a population of 22±3. Comparatively, in this work, only the edge of HK-3 is detected in spectroscopy and corresponds to candidate no. 86 in Table A.8, Table 6.5 and Table 6.6, with 3±2 early type WC according to the template, but ∼11-14 WC stars according to the emission line calibration. There are no WR detections in HK-4. By contrast, the much fainter H II region around candidate 88 shows 5±2 WR stars in García-Benito et al. (2010) and 2±1 early type WC in the template, with an emission line calibration of ∼7-9 WC.

No candidates or confirmed WR stars were detected towards the centre of the galaxy. As the reddening does not show a gradient that implies a higher extinction towards the galactic centre, it is possible that the nuclear starburst (Kennicutt et al., 2008) and surrounding H II regions, have diluted WR emission lines. Regions around the core could also simply contain older stellar populations, which no longer contain WR stars.

These limitations mean that the survey is highly incomplete and we cannot calculate a reliable WC/WN or WR/O star ratio to compare with other galaxies. Given the SFRs of NGC6946 (2.39 $M_{\odot}yr^{-1}$) and the Milky Way (∼ 2 $M_{\odot}yr^{-1}$ Chomiuk & Povich 2011) remain similar, as does the metallicity; the estimated total number of WR stars in NGC6946 is ∼1400±200. Therefore only $4.5^{+4.5}_{-2.5}$% (from templates) or 4% to at most 12% (from emission line luminosities, using the maximum and minimum possible WR stars from either red or blue bumps), of the total WR population has been spectroscopically confirmed.

Due to the incompleteness of the survey, we find far fewer WR stars in NGC6946 than other extragalactic surveys. Additionally, we see a significant over-abundance of early type WC; 42 stars from the template fits, compared to 15 mid and 4 late type stars. By

contrast, in the high metallicity M83 (log[O/H]+ 12 = 9.0−9.2), Hadfield et al. (2005) find 6 times as many WC8−9 as WC4−7 within the disk population. In the Milky Way, we also find WC9 stars are much more common, comprising over 1/3 of all WC stars (101 WC9 stars, out of the ∼280 WC stars in the Galaxy). The similar metallicity and star formation rate suggests that there should be a similar population of late type WC stars in NGC6946, but these have not been detected. The WC9 stars could be obscured by dust, particularly if they are in a dust producing binary. This, combined with the high Galactic foreground extinction and internal extinction within NGC6946, may have reduced the WC9 magnitudes beyond our completeness limit. Alternatively, within the Milky-Way, WC9 are found mainly towards the Galactic centre. As stated above, within NGC6946, we do not detect any candidates within the galactic centre region. Most late type WC may therefore have their emission lines diluted, such that the He II excess above the continuum was not detectable.

Owing to its similar metallicity and star formation rate, NGC6946 would make an interesting comparison WR environment to the Milky-Way. We have included it in Table 6.7 from Chapter 1. Like M101 which is at a similar distance, NGC6946 is highly incomplete. Future, more complete surveys, may enable a more robust population comparison with less distant galaxies like M33.

Table 6.7: Table from section 1, showing measured and estimated total WR populations for different surveyed galaxies, also including NGC6946. (1) Rosslowe & Crowther (2015a), (2) Rosslowe & Crowther (2015b), (3) Chomiuk & Povich (2011), (4) Neugent et al. (2012) and references therein, (5) Shara et al. (2016), (6) Hα luminosity from Kennicutt et al. (2008), converted to SFR using Kennicutt (1998b), (7) (Neugent & Massey, 2011) and references therein, (8) Crowther et al. (2007) and references therein, (9) Bibby & Crowther (2010) and references therein, (10) Hadfield & Crowther (2007) and references therein, (11) Hadfield et al. (2005) and references therein, (12) Pledger et al. (2018) and references therein, (13) (Kennicutt et al., 1995), (14) Neugent et al. (2018) and references therein, (no ref. for dist or metallicity) (15) Neugent & Massey (2019) and references therein, (16) Monreal-Ibero et al. (2017) and references therein, (17) Tehrani et al. (2017), (18) Hadfield & Crowther (2006) and references therein, (19) Bibby & Crowther (2012) and references therein. Note: IC4662 was not included in the table, due to the uncertain number of WR stars it hosts and their subtypes.

Galaxy	Confirmed WN, WN/WC and Of/WN	Confirmed WC and WO	Current total	Estimated total	Metallicity (log[O/H]+ 12)	SFR ($M_\odot yr^{-1}$)	Distance (Mpc)	Reference
—Spiral—								
Milky Way	385	281	665	1200±200	8.85−8.55	≈2	...	1, 2, 3
M31	93	62	155	160-170	≈8.9	0.21	0.76	4, 5, 6
M33	153	53	206	214	8.72−8.29	0.26	0.84	6, 7
NGC300	16	15	31	40	8.6	0.06	1.88	8
NGC7793	27	25	52	105	8.6−8.2	$0.45^{+0.11}_{-0.13}$	3.1	9
NGC1313	51	32	83	115	8.23±0.06	0.6	4.1	10
M83	471±130	564±170	1035±300	3000	9.0−9.2	1.41	4.5±0.3	6, 11
NGC6946	0	61	61	∼1400±200	8.76±0.2	$2.39^{+1.14}_{-1.14}$	6.1	
M101	4	11	15	3000	8.23±0.06	1.7−3.3	6.4	12
–Dwarf/Irregular–								
LMC	127	27	154	...	8.37	0.22	0.05	13, 14
SMC	11	1	12	...	8.13	0.04	0.05	13, 15
NGC 625	23	5	28	...	8.14±0.02	≈2	3.9±0.2	16
IC10	15	14	29	...	8.40±0.04	0.045±0.023	0.74±0.02	17
NGC3125	200	40	240	...	≈8.4	0.37	11.5	6, 18
NGC5068	18	24	42	170	8.74−8.23	$0.63^{+0.11}_{-0.13}$	5.45	19

Chapter 7

Conclusions and Future work

This thesis has contributed to answering the questions (as outlined in Chapter 1) of WR star origins and their properties. Here, we present an overview of the methods and results from Chapters 2−6 and discuss possible considerations for future work.

7.1 Distances and Absolute magnitudes of Galactic WR stars

Determining WR star luminosities, and other key parameters, requires knowledge of their distances. Past distance estimates to Milky Way WR stars relied on absolute magnitude calibrations, derived from the small number of WR stars which were thought to be members of clusters or associations. The calibrations therefore produced large uncertainties on the resulting distances, which could be similarly reduced if parallaxes became available. Fortunately, the second data release from the *Gaia* mission (DR2) provides parallaxes and proper motions for over a billion stars in the Galaxy, enabling us to calculate distances to a much larger number of WR stars.

We used an automated script to search a 1 arcsecond region around stars from the Galactic Wolf-Rayet catalogue (version 1.23, July 2019), for sources in the *Gaia* catalogue. The search identified 415 WR stars with *Gaia* data, the majority (383) of which had parallax information. We checked that these coordinates corresponded to isolated WR stars, using images from VPHAS+ DR3 (Drew et al., 2014), IPHAS DR2 (Barentsen et al. 2014, Drew et al. 2005) and 2MASS (Skrutskie et al., 2006).

We then used a Bayesian method to estimate the distances from the parallaxes, to properly account for the non symmetric nature of the distance uncertainties. A combined H II region distribution and dust model was used for the prior, as H II regions

traced probable locations of massive stars and the dust model reproduced what could be detected by *Gaia*. We were able to calculate distances to 383 WR stars. Comparison with Bailer-Jones et al. (2018) shows good agreement between the two data sets up to ∼2 kpc, but increasingly deviates thereafter due to the difference in priors. Further comparison with Rosslowe & Crowther (2015a) shows that again, agreement is good up to ∼2 kpc, but that beyond this distance, there is significant disagreement with many previous results.

We then used existing photometry to calculate the extinctions of these stars. Combined with the new distances, we were then able to determine absolute magnitudes for large numbers of WR stars in both the narrowband optical v^{WR} and the IR K_s bands. A Monte Carlo method produced the full distributions of each absolute magnitude; to properly capture non symmetric uncertainties. We find that 187 stars have reliable distances and extinctions and therefore absolute magnitudes. We then average the absolute magnitudes to produce new calibrations for WR subtypes, which can be applied to determine distances to new WR stars or those without *Gaia* parallaxes.

Distances from the Galactic midplane allow us to find a minimum WR star runaway (travelling at ≥30 km s^{-1}) candidates, by applying a distance cutoff of $|z| \geq$156pc (3σ, when using H II region scale heights). The numbers and binary status of runaways could give an insight into WR star evolution, based on the two main mechanisms (binaries unbound by supernovae and cluster ejection) that produced the runaways. We find 31 WR star runaways (accounting for the warp in the Galactic disk), all but two of which are single.

7.2 Cluster and association membership

Gaia parallaxes and proper motions were then used to explore cluster and association membership. The dominant formation environments of WR progenitors have important implications for the formation processes of massive stars. Two possible formation mechanisms are monolithic collapse of gas clouds, which can occur in sparse or isolated environments, whilst dense clusters (historically the preferred formation environment of massive stars) may favour competitive accretion.

We used the *Gaia* data and lists of known cluster and association members from the literature to test the claimed WR star membership of 27 clusters and 14 associations. *Gaia* proper motions were plotted and grouped by eye to identify if the WR stars had the same motion as (and were therefore likely part of) the rest of the group. Distances

were also calculated, using the same Bayesian method as the previous chapters (2 and 3) and used to ensure the WR star was not in the foreground or background of the cluster or association.

We find that only 17% of stars detected in *Gaia* DR2 are members of clusters or associations. Including claimed membership from the literature for other WR stars in the Galactic disk, IR star forming regions and Galactic Centre stars, 59–75% of 663 Galactic WR stars are isolated. Using Monte Carlo simulations, we explored the possibility that these apparently isolated stars are in fact part of low mass ($<100 M_{\odot}$), faint clusters. We sampled different cluster masses and members from an IMF, finding that most isolated WR stars are unlikely to be part of these regions. Data from Chapter 3 also suggests that only a small fraction (>8%) of WR stars are runaways, and so cluster runaways are not numerous enough to have produced the large isolated fraction.

N body simulations of star forming regions were then used to test whether the original cluster environments of the WR stars had dissolved to field densities. The simulations were either sub-virial (collapsing to clusters) or super virial (expanding; association like at lower densities), with different initial densities and degrees of substructure. The most common environment to produced isolated WR stars were low density, moderately sub-structured associations which expand during the WR star lifetime to field densities ($\sim$1-10$M_{\odot}$ pc^{-3}). This makes the star appear isolated during the WR star phase.

We also used single star isochrones to estimate the ages of clusters containing WR stars. We find that all four clusters identified as young (<2 Myr) contained hydrogen rich, main sequence WN and Of/WN stars, as anticipated. The two intermediate ($\leq$5 Myr) aged clusters hosted hydrogen deficient WN and WC stars and the four old ($\geq$5 Myr) clusters mainly contained classical WN, WC and WO stars, which could have been rejuvenated by binary evolution. Overall, there was no evidence for a population of old, low mass, low luminosity WR stars, which could have been created purely through binary companion stripping.

7.3 Emission line luminosities

We can apply the *Gaia* WR distance results to extragalactic sources. Beyond the local group, most WR stars lie in unresolved star forming regions, such that photometry and spectra may include multiple WR stars. Either templates of WR subtypes, or the luminosities of red ($\sim$5600$-$5900Å) and blue ($\sim$4600$-$4700Å) bump emission line regions, are required to determine the numbers and subtypes of stars in these populations.

Using our improved distances, we were able to calculate more accurate emission line luminosities for Galactic WR subtypes. 109 WR stars had both distances (Chapter 3) and optical spectrophotometry. For each of these spectra, we subtracted the continuum by fitting a straight line to 'windows' which avoided emission lines. Gaussian profiles could then be fit to the emission lines to determine their fluxes. For WN stars, He II 4686Å and the nearby N blends comprised the blue region lines and the C III 4650Å to He II 4686Å blend was fit for WC. In the red region, we fitted C IV 5808Å and He I 5876 for both types, supplementing WC stars with fits to C III 5696Å. In some WC stars, emission lines (particularly C III 5696Å) were truncated and exhibited a flat topped profile. This meant that it was not possible to accurately fit the lines with gaussians. However, these stars were still included in the averages, as their other emission lines were still well approximated by gaussians.

We then determined the luminosities of the individual emission lines and the red and blue regions, using the distances and extinctions from Chapter 3. The results were combined to find average line luminosities for WN, WC and WO star subtypes. We found a wide spread of luminosities within a single subtype. As anticipated, WN stars had lower red bump values than WC stars, due to their weaker emission lines in this region. WC7−8 stars had a particularly large spread of luminosities, owing to some outliers.

We compared these results to WN and WC stars in the LMC. WC4−6 stars in the LMC have higher red and blue bump luminosities than those in the Galaxy. The LMC WN stars cover a similar range of red and blue bump luminosities to Galactic WN. However, in the LMC, there is an increased number of WN stars at the upper and lower extremes. This may stem from the counteracting events of the increased luminosity necessary to form single WR stars and a decreased mass loss rate, which both depend on metallicity.

7.4 Survey of NGC6946

Extragalactic surveys help to explore the effects of metallicity on WR star evolution and the ultimate fates of WR stars, by producing a catalogue of potential stripped envelope SN or direct collapse black hole progenitors. We surveyed the galaxy NGC6946, using photometry and spectroscopy from Gemini GMOS.

Photometry was taken in six wavelength bands; He II , He IIC (to detect WR emission line excesses), Hα , HαC , and Sloan r and g. We reduced the imaging data using

the Gemini GMOS reduction pipelines in IRAF. Apparent magnitudes of sources were found using the DAOPHOT routine to perform PSF fitting and subtraction. Multi object spectroscopy was obtained in six different masks, with an R150 grating at 5100 and 5300Å central wavelengths. Flux calibration used the standard star BD+284211.

The DIPSO emission line fitting procedure was used to fit gaussians to nebular lines. We then used Hα and Hβ nebular emission, together with the intrinsic intensity ratio from Case B recombination theory, to find the c(Hβ) parameter. This could be converted to E(B−V) for individual nebular regions. The average E(B−V) for the galaxy was 0.61, which could be converted to a total galactic extinction of A_V=1.88±0.09. This extinction compares well with A_V ∼1.83 from Kessler et al. (2020), who use Hα and Paβ images. The high total extinction, combined with the 6.1Mpc distance to NGC6946, make it equivalent to observing an unobscured galaxy at 14Mpc.

Using strong nebular emission lines Hα , [N II]6583, Hβ and [O III]5007, we also determine the metallicity at different galactic radii. We use the empirical relation of Pettini & Pagel (2004) to find a central metallicity of 12+log(O/H)=8.76±0.2, which is similar to the solar neighbourhood within the Milky Way, and the metallicity gradient is −0.028±0.006 dex/kpc. Both the metallicity and gradient are within the uncertainty of results from Cedrés et al. (2012) and Moustakas et al. (2010), which were obtained using the R_{23} parameter, although the agreement strongly depends on which R_{23} calibration is used.

We subtracted the Hα continuum from the Hα images, to find the net Hα emissions from H II regions. We determined the individual Hα luminosities of these regions, which could be converted to find the number of O star members. Owing to their large (>100 pc) diameters and high Hα luminosities, many of the H II regions were classified as giant H II regions. We can compare the Hα fluxes from two such regions with results from García-Benito et al. (2010), finding that our luminosities are ∼0.6–0.7 times the size of their results, possibly due to a difference in the aperture sizes. We then used the integrated emission from the galaxy to find the star formation rate; $2.39^{+1.14}_{-1.14}$ $M_\odot yr^{-1}$. This is again similar to the Milky-Way and within uncertainty of the 2.28 result from Kennicutt et al. (2008).

The narrowband He II and continuum photometry allowed us to identify 92 WR star candidate regions, either by manually detecting excesses in blinked images, or by using an WR+O star binary model, which allowed us to find excess emissions above the continuum. We also used spectroscopy to confirm 23 candidate regions contained WR stars, and used our new emission line luminosities of Galactic WR templates to estimate

the numbers and subtypes of WR stars within these regions. The two methods produced results which agreed, albeit with large uncertainties.

Using the templates, we confirmed 61 WR stars, all of which are WC and most of which are early subtypes (WC4−6). Unfortunately, this survey is highly incomplete, due to the significant galactic extinction and poor blue spectrum sensitivity of GMOS, which meant that WN stars were not detected. This incompleteness meant we were unable to calculate the WC/WN and WR/O star ratios for the galaxy. Additionally, photometric candidates fainter than the 23 mag completeness limit of the survey, may have been missed. This includes all individual, isolated WR stars.

7.5 Future work

Finally, we discuss possible directions that future work could take to build upon our results.

- Due to an increased number of observations, astrometric results from future *Gaia* data releases will improve. In particular, the early DR3 release (EDR3) anticipated in late 2020, will provide new quality indicators for the astrometric data and source image descriptors (Brown, 2020), which may help us to better identify poor astrometric data. Parallax errors are also estimated to decrease by 20% (Brown, 2020), which will reduce the proportional impact of our prior (particularly for small parallaxes). We thus expect an increase in accuracy for some distances, and a decrease in the number of distance results flagged with large uncertainties. Proper motions are also expected to be more precise by a factor of 2, improving our ability to identify WR stars as members of clusters or associations. Future data releases may also cause the number of WR stars with negative parallaxes to fall and improvements to astrometric modelling and fitting algorithms should reduce the number of unreliable results, via a reduction in astrometric excess noise.

- Distance results may also be improved by using a more complex prior. This could include spiral arms within the dust extinction map. The Gaia DR3 release also aims to provide an extinction map (Brown, 2020), which could be used as an alternative to our current extinction model.

- The number of WR stars with parallaxes may increase. In *Gaia* DR2, 32 objects only had two parameter solutions (fitting positions). Future *Gaia* data releases

may find satisfactory five parameter solutions for these stars, which would also include parallaxes.

- To properly assess the cluster membership fraction, future work should make use of clustering algorithms or machine learning methods(like those from Cantat-Gaudin et al. (2018)) to analyse the *Gaia* dataset around apparently isolated WR stars and in clusters, and associations not yet studied with this method. This would reduce the reliance on previously established literature membership, particularly as many sources in the literature often only listed a few members, or did not specify the subtypes of the stars. This limited our ability to identify WR members. Algorithms would analyse a much larger sample of the populations surrounding WR stars, potentially detecting new low mass groupings around apparently isolated WR stars, or allowing the classification of stars whose membership status is still uncertain. Future work should also account for the nature of hierarchical cluster formation, considering that WR stars may be members of a combination of clusters, associations and larger star forming regions.

- It may also be possible to obtain more accurate cluster ages by using alternatives to isochrone fitting, such as population synthesis models. An increased number of cluster members detected via the automated *Gaia* method would also improve the accuracy of the age determination.

- Poor blue region spectroscopic sensitivity and high extinction, meant that the NGC6946 survey is highly incomplete and only detected WC stars. Further work is therefore required to uncover the full WR population. The lack of detection is particularly a problem in the centres of H II regions, where bright stellar populations dilute WR emission lines. This suggests that high angular resolution Integral Field Spectroscopy (IFS) e.g MUSE, would be an appropriate follow up to our survey, detecting WR populations (particularly WN) without relying on photometric excesses. IFS could also allow us to study how the population varies across a giant H II region, rather than assuming the spectrum from a single slit is representative of the whole area. However, the small fields of view in IFS instruments present a limitation on using this technique for full galactic WR surveys.

- As NGC6946 contains several giant H II regions, an alternative technique could be to apply templates of nearby giant H II regions (such as 30 Doradus), to estimate their WR content and properties.

Bibliography

Adams S. M., Kochanek C. S., Gerke J. R., Stanek K. Z., Dai X., 2017, MNRAS, 468, 4968

Aghakhanloo M., et al., 2020, MNRAS, 492, 2497

Allison R. J., Goodwin S. P., Parker R. J., Portegies Zwart S. F., de Grijs R., 2010, MNRAS, 407, 1098

Anderson J. P., Habergham S. M., James P. A., Hamuy M., 2012, MNRAS, 424, 1372

Andrews H., Fenech D., Prinja R. K., Clark J. S., Hindson L., 2019, A&A, 632, A38

Arenou F., et al., 2018, A&A, 616, A17

Astropy Collaboration et al., 2013a, A&A, 558, A33

Astropy Collaboration et al., 2013b, A&A, 558, A33

Astropy Collaboration et al., 2018, AJ, 156, 123

Bailer-Jones C. A. L., 2015, Publications of the Astronomical Society of the Pacific, 127, 994

Bailer-Jones C. A. L., Rybizki J., Fouesneau M., Mantelet G., Andrae R., 2018, AJ, 156, 58

Barentsen G., et al., 2014, MNRAS, 444, 3230

Barkat Z., Rakavy G., Sack N., 1967, Physical Review Letters, 18, 379

Barlow M. J., Hummer D. G., 1982, in De Loore C. W. H., Willis A. J., eds, IAU Symposium Vol. 99, Wolf-Rayet Stars: Observations, Physics, Evolution. pp 387–392

Bastian N., Covey K. R., Meyer M. R., 2010, ARAA, 48, 339

Baug T., de Grijs R., Dewangan L. K., Herczeg G. J., Ojha D. K., Wang K., Deng L., Bhatt B. C., 2019, ApJ, 885, 68

Baume G., Vázquez R. A., Carraro G., 2004, MNRAS, 355, 475

Baume G., Carraro G., Comeron F., de Elía G. C., 2011, A&A, 531, A73

Baumgardt H., Kroupa P., 2007, MNRAS, 380, 1589

Beals C. S., Plaskett J. S., 1936, Transactions of the International Astronomical Union, 29, 178

Bennett M., Bovy J., 2019, MNRAS, 482, 1417

Berlanas S. R., Wright N. J., Herrero A., Drew J. E., Lennon D. J., 2019, MNRAS, 484, 1838

Bessell M. S., 1979, Publications of the Astronomical Society of the Pacific, 91, 589

Bibby J. L., Crowther P. A., 2010, MNRAS, 405, 2737

Bibby J. L., Crowther P. A., 2012, MNRAS, 420, 3091

Bibby J. L., Crowther P. A., Furness J. P., Clark J. S., 2008, MNRAS, 386, L23

Blaauw A., 1961, Bull. Astron Inst. Neth., 15, 265

Blum R. D., Damineli A., Conti P. S., 1999, AJ, 117, 1392

Bobylev V. V., Bajkova A. T., 2016, Astronomy Letters, 42, 1

Bonnell I. A., Bate M. R., Clarke C. J., Pringle J. E., 1997, MNRAS, 285, 201

Bonnell I. A., Bate M. R., Clarke C. J., Pringle J. E., 2001, MNRAS, 323, 785

Borissova J., et al., 2012, A&A, 546, A110

Bressert E., et al., 2010, MNRAS, 409, L54

Brott I., et al., 2011, A&A, 530, A115

Brown A. G., 2020, Gaia data processing status and the promise of Gaia EDR3, `http://great.ast.cam.ac.uk/Greatwiki/GreatMeet-PM13`

Buckner A. S. M., et al., 2019, A&A, 622, A184

Campbell W. W., 1894, Astronomy and Astro-Physics (formerly The Sidereal Messenger), 13, 448

Cantat-Gaudin T., et al., 2018, A&A, 618, A93

Cantat-Gaudin T., Mapelli M., Balaguer-Núñez L., Jordi C., Sacco G., Vallenari A., 2019, A&A, 621, A115

Cardelli J. A., Clayton G. C., Mathis J. S., 1989, ApJ, 345, 245

Carroll B. W., Ostlie D. A., 1996, An Introduction to Modern Astrophysics. Addison-Wesley, (Reading, MA, USA)

Cartwright A., Whitworth A. P., 2004, MNRAS, 348, 589

Castor J. I., Abbott D. C., Klein R. I., 1975, ApJ, 195, 157

Cedrés B., Cepa J., Bongiovanni Á., Castañeda H., Sánchez-Portal M., Tomita A., 2012, A&A, 545, A43

Chabrier G., 2003, ApJ, 586, L133

Chambers K. C., et al., 2016, preprint, (arXiv:1612.05560)

Chené A. N., et al., 2013, A&A, 549, A98

Chené A. N., et al., 2015, A&A, 584, A31

Chené A. N., et al., 2019, MNRAS, 484, 5834

Chomiuk L., Povich M. S., 2011, AJ, 142, 197

Clark J. S., Negueruela I., 2002, A&A, 396, L25

Clark J. S., Negueruela I., Crowther P. A., Goodwin S. P., 2005, A&A, 434, 949

Clark J. S., Lohr M. E., Najarro F., Dong H., Martins F., 2018a, A&A, 617, A65

Clark J. S., Lohr M. E., Patrick L. R., Najarro F., Dong H., Figer D. F., 2018b, A&A, 618, A2

Clark J. S., Ritchie B. W., Negueruela I., 2020, A&A, 635, A187

Cohen M., van der Hucht K. A., Williams P. M., The P. S., 1991, ApJ, 378, 302

Conti P. S., 1975, Memoires of the Societe Royale des Sciences de Liege, 9, 193

Conti P. S., 1984, in Maeder A., Renzini A., eds, IAU Symposium Vol. 105, Observational Tests of the Stellar Evolution Theory. p. 233

Conti P. S., Crowther P. A., 2004, MNRAS, 355, 899

Conti P. S., Massey P., 1989, ApJ, 337, 251

Conti P. S., Vacca W. D., 1990, AJ, 100, 431

Conti P. S., Vacca W. D., 1994, ApJ, 423, L97

Conti P. S., Garmany C. D., De Loore C., Vanbeveren D., 1983, ApJ, 274, 302

Conti P. S., Crowther P. A., Leitherer C., 2008, From Luminous Hot Stars to Starburst Galaxies. Cambridge University Press, (Cambridge, UK)

Corti M., Bosch G., Niemela V., 2007, A&A, 467, 137

Corti M. A., Orellana R. B., Bosch G. L., 2018a, VizieR Online Data Catalog, pp J/A+A/616/A40

Corti M. A., Orellana R. B., Bosch G. L., 2018b, A&A, 616, A40

Cox A. N., 2000, Allen's astrophysical quantities. Springer-Verlag, (New York, NY, USA)

Crowther P. A., 1997, MNRAS, 290, L59

Crowther P. A., 2007, ARAA, 45, 177

Crowther P. A., 2013, MNRAS, 428, 1927

Crowther P. A., Dessart L., 1998, MNRAS, 296, 622

Crowther P. A., Hadfield L. J., 2006, A&A, 449, 711

Crowther P. A., Hadfield L. J., 2007, The Messenger, 129, 53

Crowther P. A., Smith L. J., 1997, A&A, 320, 500

Crowther P. A., Smith L. J., 1999, MNRAS, 308, 82

Crowther P. A., Walborn N. R., 2011, MNRAS, 416, 1311

Crowther P. A., Smith L. J., Hillier D. J., Schmutz W., 1995, A&A, 293, 427

Crowther P. A., De Marco O., Barlow M. J., 1998, MNRAS, 296, 367

Crowther P. A., Dessart L., Hillier D. J., Abbott J. B., Fullerton A. W., 2002, A&A, 392, 653

Crowther P. A., Drissen L., Abbott J. B., Royer P., Smartt S. J., 2003, A&A, 404, 483

Crowther P. A., Hadfield L. J., Clark J. S., Negueruela I., Vacca W. D., 2006a, MNRAS, 372, 1407

Crowther P. A., Lennon D. J., Walborn N. R., 2006b, A&A, 446, 279

Crowther P. A., Carpano S., Hadfield L. J., Pollock A. M. T., 2007, A&A, 469, L31

Crowther P. A., Schnurr O., Hirschi R., Yusof N., Parker R. J., Goodwin S. P., Kassim H. A., 2010, MNRAS, 408, 731

Csengeri T., et al., 2018, A&A, 617, A89

Davidson K., Helmel G., Humphreys R. M., 2018, Research Notes of the American Astronomical Society, 2, 133

Davies B., Beasor E. R., 2019, MNRAS, 486, L10

Davies B., et al., 2012a, MNRAS, 419, 1871

Davies B., de La Fuente D., Najarro F., Hinton J. A., Trombley C., Figer D. F., Puga E., 2012b, MNRAS, 419, 1860

Davies B., Crowther P. A., Beasor E. R., 2018, MNRAS, 478, 3138

De Loore C., De Greve J. P., Lamers H. J. G. L. M., 1977, A&A, 61, 251

De Marco O., Schmutz W., Crowther P. A., Hillier D. J., Dessart L., de Koter A., Schweickhardt J., 2000, A&A, 358, 187

Dias W. S., Alessi B. S., Moitinho A., Lépine J. R. D., 2002, A&A, 389, 871

Dias W. S., Alessi B. S., Moitinho A., Lepine J. R. D., 2014a, VizieR Online Data Catalog, p. B/ocl

Dias W. S., Monteiro H., Caetano T. C., Lepine J. R. D., Assafin M., Oliveira A. F., 2014b, VizieR Online Data Catalog, pp J/A+A/564/A79

Dias W. S., Monteiro H., Caetano T. C., Lépine J. R. D., Assafin M., Oliveira A. F., 2014c, A&A, 564, A79

Draper P. W., Gray N., Berry D. S., Taylor M., 2014, GAIA: Graphical Astronomy and Image Analysis Tool (ascl:1403.024)

Drew J. E., Barlow M. J., Unruh Y. C., Parker Q. A., Wesson R., Pierce M. J., Masheder M. R. W., Phillipps S., 2004, MNRAS, 351, 206

Drew J. E., et al., 2005, MNRAS, 362, 753

Drew J. E., et al., 2014, MNRAS, 440, 2036

Drew J. E., Herrero A., Mohr-Smith M., Monguió M., Wright N. J., Kupfer T., Napiwotzki R., 2018, MNRAS, 480, 2109

Drew J. E., Monguió M., Wright N. J., 2019, MNRAS, 486, 1034

Dreyer J. L. E., 1888, Memoirs of the Royal Astronomical Society, 49, 1

Dreyer J. L. E., 1910, Memoirs of the Royal Astronomical Society, 59, 105

Drissen L., Lamontagne R., Moffat A. F. J., Bastien P., Seguin M., 1986, ApJ, 304, 188

Ducati J. R., Bevilacqua C. M., Rembold S. r. B., Ribeiro D., 2001, ApJ, 558, 309

Ekström S., et al., 2012, A&A, 537, A146

Eldridge J. J., Maund J. R., 2016, MNRAS, 461, L117

Eldridge J. J., Izzard R. G., Tout C. A., 2008, MNRAS, 384, 1109

Eldridge J. J., Fraser M., Smartt S. J., Maund J. R., Crockett R. M., 2013, MNRAS, 436, 774

Evans D. W., et al., 2018, A&A, 616, A4

Fitzpatrick E. L., Massa D., 2009, ApJ, 699, 1209

Flewelling H. A., et al., 2016, preprint, (arXiv:1612.05243)

Foellmi C., Moffat A. F. J., Guerrero M. A., 2003a, MNRAS, 338, 360

Foellmi C., Moffat A. F. J., Guerrero M. A., 2003b, MNRAS, 338, 1025

Franciosini E., Sacco G. G., Jeffries R. D., Damiani F., Roccatagliata V., Fedele D., Rand ich S., 2018, A&A, 616, L12

Fritz T. K., et al., 2010, ApJ, 721, 395

Fritz T. K., et al., 2011, ApJ, 737, 73

Fruchter A. S., et al., 2006, Nature, 441, 463

Gaia Collaboration et al., 2018a, A&A, 616, A1

Gaia Collaboration et al., 2018b, A&A, 616, A10

García-Benito R., et al., 2010, MNRAS, 408, 2234

Georgy C., Meynet G., Walder R., Folini D., Maeder A., 2009, A&A, 502, 611

Georgy C., Ekström S., Meynet G., Massey P., Levesque E. M., Hirschi R., Eggenberger P., Maeder A., 2012, A&A, 542, A29

Giammichele N., Bergeron P., Dufour P., 2012, ApJS, 199, 29

Gieles M., Moeckel N., Clarke C. J., 2012, MNRAS, 426, L11

Gies D. R., Bolton C. T., 1986, ApJS, 61, 419

Goodwin S. P., 1997, MNRAS, 284, 785

Goodwin S. P., Whitworth A. P., 2004, A&A, 413, 929

Götberg Y., de Mink S. E., Groh J. H., 2017, A&A, 608, A11

Götberg Y., de Mink S. E., Groh J. H., Kupfer T., Crowther P. A., Zapartas E., Renzo M., 2018, A&A, 615, A78

Götberg Y., de Mink S. E., Groh J. H., Leitherer C., Norman C., 2019, A&A, 629, A134

Graczyk D., et al., 2019, ApJ, 872, 85

Gräfener G., Hamann W.-R., 2005, A&A, 432, 633

Gravity Collaboration et al., 2018, A&A, 615, L15

Green G. M., et al., 2015, ApJ, 810, 25

Groh J. H., et al., 2019, A&A, 627, A24

Hadfield L. J., Crowther P. A., 2006, MNRAS, 368, 1822

Hadfield L. J., Crowther P. A., 2007, MNRAS, 381, 418

Hadfield L. J., Crowther P. A., Schild H., Schmutz W., 2005, A&A, 439, 265

Hadfield L. J., van Dyk S. D., Morris P. W., Smith J. D., Marston A. P., Peterson D. E., 2007, MNRAS, 376, 248

Hainich R., et al., 2014, A&A, 565, A27

Hainich R., Pasemann D., Todt H., Shenar T., Sander A., Hamann W.-R., 2015, A&A, 581, A21

Hainich R., Ramachandran V., Shenar T., Sand er A. A. C., Todt H., Gruner D., Oskinova L. M., Hamann W. R., 2019, A&A, 621, A85

Hamann W. R., Gräfener G., 2004, A&A, 427, 697

Hamann W. R., Koesterke L., 1998, A&A, 335, 1003

Hamann W.-R., Schmutz W., 1987, A&A, 174, 173

Hamann W. R., Koesterke L., Wessolowski U., 1993, A&A, 274, 397

Hamann W.-R., Gräfener G., Liermann A., 2006, A&A, 457, 1015

Hamann W. R., et al., 2019, A&A, 625, A57

Hambly N., et al., 2018, Technical report, Gaia DR2 documentation Chapter 14: Datamodel description, `https://gea.esac.esa.int/archive/documentation/GDR2/`. European Space Agency, Gaia Data Processing and Analysis Consortium., `https://gea.esac.esa.int/archive/documentation/GDR2/`

Hanson M. M., Kurtev R., Borissova J., Georgiev L., Ivanov V. D., Hillier D. J., Minniti D., 2010, A&A, 516, A35

Herrmann K. A., Ciardullo R., Feldmeier J. J., Vinciguerra M., 2008, ApJ, 683, 630

Hillier D. J., 2012, in Richards M. T., Hubeny I., eds, IAU Symposium Vol. 282, From Interacting Binaries to Exoplanets: Essential Modeling Tools. pp 229–234, doi:10.1017/S1743921311027426

Hillier D. J., Miller D. L., 1998, ApJ, 496, 407

Hiltner W. A., Schild R. E., 1966, ApJ, 143, 770

Hodge P. W., Kennicutt Jr. R. C., 1983, AJ, 88, 296

Hogg D. W., 2018, preprint, p. arXiv:1804.07766 (arXiv:1804.07766)

Hopewell E. C., et al., 2005, MNRAS, 363, 857

Hubeny I., Lanz T., 1995, ApJ, 439, 875

Hummer D. G., Storey P. J., 1987, MNRAS, 224, 801

Humphreys R. M., 1978, ApJS, 38, 309

Humphreys R. M., 2019, Research Notes of the American Astronomical Society, 3, 164

Humphreys R. M., Davidson K., 1979, ApJ, 232, 409

Hur H., Park B.-G., Sung H., Bessell M. S., Lim B., Chun M.-Y., Sohn S. T., 2015, MNRAS, 446, 3797

Jeffries R. D., et al., 2014a, VizieR Online Data Catalog, pp J/A+A/563/A94

Jeffries R. D., et al., 2014b, A&A, 563, A94

Jordi C., et al., 2010, A&A, 523, A48

Jrgensen I., 2009, Publications of the Astronomical Society of Australia, 26, 1730

Kaltcheva N., Makarov V., 2007, ApJ, 667, L155

Kanarek G., Shara M., Faherty J., Zurek D., Moffat A., 2015, MNRAS, 452, 2858

Kelly P. L., Kirshner R. P., 2012, ApJ, 759, 107

Kelly P. L., Kirshner R. P., Pahre M., 2008, ApJ, 687, 1201

Kennicutt R. C. J., 1984, ApJ, 287, 116

Kennicutt Jr. R. C., 1998a, ARAA, 36, 189

Kennicutt Jr. R. C., 1998b, ApJ, 498, 541

Kennicutt Robert C. J., Bresolin F., Bomans D. J., Bothun G. D., Thompson I. B., 1995, AJ, 109, 594

Kennicutt Jr. R. C., Lee J. C., Funes J. G., J. S., Sakai S., Akiyama S., 2008, ApJS, 178, 247

Kessler S., Leroy A., Querejeta M., Murphy E., Rebolledo D., Sandstrom K., Schinnerer E., Wong T., 2020, ApJ, 892, 23

Kharchenko N. V., Piskunov A. E., Schilbach E., Röser S., Scholz R. D., 2013, A&A, 558, A53

Kingsburgh R. L., Barlow M. J., Storey P. J., 1995, A&A, 295, 75

Kippenhahn R., Weigert A., 1967, Zeitschrift für Astrophysik, 65, 251

Kobulnicky H. A., Kewley L. J., 2004, ApJ, 617, 240

Korchagin V. I., Girard T. M., Borkova T. V., Dinescu D. I., van Altena W. F., 2003, AJ, 126, 2896

Krabbe A., et al., 1995, ApJ, 447, L95

Kroupa P., 2001, MNRAS, 322, 231

Kruijssen J. M. D., Maschberger T., Moeckel N., Clarke C. J., Bastian N., Bonnell I. A., 2012, MNRAS, 419, 841

Kuncarayakti H., et al., 2018, A&A, 613, A35

Kurtev R., Borissova J., Georgiev L., Ortolani S., Ivanov V. D., 2007, A&A, 475, 209

Kurucz R. L., 1979, ApJS, 40, 1

Lada C. J., Lada E. A., 2003, ARAA, 41, 57

Lada C. J., Margulis M., Dearborn D., 1984, ApJ, 285, 141

Lamers H. J. G. L. M., Levesque E. M., 2017, Understanding Stellar Evolution. IOP Publishing, (Bristol, UK), doi:10.1088/978-0-7503-1278-3

Lamers H. J. G. L. M., Maeder A., Schmutz W., Cassinelli J. P., 1991, ApJ, 368, 538

Langer N., Hamann W.-R., Lennon M., Najarro F., Pauldrach A. W. A., Puls J., 1994, A&A, 290, 819

Lanz T., Hubeny I., 2007, ApJS, 169, 83

Lasker B. M., Sturch C. R., McLean B. J., Russell J. L., Jenkner H., Shara M. M., 1990, AJ, 99, 2019

Leloudas G., 2012, in Roming P., Kawai N., Pian E., eds, IAU Symposium Vol. 279, Death of Massive Stars: Supernovae and Gamma-Ray Bursts. pp 191–198 (arXiv:1205.0571), doi:10.1017/S1743921312012914

Leloudas G., Sollerman J., Levan A. J., Fynbo J. P. U., Malesani D., Maund J. R., 2010, A&A, 518, A29

Li C., Zhao G., Jia Y., Liao S., Yang C., Wang Q., 2019, ApJ, 871, 208

Lindegren L., et al., 2018a, Gaia DR2 astrometry, https://www.cosmos.esa.int/web/gaia/dr2-known-issues

Lindegren L., et al., 2018b, A&A, 616, A2

López-Sánchez Á. R., Esteban C., 2010, A&A, 516, A104

Lucy L. B., Solomon P. M., 1970, ApJ, 159, 879

Lundström I., Stenholm B., 1984, A&A Suppl., 58, 163

Luri X., et al., 2018, A&A, 616, A9

MacConnell D. J., Sanduleak N., 1970, PASP, 82, 80

Maeder A., 1983, A&A, 120, 113

Maeder A., Lequeux J., Azzopardi M., 1980, A&A, 90, L17

Magnier E. A., et al., 2016, preprint, (arXiv:1612.05240)

Maíz Apellániz J., Barbá R. H., 2018, A&A, 613, A9

Maíz Apellániz J., Weiler M., 2018, A&A, 619, A180

Maíz Apellániz J., et al., 2013, in Massive Stars: From alpha to Omega. p. 198 (arXiv:1306.6417)

Maíz Apellániz J., Pantaleoni González M., Barbá R. H., Simón-Díaz S., Negueruela I., Lennon D. J., Sota A., Trigueros Páez E., 2018, A&A, 616, A149

Maíz Apellániz J., Crespo Bellido P., Barbá R. H., Fernández Aranda R., Sota A., 2020, arXiv e-prints, p. arXiv:2009.05773

Makarov D., Prugniel P., Terekhova N., Courtois H., Vauglin I., 2014, A&A, 570, A13

Marchenko S. V., Moffat A. F. J., Crowther P. A., 2010, ApJ, 724, L90

Martins F., Plez B., 2006a, VizieR Online Data Catalog, pp J/A+A/457/637

Martins F., Plez B., 2006b, A&A, 457, 637

Martins F., Schaerer D., Hillier D. J., 2005, A&A, 436, 1049

Martins F., Chené A. N., Bouret J. C., Borissova J., Groh J., Ramírez Alegría S., Minniti D., 2019, A&A, 627, A170

Maschberger T., 2013, MNRAS, 429, 1725

Mason B. D., Hartkopf W. I., Gies D. R., Henry T. J., Helsel J. W., 2009, AJ, 137, 3358

Massey P., 1984, ApJ, 281, 789

Massey P., Conti P. S., 1983, ApJ, 273, 576

Massey P., Johnson J., 1993, AJ, 105, 980

Massey P., Johnson O., 1998, ApJ, 505, 793

Massey P., Thompson A. B., 1991, AJ, 101, 1408

Massey P., Johnson K. E., Degioia-Eastwood K., 1995, ApJ, 454, 151

Massey P., DeGioia-Eastwood K., Waterhouse E., 2001, AJ, 121, 1050

Mattila S., Smartt S. J., Eldridge J. J., Maund J. R., Crockett R. M., Danziger I. J., 2008, ApJ, 688, L91

Mauerhan J. C., Van Dyk S. D., Morris P. W., 2009, PASP, 121, 591

Mauerhan J. C., Van Dyk S. D., Morris P. W., 2011, AJ, 142, 40

Maund J. R., Ramirez-Ruiz E., 2016, MNRAS, 456, 3175

Maund J. R., Smartt S. J., Kudritzki R. P., Podsiadlowski P., Gilmore G. F., 2004, Nature, 427, 129

McGaugh S. S., 1991, ApJ, 380, 140

McKee C. F., Tan J. C., 2003, ApJ, 585, 850

McLeod A. F., et al., 2020, ApJ, 891, 25

Melena N. W., Massey P., Morrell N. I., Zangari A. M., 2008, AJ, 135, 878

Melnick J., Tapia M., Terlevich R., 1989, A&A, 213, 89

Mel'nik A. M., Dambis A. K., 2017, MNRAS, 472, 3887

Melnik A. M., Dambis A. K., 2020, Astrophysics and Space Science, 365, 112

Messineo M., Davies B., Ivanov V. D., Figer D. F., Schuller F., Habing H. J., Menten K. M., Petr-Gotzens M. G., 2009, ApJ, 697, 701

Messineo M., Davies B., Figer D. F., Kudritzki R. P., Valenti E., Trombley C., Najarro F., Rich R. M., 2011, ApJ, 733, 41

Meynet G., Maeder A., 2005, A&A, 429, 581

Miralles-Caballero D., et al., 2016, A&A, 592, A105

Modjaz M., et al., 2008, AJ, 135, 1136

Moeckel N., Holland C., Clarke C. J., Bonnell I. A., 2012, MNRAS, 425, 450

Moffat A. F. J., 1989, ApJ, 347, 373

Moffat A. F. J., Shara M. M., 1983, ApJ, 273, 544

Moffat A. F. J., Fitzgerald M. P., Jackson P. D., 1977, ApJ, 215, 106

Moffat A. F. J., Lamontagne R., Seggewiss W., 1982, A&A, 114, 135

Moffat A. F. J., et al., 2002, ApJ, 573, 191

Molina-Lera J. A., Baume G., Gamen R., Costa E., Carraro G., 2016, A&A, 592, A149

Monreal-Ibero A., Walsh J. R., Iglesias-Páramo J., Sandin C., Relaño M., Pérez-Montero E., Vílchez J., 2017, A&A, 603, A130

Morello G., Morris P. W., Van Dyk S. D., Marston A. P., Mauerhan J. C., 2018, MNRAS, 473, 2565

Morris P. W., van der Hucht K. A., Crowther P. A., Hillier D. J., Dessart L., Williams P. M., Willis A. J., 2000, A&A, 353, 624

Moustakas J., Kennicutt Jr. R. C., Tremonti C. A., Dale D. A., Smith J.-D. T., Calzetti D., 2010, ApJS, 190, 233

Munoz M., Moffat A. F. J., Hill G. M., Shenar T., Richardson N. D., Pablo H., St-Louis N., Ramiaramanantsoa T., 2017, MNRAS, 467, 3105

Neugent K. F., Massey P., 2011, ApJ, 733, 123

Neugent K., Massey P., 2019, Galaxies, 7, 74

Neugent K. F., Massey P., Georgy C., 2012, ApJ, 759, 11

Neugent K. F., Massey P., Morrell N., 2018, ApJ, 863, 181

Nugis T., Lamers H. J. G. L. M., 2000, A&A, 360, 227

Nugis T., Lamers H. J. G. L. M., 2002, A&A, 389, 162

Oh S., Kroupa P., 2016, A&A, 590, A107

Paczynski B., 1973, in Bappu M. K. V., Sahade J., eds, IAU Symposium Vol. 49, Wolf-Rayet and High-Temperature Stars. p. 143

Paladini R., Burigana C., Davies R. D., Maino D., Bersanelli M., Cappellini B., Platania P., Smoot G., 2003, A&A, 397, 213

Paladini R., Davies R. D., De Zotti G., 2004, MNRAS, 347, 237

Parker R. J., Goodwin S. P., 2007, MNRAS, 380, 1271

Parker R. J., Meyer M. R., 2012, MNRAS, 427, 637

Parker R. J., Church R. P., Davies M. B., Meyer M. R., 2014a, MNRAS, 437, 946

Parker R. J., Wright N. J., Goodwin S. P., Meyer M. R., 2014b, MNRAS, 438, 620

Patat F., Carraro G., 2001, MNRAS, 325, 1591

Paumard T., et al., 2006, ApJ, 643, 1011

Pedregosa F., et al., 2011, Journal of Machine Learning Research, 12, 2825

Perren G., Vázquez R. A., Carraro G., 2012, A&A, 548, A125

Pettini M., Pagel B. E. J., 2004, MNRAS, 348, L59

Pilyugin L. S., Thuan T. X., 2005, ApJ, 631, 231

Pledger J. L., Shara M. M., Wilde M., Crowther P. A., Long K. S., Zurek D., Moffat A. F. J., 2018, MNRAS, 473, 148

Portegies Zwart S. F., Verbunt F., 1996, A&A, 309, 179

Portegies Zwart S. F., Makino J., McMillan S. L. W., Hut P., 1999, A&A, 348, 117

Poveda A., Ruiz J., Allen C., 1967, Boletin de los Observatorios Tonantzintla y Tacubaya, 4, 86

Price-Whelan A. M., et al., 2018, AJ, 156, 123

Prisinzano L., et al., 2016, A&A, 589, A70

Rahman M., Murray N., 2010, ApJ, 719, 1104

Rahman M., Moon D.-S., Matzner C. D., 2011, ApJ, 743, L28

Rakavy G., Shaviv G., 1967, ApJ, 148, 803

Ramachandran V., Hamann W. R., Hainich R., Oskinova L. M., Shenar T., Sander A. A. C., Todt H., Gallagher J. S., 2018, A&A, 615, A40

Rate G., Crowther P. A., 2020, MNRAS, 493, 1512

Rate G., Crowther P. A., Parker R. J., 2020, MNRAS, 495, 1209

Rauw G., Manfroid J., Gosset E., Nazé Y., Sana H., De Becker M., Foellmi C., Moffat A. F. J., 2007, A&A, 463, 981

Rauw G., Sana H., Nazé Y., 2011, A&A, 535, A40

Reid M. J., et al., 2019, ApJ, 885, 131

Reiter M., Parker R. J., 2019, MNRAS, 486, 4354

Renzo M., et al., 2019, A&A, 624, A66

Riess A. G., et al., 2018, ApJ, 861, 126

Rodgers A. W., Campbell C. T., Whiteoak J. B., 1960, MNRAS, 121, 103

Rogstad D. H., Shostak G. S., Rots A. H., 1973, A&A, 22, 111

Romero-Gómez M., Mateu C., Aguilar L., Figueras F., Castro-Ginard A., 2019, A&A, 627, A150

Rosslowe C. K., Crowther P. A., 2015a, MNRAS, 447, 2322

Rosslowe C. K., Crowther P. A., 2015b, MNRAS, 449, 2436

Rosslowe C. K., Crowther P. A., 2018, MNRAS, 473, 2853

Russeil D., 2003, A&A, 397, 133

Salgado J., González-Núñez J., Gutiérrez-Sánchez R., Segovia J. C., Durán J., Hernández J. L., Arviset C., 2017, Astronomy and Computing, 21, 22

Salpeter E. E., 1955, ApJ, 121, 161

Sana H., et al., 2012, Science, 337, 444

Sana H., et al., 2013, A&A, 550, A107

Sander A., Hamann W.-R., Todt H., 2012, A&A, 540, A144

Sander A. A. C., Hamann W. R., Todt H., Hainich R., Shenar T., Ramachandran V., Oskinova L. M., 2019, A&A, 621, A92

Sander A. A. C., Vink J. S., Hamann W. R., 2020, MNRAS, 491, 4406

Schaerer D., Vacca W. D., 1998, ApJ, 497, 618

Schilbach E., Röser S., 2008, A&A, 489, 105

Schlafly E. F., Finkbeiner D. P., 2011, ApJ, 737, 103

Schmutz W., Hamann W. R., Wessolowski U., 1989, A&A, 210, 236

Schneider F. R. N., et al., 2014, ApJ, 780, 117

Schneider F. R. N., et al., 2018, Science, 359, 69

Schnurr O., Moffat A. F. J., St-Louis N., Morrell N. I., Guerrero M. A., 2008, MNRAS, 389, 806

Schönrich R., McMillan P., Eyer L., 2019, MNRAS, 487, 3568

Shara M. M., Moffat A. F. J., Smith L. F., Niemela V. S., Potter M., Lamontagne R., 1999, AJ, 118, 390

Shara M. M., et al., 2009, AJ, 138, 402

Shara M. M., Faherty J. K., Zurek D., Moffat A. F. J., Gerke J., Doyon R., Artigau E., Drissen L., 2012, AJ, 143, 149

Shara M. M., Mikołajewska J., Caldwell N., Iłkiewicz K., Drozd K., Zurek D., 2016, MNRAS, 455, 3453

Sharpless S., 1959, ApJS, 4, 257

Shenar T., et al., 2016, A&A, 591, A22

Shenar T., et al., 2019, A&A, 627, A151

Shenar T., Gilkis A., Vink J. S., Sana H., Sand er A. A. C., 2020, A&A, 634, A79

Shukirgaliyev B., Parmentier G., Just A., Berczik P., 2018, ApJ, 863, 171

Shull J. M., Danforth C. W., 2019, ApJ, 882, 180

Sidoli F., Smith L. J., Crowther P. A., 2006, MNRAS, 370, 799

Skrutskie M. F., et al., 2006, AJ, 131, 1163

Smartt S. J., Eldridge J. J., Crockett R. M., Maund J. R., 2009, MNRAS, 395, 1409

Smith L. F., 1968a, MNRAS, 138, 109

Smith L. F., 1968b, MNRAS, 140, 409

Smith N., 2006a, MNRAS, 367, 763

Smith N., 2006b, MNRAS, 368, 1983

Smith N., 2006c, ApJ, 644, 1151

Smith N., 2014, ARAA, 52, 487

Smith N., Owocki S. P., 2006, ApJ, 645, L45

Smith N., Tombleson R., 2015, MNRAS, 447, 598

Smith L. F., Shara M. M., Moffat A. F. J., 1990, ApJ, 358, 229

Smith L. J., Crowther P. A., Prinja R. K., 1994, A&A, 281, 833

Smith L. J., Crowther P. A., Willis A. J., 1995, A&A, 302, 830

Smith L. F., Shara M. M., Moffat A. F. J., 1996, MNRAS, 281, 163

Smith N., Li W., Filippenko A. V., Chornock R., 2011, MNRAS, 412, 1522

Smith N., Aghakhanloo M., Murphy J. W., Drout M. R., Stassun K. G., Groh J. H., 2019, MNRAS, 488, 1760

Smith N., et al., 2020, MNRAS, 492, 5897

Sofue Y., Tutui Y., Honma M., Tomita A., Takamiya T., Koda J., Takeda Y., 1999, ApJ, 523, 136

Stassun K. G., Torres G., 2018, ApJ, 862, 61

Stead J. J., Hoare M. G., 2009, MNRAS, 400, 731

Stetson P. B., 1987, PASP, 99, 191

Stevance H. F., Eldridge J. J., McLeod A., Stanway E. R., Chrimes A. A., 2020, arXiv e-prints, p. arXiv:2004.02883

Sun N.-C., Maund J. R., Hirai R., Crowther P. A., Podsiadlowski P., 2020, MNRAS, 491, 6000

Sung H., Bessell M. S., 2004, AJ, 127, 1014

Sung H., Bessell M. S., Park B. G., Kang Y. H., 1999, Journal of Korean Astronomical Society, 32, 109

Tanner A., Ghez A. M., Morris M. R., Christou J. C., 2005, ApJ, 624, 742

Tehrani K., Crowther P. A., Archer I., 2017, MNRAS, 472, 4618

Tehrani K. A., Crowther P. A., Bestenlehner J. M., Littlefair S. P., Pollock A. M. T., Parker R. J., Schnurr O., 2019, MNRAS, 484, 2692

Tetzlaff N., Neuhäuser R., Hohle M. M., 2011, MNRAS, 410, 190

Todt H., Sander A., Hainich R., Hamann W.-R., Quade M., Shenar T., 2015, A&A, 579, A75

Torres-Dodgen A. V., Massey P., 1988, AJ, 96, 1076

Torres A. V., Conti P. S., Massey P., 1986, ApJ, 300, 379

Tramper F., et al., 2015, A&A, 581, A110

Turner D. G., 1981, AJ, 86, 222

Turner D. G., 1982, in De Loore C. W. H., Willis A. J., eds, IAU Symposium Vol. 99, Wolf-Rayet Stars: Observations, Physics, Evolution. pp 57–60

Turner D. G., Forbes D., 1982, PASP, 94, 789

Turner D. G., Moffat A. F. J., Lamontagne R., Maitzen H. M., 1983, AJ, 88, 1199

Tutukov A. V., 1978, A&A, 70, 57

Urquhart J. S., Figura C. C., Moore T. J. T., Hoare M. G., Lumsden S. L., Mottram J. C., Thompson M. A., Oudmaijer R. D., 2014, MNRAS, 437, 1791

Vanbeveren D., Conti P. S., 1980, A&A, 88, 230

Vargas Álvarez C. A., Kobulnicky H. A., Bradley D. R., Kannappan S. J., Norris M. A., Cool R. J., Miller B. P., 2013, AJ, 145, 125

Vázquez R. A., Baume G., 2001, A&A, 371, 908

Vink J. S., 2017, A&A, 607, L8

Vink J. S., de Koter A., 2005, A&A, 442, 587

Vogt N., Moffat A. F. J., 1972, A&A Suppl., 7, 133

Wallace D. J., Gies D. R., Moffat A. F. J., Shara M. M., Niemela V. S., 2005, AJ, 130, 126

Wang S., Chen X., 2019, ApJ, 877, 116

Ward J. L., Kruijssen J. M. D., Rix H.-W., 2020, MNRAS, 495, 663

Wegner W., 1994, MNRAS, 270, 229

Wenger M., et al., 2000, A&A Suppl., 143, 9

Williams P. M., van der Hucht K. A., 2000, MNRAS, 314, 23

Wolf C. J. E., Rayet G., 1867, Academie des Sciences Paris Comptes Rendus, 65, 292

Wray J. D., Corso G. J., 1972, ApJ, 172, 577

Wright A. E., Barlow M. J., 1975, MNRAS, 170, 41

Wright N. J., Parker R. J., Goodwin S. P., Drake J. J., 2014, MNRAS, 438, 639

Wright N. J., Drew J. E., Mohr-Smith M., 2015, MNRAS, 449, 741

Zhekov S. A., Tomov T., Gawronski M. P., Georgiev L. N., Borissova J., Kurtev R., Gagné M., Hajduk M., 2014, MNRAS, 445, 1663

Zinn J. C., Pinsonneault M. H., Huber D., Stello D., 2019, ApJ, 878, 136

Zinnecker H., Yorke H. W., 2007, ARAA, 45, 481

de Mink S. E., Sana H., Langer N., Izzard R. G., Schneider F. R. N., 2014, ApJ, 782, 7

de Vaucouleurs G., de Vaucouleurs A., Corwin H. G., Buta R. J., Paturel G., Fouque P., 1995, VizieR Online Data Catalog, 7155

de Wit W. J., Testi L., Palla F., Zinnecker H., 2005, A&A, 437, 247

de la Fuente D., Najarro F., Trombley C., Davies B., Figer D. F., 2015, A&A, 575, A10

de la Fuente D., et al., 2016, A&A, 589, A69

van Leeuwen F., 2007, A&A, 474, 653

van der Hucht K. A., 2001, New Astronomy Reviews, 45, 135

van der Hucht K. A., Conti P. S., Lundstrom I., Stenholm B., 1981, Space Science Reviews, 28, 227

Appendix A

Appendix

A.1 Distances to Galactic WR stars from *Gaia* DR2

Table A.1: Gaia DR2 astrometric, photometric and parallax properties for 383 Galactic WR stars, including WR11 using a parallax and photometry from Hipparcos (van Leeuwen, 2007) (Chapter 3). The distance for WR11 was calculated in the same manner as WR with *Gaia* results, except the adjustments to calculate ω and σ_ω were not applied. Stellar luminosities, updated from Hamann et al. (2019) and Sander et al. (2019) according to our revised distances, are restricted to sources with no error flags.

WR Number	Spectral Type	Alias	RA J2015	Dec J2015	$\omega \pm \sigma_w$ (mas)	d (kpc)	$\lvert z \rvert$ (pc)	G (mag)	$G_{BP} - G_{RP}$ (mag)	Excess noise	$\log L/L_\odot$	Flags
WR1	WN4b	HD 4004	00 43 28.39	+64 45 35.4	0.314±0.040	$3.15^{+0.47}_{-0.36}$	125^{+15}_{-12}	9.79	1.05	0.00		g
WR3	WN3ha	HD 9974	01 38 55.62	+58 09 22.6	0.342±0.051	$2.90^{+0.52}_{-0.39}$	188^{+37}_{-27}	10.58	0.18	0.10	5.56	g
WR4	WC5+?	HD 16523	02 41 11.67	+56 43 49.8	0.258±0.051	$3.75^{+0.89}_{-0.62}$	174^{+46}_{-32}	9.68	0.51	0.06	5.72	g
WR5	WC6	HD 17638	02 52 11.66	+56 56 07.1	0.334±0.042	$2.97^{+0.43}_{-0.33}$	90^{+16}_{-12}	10.06	0.94	0.00	5.53	g
WR6	WN4b	EZ CMa	06 54 13.04	−23 55 42.0	0.441±0.065	$2.27^{+0.42}_{-0.31}$	376^{+73}_{-53}	6.57	0.04	0.18	5.78	g
WR7	WN4b	HD 56925	07 18 29.13	−13 13 01.5	0.221±0.051	$4.23^{+1.08}_{-0.74}$	11^{+2}_{-1}	11.17	0.73	0.00	5.33	g
WR8	WN7o/CE	HD 62910	07 44 58.22	−31 54 29.5	0.263±0.038	$3.74^{+0.63}_{-0.48}$	226^{+41}_{-31}	9.92	0.84	0.00		g
WR9	WC5+O7	HD 63099	07 45 50.40	−34 19 48.5	0.212±0.035	$4.57^{+0.84}_{-0.63}$	256^{+70}_{-52}	10.14	1.30	0.00		g
WR10	WN5h	HD 65865	07 59 46.24	−28 44 03.0	0.162±0.040	$5.46^{+1.25}_{-0.91}$	75^{+12}_{-9}	10.94	0.60	0.09	5.78	g
WR11	WC8+O7.5III-V	γ Vel	08 09 31.96	−47 20 11.8	2.920±0.300	$0.34^{+0.04}_{-0.03}$	24^{+5}_{-4}	1.70				
WR12	WN8h	Ve5-5	08 44 47.29	−45 58 55.4	0.154±0.037	$5.71^{+1.24}_{-0.92}$	175^{+42}_{-31}	10.36	1.15	0.00	5.93	g
WR13	WC6	Ve6-15	08 49 52.95	−45 10 24.0	0.189±0.042	$4.80^{+1.09}_{-0.78}$	43^{+14}_{-10}	12.39	1.60	0.00	5.55	g
WR14	WC7+?	HD 76536	08 54 59.16	−47 35 32.6	0.449±0.041	$2.22^{+0.22}_{-0.19}$	42^{+6}_{-5}	8.61	0.73	0.00	5.78	g
WR15	WC6	HD 79573	09 13 11.76	−50 06 25.5	0.334±0.034	$2.96^{+0.34}_{-0.28}$	35^{+6}_{-5}	10.16	1.66	0.00	5.98	g
WR16	WN8h	HD 86161	09 54 52.89	−57 43 38.2	0.378±0.040	$2.63^{+0.32}_{-0.26}$	96^{+14}_{-11}	8.05	0.72	0.00	5.72	g
WR17	WC5	HD 88500	10 10 31.90	−60 38 42.4	0.090±0.051	$6.75^{+1.74}_{-1.33}$	413^{+111}_{-85}	10.42	0.12	0.14	5.56	g
WR17-1	WN5b	SMG09 668-4	10 16 26.21	−57 28 05.7	0.188±0.165	$3.09^{+1.52}_{-0.91}$	13^{+16}_{-10}	16.97		0.79		g

WR Number	Spectral Type	Alias	RA J2015	Dec J2015	$\omega \pm \sigma_w$ (mas)	d (kpc)	$\lvert z \rvert$ (pc)	G (mag)	$G_{BP} - G_{RP}$ (mag)	Excess noise	$\log L/L_\odot$	Flags
WR18	WN4b	HD 89358	10 17 02.26	−57 54 46.8	0.244±0.049	$3.82^{+0.84}_{-0.60}$	43^{+14}_{-10}	10.34	1.18	0.00	6.07	g
WR19	WC5	LS 3	10 18 04.98	−58 16 26.2	0.219±0.036	$4.33^{+0.78}_{-0.58}$	69^{+16}_{-12}	12.40	1.94	0.00		g
WR19a	WN7:(h)	SMSP 1	10 18 53.38	−58 07 52.9	0.113±0.087	$4.77^{+1.66}_{-1.14}$	63^{+29}_{-20}	12.83	2.87	0.31		g
WR20	WN5o	BS 1	10 19 18.39	−59 09 38.8	0.125±0.025	$6.98^{+1.18}_{-0.93}$	203^{+38}_{-29}	13.54	1.73	0.00	5.77	g
WR20-2	O2If*/WN6	SS215	10 23 23.48	−58 00 20.8	0.147±0.038	$5.53^{+1.15}_{-0.87}$	35^{+11}_{-8}	11.86	1.98	0.00		g
WR20-1	WN7-8	MDM 1	10 23 28.79	−57 46 29.4	0.271±0.164	$2.72^{+1.31}_{-0.77}$	2^{+8}_{-5}	15.90	4.21	0.85		g
WR20a	O3If*/WN6+ O3If*/WN6	SMSP 2	10 23 58.00	−57 45 48.9	0.152±0.049	$5.03^{+1.18}_{-0.87}$	8^{+6}_{-5}	12.25	2.61	0.00		g
WR20b	WN6ha	SMSP 3	10 24 18.39	−57 48 29.7	0.309±0.057	$3.07^{+0.64}_{-0.46}$	1^{+3}_{-2}	12.11	2.74	0.13		g
WR20-3	O2If*/WN6	WR20c	10 25 02.60	−57 21 47.3	0.356±0.128	$2.50^{+1.04}_{-0.61}$	24^{+1}_{-0}	14.85	3.86	0.66		g
WR21a	O2If/WN5	1E 1024.0-5732	10 25 56.49	−57 48 43.5	0.211±0.036	$4.38^{+0.75}_{-0.57}$	2^{+3}_{-2}	11.69	2.28	0.00		g
WR21	WN5o+O4-6	HD 90657	10 26 31.40	−58 38 26.1	0.240±0.034	$3.99^{+0.62}_{-0.48}$	42^{+9}_{-7}	9.49	0.76	0.00		g
WR22	WN7h+O9III-V	HD 92740	10 41 17.50	−59 40 36.8	0.424±0.045	$2.33^{+0.28}_{-0.22}$	13^{+4}_{-3}	6.23	0.33	0.00	6.25	g
WR23	WC6	HD 92809	10 41 38.31	−58 46 18.7	0.386±0.046	$2.55^{+0.34}_{-0.27}$	19^{+0}_{-0}	8.87	0.56	0.00	5.60	g
WR24	WN6ha	HD 93131	10 43 52.24	−60 07 04.0	0.269±0.044	$3.55^{+0.66}_{-0.49}$	46^{+12}_{-9}	6.35	0.13	0.11	6.45	g
WR25	O2.5If*/WN6+O	HD 93162	10 44 10.37	−59 43 11.1	0.505±0.042	$1.97^{+0.18}_{-0.15}$	3^{+2}_{-1}	7.79	0.99	0.00	6.37	g
WR26	WN7b/CE	MS 1	10 44 32.11	−57 50 23.9	0.134±0.023	$6.70^{+1.05}_{-0.83}$	134^{+17}_{-14}	13.17	1.33	0.00	5.68	g
WR27	WC6+a	Ls 4	10 44 38.04	−58 48 28.8	0.375±0.042	$2.62^{+0.33}_{-0.26}$	26^{+0}_{-0}	12.82	2.24	0.00	5.26	g
WR28	WN6(h)+OB?	MS 2	10 48 58.71	−59 03 37.3	0.134±0.039	$5.74^{+1.18}_{-0.90}$	36^{+3}_{-2}	12.06	1.72	0.00	5.94	g
WR29	WN7h+O	MS 3	10 50 46.28	−60 28 41.2	0.148±0.038	$5.64^{+1.21}_{-0.90}$	78^{+21}_{-15}	11.90	1.48	0.00		g
WR30	WC6+O6-8	HD 94305	10 51 05.99	−62 17 01.6	0.185±0.034	$5.09^{+0.99}_{-0.74}$	210^{+45}_{-33}	11.16	0.69	0.00		g

WR Number	Spectral Type	Alias	RA J2015	Dec J2015	$\omega \pm \sigma_w$ (mas)	d (kpc)	$\lvert z \rvert$ (pc)	G (mag)	$G_{BP} - G_{RP}$ (mag)	Excess noise	$\log L/L_\odot$	Flags
WR30a	WO4+O5-5.5	MS 4	10 51 38.89	−60 56 34.9	0.113±0.035	$6.72^{+1.40}_{-1.09}$	140^{+33}_{-26}	12.39	1.49	0.00		g
WR31	WN4o+O8V	HD 94546	10 53 44.81	−59 30 46.6	-1.657±0.229	$6.11^{+1.67}_{-1.37}$	22^{+0}_{-0}	10.39	0.77	0.94		n
WR31a	WN11h	He3-519	10 53 59.57	−60 26 44.3	0.071±0.037	$7.35^{+1.45}_{-1.18}$	82^{+20}_{-16}	10.27	1.83	0.00		g
WR31b	WN11h	AG Car	10 56 11.57	−60 27 12.8	0.182±0.037	$4.85^{+0.93}_{-0.70}$	38^{+11}_{-8}	7.32	0.91	0.00		g
WR31c	WC6	SMSP 4	10 57 42.85	−60 34 00.4	0.083±0.052	$6.06^{+1.45}_{-1.11}$	55^{+18}_{-13}	14.06	2.27	0.28		g
WR31-1	O3.5If/WN7	THA 35-II-153	10 59 00.86	−60 08 50.1	0.182±0.046	$4.59^{+0.96}_{-0.72}$	0^{+4}_{-3}	15.61	1.97	0.07		g
WR32	WC5+OB?	MS 5	10 59 52.91	−59 52 43.4	0.128±0.039	$5.77^{+1.15}_{-0.88}$	22^{+0}_{-0}	14.52	1.85	0.13		g
WR33	WC6	HD 95435	11 00 00.71	−57 48 59.2	0.072±0.040	$7.59^{+1.62}_{-1.30}$	272^{+53}_{-43}	11.47	0.47	0.00	5.43	g
WR34	WN5o	Ls 5	11 00 06.45	−61 26 30.1	0.102±0.029	$7.41^{+1.37}_{-1.09}$	159^{+33}_{-26}	13.66	1.66	0.00	5.61	g
WR35	WN6h+OB?	MS 6	11 00 21.84	−61 13 52.4	0.123±0.027	$6.86^{+1.19}_{-0.94}$	121^{+24}_{-19}	13.13	1.64	0.00	5.60	g
WR35a	WN6h+O8.5V	SMSP 5	11 00 24.33	−59 59 35.6	0.131±0.035	$5.84^{+1.09}_{-0.85}$	14^{+1}_{-0}	12.88	1.80	0.00		g
WR35b	WN4b	SMSP 6	11 01 02.08	−60 14 01.0	0.156±0.034	$5.36^{+0.95}_{-0.74}$	2^{+4}_{-3}	13.86	2.01	0.10		g
WR36	WN5-6b+OB?	Ls 6	11 02 32.97	−59 26 20.9	0.156±0.038	$5.43^{+1.15}_{-0.85}$	73^{+11}_{-8}	12.69	1.54	0.00	5.21	g
WR37	WN4b	MS 7	11 05 13.89	−61 20 41.1	0.110±0.035	$6.71^{+1.36}_{-1.06}$	102^{+25}_{-19}	14.14	2.24	0.14		g
WR38	WC4	MS 8	11 05 46.43	−61 13 48.6	0.136±0.033	$6.04^{+1.18}_{-0.90}$	76^{+18}_{-14}	14.63	1.44	0.00	5.86	g
WR38a	WN5o	SMSP 7	11 05 48.95	−61 13 41.3	0.163±0.032	$5.42^{+1.00}_{-0.76}$	65^{+15}_{-12}	14.44	1.94	0.00	5.08	g
WR40	WN8h	HD 96548	11 06 17.20	−65 30 35.3	0.257±0.038	$3.83^{+0.67}_{-0.50}$	301^{+56}_{-42}	7.46	0.52	0.00	5.88	g
WR38b	WC7	SMSP 8	11 06 18.56	−61 14 13.7	0.195±0.055	$4.32^{+1.12}_{-0.78}$	47^{+17}_{-12}	13.74	2.63	0.29		g
WR39	WC7+OB?	MS 9	11 06 18.72	−61 14 18.4	0.008±0.166	$3.84^{+1.72}_{-1.11}$	39^{+27}_{-17}	12.62	2.49	0.57		e
WR41	WC5+OB?	Ls 7	11 07 54.06	−61 27 40.8	0.146±0.029	$6.01^{+1.06}_{-0.82}$	87^{+19}_{-14}	13.79	1.57	0.00		g
WR42	WC7+O7V	HD 97152	11 10 04.07	−60 58 44.9	0.400±0.058	$2.44^{+0.41}_{-0.31}$	0^{+3}_{-2}	7.92	0.20	0.00		g

WR Number	Spectral Type	Alias	RA J2015	Dec J2015	$\omega \pm \sigma_w$ (mas)	d (kpc)	$\lvert z \rvert$ (pc)	G (mag)	$G_{BP} - G_{RP}$ (mag)	Excess noise	$\log L/L_\odot$	Flags
WR42a	WN5b	SMSP 9	11 12 15.73	−61 05 04.8	0.065±0.061	$5.63^{+1.37}_{-1.05}$	26^{+11}_{-8}	15.28	2.46	0.23		g
WR42b	WN4b	SMSP 10	11 13 03.61	−62 14 18.4	0.068±0.061	$6.33^{+1.70}_{-1.31}$	147^{+45}_{-34}	14.81	2.70	0.31		g
WR42c	WN5o	SMSP 11	11 14 01.47	−61 03 47.7	0.044±0.046	$6.72^{+1.35}_{-1.09}$	24^{+9}_{-7}	14.47	2.50	0.21		e
WR42d	WN5b	SMSP 12	11 14 38.63	−61 11 16.3	0.182±0.141	$3.20^{+1.26}_{-0.83}$	5^{+10}_{-6}	13.65	2.54	0.94		g
WR42-1	O3If*/WN6	WR42e	11 14 45.50	−61 15 00.3	0.196±0.048	$4.34^{+0.94}_{-0.69}$	19^{+8}_{-6}	13.45	2.47	0.28		g
WR43-2	O2If*/WN5	MTT 58	11 15 07.57	−61 16 54.7	0.098±0.042	$6.16^{+1.27}_{-0.99}$	37^{+12}_{-9}	13.77	2.28	0.20		g
WR43-3	O2.5If*/WN6	RFS7	11 15 15.36	−60 51 17.7	0.105±0.032	$6.56^{+1.13}_{-0.91}$	4^{+2}_{-2}	12.26	1.86	0.00		g
WR43-1	WN4b	SMG09 740_21	11 16 03.52	−61 26 58.3	0.542±0.619	$1.34^{+1.45}_{-0.59}$	5^{+16}_{-6}	18.94		1.77		e a
WR44	WN4o+OB?	LSS 2289	11 16 57.83	−59 26 23.8	0.141±0.034	$6.07^{+1.22}_{-0.93}$	154^{+26}_{-20}	12.53	0.78	0.00	5.55	g
WR44a	WN5b	SMSP 13	11 18 43.09	−61 26 35.8	0.147±0.047	$5.06^{+1.12}_{-0.84}$	26^{+10}_{-7}	15.20	2.34	0.19		g
WR44-1	WCE	SMG09 740_16	11 19 43.01	−61 27 12.3	-0.339±0.423	$2.67^{+1.46}_{-0.96}$	2^{+12}_{-8}	16.13		1.51		n e a
WR45	WC6	LSS 2423	11 38 05.08	−62 16 01.9	0.228±0.022	$4.25^{+0.43}_{-0.36}$	23^{+4}_{-3}	13.24	1.92	0.00	5.43	g
WR45-1	WN9-10h	HDM 1	11 42 37.64	−62 41 19.2	0.050±0.093	$4.88^{+1.58}_{-1.12}$	52^{+23}_{-16}	15.58	3.32	0.44		e
WR45-2	WN5	SMG09 768_6	11 46 06.64	−62 47 12.7	0.173±0.062	$4.39^{+1.21}_{-0.84}$	44^{+18}_{-12}	15.46	2.62	0.31		g
WR45a	WN5o	SMSNPL 1	11 46 18.14	−61 24 41.5	0.197±0.087	$3.79^{+1.27}_{-0.84}$	52^{+10}_{-7}	15.12	2.42	0.47		g
WR45b	WN4b	SMSNPL 2	11 48 46.02	−62 23 02.6	-0.024±0.068	$5.95^{+1.34}_{-1.07}$	19^{+9}_{-7}	15.09	2.74	0.33		n e
WR45-3	WN5b	SMG09 772_17	11 50 04.23	−62 52 15.4	-0.171±0.128	$5.21^{+1.68}_{-1.26}$	54^{+24}_{-18}	16.82	3.41	0.71		n
WR45-4	WN6	SMG09 773_3	11 55 52.10	−62 45 02.3	0.020±0.068	$5.65^{+1.36}_{-1.06}$	34^{+13}_{-10}	15.54	3.00	0.35		e
WR45-5	WN7/Of	VVV CL009-6	11 56 03.75	−63 18 54.4	0.099±0.046	$6.27^{+1.48}_{-1.13}$	100^{+28}_{-21}	13.60	2.37	0.22		g
WR45c	WN5o	SMSNPL 3	11 56 04.74	−62 44 05.1	0.130±0.028	$6.14^{+0.97}_{-0.77}$	37^{+9}_{-7}	14.00	1.93	0.00		g
WR46	WN3b pec	HD 104994	12 05 18.71	−62 03 10.1	0.379±0.043	$2.60^{+0.32}_{-0.26}$	36^{+1}_{-1}	10.70	0.19	0.08	5.41	g

WR Number	Spectral Type	Alias	RA J2015	Dec J2015	$\omega \pm \sigma_w$ (mas)	d (kpc)	$\lvert z \rvert$ (pc)	G (mag)	$G_{BP} - G_{RP}$ (mag)	Excess noise	$\log L/L_\odot$	Flags
WR46-1	WN6o	HDM 2	12 06 56.47	−62 38 30.4	0.048±0.083	$4.72^{+1.18}_{-0.91}$	3^{+4}_{-3}	15.07	2.78	0.42		e
WR46-18	WC6-7	RC17 E3	12 08 52.47	−62 50 54.6	0.291±0.470	$1.81^{+1.26}_{-0.71}$	8^{+8}_{-4}	19.38	3.22	2.02		e a
WR46-7	WC5-7	2MASS J12100795-6244194	12 10 07.95	−62 44 19.4	0.009±0.221	$3.06^{+1.21}_{-0.86}$	7^{+5}_{-3}	18.26	4.37	0.96		e
WR46-8	WN6	2MASS J12110256-6257476	12 11 02.55	−62 57 47.6	0.258±0.181	$2.59^{+1.11}_{-0.71}$	0^{+8}_{-5}	17.43	4.33	0.96		g
WR46-16	WN9	RMM11 #5	12 11 54.06	−63 17 03.8	0.247±0.214	$2.47^{+1.26}_{-0.75}$	11^{+16}_{-9}	18.34	2.64	0.79		g
WR46-9	WN5	2MASS J12121681-6246145	12 12 16.80	−62 46 14.6	0.098±0.189	$3.05^{+1.17}_{-0.82}$	8^{+4}_{-3}	17.49	4.54	0.98		e
WR46-17	WN9/OIf+	VVV CL011-2	12 12 41.12	−62 42 30.7	-0.034±0.265	$2.89^{+1.23}_{-0.87}$	12^{+3}_{-2}	16.47	4.05	1.63		n e a
WR46a	WN4o	SMSNPL 4	12 13 02.34	−63 42 25.4	0.072±0.048	$6.73^{+1.56}_{-1.23}$	114^{+31}_{-24}	14.88	2.06	0.12		g
WR46-10	WCE	SMG09 791_12c	12 13 28.27	−62 41 43.0	0.727±0.524	$1.25^{+1.22}_{-0.50}$	17^{+3}_{-1}	19.36	3.41	1.77		a
WR46-2	WN7h	HDM 3	12 13 38.78	−63 08 58.1	0.168±0.088	$3.81^{+1.12}_{-0.80}$	18^{+11}_{-8}	14.63	3.29	0.43		g
WR46-3	O6-7.5If+	KBG2007-4	12 14 31.53	−62 58 54.3	-0.108±0.151	$4.07^{+1.26}_{-0.96}$	8^{+9}_{-6}	15.30	4.51	0.89		n e
WR46-4	Ofpe/WN9	KBG2007-3	12 14 31.71	−62 58 52.1	-0.499±0.411	$2.81^{+1.29}_{-0.92}$	0^{+9}_{-6}	15.81	4.54	2.50		n a
WR46-5	WN6	KBG2007-2	12 14 33.08	−62 58 51.0	-0.041±0.160	$3.73^{+1.24}_{-0.92}$	5^{+8}_{-6}	16.53	4.46	0.83		n e
WR46-6	WN7	KBG2007-1	12 14 33.90	−62 58 48.7	-0.123±0.164	$3.93^{+1.26}_{-0.96}$	7^{+8}_{-6}	16.86	4.31	0.93		n e
WR46-15	WN8	MDM 2	12 15 12.48	−62 46 43.9	-1.846±1.211	$1.99^{+1.32}_{-0.89}$	13^{+4}_{-3}	20.49		4.83		n a
WR46-11	WCE	SMG09 808_14	12 28 41.90	−63 25 46.1	-0.130±0.121	$4.85^{+1.44}_{-1.09}$	35^{+16}_{-12}	16.97	3.49	0.58		n
WR46-12	WN4b	SMG09 808_23	12 28 50.98	−63 17 00.1	0.093±0.194	$3.00^{+1.20}_{-0.83}$	6^{+10}_{-7}	18.04	3.33	0.66		e

WR Number	Spectral Type	Alias	RA J2015	Dec J2015	$\omega \pm \sigma_w$ (mas)	d (kpc)	$\lvert z \rvert$ (pc)	G (mag)	$G_{BP} - G_{RP}$ (mag)	Excess noise	$\log L/L_\odot$	Flags
WR46-13	WC7	SMG09 807_16	12 30 03.86	−62 50 17.1	-0.046±0.174	$3.58^{+1.19}_{-0.90}$	16^{+1}_{-1}	17.84	3.61	0.82		n e
WR46-14	WN5b	SMG09 816_10	12 38 18.75	−63 24 19.7	1.538±0.589	$0.65^{+0.70}_{-0.23}$	14^{+6}_{-2}	17.78	4.00	4.25		a
WR47	WN6o+O5V	HD 311884	12 43 50.99	−63 05 14.8	0.263±0.047	$3.49^{+0.61}_{-0.47}$	6^{+2}_{-1}	10.29	1.44	0.00		g
WR47a	WN8h	SMSNPL 5	12 45 51.24	−64 09 38.0	0.146±0.064	$4.89^{+1.46}_{-1.02}$	89^{+33}_{-23}	13.96	2.75	0.32		g
WR47-1	WN6o	HDM 4	12 46 16.13	−62 57 23.5	0.139±0.123	$3.45^{+1.06}_{-0.78}$	15^{+1}_{-1}	16.49	3.56	0.63		g
WR47b	WN9h	SMSNPL 6	12 48 07.60	−63 38 39.8	-0.075±0.089	$5.63^{+1.49}_{-1.16}$	55^{+20}_{-15}	14.22	3.34	0.50		n e
WR47-5	WN6(h)	RC17 B13	12 50 48.96	−62 24 39.8	-0.271±0.345	$2.96^{+1.55}_{-1.01}$	44^{+12}_{-8}	19.07	4.33	1.27		n e a
WR47c	WC5	SMSNPL 7	12 52 55.67	−63 46 38.0	0.058±0.044	$6.81^{+1.43}_{-1.15}$	86^{+22}_{-18}	14.22	2.35	0.19		g
WR47-2	WC5-6	SMG09 832_25	12 55 44.24	−63 35 50.1	0.053±0.158	$3.45^{+1.30}_{-0.90}$	23^{+16}_{-11}	17.77	4.48	0.76		e
WR47-3	WC5-6	SMG09 856_13c	13 03 11.06	−63 42 16.4	0.620±0.349	$1.41^{+1.07}_{-0.48}$	0^{+16}_{-7}	18.22	4.11	2.12		a
WR48	WC6(+O9.5/B0Iab)	theta Mus	13 08 07.14	−65 18 21.7	0.388±0.128	$2.39^{+1.23}_{-0.62}$	83^{+53}_{-26}	5.58	0.00	0.45		g
WR48-1	WC7	HDM 5	13 10 12.06	−62 39 06.6	0.250±0.125	$2.93^{+1.02}_{-0.68}$	28^{+2}_{-1}	15.13	3.58	0.55		g
WR48b	WC9d	SMSNPL 8	13 11 27.69	−63 45 59.9	0.141±0.051	$5.12^{+1.25}_{-0.92}$	66^{+21}_{-15}	14.15	2.50	0.25		g
WR48-6	WN9	MDM11 3	13 12 09.05	−62 43 26.7	0.043±0.210	$3.02^{+1.16}_{-0.83}$	23^{+1}_{-0}	16.32		1.25		e a
WR48-10	WN9h	DCT12 D1-2	13 12 24.97	−62 42 00.2	0.321±0.144	$2.52^{+0.95}_{-0.61}$	24^{+1}_{-0}	14.39	4.40	0.76		g
WR48-7	WN8	MDM11 5	13 12 25.46	−62 44 41.8	0.285±0.154	$2.61^{+0.99}_{-0.65}$	22^{+0}_{-0}	15.06	4.77	0.83		g
WR48-4	WC6	SMG09 845_35	13 12 27.65	−62 44 22.0	0.255±0.208	$2.48^{+1.08}_{-0.70}$	22^{+0}_{-0}	18.08	4.39	1.02		a
WR48-8	WN9	MDM11 7	13 12 28.49	−62 41 51.0	0.226±0.103	$3.22^{+0.97}_{-0.68}$	25^{+1}_{-0}	13.98	3.75	0.59		g
WR48-9	WN9h	MDM11 8	13 12 28.55	−62 41 43.8	0.318±0.092	$2.78^{+0.78}_{-0.53}$	24^{+1}_{-0}	12.61	3.68	0.31		g
WR48a	WC8ed+?	D83 1	13 12 39.59	−62 42 55.9	0.374±0.159	$2.27^{+0.92}_{-0.57}$	23^{+0}_{-0}	13.83	4.62	0.84		g
WR48-5	WN6b	SMG09 847_8	13 12 45.33	−63 05 52.0	0.099±0.456	$2.06^{+1.16}_{-0.76}$	9^{+6}_{-4}	19.43	4.00	2.03		e a

WR Number	Spectral Type	Alias	RA J2015	Dec J2015	$\omega \pm \sigma_w$ (mas)	d (kpc)	$\lvert z \rvert$ (pc)	G (mag)	$G_{BP} - G_{RP}$ (mag)	Excess noise	$\log L/L_\odot$	Flags
WR48c	WN3h/C4	SMSNPL 9	13 12 52.36	−63 23 45.9	0.371±0.029	$2.67^{+0.22}_{-0.19}$	8^{+2}_{-2}	13.71	0.91	0.00		g
WR48-2	WC7-8	MV09 J13125770-6240599	13 12 57.69	−62 40 59.9	0.175±0.127	$3.25^{+1.07}_{-0.76}$	25^{+1}_{-1}	15.05	3.86	0.67		g
WR49	WN5(h)	LSS 2979	13 13 51.30	−65 18 08.9	0.089±0.025	$8.35^{+1.44}_{-1.17}$	348^{+63}_{-51}	13.24	1.02	0.00	5.24	g
WR50	WC7+OB	V864 Cen	13 18 01.03	−62 26 04.8	0.273±0.041	$3.48^{+0.54}_{-0.42}$	37^{+2}_{-2}	11.52	1.34	0.00		g
WR51	WN4o	MR45	13 18 23.35	−62 28 21.2	0.260±0.033	$3.67^{+0.48}_{-0.39}$	35^{+2}_{-1}	13.61	2.00	0.06	5.07	g
WR52	WC4	HD 115473	13 18 27.99	−58 08 13.7	0.572±0.047	$1.75^{+0.16}_{-0.13}$	159^{+12}_{-10}	9.05	0.27	0.00		g
WR52-2	WN6	SMG09 858_26	13 28 15.87	−62 06 23.6	0.284±0.160	$2.63^{+1.20}_{-0.71}$	41^{+9}_{-5}	17.51	4.31	0.86		g
WR53	WC8d	HD 117297	13 30 53.24	−62 04 51.9	0.221±0.040	$4.14^{+0.74}_{-0.56}$	52^{+5}_{-4}	10.26	0.97	0.00	5.47	g
WR54	WN5o	MR 48	13 32 43.74	−65 01 27.9	0.128±0.035	$6.52^{+1.37}_{-1.05}$	263^{+59}_{-45}	12.35	1.04	0.00	5.58	g
WR55	WN7o	HD 117688	13 33 30.10	−62 19 01.2	0.315±0.054	$3.00^{+0.55}_{-0.41}$	29^{+1}_{-1}	10.23	0.94	0.00	5.35	g
WR56	WC7	Ls 8	13 33 45.37	−64 07 31.3	0.072±0.026	$8.67^{+1.46}_{-1.20}$	226^{+41}_{-34}	13.18	0.91	0.00	5.13	g
WR56a	WN6o	SMSNPL 10	13 41 14.01	−60 53 54.0	0.208±0.055	$4.36^{+1.20}_{-0.82}$	126^{+29}_{-19}	14.13	2.37	0.22		g
WR57	WC8	HD 119078	13 43 16.35	−67 24 05.1	0.160±0.049	$5.50^{+1.49}_{-1.06}$	461^{+131}_{-93}	9.52	0.24	0.12	5.69	g
WR58	WN4b/CE	MR 51	13 49 04.47	−65 41 56.2	0.148±0.041	$5.88^{+1.42}_{-1.04}$	336^{+86}_{-63}	12.53	0.83	0.00	4.89	g
WR59	WC9d	LSS 3164	13 49 32.55	−61 31 42.3	0.262±0.047	$3.57^{+0.69}_{-0.51}$	56^{+6}_{-5}	12.04	2.59	0.12	5.72	g
WR59-2	WC5-6	SMG09 885_11	13 54 13.43	−61 50 01.9	0.330±0.573	$1.65^{+1.25}_{-0.68}$	24^{+3}_{-1}	19.32	3.99	2.02		e a
WR60	WC8	HD 121194	13 55 48.44	−61 09 48.5	0.271±0.045	$3.51^{+0.65}_{-0.48}$	66^{+8}_{-6}	11.43	2.10	0.12	5.77	g
WR60-7	WC7-8	RC17 B51	14 02 33.42	−61 20 27.4	0.035±0.479	$2.06^{+1.38}_{-0.80}$	33^{+8}_{-5}	19.33	3.79	2.21		e a
WR60-5	WC7	WR60a	14 06 03.60	−60 27 29.6	0.373±0.125	$2.44^{+1.13}_{-0.61}$	67^{+21}_{-11}	14.62	3.44	0.49		g
WR60-2	WC8	SMG09 903_15c	14 12 36.53	−61 45 32.8	-2.232±1.175	$2.09^{+1.16}_{-0.85}$	6^{+7}_{-5}	20.26	3.80	6.58		n a

WR Number	Spectral Type	Alias	RA J2015	Dec J2015	$\omega \pm \sigma_w$ (mas)	d (kpc)	$\lvert z \rvert$ (pc)	G (mag)	$G_{BP} - G_{RP}$ (mag)	Excess noise	$\log L/L_\odot$	Flags
WR61	WN5o	MR 53	14 13 03.51	−65 26 52.8	0.168±0.039	$5.49^{+1.25}_{-0.91}$	353^{+85}_{-62}	12.03	0.67	0.00	4.99	g
WR61-3	WC9	MDM11 13	14 20 30.74	−60 48 22.2	1.015±1.116	$0.91^{+1.40}_{-0.46}$	24^{+5}_{-1}	20.50	3.11	3.72		e a
WR61-1	WN6	2MASS J14212314-6018041	14 21 23.13	−60 18 04.1	-0.022±0.174	$3.88^{+1.65}_{-1.12}$	64^{+18}_{-12}	16.93	5.21	0.91		n e
WR62	WN6b	NS 2	14 31 06.13	−61 20 59.7	0.189±0.049	$4.28^{+0.89}_{-0.66}$	35^{+11}_{-8}	12.40	2.62	0.09	5.82	g
WR62a	WN6o	SMSNPL 11	14 32 37.69	−61 29 54.2	0.262±0.050	$3.50^{+0.70}_{-0.51}$	37^{+11}_{-8}	12.22	2.02	0.00		g
WR62-2	WN8-9h	VVV CL041-8	14 46 26.37	−59 23 29.2	0.380±0.177	$2.20^{+0.98}_{-0.58}$	31^{+4}_{-2}	13.07	4.46	0.88		g
WR62b	WN5o	SMSNPL 12	14 46 40.84	−61 06 57.1	0.108±0.064	$5.50^{+1.59}_{-1.17}$	103^{+35}_{-26}	15.24	2.58	0.26		g
WR62-1	WN7-8h	AX J144701-5919	14 46 53.56	−59 19 38.3	0.199±0.290	$2.30^{+1.23}_{-0.75}$	33^{+6}_{-4}	14.65	5.79	1.25		e a
WR64	WC7	BS 3	14 56 55.18	−55 50 58.6	0.062±0.040	$7.98^{+1.67}_{-1.37}$	413^{+82}_{-67}	14.31	1.40	0.00	5.07	g
WR64-3	WN6o	RC17 B87	15 02 46.14	−58 27 06.8	-0.049±0.256	$2.90^{+1.11}_{-0.83}$	28^{+2}_{-2}	17.68	4.60	1.19		n e a
WR64-4	WN6o+OB	RC17 B88	15 04 11.16	−58 27 21.7	0.613±0.285	$1.54^{+0.91}_{-0.47}$	22^{+0}_{-0}	17.08	5.22	1.60		a
WR64-5	WN6o	RC17 B91	15 07 31.84	−58 15 09.9	0.361±0.421	$1.83^{+1.09}_{-0.66}$	21^{+0}_{-0}	19.23	3.69	1.38		e a
WR65	WC9d+OB?	Wra 1297	15 13 41.70	−59 11 45.0	0.292±0.066	$3.13^{+0.80}_{-0.54}$	44^{+16}_{-11}	12.18	2.92	0.20	5.82	g
WR66	WN8(h)	HD 134877	15 14 57.71	−59 50 30.2	-21.626±1.436	$5.18^{+2.08}_{-1.81}$	144^{+66}_{-57}	10.91	1.46	2.11		n a
WR67	WN6o	MR 55	15 15 32.62	−59 02 30.7	0.426±0.085	$2.23^{+0.54}_{-0.37}$	25^{+11}_{-7}	11.05	1.49	0.00	5.05	g
WR67-3	WN10	G321.0331-0.4274	15 15 39.42	−58 08 16.1	0.261±0.106	$2.93^{+0.79}_{-0.58}$	1^{+5}_{-4}	13.47	3.44	0.39		g
WR67-1	WN6h	WR67a	15 16 36.95	−58 09 58.8	0.135±0.120	$3.36^{+0.92}_{-0.70}$	9^{+8}_{-6}	13.45	3.01	0.55		g
WR67-2	WC7	WR67b	15 17 46.29	−57 56 59.3	0.208±0.338	$2.17^{+1.00}_{-0.69}$	5^{+7}_{-5}	15.41	4.42	1.45		e a
WR68	WC7	BS 4	15 18 20.75	−59 38 17.4	0.188±0.041	$4.93^{+1.12}_{-0.81}$	141^{+36}_{-26}	12.53	2.00	0.00	5.71	g

WR Number	Spectral Type	Alias	RA J2015	Dec J2015	$\omega \pm \sigma_w$ (mas)	d (kpc)	$\lvert z \rvert$ (pc)	G (mag)	$G_{BP} - G_{RP}$ (mag)	Excess noise	$\log L/L_\odot$	Flags
WR68-1	WN4b	SMG09 979_11	15 20 35.91	−57 27 12.0	-3.509±2.036	$1.88^{+1.10}_{-0.85}$	14^{+3}_{-2}	20.74	2.44	5.36		n a
WR68a	WN6o	SMSNPL 13	15 23 16.60	−57 44 19.9	0.154±0.073	$3.97^{+0.92}_{-0.70}$	22^{+10}_{-7}	12.69	2.69	0.13		g
WR69	WC9d+OB	HD 136488	15 24 11.30	−62 40 37.6	0.285±0.043	$3.48^{+0.64}_{-0.47}$	271^{+53}_{-39}	9.01	0.74	0.00	5.32	g
WR70	WC9vd+B0I	HD 137603	15 29 44.68	−58 34 51.3	0.326±0.042	$3.01^{+0.44}_{-0.34}$	74^{+14}_{-10}	9.20	1.69	0.00		g
WR70-1	WN7	MV09 J15352652-5604123	15 35 26.52	−56 04 12.4	0.128±0.605	$1.93^{+1.04}_{-0.74}$	14^{+3}_{-2}	19.93	3.47	2.01		e a
WR70-13	WC8d	RC17 B105	15 37 46.50	−56 08 45.5	-0.365±0.348	$2.78^{+0.98}_{-0.79}$	0^{+7}_{-6}	18.57	4.24	1.57		n a
WR70-3	WC7	SMG09 1011_24	15 43 04.66	−55 11 12.8	0.337±0.174	$2.36^{+0.84}_{-0.58}$	15^{+1}_{-1}	15.34	4.22	0.83		g
WR70-5	WC9	WM10 11b	15 48 42.10	−55 07 54.3	0.469±0.168	$1.95^{+0.75}_{-0.47}$	1^{+7}_{-4}	16.44		0.83		g
WR70a	WN6o	SMSNPL 14	15 59 25.28	−54 12 42.8	0.123±0.090	$3.99^{+1.21}_{-0.84}$	38^{+18}_{-12}	14.42	2.94	0.35		g
WR70-2	WN5b	2MASS J15595671-5159299	15 59 56.71	−51 59 30.0	-0.131±0.236	$3.66^{+1.84}_{-1.17}$	70^{+25}_{-15}	16.76	5.82	1.21		n e a
WR70-11	WN7	1042-25L	16 00 25.26	−52 03 29.6	-0.360±0.233	$4.17^{+1.77}_{-1.24}$	70^{+21}_{-14}	17.82	5.12	1.10		n a
WR70-16	WC7d+WN or WN/Cd+O	2XMM J160050.7-514245	16 00 50.49	−51 42 45.3	1.813±0.410	$0.55^{+0.20}_{-0.12}$	29^{+3}_{-1}	15.44		1.24		a
WR71	WN6o	HD 143414	16 03 49.33	−62 41 36.1	0.313±0.052	$3.19^{+0.67}_{-0.48}$	401^{+88}_{-63}	9.89	0.25	0.13	5.07	g
WR71-1	WN9	1040-B6C	16 04 03.78	−53 10 44.5	-0.094±0.307	$2.63^{+0.98}_{-0.75}$	3^{+8}_{-6}	18.85	3.44	1.06		n e a
WR72-5	WN6o	RC17 B132	16 07 01.46	−51 58 18.6	-0.204±0.378	$2.57^{+1.02}_{-0.79}$	24^{+1}_{-1}	18.69	4.43	1.56		n e a
WR72-1	WC9	HDM6	16 11 39.26	−52 05 45.9	0.211±0.122	$3.00^{+0.83}_{-0.62}$	5^{+7}_{-5}	14.26	3.89	0.50		g
WR72-2	WC8	SMG09 1053_27	16 11 43.70	−51 10 16.7	-1.296±0.544	$2.79^{+1.11}_{-0.87}$	28^{+3}_{-2}	16.20	6.01	2.92		n a
WR73	WC9d	NS 3	16 12 37.47	−46 37 36.9	0.051±0.067	$6.81^{+1.85}_{-1.47}$	422^{+109}_{-86}	13.58	2.29	0.23		e

WR Number	Spectral Type	Alias	RA J2015	Dec J2015	$\omega \pm \sigma_w$ (mas)	d (kpc)	$\lvert z \rvert$ (pc)	G (mag)	$G_{BP} - G_{RP}$ (mag)	Excess noise	$\log L/L_\odot$	Flags
WR74	WN7o	BP 1	16 16 13.79	−51 36 41.8	0.166±0.065	$3.98^{+0.86}_{-0.66}$	23^{+9}_{-7}	12.60	2.22	0.00	5.41	g
WR75	WN6b	HD 147419	16 24 26.22	−51 32 06.1	0.282±0.057	$3.32^{+0.80}_{-0.55}$	64^{+20}_{-14}	10.43	1.23	0.00	5.55	g
WR75-1	WC8	SMG09 1081_21	16 24 58.87	−48 56 52.5	-0.343±0.598	$2.17^{+1.19}_{-0.84}$	31^{+5}_{-3}	19.31	4.08	2.27		n e a
WR75aa	WC9d	HBD 1	16 26 20.14	−45 59 45.8	0.165±0.075	$4.88^{+1.63}_{-1.14}$	205^{+61}_{-42}	15.25	2.43	0.21		g
WR75a	WC9	SMSNPL 15	16 26 37.23	−50 19 23.0	0.215±0.109	$3.14^{+1.07}_{-0.70}$	27^{+16}_{-10}	13.62	3.15	0.49		g
WR75b	WC9	SMSNPL 16	16 28 17.23	−48 17 40.8	0.578±0.121	$1.69^{+0.45}_{-0.30}$	30^{+2}_{-1}	13.56	3.51	0.53		g
WR75-21	WC7:	SFZ12 1095-189L	16 33 48.13	−47 52 52.8	0.795±0.041	$1.26^{+0.07}_{-0.06}$	19^{+0}_{-0}	13.24	2.15	0.13		g
WR75ab	WN7h	PCG1	16 33 48.73	−49 28 44.1	0.180±0.090	$3.79^{+1.47}_{-0.88}$	54^{+29}_{-17}	13.56	2.81	0.36		g
WR75c	WC9	HBD 2	16 34 03.58	−43 40 24.9	0.040±0.061	$7.15^{+1.78}_{-1.45}$	365^{+86}_{-69}	14.20	2.22	0.14		e
WR75d	WC9	HBD 3	16 34 17.44	−46 08 53.1	0.217±0.111	$3.57^{+1.61}_{-0.94}$	86^{+29}_{-17}	14.26	3.21	0.46		g
WR75-23	WC9	SFZ12 1106-31L	16 37 23.98	−46 26 28.8	0.241±0.103	$3.17^{+1.08}_{-0.70}$	46^{+8}_{-5}	13.80	3.31	0.42		g
WR76	WC9d	LSS 3693	16 40 05.25	−45 41 12.7	0.122±0.133	$3.65^{+1.55}_{-0.96}$	60^{+16}_{-10}	13.06	3.19	0.54		e
WR77	WC8+OB	He3-1239	16 41 19.25	−48 01 59.2	0.334±0.052	$2.85^{+0.50}_{-0.37}$	33^{+9}_{-7}	12.36	2.02	0.00		g
WR77-5	WN6	SFZ12 1115-197L	16 43 40.37	−45 57 57.7	0.395±0.183	$2.18^{+0.80}_{-0.55}$	19^{+0}_{-0}	14.69	3.77	0.58		g
WR77-1	WN7b	2MASS J16441069-4524246	16 44 10.68	−45 24 24.6	0.148±0.211	$2.71^{+1.08}_{-0.75}$	33^{+5}_{-3}	14.79	4.46	0.75		e
WR77aa	WC9d	HBD 4	16 46 46.28	−45 47 58.3	0.274±0.171	$2.53^{+0.80}_{-0.60}$	6^{+4}_{-3}	14.98	4.52	0.61		g
WR77-2	WN7	2MASS J16465342-4535590	16 46 53.42	−45 35 59.0	0.149±0.209	$2.66^{+0.84}_{-0.66}$	10^{+3}_{-2}	16.11	5.31	0.88		e
WR77a	WN6o		16 46 55.53	−45 51 34.5	0.103±0.212	$2.72^{+0.86}_{-0.67}$	2^{+5}_{-4}	16.82	4.61	0.89		e

WR Number	Spectral Type	Alias	RA J2015	Dec J2015	$\omega \pm \sigma_w$ (mas)	d (kpc)	$\lvert z \rvert$ (pc)	G (mag)	$G_{BP} - G_{RP}$ (mag)	Excess noise	$\log L/L_\odot$	Flags
WR77b	WC9d		16 46 59.91	−45 55 25.7	-0.250±0.258	$3.00^{+0.91}_{-0.74}$	2^{+7}_{-5}	15.23		1.11		n e a
WR77c	WN8o		16 47 00.88	−45 51 20.6	0.028±0.196	$2.94^{+0.87}_{-0.69}$	0^{+6}_{-4}	16.32	5.48	0.88		e
WR77d	WN7o	Wd1-57c	16 47 01.59	−45 51 45.3	0.121±0.216	$2.67^{+0.86}_{-0.67}$	1^{+6}_{-4}	16.23	4.89	1.00		e
WR77f	WN10-11h	Wd1-5	16 47 02.97	−45 50 19.8	0.268±0.217	$2.38^{+0.84}_{-0.63}$	4^{+5}_{-4}	14.46	4.64	0.74		g
WR77h	WN8o		16 47 03.80	−45 50 38.8	0.563±0.227	$1.72^{+0.78}_{-0.46}$	8^{+5}_{-3}	15.80		0.96		g
WR77i	WC9d	Wd1-66	16 47 03.96	−45 51 37.7	0.315±0.217	$2.28^{+0.84}_{-0.61}$	4^{+6}_{-4}	15.98	5.38	0.98		g
WR77j	WN7o		16 47 04.01	−45 51 25.1	-0.522±0.269	$3.21^{+0.91}_{-0.75}$	2^{+6}_{-5}	16.75	4.88	1.30		n a
WR77m	WC9d		16 47 04.41	−45 51 03.7	-0.002±0.277	$2.62^{+0.89}_{-0.71}$	2^{+6}_{-4}	16.80	5.17	1.33		n e a
WR77n	WC9d	Wd1-241	16 47 05.21	−45 52 25.0	0.122±0.204	$2.72^{+0.86}_{-0.67}$	0^{+6}_{-4}	14.83	4.64	0.86		e
WR77o	WN7o	Wd1-14c	16 47 05.37	−45 51 04.9	-0.065±0.189	$3.15^{+0.88}_{-0.70}$	1^{+6}_{-5}	16.48	5.75	0.60		n e
WR77p	WC9		16 47 06.06	−45 52 08.3	3.936±0.712	$0.30^{+0.07}_{-0.00}$	18^{+0}_{-0}	15.01	4.73	3.03		a
WR77q	WN5o		16 47 06.10	−45 50 22.5	0.188±0.324	$2.25^{+0.90}_{-0.69}$	5^{+6}_{-4}	16.94		0.84		e
WR77r	WN7o		16 47 06.25	−45 51 26.5	-0.583±0.308	$3.06^{+0.91}_{-0.75}$	1^{+6}_{-5}	17.53	4.25	1.17		n a
WR77s	WN6o	GDTB 1	16 47 06.54	−45 50 39.1	0.473±0.210	$1.93^{+0.79}_{-0.51}$	7^{+5}_{-3}	16.26	4.88	0.96		g
WR77sa	WN6h	GDTB 3	16 47 07.62	−45 49 22.1	0.023±0.294	$2.54^{+0.89}_{-0.71}$	3^{+6}_{-4}	18.15	4.91	1.15		e a
WR77sb	WN6o		16 47 07.66	−45 52 36.0	0.228±0.200	$2.52^{+0.85}_{-0.63}$	1^{+6}_{-4}	16.07	5.07	0.87		g
WR77sc	WN7b	Wd1-72	16 47 08.35	−45 50 45.5	0.095±0.224	$2.68^{+0.87}_{-0.68}$	1^{+6}_{-4}	15.84	5.44	0.84		e
WR77sd	WN5o	GDTB 2	16 47 14.14	−45 48 32.0	0.547±0.291	$1.72^{+0.87}_{-0.53}$	8^{+6}_{-3}	18.11	3.87	1.15		a
WR77-3	WN6	MDM11 30	16 47 46.03	−45 59 04.9	-0.019±0.256	$2.70^{+0.97}_{-0.73}$	6^{+9}_{-7}	16.84	6.02	1.13		n e a
WR77t	WC9d	HBD 5	16 50 57.63	−43 40 27.8	0.234±0.179	$2.68^{+1.22}_{-0.75}$	42^{+9}_{-6}	15.27	4.50	0.76		g
WR77-6	WN6b	SFZ12 1138-133L	16 51 19.33	−43 26 55.3	-1.068±0.963	$1.96^{+1.57}_{-0.92}$	39^{+15}_{-8}	19.99	3.06	3.11		n a

WR Number	Spectral Type	Alias	RA J2015	Dec J2015	$\omega \pm \sigma_w$ (mas)	d (kpc)	$\lvert z \rvert$ (pc)	G (mag)	$G_{BP} - G_{RP}$ (mag)	Excess noise	$\log L/L_\odot$	Flags
WR78	WN7h	HD 151932	16 52 19.25	−41 51 16.3	0.797±0.084	$1.25^{+0.15}_{-0.12}$	52^{+3}_{-3}	6.28	0.60	0.00	5.79	g
WR79	WC7+O5-8	HD 152270	16 54 19.70	−41 49 11.6	0.729±0.057	$1.37^{+0.12}_{-0.10}$	48^{+2}_{-2}	6.54	0.38	0.00		g
WR79a	WN9ha	HD 152408	16 54 58.50	−41 09 03.1	0.475±0.141	$2.02^{+0.98}_{-0.51}$	73^{+25}_{-13}	5.67	0.36	0.33		g
WR79b	WN9ha	HD 152386	16 55 06.45	−44 59 21.4	-2.210±0.312	$5.32^{+1.65}_{-1.40}$	66^{+27}_{-22}	7.92	0.85	0.67		n
WR80	WC9d	Wra 1581	16 59 02.19	−45 43 10.1	0.249±0.098	$3.50^{+1.59}_{-0.90}$	97^{+53}_{-30}	13.27	2.70	0.30	5.16	g
WR81	WC9	He3-1316	17 02 40.38	−45 59 15.5	0.467±0.073	$2.11^{+0.42}_{-0.30}$	74^{+18}_{-13}	11.07	2.32	0.12	5.24	g
WR82	WN7(h)	Ls 11	17 04 04.63	−45 12 15.1	0.258±0.055	$3.74^{+0.98}_{-0.66}$	130^{+39}_{-26}	11.59	1.53	0.00	5.25	g
WR82-2	WC9	1178-66B	17 07 23.95	−39 19 54.5	0.269±0.357	$2.02^{+1.65}_{-0.79}$	46^{+21}_{-10}	18.51	5.03	1.27		e a
WR83	WN5o	He 3-1344	17 10 54.63	−46 36 00.6	0.257±0.059	$3.80^{+1.10}_{-0.72}$	250^{+78}_{-51}	12.07	1.27	0.00		g
WR83-1	WC6:	SFZ12 1179-129L	17 11 00.81	−39 49 31.4	-0.150±1.713	$1.75^{+1.01}_{-0.88}$	17^{+2}_{-1}	20.46	2.63	4.12		n e a
WR84	WN7o	LS 12	17 11 21.70	−39 53 22.0	0.304±0.056	$3.01^{+0.51}_{-0.40}$	9^{+1}_{-1}	12.13	2.05	0.00	5.28	g
WR84-4	WN7ha	SFZ12 1181-211L	17 11 46.13	−39 20 27.8	0.419±0.184	$2.10^{+0.81}_{-0.53}$	22^{+0}_{-0}	15.34	4.24	0.58		g
WR84-11	WN9h	1176-B49	17 12 34.87	−40 37 13.7	-0.860±0.335	$3.27^{+1.43}_{-0.94}$	26^{+20}_{-13}	18.36	4.86	1.16		n a
WR84-9	WN6	VVV CL099-5	17 14 25.40	−38 09 50.5	2.946±1.402	$0.35^{+1.19}_{-0.05}$	22^{+6}_{-0}	20.38		4.87		a
WR84-10	WC8	VVV CL099-7	17 14 25.65	−38 09 53.8	0.179±0.369	$2.13^{+1.17}_{-0.75}$	32^{+6}_{-4}	18.47	4.25	1.55		e a
WR85	WN6h	HD 155603B	17 14 27.12	−39 45 47.1	0.495±0.067	$1.99^{+0.30}_{-0.24}$	0^{+3}_{-2}	10.03	1.13	0.00	5.38	g
WR88	WC9	The 1	17 18 49.73	−33 57 41.4	0.284±0.058	$3.44^{+0.88}_{-0.60}$	142^{+31}_{-21}	11.75	2.15	0.00	5.47	g
WR87	WN7h+abs	LSS 4064	17 18 52.87	−38 50 03.6	0.305±0.072	$2.91^{+0.66}_{-0.47}$	18^{+8}_{-6}	10.88	2.40	0.13	6.10	g
WR89	WN8h+abs	LSS 4065	17 19 00.52	−38 48 51.3	0.297±0.079	$2.90^{+0.72}_{-0.51}$	18^{+9}_{-6}	10.11	2.19	0.00	6.21	g
WR90	WC7	HD 156385	17 19 29.90	−45 38 23.9	0.871±0.073	$1.15^{+0.11}_{-0.09}$	74^{+8}_{-7}	6.75	0.27	0.06	5.55	g
WR91	WN7b	StSa 1	17 20 22.02	−38 56 48.4	0.155±0.087	$4.04^{+1.52}_{-0.92}$	55^{+28}_{-17}	13.24	3.03	0.31	5.70	g

WR Number	Spectral Type	Alias	RA J2015	Dec J2015	$\omega \pm \sigma_w$ (mas)	d (kpc)	$\lvert z \rvert$ (pc)	G (mag)	$G_{BP} - G_{RP}$ (mag)	Excess noise	$\log L/L_\odot$	Flags
WR93	WC7+O7-9	HD 157504	17 25 08.85	−34 11 12.6	0.565±0.053	$1.76^{+0.19}_{-0.15}$	46^{+2}_{-2}	9.84	2.14	0.00		g
WR92	WC9	HD 157451	17 25 23.28	−43 29 31.5	0.257±0.067	$3.78^{+1.25}_{-0.79}$	270^{+96}_{-60}	10.12	0.62	0.00	4.93	g
WR93a	WN6h	Th3-28	17 30 56.80	−26 59 11.0	0.117±0.177	$4.41^{+2.15}_{-1.49}$	311^{+141}_{-98}	17.58	2.35	0.24		e
WR93b	WO3	DBU 1	17 32 03.31	−35 04 32.7	0.403±0.099	$2.29^{+0.61}_{-0.42}$	12^{+8}_{-6}	14.58	2.06	0.24		g
WR94	WN5o	HD 158860	17 33 07.07	−33 38 23.4	1.052±0.066	$0.95^{+0.06}_{-0.06}$	16^{+0}_{-0}	9.87	2.31	0.00	5.52	g
WR95	WC9d	He3-1434	17 36 19.89	−33 26 12.3	0.468±0.085	$2.07^{+0.43}_{-0.31}$	4^{+5}_{-3}	11.98	2.66	0.06	5.19	g
WR96	WC9d	LSS 4265	17 36 24.45	−32 54 31.5	0.342±0.083	$2.64^{+0.58}_{-0.43}$	1^{+4}_{-3}	12.47	2.48	0.00		g
WR97	WN5b+O7	HDE 320102	17 36 53.62	−34 02 36.8	0.454±0.060	$2.15^{+0.32}_{-0.25}$	21^{+6}_{-4}	10.39	1.44	0.00		g
WR98	WN8o/C7	HDE 318016	17 37 13.74	−33 27 56.0	0.500±0.070	$1.96^{+0.31}_{-0.24}$	9^{+4}_{-3}	10.90	2.19	0.00		g
WR98a	WC8-9vd+?	IRAS 17380-3031	17 41 13.04	−30 32 30.4	0.849±0.349	$1.26^{+0.87}_{-0.41}$	20^{+0}_{-0}	15.46	5.64	1.46		a
WR100	WN7b	HDE 318139	17 42 09.76	−32 33 24.9	0.249±0.064	$3.55^{+1.06}_{-0.67}$	57^{+23}_{-14}	11.75	2.21	0.00	5.67	g
WR101	WC8	DA 3	17 45 09.01	−31 50 15.9	0.365±0.153	$2.28^{+1.26}_{-0.63}$	35^{+31}_{-15}	13.19	3.20	0.60		g
WR102	WO2	Sand 4	17 45 47.54	−26 10 26.8	0.376±0.041	$2.64^{+0.33}_{-0.27}$	85^{+8}_{-6}	13.76	1.47	0.00	5.57	g
WR102-19	WN5	SFZ12 1322-220L	17 55 20.21	−24 07 38.4	0.369±0.131	$2.39^{+0.96}_{-0.57}$	45^{+10}_{-5}	16.13	3.81	0.37		g
WR102-20	WC9	SFZ12 1327-25L	17 59 02.85	−24 20 50.7	0.511±1.356	$1.92^{+0.92}_{-0.89}$	12^{+3}_{-3}	20.40		2.98		e a
WR102-25	WN6	KW03-083	17 59 35.60	−30 51 32.5	0.028±0.088	$6.42^{+1.95}_{-1.55}$	380^{+121}_{-96}	15.29	1.66	0.16		e
WR102-21	WN6	SFZ12 1342-208L	17 59 48.22	−22 14 52.3	0.358±0.245	$2.11^{+1.33}_{-0.69}$	44^{+15}_{-7}	16.45	4.50	0.75		g
WR102l	WN8o	SMSNPL 17	18 00 34.33	−22 47 39.9	0.192±0.092	$3.43^{+0.88}_{-0.65}$	34^{+3}_{-2}	12.62	3.20	0.17		g

WR Number	Spectral Type	Alias	RA J2015	Dec J2015	$\omega \pm \sigma_w$ (mas)	d (kpc)	$\lvert z \rvert$ (pc)	G (mag)	$G_{BP} - G_{RP}$ (mag)	Excess noise	$\log L/L_\odot$	Flags
WR103	WC9d+?	HD 164270	18 01 43.15	−32 42 55.2	0.283±0.077	$3.46^{+1.28}_{-0.77}$	274^{+108}_{-65}	8.57	0.62	0.00	5.46	g
WR104	WC9d+B0.5V (+VB)	Ve2-45	18 02 04.12	−23 37 42.2	0.272±0.124	$2.74^{+0.72}_{-0.55}$	2^{+6}_{-4}	11.73	2.85	0.34		g
WR105	WN9h	NS 4	18 02 23.46	−23 34 37.5	0.577±0.088	$1.73^{+0.32}_{-0.23}$	4^{+2}_{-2}	10.60	2.97	0.16	5.89	g
WR105-2	WN8-9	1343-284	18 03 28.36	−22 22 59.0	0.367±0.152	$2.38^{+0.71}_{-0.53}$	14^{+1}_{-1}	14.50	3.58	0.51		g
WR106	WC9d	HDE 313643	18 04 43.66	−21 09 30.6	0.299±0.058	$3.07^{+0.56}_{-0.43}$	31^{+1}_{-1}	11.10	1.95	0.00	5.16	g
WR107	WN8o	DA 1	18 04 46.10	−21 51 27.2	-0.284±0.297	$2.87^{+0.81}_{-0.69}$	12^{+2}_{-1}	12.37	2.40	0.66		n e
WR107a	WC5-7	SMSNPL 18	18 05 11.49	−22 13 24.7	0.235±0.111	$2.95^{+0.70}_{-0.55}$	0^{+5}_{-4}	14.46	2.71	0.25		g
WR108	WN9ha	HDE 313846	18 05 25.73	−23 00 20.4	0.342±0.052	$2.79^{+0.45}_{-0.35}$	20^{+6}_{-5}	9.44	1.37	0.00	5.74	g
WR108-1	WN9	WR1361-1583	18 07 05.16	−20 15 16.7	0.135±0.415	$2.22^{+0.98}_{-0.75}$	26^{+2}_{-2}	19.44	2.92	0.00		e
WR109	WN5h	NS 3	18 07 50.90	−35 10 25.2	0.072±0.061	$6.84^{+1.85}_{-1.45}$	835^{+232}_{-181}	14.44	0.32	0.04		g
WR110	WN5-6b	HD 165688	18 07 56.96	−19 23 56.9	0.633±0.053	$1.58^{+0.15}_{-0.12}$	31^{+0}_{-0}	9.21	1.42	0.00	5.51	g
WR111	WC5	HD 165763	18 08 28.47	−21 15 11.2	0.612±0.097	$1.63^{+0.32}_{-0.23}$	3^{+3}_{-2}	7.49	-0.04	0.16	5.37	g
WR111-1	WN6o	HDM7	18 09 45.06	−20 17 10.4	1.733±0.562	$0.63^{+0.80}_{-0.22}$	16^{+5}_{-1}	18.70	3.56	1.83		a
WR111-9	WC9	1381-19L	18 12 02.42	−18 06 55.3	0.050±0.168	$3.17^{+0.91}_{-0.71}$	30^{+2}_{-2}	13.63	3.60	0.63		e
WR111-2	WN7b	HDM8	18 13 14.20	−17 53 43.5	0.497±0.179	$1.98^{+0.73}_{-0.48}$	21^{+0}_{-0}	14.49	4.37	0.69		g
WR111-4	WN7	MDM11 34	18 13 22.49	−17 53 50.3	0.340±0.199	$2.37^{+0.79}_{-0.60}$	20^{+0}_{-0}	15.18	4.38	0.80		g
WR111-13	WN6b	MCF15 1	18 13 34.82	−18 05 41.5	0.209±0.341	$2.36^{+0.82}_{-0.69}$	14^{+2}_{-1}	15.39	4.60	1.23		e a
WR111-3	WC8	SMG09 1385_24	18 13 42.47	−17 28 12.3	-0.003±0.392	$2.42^{+0.94}_{-0.75}$	26^{+2}_{-1}	16.89	5.83	1.76		n e a
WR111-10	WC7	1389-4AB6	18 14 14.11	−17 21 02.8	0.964±0.462	$1.23^{+1.03}_{-0.46}$	22^{+1}_{-0}	19.49	1.95	0.82		g

WR Number	Spectral Type	Alias	RA J2015	Dec J2015	$\omega \pm \sigma_w$ (mas)	d (kpc)	$\lvert z \rvert$ (pc)	G (mag)	$G_{BP} - G_{RP}$ (mag)	Excess noise	$\log L/L_\odot$	Flags
WR111-12	WC9	THA 34-30	18 14 32.98	−18 25 14.8	0.406±0.160	$2.23^{+0.71}_{-0.51}$	1^{+6}_{-4}	13.26	3.20	0.47		g
WR112	WC9d+OB?	GL 2104	18 16 33.49	−18 58 42.4	-1.384±0.483	$3.16^{+2.06}_{-1.07}$	44^{+42}_{-22}	14.59	4.47	1.34		n a
WR113	WC8d+O8-9IV	HD 168206	18 19 07.36	−11 37 59.2	0.553±0.063	$1.80^{+0.24}_{-0.19}$	75^{+7}_{-5}	8.78	1.22	0.00		g
WR113-1	WN7o	HDM9	18 19 22.19	−16 03 12.5	0.452±0.192	$2.13^{+0.73}_{-0.53}$	6^{+4}_{-3}	12.99	3.20	0.66		g
WR113-2	WC5-6	SMG09 1425_47	18 23 03.43	−13 10 00.5	0.517±0.269	$1.86^{+0.90}_{-0.56}$	26^{+2}_{-1}	14.54	3.20	0.61		g
WR114	WC5+OB?	IC14-17	18 23 16.34	−13 43 26.1	0.479±0.046	$2.09^{+0.22}_{-0.18}$	16^{+0}_{-0}	11.43	1.73	0.00	5.39	g
WR114-2	WC8	SFZ12 1434-43L	18 23 32.32	−12 03 58.7	-1.121±1.222	$1.81^{+1.50}_{-0.90}$	39^{+15}_{-9}	20.04	2.92	3.17		n e a
WR114-1	WN6	HDM10	18 25 00.23	−10 33 23.7	0.295±0.242	$2.38^{+1.65}_{-0.82}$	61^{+28}_{-14}	16.56	4.02	0.61		g
WR115	WN6o	MR 87	18 25 30.01	−14 38 41.0	2.107±0.763	$0.48^{+0.54}_{-0.17}$	12^{+9}_{-3}	10.90	2.13	2.67		a
WR115-1	WN6o	HDM11	18 25 53.09	−13 28 32.3	0.151±0.119	$3.19^{+0.77}_{-0.61}$	11^{+7}_{-6}	13.94	3.10	0.41		g
WR115-2	WN8	SFZ12 1431-34L	18 25 53.62	−12 50 03.2	0.472±0.369	$2.14^{+0.81}_{-0.69}$	10^{+3}_{-3}	17.22	4.68	1.67		a
WR115-3	WN7	MDM11 36	18 26 06.12	−13 04 10.6	0.335±0.089	$2.68^{+0.58}_{-0.45}$	0^{+4}_{-3}	13.27	2.94	0.36		g
WR116	WN8h	AS 306	18 27 04.29	−12 22 52.7	0.402±0.061	$2.44^{+0.39}_{-0.30}$	7^{+2}_{-1}	11.50	2.60	0.00	5.41	g
WR116-1	WC9+OBI	2MASS J18281180-1025424	18 28 11.80	−10 25 42.4	0.243±0.196	$2.58^{+1.00}_{-0.70}$	36^{+6}_{-4}	12.74	3.82	0.35		g
WR116-2	WN5	SMG09 1462_54	18 29 33.84	−08 39 02.2	-0.465±0.764	$2.09^{+1.82}_{-0.97}$	52^{+27}_{-14}	19.69	3.38	2.16		n e a
WR116-3	WN6ha	MDM11 37	18 30 53.20	−10 19 37.2	0.217±0.138	$2.89^{+0.68}_{-0.56}$	11^{+2}_{-1}	14.09	3.18	0.42		g
WR117	WC9d	IC14-22	18 31 02.51	−06 35 49.7	0.236±0.099	$3.66^{+1.45}_{-0.91}$	116^{+37}_{-23}	12.46	2.22	0.00	5.30	g
WR117-1	WN7	XGPS-I J183116-100921	18 31 16.53	−10 09 25.1	0.025±0.128	$3.41^{+0.68}_{-0.59}$	9^{+2}_{-2}	13.12	3.51	0.53		e

WR Number	Spectral Type	Alias	RA J2015	Dec J2015	$\omega \pm \sigma_w$ (mas)	d (kpc)	$\lvert z \rvert$ (pc)	G (mag)	$G_{BP} - G_{RP}$ (mag)	Excess noise	$\log L/L_\odot$	Flags
WR118	WC9d	GL 2179	18 31 42.21	−09 59 16.8	0.155±0.328	$2.49^{+0.78}_{-0.68}$	11^{+2}_{-2}	15.18	5.93	1.53		e a
WR118-4	WC8	SFZ12 1463-7L	18 33 47.63	−09 23 07.9	0.143±0.460	$2.34^{+0.82}_{-0.73}$	4^{+5}_{-4}	18.63	4.63	2.30		e a
WR118-2	WN9	MDI09 Quartet 2	18 36 16.68	−07 04 59.4	0.109±0.372	$2.41^{+0.91}_{-0.74}$	25^{+1}_{-1}	17.86		1.97		e a
WR118-3	WN9	MDI09 Quartet 1	18 36 17.28	−07 05 07.1	1.725±0.784	$0.70^{+1.33}_{-0.28}$	22^{+2}_{-0}	18.09	5.89	4.61		a
WR118-10	WN6	1485-6C4	18 36 55.53	−06 31 02.1	1.904±0.571	$0.55^{+0.50}_{-0.17}$	23^{+2}_{-0}	17.41	4.55	2.77		a
WR118-5	WC9d	MDM11 40	18 37 51.49	−06 08 41.8	-1.535±0.568	$2.87^{+0.98}_{-0.82}$	31^{+3}_{-2}	19.22	4.67	1.81		n a
WR118-6	WN7:	SFZ12 1483-212L	18 38 27.21	−07 10 45.2	-2.154±1.676	$2.29^{+0.87}_{-0.83}$	4^{+6}_{-5}	20.33	2.92	3.72		n a
WR119	WC9d	The 2	18 39 17.90	−10 05 31.0	0.284±0.086	$3.22^{+1.24}_{-0.73}$	87^{+41}_{-24}	11.57	1.54	0.00	4.63	g
WR119-2	WC8	SFZ12 1493-9L	18 39 34.58	−05 44 23.1	0.393±0.363	$2.19^{+0.86}_{-0.70}$	21^{+0}_{-0}	17.55	4.91	1.52		a
WR119-1	WN7o	HDM12	18 40 08.65	−03 29 31.2	-0.040±0.166	$4.27^{+1.63}_{-1.20}$	88^{+26}_{-19}	15.85	3.87	0.58		n e
WR120	WN7o	MR 89	18 41 00.87	−04 26 14.5	0.666±0.193	$1.50^{+0.64}_{-0.36}$	28^{+3}_{-1}	11.22	1.79	0.25	4.87	g
WR120-16	WC8	1514-AA0	18 41 06.81	−02 56 01.3	0.127±0.429	$2.21^{+1.80}_{-0.91}$	57^{+30}_{-15}	18.72	3.74	1.18		e a
WR120-1	WC9	HDM13	18 41 10.70	−04 51 27.1	0.001±0.221	$2.94^{+0.82}_{-0.69}$	23^{+0}_{-0}	15.26	4.00	0.71		e
WR120-11	WC8	SFZ12 1495-32L	18 41 23.35	−05 40 58.2	-1.716±0.726	$2.66^{+0.80}_{-0.73}$	3^{+5}_{-4}	18.48		2.40		n a
WR120-7	WN7	SFZ12 1503-160L	18 41 34.07	−05 04 01.3	-0.408±0.326	$2.93^{+0.77}_{-0.68}$	14^{+1}_{-1}	15.07	4.62	0.93		n
WR120-3	WN9h	2MASS J18420630-0348224	18 42 06.31	−03 48 22.5	1.046±0.759	$1.08^{+1.29}_{-0.49}$	27^{+7}_{-2}	18.68	4.27	2.44		a

WR Number	Spectral Type	Alias	RA J2015	Dec J2015	$\omega \pm \sigma_w$ (mas)	d (kpc)	$\lvert z \rvert$ (pc)	G (mag)	$G_{BP} - G_{RP}$ (mag)	Excess noise	$\log L/L_\odot$	Flags
WR120-4	WN9h	2MASS J18420827-0351029	18 42 08.27	−03 51 03.0	-0.283±0.567	$2.33^{+1.09}_{-0.85}$	33^{+5}_{-4}	18.27	3.90	1.67		n e a
WR120-5	WC8	SCB12 2w02	18 42 08.47	−03 49 35.3	-0.054±0.742	$1.98^{+1.14}_{-0.83}$	31^{+6}_{-4}	18.24	4.72	2.05		n e a
WR120-6	WN6	PN G029.0+00.4	18 42 46.92	−03 13 17.3	0.248±0.101	$3.14^{+0.94}_{-0.66}$	45^{+7}_{-5}	16.78	2.68	0.00		g
WR120-15	WC8	SCB12 2w04	18 43 17.23	−03 08 56.7	-0.115±0.265	$3.01^{+1.11}_{-0.84}$	40^{+7}_{-5}	18.20	4.36	1.04		n e a
WR120-10	WN7	SFZ12 1517-138L	18 43 58.03	−02 45 17.3	0.322±0.135	$2.59^{+0.90}_{-0.60}$	39^{+6}_{-4}	14.12	3.70	0.49		g
WR121	WC9d	AS 320	18 44 13.15	−03 47 57.8	0.448±0.055	$2.23^{+0.30}_{-0.24}$	15^{+0}_{-0}	11.08	2.08	0.00	5.16	g
WR121-15	WN4-5	2MASS J18442065-0236510	18 44 20.66	−02 36 51.2	-0.108±0.269	$2.98^{+1.12}_{-0.85}$	40^{+7}_{-5}	18.03	4.47	1.15		n e a
WR121-12	WN5	1530-8FA	18 46 00.97	−01 14 35.0	-0.027±0.412	$2.40^{+1.45}_{-0.90}$	47^{+16}_{-10}	18.33	4.92	1.26		n e a
WR121-1	WN7h	WM10 52	18 49 27.34	−01 04 20.7	0.097±0.143	$3.19^{+0.73}_{-0.62}$	18^{+0}_{-0}	15.21	3.63	0.54		e
WR121-6	WN5	SFZ12 1536-180L	18 51 10.76	−01 30 03.5	0.288±0.098	$2.86^{+0.69}_{-0.52}$	10^{+7}_{-5}	13.98	2.95	0.37		g
WR122	WN	NaSt1	18 52 17.55	+00 59 44.3	0.303±0.063	$3.03^{+0.60}_{-0.45}$	34^{+2}_{-2}	13.18	2.38	0.28		g
WR122-2	WN9	MDM11 51	18 52 43.69	+00 08 41.6	0.227±1.115	$2.21^{+0.89}_{-0.85}$	12^{+3}_{-3}	19.63	3.82	2.97		e a
WR122-3	WN6	MDM11 52	18 54 03.12	+01 24 50.8	-0.300±0.593	$2.41^{+0.93}_{-0.80}$	23^{+1}_{-0}	19.48	3.78	1.62		n e a
WR122-1	WC8	IPHAS J190015.86+000517.3	19 00 15.86	+00 05 17.3	0.170±0.077	$4.63^{+1.55}_{-1.08}$	134^{+52}_{-36}	14.90	2.14	0.24		g
WR122-15	WN6	1602-9AF	19 02 42.35	+06 54 44.8	0.262±0.342	$2.10^{+1.45}_{-0.76}$	44^{+16}_{-8}	18.45	4.39	1.42		e a

WR Number	Spectral Type	Alias	RA J2015	Dec J2015	$\omega \pm \sigma_w$ (mas)	d (kpc)	$\lvert z \rvert$ (pc)	G (mag)	$G_{BP} - G_{RP}$ (mag)	Excess noise	$\log L/L_\odot$	Flags
WR123	WN8o	HD 177230	19 03 59.02	−04 19 02.0	0.164±0.054	$5.35^{+1.56}_{-1.09}$	422^{+129}_{-90}	10.86	0.93	0.00	5.22	g
WR123-1	WN6o	HDM14	19 08 17.97	+08 29 10.5	0.157±0.231	$2.67^{+0.97}_{-0.73}$	27^{+2}_{-1}	15.59	4.68	0.90		e
WR123-3	WN8	MDM11 55	19 08 38.09	+09 28 20.9	-0.330±0.320	$3.18^{+1.41}_{-1.01}$	50^{+12}_{-9}	18.28	4.18	1.51		n a
WR123-8	WN9h	1629-14D6	19 10 06.40	+09 45 25.4	-0.057±0.888	$1.75^{+1.29}_{-0.81}$	31^{+7}_{-4}	19.95	4.02	3.37		n e a
WR124	WN8h	209 BAC	19 11 30.87	+16 51 38.1	0.144±0.045	$5.87^{+1.48}_{-1.09}$	359^{+85}_{-62}	10.61	1.56	0.00	5.69	g
WR124-1B	WC8	MDI09 GLIMPSE20 6	19 12 24.01	+09 57 29.3	1.298±1.160	$1.56^{+1.05}_{-0.90}$	18^{+1}_{-1}	20.01		4.56		a
WR124-1A	WC8	MDI09 GLIMPSE20 6	19 12 24.13	+09 57 28.8	-0.083±0.516	$2.34^{+0.97}_{-0.79}$	17^{+1}_{-0}	19.17	4.68	1.92		n e a
WR124-3	WC8	SFZ12 1657-51L	19 16 18.38	+12 46 49.3	-0.415±0.255	$3.66^{+1.30}_{-1.00}$	45^{+8}_{-6}	17.72		1.02		n a
WR124-9	WC6:	SFZ12 1670-57L	19 17 32.80	+14 08 28.0	-0.144±0.392	$2.66^{+1.73}_{-1.00}$	56^{+23}_{-13}	18.84	3.91	1.56		n e a
WR124-18	WN9h	1669-3DF	19 18 31.35	+13 43 39.1	-0.608±0.516	$2.60^{+1.32}_{-0.92}$	37^{+8}_{-5}	19.41	3.65	2.04		n a
WR124-19	WC6:	1660-1169	19 20 02.47	+12 08 20.2	-1.118±0.733	$2.32^{+1.18}_{-0.86}$	8^{+14}_{-10}	20.05	2.46	2.34		n a
WR124-2	WC8	SMG09 1671_5	19 20 40.39	+13 50 35.1	-2.755±0.791	$2.77^{+1.03}_{-0.85}$	18^{+0}_{-0}	20.01	3.08	2.90		n a
WR124-6	WC6	SFZ12 1675-17L	19 22 53.61	+14 08 49.8	-0.694±0.469	$2.73^{+1.00}_{-0.81}$	2^{+6}_{-5}	18.83	4.64	1.76		n a
WR124-7	WC7	SFZ12 175-10L	19 22 54.45	+14 11 27.9	-1.729±0.585	$2.88^{+1.00}_{-0.83}$	2^{+6}_{-5}	18.48	4.59	1.48		n a
WR124-11	WN6b	SFZ12 1698-70L	19 24 46.91	+17 14 25.0	0.197±0.272	$2.45^{+1.53}_{-0.84}$	50^{+18}_{-10}	18.45	4.44	1.17		e a
WR124-20	WC9	1697-38F	19 25 18.14	+17 02 15.5	1.477±0.417	$0.68^{+0.38}_{-0.18}$	26^{+3}_{-1}	19.23	3.76	1.31		a

WR Number	Spectral Type	Alias	RA J2015	Dec J2015	$\omega \pm \sigma_w$ (mas)	d (kpc)	$\lvert z \rvert$ (pc)	G (mag)	$G_{BP} - G_{RP}$ (mag)	Excess noise	$\log L/L_\odot$	Flags
WR124-21	WC8	1702-23L	19 26 08.35	+17 46 22.9	-0.353±0.136	$5.85^{+1.58}_{-1.32}$	87^{+17}_{-14}	15.98	3.75	0.61		n
WR124-22	WC9	1695-2B7	19 27 17.98	+16 05 24.5	0.335±0.476	$1.91^{+1.07}_{-0.72}$	7^{+7}_{-4}	19.29	4.48	1.83		e a
WR125	WC7ed+O9III	IC14-36	19 28 15.61	+19 33 21.4	0.273±0.070	$3.36^{+0.99}_{-0.65}$	82^{+18}_{-11}	11.94	2.24	0.00		g
WR125-4	WN7	MDM11 61	19 30 05.31	+17 46 01.0	-1.173±0.484	$2.96^{+1.05}_{-0.86}$	11^{+3}_{-2}	19.17	3.63	1.72		n a
WR125-3	WN7ha	Mercer 23 #2	19 30 13.56	+18 32 02.4	-0.190±0.304	$2.93^{+1.18}_{-0.88}$	29^{+3}_{-2}	12.81	3.41	0.92		n e
WR125-2	WN8-9	IPHAS J193038.84+183909.8	19 30 38.84	+18 39 09.7	0.222±0.099	$3.28^{+0.93}_{-0.67}$	28^{+2}_{-1}	12.44	3.68	0.28		g
WR125-1	WC8	HDM15	19 33 44.01	+19 22 47.4	0.121±0.051	$4.80^{+0.85}_{-0.70}$	7^{+2}_{-1}	13.33	2.69	0.25		g
WR126	WC5/WN	ST 2	19 39 56.19	+26 34 42.4	0.091±0.033	$7.57^{+1.49}_{-1.19}$	299^{+55}_{-43}	12.42	1.21	0.00	5.90	g
WR127	WN3b+O9.5V	HD 186943	19 46 15.94	+28 16 19.0	0.321±0.032	$3.09^{+0.35}_{-0.29}$	114^{+10}_{-8}	10.00	0.57	0.00		g
WR129	WN4o	MR 96	19 48 18.26	+30 26 52.6	0.165±0.039	$5.47^{+1.22}_{-0.90}$	254^{+52}_{-38}	12.71	1.14	0.00		g
WR128	WN4(h)	HD 187282	19 48 32.20	+18 12 03.6	0.342±0.052	$2.90^{+0.54}_{-0.39}$	170^{+35}_{-26}	10.35	0.21	0.09	5.22	g
WR130	WN8(h)	LS 16	19 59 12.59	+31 27 08.9	-0.474±0.145	$6.67^{+1.89}_{-1.57}$	131^{+31}_{-26}	11.23	2.17	0.52		n
WR131	WN7h+abs	MR 97	20 00 19.12	+33 15 51.0	0.113±0.033	$6.92^{+1.40}_{-1.09}$	227^{+41}_{-32}	11.52	1.53	0.00	6.02	g
WR132	WC6+?	HD 190002	20 01 39.73	+32 34 17.9	0.232±0.035	$4.15^{+0.68}_{-0.52}$	100^{+13}_{-10}	12.12	1.43	0.00	5.32	g
WR133	WN5o+O9I	HD 190918	20 05 57.32	+35 47 18.0	0.541±0.042	$1.85^{+0.16}_{-0.14}$	87^{+5}_{-4}	6.73	0.26	0.05		g
WR134	WN6b	HD 191765	20 10 14.19	+36 10 34.9	0.571±0.039	$1.75^{+0.13}_{-0.11}$	67^{+3}_{-3}	7.74	0.57	0.00	5.62	g
WR135	WC8	HD 192103	20 11 53.52	+36 11 50.4	0.504±0.041	$1.98^{+0.18}_{-0.15}$	64^{+3}_{-3}	7.88	0.40	0.00	5.39	g
WR136	WN6b(h)	HD 192163	20 12 06.53	+38 21 17.7	0.515±0.043	$1.93^{+0.18}_{-0.15}$	102^{+7}_{-6}	7.18	0.59	0.00	5.79	g
WR137	WC7pd+O9	HD 192641	20 14 31.76	+36 39 39.5	0.473±0.038	$2.10^{+0.18}_{-0.16}$	60^{+3}_{-2}	7.75	0.54	0.00		g

WR Number	Spectral Type	Alias	RA J2015	Dec J2015	$\omega \pm \sigma_w$ (mas)	d (kpc)	$\lvert z \rvert$ (pc)	G (mag)	$G_{BP} - G_{RP}$ (mag)	Excess noise	$\log L/L_\odot$	Flags
WR138	WN6o	HD 193077	20 17 00.02	+37 25 23.7	0.397±0.055	$2.47^{+0.40}_{-0.31}$	68^{+7}_{-5}	7.92	0.62	0.00		g
WR138-1	WN8-9h	HBHA 4202-22	20 17 08.11	+41 07 26.9	-0.015±0.072	$12.51^{+2.49}_{-2.71}$	709^{+136}_{-149}	13.82	2.89	0.40		n e
WR139	WN5o+O6III-V	HD 193576	20 19 32.42	+38 43 53.9	0.765±0.037	$1.31^{+0.07}_{-0.06}$	53^{+1}_{-1}	7.75	0.82	0.00		g
WR140	WC7pd+O4-5	HD 193793	20 20 27.97	+43 51 16.3	0.611±0.037	$1.64^{+0.11}_{-0.09}$	140^{+7}_{-6}	6.62	0.72	0.00		g
WR141	WN5o+O5V-III	HD 193928	20 21 31.73	+36 55 12.7	0.516±0.036	$1.92^{+0.14}_{-0.12}$	23^{+0}_{-0}	9.33	1.46	0.00		g
WR142	WO2	Sand 5	20 21 44.34	+37 22 30.4	0.605±0.036	$1.65^{+0.11}_{-0.09}$	29^{+0}_{-0}	12.23	1.96	0.00		g
WR142a	WC8	PCG02 1	20 24 06.19	+41 25 33.8	0.536±0.124	$1.81^{+0.61}_{-0.37}$	91^{+24}_{-14}	13.77	3.90	0.64		g
WR142-1	WN6o	HBHalpha 4203-27	20 28 14.55	+43 39 25.4	0.561±0.062	$1.77^{+0.23}_{-0.18}$	110^{+11}_{-9}	12.80	3.25	0.24		g
WR143	WC4+OB?	HD 195177	20 28 22.66	+38 37 18.9	0.417±0.039	$2.22^{+0.18}_{-0.16}$	19^{+0}_{-0}	10.80	1.73	0.00		g
WR144	WC4	HM19-1	20 32 03.02	+41 15 20.4	0.565±0.069	$1.75^{+0.24}_{-0.19}$	49^{+3}_{-3}	12.87	2.65	0.28	5.19	g
WR145	WN7o/CE+?	AS 422	20 32 06.27	+40 48 29.5	0.684±0.051	$1.46^{+0.12}_{-0.10}$	37^{+1}_{-1}	10.63	2.64	0.11	5.61	g
WR146	WC6+O8	MR 112	20 35 47.08	+41 22 44.6	0.863±0.456	$1.10^{+0.67}_{-0.36}$	29^{+5}_{-2}	11.05	3.32	2.04		a
WR147	WN8(h)+B0.5V	AS 431	20 36 43.63	+40 21 07.4	-1.244±0.390	$1.79^{+0.28}_{-0.26}$	10^{+1}_{-1}	10.82	4.21	1.81		n a
WR148	WN8h+	HD 197406	20 41 21.54	+52 35 15.1	0.028±0.035	$9.47^{+1.77}_{-1.49}$	1087^{+199}_{-168}	10.15	0.92	0.00		e
WR149	WN5o	St 4	21 07 11.69	+48 25 36.2	0.194±0.031	$4.89^{+0.83}_{-0.63}$	76^{+9}_{-7}	13.35	2.01	0.07	5.41	g
WR150	WC5	ST 5	21 50 05.57	+50 42 24.7	0.053±0.033	$8.73^{+1.70}_{-1.38}$	357^{+73}_{-59}	12.26	0.98	0.00	5.75	g
WR151	WN4o+O5V	CX Cep	22 09 33.44	+57 44 30.5	0.158±0.046	$5.38^{+1.31}_{-0.96}$	151^{+31}_{-23}	11.71	1.34	0.00		g
WR152	WN3(h)	HD 211564	22 16 24.03	+55 37 36.7	0.205±0.054	$4.36^{+1.12}_{-0.79}$	46^{+17}_{-12}	11.40	0.51	0.00	5.64	g
WR153	WN6o/CE+O6I	HD 211853	22 18 45.60	+56 07 33.9	0.236±0.037	$4.06^{+0.68}_{-0.52}$	25^{+7}_{-5}	8.81	0.70	0.00	5.88	g
WR154	WC6	HD 213049	22 27 17.81	+56 15 11.7	0.162±0.041	$5.38^{+1.20}_{-0.89}$	90^{+24}_{-18}	10.67	0.90	0.00		g

WR Number	Spectral Type	Alias	RA J2015	Dec J2015	$\omega \pm \sigma_w$ (mas)	d (kpc)	$\lvert z \rvert$ (pc)	G (mag)	$G_{BP} - G_{RP}$ (mag)	Excess noise	$\log L/L_\odot$	Flags
WR155	WN6o+O9II-Ib	CQ Cep	22 36 53.95	+56 54 20.9	0.330±0.043	$2.99^{+0.45}_{-0.35}$	46^{+10}_{-7}	8.71	0.74	0.00		g
WR156	WN8h	MR 119	23 00 10.12	+60 55 38.4	0.238±0.031	$4.10^{+0.60}_{-0.47}$	86^{+9}_{-7}	10.30	1.70	0.00	6.00	g
WR157	WN5o(+B1II)	HD 219460	23 15 12.39	+60 27 01.8	0.387±0.043	$2.57^{+0.32}_{-0.26}$	10^{+1}_{-1}	10.26	0.93	0.00		g
WR158	WN7h	MR 112	23 43 30.59	+61 55 48.1	0.184±0.032	$5.00^{+0.83}_{-0.65}$	29^{+1}_{-1}	10.71	1.53	0.00	6.02	g
WR159	WN4	BCC 1	23 47 20.38	+63 13 14.2	0.542±0.122	$1.82^{+0.60}_{-0.37}$	60^{+13}_{-7}	10.53	1.55	0.37		g

Columns are: (1) WR Number, (2) Spectral type, (3) Alternative name, (4) *Gaia* Right Ascension, (5) *Gaia* Declination, (6) Zero point corrected parallax ω and inflated error σ_ω, (7) Distance from the Sun, (8) Distance from the midplane, (9) *Gaia* G band apparent magnitude, (10) *Gaia* colour index, (11) Astrometric excess noise, (12) Stellar luminosity, (13) Error flags, a = astrometric excess noise > 1 mas; e = large parallax uncertainty $|\sigma_\omega/\omega|$>1; n = negative parallax ω<0, g = good astrometry.

A.2 Absolute magnitudes of Galactic WR stars

Table A.2: K_s absolute magnitudes of Galactic WR stars, from Chapter 3.

WR Number	Spectral type	K_s (mag)	μ (mag)	J-K_s (mag)	H-K_s (mag)	A_{Ks} (mag)	$M_{K_s}^{Sys}$ (mag)	$F_{WR}^{K_s}/F_{Sys}^{K_s}$	$M_{K_s}^{WR}$ (mag)	Flags
WR1	WN4b	7.48	12.49	0.73	0.38	0.30±0.08			$-5.4^{+0.3}_{-0.3}$	b:
WR3	WN3ha	10.01	12.31	0.23	0.12	0.11±0.08			$-2.5^{+0.3}_{-0.4}$	b:
WR4	WC5+?	7.88	12.87	0.87	0.69	0.18±0.11			$-5.2^{+0.4}_{-0.5}$	b
WR5	WC6	7.65	12.36	0.98	0.69	0.30±0.11			$-5.1^{+0.3}_{-0.3}$	g
WR6	WN4b	5.89	11.78	0.46	0.34	0.05±0.08			$-6.0^{+0.3}_{-0.4}$	b
WR7	WN4b	9.27	13.13	0.70	0.40	0.24±0.08			$-4.2^{+0.4}_{-0.5}$	g
WR8	WN7o/CE	7.93	12.87	0.64	0.39	0.31±0.08			$-5.3^{+0.3}_{-0.3}$	b:
WR9	WC5+O7	7.54	13.3	0.91	0.57	0.45±0.08	$-6.3^{+0.3}_{-0.4}$	0.60 ± 0.24	$-5.7^{+0.9}_{-0.7}$	b
WR10	WN5h	9.61	13.69	0.44	0.28	0.24±0.17			$-4.4^{+0.5}_{-0.5}$	g
WR11	WC8+O7.5III-V	2.10	7.67	0.05	0.15	0.00±0.11	$-5.6^{+0.4}_{-0.4}$	0.45 ± 0.02	$-4.8^{+0.4}_{-0.4}$	b:
WR12	WN8h	7.87	13.78	0.75	0.39	0.25±0.08			$-6.3^{+0.4}_{-0.4}$	g
WR13	WC6	8.86	13.41	1.27	0.77	0.45±0.11			$-5.1^{+0.4}_{-0.4}$	g

WR Number	Spectral type	K_s (mag)	μ (mag)	J-K_s (mag)	H-K_s (mag)	A_{Ks} (mag)	$M_{K_s}^{Sys}$ (mag)	$F_{WR}^{K_s}/F_{Sys}^{K_s}$	$M_{K_s}^{WR}$ (mag)	Flags
WR14	WC7+?	6.61	11.73	0.88	0.64	0.15±0.11			$-5.3^{+0.2}_{-0.2}$	g
WR15	WC6	6.60	12.36	1.25	0.74	0.41±0.11			$-6.2^{+0.3}_{-0.3}$	b
WR16	WN8h	6.38	12.1	0.59	0.33	0.20±0.08			$-6.0^{+0.2}_{-0.2}$	g
WR17	WC5	9.17	14.15	0.76	0.57	0.15±0.11			$-5.2^{+0.5}_{-0.5}$	b
WR17-1	WN5b	9.53	12.45	2.20	0.85	0.85±0.20			$-4.1^{+0.8}_{-0.8}$	g
WR18	WN4b	7.68	12.91	0.89	0.53	0.32±0.08			$-5.6^{+0.4}_{-0.5}$	b:
WR19	WC5	8.53	13.18	1.22	0.60	0.56±0.11			$-5.3^{+0.3}_{-0.4}$	b
WR19a	WN7:(h)	7.50	13.39	1.57	0.63	0.82±0.08			$-6.9^{+0.6}_{-0.6}$	b
WR20	WN5o	9.93	14.22	1.07	0.50	0.51±0.08			$-4.9^{+0.3}_{-0.3}$	b:
WR20-2	O2If*/WN6	8.38	13.72	0.90	0.35	0.53±0.13			$-6.0^{+0.4}_{-0.4}$	b
WR20-1	WN7-8	8.34	12.17	2.26	0.86	1.03±0.23			$-5.2^{+0.8}_{-0.8}$	b:
WR20a	O3If*/WN6+ O3If*/WN6	7.59	13.51	1.27	0.49	0.76±0.08	$-6.8^{+0.4}_{-0.4}$	0.50 ± 0.00	$-6.0^{+0.4}_{-0.4}$	g

WR Number	Spectral type	K_s (mag)	μ (mag)	J-K_s (mag)	H-K_s (mag)	A_{Ks} (mag)	$M_{K_s}^{Sys}$ (mag)	$F_{WR}^{K_s}/F_{Sys}^{K_s}$	$M_{K_s}^{WR}$ (mag)	Flags
WR20b	WN6ha	7.18	12.44	1.47	0.62	0.89±0.08			$-6.2^{+0.3}_{-0.4}$	g
WR20-3	O2If*/WN6	9.04	11.99	1.47	0.53	0.80±0.18			$-3.9^{+0.6}_{-0.8}$	b
WR21a	O2If/WN5	7.83	13.21	0.98	0.37	0.57±0.14			$-6.0^{+0.3}_{-0.4}$	g
WR21	WN5o+O4-6	8.03	13.0	0.38	0.19	0.25±0.08	$-5.3^{+0.3}_{-0.3}$	0.92 ± 0.22	$-5.2^{+0.6}_{-0.4}$	b
WR22	WN7h+O9III-V	5.39	11.84	0.32	0.19	0.18±0.08			$-6.7^{+0.2}_{-0.2}$	b:
WR23	WC6	7.05	12.03	0.84	0.55	0.07±0.11			$-5.1^{+0.3}_{-0.3}$	g
WR24	WN6ha	5.82	12.75	0.28	0.19	0.13±0.08			$-7.1^{+0.3}_{-0.4}$	b
WR25	O2.5If*/WN6+O	5.72	11.47	0.54	0.25	0.34±0.11			$-6.1^{+0.2}_{-0.2}$	b:
WR26	WN7b/CE	9.68	14.13	1.16	0.59	0.51±0.08			$-5.0^{+0.3}_{-0.3}$	g
WR27	WC6+a	8.29	12.09	1.59	0.88	0.66±0.11			$-4.5^{+0.3}_{-0.3}$	g
WR28	WN6(h)+OB?	8.73	13.79	0.98	0.43	0.48±0.08			$-5.6^{+0.4}_{-0.4}$	b
WR29	WN7h+O	9.12	13.76	0.79	0.34	0.40±0.14	$-5.1^{+0.4}_{-0.4}$	0.32 ± 0.89	$-3.9^{+1.6}_{-1.6}$	b
WR30	WC6+O6-8	9.21	13.54	0.84	0.55	0.23±0.08	$-4.6^{+0.4}_{-0.4}$	0.72 ± 0.29	$-4.3^{+0.9}_{-0.7}$	b:

WR Number	Spectral type	K_s (mag)	μ (mag)	J-K_s (mag)	H-K_s (mag)	A_{Ks} (mag)	$M_{K_s}^{Sys}$ (mag)	$F_{WR}^{K_s}/F_{Sys}^{K_s}$	$M_{K_s}^{WR}$ (mag)	Flags
WR30a	WO4+O5-5.5	9.56	14.14	0.69	0.27	0.48±0.07	$-5.2^{+0.4}_{-0.4}$	0.22 ± 0.02	$-3.5^{+0.5}_{-0.5}$	g
WR31	WN4o+O8V	8.69	13.93	0.48	0.27	0.26±0.08			$-5.6^{+0.5}_{-0.5}$	b
WR31a	WN11h	6.10	14.33	1.22	0.62	0.60±0.14			$-8.9^{+0.4}_{-0.4}$	g
WR31b	WN11h	4.53	13.43	0.89	0.55	0.47±0.11			$-9.5^{+0.4}_{-0.4}$	g
WR31c	WC6	9.49	13.91	1.55	0.85	0.51±0.11			$-5.0^{+0.5}_{-0.5}$	g
WR31-1	O3.5If/WN7		13.31							u
WR32	WC5+OB?	10.23	13.8	1.49	0.81	0.68±0.08	$-4.3^{+0.4}_{-0.4}$	0.72 ± 0.31	$-4.0^{+1.0}_{-0.7}$	g
WR33	WC6	9.69	14.4	0.93	0.66	0.16±0.11			$-5.0^{+0.4}_{-0.4}$	g
WR34	WN5o	10.04	14.35	1.16	0.55	0.46±0.08			$-4.8^{+0.4}_{-0.4}$	b:
WR35	WN6h+OB?	9.62	14.18	1.08	0.47	0.39±0.24	$-5.0^{+0.4}_{-0.4}$	0.56 ± 1.27	$-4.4^{+1.0}_{-1.0}$	g
WR35a	WN6h+O8.5V	9.65	13.83	0.82	0.32	0.51±0.08	$-4.8^{+0.4}_{-0.4}$	0.12 ± 0.01	$-2.4^{+0.5}_{-0.5}$	b
WR35b	WN4b	9.76	13.65	1.19	0.59	0.64±0.08			$-4.6^{+0.3}_{-0.3}$	g
WR36	WN5-6b+OB?	9.40	13.67	1.00	0.51	0.40±0.09	$-4.8^{+0.4}_{-0.4}$	0.83 ± 0.48	$-4.6^{+1.4}_{-0.6}$	g

WR Number	Spectral type	K_s (mag)	μ (mag)	J-K_s (mag)	H-K_s (mag)	A_{Ks} (mag)	$M_{K_s}^{Sys}$ (mag)	$F_{WR}^{K_s}/F_{Sys}^{K_s}$	$M_{K_s}^{WR}$ (mag)	Flags
WR37	WN4b	9.67	14.13	1.36	0.67	0.62±0.08			$-5.2^{+0.4}_{-0.4}$	g
WR38	WC4	10.79	13.91	1.20	0.71	0.50±0.11			$-3.7^{+0.4}_{-0.4}$	b
WR38a	WN5o	10.71	13.67	0.82	0.50	0.49±0.08			$-3.5^{+0.4}_{-0.4}$	g
WR40	WN8h	6.11	12.92	0.51	0.30	0.15±0.08			$-7.0^{+0.3}_{-0.4}$	b:
WR38b	WC7	8.61	13.18	1.78	0.67	0.75±0.11			$-5.4^{+0.4}_{-0.5}$	b:
WR39	WC7+OB?	8.21	12.92	1.30	0.53	0.68±0.08	$-5.7^{+0.7}_{-0.7}$	0.53 ± 0.27	$-5.0^{+1.5}_{-1.2}$	g
WR41	WC5+OB?	10.12	13.89	1.41	0.86	0.46±0.10	$-4.3^{+0.3}_{-0.3}$	0.87 ± 0.35	$-4.2^{+0.9}_{-0.5}$	g
WR42	WC7+O7V	7.08	11.93	0.51	0.44	0.14±0.08	$-5.1^{+0.3}_{-0.3}$	0.66 ± 0.33	$-4.6^{+1.1}_{-0.8}$	g
WR42a	WN5b	10.81	13.75	1.27	0.50	0.72±0.08			$-3.8^{+0.5}_{-0.5}$	b:
WR42b	WN4b	9.90	14.01	1.45	0.62	1.15±0.08			$-5.4^{+0.5}_{-0.5}$	b
WR42c	WN5o	9.90	14.14	1.25	0.57	0.72±0.08			$-5.0^{+0.4}_{-0.4}$	b
WR42d	WN5b	8.91	12.53	1.29	0.61	0.67±0.08			$-4.5^{+0.7}_{-0.7}$	g
WR42-1	O3If*/WN6	9.04	13.19	1.14	0.43	0.65±0.15			$-4.9^{+0.4}_{-0.4}$	b

WR Number	Spectral type	K_s (mag)	μ (mag)	J-K_s (mag)	H-K_s (mag)	A_{Ks} (mag)	$M_{K_s}^{Sys}$ (mag)	$F_{WR}^{K_s}/F_{Sys}^{K_s}$	$M_{K_s}^{WR}$ (mag)	Flags
WR43-2	O2If*/WN5	9.24	13.95	1.23	0.44	0.68±0.16			$-5.5^{+0.4}_{-0.4}$	b
WR43-3	O2.5If*/WN6	9.12	14.08	0.73	0.27	0.44±0.12			$-5.5^{+0.4}_{-0.4}$	b
WR43-1	WN4b	10.47	10.63	2.69	1.10	1.13±0.25			$-2.1^{+1.2}_{-1.3}$	b
WR44	WN4o+OB?	10.47	13.92	0.69	0.42	0.30±0.07	$-3.8^{+0.4}_{-0.4}$	0.15 ± 0.09	$-1.8^{+1.3}_{-0.9}$	b
WR44a	WN5b	10.82	13.52	1.25	0.52	0.76±0.08			$-3.6^{+0.4}_{-0.4}$	b:
WR45	WC6	9.20	13.14	1.40	0.79	0.58±0.11			$-4.6^{+0.2}_{-0.2}$	g
WR45-1	WN9-10h	9.81	13.44	1.69	0.73	0.80±0.18			$-4.6^{+0.6}_{-0.6}$	b:
WR45-2	WN5	10.78	13.21	1.37	0.58	0.58±0.15			$-3.2^{+0.5}_{-0.5}$	b:
WR45a	WN5o	10.73	12.89	1.17	0.51	0.65±0.08			$-3.0^{+0.6}_{-0.6}$	b:
WR45b	WN4b	9.92	13.87	1.53	0.69	0.70±0.08			$-4.7^{+0.4}_{-0.4}$	g
WR45-3	WN5b	10.94	13.58	1.63	0.63	0.56±0.15			$-3.4^{+0.6}_{-0.6}$	b
WR45-4	WN6	10.14	13.76	1.51	0.62	0.64±0.16			$-4.4^{+0.5}_{-0.5}$	g
WR45c	WN5o	10.32	13.94	1.03	0.47	0.52±0.08			$-4.2^{+0.3}_{-0.3}$	g

WR Number	Spectral type	K_s (mag)	μ (mag)	J-K_s (mag)	H-K_s (mag)	A_{Ks} (mag)	$M_{K_s}^{Sys}$ (mag)	$F_{WR}^{K_s}/F_{Sys}^{K_s}$	$M_{K_s}^{WR}$ (mag)	Flags
WR46	WN3b pec	9.83	12.07	0.37	0.25	0.07±0.08			$-2.3^{+0.3}_{-0.3}$	b:
WR46-1	WN6o	10.22	13.37	1.33	0.60	0.58±0.14			$-3.8^{+0.5}_{-0.5}$	g
WR46-18	WC6-7	10.47	11.29	2.87	1.20	0.97±0.27			$-2.3^{+1.0}_{-1.1}$	b
WR46-7	WC5-7	9.74	12.43	3.01	1.34	1.11±0.28			$-4.0^{+0.7}_{-0.7}$	g
WR46-8	WN6	9.85	12.06	2.17	0.85	0.97±0.22			$-3.5^{+0.7}_{-0.7}$	g
WR46-16	WN9	11.54	11.96	1.90	0.51	0.71±0.19			$-1.5^{+0.8}_{-0.8}$	b
WR46-9	WN5	9.88	12.42	2.19	0.84	0.96±0.22			$-3.7^{+0.7}_{-0.7}$	g
WR46-17	WN9/OIf+		12.3							u
WR46a	WN4o	10.92	14.14	1.16	0.50	0.60±0.08			$-3.9^{+0.4}_{-0.4}$	b:
WR46-2	WN7h	9.03	12.91	1.53	0.61	0.69±0.16			$-4.7^{+0.5}_{-0.5}$	g
WR46-3	O6-7.5If+		13.05							u
WR46-4	Ofpe/WN9		12.24							u
WR46-5	WN6	9.67	12.86	1.85	0.58	0.69±0.19			$-4.1^{+0.6}_{-0.6}$	b

WR Number	Spectral type	K_s (mag)	μ (mag)	J-K_s (mag)	H-K_s (mag)	A_{Ks} (mag)	$M_{K_s}^{Sys}$ (mag)	$F_{WR}^{K_s}/F_{Sys}^{K_s}$	$M_{K_s}^{WR}$ (mag)	Flags
WR46-6	WN7	9.64	12.97	2.02	0.66	0.84±0.21			$-4.3^{+0.6}_{-0.6}$	b:
WR46-15	WN8	9.84	11.5	3.29	1.19	1.51±0.33			$-3.5^{+1.0}_{-1.2}$	b
WR46-12	WN4b	11.84	12.39	1.72	0.71	0.64±0.16			$-1.4^{+0.7}_{-0.7}$	b
WR46-13	WC7	11.09	12.77	2.07	0.96	0.61±0.21			$-2.5^{+0.6}_{-0.6}$	b
WR46-14	WN5b	10.96	9.06	1.97	0.80	0.75±0.18			$0.5^{+1.1}_{-1.3}$	b
WR47	WN6o+O5V	7.55	12.72	0.77	0.37	0.46±0.22	$-5.7^{+0.4}_{-0.4}$	0.53 ± 1.20	$-5.0^{+1.1}_{-1.1}$	b
WR47a	WN8h	9.06	13.45	1.38	0.62	0.83±0.08			$-5.4^{+0.5}_{-0.5}$	g
WR47-1	WN6o	10.55	12.69	1.63	0.67	0.70±0.17			$-3.0^{+0.6}_{-0.6}$	b:
WR47b	WN9h	8.84	13.75	1.45	0.60	0.92±0.08			$-6.0^{+0.5}_{-0.5}$	g
WR47-5	WN6(h)	11.09	12.36	2.23	0.83	0.96±0.22			$-2.6^{+0.9}_{-0.9}$	b
WR47c	WC5	9.89	14.16	1.35	0.59	0.71±0.11			$-5.1^{+0.4}_{-0.4}$	b:
WR47-2	WC5-6	10.22	12.69	2.26	0.90	0.62±0.22			$-3.3^{+0.7}_{-0.7}$	b
WR47-3	WC5-6	11.05	10.74	2.08	0.87	0.55±0.21			$-0.7^{+0.9}_{-1.1}$	b

WR Number	Spectral type	K_s (mag)	μ (mag)	J-K_s (mag)	H-K_s (mag)	A_{Ks} (mag)	$M_{K_s}^{Sys}$ (mag)	$F_{WR}^{K_s}/F_{Sys}^{K_s}$	$M_{K_s}^{WR}$ (mag)	Flags
WR48	WC6 (+O9.5/B0Iab)	5.43	11.9	0.14	0.14	0.08±0.08	$-6.8^{+0.7}_{-0.8}$	0.99 ± 0.44	$-6.8^{+1.3}_{-0.8}$	b
WR48-1	WC7	9.31	12.34	1.74	0.78	0.40±0.19			$-3.6^{+0.6}_{-0.6}$	b
WR48b	WC9d	8.58	13.55	2.41	1.20	0.61±0.08			$-5.7^{+0.5}_{-0.5}$	b:
WR48-6	WN9	7.58	12.4	2.63	0.99	1.22±0.27			$-6.3^{+0.7}_{-0.7}$	g
WR48-10	WN9h	7.48	12.01	1.94	0.67	0.83±0.20			$-5.6^{+0.7}_{-0.7}$	g
WR48-7	WN8	7.65	12.09	2.16	0.83	0.99±0.22			$-5.7^{+0.7}_{-0.7}$	g
WR48-4	WC6	10.71	11.97	2.45	1.11	0.81±0.24			$-2.4^{+0.8}_{-0.8}$	b
WR48-8	WN9	8.15	12.54	1.66	0.68	0.77±0.18			$-5.3^{+0.6}_{-0.6}$	g
WR48-9	WN9h	6.61	12.22	1.65	0.66	0.75±0.17			$-6.5^{+0.5}_{-0.5}$	b:
WR48a	WC8ed+?	5.08	11.78	3.66	1.72	0.89±0.08	$-7.8^{+0.6}_{-0.7}$	0.30 ± 0.17	$-6.5^{+1.6}_{-1.2}$	b
WR48-5	WN6b	10.26	11.57	2.80	1.08	1.15±0.26			$-2.8^{+0.9}_{-1.0}$	b
WR48c	WN3h/C4	11.16	12.13	0.70	0.36	0.27±0.08			$-1.3^{+0.2}_{-0.2}$	b

WR Number	Spectral type	K_s (mag)	μ (mag)	J-K_s (mag)	H-K_s (mag)	A_{Ks} (mag)	$M_{K_s}^{Sys}$ (mag)	$F_{WR}^{K_s}/F_{Sys}^{K_s}$	$M_{K_s}^{WR}$ (mag)	Flags
WR48-2	WC7-8	8.98	12.56	1.84	0.85	0.48±0.20			$-4.2^{+0.6}_{-0.6}$	b
WR49	WN5(h)	11.21	14.61	0.68	0.36	0.27±0.08			$-3.7^{+0.3}_{-0.3}$	g
WR50	WC7+OB	8.81	12.7	0.94	0.57	0.34±0.10	$-4.3^{+0.3}_{-0.3}$	0.84 ± 0.42	$-4.1^{+1.1}_{-0.5}$	b:
WR51	WN4o	13.46	12.82	0.67	0.17	0.60±0.08			$-0.0^{+0.3}_{-0.3}$	b
WR52	WC4	7.55	11.21	0.86	0.66	0.22±0.11			$-3.9^{+0.2}_{-0.2}$	b:
WR52-2	WN6	10.68	12.1	1.85	0.72	0.79±0.19			$-2.5^{+0.7}_{-0.8}$	b
WR53	WC8d	6.83	13.08	1.91	1.09	0.35±0.08			$-6.7^{+0.3}_{-0.3}$	b
WR54	WN5o	10.09	14.07	0.76	0.39	0.33±0.08			$-4.4^{+0.4}_{-0.4}$	g
WR55	WN7o	8.01	12.38	0.76	0.48	0.24±0.08			$-4.7^{+0.3}_{-0.4}$	g
WR56	WC7	10.77	14.69	1.07	0.71	0.28±0.11			$-4.3^{+0.3}_{-0.3}$	b:
WR56a	WN6o	9.73	13.2	1.17	0.55	0.71±0.08			$-4.3^{+0.5}_{-0.5}$	g
WR57	WC8	8.01	13.7	1.08	0.74	0.21±0.08			$-6.0^{+0.5}_{-0.5}$	b:
WR58	WN4b/CE	10.54	13.85	0.76	0.44	0.35±0.08			$-3.8^{+0.4}_{-0.4}$	b:

WR Number	Spectral type	K_s (mag)	μ (mag)	J-K_s (mag)	H-K_s (mag)	A_{Ks} (mag)	$M_{K_s}^{Sys}$ (mag)	$F_{WR}^{K_s}/F_{Sys}^{K_s}$	$M_{K_s}^{WR}$ (mag)	Flags
WR59	WC9d	6.61	12.77	2.18	1.10	0.69±0.08			$-6.9^{+0.3}_{-0.4}$	g
WR59-2	WC5-6	10.86	11.08	2.74	1.21	0.94±0.26			$-1.7^{+1.0}_{-1.2}$	b
WR60	WC8	7.70	12.73	1.21	0.67	0.62±0.08			$-5.7^{+0.3}_{-0.4}$	g
WR60-7	WC7-8	10.28	11.57	3.00	1.29	1.07±0.28			$-2.8^{+1.0}_{-1.0}$	b
WR60-5	WC7	9.39	11.94	1.45	0.73	0.30±0.17			$-3.1^{+0.6}_{-0.8}$	b
WR60-2	WC8	9.71	11.6	3.87	1.62	1.69±0.36			$-3.8^{+1.0}_{-1.1}$	b
WR61	WN5o	10.35	13.7	0.61	0.32	0.28±0.08			$-3.7^{+0.4}_{-0.4}$	g
WR61-3	WC9	10.38	9.8	3.24	1.25	1.41±0.31			$-2.1^{+1.4}_{-1.5}$	b
WR61-1	WN6	9.62	12.95	2.06	0.81	0.90±0.21			$-4.5^{+0.7}_{-0.7}$	b
WR62	WN6b	7.75	13.15	1.36	0.60	0.78±0.08			$-6.3^{+0.4}_{-0.4}$	b
WR62a	WN6o	9.06	12.72	0.73	0.30	0.67±0.08			$-4.4^{+0.3}_{-0.4}$	g
WR62-2	WN8-9h	6.87	11.71	1.54	0.55	0.65±0.16			$-5.7^{+0.7}_{-0.8}$	b
WR62b	WN5o	10.97	13.7	1.04	0.47	0.90±0.08			$-3.8^{+0.5}_{-0.5}$	g

WR Number	Spectral type	K_s (mag)	μ (mag)	J-K_s (mag)	H-K_s (mag)	A_{Ks} (mag)	$M_{\mathrm{K_s}}^{\mathrm{Sys}}$ (mag)	$\mathrm{F}_{\mathrm{WR}}^{\mathrm{K_s}}/\mathrm{F}_{\mathrm{Sys}}^{\mathrm{K_s}}$	$M_{\mathrm{K_s}}^{\mathrm{WR}}$ (mag)	Flags
WR62-1	WN7-8h	6.82	11.81	2.11	0.78	0.95±0.22			$-6.3^{+0.9}_{-0.9}$	b
WR64	WC7	11.33	14.51	1.17	0.70	0.16±0.11			$-3.4^{+0.4}_{-0.4}$	b
WR64-3	WN6o	10.18	12.31	2.21	0.86	0.98±0.22			$-3.3^{+0.7}_{-0.7}$	b:
WR64-4	WN6o+OB	9.10	10.93	2.25	0.91	1.14±0.24	$-3.3^{+0.8}_{-1.0}$	0.63 ± 0.42	$-2.8^{+2.0}_{-1.5}$	b
WR64-5	WN6o	10.80	11.31	2.31	0.86	1.00±0.24			$-1.9^{+0.9}_{-1.0}$	b
WR65	WC9d+OB?	6.17	12.48	2.29	1.11	0.76±0.08	$-7.1^{+0.4}_{-0.5}$	0.34 ± 0.22	$-6.0^{+1.5}_{-1.0}$	g
WR66	WN8(h)	8.15	13.57	0.78	0.33	0.39±0.08			$-5.9^{+0.7}_{-0.8}$	g
WR67	WN6o	8.45	11.75	0.83	0.41	0.51±0.08			$-3.9^{+0.4}_{-0.5}$	g
WR67-3	WN10	7.74	12.34	1.63	0.72	0.77±0.17			$-5.5^{+0.5}_{-0.5}$	b
WR67-1	WN6h	8.82	12.63	1.04	0.36	0.34±0.12			$-4.3^{+0.5}_{-0.5}$	b
WR67-2	WC7	8.46	11.68	1.88	0.80	0.46±0.20			$-3.9^{+0.8}_{-0.8}$	b
WR68	WC7	8.75	13.46	1.15	0.63	0.52±0.11			$-5.3^{+0.4}_{-0.4}$	g
WR68-1	WN4b	11.06	11.37	2.82	1.09	1.16±0.26			$-1.7^{+1.0}_{-1.1}$	b

WR Number	Spectral type	K_s (mag)	μ (mag)	J-K_s (mag)	H-K_s (mag)	A_{Ks} (mag)	$M_{K_s}^{Sys}$ (mag)	$F_{WR}^{K_s}/F_{Sys}^{K_s}$	$M_{K_s}^{WR}$ (mag)	Flags
WR68a	WN6o	8.62	12.99	0.97	0.40	0.77±0.08			$-5.2^{+0.4}_{-0.4}$	b
WR69	WC9d+OB	6.40	12.71	1.56	0.88	0.20±0.08	$-6.5^{+0.3}_{-0.4}$	0.47 ± 0.30	$-5.7^{+1.4}_{-0.9}$	b:
WR70	WC9vd+B0I	5.74	12.39	1.33	0.82	0.56±0.08	$-7.3^{+0.3}_{-0.3}$	0.11 ± 0.07	$-4.9^{+1.4}_{-0.8}$	b
WR70-1	WN7	11.46	11.42	2.38	0.93	1.11±0.24			$-1.3^{+0.9}_{-1.0}$	b
WR70-13	WC8d		12.22							u
WR70-3	WC7	9.06	11.87	1.90	0.88	0.52±0.20			$-3.5^{+0.6}_{-0.6}$	b
WR70-5	WC9	8.49	11.45	2.70	1.22	1.26±0.26			$-4.4^{+0.7}_{-0.7}$	g
WR70a	WN6o	9.76	13.01	1.18	0.48	0.67±0.08			$-4.1^{+0.5}_{-0.5}$	g
WR70-2	WN5b	8.66	12.82	2.22	0.86	0.86±0.20			$-5.3^{+0.8}_{-0.9}$	b:
WR70-11	WN7	9.88	13.1	2.14	0.77	0.94±0.22			$-4.4^{+0.8}_{-0.8}$	b:
WR70-16	WC7d+WN or WN/Cd+O		8.7							u
WR71	WN6o	9.09	12.52	0.39	0.22	0.10±0.08			$-3.6^{+0.3}_{-0.4}$	g

WR Number	Spectral type	K_s (mag)	μ (mag)	J-K_s (mag)	H-K_s (mag)	A_{Ks} (mag)	$M_{K_s}^{Sys}$ (mag)	$F_{WR}^{K_s}/F_{Sys}^{K_s}$	$M_{K_s}^{WR}$ (mag)	Flags
WR71-1	WN9	11.17	12.1	1.96	0.73	0.87±0.20			$-2.0^{+0.7}_{-0.7}$	b
WR72-5	WN6o	10.27	12.05	2.29	0.87	1.00±0.23			$-3.0^{+0.7}_{-0.8}$	b:
WR72-1	WC9	8.46	12.38	1.70	0.79	0.72±0.17			$-4.8^{+0.5}_{-0.5}$	g
WR72-2	WC8	8.10	12.23	2.16	0.87	0.76±0.19			$-5.0^{+0.7}_{-0.8}$	g
WR73	WC9d	7.47	14.17	2.85	1.32	0.68±0.08			$-7.5^{+0.5}_{-0.5}$	b:
WR74	WN7o	8.80	13.0	0.93	0.42	0.76±0.08			$-5.1^{+0.4}_{-0.4}$	g
WR75	WN6b	7.84	12.6	0.76	0.40	0.39±0.08			$-5.2^{+0.4}_{-0.5}$	g
WR75-1	WC8	10.73	11.68	2.55	1.03	0.96±0.23			$-2.2^{+0.9}_{-1.0}$	b
WR75aa	WC9d		13.44							u
WR75a	WC9	8.50	12.49	1.46	0.68	0.82±0.08			$-4.9^{+0.5}_{-0.6}$	g
WR75b	WC9	8.36	11.14	1.40	0.64	0.89±0.08			$-3.7^{+0.4}_{-0.5}$	b
WR75-21	WC7:	9.35	10.5	1.08	0.27	- 0.11±0.16			$-1.1^{+0.2}_{-0.2}$	b

WR Number	Spectral type	K_s (mag)	μ (mag)	J-K_s (mag)	H-K_s (mag)	A_{Ks} (mag)	$M_{K_s}^{Sys}$ (mag)	$F_{WR}^{K_s}/F_{Sys}^{K_s}$	$M_{K_s}^{WR}$ (mag)	Flags
WR75ab	WN7h	8.91	12.9	1.31	0.38	0.47±0.15			$-4.6^{+0.6}_{-0.7}$	g
WR75c	WC9	10.52	14.27	1.10	0.60	0.45±0.12			$-4.3^{+0.5}_{-0.5}$	b:
WR75d	WC9	9.12	12.76	1.56	0.76	0.67±0.16			$-4.6^{+0.7}_{-0.8}$	g
WR75-23	WC9	8.93	12.5	1.34	0.66	0.55±0.14			$-4.3^{+0.5}_{-0.6}$	b
WR76	WC9d	4.88	12.81	3.58	1.63	0.63±0.08			$-8.8^{+0.7}_{-0.7}$	b
WR77	WC8+OB	8.53	12.27	1.33	0.74	0.42±0.10	$-4.2^{+0.3}_{-0.4}$	0.76 ± 0.45	$-3.9^{+1.3}_{-0.7}$	b
WR77-5	WN6	9.14	11.69	1.42	0.57	0.58±0.15			$-3.4^{+0.7}_{-0.7}$	b
WR77-1	WN7b	8.29	12.16	1.77	0.71	0.64±0.16			$-4.8^{+0.7}_{-0.7}$	b
WR77aa	WC9d		12.01							u
WR77-2	WN7	8.73	12.13	2.02	0.80	0.93±0.21			$-4.5^{+0.6}_{-0.6}$	b
WR77a	WN6o	10.00	12.17	1.72	0.67	0.73±0.20			$-3.0^{+0.6}_{-0.6}$	b
WR77b	WC9d		12.38							u
WR77c	WN8o	8.86	12.34	2.03	0.71	0.87±0.23			$-4.5^{+0.6}_{-0.6}$	b

WR Number	Spectral type	K_s (mag)	μ (mag)	J-K_s (mag)	H-K_s (mag)	A_{Ks} (mag)	$M_{K_s}^{Sys}$ (mag)	$F_{WR}^{K_s}/F_{Sys}^{K_s}$	$M_{K_s}^{WR}$ (mag)	Flags
WR77d	WN7o	9.26	12.13	1.80	0.57	0.72±0.21			$-3.7^{+0.6}_{-0.6}$	b
WR77f	WN10-11h	8.29	11.89	1.52	0.51	0.59±0.19			$-4.4^{+0.7}_{-0.7}$	b
WR77h	WN8o	8.76	11.17	1.99	0.66	0.83±0.23			$-3.5^{+0.8}_{-0.8}$	b
WR77i	WC9d		11.79							u
WR77j	WN7o	9.28	12.53	2.08	0.69	0.87±0.24			$-4.2^{+0.6}_{-0.6}$	b:
WR77m	WC9d		12.09							u
WR77n	WC9d		12.17							u
WR77o	WN7o	9.18	12.49	1.73	0.61	0.73±0.21			$-4.2^{+0.6}_{-0.6}$	b
WR77p	WC9	8.29	7.39	1.83	0.80	0.76±0.21			$-0.1^{+0.3}_{-0.4}$	b
WR77q	WN5o	9.18	11.76	1.73	0.61	0.69±0.20			$-3.5^{+0.7}_{-0.8}$	g
WR77r	WN7o	10.26	12.43	1.66	0.58	0.70±0.20			$-3.0^{+0.6}_{-0.6}$	b
WR77s	WN6o	6.17	11.43	0.43	0.87	0.56±0.13			$-6.1^{+0.7}_{-0.7}$	b
WR77sa	WN6h	10.17	12.02	2.06	0.25	0.52±7.04			$-2.5^{+7.0}_{-7.1}$	b

WR Number	Spectral type	K_s (mag)	μ (mag)	J-K_s (mag)	H-K_s (mag)	A_{Ks} (mag)	$M_{K_s}^{Sys}$ (mag)	$F_{WR}^{K_s}/F_{Sys}^{K_s}$	$M_{K_s}^{WR}$ (mag)	Flags
WR77sb	WN6o	8.33	12.0	1.65	0.48	0.58±0.27			$-4.4^{+0.7}_{-0.7}$	b
WR77sc	WN7b	6.33	12.14	1.69	0.59	0.54±0.15			$-6.5^{+0.6}_{-0.6}$	b
WR77sd	WN5o	10.25	11.18	2.11	0.83	0.93±0.21			$-2.2^{+0.8}_{-0.8}$	b
WR77-3	WN6	9.10	12.16	2.02	0.74	0.85±0.20			$-4.1^{+0.7}_{-0.7}$	g
WR77t	WC9d		12.14							u
WR77-6	WN6b	10.95	11.46	2.61	0.98	1.04±0.24			$-2.1^{+1.1}_{-1.2}$	b
WR78	WN7h	4.98	10.48	0.46	0.29	0.16±0.08			$-5.7^{+0.2}_{-0.2}$	b
WR79	WC7+O5-8	5.39	10.68	0.57	0.42	0.11±0.09	$-5.4^{+0.2}_{-0.2}$	0.80 ± 0.41	$-5.2^{+1.0}_{-0.4}$	g
WR79a	WN9ha	4.90	11.52	0.25	0.19	0.21±0.08			$-7.1^{+0.6}_{-0.8}$	g
WR79b	WN9ha	6.47	13.63	0.29	0.15	0.38±0.08			$-7.6^{+0.6}_{-0.7}$	b
WR80	WC9d	6.31	12.72	3.15	1.46	0.85±0.08			$-7.5^{+0.6}_{-0.8}$	b:
WR81	WC9	7.12	11.62	1.17	0.64	0.63±0.08			$-5.2^{+0.3}_{-0.4}$	g
WR82	WN7(h)	8.69	12.87	0.78	0.35	0.44±0.08			$-4.7^{+0.4}_{-0.5}$	g

WR Number	Spectral type	K_s (mag)	μ (mag)	J-K_s (mag)	H-K_s (mag)	A_{Ks} (mag)	$M_{K_s}^{Sys}$ (mag)	$F_{WR}^{K_s}/F_{Sys}^{K_s}$	$M_{K_s}^{WR}$ (mag)	Flags
WR82-2	WC9	10.26	11.53	2.23	0.86	0.90±0.22			$-2.7^{+1.0}_{-1.2}$	b
WR83	WN5o	15.17	12.9	0.87	0.02	0.47±0.08			$1.7^{+0.5}_{-0.6}$	b
WR83-1	WC6:	12.81	11.21	2.45	1.08	0.79±0.25			$0.6^{+1.0}_{-1.2}$	b
WR84	WN7o	8.50	12.39	1.08	0.46	0.53±0.08			$-4.5^{+0.3}_{-0.3}$	g
WR84-4	WN7ha	9.49	11.62	1.39	0.51	0.69±0.16			$-3.1^{+0.7}_{-0.7}$	b
WR84-11	WN9h	10.41	12.57	2.25	0.81	1.00±0.23			$-3.4^{+0.8}_{-0.8}$	b:
WR84-9	WN6	10.64	7.7	2.79	1.06	1.26±0.29			$-0.5^{+1.7}_{-1.8}$	b
WR84-10	WC8	9.26	11.64	2.41	0.80	0.77±0.24			$-3.5^{+0.9}_{-0.9}$	b
WR85	WN6h	7.47	11.49	0.73	0.47	0.37±0.08			$-4.5^{+0.3}_{-0.3}$	g
WR88	WC9	8.05	12.68	0.98	0.51	0.58±0.08			$-5.3^{+0.4}_{-0.5}$	g
WR87	WN7h+abs	7.08	12.32	0.90	0.37	0.84±0.08			$-6.1^{+0.4}_{-0.5}$	g
WR89	WN8h+abs	6.58	12.31	0.80	0.38	0.68±0.08			$-6.5^{+0.4}_{-0.5}$	g
WR90	WC7	5.52	10.3	0.73	0.57	0.04±0.11			$-4.8^{+0.2}_{-0.2}$	g

WR Number	Spectral type	K_s (mag)	μ (mag)	J-K_s (mag)	H-K_s (mag)	A_{Ks} (mag)	$M_{K_s}^{Sys}$ (mag)	$F_{WR}^{K_s}/F_{Sys}^{K_s}$	$M_{K_s}^{WR}$ (mag)	Flags
WR91	WN7b	8.20	13.03	1.33	0.57	0.74±0.08			$-5.8^{+0.6}_{-0.7}$	b
WR93	WC7+O7-9	5.87	11.23	1.17	0.66	0.61±0.08	$-6.0^{+0.2}_{-0.2}$	0.71 ± 0.36	$-5.6^{+1.0}_{-0.6}$	b:
WR92	WC9	8.82	12.89	0.68	0.40	0.17±0.08			$-4.4^{+0.5}_{-0.6}$	b:
WR93a	WN6h	12.72	13.22	1.16	0.50	0.12±0.08			$-0.9^{+0.8}_{-0.9}$	b
WR93b	WO3	10.17	11.8	1.16	0.38	0.52±0.14			$-2.2^{+0.4}_{-0.5}$	b:
WR94	WN5o	5.91	9.9	1.18	0.28	0.45±0.08			$-4.4^{+0.2}_{-0.2}$	g
WR95	WC9d	5.27	11.57	3.02	1.40	0.71±0.08			$-7.1^{+0.4}_{-0.4}$	g
WR96	WC9d	6.20	12.11	2.84	1.32	0.59±0.08			$-6.6^{+0.4}_{-0.4}$	g
WR97	WN5b+O7	8.01	11.66	0.49	0.20	0.43±0.08	$-4.1^{+0.3}_{-0.3}$	0.17 ± 0.10	$-2.2^{+1.2}_{-0.8}$	b
WR98	WN8o/C7	7.04	11.46	1.05	0.51	0.58±0.08			$-5.1^{+0.3}_{-0.3}$	b:
WR98a	WC8-9vd+?	4.33	10.5	4.81	2.17	0.13±0.08	$-6.8^{+0.9}_{-1.0}$	0.35 ± 0.22	$-5.6^{+2.0}_{-1.5}$	g
WR100	WN7b	7.71	12.75	1.14	0.56	0.60±0.08			$-5.7^{+0.5}_{-0.6}$	b
WR101	WC8	7.89	11.79	1.73	0.89	0.82±0.08			$-5.0^{+0.7}_{-0.9}$	g

WR Number	Spectral type	K_s (mag)	μ (mag)	J-K_s (mag)	H-K_s (mag)	A_{Ks} (mag)	$M_{K_s}^{Sys}$ (mag)	$F_{WR}^{K_s}/F_{Sys}^{K_s}$	$M_{K_s}^{WR}$ (mag)	Flags
WR102	WO2	11.29	12.11	0.63	0.42	0.50±0.08			$-1.4^{+0.3}_{-0.3}$	b
WR102-19	WN5	10.32	11.89	1.52	0.63	0.65±0.16			$-2.4^{+0.6}_{-0.7}$	b
WR102-20	WC9	10.89	11.42	2.89	1.49	1.50±0.29			$-2.1^{+1.0}_{-1.1}$	b
WR102-25	WN6	12.83	14.04	0.89	0.45	0.37±0.13			$-1.7^{+0.6}_{-0.6}$	b
WR102-21	WN6	9.47	11.62	1.93	0.82	0.88±0.19			$-3.4^{+0.9}_{-1.0}$	b:
WR102l	WN8o	7.57	12.67	1.26	0.53	0.86±0.08			$-6.1^{+0.5}_{-0.5}$	g
WR103	WC9d+?	6.37	12.7	1.38	0.84	0.15±0.09	$-6.6^{+0.5}_{-0.7}$	0.71 ± 0.45	$-6.3^{+1.6}_{-1.0}$	g
WR104	WC9d+B0.5V (+VB)	2.42	12.19	4.25	1.92	0.71±0.07	$-10.6^{+0.6}_{-0.6}$	0.72 ± 0.14	$-10.2^{+0.8}_{-0.8}$	b
WR105	WN9h	5.73	11.19	1.31	0.52	0.88±0.08			$-6.4^{+0.3}_{-0.4}$	g
WR105-2	WN8-9	9.02	11.88	1.45	0.58	0.65±0.16			$-3.7^{+0.6}_{-0.6}$	b
WR106	WC9d	4.82	12.43	3.12	1.46	0.49±0.08			$-8.2^{+0.4}_{-0.4}$	b:
WR107	WN8o	8.19	12.29	1.19	0.50	0.65±0.08			$-4.8^{+0.5}_{-0.6}$	b:

WR Number	Spectral type	K_s (mag)	μ (mag)	J-K_s (mag)	H-K_s (mag)	A_{Ks} (mag)	$M_{\mathrm{K_s}}^{\mathrm{Sys}}$ (mag)	$\mathrm{F}_{\mathrm{WR}}^{\mathrm{K_s}}/\mathrm{F}_{\mathrm{Sys}}^{\mathrm{K_s}}$	$M_{\mathrm{K_s}}^{\mathrm{WR}}$ (mag)	Flags
WR107a	WC5-7	9.38	12.35	1.79	0.93	0.67±0.11			$-3.7^{+0.5}_{-0.5}$	b
WR108	WN9ha	7.10	12.22	0.57	0.24	0.49±0.08			$-5.7^{+0.3}_{-0.3}$	b
WR108-1	WN9	11.16	11.73	3.71	1.51	1.84±0.37			$-2.6^{+0.9}_{-0.9}$	b
WR109	WN5h	13.27	14.18	0.25	0.52	0.12±0.08			$-1.2^{+0.5}_{-0.5}$	b
WR110	WN5-6b	6.22	10.99	0.90	0.50	0.41±0.08			$-5.2^{+0.2}_{-0.2}$	g
WR111	WC5	6.51	11.06	0.77	0.63	0.08±0.11			$-4.7^{+0.3}_{-0.4}$	g
WR111-1	WN6o	10.13	9.01	2.45	0.93	1.08±0.24			$-0.8^{+1.2}_{-1.3}$	b
WR111-9	WC9	7.79	12.5	1.87	0.83	0.79±0.18			$-5.6^{+0.6}_{-0.6}$	b:
WR111-2	WN7b	7.94	11.48	1.68	0.66	0.59±0.15			$-4.4^{+0.6}_{-0.6}$	b
WR111-4	WN7	8.66	11.87	1.64	0.61	0.71±0.17			$-4.1^{+0.6}_{-0.6}$	b
WR111-13	WN6b	8.02	11.87	2.15	0.87	0.84±0.20			$-4.8^{+0.7}_{-0.8}$	g
WR111-3	WC8	8.57	11.91	2.64	1.13	1.05±0.24			$-4.5^{+0.7}_{-0.8}$	b:
WR111-10	WC7	12.24	10.44	3.89	2.02	1.80±0.37			$-0.6^{+1.0}_{-1.2}$	b

WR Number	Spectral type	K_s (mag)	μ (mag)	J-K_s (mag)	H-K_s (mag)	A_{Ks} (mag)	$M_{K_s}^{Sys}$ (mag)	$F_{WR}^{K_s}/F_{Sys}^{K_s}$	$M_{K_s}^{WR}$ (mag)	Flags
WR111-12	WC9	5.76	11.74	3.28	1.49	1.59±0.32			$-7.7^{+0.7}_{-0.7}$	b
WR112	WC9d+OB?	4.25	12.5	4.43	2.01	0.71±0.08	$-9.4^{+0.9}_{-1.0}$	0.18 ± 0.11	$-7.5^{+2.0}_{-1.5}$	b:
WR113	WC8d+O8-9IV	5.49	11.28	1.53	0.79	0.34±0.08	$-6.2^{+0.3}_{-0.3}$	0.48 ± 0.28	$-5.4^{+1.2}_{-0.8}$	g
WR113-1	WN7o	7.76	11.64	1.33	0.54	0.59±0.15			$-4.7^{+0.6}_{-0.6}$	g
WR113-2	WC5-6	8.27	11.34	2.07	1.01	0.65±0.21			$-4.1^{+0.8}_{-0.8}$	g
WR114	WC5+OB?	7.61	11.6	1.37	0.82	0.49±0.11			$-4.5^{+0.2}_{-0.2}$	g
WR114-2	WC8	11.69	11.29	2.76	1.21	1.14±0.25			$-1.3^{+1.2}_{-1.3}$	b
WR114-1	WN6	10.61	11.89	1.60	0.63	0.67±0.17			$-2.4^{+0.9}_{-1.0}$	b
WR115	WN6o	6.95	8.39	1.04	0.47	0.61±0.08			$-2.7^{+1.1}_{-1.3}$	b
WR115-1	WN6o	8.96	12.52	1.36	0.56	0.56±0.14			$-4.2^{+0.5}_{-0.5}$	g
WR115-2	WN8	9.28	11.65	2.25	0.85	1.02±0.23			$-3.5^{+0.7}_{-0.8}$	b
WR115-3	WN7	8.30	12.14	1.29	0.52	0.57±0.14			$-4.5^{+0.4}_{-0.4}$	g
WR116	WN8h	6.96	11.94	1.25	0.61	0.25±0.08			$-5.3^{+0.3}_{-0.3}$	b

WR Number	Spectral type	K_s (mag)	μ (mag)	J-K_s (mag)	H-K_s (mag)	A_{Ks} (mag)	$M_{K_s}^{Sys}$ (mag)	$F_{WR}^{K_s}/F_{Sys}^{K_s}$	$M_{K_s}^{WR}$ (mag)	Flags
WR116-1	WC9+OBI	5.63	12.06	2.73	1.30	1.65±0.30	$-8.3^{+0.7}_{-0.7}$	0.10 ± 0.07	$-5.9^{+1.8}_{-1.3}$	b
WR116-2	WN5	11.93	11.6	2.14	0.82	0.94±0.21			$-1.2^{+1.1}_{-1.2}$	b
WR116-3	WN6ha	9.43	12.3	1.25	0.48	0.62±0.15			$-3.6^{+0.5}_{-0.5}$	b
WR117	WC9d	7.36	12.81	2.31	1.13	0.65±0.08			$-6.3^{+0.6}_{-0.7}$	g
WR117-1	WN7	7.63	12.66	1.46	0.66	0.70±0.16			$-5.8^{+0.4}_{-0.4}$	b
WR118	WC9d	3.65	11.98	4.45	1.76	1.46±0.08			$-9.8^{+0.6}_{-0.7}$	b
WR118-4	WC8	9.36	11.85	2.82	1.16	1.12±0.25			$-3.7^{+0.7}_{-0.8}$	b
WR118-2	WN9	7.58	11.91	2.99	1.08	1.36±0.30			$-5.8^{+0.7}_{-0.8}$	g
WR118-3	WN9	7.38	9.22	2.96	1.02	1.31±0.30			$-4.7^{+1.4}_{-1.5}$	b:
WR118-10	WN6	10.02	8.68	2.02	0.79	0.88±0.20			$-0.1^{+1.0}_{-1.2}$	b
WR118-5	WC9d		12.29							u
WR118-6	WN7:	10.59	11.8	3.05	1.14	1.42±0.31			$-2.7^{+0.8}_{-0.9}$	b
WR119	WC9d	7.26	12.54	2.24	1.17	0.42±0.08			$-5.9^{+0.6}_{-0.7}$	g

WR Number	Spectral type	K_s (mag)	μ (mag)	J-K_s (mag)	H-K_s (mag)	A_{Ks} (mag)	$M_{K_s}^{Sys}$ (mag)	$F_{WR}^{K_s}/F_{Sys}^{K_s}$	$M_{K_s}^{WR}$ (mag)	Flags
WR119-2	WC8	9.56	11.7	2.27	0.93	0.83±0.20			$-3.1^{+0.7}_{-0.8}$	b
WR119-1	WN7o	10.29	13.15	1.48	0.57	0.64±0.16			$-3.7^{+0.7}_{-0.7}$	b
WR120	WN7o	8.01	10.89	0.89	0.40	0.52±0.08			$-3.6^{+0.6}_{-0.7}$	b
WR120-16	WC8	10.54	11.72	2.38	0.70	0.70±0.21			$-2.5^{+1.1}_{-1.2}$	b
WR120-1	WC9	9.45	12.34	1.60	0.72	0.65±0.16			$-3.7^{+0.6}_{-0.6}$	b
WR120-11	WC8	10.25	12.12	2.10	0.90	0.76±0.19			$-2.7^{+0.6}_{-0.7}$	b
WR120-7	WN7	8.51	12.33	1.71	0.70	0.79±0.18			$-4.7^{+0.5}_{-0.6}$	b
WR120-3	WN9h	9.16	10.16	2.79	1.06	1.30±0.28			$-3.2^{+1.3}_{-1.4}$	b
WR120-4	WN9h	9.27	11.83	2.58	0.99	1.20±0.26			$-3.9^{+0.8}_{-0.9}$	b:
WR120-5	WC8		11.49							u
WR120-6	WN6	12.32	12.48	1.19	0.51	0.48±0.13			$-0.8^{+0.5}_{-0.5}$	b
WR120-15	WC8	10.66	12.39	2.03	0.71	0.62±0.18			$-2.5^{+0.7}_{-0.7}$	b
WR120-10	WN7	8.53	12.06	1.47	0.63	0.68±0.16			$-4.4^{+0.6}_{-0.6}$	b:

WR Number	Spectral type	K_s (mag)	μ (mag)	J-K_s (mag)	H-K_s (mag)	A_{Ks} (mag)	$M_{\mathrm{K_s}}^{\mathrm{Sys}}$ (mag)	$\mathrm{F}_{\mathrm{WR}}^{\mathrm{K_s}}/\mathrm{F}_{\mathrm{Sys}}^{\mathrm{K_s}}$	$M_{\mathrm{K_s}}^{\mathrm{WR}}$ (mag)	Flags
WR121	WC9d	5.77	11.74	2.52	1.29	0.57±0.08			$-6.6^{+0.3}_{-0.3}$	g
WR121-15	WN4-5	10.72	12.37	2.02	0.85	1.13±0.23			$-3.0^{+0.7}_{-0.7}$	g
WR121-12	WN5	10.64	11.9	2.12	0.79	0.90±0.21			$-2.6^{+0.9}_{-1.0}$	b
WR121-1	WN7h	9.47	12.52	1.47	0.60	0.66±0.16			$-3.8^{+0.5}_{-0.5}$	b
WR121-6	WN5	9.34	12.28	1.08	0.42	0.39±0.12			$-3.4^{+0.5}_{-0.5}$	b
WR122-2	WN9	9.61	11.72	2.88	1.07	1.33±0.29			$-3.5^{+0.8}_{-0.9}$	b:
WR122-3	WN6	9.99	11.91	2.82	1.07	1.27±0.28			$-3.3^{+0.8}_{-0.9}$	b:
WR122-1	WC8	10.30	13.33	1.88	1.00	0.78±0.17			$-4.0^{+0.6}_{-0.6}$	b
WR122-15	WN6	11.05	11.61	2.06	0.57	0.74±0.21			$-1.8^{+1.0}_{-1.0}$	b
WR123	WN8o	8.92	13.64	0.60	0.36	0.26±0.08			$-5.1^{+0.5}_{-0.5}$	b:
WR123-1	WN6o	8.71	12.13	1.88	0.76	0.83±0.19			$-4.4^{+0.7}_{-0.7}$	b
WR123-3	WN8	9.94	12.51	2.28	0.87	1.05±0.23			$-3.9^{+0.8}_{-0.8}$	b
WR123-8	WN9h	12.62	11.21	2.11	0.82	0.97±0.22			$-0.0^{+1.1}_{-1.2}$	b

WR Number	Spectral type	K_s (mag)	μ (mag)	J-K_s (mag)	H-K_s (mag)	A_{Ks} (mag)	$M_{\mathrm{K_s}}^{\mathrm{Sys}}$ (mag)	$\mathrm{F}_{\mathrm{WR}}^{\mathrm{K_s}}/\mathrm{F}_{\mathrm{Sys}}^{\mathrm{K_s}}$	$M_{\mathrm{K_s}}^{\mathrm{WR}}$ (mag)	Flags
WR124	WN8h	7.73	13.84	0.85	0.45	0.42±0.08			$-6.7^{+0.5}_{-0.5}$	g
WR124-1B	WC8	9.19	10.96	2.85	1.19	1.15±0.26			$-3.3^{+1.2}_{-1.3}$	b
WR124-1A	WC8	9.19	11.85	2.85	1.19	1.15±0.26			$-3.9^{+0.8}_{-0.9}$	b
WR124-3	WC8	10.77	12.82	2.19	1.05	0.89±0.20			$-3.1^{+0.7}_{-0.7}$	b
WR124-9	WC6:	11.67	12.12	2.23	1.05	0.72±0.22			$-1.6^{+0.9}_{-1.0}$	b
WR124-18	WN9h	9.97	12.07	2.82	1.07	1.32±0.28			$-3.7^{+0.9}_{-0.9}$	b:
WR124-19	WC6:	12.08	11.83	2.57	1.21	0.91±0.25			$-0.9^{+0.9}_{-1.0}$	b
WR124-2	WC8	10.76	12.21	2.81	1.04	1.03±0.25			$-2.6^{+0.7}_{-0.8}$	b
WR124-6	WC6	9.68	12.18	2.99	1.23	1.03±0.28			$-3.7^{+0.7}_{-0.8}$	b
WR124-7	WC7	9.58	12.3	3.25	1.44	1.23±0.31			$-4.0^{+0.7}_{-0.8}$	b
WR124-11	WN6b	10.25	11.95	2.40	0.94	0.95±0.22			$-3.1^{+0.9}_{-1.0}$	b
WR124-20	WC9	9.92	9.15	3.05	1.26	1.37±0.30			$-0.9^{+0.7}_{-0.9}$	b
WR124-21	WC8	10.21	13.83	1.65	0.76	0.56±0.15			$-4.3^{+0.5}_{-0.5}$	b

WR Number	Spectral type	K_s (mag)	μ (mag)	J-K_s (mag)	H-K_s (mag)	A_{Ks} (mag)	$M_{K_s}^{Sys}$ (mag)	$F_{WR}^{K_s}/F_{Sys}^{K_s}$	$M_{K_s}^{WR}$ (mag)	Flags
WR124-22	WC9	9.64	11.41	3.37	1.45	1.58±0.33			$-3.6^{+0.9}_{-1.0}$	b
WR125	WC7ed+O9III	8.21	12.63	1.09	0.53	0.69±0.09	$-5.2^{+0.5}_{-0.6}$	0.76 ± 0.39	$-4.9^{+1.2}_{-0.9}$	g
WR125-4	WN7	10.12	12.35	2.59	0.95	1.18±0.26			$-3.5^{+0.7}_{-0.7}$	b
WR125-3	WN7ha	7.33	12.34	1.32	0.50	0.67±0.16			$-5.9^{+0.7}_{-0.7}$	g
WR125-2	WN8-9	6.60	12.58	1.61	0.68	0.75±0.17			$-6.9^{+0.5}_{-0.5}$	b:
WR125-1	WC8	9.07	13.4	1.13	0.54	0.27±0.10			$-4.7^{+0.4}_{-0.4}$	b
WR126	WC5/WN	10.09	14.4	0.61	0.31	0.40±0.11			$-4.8^{+0.4}_{-0.4}$	b:
WR127	WN3b+O9.5V	8.76	12.45	0.42	0.26	0.19±0.07	$-3.9^{+0.2}_{-0.2}$	0.40 ± 0.23	$-2.9^{+1.2}_{-0.7}$	g
WR129	WN4o	10.40	13.69	0.68	0.32	0.38±0.08			$-3.8^{+0.4}_{-0.4}$	b:
WR128	WN4(h)	9.62	12.31	0.35	0.22	0.14±0.08			$-2.9^{+0.3}_{-0.4}$	g
WR130	WN8(h)	7.45	14.12	1.00	0.42	0.59±0.08			$-7.4^{+0.5}_{-0.6}$	b
WR131	WN7h+abs	8.86	14.2	0.66	0.29	0.47±0.08			$-5.9^{+0.4}_{-0.4}$	g
WR132	WC6+?	9.05	13.09	1.13	0.71	0.40±0.11			$-4.5^{+0.3}_{-0.3}$	g

WR Number	Spectral type	K_s (mag)	μ (mag)	J-K_s (mag)	H-K_s (mag)	A_{Ks} (mag)	$M_{\mathrm{K_s}}^{\mathrm{Sys}}$ (mag)	$\mathrm{F}_{\mathrm{WR}}^{\mathrm{K_s}}/\mathrm{F}_{\mathrm{Sys}}^{\mathrm{K_s}}$	$M_{\mathrm{K_s}}^{\mathrm{WR}}$ (mag)	Flags
WR133	WN5o+O9I	6.25	11.33	0.07	0.07	0.13±0.07	$-5.2^{+0.2}_{-0.2}$	0.23 ± 0.14	$-3.7^{+1.1}_{-0.7}$	g
WR134	WN6b	6.16	11.21	0.55	0.36	0.17±0.08			$-5.2^{+0.2}_{-0.2}$	g
WR135	WC8	6.66	11.48	0.57	0.45	0.15±0.08			$-5.0^{+0.2}_{-0.2}$	g
WR136	WN6b(h)	5.56	11.43	0.57	0.34	0.18±0.08			$-6.1^{+0.2}_{-0.2}$	b
WR137	WC7pd+O9	6.18	11.61	0.80	0.59	0.18±0.08	$-5.6^{+0.2}_{-0.2}$	0.56 ± 0.28	$-5.0^{+1.0}_{-0.6}$	g
WR138	WN6o	6.58	11.96	0.38	0.22	0.22±0.08			$-5.7^{+0.3}_{-0.3}$	b
WR138-1	WN8-9h	8.65	15.49	1.50	0.62	0.68±0.16			$-7.3^{+0.5}_{-0.6}$	b
WR139	WN5o+O6III-V	6.33	10.58	0.37	0.19	0.30±0.09	$-4.6^{+0.1}_{-0.1}$	0.62 ± 0.36	$-4.0^{+1.1}_{-0.6}$	g
WR140	WC7pd+O4-5	5.04	11.07	0.51	0.39	0.24±0.08	$-6.3^{+0.2}_{-0.2}$	0.62 ± 0.31	$-5.8^{+0.9}_{-0.6}$	b
WR141	WN5o+O5V-III	6.54	11.42	0.80	0.39	0.44±0.08			$-5.3^{+0.2}_{-0.2}$	b
WR142	WO2	8.60	11.08	0.94	0.29	0.78±0.08			$-3.3^{+0.2}_{-0.2}$	g
WR142a	WC8	7.12	11.29	2.15	0.97	0.83±0.19			$-5.1^{+0.5}_{-0.7}$	g
WR142-1	WN6o	7.19	11.24	1.58	0.67	0.69±0.16			$-4.8^{+0.3}_{-0.3}$	b:

WR Number	Spectral type	K_s (mag)	μ (mag)	J-K_s (mag)	H-K_s (mag)	A_{Ks} (mag)	$M_{\mathrm{K_s}}^{\mathrm{Sys}}$ (mag)	$\mathrm{F}_{\mathrm{WR}}^{\mathrm{K_s}}/\mathrm{F}_{\mathrm{Sys}}^{\mathrm{K_s}}$	$M_{\mathrm{K_s}}^{\mathrm{WR}}$ (mag)	Flags
WR143	WC4+OB?	7.46	11.73	1.12	0.64	0.65±0.08	$-4.9^{+0.2}_{-0.2}$	0.67 ± 0.26	$-4.5^{+0.7}_{-0.5}$	g
WR144	WC4	7.71	11.21	1.70	0.88	0.47±0.19			$-4.0^{+0.3}_{-0.3}$	g
WR145	WN7o/CE+?	6.24	10.81	1.13	0.47	0.83±0.14	$-5.4^{+0.2}_{-0.2}$	0.86 ± 0.75	$-5.3^{+2.4}_{-0.4}$	b:
WR146	WC6+O8	5.49	10.21	1.58	0.75	1.16±0.08	$-6.3^{+0.8}_{-0.9}$	0.71 ± 0.31	$-5.9^{+1.4}_{-1.3}$	b
WR147	WN8(h)+B0.5V	4.11	11.26	1.90	0.75	1.01±0.08			$-8.2^{+0.3}_{-0.3}$	b
WR148	WN8h+	8.32	14.88	0.44	0.21	0.22±0.08			$-6.9^{+0.4}_{-0.4}$	b:
WR149	WN5o	9.61	13.45	1.01	0.45	0.65±0.08			$-4.6^{+0.3}_{-0.3}$	b:
WR150	WC5	9.60	14.71	1.12	0.71	0.32±0.11			$-5.5^{+0.4}_{-0.4}$	b
WR151	WN4o+O5V	9.01	13.65	0.75	0.35	0.43±0.11	$-5.2^{+0.5}_{-0.5}$	0.83 ± 0.49	$-5.0^{+1.4}_{-0.7}$	b
WR152	WN3(h)	10.04	13.2	0.45	0.28	0.22±0.08			$-3.5^{+0.4}_{-0.5}$	g
WR153	WN6o/CE+O6I	7.41	13.04	0.37	0.19	0.23±0.10	$-5.9^{+0.3}_{-0.3}$	0.81 ± 0.47	$-5.7^{+1.3}_{-0.6}$	b
WR154	WC6	8.29	13.65	1.01	0.72	0.25±0.11			$-5.7^{+0.4}_{-0.4}$	b:
WR155	WN6o+O9II-Ib	7.16	12.38	0.32	0.18	0.25±0.11	$-5.5^{+0.3}_{-0.3}$	0.24 ± 0.54	$-4.0^{+1.9}_{-1.6}$	g

WR Number	Spectral type	K_s (mag)	μ (mag)	J-K_s (mag)	H-K_s (mag)	A_{Ks} (mag)	$M_{\mathrm{K_s}}^{\mathrm{Sys}}$ (mag)	$\mathrm{F}_{\mathrm{WR}}^{\mathrm{K_s}}/\mathrm{F}_{\mathrm{Sys}}^{\mathrm{K_s}}$	$M_{\mathrm{K_s}}^{\mathrm{WR}}$ (mag)	Flags
WR156	WN8h	7.03	13.07	0.91	0.41	0.43±0.08			$-6.5^{+0.3}_{-0.3}$	g
WR157	WN5o(+B1II)	7.73	12.05	0.49	0.21	0.33±0.08	$-4.7^{+0.3}_{-0.3}$	0.38 ± 0.22	$-3.6^{+1.2}_{-0.8}$	g
WR158	WN7h	7.81	13.49	0.83	0.39	0.40±0.08	$-6.1^{+0.3}_{-0.3}$	0.37 ± 1.00	$-5.1^{+1.4}_{-1.4}$	g
WR159	WN4	5.53	11.3	0.57	0.23	0.34±0.10			$-6.2^{+0.5}_{-0.6}$	b

Columns: (1) WR Number, (2) Spectral type, (3) $\mathrm{K_s}$ apparent magnitude, (4) Distance modulus μ, (5) J$-\mathrm{K_s}$ colour, (6) H$-\mathrm{K_s}$ colour, (7) $\mathrm{K_s}$ band extinction A_{Ks}, (8) Absolute magnitude of binary system (including companion), (9) Fraction of light contributed to the binary system by the WR component, (10) Absolute magnitude of WR star, (11) Error flags, where M>upper$_{\mathrm{initial}}$ or M<lower$_{\mathrm{initial}}$ = b, M> upper$_{\mathrm{final}}$ or M<lower$_{\mathrm{final}}$ = b: ($_{\mathrm{initial}}$ denotes the averages calculated before sigma clipping, $_{\mathrm{final}}$ are the final absolute magnitude boundaries) and g are results with no issues.

Table A.3: Absolute v^{WR} magnitudes of Galactic WR stars, from Chapter 3.

WR Number	Spectral type	$v^{WR}\pm0.1$ (mag)	μ (mag)	$(b-v)^{WR}$ (mag)	A_v^{WR} (mag)	M_v^{Sys} (mag)	F_v^{WR}/F_v^{Sys}	M_v^{WR} (mag)	Flags
WR1	WN4b	10.51	12.49	0.51	2.84±0.71			$-4.9^{+0.8}_{-0.8}$	g
WR3	WN3ha	10.70	12.31	-0.06	1.07±0.71			$-2.8^{+0.8}_{-0.8}$	b:
WR4	WC5+?	10.53	12.87	0.20	1.65±1.01			$-4.2^{+1.1}_{-1.1}$	g
WR5	WC6	11.02	12.36	0.47	2.76±1.01			$-4.2^{+1.1}_{-1.1}$	g
WR6	WN4b	6.94	11.78	-0.07	0.45±0.71			$-5.4^{+0.8}_{-0.8}$	b:
WR7	WN4b	11.75	13.13	0.36	2.22±0.71			$-3.8^{+0.9}_{-0.9}$	b:
WR8	WN7o/CE	10.48	12.87	0.47	2.88±0.71			$-5.4^{+0.8}_{-0.8}$	b:
WR9	WC5+O7	10.93	13.3	0.74	4.16±0.72	$-6.6^{+0.8}_{-0.8}$	0.29 ± 0.12	$-5.3^{+1.4}_{-1.2}$	b
WR10	WN5h	11.08	13.69	0.22	2.26±1.61			$-5.0^{+1.7}_{-1.7}$	b:
WR11	WC8+O7.5III-V	1.74	7.67	-0.32	0.00±1.03	$-6.0^{+1.1}_{-1.1}$	0.24 ± 0.03	$-4.4^{+1.2}_{-1.2}$	g
WR12	WN8h	10.99	13.78	0.42	2.35±0.71			$-5.3^{+0.8}_{-0.8}$	g
WR13	WC6	13.78	13.41	0.82	4.20±1.01			$-4.0^{+1.1}_{-1.1}$	g

WR Number	Spectral type	v^{WR}±0.1 (mag)	μ (mag)	$(b-v)^{WR}$ (mag)	A_v^{WR} (mag)	$M_{\rm v}^{\rm Sys}$ (mag)	$\rm F_{v}^{WR}$/ $\rm F_{v}^{Sys}$	$M_{\rm v}^{\rm WR}$ (mag)	Flags
WR14	WC7+?	9.40	11.73	0.14	1.40±1.01			$-3.8^{+1.0}_{-1.0}$	g
WR15	WC6	11.72	12.36	0.72	3.79±1.01			$-4.5^{+1.0}_{-1.0}$	b:
WR16	WN8h	8.44	12.1	0.30	1.85±0.71			$-5.6^{+0.8}_{-0.8}$	g
WR17	WC5	11.03	14.15	0.14	1.40±1.01			$-4.6^{+1.1}_{-1.1}$	g
WR17-1	WN5b		12.45						u
WR18	WN4b	11.11	12.91	0.55	3.01±0.71			$-5.0^{+0.8}_{-0.8}$	g
WR19	WC5	13.75	13.18	1.06	5.19±1.01			$-4.7^{+1.1}_{-1.1}$	b:
WR19a	WN7:(h)	17.45	13.39	1.71	7.66±0.71			$-3.8^{+0.9}_{-0.9}$	b:
WR20	WN5o	14.45	14.22	0.88	4.78±0.71			$-4.6^{+0.8}_{-0.8}$	g
WR20-2	O2If*/WN6		13.72						u
WR20-1	WN7-8		12.17						u
WR20a	O3If*/WN6+ O3If*/WN6	14.14	13.51	1.38	7.09±0.71	$-6.6^{+0.8}_{-0.8}$	0.50 ± 0.00	$-5.8^{+0.8}_{-0.8}$	g

WR Number	Spectral type	v^{WR}±0.1 (mag)	μ (mag)	$(b-v)^{WR}$ (mag)	A_v^{WR} (mag)	$M_{\rm v}^{\rm Sys}$ (mag)	$F_{\rm v}^{\rm WR}/\ F_{\rm v}^{\rm Sys}$	$M_{\rm v}^{\rm WR}$ (mag)	Flags
WR20b	WN6ha	15.40	12.44	1.69	8.32±0.71			$-5.5^{+0.8}_{-0.8}$	b
WR20-3	O2If*/WN6		11.99						u
WR21a	O2If/WN5	12.80	13.21						u
WR21	WN5o+O4-6	9.76	13.0	0.27	2.32±0.76	$-5.6^{+0.8}_{-0.8}$	0.86 ± 0.20	$-5.5^{+1.1}_{-1.0}$	b
WR22	WN7h+O9III-V	7.16	11.84	0.08	1.69±0.71			$-6.4^{+0.8}_{-0.8}$	g
WR23	WC6	9.67	12.03	-0.05	0.62±1.01			$-3.0^{+1.0}_{-1.0}$	b
WR24	WN6ha	7.20	12.75	-0.04	1.19±0.71			$-6.9^{+0.8}_{-0.8}$	b:
WR25	O2.5If*/WN6+O	8.84	11.47	0.17	3.16±1.07			$-5.8^{+1.1}_{-1.1}$	b
WR26	WN7b/CE	14.61	14.13	0.92	4.74±0.71			$-4.3^{+0.8}_{-0.8}$	g
WR27	WC6+a	14.96	12.09	1.29	6.14±1.01			$-3.3^{+1.0}_{-1.0}$	b:
WR28	WN6(h)+OB?	13.00	13.79	0.77	4.53±0.71			$-5.4^{+0.8}_{-0.8}$	b
WR29	WN7h+O	12.65	13.76	0.65	3.76±1.32	$-5.0^{+1.4}_{-1.4}$	0.26 ± 0.82	$-3.5^{+2.9}_{-2.9}$	b
WR30	WC6+O6-8	11.73	13.54	0.27	2.18±0.77	$-4.1^{+0.9}_{-0.9}$	0.44 ± 0.18	$-3.2^{+1.4}_{-1.2}$	b:

WR Number	Spectral type	v^{WR}±0.1 (mag)	μ (mag)	$(b-v)^{WR}$ (mag)	A_v^{WR} (mag)	M_v^{Sys} (mag)	F_v^{WR}/F_v^{Sys}	M_v^{WR} (mag)	Flags
WR30a	WO4+O5-5.5	13.33	14.14	0.79	4.52±0.70	$-5.4^{+0.8}_{-0.8}$	0.10 ± 0.05	$-2.9^{+1.6}_{-1.2}$	g
WR31	WN4o+O8V	10.69	13.93	0.28	2.47±0.71			$-5.8^{+0.9}_{-0.9}$	b
WR31a	WN11h		14.33						u
WR31b	WN11h		13.43						u
WR31c	WC6	16.37	13.91	0.96	4.78±1.01			$-2.4^{+1.1}_{-1.1}$	b
WR31-1	O3.5If/WN7		13.31						u
WR32	WC5+OB?	15.90	13.8	1.29	6.37±0.77	$-4.4^{+0.9}_{-0.9}$	0.44 ± 0.18	$-3.5^{+1.4}_{-1.2}$	g
WR33	WC6	12.35	14.4	0.16	1.48±1.01			$-3.6^{+1.1}_{-1.1}$	g
WR34	WN5o	14.50	14.35	0.76	4.28±0.71			$-4.2^{+0.8}_{-0.8}$	g
WR35	WN6h+OB?	13.90	14.18	0.59	3.63±2.21	$-4.0^{+2.2}_{-2.2}$	0.48 ± 1.25	$-3.2^{+3.0}_{-3.0}$	b:
WR35a	WN6h+O8.5V	13.92	13.83	0.86	4.77±0.71	$-4.8^{+0.8}_{-0.8}$	0.09 ± 0.09	$-2.1^{+5.3}_{-1.5}$	b
WR35b	WN4b	14.49	13.65	1.27	5.97±0.71			$-5.2^{+0.8}_{-0.8}$	b:
WR36	WN5-6b+OB?	13.70	13.67	0.68	3.75±0.82	$-3.8^{+0.9}_{-0.9}$	0.59 ± 0.34	$-3.3^{+1.9}_{-1.4}$	b:

WR Number	Spectral type	v^{WR}±0.1 (mag)	μ (mag)	$(b-v)^{WR}$ (mag)	A_v^{WR} (mag)	M_v^{Sys} (mag)	F_v^{WR}/F_v^{Sys}	M_v^{WR} (mag)	Flags
WR37	WN4b	15.77	14.13	1.23	5.81±0.71			$-4.3^{+0.8}_{-0.8}$	g
WR38	WC4	15.40	13.91	0.93	4.66±1.01			$-3.3^{+1.1}_{-1.1}$	b:
WR38a	WN5o	16.21	13.67	0.83	4.57±0.71			$-2.1^{+0.8}_{-0.8}$	b
WR40	WN8h	7.60	12.92	0.19	1.40±0.71			$-6.8^{+0.8}_{-0.8}$	b
WR38b	WC7	16.21	13.18	1.50	7.00±1.01			$-4.1^{+1.1}_{-1.1}$	g
WR39	WC7+OB?	14.50	12.92	1.26	6.32±0.72	$-5.0^{+1.0}_{-1.0}$	0.25 ± 0.13	$-3.5^{+1.8}_{-1.5}$	g
WR41	WC5+OB?	14.80	13.89	0.80	4.26±0.90	$-3.4^{+1.0}_{-1.0}$	0.66 ± 0.27	$-3.0^{+1.5}_{-1.3}$	b
WR42	WC7+O7V	8.25	11.93	0.06	1.33±0.76	$-5.1^{+0.8}_{-0.8}$	0.37 ± 0.19	$-4.0^{+1.6}_{-1.3}$	g
WR42a	WN5b	17.61	13.75	1.46	6.76±0.71			$-3.0^{+0.8}_{-0.8}$	b
WR42b	WN4b	16.96	14.01	2.43	10.75±0.71			$-7.9^{+0.9}_{-0.9}$	b
WR42c	WN5o	16.56	14.14	1.36	6.76±0.71			$-4.4^{+0.8}_{-0.8}$	g
WR42d	WN5b	15.28	12.53	1.33	6.22±0.71			$-3.7^{+1.0}_{-1.0}$	b:
WR42-1	O3If*/WN6		13.19						u

WR Number	Spectral type	v^{WR}±0.1 (mag)	μ (mag)	$(b-v)^{WR}$ (mag)	A_v^{WR} (mag)	M_v^{Sys} (mag)	F_v^{WR}/F_v^{Sys}	M_v^{WR} (mag)	Flags
WR43-2	O2If*/WN5		13.95						u
WR43-3	O2.5If*/WN6		14.08						u
WR43-1	WN4b		10.63						u
WR44	WN4o+OB?	12.96	13.92	0.37	2.77±0.70	$-3.8^{+0.8}_{-0.8}$	0.10 ± 0.06	$-1.4^{+1.8}_{-1.3}$	b
WR44a	WN5b	16.20	13.52	1.55	7.13±0.71			$-4.6^{+0.8}_{-0.8}$	g
WR45	WC6	14.80	13.14	1.12	5.44±1.01			$-3.8^{+1.0}_{-1.0}$	g
WR45-1	WN9-10h		13.44						u
WR45-2	WN5		13.21						u
WR45a	WN5o	16.69	12.89	1.19	6.06±0.71			$-2.5^{+0.9}_{-0.9}$	b
WR45b	WN4b	18.08	13.87	1.40	6.51±0.71			$-2.4^{+0.8}_{-0.8}$	b
WR45-3	WN5b		13.58						u
WR45-4	WN6		13.76						u
WR45c	WN5o	15.44	13.94	0.91	4.90±0.71			$-3.5^{+0.8}_{-0.8}$	b:

WR Number	Spectral type	v^{WR}±0.1 (mag)	μ (mag)	$(b-v)^{WR}$ (mag)	A_v^{WR} (mag)	$M_{\rm v}^{\rm Sys}$ (mag)	$F_{\rm v}^{\rm WR}/\ F_{\rm v}^{\rm Sys}$	$M_{\rm v}^{\rm WR}$ (mag)	Flags
WR46	WN3b pec	10.87	12.07	-0.03	0.62±0.71			$-1.9^{+0.8}_{-0.8}$	b
WR46-1	WN6o		13.37						u
WR46-18	WC6-7		11.29						u
WR46-7	WC5-7		12.43						u
WR46-8	WN6		12.06						u
WR46-16	WN9		11.96						u
WR46-9	WN5		12.42						u
WR46-17	WN9/OIf+		12.3						u
WR46a	WN4o	16.00	14.14	1.04	5.60±0.71			$-3.8^{+0.8}_{-0.8}$	g
WR46-2	WN7h		12.91						u
WR46-3	O6-7.5If+		13.05						u
WR46-4	Ofpe/WN9		12.24						u
WR46-5	WN6		12.86						u

WR Number	Spectral type	v^{WR}±0.1 (mag)	μ (mag)	$(b-v)^{WR}$ (mag)	A_v^{WR} (mag)	$M_{\rm v}^{\rm Sys}$ (mag)	$F_{\rm v}^{\rm WR}/\ F_{\rm v}^{\rm Sys}$	$M_{\rm v}^{\rm WR}$ (mag)	Flags
WR46-6	WN7		12.97						u
WR46-15	WN8		11.5						u
WR46-12	WN4b		12.39						u
WR46-13	WC7		12.77						u
WR46-14	WN5b		9.06						u
WR47	WN6o+O5V	11.08	12.72	0.76	4.33±2.08	$-6.1^{+2.1}_{-2.1}$	0.45 ± 1.17	$-5.2^{+3.0}_{-3.0}$	b:
WR47a	WN8h	15.98	13.45	1.73	7.75±0.71			$-5.4^{+0.9}_{-0.9}$	g
WR47-1	WN6o		12.69						u
WR47b	WN9h	17.05	13.75	1.93	8.57±0.71			$-5.4^{+0.9}_{-0.9}$	g
WR47-5	WN6(h)		12.36						u
WR47c	WC5	16.09	14.16	1.40	6.59±1.01			$-4.8^{+1.1}_{-1.1}$	b:
WR47-2	WC5-6		12.69						u
WR47-3	WC5-6		10.74						u

WR Number	Spectral type	v^{WR}±0.1 (mag)	μ (mag)	$(b-v)^{WR}$ (mag)	A_v^{WR} (mag)	$M_{\rm v}^{\rm Sys}$ (mag)	$\rm F_{v}^{WR}$/ $\rm F_{v}^{Sys}$	$M_{\rm v}^{\rm WR}$ (mag)	Flags
WR48	WC6 (+O9.5/B0Iab)	5.88	11.9	-0.12	0.72±0.70	$-7.2^{+1.0}_{-1.0}$	0.96 ± 0.42	$-7.1^{+1.7}_{-1.1}$	b
WR48-1	WC7		12.34						u
WR48b	WC9d	15.96	13.55	1.07	5.73±0.71			$-3.5^{+0.8}_{-0.8}$	b
WR48-6	WN9		12.4						u
WR48-10	WN9h		12.01						u
WR48-7	WN8		12.09						u
WR48-4	WC6		11.97						u
WR48-8	WN9		12.54						u
WR48-9	WN9h		12.22						u
WR48a	WC8ed+?	16.80	11.78	1.70	8.28±0.70	$-3.5^{+1.0}_{-1.0}$	0.12 ± 0.07	$-1.3^{+1.9}_{-1.5}$	b
WR48-5	WN6b		11.57						u
WR48c	WN3h/C4	13.98	12.13	0.39	2.55±0.71			$-0.7^{+0.7}_{-0.7}$	b

WR Number	Spectral type	v^{WR}±0.1 (mag)	μ (mag)	$(b-v)^{WR}$ (mag)	A_v^{WR} (mag)	$M_{\rm v}^{\rm Sys}$ (mag)	$\rm F_{v}^{WR}$/ $\rm F_{v}^{Sys}$	$M_{\rm v}^{\rm WR}$ (mag)	Flags
WR48-2	WC7-8		12.56						u
WR49	WN5(h)	13.84	14.61	0.34	2.55±0.71			$-3.4^{+0.8}_{-0.8}$	b:
WR50	WC7+OB	12.49	12.7	0.54	3.21±0.91	$-3.5^{+1.0}_{-1.0}$	0.60 ± 0.31	$-3.0^{+1.8}_{-1.4}$	b
WR51	WN4o	14.64	12.82	1.04	5.60±0.71			$-3.9^{+0.8}_{-0.8}$	g
WR52	WC4	9.86	11.21	0.29	2.02±1.01			$-3.4^{+1.0}_{-1.0}$	b:
WR52-2	WN6		12.1						u
WR53	WC8d	10.88	13.08	0.42	3.25±0.71			$-5.6^{+0.8}_{-0.8}$	b:
WR54	WN5o	12.99	14.07	0.46	3.05±0.71			$-4.2^{+0.8}_{-0.8}$	g
WR55	WN7o	10.87	12.38	0.40	2.27±0.71			$-3.9^{+0.8}_{-0.8}$	b:
WR56	WC7	13.87	14.69	0.44	2.64±1.01			$-3.5^{+1.1}_{-1.1}$	g
WR56a	WN6o	15.91	13.2	1.32	6.59±0.71			$-4.1^{+0.9}_{-0.9}$	g
WR57	WC8	10.02	13.7	0.10	1.94±0.71			$-5.8^{+0.9}_{-0.9}$	b
WR58	WN4b/CE	13.05	13.85	0.57	3.30±0.71			$-4.2^{+0.8}_{-0.8}$	g

WR Number	Spectral type	v^{WR}±0.1 (mag)	μ (mag)	$(b-v)^{WR}$ (mag)	A_v^{WR} (mag)	$M_{\rm v}^{\rm Sys}$ (mag)	$F_{\rm v}^{\rm WR}/F_{\rm v}^{\rm Sys}$	$M_{\rm v}^{\rm WR}$ (mag)	Flags
WR59	WC9d	13.90	12.77	1.24	6.43±0.71			$-5.4^{+0.8}_{-0.8}$	b
WR59-2	WC5-6		11.08						u
WR60	WC8	13.25	12.73	1.04	5.81±0.71			$-5.4^{+0.8}_{-0.8}$	b:
WR60-7	WC7-8		11.57						u
WR60-5	WC7		11.94						u
WR60-2	WC8		11.6						u
WR61	WN5o	12.41	13.7	0.36	2.64±0.71			$-4.1^{+0.8}_{-0.8}$	g
WR61-3	WC9		9.8						u
WR61-1	WN6		12.95						u
WR62	WN6b	14.22	13.15	1.60	7.33±0.71			$-6.4^{+0.8}_{-0.8}$	b
WR62a	WN6o	13.80	12.72	1.24	6.26±0.71			$-5.3^{+0.8}_{-0.8}$	b:
WR62-2	WN8-9h		11.71						u
WR62b	WN5o	17.26	13.7	1.77	8.45±0.71			$-5.0^{+0.9}_{-0.9}$	b:

WR Number	Spectral type	v^{WR}±0.1 (mag)	μ (mag)	$(b-v)^{WR}$ (mag)	A_v^{WR} (mag)	M_v^{Sys} (mag)	F_v^{WR}/F_v^{Sys}	M_v^{WR} (mag)	Flags
WR62-1	WN7-8h		11.81						u
WR64	WC7	15.57	14.51	0.16	1.48±1.01			$-0.5^{+1.1}_{-1.1}$	b
WR64-3	WN6o		12.31						u
WR64-4	WN6o+OB		10.93						u
WR64-5	WN6o		11.31						u
WR65	WC9d+OB?	14.50	12.48	1.41	7.06±0.71	$-5.2^{+0.9}_{-0.9}$	0.17 ± 0.11	$-3.3^{+2.0}_{-1.4}$	b
WR66	WN8(h)	11.66	13.57	0.73	3.63±0.71			$-5.7^{+1.1}_{-1.1}$	g
WR67	WN6o	12.12	11.75	0.87	4.74±0.71			$-4.5^{+0.8}_{-0.8}$	g
WR67-3	WN10		12.34						u
WR67-1	WN6h		12.63						u
WR67-2	WC7		11.68						u
WR68	WC7	14.09	13.46	0.97	4.82±1.01			$-4.3^{+1.1}_{-1.1}$	b:
WR68-1	WN4b		11.37						u

WR Number	Spectral type	v^{WR}±0.1 (mag)	μ (mag)	$(b-v)^{WR}$ (mag)	A_v^{WR} (mag)	M_v^{Sys} (mag)	F_v^{WR}/F_v^{Sys}	M_v^{WR} (mag)	Flags
WR68a	WN6o	14.41	12.99	1.46	7.17±0.71			$-5.9^{+0.8}_{-0.8}$	b
WR69	WC9d+OB	9.43	12.71	0.14	1.83±0.73	$-5.2^{+0.8}_{-0.8}$	0.25 ± 0.16	$-3.7^{+1.9}_{-1.3}$	b:
WR70	WC9vd+B0I	10.10	12.39	0.96	5.20±0.71	$-7.6^{+0.8}_{-0.8}$	0.05 ± 0.03	$-4.3^{+2.0}_{-1.3}$	g
WR70-1	WN7		11.42						u
WR70-13	WC8d		12.22						u
WR70-3	WC7		11.87						u
WR70-5	WC9		11.45						u
WR70a	WN6o	16.90	13.01	1.23	6.22±0.71			$-2.5^{+0.9}_{-0.9}$	b
WR70-2	WN5b		12.82						u
WR70-11	WN7		13.1						u
WR70-16	WC7d+WN or WN/Cd+O		8.7						u
WR71	WN6o	10.23	12.52	-0.05	0.95±0.71			$-3.4^{+0.8}_{-0.8}$	b:

WR Number	Spectral type	v^{WR}±0.1 (mag)	μ (mag)	$(b-v)^{WR}$ (mag)	A_v^{WR} (mag)	$M_{\rm v}^{\rm Sys}$ (mag)	$F_{\rm v}^{\rm WR}/\ F_{\rm v}^{\rm Sys}$	$M_{\rm v}^{\rm WR}$ (mag)	Flags
WR71-1	WN9		12.1						u
WR72-5	WN6o		12.05						u
WR72-1	WC9		12.38						u
WR72-2	WC8		12.23						u
WR73	WC9d	15.20	14.17	1.23	6.39±0.71			$-5.5^{+0.9}_{-0.9}$	b
WR74	WN7o	13.98	13.0	1.58	7.13±0.71			$-6.3^{+0.8}_{-0.8}$	b
WR75	WN6b	11.23	12.6	0.71	3.67±0.71			$-5.2^{+0.8}_{-0.8}$	b:
WR75-1	WC8		11.68						u
WR75aa	WC9d		13.44						u
WR75a	WC9	14.51	12.49	1.53	7.62±0.71			$-5.8^{+0.9}_{-0.9}$	b
WR75b	WC9	16.09	11.14	1.71	8.36±0.71			$-3.6^{+0.9}_{-0.9}$	b
WR75-21	WC7:		10.5						u
WR75ab	WN7h		12.9						u

WR Number	Spectral type	v^{WR}±0.1 (mag)	μ (mag)	$(b-v)^{WR}$ (mag)	A_v^{WR} (mag)	M_v^{Sys} (mag)	F_v^{WR}/F_v^{Sys}	M_v^{WR} (mag)	Flags
WR75c	WC9		14.27						u
WR75d	WC9		12.76						u
WR75-23	WC9		12.5						u
WR76	WC9d	15.46	12.81	1.12	5.93±0.71			$-3.6^{+1.0}_{-1.0}$	b
WR77	WC8+OB	13.00	12.27	0.61	3.90±0.90	$-3.3^{+1.0}_{-1.0}$	0.52 ± 0.32	$-2.6^{+2.0}_{-1.5}$	b
WR77-5	WN6		11.69						u
WR77-1	WN7b		12.16						u
WR77aa	WC9d		12.01						u
WR77-2	WN7		12.13						u
WR77a	WN6o		12.17						u
WR77b	WC9d		12.38						u
WR77c	WN8o		12.34						u
WR77d	WN7o		12.13						u

WR Number	Spectral type	$v^{WR}\pm0.1$ (mag)	μ (mag)	$(b-v)^{WR}$ (mag)	A_v^{WR} (mag)	$M_{\rm v}^{\rm Sys}$ (mag)	$\rm F_{v}^{WR}/\ F_{v}^{Sys}$	$M_{\rm v}^{\rm WR}$ (mag)	Flags
WR77f	WN10-11h		11.89						u
WR77h	WN8o		11.17						u
WR77i	WC9d		11.79						u
WR77j	WN7o		12.53						u
WR77m	WC9d		12.09						u
WR77n	WC9d		12.17						u
WR77o	WN7o		12.49						u
WR77p	WC9		7.39						u
WR77q	WN5o		11.76						u
WR77r	WN7o		12.43						u
WR77s	WN6o		11.43						u
WR77sa	WN6h		12.02						u
WR77sb	WN6o		12.0						u

WR Number	Spectral type	v^{WR}±0.1 (mag)	μ (mag)	$(b-v)^{WR}$ (mag)	A_v^{WR} (mag)	M_v^{Sys} (mag)	F_v^{WR}/F_v^{Sys}	M_v^{WR} (mag)	Flags
WR77sc	WN7b		12.14						u
WR77sd	WN5o		11.18						u
WR77-3	WN6		12.16						u
WR77t	WC9d		12.14						u
WR77-6	WN6b		11.46						u
WR78	WN7h	6.61	10.48	0.21	1.48±0.71			$-5.4^{+0.8}_{-0.8}$	b:
WR79	WC7+O5-8	6.95	10.68	0.01	1.05±0.87	$-4.8^{+0.9}_{-0.9}$	0.54 ± 0.29	$-4.2^{+1.7}_{-1.4}$	g
WR79a	WN9ha	5.29	11.52	0.15	1.94±0.71			$-8.6^{+1.0}_{-1.0}$	b
WR79b	WN9ha	8.32	13.63	0.55	3.58±0.71			$-9.0^{+0.9}_{-0.9}$	b
WR80	WC9d	14.63	12.72	1.60	7.91±0.71			$-6.3^{+1.0}_{-1.0}$	b
WR81	WC9	12.71	11.62	1.10	5.85±0.71			$-4.9^{+0.8}_{-0.8}$	g
WR82	WN7(h)	12.41	12.87	0.85	4.12±0.71			$-4.8^{+0.9}_{-0.9}$	g
WR82-2	WC9		11.53						u

WR Number	Spectral type	v^{WR}±0.1 (mag)	μ (mag)	$(b-v)^{WR}$ (mag)	A_v^{WR} (mag)	M_v^{Sys} (mag)	F_v^{WR}/F_v^{Sys}	M_v^{WR} (mag)	Flags
WR83	WN5o	12.80	12.9	0.79	4.41±0.71			$-4.7^{+0.9}_{-0.9}$	g
WR83-1	WC6:		11.21						u
WR84	WN7o	13.60	12.39	1.06	4.99±0.71			$-3.9^{+0.8}_{-0.8}$	b:
WR84-4	WN7ha		11.62						u
WR84-11	WN9h		12.57						u
WR84-9	WN6		7.7						u
WR84-10	WC8		11.64						u
WR85	WN6h	10.60	11.49	0.57	3.50±0.71			$-4.5^{+0.8}_{-0.8}$	g
WR88	WC9	13.25	12.68	1.00	5.44±0.71			$-5.1^{+0.9}_{-0.9}$	b:
WR87	WN7h+abs	12.50	12.32	1.58	7.87±0.71			$-7.8^{+0.8}_{-0.8}$	b
WR89	WN8h+abs	11.50	12.31	1.22	6.34±0.71			$-7.3^{+0.8}_{-0.8}$	g
WR90	WC7	7.45	10.3	-0.12	0.33±1.01			$-3.2^{+1.0}_{-1.0}$	b:
WR91	WN7b	15.76	13.03	1.50	6.92±0.71			$-4.5^{+0.9}_{-0.9}$	g

WR Number	Spectral type	v^{WR}±0.1 (mag)	μ (mag)	$(b-v)^{WR}$ (mag)	A_v^{WR} (mag)	M_v^{Sys} (mag)	F_v^{WR}/F_v^{Sys}	M_v^{WR} (mag)	Flags
WR93	WC7+O7-9	11.46	11.23	1.12	5.68±0.79	$-5.5^{+0.8}_{-0.8}$	0.42 ± 0.22	$-4.6^{+1.6}_{-1.3}$	b:
WR92	WC9	10.43	12.89	0.07	1.61±0.71			$-4.3^{+0.9}_{-0.9}$	g
WR93a	WN6h	13.90	13.22	0.00	1.15±0.71			$-0.8^{+1.1}_{-1.1}$	b
WR93b	WO3		11.8						u
WR94	WN5o	12.27	9.9	0.74	4.20±0.71			$-1.8^{+0.7}_{-0.7}$	b
WR95	WC9d	14.00	11.57	1.29	6.63±0.71			$-4.3^{+0.8}_{-0.8}$	g
WR96	WC9d	14.14	12.11	1.01	5.48±0.71			$-3.6^{+0.8}_{-0.8}$	b
WR97	WN5b+O7	11.14	11.66	0.68	4.01±0.70	$-4.6^{+0.8}_{-0.8}$	0.06 ± 0.03	$-1.5^{+1.7}_{-1.3}$	b
WR98	WN8o/C7	12.51	11.46	1.08	5.40±0.71			$-4.4^{+0.8}_{-0.8}$	b
WR98a	WC8-9vd+?	19.70	10.5	0.00	1.25±0.71	$7.4^{+1.1}_{-1.2}$	0.17 ± 0.11	$9.3^{+2.2}_{-1.7}$	b
WR100	WN7b	13.44	12.75	1.17	5.56±0.71			$-5.1^{+0.9}_{-0.9}$	g
WR101	WC8	16.40	11.79	1.50	7.70±0.71			$-3.5^{+1.1}_{-1.1}$	b:
WR102	WO2	15.10	12.11	0.77	4.70±0.71			$-1.8^{+0.8}_{-0.8}$	g

WR Number	Spectral type	v^{WR}±0.1 (mag)	μ (mag)	$(b-v)^{WR}$ (mag)	A_v^{WR} (mag)	$M_{\rm v}^{\rm Sys}$ (mag)	$F_{\rm v}^{\rm WR}/\ F_{\rm v}^{\rm Sys}$	$M_{\rm v}^{\rm WR}$ (mag)	Flags
WR102-19	WN5		11.89						u
WR102-20	WC9		11.42						u
WR102-25	WN6		14.04						u
WR102-21	WN6		11.62						u
WR102l	WN8o	15.53	12.67	1.80	8.03±0.71			$-5.3^{+0.9}_{-0.9}$	g
WR103	WC9d+?	9.01	12.7	0.03	1.40±0.88	$-5.4^{+1.1}_{-1.1}$	0.48 ± 0.32	$-4.6^{+2.3}_{-1.6}$	g
WR104	WC9d+B0.5V (+VB)	13.54	12.19	1.31	6.67±0.68	$-5.5^{+0.8}_{-0.8}$	0.50 ± 0.10	$-4.7^{+1.1}_{-1.0}$	g
WR105	WN9h	12.92	11.19	1.84	8.20±0.71			$-6.6^{+0.8}_{-0.8}$	g
WR105-2	WN8-9		11.88						u

WR Number	Spectral type	v^{WR}±0.1 (mag)	μ (mag)	$(b-v)^{WR}$ (mag)	A_v^{WR} (mag)	M_v^{Sys} (mag)	F_v^{WR}/F_v^{Sys}	M_v^{WR} (mag)	Flags
WR106	WC9d	12.33	12.43	0.80	4.61±0.71			$-4.8^{+0.8}_{-0.8}$	g
WR107	WN8o	14.10	12.29	1.32	6.06±0.71			$-4.3^{+0.9}_{-0.9}$	b
WR107a	WC5-7	16.43	12.35	1.32	6.26±1.01			$-2.3^{+1.1}_{-1.1}$	b
WR108	WN9ha	10.16	12.22	0.80	4.61±0.71			$-6.8^{+0.8}_{-0.8}$	g
WR108-1	WN9		11.73						u
WR109	WN5h	14.48	14.18	0.00	1.15±0.71			$-1.0^{+0.9}_{-0.9}$	b
WR110	WN5-6b	10.30	10.99	0.75	3.83±0.71			$-4.6^{+0.7}_{-0.7}$	g
WR111	WC5	8.23	11.06	-0.02	0.74±1.01			$-3.7^{+1.1}_{-1.1}$	g
WR111-1	WN6o		9.01						u
WR111-9	WC9		12.5						u
WR111-2	WN7b		11.48						u
WR111-4	WN7		11.87						u

WR Number	Spectral type	v^{WR}±0.1 (mag)	μ (mag)	$(b-v)^{WR}$ (mag)	A_v^{WR} (mag)	M_v^{Sys} (mag)	F_v^{WR}/F_v^{Sys}	M_v^{WR} (mag)	Flags
WR111-13	WN6b		11.87						u
WR111-3	WC8		11.91						u
WR111-10	WC7		10.44						u
WR111-12	WC9		11.74						u
WR112	WC9d+OB?	18.80	12.5	1.30	6.60±0.70	$-0.8^{+1.1}_{-1.1}$	0.08 ± 0.05	$2.0^{+2.3}_{-1.7}$	b
WR113	WC8d+O8-9IV	9.43	11.28	0.46	3.20±0.73	$-5.1^{+0.8}_{-0.8}$	0.24 ± 0.15	$-3.6^{+1.8}_{-1.3}$	b:
WR113-1	WN7o		11.64						u
WR113-2	WC5-6		11.34						u
WR114	WC5+OB?	12.95	11.6	0.91	4.57±1.01			$-3.3^{+1.0}_{-1.0}$	b:
WR114-2	WC8		11.29						u
WR114-1	WN6		11.89						u

WR Number	Spectral type	v^{WR}±0.1 (mag)	μ (mag)	$(b-v)^{WR}$ (mag)	A_v^{WR} (mag)	$M_{\rm v}^{\rm Sys}$ (mag)	$\rm F_{v}^{WR}$/ $\rm F_{v}^{Sys}$	$M_{\rm v}^{\rm WR}$ (mag)	Flags
WR115	WN6o	12.32	8.39	1.10	5.69±0.71			$-2.5^{+1.3}_{-1.5}$	b
WR115-1	WN6o		12.52						u
WR115-2	WN8		11.65						u
WR115-3	WN7		12.14						u
WR116	WN8h	13.38	11.94	0.41	2.31±0.71			$-0.9^{+0.8}_{-0.8}$	b
WR116-1	WC9+OBI		12.06				0.04 ± 0.03		u
WR116-2	WN5		11.6						u
WR116-3	WN6ha		12.3						u
WR117	WC9d	14.19	12.81	1.15	6.06±0.71			$-5.0^{+1.0}_{-1.0}$	b:
WR117-1	WN7		12.66						u
WR118	WC9d	22.00	11.98	3.00	13.68±0.71			$-3.7^{+0.9}_{-0.9}$	b:
WR118-4	WC8		11.85						u
WR118-2	WN9		11.91						u

WR Number	Spectral type	v^{WR}±0.1 (mag)	μ (mag)	$(b-v)^{WR}$ (mag)	A_v^{WR} (mag)	$M_{\rm v}^{\rm Sys}$ (mag)	$F_{\rm v}^{\rm WR}/\ F_{\rm v}^{\rm Sys}$	$M_{\rm v}^{\rm WR}$ (mag)	Flags
WR118-3	WN9		9.22						u
WR118-10	WN6		8.68						u
WR118-5	WC9d		12.29						u
WR118-6	WN7:		11.8						u
WR119	WC9d	12.41	12.54	0.63	3.91±0.71			$-4.3^{+0.9}_{-0.9}$	g
WR119-2	WC8		11.7						u
WR119-1	WN7o		13.15						u
WR120	WN7o	12.30	10.89	1.02	4.82±0.71			$-3.7^{+1.0}_{-1.0}$	b
WR120-16	WC8		11.72						u
WR120-1	WC9		12.34						u
WR120-11	WC8		12.12						u

WR Number	Spectral type	v^{WR}±0.1 (mag)	μ (mag)	$(b-v)^{WR}$ (mag)	A_v^{WR} (mag)	$M_{\rm v}^{\rm Sys}$ (mag)	$F_{\rm v}^{\rm WR}/\ F_{\rm v}^{\rm Sys}$	$M_{\rm v}^{\rm WR}$ (mag)	Flags
WR120-7	WN7		12.33						u
WR120-3	WN9h		10.16						u
WR120-4	WN9h		11.83						u
WR120-5	WC8		11.49						u
WR120-6	WN6		12.48						u
WR120-15	WC8		12.39						u
WR120-10	WN7		12.06						u
WR121	WC9d	12.41	11.74	0.97	5.31±0.71			$-4.7^{+0.8}_{-0.8}$	g
WR121-15	WN4-5		12.37						u
WR121-12	WN5		11.9						u

WR Number	Spectral type	v^{WR}±0.1 (mag)	μ (mag)	$(b-v)^{WR}$ (mag)	A_v^{WR} (mag)	$M_{\rm v}^{\rm Sys}$ (mag)	$F_{\rm v}^{\rm WR}/\ F_{\rm v}^{\rm Sys}$	$M_{\rm v}^{\rm WR}$ (mag)	Flags
WR121-1	WN7h		12.52						u
WR121-6	WN5		12.28						u
WR122-2	WN9		11.72						u
WR122-3	WN6		11.91						u
WR122-1	WC8		13.33						u
WR122-15	WN6		11.61						u
WR123	WN8o	11.26	13.64	0.43	2.39±0.71			$-5.0^{+0.9}_{-0.9}$	b:
WR123-1	WN6o		12.13						u
WR123-3	WN8		12.51						u
WR123-8	WN9h		11.21						u
WR124	WN8h	11.58	13.84	0.81	3.96±0.71			$-6.4^{+0.9}_{-0.9}$	b:

WR Number	Spectral type	$v^{WR}\pm0.1$ (mag)	μ (mag)	$(b-v)^{WR}$ (mag)	A_v^{WR} (mag)	$M_{\rm v}^{\rm Sys}$ (mag)	$F_{\rm v}^{\rm WR}/\ F_{\rm v}^{\rm Sys}$	$M_{\rm v}^{\rm WR}$ (mag)	Flags
WR124-1B	WC8		10.96						u
WR124-1A	WC8		11.85						u
WR124-3	WC8		12.82						u
WR124-9	WC6:		12.12						u
WR124-18	WN9h		12.07						u
WR124-19	WC6:		11.83						u
WR124-2	WC8		12.21						u
WR124-6	WC6		12.18						u
WR124-7	WC7		12.3						u

WR Number	Spectral type	v^{WR}±0.1 (mag)	μ (mag)	$(b-v)^{WR}$ (mag)	A_v^{WR} (mag)	$M_{\rm v}^{\rm Sys}$ (mag)	$\rm F_{v}^{WR}$/ $\rm F_{v}^{Sys}$	$M_{\rm v}^{\rm WR}$ (mag)	Flags
WR124-11	WN6b		11.95						u
WR124-20	WC9		9.15						u
WR124-21	WC8		13.83						u
WR124-22	WC9		11.41						u
WR125	WC7ed+O9III	13.52	12.63	1.32	6.48±0.83	$-5.8^{+1.0}_{-1.0}$	0.48 ± 0.26	$-5.0^{+1.8}_{-1.4}$	b
WR125-4	WN7		12.35						u
WR125-3	WN7ha		12.34						u
WR125-2	WN8-9		12.58						u
WR125-1	WC8		13.4						u
WR126	WC5/WN	13.29	14.4	0.70	3.71±1.01			$-4.9^{+1.1}_{-1.1}$	b

WR Number	Spectral type	v^{WR}±0.1 (mag)	μ (mag)	$(b-v)^{WR}$ (mag)	A_v^{WR} (mag)	M_v^{Sys} (mag)	F_v^{WR}/F_v^{Sys}	M_v^{WR} (mag)	Flags
WR127	WN3b+O9.5V	10.33	12.45	0.15	1.77±0.69	$-3.9^{+0.7}_{-0.7}$	0.17 ± 0.10	$-2.0^{+1.7}_{-1.2}$	b
WR129	WN4o	13.27	13.69	0.55	3.58±0.71			$-4.1^{+0.8}_{-0.8}$	b:
WR128	WN4(h)	10.54	12.31	-0.01	1.28±0.71			$-3.2^{+0.8}_{-0.8}$	g
WR130	WN8(h)	12.60	14.12	1.18	5.48±0.71			$-7.1^{+0.9}_{-0.9}$	b
WR131	WN7h+abs	12.36	14.2	0.73	4.37±0.71			$-6.3^{+0.8}_{-0.8}$	g
WR132	WC6+?	13.49	13.09	0.70	3.71±1.01			$-3.4^{+1.1}_{-1.1}$	b:
WR133	WN5o+O9I	6.70	11.33	0.00	1.22±0.70	$-5.9^{+0.7}_{-0.7}$	0.16 ± 0.09	$-3.9^{+1.7}_{-1.2}$	g
WR134	WN6b	8.23	11.21	0.20	1.57±0.71			$-4.6^{+0.7}_{-0.7}$	g
WR135	WC8	8.36	11.48	-0.03	1.40±0.71			$-4.6^{+0.7}_{-0.7}$	g
WR136	WN6b(h)	7.65	11.43	0.23	1.69±0.71			$-5.5^{+0.7}_{-0.7}$	b
WR137	WC7pd+O9	8.15	11.61	0.14	1.70±0.73	$-5.2^{+0.8}_{-0.8}$	0.28 ± 0.15	$-3.8^{+1.6}_{-1.2}$	g
WR138	WN6o	8.10	11.96	0.22	2.06±0.71			$-6.0^{+0.8}_{-0.8}$	b
WR138-1	WN8-9h		15.49						u

WR Number	Spectral type	v^{WR}±0.1 (mag)	μ (mag)	$(b-v)^{WR}$ (mag)	A_v^{WR} (mag)	M_v^{Sys} (mag)	F_v^{WR}/F_v^{Sys}	M_v^{WR} (mag)	Flags
WR139	WN5o+O6III-V	8.10	10.58	0.38	2.76±0.83	$-5.3^{+0.8}_{-0.8}$	0.51 ± 0.30	$-4.5^{+1.8}_{-1.3}$	g
WR140	WC7pd+O4-5	7.07	11.07	0.27	2.21±0.74	$-6.2^{+0.8}_{-0.8}$	0.33 ± 0.17	$-5.0^{+1.5}_{-1.2}$	b
WR141	WN5o+O5V-III	10.14	11.42	0.71	4.08±0.71			$-5.4^{+0.7}_{-0.7}$	b
WR142	WO2	13.82	11.08	1.39	7.25±0.71			$-4.5^{+0.7}_{-0.7}$	b
WR142a	WC8		11.29						u
WR142-1	WN6o		11.24						u
WR143	WC4+OB?	11.95	11.73	1.21	6.07±0.74	$-5.9^{+0.8}_{-0.8}$	0.36 ± 0.15	$-4.8^{+1.3}_{-1.1}$	b:
WR144	WC4	15.49	11.21						u
WR145	WN7o/CE+?	12.55	10.81	1.63	7.76±1.31	$-6.1^{+1.3}_{-1.3}$	0.65 ± 0.64	$-5.6^{+6.3}_{-1.8}$	b
WR146	WC6+O8	13.91	10.21	2.38	10.87±0.77	$-7.6^{+1.2}_{-1.2}$	0.43 ± 0.19	$-6.7^{+1.8}_{-1.6}$	b
WR147	WN8(h)+B0.5V	14.89	11.26	2.15	9.48±0.71			$-5.9^{+0.8}_{-0.8}$	g
WR148	WN8h+	10.46	14.88	0.36	2.10±0.71			$-6.6^{+0.8}_{-0.8}$	b:
WR149	WN5o	14.70	13.45	1.20	6.10±0.71			$-4.9^{+0.8}_{-0.8}$	b:

WR Number	Spectral type	v^{WR}±0.1 (mag)	μ (mag)	$(b-v)^{WR}$ (mag)	A_v^{WR} (mag)	$M_{\rm v}^{\rm Sys}$ (mag)	$F_{\rm v}^{\rm WR}$/ $F_{\rm v}^{\rm Sys}$	$M_{\rm v}^{\rm WR}$ (mag)	Flags
WR150	WC5	13.47	14.71	0.53	3.01±1.01			$-4.3^{+1.1}_{-1.1}$	g
WR151	WN4o+O5V	12.37	13.65	0.65	3.98±1.04	$-5.4^{+1.1}_{-1.1}$	0.76 ± 0.44	$-5.1^{+2.1}_{-1.4}$	b
WR152	WN3(h)	11.67	13.2	0.17	2.02±0.71			$-3.7^{+0.9}_{-0.9}$	g
WR153	WN6o/CE+O6I	9.08	13.04	0.27	2.19±0.96	$-6.2^{+1.0}_{-1.0}$	0.56 ± 0.37	$-5.6^{+2.2}_{-1.6}$	b
WR154	WC6	11.54	13.65	0.36	2.31±1.01			$-4.6^{+1.1}_{-1.1}$	b:
WR155	WN6o+O9II-Ib	8.75	12.38	0.28	2.37±1.07	$-6.1^{+1.1}_{-1.1}$	0.19 ± 0.49	$-4.3^{+2.9}_{-2.5}$	g
WR156	WN8h	11.09	13.07	0.83	4.04±0.71			$-6.1^{+0.8}_{-0.8}$	g
WR157	WN5o(+B1II)	9.91	12.05	0.46	3.11±0.72	$-5.3^{+0.8}_{-0.8}$	0.28 ± 0.16	$-3.9^{+1.7}_{-1.3}$	g
WR158	WN7h	11.46	13.49	0.75	3.71±0.71	$-5.8^{+0.8}_{-0.8}$	0.30 ± 0.94	$-4.5^{+2.1}_{-2.1}$	g
WR159	WN4		11.3						u

Columns: (1) WR Number, (2) Spectral type, (3) v^{WR} apparent magnitude and error, (4) Distance modulus μ, (5) $(b-v)^{WR}$ colour, (6) v^{WR} band extinction A_v, (7) Absolute magnitude of binary system (including companion), (8) Fraction

of light contributed to the binary system by the WR component, (9) Absolute magnitude of WR star, (10) Error flags, where $M >$ upper$_{\text{initial}}$ or $M <$lower$_{\text{initial}} =$ b, $M >$upper$_{\text{final}}$ or $M <$lower$_{\text{final}} =$ b: ($_{\text{initial}}$ denotes the averages calculated before sigma clipping, $_{\text{final}}$ are the final absolute magnitude boundaries) and g are results with no issues.

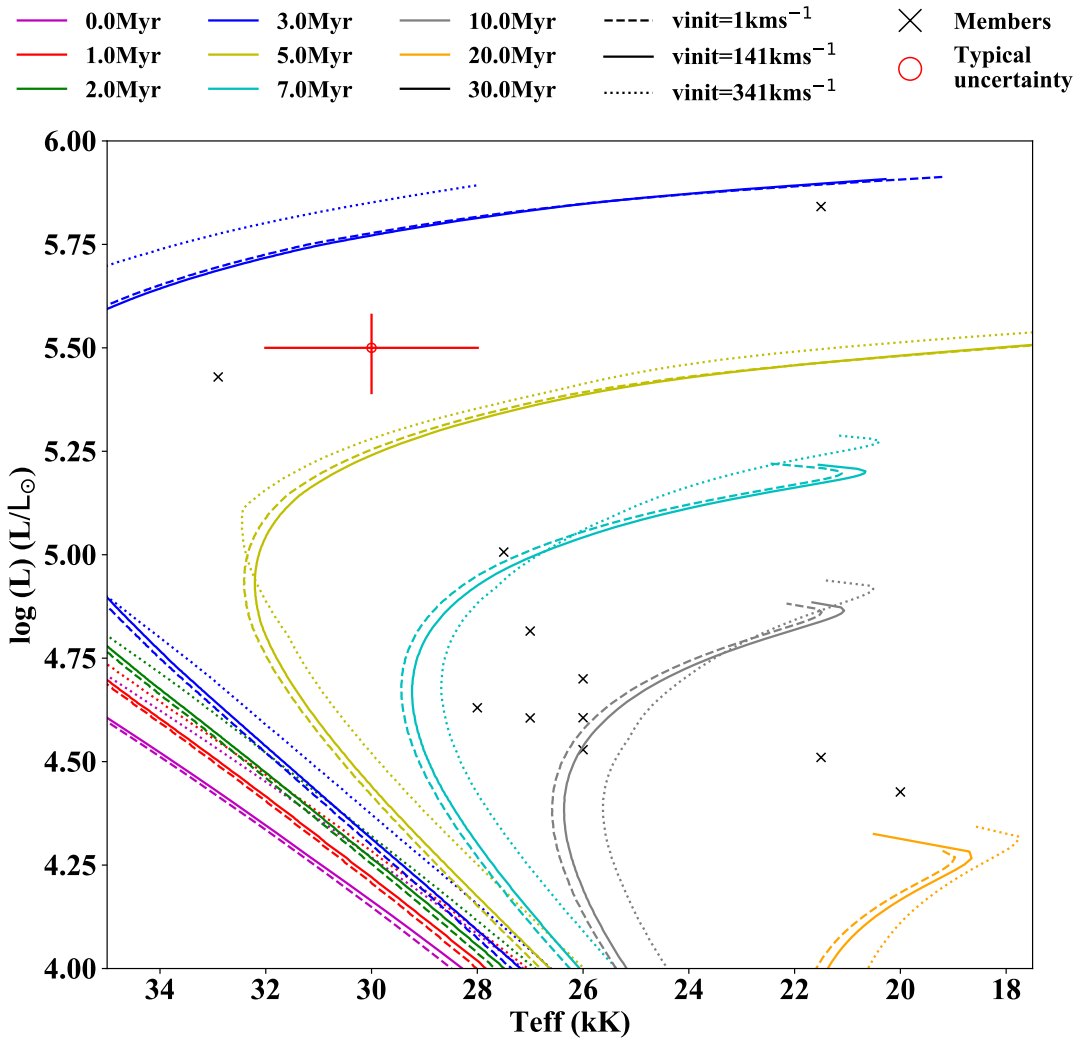

Figure A.1: Berkeley 87 cluster members and 0-30 Myr isochrones from Brott et al. (2011). Berkeley 87 was assigned an age of 8−9 Myr, as most member data fitted between the 7 and 10 Myr isochrones. The solid lines denote stars with a 'typical' 141 km s^{-1}(the closest value to the mean from Brott et al. (2011)) rotation rate, whilst the dashed line is for a 1 km s^{-1}'non rotating' star and the dotted line is for a 341 km s^{-1}rapid rotator.

A.3 Isochrone fits

Isochrone fits to the members of clusters with ages, from Table 4.9 of Chapter 4.

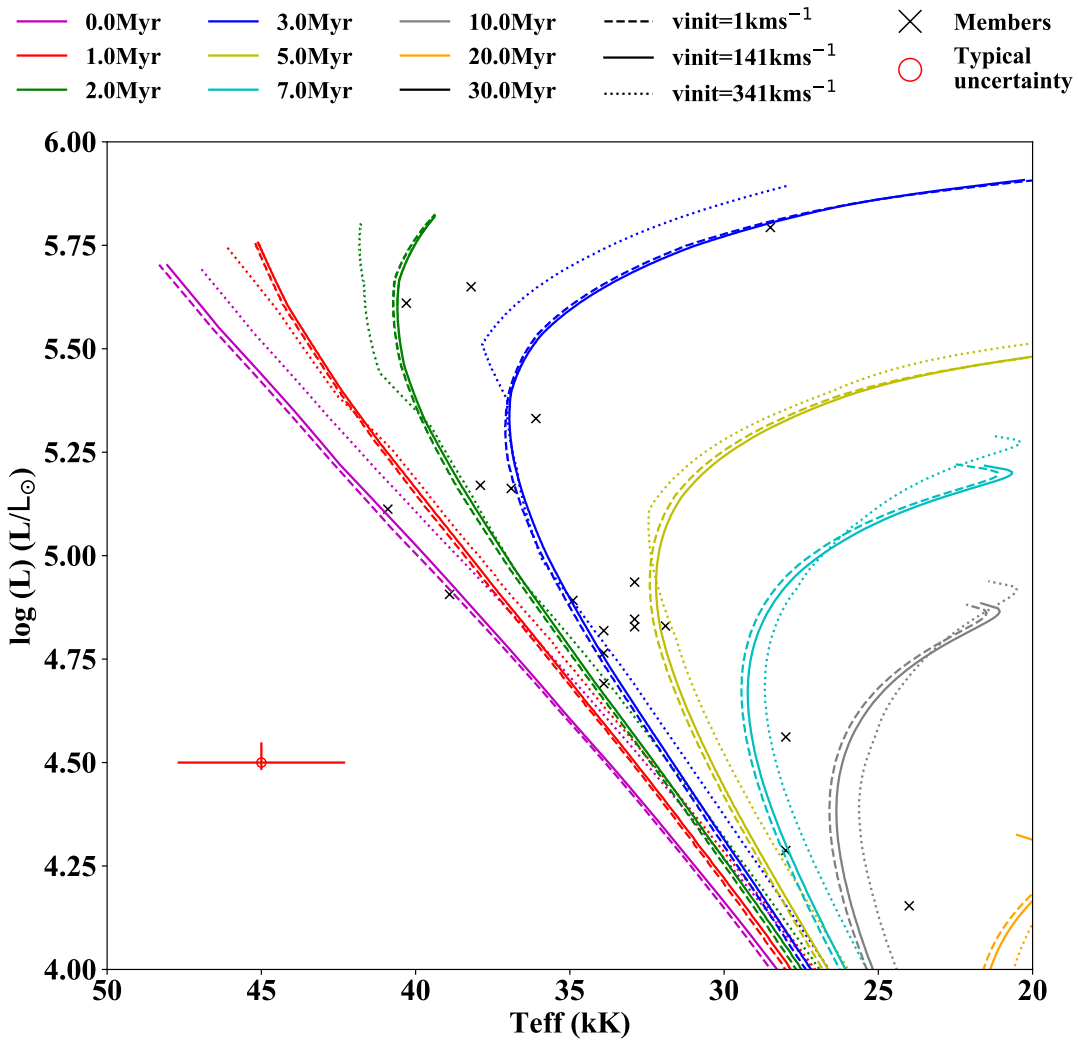

Figure A.2: Collinder 228 cluster members and 0-30 Myr isochrones from Brott et al. (2011). Collinder 228 was assigned an age of ∼2 Myr, based on the closest isochrone to most member data. The solid lines denote stars with a 'typical' 141 km s^{-1}(the closest value to the mean from Brott et al. (2011)) rotation rate, whilst the dashed line is for a 1 km s^{-1}'non rotating' star and the dotted line is for a 341 km s^{-1}rapid rotator.

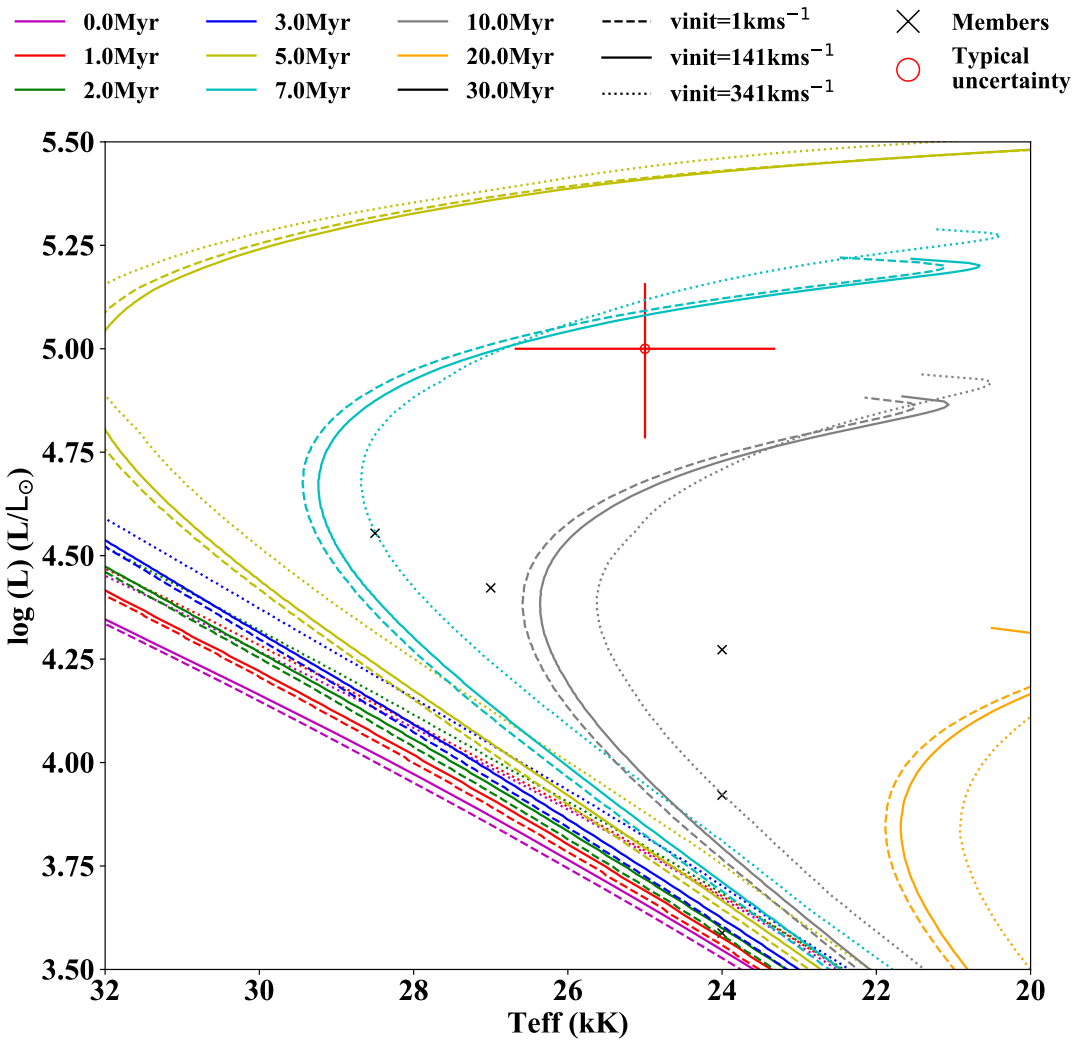

Figure A.3: Markierien 50 cluster members and 0-30 Myr isochrones from Brott et al. (2011). Markierien 50 was assigned an age of ∼10 Myr, as most member data is around this isochrone. The solid lines denote stars with a 'typical' 141 km s^{-1}(the closest value to the mean from Brott et al. (2011)) rotation rate, whilst the dashed line is for a 1 km s^{-1}'non rotating' star and the dotted line is for a 341 km s^{-1}rapid rotator.

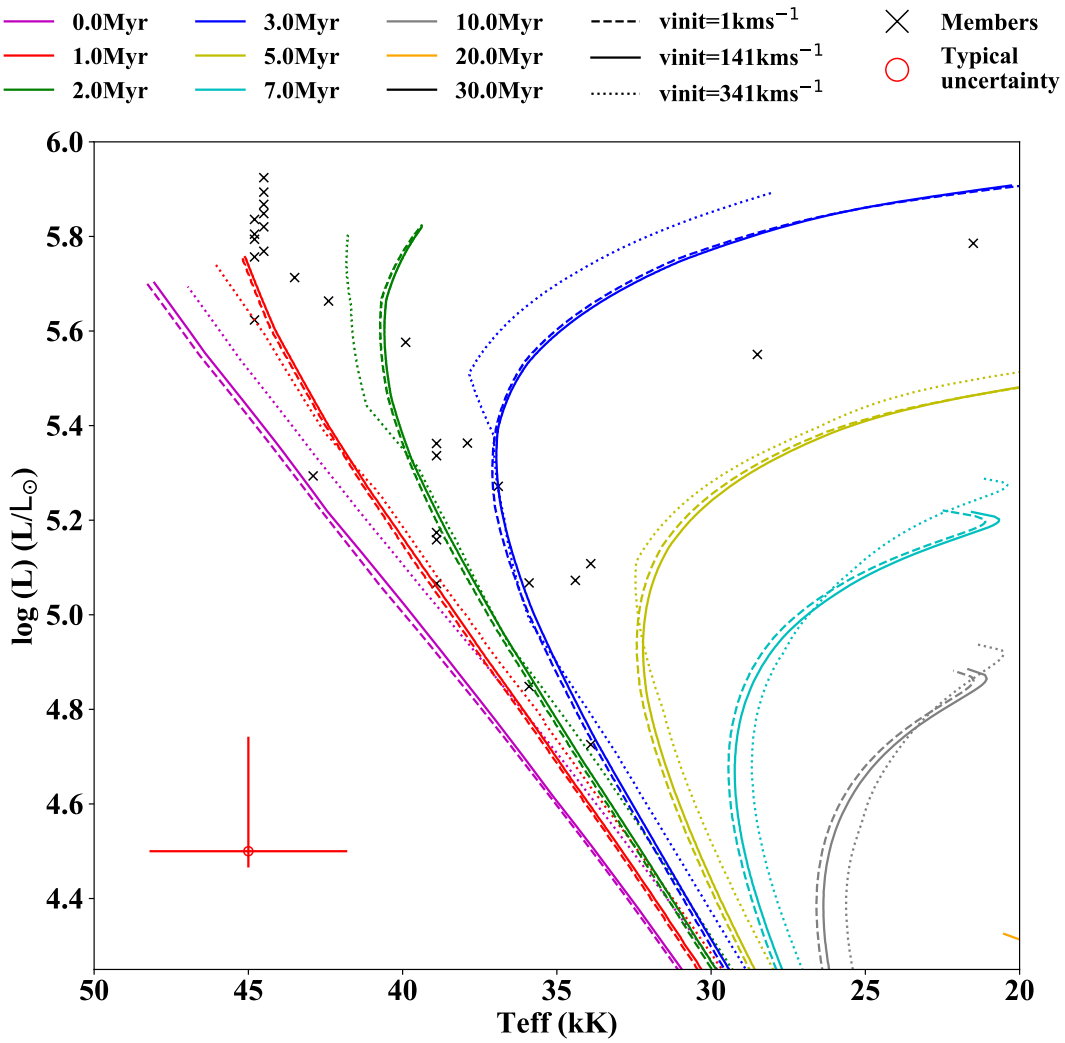

Figure A.4: NGC 3603 cluster members and 0-30 Myr isochrones from Brott et al. (2011). NGC 3603 was assigned an age of 1±1 Myr, based on the closest isochrone to most member data. The solid lines denote stars with a 'typical' 141 km s^{-1}(the closest value to the mean from Brott et al. (2011)) rotation rate, whilst the dashed line is for a 1 km s^{-1}'non rotating' star and the dotted line is for a 341 km s^{-1}rapid rotator.

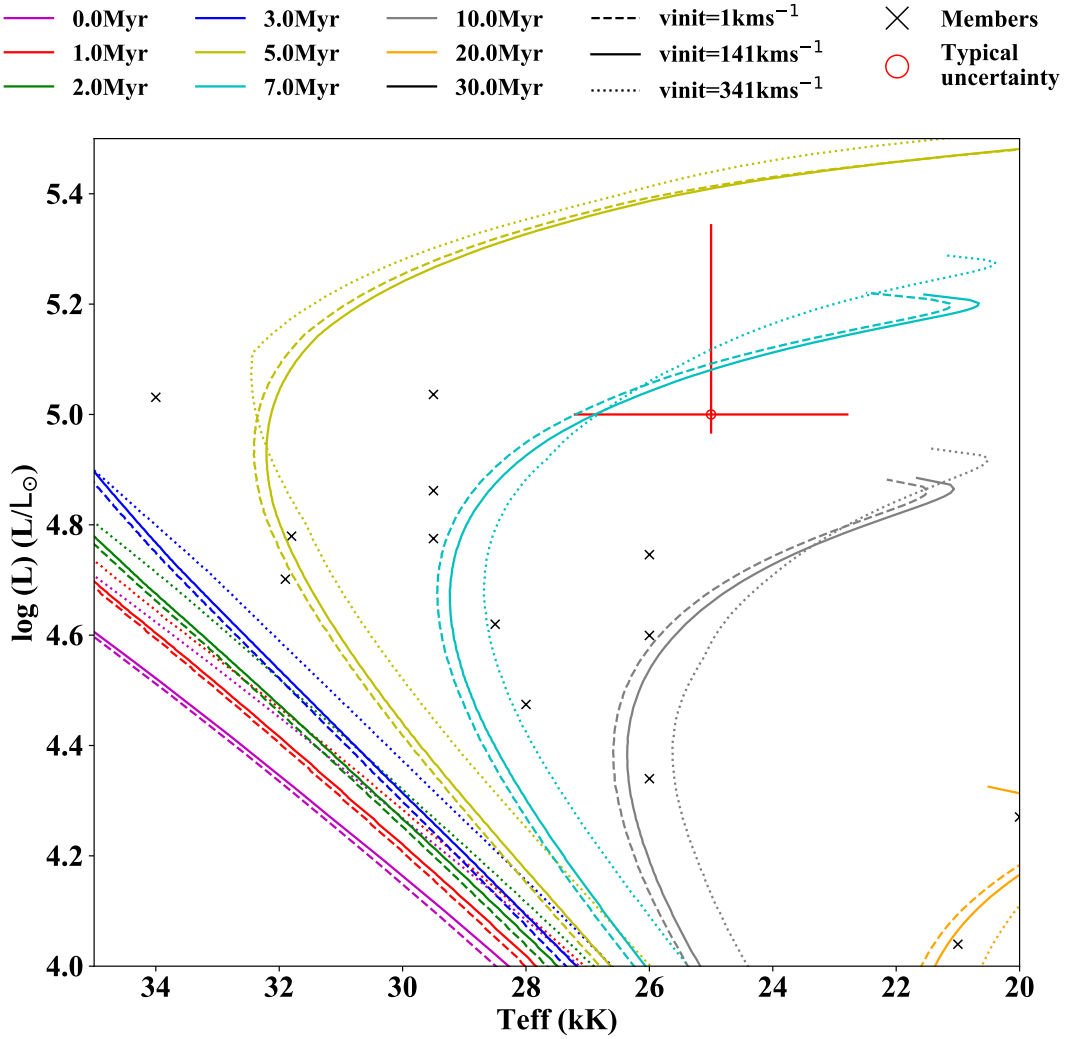

Figure A.5: Ruprecht 44 cluster members and 0-30 Myr isochrones from Brott et al. (2011). Ruprecht 44 was assigned an age of 7±3 Myr, as most member data fitted between the 5 and 10 Myr isochrones. The solid lines denote stars with a 'typical' 141 km s^{-1}(the closest value to the mean from Brott et al. (2011)) rotation rate, whilst the dashed line is for a 1 km s^{-1}'non rotating' star and the dotted line is for a 341 km s^{-1}rapid rotator.

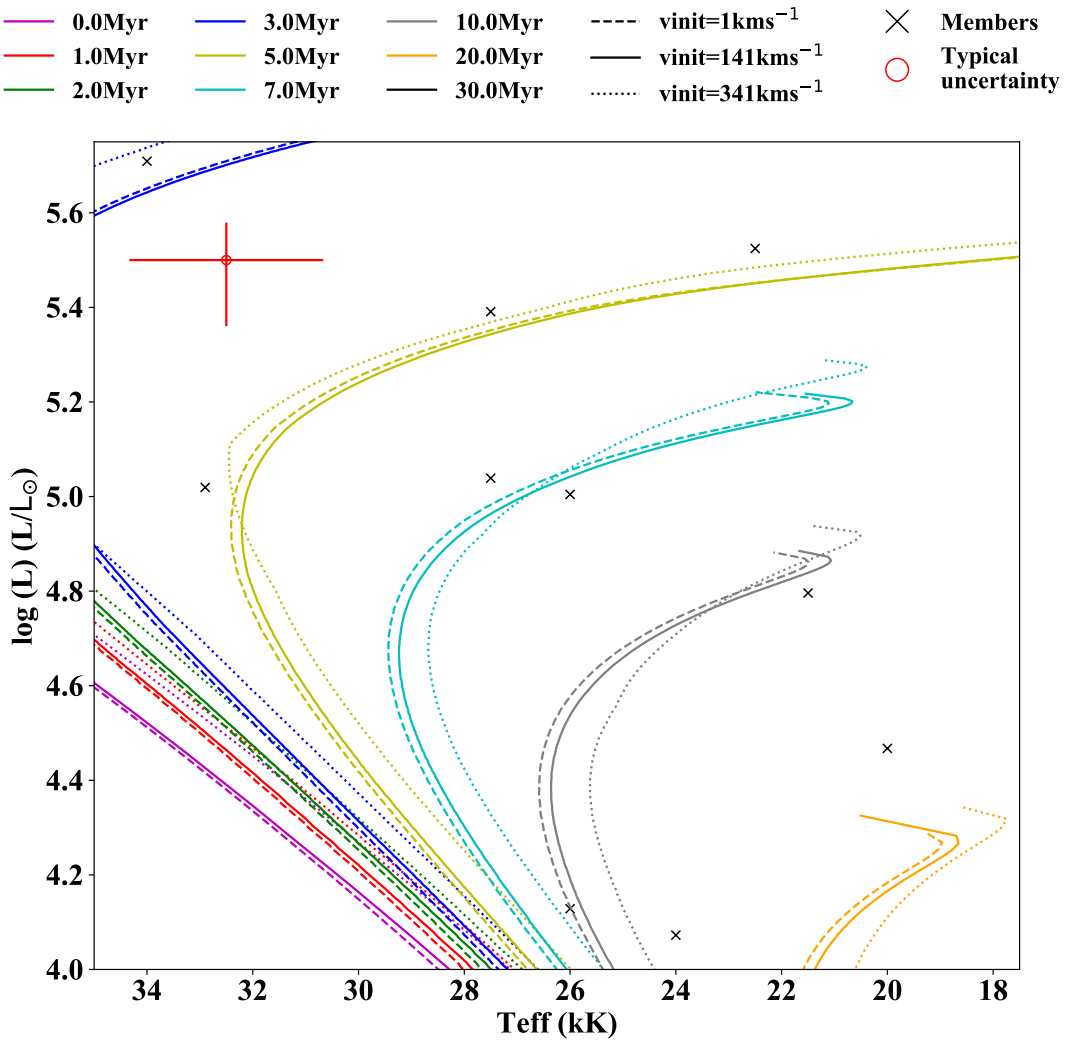

Figure A.6: Trumpler 27 cluster members and 0-30 Myr isochrones from Brott et al. (2011). Trumpler 27 was assigned an age of 7 $^{+3}_{-2}$ Myr, based on the closest isochrones to most member data. The solid lines denote stars with a 'typical' 141 km s^{-1}(the closest value to the mean from Brott et al. 2011) rotation rate, whilst the dashed line is for a 1 km s^{-1}'non rotating' star and the dotted line is for a 341 km s^{-1}rapid rotator.

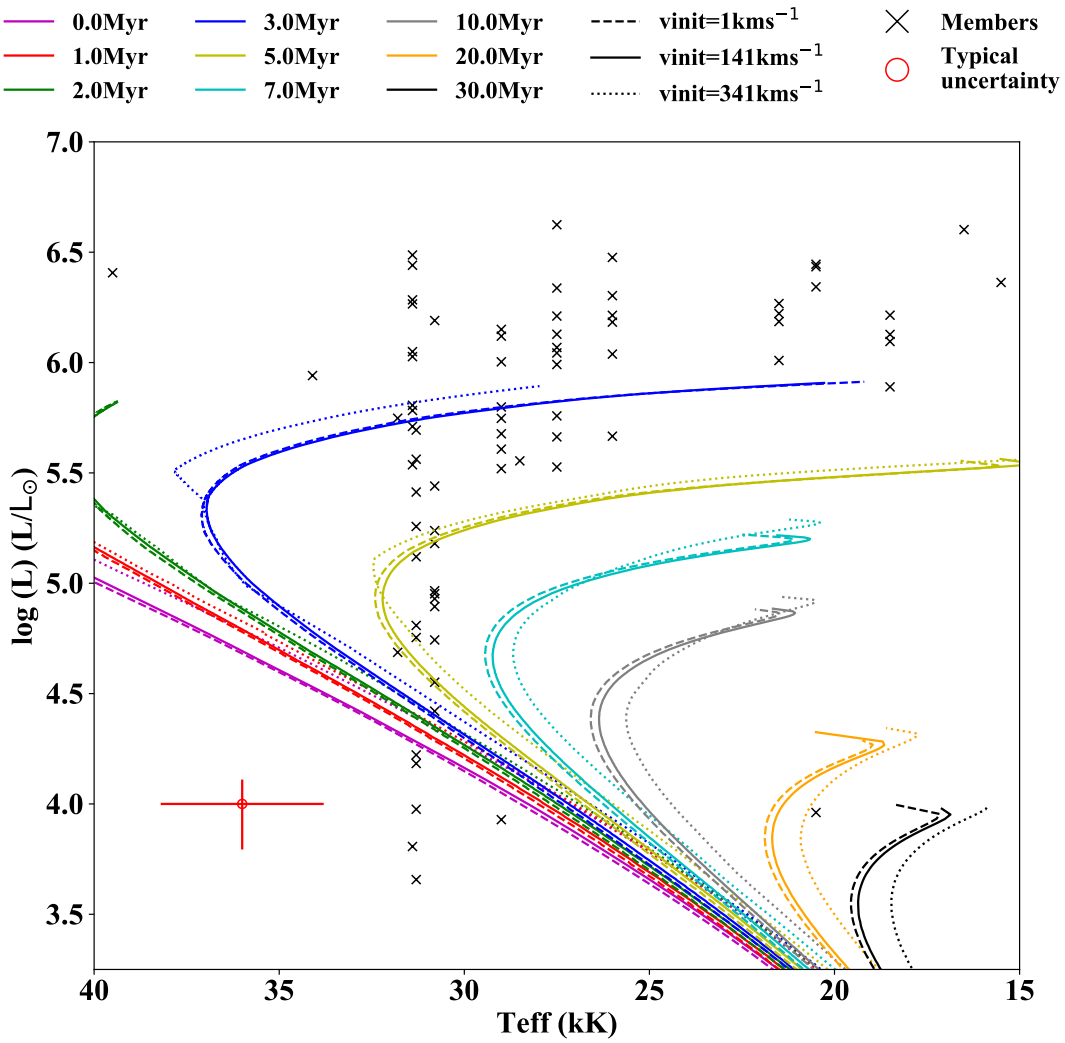

Figure A.7: Westerlund 1 cluster members and 0-30 Myr isochrones from Brott et al. (2011). Westerlund 1 was assigned an age of <5 Myr, as most member data were around the 3−4 Myr isochrones. The solid lines denote stars with a 'typical' 141 km s^{-1}(the closest value to the mean from Brott et al. (2011)) rotation rate, whilst the dashed line is for a 1 km s^{-1}'non rotating' star and the dotted line is for a 341 km s^{-1}rapid rotator.

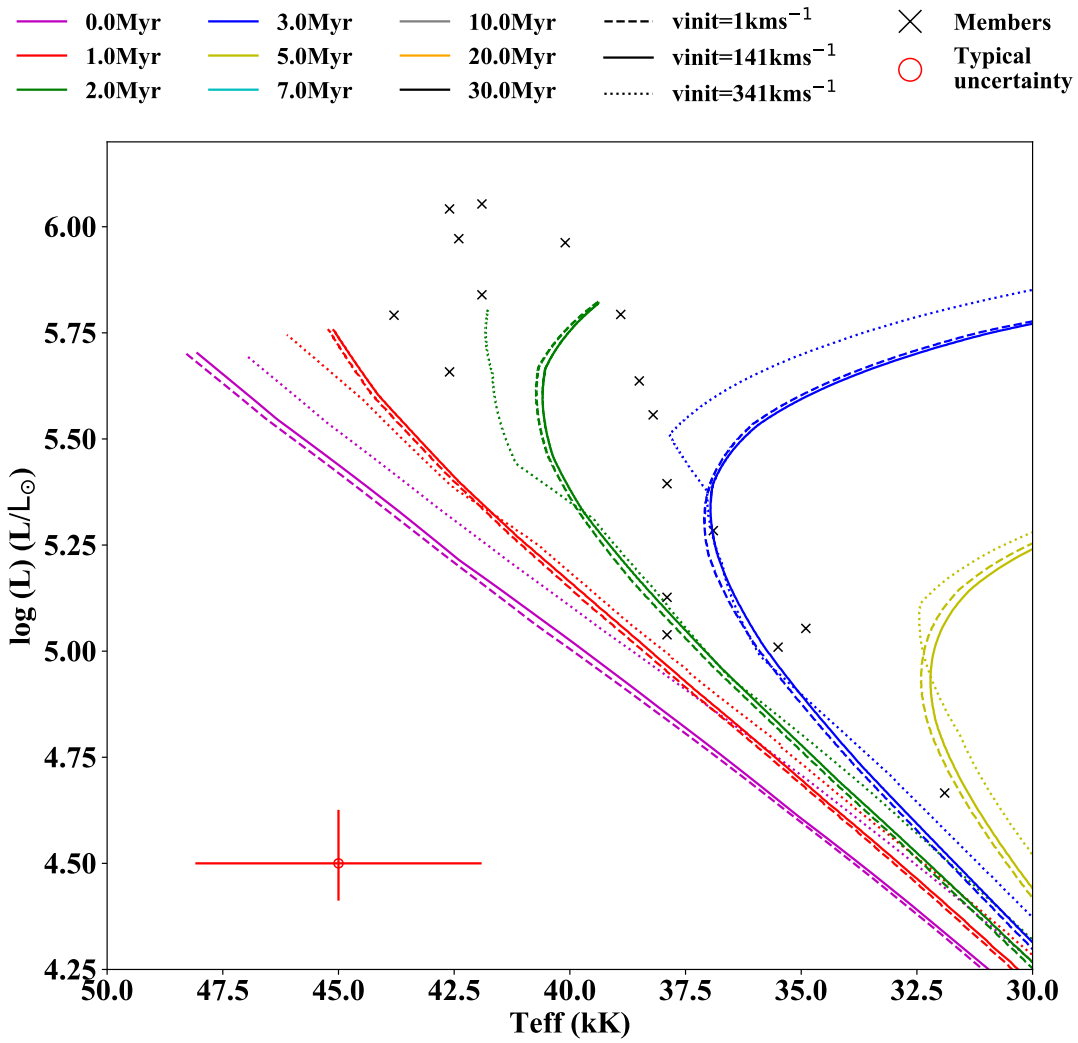

Figure A.8: Westerlund 2 cluster members and 0-30 Myr isochrones from Brott et al. (2011). Westerlund 2 was assigned an age of 2±1 Myr, based on the closest isochrone to most member data. The solid lines denote stars with a 'typical' 141 km s^{-1}(the closest value to the mean from Brott et al. (2011)) rotation rate, whilst the dashed line is for a 1 km s^{-1}'non rotating' star and the dotted line is for a 341 km s^{-1}rapid rotator.

A.4 Emission line data for Galactic WR stars

Table A.4: WN blue region emission line fluxes, intensities and luminosities for individual stars, from Chapter 5.

WR Number	Distance (kpc)	A_V (mag)	F_{Nblend} (10^{-11}ergs s^{-1}Å^{-1})	I_{Nblend} (10^{-11}ergs s^{-1}Å^{-1})	L_{Nblend} (10^{35}ergs s^{-1})	F_{4686} (10^{-11}ergs s^{-1}Å^{-1})	I_{4686} (10^{-11}ergs s^{-1}Å^{-1})	L_{4686} (10^{35}ergs s^{-1})	Source
1	$3.15^{+0.47}_{-0.36}$	2.58±0.65	1.2±0.059	23^{+28}_{-13}	$2.7^{+3.3}_{-1.5}$	6.7±0.33	120^{+140}_{-66}	$15^{+17}_{-8.1}$	INT91
3	$2.90^{+0.52}_{-0.39}$	0.97±0.65	0.83±0.037	$2.5^{+2.8}_{-1.2}$	$0.26^{+0.28}_{-0.13}$	1.1±0.056	$3.4^{+4}_{-1.8}$	$0.34^{+0.4}_{-0.19}$	INT91
6	$2.27^{+0.42}_{-0.31}$	0.41±0.65	46±2.3	74^{+90}_{-41}	$4.6^{+5.6}_{-2.6}$	220±11	350^{+420}_{-190}	22^{+26}_{-12}	CTIO
7	$4.23^{+1.08}_{-0.74}$	2.02±0.65	0.6±0.03	$6.2^{+7.5}_{-3.4}$	$1.3^{+1.7}_{-0.77}$	3.3±0.17	32^{+38}_{-17}	$6.9^{+8.4}_{-3.9}$	AAT92
8	$3.74^{+0.63}_{-0.48}$	2.62±0.65	8.1±0.33	160^{+160}_{-71}	27^{+27}_{-12}	3.3±0.17	63^{+75}_{-34}	$11^{+13}_{-5.9}$	CTIO
10	$5.46^{+1.25}_{-0.91}$	2.06±1.46	0.13±0.0045	$1.3^{+4.4}_{-0.78}$	$0.48^{+1.6}_{-0.28}$	1.2±0.058	$12^{+52}_{-9.6}$	$4.2^{+19}_{-3.5}$	CTIO
12	$5.71^{+1.24}_{-0.92}$	2.13±0.65	0.55±0.028	$6.3^{+7.6}_{-3.4}$	$2.5^{+3}_{-1.4}$	1.9±0.094	21^{+25}_{-11}	$8.2^{+9.8}_{-4.6}$	CTIO
16	$2.63^{+0.32}_{-0.26}$	1.69±0.65	6.4±0.32	44^{+53}_{-24}	$3.6^{+4.4}_{-2}$	14±0.69	93^{+110}_{-50}	$7.7^{+9.1}_{-4.2}$	CTIO
18	$3.82^{+0.84}_{-0.60}$	2.73±0.65	1±0.051	24^{+29}_{-13}	$4.1^{+5.1}_{-2.4}$	5.3±0.26	120^{+140}_{-62}	20^{+24}_{-11}	AAT92
20	$6.98^{+1.18}_{-0.93}$	4.34±0.65	0.02±0.00073	$2.8^{+2.6}_{-1.2}$	$1.7^{+1.5}_{-0.7}$	0.12±0.0059	$16^{+19}_{-8.6}$	$9.2^{+11}_{-5.1}$	CTIO
22	$2.33^{+0.28}_{-0.22}$	1.54±0.65	11±0.53	61^{+73}_{-33}	$4^{+4.8}_{-2.2}$	29±1.5	160^{+190}_{-88}	$11^{+13}_{-5.8}$	CTIO
24	$3.55^{+0.66}_{-0.49}$	1.09±0.65	6.5±0.25	$22^{+21}_{-9.6}$	$3.4^{+3.2}_{-1.5}$	20±1	69^{+81}_{-37}	$10^{+12}_{-5.8}$	AAT92
25	$1.97^{+0.18}_{-0.15}$	2.87±0.98	1.3±0.049	35^{+56}_{-18}	$1.6^{+2.6}_{-0.83}$	2.9±0.14	73^{+160}_{-50}	$3.4^{+7.3}_{-2.3}$	CTIO
26	$6.70^{+1.05}_{-0.83}$	4.31±0.65	0.1±0.0039	$14^{+13}_{-5.9}$	$7.7^{+7.1}_{-3.3}$	0.24±0.012	30^{+36}_{-16}	$16^{+19}_{-9.1}$	CTIO
34	$7.41^{+1.37}_{-1.09}$	3.90±0.65	0.022±0.00081	$2^{+1.7}_{-0.78}$	$1.3^{+1.1}_{-0.53}$	0.091±0.0045	$7.3^{+8.6}_{-3.9}$	$4.8^{+5.7}_{-2.7}$	CTIO
35	$6.86^{+1.19}_{-0.94}$	3.30±2.01	0.052±0.0021	$2.3^{+17}_{-1.6}$	$1.3^{+9.6}_{-0.93}$	0.2±0.0098	$8^{+73}_{-7.2}$	$4.5^{+41}_{-4.1}$	CTIO
36	$5.43^{+1.15}_{-0.85}$	3.41±0.75	0.067±0.0034	$3.3^{+4.9}_{-2}$	$1.2^{+1.8}_{-0.73}$	0.32±0.016	$15^{+21}_{-8.7}$	$5.2^{+7.5}_{-3.2}$	CTIO
37	$6.71^{+1.36}_{-1.06}$	5.28±0.65	0.012±0.00061	$5.2^{+6.3}_{-2.9}$	$2.8^{+3.5}_{-1.6}$	0.059±0.003	23^{+27}_{-12}	$12^{+15}_{-6.9}$	CTIO
40	$3.83^{+0.67}_{-0.50}$	1.27±0.65	15±0.76	65^{+78}_{-36}	$11^{+14}_{-6.5}$	34±1.7	140^{+170}_{-77}	25^{+30}_{-14}	CTIO
46	$2.60^{+0.32}_{-0.26}$	0.56±0.65	1.5±0.077	$2.9^{+3.6}_{-1.6}$	$0.24^{+0.29}_{-0.13}$	2.2±0.11	$4.2^{+4.9}_{-2.3}$	$0.34^{+0.4}_{-0.19}$	CTIO
47	$3.49^{+0.61}_{-0.47}$	3.94±1.89	0.4±0.014	36^{+210}_{-23}	$5.2^{+30}_{-3.3}$	1.3±0.063	110^{+840}_{-95}	16^{+120}_{-14}	CTIO
49	$8.35^{+1.44}_{-1.17}$	2.32±0.65	0.043±0.0017	$0.61^{+0.57}_{-0.26}$	$0.51^{+0.48}_{-0.22}$	0.19±0.0095	$2.6^{+3.1}_{-1.4}$	$2.2^{+2.6}_{-1.2}$	CTIO
51	$3.67^{+0.48}_{-0.39}$	5.09±0.65	0.013±0.00067	$4.7^{+5.6}_{-2.6}$	$0.75^{+0.92}_{-0.42}$	0.061±0.003	19^{+22}_{-10}	$3.1^{+3.6}_{-1.7}$	CTIO
54	$6.52^{+1.37}_{-1.05}$	2.77±0.65	0.11±0.0048	$2.6^{+2.8}_{-1.3}$	$1.3^{+1.5}_{-0.68}$	0.43±0.021	$9.7^{+11}_{-5.3}$	$4.9^{+5.9}_{-2.8}$	CTIO
55	$3.00^{+0.55}_{-0.41}$	2.06±0.65	1.3±0.051	$14^{+13}_{-5.8}$	$1.5^{+1.4}_{-0.65}$	2.4±0.12	25^{+29}_{-13}	$2.6^{+3.2}_{-1.5}$	CTIO

WR Number	Distance (kpc)	A_V (mag)	F_{Nblend} (10^{-11}ergs s^{-1}Å^{-1})	I_{Nblend} (10^{-11}ergs s^{-1}Å^{-1})	L_{Nblend} (10^{35}ergs s^{-1})	F_{4686} (10^{-11}ergs s^{-1}Å^{-1})	I_{4686} (10^{-11}ergs s^{-1}Å^{-1})	L_{4686} (10^{35}ergs s^{-1})	Source
58	$5.88^{+1.42}_{-1.04}$	3.00±0.65	0.23±0.011	$7^{+8.5}_{-3.9}$	$2.9^{+3.6}_{-1.7}$	0.76±0.038	22^{+26}_{-12}	$9.2^{+11}_{-5.3}$	CTIO
61	$5.49^{+1.25}_{-0.91}$	2.40±0.65	0.22±0.0084	$3.4^{+3.2}_{-1.4}$	$1.2^{+1.2}_{-0.54}$	0.92±0.046	$14^{+16}_{-7.4}$	$4.9^{+5.9}_{-2.8}$	CTIO
67	$2.23^{+0.54}_{-0.37}$	4.31±0.65	0.26±0.01	35^{+34}_{-15}	$2.1^{+2.1}_{-0.97}$	0.85±0.042	110^{+130}_{-59}	$6.5^{+7.8}_{-3.7}$	CTIO
71	$3.19^{+0.67}_{-0.48}$	0.86±0.65	2.6±0.093	$7^{+6}_{-2.7}$	$0.85^{+0.74}_{-0.34}$	7.9±0.4	21^{+25}_{-11}	$2.6^{+3.1}_{-1.4}$	CTIO
74	$3.98^{+0.86}_{-0.66}$	6.48±0.65	0.036±0.0014	60^{+55}_{-25}	$11^{+11}_{-4.9}$	0.066±0.0033	97^{+110}_{-53}	18^{+22}_{-10}	CTIO
75	$3.32^{+0.80}_{-0.55}$	3.33±0.65	1.7±0.085	77^{+92}_{-42}	$10^{+12}_{-5.8}$	3.3±0.16	140^{+160}_{-75}	18^{+22}_{-10}	CTIO
82	$3.74^{+0.98}_{-0.66}$	3.75±0.65	0.21±0.0081	$15^{+14}_{-6.4}$	$2.6^{+2.4}_{-1.1}$	0.47±0.024	32^{+38}_{-17}	$5.4^{+6.5}_{-3.1}$	CTIO
83	$3.80^{+1.10}_{-0.72}$	4.01±0.65	0.16±0.0058	$16^{+14}_{-6.2}$	$2.8^{+2.4}_{-1.1}$	0.48±0.024	43^{+51}_{-23}	$7.5^{+9.1}_{-4.3}$	CTIO
84	$3.01^{+0.51}_{-0.40}$	4.53±0.65	0.065±0.0033	$12^{+14}_{-6.3}$	$1.3^{+1.5}_{-0.71}$	0.19±0.0094	31^{+37}_{-17}	$3.4^{+4}_{-1.9}$	CTIO
85	$1.99^{+0.30}_{-0.24}$	3.18±0.65	1±0.052	40^{+47}_{-22}	$1.9^{+2.3}_{-1}$	3±0.15	110^{+130}_{-58}	$5.1^{+6.1}_{-2.8}$	CTIO
87	$2.91^{+0.66}_{-0.47}$	7.15±0.65	0.04±0.002	140^{+170}_{-77}	$14^{+17}_{-8.1}$	0.075±0.0038	240^{+280}_{-130}	24^{+29}_{-14}	CTIO
89	$2.90^{+0.72}_{-0.51}$	5.77±0.65	0.11±0.0043	83^{+75}_{-34}	$8.4^{+7.7}_{-3.6}$	0.25±0.013	170^{+200}_{-91}	$17^{+20}_{-9.7}$	CTIO
91	$4.04^{+1.52}_{-0.92}$	6.29±0.65	0.01±0.0004	$14^{+13}_{-5.8}$	$2.7^{+2.6}_{-1.2}$	0.022±0.0011	26^{+30}_{-14}	$5^{+6.2}_{-3}$	CTIO
94	$0.95^{+0.06}_{-0.06}$	3.82±0.65	0.23±0.0083	$18^{+16}_{-7.1}$	$0.2^{+0.17}_{-0.078}$	0.66±0.033	49^{+57}_{-26}	$0.53^{+0.63}_{-0.29}$	CTIO
98	$1.96^{+0.31}_{-0.24}$	4.91±0.65	0.34±0.013	91^{+84}_{-38}	$4.2^{+3.9}_{-1.8}$	0.17±0.0085	43^{+50}_{-23}	$2^{+2.3}_{-1.1}$	CTIO
100	$3.55^{+1.06}_{-0.67}$	5.06±0.65	0.14±0.0054	47^{+42}_{-19}	$7.1^{+6.6}_{-3.1}$	0.29±0.015	87^{+100}_{-47}	$13^{+16}_{-7.5}$	CTIO
105	$1.73^{+0.32}_{-0.23}$	7.45±0.65	0.017±0.00073	84^{+86}_{-39}	$3^{+3.1}_{-1.4}$	0.0084±0.00042	37^{+44}_{-20}	$1.3^{+1.6}_{-0.74}$	WHT94
107	$2.87^{+0.81}_{-0.69}$	5.51±0.65	0.039±0.002	21^{+25}_{-11}	$2.1^{+2.6}_{-1.2}$	0.034±0.0017	17^{+20}_{-9}	$1.7^{+2}_{-0.98}$	INT96
108	$2.79^{+0.45}_{-0.35}$	4.19±0.65	0.55±0.024	66^{+69}_{-31}	$6.1^{+6.5}_{-3}$	0.74±0.037	83^{+98}_{-45}	$7.7^{+9.2}_{-4.3}$	INT91
110	$1.58^{+0.15}_{-0.12}$	3.48±0.65	3.2±0.16	180^{+210}_{-97}	$5.3^{+6.4}_{-2.9}$	11±0.56	570^{+670}_{-310}	$17^{+20}_{-9.3}$	INT91
123	$5.35^{+1.56}_{-1.09}$	2.17±0.65	0.62±0.031	$7.4^{+8.8}_{-4}$	$2.5^{+3.1}_{-1.5}$	0.35±0.017	$4^{+4.7}_{-2.2}$	$1.4^{+1.7}_{-0.79}$	INT91
124	$5.87^{+1.48}_{-1.09}$	3.60±0.65	0.28±0.013	$17^{+19}_{-8.6}$	$6.9^{+8}_{-3.8}$	0.25±0.012	$14^{+17}_{-7.6}$	$5.8^{+7}_{-3.3}$	INT91
128	$2.90^{+0.54}_{-0.39}$	1.16±0.65	0.86±0.031	$3.3^{+2.9}_{-1.3}$	$0.33^{+0.29}_{-0.13}$	2.5±0.13	9.3^{+11}_{-5}	$0.94^{+1.1}_{-0.52}$	INT91
131	$6.92^{+1.40}_{-1.09}$	3.97±0.65	0.046±0.0023	$4.2^{+5.1}_{-2.3}$	$2.4^{+3}_{-1.4}$	0.11±0.0053	9.2^{+11}_{-5}	$5.3^{+6.3}_{-3}$	WHT94
133	$1.85^{+0.16}_{-0.14}$	1.11±0.64	4.1±0.2	$15^{+17}_{-7.9}$	$0.6^{+0.71}_{-0.33}$	20±0.99	69^{+79}_{-37}	$2.8^{+3.2}_{-1.5}$	INT91
134	$1.75^{+0.13}_{-0.11}$	1.42±0.65	14±0.71	73^{+88}_{-40}	$2.7^{+3.2}_{-1.5}$	86±4.3	420^{+500}_{-230}	$16^{+18}_{-8.5}$	INT91
139	$1.31^{+0.07}_{-0.06}$	2.51±0.75	2.3±0.093	41^{+47}_{-19}	$0.84^{+0.97}_{-0.39}$	6.3±0.31	100^{+150}_{-62}	$2.1^{+3.1}_{-1.3}$	INT91

WR Number	Distance (kpc)	A_V (mag)	F_{Nblend} (10^{-11}ergs $s^{-1}Å^{-1}$)	I_{Nblend} (10^{-11}ergs $s^{-1}Å^{-1}$)	L_{Nblend} (10^{35}ergs s^{-1})	F_{4686} (10^{-11}ergs $s^{-1}Å^{-1}$)	I_{4686} (10^{-11}ergs $s^{-1}Å^{-1}$)	L_{4686} (10^{35}ergs s^{-1})	Source
145	$1.46^{+0.12}_{-0.10}$	7.06±1.19	0.098±0.0039	310^{+750}_{-180}	$7.8^{+19}_{-4.7}$	0.1±0.005	280^{+850}_{-210}	$7.2^{+22}_{-5.4}$	WHT94
148	$9.47^{+1.77}_{-1.49}$	1.91±0.65	0.24±0.0092	$2.1^{+2}_{-0.89}$	$2.3^{+2.1}_{-0.99}$	1.7±0.087	$15^{+18}_{-8.1}$	16^{+19}_{-9}	INT91
149	$4.89^{+0.83}_{-0.63}$	5.54±0.65	0.018±0.00065	$10^{+9}_{-4.1}$	$3^{+2.6}_{-1.2}$	0.11±0.0056	58^{+68}_{-31}	$17^{+20}_{-9.2}$	INT13
155	$2.99^{+0.45}_{-0.35}$	2.16±0.97	1.3±0.064	15^{+33}_{-10}	$1.6^{+3.5}_{-1.1}$	3.1±0.16	35^{+75}_{-24}	$3.8^{+8.1}_{-2.6}$	INT91
156	$4.10^{+0.60}_{-0.47}$	3.67±0.65	0.49±0.023	32^{+36}_{-16}	$6.5^{+7.2}_{-3.3}$	0.37±0.019	23^{+27}_{-13}	$4.7^{+5.5}_{-2.6}$	INT91
157	$2.57^{+0.32}_{-0.26}$	2.83±0.65	0.18±0.0067	$4.7^{+4.1}_{-1.8}$	$0.37^{+0.32}_{-0.15}$	0.93±0.046	22^{+26}_{-12}	$1.8^{+2.1}_{-0.97}$	INT91

Table A.5: WN red region emission line fluxes, intensities and luminosities for individual stars, from Chapter 5.

WR Number	Distance (kpc)	A_V (mag)	F_{5808} (10^{-11}ergs $s^{-1}Å^{-1}$)	I_{5808} (10^{-11}ergs $s^{-1}Å^{-1}$)	L_{5808} (10^{35}ergs s^{-1})	F_{5876} (10^{-11}ergs $s^{-1}Å^{-1}$)	I_{5876} (10^{-11}ergs $s^{-1}Å^{-1}$)	L_{5876} (10^{35}ergs s^{-1})	Source
1	$3.15^{+0.47}_{-0.36}$	2.58±0.65	1.3±0.063	$12^{+10}_{-5.4}$	$1.4^{+1.2}_{-0.67}$	0.38±0.019	$3.5^{+2.9}_{-1.6}$	$0.41^{+0.35}_{-0.19}$	INT91
3	$2.90^{+0.52}_{-0.39}$	0.97±0.65	0.041±0.0021	$0.096^{+0.08}_{-0.044}$	$0.0096^{+0.0083}_{-0.0046}$				INT91
6	$2.27^{+0.42}_{-0.31}$	0.41±0.65	13±0.67	$19^{+16}_{-8.8}$	$1.2^{+1}_{-0.57}$	7.2±0.36	$10^{+8.5}_{-4.6}$	$0.63^{+0.53}_{-0.3}$	CTIO
7	$4.23^{+1.08}_{-0.74}$	2.02±0.65	0.4±0.02	$2.3^{+1.9}_{-1.1}$	$0.5^{+0.44}_{-0.24}$	0.054±0.0027	$0.31^{+0.25}_{-0.14}$	$0.066^{+0.057}_{-0.032}$	AAT92
8	$3.74^{+0.63}_{-0.48}$	2.62±0.65	3.4±0.17	33^{+28}_{-15}	$5.6^{+4.8}_{-2.7}$	0.93±0.047	$8.7^{+7.2}_{-4}$	$1.5^{+1.2}_{-0.69}$	CTIO
10	$5.46^{+1.25}_{-0.91}$	2.06±1.46	0.025±0.0012	$0.15^{+0.4}_{-0.11}$	$0.053^{+0.14}_{-0.04}$				CTIO
12	$5.71^{+1.24}_{-0.92}$	2.13±0.65	0.061±0.0031	$0.39^{+0.33}_{-0.18}$	$0.15^{+0.13}_{-0.074}$	0.45±0.022	$2.8^{+2.3}_{-1.3}$	$1.1^{+0.93}_{-0.52}$	CTIO
16	$2.63^{+0.32}_{-0.26}$	1.69±0.65	0.41±0.02	$1.8^{+1.5}_{-0.8}$	$0.15^{+0.12}_{-0.068}$	3±0.15	$13^{+11}_{-5.8}$	$1.1^{+0.88}_{-0.49}$	CTIO
18	$3.82^{+0.84}_{-0.60}$	2.73±0.65	0.99±0.05	$11^{+9}_{-4.9}$	$1.9^{+1.6}_{-0.9}$	0.29±0.015	$3.1^{+2.5}_{-1.4}$	$0.54^{+0.46}_{-0.26}$	AAT92
20	$6.98^{+1.18}_{-0.93}$	4.34±0.65	0.026±0.0013	$1.1^{+0.96}_{-0.52}$	$0.67^{+0.57}_{-0.32}$	0.0083±0.00042	$0.34^{+0.28}_{-0.16}$	$0.2^{+0.17}_{-0.095}$	CTIO
22	$2.33^{+0.28}_{-0.22}$	1.54±0.65	1.6±0.078	$5.9^{+4.9}_{-2.7}$	$0.38^{+0.32}_{-0.18}$	0.63±0.031	$2.3^{+1.9}_{-1.1}$	$0.15^{+0.13}_{-0.07}$	CTIO
24	$3.55^{+0.66}_{-0.49}$	1.09±0.65	1.6±0.079	$4^{+3.4}_{-1.8}$	$0.61^{+0.52}_{-0.29}$				AAT92
25	$1.97^{+0.18}_{-0.15}$	2.87±0.98	0.12±0.0058	$1.4^{+2}_{-0.83}$	$0.065^{+0.094}_{-0.039}$				CTIO
26	$6.70^{+1.05}_{-0.83}$	4.31±0.65	0.74±0.037	31^{+26}_{-14}	$17^{+14}_{-7.9}$	0.061±0.0031	$2.4^{+2}_{-1.1}$	$1.3^{+1.1}_{-0.61}$	CTIO
34	$7.41^{+1.37}_{-1.09}$	3.90±0.65							CTIO
35	$6.86^{+1.19}_{-0.94}$	3.30±2.01	0.017±0.00085	$0.3^{+1.5}_{-0.25}$	$0.17^{+0.84}_{-0.14}$	0.0068±0.00034	$0.11^{+0.55}_{-0.094}$	$0.064^{+0.31}_{-0.054}$	CTIO
36	$5.43^{+1.15}_{-0.85}$	3.41±0.75	0.066±0.0033	$1.3^{+1.3}_{-0.63}$	$0.44^{+0.45}_{-0.23}$	0.059±0.0029	$1.1^{+1.1}_{-0.54}$	$0.38^{+0.39}_{-0.2}$	CTIO
37	$6.71^{+1.36}_{-1.06}$	5.28±0.65	0.022±0.0011	$2.1^{+1.8}_{-0.98}$	$1.2^{+1}_{-0.56}$	0.0063±0.00031	$0.57^{+0.47}_{-0.26}$	$0.31^{+0.26}_{-0.15}$	CTIO
40	$3.83^{+0.67}_{-0.50}$	1.27±0.65	1.9±0.096	$5.8^{+4.9}_{-2.7}$	$1^{+0.88}_{-0.49}$	8.3±0.41	25^{+20}_{-11}	$4.3^{+3.7}_{-2}$	CTIO
46	$2.60^{+0.32}_{-0.26}$	0.56±0.65							CTIO
47	$3.49^{+0.61}_{-0.47}$	3.94±1.89	0.19±0.0094	$5.7^{+25}_{-4.7}$	$0.84^{+3.7}_{-0.69}$	0.18±0.0091	$5.3^{+23}_{-4.3}$	$0.77^{+3.3}_{-0.64}$	CTIO
49	$8.35^{+1.44}_{-1.17}$	2.32±0.65	0.014±0.0007	$0.11^{+0.088}_{-0.048}$	$0.088^{+0.076}_{-0.042}$	0.0026±0.00013	$0.019^{+0.015}_{-0.0085}$	$0.016^{+0.013}_{-0.0074}$	CTIO
51	$3.67^{+0.48}_{-0.39}$	5.09±0.65	0.01±0.00052	$0.86^{+0.72}_{-0.39}$	$0.14^{+0.12}_{-0.065}$	0.002±0.0001	$0.16^{+0.13}_{-0.073}$	$0.026^{+0.022}_{-0.012}$	CTIO
54	$6.52^{+1.37}_{-1.05}$	2.77±0.65							CTIO

WR Number	Distance (kpc)	A_V (mag)	F_{5808} (10^{-11}ergs s^{-1}Å^{-1})	I_{5808} (10^{-11}ergs s^{-1}Å^{-1})	L_{5808} (10^{35}ergs s^{-1})	F_{5876} (10^{-11}ergs s^{-1}Å^{-1})	I_{5876} (10^{-11}ergs s^{-1}Å^{-1})	L_{5876} (10^{35}ergs s^{-1})	Source
55	$3.00^{+0.55}_{-0.41}$	2.06±0.65							CTIO
58	$5.88^{+1.42}_{-1.04}$	3.00±0.65	0.37±0.018	$4.9^{+4.1}_{-2.2}$	$2^{+1.8}_{-1}$	0.015±0.00075	$0.19^{+0.16}_{-0.088}$	$0.08^{+0.069}_{-0.039}$	CTIO
61	$5.49^{+1.25}_{-0.91}$	2.40±0.65	0.11±0.0053	$0.85^{+0.72}_{-0.39}$	$0.31^{+0.27}_{-0.15}$	0.035±0.0017	$0.27^{+0.22}_{-0.12}$	$0.097^{+0.083}_{-0.047}$	CTIO
67	$2.23^{+0.54}_{-0.37}$	4.31±0.65	0.1±0.005	$4.2^{+3.5}_{-1.9}$	$0.25^{+0.22}_{-0.12}$	0.057±0.0029	$2.3^{+1.9}_{-1}$	$0.14^{+0.12}_{-0.066}$	CTIO
71	$3.19^{+0.67}_{-0.48}$	0.86±0.65	0.43±0.021	$0.9^{+0.76}_{-0.41}$	$0.11^{+0.095}_{-0.053}$	0.36±0.018	$0.75^{+0.62}_{-0.34}$	$0.091^{+0.078}_{-0.044}$	CTIO
74	$3.98^{+0.86}_{-0.66}$	6.48±0.65	0.015±0.00077	$4.2^{+3.5}_{-1.9}$	$0.8^{+0.69}_{-0.39}$	0.024±0.0012	$6^{+5}_{-2.7}$	$1.1^{+0.98}_{-0.55}$	CTIO
75	$3.32^{+0.80}_{-0.55}$	3.33±0.65	0.52±0.026	$9.4^{+8}_{-4.3}$	$1.2^{+1.1}_{-0.61}$	0.82±0.041	$14^{+12}_{-6.5}$	$1.9^{+1.6}_{-0.91}$	CTIO
82	$3.74^{+0.98}_{-0.66}$	3.75±0.65	0.023±0.0012	$0.6^{+0.5}_{-0.27}$	$0.1^{+0.088}_{-0.049}$	0.09±0.0045	$2.2^{+1.8}_{-1}$	$0.37^{+0.32}_{-0.18}$	CTIO
83	$3.80^{+1.10}_{-0.72}$	4.01±0.65	0.044±0.0022	$1.4^{+1.2}_{-0.65}$	$0.25^{+0.22}_{-0.12}$	0.024±0.0012	$0.75^{+0.62}_{-0.34}$	$0.13^{+0.11}_{-0.064}$	CTIO
84	$3.01^{+0.51}_{-0.40}$	4.53±0.65	0.033±0.0016	$1.7^{+1.4}_{-0.77}$	$0.18^{+0.16}_{-0.087}$	0.042±0.0021	$2^{+1.7}_{-0.92}$	$0.22^{+0.19}_{-0.1}$	CTIO
85	$1.99^{+0.30}_{-0.24}$	3.18±0.65	0.16±0.0082	$2.6^{+2.2}_{-1.2}$	$0.12^{+0.11}_{-0.058}$	0.076±0.0038	$1.2^{+0.95}_{-0.52}$	$0.055^{+0.046}_{-0.026}$	CTIO
87	$2.91^{+0.66}_{-0.47}$	7.15±0.65	0.021±0.0011	$10^{+8.6}_{-4.7}$	$1^{+0.9}_{-0.51}$	0.0047±0.00023	$2.1^{+1.7}_{-0.96}$	$0.21^{+0.18}_{-0.1}$	CTIO
89	$2.90^{+0.72}_{-0.51}$	5.77±0.65				0.0094±0.00047	$1.3^{+1.1}_{-0.59}$	$0.13^{+0.11}_{-0.064}$	CTIO
91	$4.04^{+1.52}_{-0.92}$	6.29±0.65	0.0067±0.00033	$1.6^{+1.3}_{-0.71}$	$0.3^{+0.28}_{-0.16}$	0.024±0.0012	$5.1^{+4.2}_{-2.3}$	$1^{+0.91}_{-0.51}$	CTIO
94	$0.95^{+0.06}_{-0.06}$	3.82±0.65							CTIO
98	$1.96^{+0.31}_{-0.24}$	4.91±0.65	0.29±0.015	$21^{+17}_{-9.4}$	$0.95^{+0.81}_{-0.45}$	0.23±0.011	$15^{+13}_{-6.9}$	$0.7^{+0.59}_{-0.33}$	CTIO
100	$3.55^{+1.06}_{-0.67}$	5.06±0.65							CTIO
105	$1.73^{+0.32}_{-0.23}$	7.45±0.65				0.079±0.004	46^{+38}_{-21}	$1.7^{+1.4}_{-0.78}$	WHT94
107	$2.87^{+0.81}_{-0.69}$	5.51±0.65							INT96
108	$2.79^{+0.45}_{-0.35}$	4.19±0.65	0.11±0.0054	$4^{+3.4}_{-1.8}$	$0.37^{+0.32}_{-0.18}$	0.05±0.0025	$1.8^{+1.5}_{-0.82}$	$0.17^{+0.14}_{-0.079}$	INT91
110	$1.58^{+0.15}_{-0.12}$	3.48±0.65	2.1±0.1	42^{+35}_{-19}	$1.3^{+1.1}_{-0.58}$	1.3±0.065	25^{+21}_{-11}	$0.75^{+0.63}_{-0.35}$	INT91
123	$5.35^{+1.56}_{-1.09}$	2.17±0.65							INT91
124	$5.87^{+1.48}_{-1.09}$	3.60±0.65	0.034±0.0017	$0.76^{+0.64}_{-0.35}$	$0.31^{+0.28}_{-0.16}$	0.36±0.018	$7.8^{+6.4}_{-3.5}$	$3.2^{+2.8}_{-1.6}$	INT91
128	$2.90^{+0.54}_{-0.39}$	1.16±0.65	0.098±0.0049	$0.27^{+0.23}_{-0.12}$	$0.027^{+0.023}_{-0.013}$	0.02±0.001	$0.054^{+0.045}_{-0.025}$	$0.0055^{+0.0046}_{-0.0026}$	INT91
131	$6.92^{+1.40}_{-1.09}$	3.97±0.65	0.012±0.00058	$0.36^{+0.3}_{-0.16}$	$0.21^{+0.18}_{-0.099}$	0.023±0.0011	$0.67^{+0.56}_{-0.31}$	$0.39^{+0.33}_{-0.19}$	WHT94
133	$1.85^{+0.16}_{-0.14}$	1.11±0.64	3.1±0.16	$8.1^{+6.7}_{-3.7}$	$0.33^{+0.27}_{-0.15}$	0.43±0.022	$1.1^{+0.91}_{-0.51}$	$0.046^{+0.038}_{-0.021}$	INT91
134	$1.75^{+0.13}_{-0.11}$	1.42±0.65	5.3±0.26	$18^{+15}_{-8.3}$	$0.66^{+0.56}_{-0.31}$	3.9±0.19	13^{+11}_{-6}	$0.48^{+0.4}_{-0.22}$	INT91

WR Number	Distance (kpc)	A_V (mag)	F_{5808} (10^{-11}ergs s^{-1}Å^{-1})	I_{5808} (10^{-11}ergs s^{-1}Å^{-1})	L_{5808} (10^{35}ergs s^{-1})	F_{5876} (10^{-11}ergs s^{-1}Å^{-1})	I_{5876} (10^{-11}ergs s^{-1}Å^{-1})	L_{5876} (10^{35}ergs s^{-1})	Source
139	$1.31^{+0.07}_{-0.06}$	2.51±0.75	1.5±0.076	$13^{+14}_{-6.8}$	$0.27^{+0.28}_{-0.14}$	0.61±0.031	$5.2^{+5.2}_{-2.6}$	$0.11^{+0.11}_{-0.054}$	INT91
145	$1.46^{+0.12}_{-0.10}$	7.06±1.19	0.43±0.021	190^{+370}_{-130}	$4.9^{+9.5}_{-3.2}$	0.098±0.0049	41^{+77}_{-27}	$1^{+2}_{-0.68}$	WHT94
148	$9.47^{+1.77}_{-1.49}$	1.91±0.65	0.052±0.0026	$0.27^{+0.23}_{-0.12}$	$0.29^{+0.25}_{-0.14}$	0.0077±0.00039	$0.04^{+0.033}_{-0.018}$	$0.043^{+0.036}_{-0.02}$	INT91
149	$4.89^{+0.83}_{-0.63}$	5.54±0.65	0.03±0.0015	$3.6^{+3}_{-1.6}$	$1^{+0.89}_{-0.49}$	0.0055±0.00027	$0.63^{+0.52}_{-0.28}$	$0.18^{+0.15}_{-0.085}$	INT13
155	$2.99^{+0.45}_{-0.35}$	2.16±0.97	0.28±0.014	$1.8^{+2.6}_{-1.1}$	$0.19^{+0.28}_{-0.12}$	0.13±0.0067	$0.85^{+1.2}_{-0.5}$	$0.091^{+0.13}_{-0.054}$	INT91
156	$4.10^{+0.60}_{-0.47}$	3.67±0.65	0.078±0.0039	$1.9^{+1.6}_{-0.85}$	$0.38^{+0.32}_{-0.18}$	0.021±0.001	$0.48^{+0.4}_{-0.22}$	$0.098^{+0.082}_{-0.046}$	INT91
157	$2.57^{+0.32}_{-0.26}$	2.83±0.65							INT91

Table A.6: WC blue region emission line fluxes, intensities and luminosities for individual stars, from Chapter 5.

WR Number	Distance (kpc)	A_V (mag)	F_{4650} (10^{-11}ergs s^{-1}Å^{-1})	I_{4650} (10^{-11}ergs s^{-1}Å^{-1})	L_{4650} (10^{35}ergs s^{-1})	F_{4686} (10^{-11}ergs s^{-1}Å^{-1})	I_{4686} (10^{-11}ergs s^{-1}Å^{-1})	L_{4686} (10^{35}ergs s^{-1})	Source
4	$3.75^{+0.89}_{-0.62}$	1.50±0.92	16±0.81	89^{+180}_{-59}	15^{+30}_{-10}	8.3±0.41	45^{+88}_{-30}	$7.6^{+15}_{-5.2}$	INT91
5	$2.97^{+0.43}_{-0.33}$	2.51±0.92	9.2±0.46	160^{+320}_{-110}	17^{+34}_{-11}	4.7±0.23	80^{+160}_{-53}	$8.4^{+17}_{-5.7}$	WHT02
13	$4.80^{+1.09}_{-0.78}$	3.82±0.92	0.51±0.026	40^{+78}_{-26}	$11^{+22}_{-7.5}$	0.29±0.015	22^{+43}_{-14}	$6^{+12}_{-4.1}$	CTIO
14	$2.22^{+0.22}_{-0.19}$	1.27±0.92	43±2.2	190^{+370}_{-120}	$11^{+22}_{-7.3}$	9.2±0.46	38^{+75}_{-25}	$2.3^{+4.4}_{-1.5}$	AAT92
15	$2.96^{+0.34}_{-0.28}$	3.45±0.92	2.9±0.14	150^{+290}_{-97}	15^{+30}_{-10}	2.7±0.14	130^{+260}_{-88}	$14^{+27}_{-9.3}$	CTIO
17	$6.75^{+1.74}_{-1.33}$	1.27±0.92	15±0.75	64^{+130}_{-43}	35^{+70}_{-24}	2.5±0.12	$10^{+20}_{-6.9}$	$5.7^{+11}_{-3.9}$	ANU97
19	$4.33^{+0.78}_{-0.58}$	4.72±0.92	0.34±0.017	73^{+140}_{-48}	16^{+32}_{-11}	0.036±0.0018	$7.3^{+14}_{-4.9}$	$1.7^{+3.2}_{-1.1}$	ANU97
23	$2.55^{+0.34}_{-0.27}$	0.56±0.92	37±1.8	70^{+140}_{-46}	$5.4^{+11}_{-3.7}$	19±0.95	36^{+70}_{-24}	$2.8^{+5.5}_{-1.9}$	ANU97
27	$2.62^{+0.33}_{-0.26}$	5.58±0.92	0.25±0.013	150^{+290}_{-97}	$12^{+24}_{-8.1}$	0.095±0.0047	52^{+100}_{-34}	$4.3^{+8.4}_{-2.9}$	CTIO
30	$5.09^{+0.99}_{-0.74}$	1.98±0.70	2.2±0.11	21^{+27}_{-12}	$6.4^{+8.6}_{-3.8}$	1.1±0.054	$10^{+13}_{-5.7}$	$3.1^{+4.1}_{-1.8}$	CTIO
330	$6.72^{+1.40}_{-1.09}$	4.11±0.64				0.19±0.0095	20^{+23}_{-11}	$11^{+13}_{-6.1}$	ANU97
33	$7.59^{+1.62}_{-1.30}$	1.35±0.92	3.5±0.17	16^{+32}_{-11}	$11^{+22}_{-7.7}$	1.1±0.055	$5.1^{+9.9}_{-3.4}$	$3.5^{+6.9}_{-2.4}$	CTIO
38	$6.04^{+1.18}_{-0.90}$	4.23±0.92	0.11±0.0053	$13^{+26}_{-8.9}$	5.8^{+12}_{-4}	0.046±0.0023	$5.5^{+11}_{-3.6}$	$2.4^{+4.7}_{-1.6}$	ANU97
39	$3.84^{+1.72}_{-1.11}$	5.75±0.65	0.091±0.0046	63^{+76}_{-35}	11^{+14}_{-7}	0.053±0.0026	35^{+41}_{-19}	$6.2^{+7.8}_{-3.8}$	CTIO
42	$2.44^{+0.41}_{-0.31}$	1.21±0.69	84±4.2	330^{+430}_{-190}	24^{+31}_{-14}	20±1	78^{+100}_{-44}	$5.6^{+7.2}_{-3.2}$	CTIO
45	$4.25^{+0.43}_{-0.36}$	4.94±0.92	0.23±0.012	64^{+130}_{-43}	$14^{+28}_{-9.3}$	0.048±0.0024	$12^{+24}_{-8.2}$	$2.7^{+5.2}_{-1.8}$	CTIO
50	$3.48^{+0.54}_{-0.42}$	2.92±0.83	0.87±0.043	24^{+41}_{-15}	$3.5^{+5.9}_{-2.2}$	0.47±0.023	$13^{+21}_{-7.9}$	$1.8^{+3.1}_{-1.2}$	CTIO
53	$4.14^{+0.74}_{-0.56}$	2.96±0.65	4.6±0.23	130^{+160}_{-73}	27^{+33}_{-15}	1.2±0.062	35^{+41}_{-19}	$7.1^{+8.5}_{-4}$	ANU97
56	$8.67^{+1.46}_{-1.20}$	2.40±0.92	0.44±0.022	$6.8^{+13}_{-4.5}$	$6.1^{+12}_{-4.1}$	0.21±0.01	$3.1^{+6.1}_{-2.1}$	$2.8^{+5.5}_{-1.9}$	CTIO
57	$5.50^{+1.49}_{-1.06}$	1.76±0.65	20±1	150^{+180}_{-81}	54^{+66}_{-31}	4.6±0.23	33^{+39}_{-18}	12^{+15}_{-7}	CTIO
59	$3.57^{+0.69}_{-0.51}$	5.84±0.65	0.037±0.0018	28^{+34}_{-15}	$4.3^{+5.2}_{-2.4}$	0.014±0.00071	$10^{+12}_{-5.5}$	$1.6^{+1.9}_{-0.87}$	CTIO
60	$3.51^{+0.65}_{-0.48}$	5.28±0.65	0.45±0.023	190^{+220}_{-100}	28^{+33}_{-16}	0.28±0.014	110^{+130}_{-59}	16^{+19}_{-9}	CTIO
65	$3.13^{+0.80}_{-0.54}$	6.42±0.64	0.027±0.0013	39^{+47}_{-21}	$4.6^{+5.6}_{-2.6}$	0.007±0.00035	$9.6^{+11}_{-5.2}$	$1.1^{+1.4}_{-0.64}$	CTIO
68	$4.93^{+1.12}_{-0.81}$	4.38±0.92	0.19±0.0095	28^{+56}_{-19}	$8.2^{+16}_{-5.6}$	0.15±0.0073	20^{+40}_{-13}	$5.9^{+12}_{-4.1}$	CTIO
69	$3.48^{+0.64}_{-0.47}$	1.67±0.66	4.6±0.23	31^{+38}_{-17}	$4.5^{+5.6}_{-2.5}$	2.2±0.11	15^{+18}_{-8}	$2.1^{+2.6}_{-1.2}$	CTIO

WR Number	Distance (kpc)	A_V (mag)	F_{4650} (10^{-11}ergs s^{-1}Å^{-1})	I_{4650} (10^{-11}ergs s^{-1}Å^{-1})	L_{4650} (10^{35}ergs s^{-1})	F_{4686} (10^{-11}ergs s^{-1}Å^{-1})	I_{4686} (10^{-11}ergs s^{-1}Å^{-1})	L_{4686} (10^{35}ergs s^{-1})	Source
70	$3.01^{+0.44}_{-0.34}$	4.72±0.64	0.5±0.025	110^{+130}_{-58}	$12^{+14}_{-6.4}$	0.14±0.0071	29^{+33}_{-16}	$3.1^{+3.7}_{-1.7}$	CTIO
73	$6.81^{+1.85}_{-1.47}$	5.81±0.65	0.033±0.0016	24^{+29}_{-13}	$13^{+16}_{-7.9}$	0.02±0.00098	$14^{+16}_{-7.5}$	$7.7^{+9.3}_{-4.5}$	CTIO
79	$1.37^{+0.12}_{-0.10}$	0.96±0.79	19±0.97	58^{+92}_{-35}	$1.3^{+2.1}_{-0.8}$	13±0.67	40^{+62}_{-24}	$0.89^{+1.4}_{-0.55}$	CTIO
80	$3.50^{+1.59}_{-0.90}$	7.19±0.65	0.028±0.0014	100^{+120}_{-55}	15^{+19}_{-9}	0.0097±0.00048	32^{+37}_{-17}	$4.7^{+5.9}_{-2.8}$	CTIO
81	$2.11^{+0.42}_{-0.30}$	5.32±0.65	0.28±0.014	120^{+140}_{-65}	$6.4^{+7.7}_{-3.6}$	0.11±0.0057	45^{+53}_{-24}	$2.4^{+2.9}_{-1.3}$	CTIO
88	$3.44^{+0.88}_{-0.60}$	4.94±0.65	0.13±0.0063	35^{+42}_{-19}	$5^{+6.1}_{-2.8}$	0.075±0.0037	20^{+23}_{-11}	$2.8^{+3.4}_{-1.6}$	CTIO
90	$1.15^{+0.11}_{-0.09}$	0.30±0.92	210±10	290^{+580}_{-190}	$4.6^{+9.1}_{-3.1}$	180±8.8	250^{+490}_{-160}	$3.9^{+7.7}_{-2.6}$	CTIO
93	$1.76^{+0.19}_{-0.15}$	5.16±0.72	0.92±0.046	330^{+460}_{-190}	$12^{+17}_{-7.2}$	1.5±0.075	510^{+690}_{-290}	19^{+26}_{-11}	CTIO
92	$3.78^{+1.25}_{-0.79}$	1.46±0.65	4.2±0.21	22^{+26}_{-12}	$3.8^{+4.7}_{-2.2}$	1.1±0.057	$5.9^{+7}_{-3.2}$	$1^{+1.2}_{-0.59}$	CTIO
95	$2.07^{+0.43}_{-0.31}$	6.03±0.65	0.088±0.0044	84^{+100}_{-46}	$4.3^{+5.2}_{-2.4}$	0.027±0.0014	24^{+29}_{-13}	$1.2^{+1.5}_{-0.7}$	CTIO
103	$3.46^{+1.28}_{-0.77}$	1.27±0.80	17±0.84	72^{+110}_{-44}	$10^{+17}_{-6.7}$	5.2±0.26	22^{+34}_{-13}	$3.2^{+5.1}_{-2.1}$	AAT92
104	$2.74^{+0.72}_{-0.55}$	6.07±0.62	0.04±0.002	40^{+45}_{-21}	$3.6^{+4.1}_{-2}$	0.0066±0.00033	$6.1^{+6.8}_{-3.2}$	$0.55^{+0.63}_{-0.31}$	WHT02
106	$3.07^{+0.56}_{-0.43}$	4.19±0.65	0.33±0.016	39^{+46}_{-21}	$4.4^{+5.3}_{-2.5}$	0.1±0.0052	$12^{+14}_{-6.3}$	$1.3^{+1.6}_{-0.74}$	INT96
111	$1.63^{+0.32}_{-0.23}$	0.67±0.92	150±7.6	330^{+640}_{-220}	$10^{+21}_{-7.1}$	51±2.5	110^{+210}_{-72}	$3.5^{+6.8}_{-2.3}$	INT91
113	$1.80^{+0.24}_{-0.19}$	2.91±0.66	2.7±0.13	73^{+89}_{-40}	$2.8^{+3.5}_{-1.6}$	0.75±0.038	20^{+24}_{-11}	$0.77^{+0.94}_{-0.43}$	INT91
114	$2.09^{+0.22}_{-0.18}$	4.16±0.92	1.3±0.065	150^{+290}_{-98}	$7.7^{+15}_{-5.2}$	0.65±0.032	70^{+140}_{-47}	$3.7^{+7.2}_{-2.5}$	CTIO
117	$3.66^{+1.45}_{-0.91}$	5.51±0.65	0.13±0.0064	67^{+80}_{-36}	$11^{+13}_{-6.4}$	0.043±0.0021	21^{+25}_{-11}	$3.4^{+4.2}_{-2}$	WHT02
126	$7.57^{+1.49}_{-1.19}$	3.37±0.92	0.13±0.0067	$6.2^{+12}_{-4.1}$	$4.3^{+8.5}_{-2.9}$	0.11±0.0055	$4.9^{+9.6}_{-3.3}$	$3.4^{+6.6}_{-2.3}$	WHT94
135	$1.98^{+0.18}_{-0.15}$	1.27±0.65	100±5.1	430^{+520}_{-240}	20^{+24}_{-11}	28±1.4	120^{+140}_{-63}	$5.4^{+6.4}_{-3}$	INT91
137	$2.10^{+0.18}_{-0.16}$	1.54±0.66	43±2.2	250^{+310}_{-140}	$13^{+16}_{-7.4}$	8.7±0.44	49^{+60}_{-27}	$2.6^{+3.2}_{-1.5}$	INT91
142	$1.65^{+0.11}_{-0.09}$	6.59±0.65				0.095±0.0047	170^{+210}_{-95}	$5.7^{+6.8}_{-3.1}$	WHT02
144	$1.75^{+0.24}_{-0.19}$		0.079±0.004			0.072±0.0036			WHT02
154	$5.38^{+1.20}_{-0.89}$	2.10±0.92	5.8±0.29	63^{+130}_{-42}	22^{+44}_{-15}	3.5±0.17	37^{+73}_{-25}	$13^{+26}_{-8.8}$	INT91

Table A.7: WC red region emission line fluxes, intensities and luminosities for individual stars, from Chapter 5.

WR Number	Distance (kpc)	A_V (mag)	F_{5696} (10^{-11}ergs $s^{-1}Å^{-1}$)	I_{5696} (10^{-11}ergs $s^{-1}Å^{-1}$)	L_{5696} (10^{35}ergs s^{-1})	F_{5808} (10^{-11}ergs $s^{-1}Å^{-1}$)	I_{5808} (10^{-11}ergs $s^{-1}Å^{-1}$)	L_{5808} (10^{35}ergs s^{-1})	F_{5876} (10^{-11}ergs $s^{-1}Å^{-1}$)	I_{5876} (10^{-11}ergs $s^{-1}Å^{-1}$)	L_{5876} (10^{35}ergs s^{-1})	Source
4	$3.75^{+0.89}_{-0.62}$	1.50±0.92	2±0.098	$7.4^{+10}_{-4.3}$	$1.2^{+1.7}_{-0.75}$	19±0.95	70^{+92}_{-40}	12^{+16}_{-7}	1.7±0.086	$6.2^{+8.1}_{-3.5}$	$1^{+1.4}_{-0.62}$	INT91
5	$2.97^{+0.43}_{-0.33}$	2.51±0.92	1.3±0.065	$12^{+16}_{-6.9}$	$1.3^{+1.7}_{-0.75}$	11±0.57	100^{+130}_{-57}	$11^{+14}_{-6.1}$	1.3±0.064	$11^{+14}_{-6.1}$	$1.1^{+1.5}_{-0.66}$	WHT02
13	$4.80^{+1.09}_{-0.78}$	3.82±0.92	0.14±0.0069	$4.1^{+5.6}_{-2.4}$	$1.1^{+1.6}_{-0.68}$	0.61±0.03	$17^{+22}_{-9.4}$	$4.6^{+6.1}_{-2.7}$	0.13±0.0064	$3.3^{+4.3}_{-1.9}$	$0.92^{+1.2}_{-0.54}$	CTIO
14	$2.22^{+0.22}_{-0.19}$	1.27±0.92	10±0.52	32^{+44}_{-19}	$1.9^{+2.6}_{-1.1}$	30±1.5	91^{+120}_{-52}	$5.4^{+7.1}_{-3.1}$	4.9±0.25	$15^{+19}_{-8.3}$	$0.86^{+1.1}_{-0.49}$	AAT92
15	$2.96^{+0.34}_{-0.28}$	3.45±0.92	1.4±0.069	29^{+40}_{-17}	$3^{+4.2}_{-1.8}$	6.8±0.34	130^{+180}_{-77}	$14^{+19}_{-8.2}$	1.9±0.096	36^{+47}_{-21}	$3.8^{+5}_{-2.2}$	CTIO
17	$6.75^{+1.74}_{-1.33}$	1.27±0.92	0.54±0.027	$1.7^{+2.3}_{-0.96}$	$0.91^{+1.3}_{-0.55}$	9±0.45	27^{+36}_{-15}	$15^{+20}_{-8.9}$	0.86±0.043	$2.6^{+3.3}_{-1.4}$	$1.4^{+1.8}_{-0.84}$	ANU97
19	$4.33^{+0.78}_{-0.58}$	4.72±0.92	0.041±0.0021	$2.7^{+3.7}_{-1.6}$	$0.61^{+0.83}_{-0.36}$	0.71±0.036	42^{+56}_{-24}	$9.5^{+13}_{-5.6}$				ANU97
23	$2.55^{+0.34}_{-0.27}$	0.56±0.92	7.5±0.38	$12^{+17}_{-7.2}$	$0.97^{+1.3}_{-0.57}$	28±1.4	46^{+60}_{-26}	$3.5^{+4.7}_{-2.1}$	4.4±0.22	$7.2^{+9.3}_{-4.1}$	$0.56^{+0.73}_{-0.32}$	ANU97
27	$2.62^{+0.33}_{-0.26}$	5.58±0.92	0.083±0.0041	$11^{+16}_{-6.6}$	$0.95^{+1.3}_{-0.56}$	0.44±0.022	54^{+72}_{-31}	$4.5^{+6}_{-2.6}$	0.048±0.0024	$5.6^{+7.3}_{-3.2}$	$0.46^{+0.61}_{-0.27}$	CTIO
30	$5.09^{+0.99}_{-0.74}$	1.98±0.70										CTIO
33	$7.59^{+1.62}_{-1.30}$	1.35±0.92	0.42±0.021	$1.4^{+1.9}_{-0.8}$	$0.96^{+1.3}_{-0.58}$	3.9±0.19	$12^{+16}_{-7.1}$	$8.6^{+12}_{-5.1}$	0.26±0.013	$0.83^{+1.1}_{-0.47}$	$0.57^{+0.76}_{-0.34}$	CTIO
38	$6.04^{+1.18}_{-0.90}$	4.23±0.92	0.0097±0.00049	$0.41^{+0.56}_{-0.24}$	$0.18^{+0.25}_{-0.11}$	0.28±0.014	$11^{+14}_{-6.2}$	$4.8^{+6.4}_{-2.8}$				ANU97
39	$3.84^{+1.72}_{-1.11}$	5.75±0.65	0.066±0.0033	$11^{+9.2}_{-5}$	$1.9^{+1.8}_{-1}$	0.12±0.0061	$18^{+15}_{-8.1}$	$3.1^{+3}_{-1.7}$	0.054±0.0027	$7.3^{+6.1}_{-3.3}$	$1.3^{+1.2}_{-0.7}$	CTIO
42	$2.44^{+0.41}_{-0.31}$	1.21±0.69										CTIO
45	$4.25^{+0.43}_{-0.36}$	4.94±0.92										CTIO
50	$3.48^{+0.54}_{-0.42}$	2.92±0.83	0.65±0.033	$8.6^{+10}_{-4.7}$	$1.3^{+1.5}_{-0.7}$	1.2±0.062	$16^{+18}_{-8.3}$	$2.3^{+2.6}_{-1.2}$	0.18±0.0091	$2.2^{+2.5}_{-1.2}$	$0.32^{+0.36}_{-0.17}$	CTIO
53	$4.14^{+0.74}_{-0.56}$	2.96±0.65	5.8±0.29	79^{+69}_{-37}	$16^{+14}_{-7.9}$	2.5±0.13	33^{+27}_{-15}	$6.7^{+5.8}_{-3.2}$	0.95±0.047	$12^{+9.8}_{-5.4}$	$2.4^{+2.1}_{-1.2}$	ANU97
56	$8.67^{+1.46}_{-1.20}$	2.40±0.92	0.21±0.011	$1.8^{+2.4}_{-1}$	$1.6^{+2.2}_{-0.96}$	0.37±0.018	$2.9^{+3.9}_{-1.7}$	$2.6^{+3.5}_{-1.5}$	0.054±0.0027	$0.42^{+0.54}_{-0.24}$	$0.38^{+0.49}_{-0.22}$	CTIO
57	$5.50^{+1.49}_{-1.06}$	1.76±0.65	9.8±0.49	46^{+40}_{-22}	$17^{+15}_{-8.5}$	9±0.45	41^{+35}_{-19}	$15^{+13}_{-7.5}$	1.6±0.079	$7.1^{+5.9}_{-3.2}$	$2.6^{+2.2}_{-1.3}$	CTIO
59	$3.57^{+0.69}_{-0.51}$	5.84±0.65	0.16±0.0082	29^{+25}_{-13}	$4.4^{+3.9}_{-2.1}$	0.059±0.0029	$9.1^{+7.7}_{-4.2}$	$1.4^{+1.2}_{-0.67}$	0.044±0.0022	$6.4^{+5.3}_{-2.9}$	$0.98^{+0.83}_{-0.47}$	CTIO
60	$3.51^{+0.65}_{-0.48}$	5.28±0.65	1.4±0.071	150^{+130}_{-71}	22^{+20}_{-11}	1±0.05	96^{+81}_{-44}	$14^{+12}_{-6.8}$	0.25±0.013	23^{+19}_{-10}	$3.4^{+2.9}_{-1.6}$	CTIO
65	$3.13^{+0.80}_{-0.54}$	6.42±0.64	0.12±0.0062	36^{+31}_{-17}	$4.2^{+3.8}_{-2.1}$	0.041±0.002	$10^{+8.7}_{-4.7}$	$1.2^{+1.1}_{-0.6}$	0.032±0.0016	$7.6^{+6.2}_{-3.4}$	$0.89^{+0.77}_{-0.43}$	CTIO
68	$4.93^{+1.12}_{-0.81}$	4.38±0.92	0.24±0.012	$12^{+16}_{-6.7}$	$3.4^{+4.7}_{-2}$	0.46±0.023	21^{+27}_{-12}	$6^{+8}_{-3.6}$	0.13±0.0063	$5.3^{+6.9}_{-3}$	$1.5^{+2}_{-0.91}$	CTIO
69	$3.48^{+0.64}_{-0.47}$	1.67±0.66										CTIO
70	$3.01^{+0.44}_{-0.34}$	4.72±0.64	1.5±0.073	95^{+81}_{-44}	$10^{+8.9}_{-4.9}$	0.83±0.041	49^{+41}_{-22}	$5.3^{+4.5}_{-2.5}$				CTIO
70	$3.01^{+0.44}_{-0.34}$	4.72±0.64	1.5±0.073	95^{+81}_{-44}	$10^{+8.9}_{-4.9}$	0.83±0.041	49^{+41}_{-22}	$5.3^{+4.5}_{-2.5}$				CTIO
70	$3.01^{+0.44}_{-0.34}$	4.72±0.64	1.5±0.073	95^{+81}_{-44}	$10^{+8.9}_{-4.9}$	0.83±0.041	49^{+41}_{-22}	$5.3^{+4.5}_{-2.5}$				CTIO
70	$3.01^{+0.44}_{-0.34}$	4.72±0.64	1.5±0.073	95^{+81}_{-44}	$10^{+8.9}_{-4.9}$	0.83±0.041	49^{+41}_{-22}	$5.3^{+4.5}_{-2.5}$				CTIO
73	$6.81^{+1.85}_{-1.47}$	5.81±0.65	0.17±0.0084	28^{+24}_{-13}	$16^{+14}_{-8.1}$	0.063±0.0031	$9.5^{+8}_{-4.3}$	$5.3^{+4.7}_{-2.7}$	0.029±0.0014	$4.1^{+3.4}_{-1.9}$	$2.3^{+2}_{-1.2}$	CTIO
79	$1.37^{+0.12}_{-0.10}$	0.96±0.79										CTIO
80	$3.50^{+1.59}_{-0.90}$	7.19±0.65	0.15±0.0074	85^{+73}_{-40}	$12^{+12}_{-6.6}$	0.051±0.0025	25^{+21}_{-12}	$3.7^{+3.6}_{-2}$	0.028±0.0014	13^{+11}_{-6}	$1.9^{+1.8}_{-1}$	CTIO
81	$2.11^{+0.42}_{-0.30}$	5.32±0.65	0.96±0.048	110^{+91}_{-49}	$5.6^{+5}_{-2.7}$	0.33±0.017	33^{+28}_{-15}	$1.8^{+1.5}_{-0.84}$	0.31±0.016	29^{+24}_{-13}	$1.6^{+1.3}_{-0.74}$	CTIO
88	$3.44^{+0.88}_{-0.60}$	4.94±0.65	0.41±0.021	33^{+28}_{-15}	$4.6^{+4.2}_{-2.3}$	0.16±0.0082	$12^{+9.9}_{-5.4}$	$1.7^{+1.5}_{-0.82}$	0.13±0.0063	$8.6^{+7.1}_{-3.9}$	$1.2^{+1.1}_{-0.59}$	CTIO

WR Number	Distance (kpc)	A_V (mag)	F_{5696} (10^{-11}ergs $s^{-1}Å^{-1}$)	I_{5696} (10^{-11}ergs $s^{-1}Å^{-1}$)	L_{5696} (10^{35}ergs s^{-1})	F_{5808} (10^{-11}ergs $s^{-1}Å^{-1}$)	I_{5808} (10^{-11}ergs $s^{-1}Å^{-1}$)	L_{5808} (10^{35}ergs s^{-1})	F_{5876} (10^{-11}ergs $s^{-1}Å^{-1}$)	I_{5876} (10^{-11}ergs $s^{-1}Å^{-1}$)	L_{5876} (10^{35}ergs s^{-1})	Source
90	$1.15^{+0.11}_{-0.09}$	0.30±0.92										CTIO
92	$3.78^{+1.25}_{-0.79}$	1.46±0.65	4.1±0.2	$15^{+13}_{-6.9}$	$2.5^{+2.3}_{-1.3}$	1.1±0.053	$3.7^{+3.1}_{-1.7}$	$0.64^{+0.58}_{-0.32}$	0.95±0.047	$3.3^{+2.7}_{-1.5}$	$0.56^{+0.5}_{-0.28}$	CTIO
93	$1.76^{+0.19}_{-0.15}$	5.16±0.72	1.7±0.087	170^{+160}_{-82}	$6.2^{+6.1}_{-3.1}$	3.9±0.19	340^{+320}_{-170}	$13^{+12}_{-6.3}$	1.5±0.073	120^{+110}_{-58}	$4.4^{+4.2}_{-2.2}$	CTIO
95	$2.07^{+0.43}_{-0.31}$	6.03±0.65	0.31±0.015	63^{+55}_{-29}	$3.2^{+2.9}_{-1.6}$	0.13±0.0065	24^{+20}_{-11}	$1.2^{+1.1}_{-0.59}$	0.08±0.004	$14^{+11}_{-6.2}$	$0.7^{+0.6}_{-0.34}$	CTIO
103	$3.46^{+1.28}_{-0.77}$	1.27±0.80	20±1	62^{+70}_{-33}	$8.9^{+11}_{-5.1}$	5.8±0.29	$17^{+19}_{-9.1}$	$2.5^{+2.9}_{-1.4}$	5.1±0.25	$15^{+16}_{-7.8}$	$2.2^{+2.5}_{-1.2}$	AAT92
104	$2.74^{+0.72}_{-0.55}$	6.07±0.62										WHT02
106	$3.07^{+0.56}_{-0.43}$	4.19±0.65	0.83±0.042	34^{+29}_{-16}	$3.8^{+3.4}_{-1.9}$	0.27±0.014	$10^{+8.6}_{-4.7}$	$1.2^{+1}_{-0.56}$	0.27±0.013	$9.5^{+7.9}_{-4.3}$	$1.1^{+0.91}_{-0.51}$	INT96
111	$1.63^{+0.32}_{-0.23}$	0.67±0.92	7.4±0.37	$13^{+18}_{-7.8}$	$0.43^{+0.59}_{-0.26}$	85±4.3	150^{+200}_{-87}	$4.9^{+6.5}_{-2.9}$	7.9±0.39	$14^{+18}_{-7.9}$	$0.45^{+0.59}_{-0.26}$	INT91
113	$1.80^{+0.24}_{-0.19}$	2.91±0.66	3.6±0.18	48^{+42}_{-22}	$1.9^{+1.7}_{-0.89}$	1.8±0.089	22^{+19}_{-10}	$0.85^{+0.74}_{-0.4}$	0.57±0.029	$6.9^{+5.8}_{-3.2}$	$0.27^{+0.23}_{-0.13}$	INT91
114	$2.09^{+0.22}_{-0.18}$	4.16±0.92	0.32±0.016	$13^{+17}_{-7.2}$	$0.66^{+0.9}_{-0.38}$	1.9±0.097	71^{+93}_{-40}	$3.7^{+4.9}_{-2.1}$	0.3±0.015	11^{+14}_{-6}	$0.56^{+0.72}_{-0.32}$	CTIO
117	$3.66^{+1.45}_{-0.91}$	5.51±0.65	0.49±0.025	64^{+55}_{-30}	$10^{+9.7}_{-5.4}$	0.19±0.0094	22^{+18}_{-10}	$3.5^{+3.3}_{-1.8}$	0.07±0.0035	$7.8^{+6.4}_{-3.5}$	$1.2^{+1.1}_{-0.64}$	WHT02
126	$7.57^{+1.49}_{-1.19}$	3.37±0.92	0.014±0.0007	$0.28^{+0.37}_{-0.16}$	$0.19^{+0.26}_{-0.11}$	0.46±0.023	$8.5^{+11}_{-4.8}$	$5.8^{+7.8}_{-3.5}$	0.022±0.0011	$0.4^{+0.51}_{-0.22}$	$0.27^{+0.36}_{-0.16}$	WHT94
135	$1.98^{+0.18}_{-0.15}$	1.27±0.65	37±1.9	110^{+99}_{-53}	$5.3^{+4.6}_{-2.5}$	35±1.8	110^{+89}_{-48}	$5^{+4.2}_{-2.3}$	9±0.45	27^{+22}_{-12}	$1.2^{+1}_{-0.57}$	INT91
137	$2.10^{+0.18}_{-0.16}$	1.54±0.66	12±0.58	46^{+40}_{-21}	$2.4^{+2.1}_{-1.1}$	20±1	76^{+65}_{-35}	$4^{+3.5}_{-1.9}$	3.6±0.18	$13^{+11}_{-6.2}$	$0.71^{+0.61}_{-0.33}$	INT91
142	$1.65^{+0.11}_{-0.09}$	6.59±0.65				0.2±0.01	78^{+69}_{-37}	$2.5^{+2.3}_{-1.2}$				WHT02
144	$1.75^{+0.24}_{-0.19}$		0.032±0.0016			0.73±0.036			0.044±0.0022			WHT02
154	$5.38^{+1.20}_{-0.89}$	2.10±0.92	1.4±0.068	8.7^{+12}_{-5}	$3^{+4.2}_{-1.8}$	6.9±0.35	43^{+56}_{-24}	$15^{+20}_{-8.8}$	1±0.051	$6.1^{+7.9}_{-3.4}$	$2.1^{+2.8}_{-1.2}$	INT91
330	$6.72^{+1.40}_{-1.09}$	4.11±0.64				0.093±0.0046	$3.8^{+3.3}_{-1.8}$	$2^{+1.8}_{-1}$				ANU97

A.5 List of WR star candidates in NGC6946

Table A.8: Table listing information on the WR candidates from Chapter 6. Column 1 is the assigned catalogue number, columns 2 and 3 are the RA and DEC, columns 4 and 5 are the He II and He IIC apparent magnitudes (mag), column 6 is the excess of He II , column 7 is the number of σ excesses, columns 9-11 are the broadband, Hα and HαC apparent magnitudes (mag). Finally, column 12 lists the detection methods for each source. (a) denotes that a sources was found from photometric excesses only, (b) indicates that a spectrum was taken at the source, (c) that the source was detected manually via excesses in the image, (d) indicates a spectroscopic WC confirmation and (e) that no WR features were observed in the spectrum (so the source is a possible WN).

ID	R.A	DEC	He II	He IIC	Δ He IIC	σ excess	g	r	Hα	HαC	Detection methods
1	$20^h34^m19.57^s$	$60°10'03.5''$		21.93±0.08					19.10±0.10		c
2	$20^h34^m20.54^s$	$60°10'03.0''$	23.09±0.04	23.51±0.05	0.42±0.06	2.44±0.37	22.83±0.04	22.28±0.06	19.65±0.11	22.45±0.05	abd
3	$20^h34^m20.60^s$	$60°10'05.0''$	21.61±0.05	21.83±0.05	0.22±0.07	2.93±0.91	21.46±0.04	21.07±0.07	18.69±0.07	21.20±0.07	a
4	$20^h34^m20.76^s$	$60°09'01.8''$	23.60±0.05	24.21±0.06	0.61±0.08	1.62±0.20		23.35±0.05			be
5	$20^h34^m21.06^s$	$60°10'44.6''$							20.47±0.09		c
6	$20^h34^m21.55^s$	$60°08'08.8''$	22.73±0.05	23.18±0.05	0.44±0.07	3.55±0.57	22.77±0.04	22.22±0.07	19.53±0.09		abce
7	$20^h34^m22.15^s$	$60°09'57.9''$	23.51±0.04				23.87±0.05				c
8	$20^h34^m22.30^s$	$60°10'22.5''$									c
9	$20^h34^m22.89^s$	$60°10'33.7''$	22.72±0.05					20.85±0.08			c
10	$20^h34^m23.16^s$	$60°08'19.2''$	23.79±0.04								bcd
11	$20^h34^m23.51^s$	$60°10'40.7''$	22.03±0.07								be
12	$20^h34^m23.64^s$	$60°08'45.6''$	23.55±0.06								bce
13	$20^h34^m23.73^s$	$60°10'33.8''$									c
14	$20^h34^m23.97^s$	$60°11'17.6''$	23.71±0.06					22.80±0.06	20.59±0.10		bce
15	$20^h34^m24.98^s$	$60°09'46.8''$	21.99±0.04	22.09±0.04	0.10±0.06	1.06±0.61	21.89±0.03	21.48±0.05	20.12±0.09	21.41±0.05	bd
16	$20^h34^m25.13^s$	$60°10'55.6''$	25.08±0.12								c
17	$20^h34^m25.16^s$	$60°11'16.2''$	22.02±0.07	22.11±0.07	0.09±0.10	0.44±0.52	21.87±0.06	21.97±0.06		21.83±0.08	bce
18	$20^h34^m25.20^s$	$60°11'38.7''$	23.04±0.05	23.28±0.06	0.24±0.08	0.39±0.13	22.99±0.04	22.80±0.06	21.06±0.10		bd
19	$20^h34^m25.22^s$	$60°07'10.2''$	23.21±0.05	23.68±0.07	0.46±0.08	1.87±0.33	23.71±0.04	23.68±0.05			bcd
20	$20^h34^m25.57^s$	$60°07'45.5''$	23.13±0.07								c
21	$20^h34^m25.85^s$	$60°11'14.1''$	23.14±0.07								c
22	$20^h34^m25.99^s$	$60°11'18.0''$	20.97±0.07	21.23±0.08	0.26±0.10	2.66±1.04	20.80±0.06	20.97±0.07		20.51±0.09	a
23	$20^h34^m27.72^s$	$60°07'46.1''$	23.25±0.04	23.94±0.05	0.68±0.06	5.02±0.43	22.91±0.03	22.02±0.04	18.98±0.05	22.21±0.05	abce
24	$20^h34^m29.98^s$	$60°11'00.8''$									c
25	$20^h34^m30.96^s$	$60°09'23.7''$	23.91±0.05						20.75±0.09		b
26	$20^h34^m31.24^s$	$60°10'23.9''$	21.73±0.03	22.00±0.04	0.27±0.05	5.09±0.89	21.68±0.03	20.74±0.04	17.75±0.07	20.82±0.04	abcd
27	$20^h34^m32.13^s$	$60°10'38.4''$	23.28±0.04								c

ID	R.A	DEC	He II	He IIC	Δ He IIC	σ excess	g	r	Hα	HαC	Detection methods
28	$20^h34^m32.67^s$	$60°10'13.2''$	25.19±0.23								bd
29	$20^h34^m32.98^s$	$60°08'02.9''$	22.01±0.05	22.28±0.08	0.27±0.10	2.20±0.79	22.12±0.06				abce
30	$20^h34^m33.05^s$	$60°07'18.6''$	23.37±0.09								bd
31	$20^h34^m33.10^s$	$60°11'10.9''$	22.50±0.06	22.59±0.08	0.09±0.10	-0.05±0.06	22.24±0.05	21.95±0.06	19.44±0.08		bd
32	$20^h34^m33.13^s$	$60°10'20.4''$	22.91±0.07				22.78±0.07				bce
33	$20^h34^m33.80^s$	$60°09'03.7''$	24.71±0.12								c
34	$20^h34^m33.95^s$	$60°08'20.9''$	22.67±0.03	23.20±0.04	0.53±0.05	7.02±0.64	22.90±0.03	22.38±0.06	20.24±0.08		abe
35	$20^h34^m34.75^s$	$60°08'48.4''$	23.17±0.05								be
36	$20^h34^m35.05^s$	$60°07'26.8''$	24.11±0.05				24.74±0.09	23.71±0.05	20.80±0.07		bd
37	$20^h34^m43.43^s$	$60°07'11.9''$	22.66±0.07								be
38	$20^h34^m45.00^s$	$60°11'42.6''$	23.65±0.04								bce
39	$20^h34^m45.99^s$	$60°10'49.4''$	21.00±0.03	21.11±0.04	0.11±0.05	2.54±1.14	20.71±0.02	19.22±0.13	18.28±0.01	18.73±0.02	a
40	$20^h34^m47.70^s$	$60°11'14.7''$	23.86±0.04								c
41	$20^h34^m47.97^s$	$60°10'57.8''$	23.26±0.04								bcd
42	$20^h34^m48.00^s$	$60°10'56.7''$	22.97±0.04	23.31±0.06	0.34±0.07	1.81±0.37	23.14±0.05	22.41±0.14	20.15±0.07		ac
43	$20^h34^m48.06^s$	$60°10'41.7''$	21.75±0.08	22.05±0.09	0.30±0.12	2.14±0.88	21.76±0.07				bd
44	$20^h34^m48.07^s$	$60°07'16.7''$	21.55±0.03	21.76±0.03	0.21±0.04	4.49±0.92	21.37±0.02	20.31±0.03	19.39±0.05	19.96±0.03	a
45	$20^h34^m48.22^s$	$60°11'00.1''$	23.74±0.03								bcd
46	$20^h34^m49.20^s$	$60°10'31.9''$	23.48±0.05					22.76±0.07	20.36±0.10		be
47	$20^h34^m50.83^s$	$60°07'46.1''$	22.57±0.05					21.23±0.06			bce
48	$20^h34^m51.39^s$	$60°12'37.8''$	25.48±0.33								c
49	$20^h34^m51.81^s$	$60°12'42.8''$	22.54±0.04				22.80±0.05	21.99±0.15	19.32±0.07		bce
50	$20^h34^m52.06^s$	$60°07'11.2''$	22.64±0.06								c
51	$20^h34^m52.31^s$	$60°07'14.8''$	23.60±0.04								c
52	$20^h34^m53.32^s$	$60°12'48.1''$	21.97±0.06	22.80±0.06	0.82±0.08	8.65±0.85	22.02±0.05	22.54±0.13			ac
53	$20^h34^m53.47^s$	$60°10'30.6''$	23.43±0.06	24.11±0.13	0.67±0.14	1.61±0.34	24.45±0.19	23.06±0.04	19.84±0.10	22.49±0.07	bd
54	$20^h34^m54.12^s$	$60°12'46.5''$	21.59±0.07								c
55	$20^h34^m56.09^s$	$60°10'55.7''$	22.35±0.07	22.80±0.08	0.45±0.11	2.98±0.73		21.77±0.08	19.08±0.11	21.39±0.08	a
56	$20^h34^m57.11^s$	$60°11'33.8''$	21.41±0.03	21.55±0.03	0.14±0.04	3.18±0.98	21.12±0.02	19.79±0.03	19.17±0.03	19.45±0.04	a
57	$20^h34^m57.68^s$	$60°08'35.0''$	22.72±0.04	22.98±0.06	0.27±0.07	1.58±0.44	23.35±0.03	22.40±0.13	19.96±0.06	22.28±0.04	bd
58	$20^h34^m57.81^s$	$60°11'27.5''$	24.92±0.12								be
59	$20^h34^m59.36^s$	$60°10'39.6''$	24.51±0.09								be
60	$20^h35^m00.49^s$	$60°10'46.2''$	25.38±0.26								be
61	$20^h35^m00.76^s$	$60°11'30.8''$	21.44±0.05	22.38±0.05	0.94±0.07	11.72±0.93	20.41±0.05	19.24±0.14	16.46±0.05	19.52±0.05	ac
62	$20^h35^m01.76^s$	$60°09'04.8''$	20.92±0.05	21.04±0.05	0.12±0.07	2.01±1.15	20.91±0.04	20.54±0.13	18.65±0.05	20.54±0.04	bd
63	$20^h35^m02.46^s$	$60°10'39.7''$	23.35±0.07								be

ID	R.A	DEC	He II	He IIC	Δ He IIC	σ excess	g	r	Hα	HαC	Detection methods
64	$20^h35^m04.34^s$	$60°11'12.7''$	22.02±0.04	22.31±0.06	0.28±0.07	3.01±0.78	22.16±0.04	21.04±0.13	18.38±0.04	21.34±0.04	abd
65	$20^h35^m04.35^s$	$60°10'49.3''$	23.79±0.04				23.79±0.06	22.83±0.14	19.80±0.06		bd
66	$20^h35^m04.97^s$	$60°10'49.8''$					22.87±0.06				be
67	$20^h35^m06.58^s$	$60°07'25.7''$	23.46±0.06								c
68	$20^h35^m07.09^s$	$60°11'47.3''$	23.94±0.04						20.26±0.07		c
69	$20^h35^m07.39^s$	$60°07'22.0''$	23.32±0.04					22.55±0.14			c
70	$20^h35^m08.55^s$	$60°07'43.9''$	23.59±0.04								c
71	$20^h35^m10.76^s$	$60°11'22.7''$	21.66±0.04	22.14±0.06	0.47±0.07	5.84±0.90	22.00±0.04	21.80±0.14		21.92±0.05	abcd
72	$20^h35^m11.08^s$	$60°11'11.5''$									c
73	$20^h35^m11.80^s$	$60°10'55.6''$	20.92±0.03	21.02±0.04	0.10±0.05	2.42±1.18	20.83±0.02	19.96±0.13	18.74±0.06	19.85±0.02	bd
74	$20^h35^m12.90^s$	$60°09'05.5''$	22.28±0.04	22.49±0.07	0.21±0.08	1.64±0.62	22.21±0.05	21.96±0.14			be
75	$20^h35^m15.02^s$	$60°10'52.1''$							20.01±0.07		be
76	$20^h35^m16.15^s$	$60°10'56.4''$	23.33±0.06								c
77	$20^h35^m16.38^s$	$60°10'53.7''$	23.45±0.04								c
78	$20^h35^m17.07^s$	$60°10'14.0''$	23.32±0.05					22.95±0.14	20.11±0.04		be
79	$20^h35^m17.69^s$	$60°10'54.3''$	21.24±0.04	21.45±0.06	0.21±0.07	2.98±1.01	21.31±0.04	20.82±0.14		20.67±0.06	abcd
80	$20^h35^m18.58^s$	$60°10'41.5''$	23.77±0.04					22.98±0.14	20.33±0.06		c
81	$20^h35^m19.50^s$	$60°10'34.5''$	23.54±0.06								bcd
82	$20^h35^m19.83^s$	$60°10'43.2''$	23.39±0.04								bcd
83	$20^h35^m20.31^s$	$60°09'48.7''$	23.32±0.06					22.41±0.14	19.11±0.07		be
84	$20^h35^m20.44^s$	$60°09'36.3''$	21.82±0.05	22.04±0.07	0.22±0.09	2.14±0.83	21.88±0.05	21.45±0.14		21.37±0.06	ac
85	$20^h35^m22.45^s$	$60°10'46.2''$	23.98±0.04								bcd
86	$20^h35^m24.68^s$	$60°10'01.9''$	20.73±0.07	21.06±0.08	0.33±0.11	3.30±1.05	20.79±0.06				abd
87	$20^h35^m24.92^s$	$60°09'52.4''$	22.85±0.05				22.67±0.09				c
88	$20^h35^m25.43^s$	$60°09'45.5''$	21.70±0.03	22.09±0.04	0.39±0.05	6.65±0.90	21.90±0.03	21.52±0.13		21.65±0.04	abcd
89	$20^h35^m25.97^s$	$60°09'55.7''$	22.05±0.04	22.50±0.06	0.45±0.07	5.14±0.81	22.15±0.05	21.64±0.14		21.67±0.06	ac
90	$20^h35^m25.98^s$	$60°09'53.2''$	23.03±0.04								c
91	$20^h35^m27.04^s$	$60°09'49.4''$	23.44±0.03								c
92	$20^h35^m28.11^s$	$60°12'01.1''$	23.53±0.03								c

A.6 Equations for the WR binary model

Equations used to calculate M_{HeIIC} and the WR binary model fit in Figures. 6.14 and 6.15 from Chapter 6. First, the combined continuum apparent magnitude was calculated using the standard equation

$$m_{cont} = -2.5log_{10}\left(\frac{100}{D^2}\left(10^{-\frac{M_{WC}}{2.5}} + 10^{-\frac{M_O}{2.5}}\right)\right) + A_v \tag{A.1}$$

where m_{cont} is the continnum apparent magnitude, M_{WC} and M_O are the WC and O star absolute continuum magnitudes, D is the distance to the binary in pc and A_v is the extinction in magnitudes. The equation for specific extinction in the He IIC band from Tehrani et al. (2017) was used to calculate A_v. This was then used to calculate the combined absolute magnitude of the continuum of the binary spectrum

$$M_{cont} = m_{cont} - 5log_{10}\left(\frac{D}{10}\right) - A_v \tag{A.2}$$

where M_{cont} is the continuum absolute magnitude. The absolute magnitude of the WC emission line could also be calculated

$$M_{line} = M_{WC} - M_{excess} \tag{A.3}$$

where M_{line} is the line absolute magnitude and M_{excess} is the WC emission line excess above the continuum. Finally, equations A.2 and A.3 can be combined to find the apparent magnitude of the WC emission line in the binary, m_{line}

$$m_{line} = -2.5log_{10}\left(\frac{100}{D^2}\left(10^{-\frac{M_{line}}{2.5}} + 10^{-\frac{M_{cont}}{2.5}}\right)\right) + A_v \tag{A.4}$$

Both m_{cont} and m_{line} can be combined to calculate the line excess in the binary

$$\Delta He_{IIC} - He_{II} = m_{cont} - m_{line} \tag{A.5}$$

A.7 Metallicities of H II and nebular regions in NGC6946 with spectra

Table A.9: Information on H II and nebular regions with spectra from Chapter 6. (1) Spectrum catalogue number from this work, (2) Catalogue numbers from Hodge & Kennicutt (1983), (3,4) RA and DEC of the slit, (5) Radius (r/r_{25}) from the galactic centre, (6) c(Hβ) used to calculate E(B−V), (7) Metallicity calculated with the N2 calibration, (8) Metallicity calculated with the O3N2 calibration, (9) Multi Object Spectroscopy mask containing the spectrum observation, (10) Metallicity calibration (N2 or O3N2) used to determine the metallicity gradient and central metallicity.

H II region ID	Hodge region	RA (spectrum slit)	DEC (spectrum slit)	Radius (r/r_{25})	c(Hβ)	log(O/H)+12$_{N2}$	log(O/H)+12$_{O3N2}$	Mask	Metallicity calibration
1	324	$20^h34^m50.83^s$	60°07′46.1″	0.29	0.47 ± 0.05	8.65±0.41		1	N2
2	492	$20^h34^m32.98^s$	60°08′02.9″	0.48		8.52±0.41		1	N2
3	481	$20^h34^m33.95^s$	60°08′20.9″	0.44	0.64 ± 0.17	8.59±0.41		1	N2
4	536	$20^h34^m19.91^s$	60°09′00.9″	0.73	1.32 ± 0.10	8.50±0.29	8.51±0.18	average 1 and 2	O3N2
5	501	$20^h34^m31.24^s$	60°10′23.9″	0.56	1.07 ± 0.04	8.59±0.41	8.71±0.25	1	O3N2
6	265	$20^h34^m53.26^s$	60°10′52.4″	0.32	0.69 ± 0.04	8.64±0.41		1	N2
7	516	$20^h34^m27.37^s$	60°07′30.8″	0.63	0.73±0.11 *larger	8.63±0.29		averaged 1 and 2	N2
8		$20^h34^m21.55^s$	60°08′08.8″	0.71	0.37±0.10	8.55±0.41	8.62±0.25	1	O3N2
9	538	$20^h34^m19.26^s$	60°10′04.4″	0.79	0.84±0.07	8.54±0.41	8.48±0.25	1	O3N2
10	509	$20^h34^m30.33^s$	60°07′18.7″	0.59		8.61±0.41		2	N2
11		$20^h34^m27.72^s$	60°07′46.1″	0.60	0.61	8.65±0.41	8.47±0.25	2	O3N2
12	230	$20^h34^m55.75^s$	60°08′08.6″	0.23	0.08	8.67±0.41	8.82±0.25	2	O3N2
13	416	$20^h34^m43.01^s$	60°08′33.5″	0.24	0.39	8.72±0.41		2	N2
14	530	$20^h34^m23.64^s$	60°08′45.6″	0.65	0.20	8.65±0.41		2	N2
15	476	$20^h34^m34.87^s$	60°08′52.3″	0.40		8.64±0.41		2	N2
16		$20^h34^m29.58^s$	60°09′36.3″	0.53	0.59	8.62±0.41	8.72±0.25	2	O3N2
17	351	$20^h34^m48.06^s$	60°10′41.7″	0.31	0.26	8.57±0.41	8.69±0.25	2	O3N2

H II region ID	Hodge region	RA (spectrum slit)	DEC (spectrum slit)	Radius (r/r_{25})	c(Hβ)	log(O/H)+12$_{N2}$	log(O/H)+12$_{O3N2}$	Mask	Metallicity calibration
18	493	$20^h34^m32.67^s$	60°10′13.2″	0.51	1.16	8.57±0.29	8.58±0.18	averaged 2 and 3	O3N2
19	256	$20^h34^m53.47^s$	60°10′30.6″	0.25	0.57	8.56±0.41		2	N2
20		$20^h34^m33.10^s$	60°11′10.9″	0.61	0.57	8.61±0.41	8.68±0.25	2	O3N2
21		$20^h34^m24.98^s$	60°09′46.8″	0.64	0.70	8.52±0.41		2	N2
22	449	$20^h34^m37.65^s$	60°09′21.2″	0.34	0.17	8.56±0.41		2	N2
23	537/8	$20^h34^m19.75^s$	60°10′06.7″	0.78	0.30	8.44±0.410	8.63±0.25	2	O3N2
24	325	$20^h34^m49.70^s$	60°10′24.7″	0.25	0.39	8.59±0.41		2	
25	352	$20^h34^m47.97^s$	60°10′57.8″	0.36				2	N2
26		$20^h34^m33.05^s$	60°07′18.6″	0.55	0.37	8.52±0.41		3	N2
27		$20^h34^m35.05^s$	60°07′26.8″	0.50	0.49	8.62±0.41		3	N2
28	251	$20^h34^m54.81^s$	60°07′37.5″	0.33	1.15	8.64±0.41	8.58±0.25	3	O3N2
29	535	$20^h34^m20.54^s$	60°10′03.0″	0.76	0.30	8.54±0.41	8.62±0.25	3	O3N2
30		$20^h34^m23.97^s$	60°11′17.6″	0.80	0.26	8.57±0.41		3	N2
31		$20^h34^m49.20^s$	60°10′31.9″	0.27	0.85	8.68±0.41	8.60±0.25	3	O3N2
32	488	$20^h34^m33.13^s$	60°10′20.4″	0.51	0.50	8.37±0.41		3	N2
33		$20^h34^m23.16^s$	60°08′19.2″	0.67	0.35			3	
34	375	$20^h34^m46.75^s$	60°06′50.1″	0.47	0.67	8.64±0.41	8.57±0.25	3	O3N2
35	412	$20^h34^m43.88^s$	60°07′53.8″	0.31	0.76	8.62±0.41		3	N2
36		$20^h34^m20.76^s$	60°09′01.8″	0.71	0.60	8.46±0.41	8.46±0.26	3	O3N2
37		$20^h34^m30.96^s$	60°09′23.7″	0.49		8.65±0.41		3	N2
38	476	$20^h34^m34.75^s$	60°08′48.4″	0.40	0.20	8.59±0.41		3	N2
39	358	$20^h34^m47.42^s$	60°11′41.1″	0.50	0.48	8.67±0.41		3	N2
40	535	$20^h34^m20.54^s$	60°10′03.0″	0.76	0.54	8.51±0.41	8.64±0.26	3	O3N2
41		$20^h34^m37.43^s$	60°11′34.1″	0.60	0.48	8.66±0.41	8.63±0.25	3	O3N2
42	95	$20^h35^m09.01^s$	60°09′32.0″	0.37	0.69	8.62±0.41	8.82±0.25	4	O3N2
43	27	$20^h35^m17.69^s$	60°10′54.3″	0.62	0.32	8.51±0.41		4	N2

H II region ID	Hodge region	RA (spectrum slit)	DEC (spectrum slit)	Radius (r/r_{25})	c(Hβ)	log(O/H)+12$_{N2}$	log(O/H)+12$_{O3N2}$	Mask	Metallicity calibration
44	29	$20^h35^m16.77^s$	60°11′00.2″	0.61	0.45	8.46±0.41	8.46±0.25	4	O3N2
45		$20^h35^m01.76^s$	60°09′04.8″	0.21		8.59±0.41		4	N2
46	205	$20^h34^m58.18^s$	60°08′31.3″	0.20	0.83	8.56±0.41		4	N2
47	374	$20^h34^m46.21^s$	60°10′46.1″	0.35	0.60	8.63±0.41		4	N2
48	226	$20^h34^m55.62^s$	60°10′53.6″	0.33		8.69±0.41		4	N2
49		$20^h34^m53.59^s$	60°12′46.7″	0.69		8.30±0.41		4	N2
50	256	$20^h34^m53.56^s$	60°10′30.5″	0.25		8.49±0.41		4	N2
51		$20^h35^m25.43^s$	60°09′45.5″	0.73	2.39	8.48±0.41	8.43±0.27	4	O3N2
52	3	$20^h35^m24.68^s$	60°10′01.9″	0.72	0.43	8.49±0.41	8.50±0.25	4	O3N2
53	17	$20^h35^m20.55^s$	60°09′36.7″	0.62	0.86	8.57±0.42		4	N2
54		$20^h35^m11.60^s$	60°09′03.0″	0.43	0.82	8.62±0.41		4	N2
55	74	$20^h35^m10.76^s$	60°11′22.7″	0.55				4	N2
56	109	$20^h35^m07.27^s$	60°11′13.7″	0.48		8.51±0.41	8.58±0.25	4	O3N2
57	4	$20^h35^m23.86^s$	60°09′49.8″	0.70	0.87	8.36±0.42	8.42±0.26	5	O3N2
58		$20^h35^m17.07^s$	60°10′14.0″	0.56	0.39	8.67±0.41	8.81±0.25	5	O3N2
59	65	$20^h35^m12.18^s$	60°08′55.8″	0.45	1.15	8.60±0.41	8.86±0.26	5	O3N2
60	129	$20^h35^m04.35^s$	60°10′49.3″	0.39	0.51	8.60±0.41		5	N2
61	120	$20^h35^m05.69^s$	60°11′09.9″	0.45		8.57±0.42		5	N2
62	277	$20^h34^m52.88^s$	60°09′30.7″	0.06	1.04	8.74±0.41	8.87±0.25	5	O3N2
63	338	$20^h34^m49.25^s$	60°10′09.2″	0.21	0.22	8.59±0.41	8.71±0.25	5	O3N2
64	347	$20^h34^m48.26^s$	60°10′38.5″	0.31		8.63±0.41		5	N2
65	358	$20^h34^m47.47^s$	60°11′40.8″	0.51	0.97	8.51±0.41	8.60±0.25	5	O3N2
66		$20^h35^m24.13^s$	60°08′36.9″	0.73	1.16	8.58±0.41	8.66±0.25	5	O3N2
67	3	$20^h35^m25.10^s$	60°10′03.6″	0.73		8.90±0.41	8.65±0.25	5	O3N2
68		$20^h35^m19.97^s$	60°09′41.3″	0.61		8.69±0.41		5	N2
69		$20^h35^m08.58^s$	60°09′42.9″	0.36	0.79	8.63±0.41	8.78±0.26	5	O3N2

H II region ID	Hodge region	RA (spectrum slit)	DEC (spectrum slit)	Radius (r/r_{25})	c(Hβ)	log(O/H)+12$_{N2}$	log(O/H)+12$_{O3N2}$	Mask	Metallicity calibration
70	62	$20^h35^m11.86^s$	$60°10'22.6''$	0.47	1.03	8.59±0.29	8.69±0.18	averaged 5 and 6	O3N2
71	108	$20^h35^m07.41^s$	$60°09'32.5''$	0.33	0.38	8.62±0.41		5	N2
72		$20^h34^m57.68^s$	$60°08'35.0''$	0.18	0.67	8.69±0.41	8.79±0.26	5	O3N2
73		$20^h34^m53.45^s$	$60°10'34.7''$	0.27		8.77±0.41		5	N2
74	219	$20^h34^m56.20^s$	$60°10'55.4''$	0.33	0.41	8.68±0.41		5	N2
75	19	$20^h35^m20.31^s$	$60°09'48.7''$	0.62	0.54	8.59±0.41	8.50±0.25	6	O3N2
76	40	$20^h35^m15.02^s$	$60°10'52.1''$	0.57	0.77	8.56±0.41	8.55±0.25	6	O3N2
77		$20^h35^m19.63^s$	$60°10'48.2''$	0.65	1.13	8.45±0.41	8.41±0.25	6	O3N2
78	26	$20^h35^m18.19^s$	$60°09'07.1''$	0.58	1.36	8.60±0.41	8.67±0.25	6	O3N2
79		$20^h35^m03.64^s$	$60°09'24.4''$	0.25		8.55±0.41		6	N2
80		$20^h35^m03.42^s$	$60°08'01.6''$	0.36		8.62±0.41		6	N2
81	127	$20^h35^m04.34^s$	$60°11'12.7''$	0.45	0.55	8.75±0.41		6	N2
82		$20^h34^m49.37^s$	$60°10'02.7''$	0.18		8.53±0.41		6	N2
83		$20^h34^m53.68^s$	$60°10'24.9''$	0.23		8.54±0.41		6	N2
84		$20^h34^m50.81^s$	$60°10'21.2''$	0.23	0.64	8.71±0.41	8.75±0.25	6	O3N2
85	265	$20^h34^m53.07^s$	$60°10'53.2''$	0.33	0.37	8.60±0.41		6	N2
86	416	$20^h34^m42.99^s$	$60°08'33.1''$	0.24	0.86	8.68±0.41	8.83±0.25	6	O3N2
87	109	$20^h35^m07.09^s$	$60°11'15.4''$	0.48	0.97	8.29±0.42	8.37±0.26	6	O3N2
88		$20^h35^m15.96^s$	$60°10'02.7''$	0.53		8.66±0.41		6	N2
89		$20^h35^m10.62^s$	$60°11'11.9''$	0.53	0.33	8.55±0.41	8.60±0.25	6	O3N2
90		$20^h35^m02.78^s$	$60°09'23.7''$	0.23		8.37±0.42		6	N2
91	309	$20^h34^m50.58^s$	$60°12'40.3''$	0.68	0.10	8.62±0.41	8.68±0.25	6	O3N2